Fakultät für Maschinenwesen

Lehrstuhl für Flugsystemdynamik

Adaptive Flight Control for Fault Tolerance

Dipl.-Ing. (Univ.) Fabian Hellmundt

Vollständiger Abdruck der von der Fakultät für Maschinenwesen
der Technischen Universität München
zur Erlangung des akademischen Grades eines

Doktor-Ingenieurs (Dr.-Ing.)

genehmigten Dissertation.

Vorsitzender:	apl. Prof. Dr.-Ing. habil. Christian Breitsamter
Prüfer der Dissertation:	1. Prof. Dr.-Ing. Florian Holzapfel
	2. Prof. Dr.-Ing. Dieter Moormann, RWTH Aachen

Die Dissertation wurde am 10.04.2017 bei der Technischen Universität München eingereicht und durch die Fakultät für Maschinenwesen am 21.10.2017 angenommen.

Fabian Hellmundt
Aschheimer Str. 24
85774 Unterföhring

fabian@hellmundt.de

Composed in LaTeX

Für Katrin und Anton

Abstract

In this PhD thesis, adaptive control methods are investigated in terms of application in aircraft Flight Control Systems (FCS). Adaptive control is a promising approach in order to increase robustness of the closed-loop containing aircraft and FCS against uncertainties, which could also be caused by faults.
More specifically, the focus of the work at hand lies on the application of L1 Adaptive Control with piecewise constant update laws. Compared to most other adaptive control approaches, L1 Adaptive Control with piecewise constant update laws offers a significant advantage, because its application results in a linear control law. This could be beneficial with regard to potential FCS certification.
For this reason, L1 Adaptive Control with piecewise constant update laws is utilized to design adaptive augmentations on the one hand, which enhance a Differential PI (DPI) baseline controller, and an adaptive standalone controller on the other hand. Delays, actuator model and filter dynamics are directly taken into account right from the beginning of the controller design process. Thereby, a hedging strategy is proposed, which restores the robust stability properties phase and gain margin to the level of a baseline-controller-only configuration. This is a major advantage, because adaptive augmentations usually decrease robust stability of the closed-loop drastically. In order to apply the hedging strategy, measurement of the actuator deflection is required. Moreover, two different augmentation architectures are presented and compared in detail.
The adaptive standalone controller uses a novel combination of L1 Adaptive Control with piecewise constant update laws and Eigenstructure Assignment, which is contributed by this thesis. L1 Adaptive Control with Eigenstructure Assignment enables to design a standalone adaptive controller and at the same time offers the possibility to precisely adjust plant dynamics according to requirements by means of exact pole placement. Thereby, delays, actuator model and filter dynamics can also be directly incorporated into the design process.
Performance and robust stability assessments of the proposed controllers are carried out in combination with a longitudinal, nonlinear F-16 aircraft model. In order to investigate the impact of reality effects on the controller performance, the analyses also include more realistic sensor models, discrete-time controller implementation with limited sampling time, filters and atmospheric disturbances, i.e. turbulence and gust. For this, the individual effects are also applied considering parameter variations.

Zusammenfassung

In dieser Doktorarbeit werden adaptive Regelungsmethoden im Bezug auf ihre Anwendbarkeit in Flugregelungssystemen untersucht. Adaptive Regelung ist ein vielversprechender Ansatz um die Robustheit des geschlossenen Regelkreises, der Flugzeug und Flugregelungssystem enthält, gegen Unsicherheiten zu erhöhen, deren Ursache ebenso Defekte sein können.
Der Fokus dieser Arbeit liegt insbesondere in der Anwendung der L1 adaptiven Regelung mit stückweise konstanten Aktualisierungsgesetzen. Im Vergleich zu den meisten anderen adaptiven Regelungsverfahren bietet die L1 adaptive Regelung mit stückweise konstanten Aktualisierungsgesetzen einen signifikaten Vorteil, da ihre Anwendung in einem linearen Regelgesetz mündet. Dies könnte sich im Bezug auf eine mögliche Flugreglerzertifizierung als günstig erweisen.
Aus diesem Grund wird die L1 adaptive Regelung mit stückweise konstanten Aktualisierungsgesetzen auf der einen Seite verwendet, um adaptive Augmentierungen zu entwerfen, die einen differenzierenden PI Basisregler erweitern, auf der anderen Seite wird hiermit ein eigenständiger adaptiver Regler gestaltet. Verzögerungen, ein Aktuatormodell und Filterdynamiken werden im Entwurfsprozess des Reglers von Anfang an mit einbezogen. Dabei wird eine Hedging Strategie vorgeschlagen, mit deren Hilfe die Robustheitseigenschaften Phasenrand und Amplitudenreserve auf das Level einer Basisreglerkonfiguration angehoben werden können. Dies ist ein großer Vorteil, da adaptive Augmentierungen üblicherweise die Robustheitseigenschaften des geschlossenen Regelkreises drastisch reduzieren. Um die Hedging Strategie anzuwenden, wird die Messung des Aktuatorausschlages benötigt. Darüber hinaus werden zwei unterschiedliche Architekturen zur Augmentierung präsentiert und detailliert verglichen.
Der eigenständige adaptive Regler nutzt eine neuartige Kombination aus L1 adaptiver Regelung mit stückweise konstanten Aktualisierungsgesetzen und Eigenstrukturvorgabe, welche durch diese Arbeit beigesteuert wird. L1 adaptive Regelung mit Eigenstrukturvorgabe ermöglicht es, einen eigenständigen adaptiven Regler zu entwerfen und bietet gleichzeitig die Möglichkeit, die Streckendynamik mit Hilfe von genauer Polvorgabe präzise anzupassen. Dabei können Verzögerungen, ein Aktuatormodell und Filterdynamiken direkt in den Entwurfsprozess eingebunden werden.
Untersuchungen bezüglich Performanz und Robustheitseigenschaften der vorgeschlagenen Regelungsentwürfe werden in Kombination mit einem nichtlinearen Längsbewegungsmodell eines F-16 Flugzeugs durchgeführt. Um in der Lage zu sein, den Einfluss

von Realitätseffekten auf die Performanz der Regler untersuchen zu können, enthalten die Analysen ebenso realistischere Sensormodelle, zeitdiskrete Reglerimplementierungen mit begrenzter Taktzeit, Filter und atmosphärische Störungen (Turbulenz und Windböen). Hierfür werden die einzelnen Effekte auch unter Berücksichtigung von Parametervariationen angewendet.

Acknowledgment

Although this thesis is written in English, I decided to formulate the acknowledgement in German, because this is the language I used to communicate with most of the people mentioned in this section and I want to thank them in my mother tongue. So here we go...
Zuerst möchte ich mich besonders bei meinem Doktorvater Prof. Dr.-Ing. Florian Holzapfel für die viele Zeit und Unterstützung bedanken, die in diese Doktorarbeit geflossen sind. Bedanken möchte ich mich auch bei Prof. Dr.-Ing. Dieter Moormann (Rheinisch-Westfälische Technische Hochschule Aachen) für die Zweitprüfung dieser Arbeit und apl. Prof. Dr.-Ing. habil. Christian Breitsamter für die Übernahme des Prüfungsvorsitzes.
Ich möchte auch Dr.-Ing. Rudolf Maier und Dr.-Ing. Andreas Wildschek meinen großen Dank aussprechen, die es mir ermöglicht haben, meine Doktorarbeit bei Airbus Group Innovations (vorher EADS Innovation Works) in meinem Wunschthema anzufertigen und gleichzeitig die Betreuung meiner Arbeit von Industrieseite übernommen haben. Ebenso möchte ich mich bei Johannes Beck und Robert Osterhuber bedanken, die das Projekt von Seiten Airbus Defence and Space, ehemals Cassidian, unterstützt haben.
Dankeschön auch für die vielen interessanten Diskussionen an meine Mitstreiter vom Lehrstuhl für Flugsystemdynamik, insbesondere Dr.-Ing. Matthias Heller für die vielen spannenden Anregungen zum Thema Robustheit. Vielen Dank an Florian Peter und Dr.-Ing. Thomas Bierling, ebenfalls vom Lehrstuhl für Flugsystemdynamik, die meine letzte Semester- bzw. meine Diplomarbeit während des Studiums betreut haben und so maßgeblich dazu beigetragen haben, dass ich letztendlich meinen Forschungsschwerpunkt in der Flugregelung gesetzt habe.
Ebenso gilt mein Dank meinen Teamkollegen bei Airbus Group Innovations, namentlich Simon Binder, Mikael Bottemanne, Dr.-Ing. Johannes Kirn, Peter Langenbacher, Dr.-Ing. Michael Meyer, Philipp Schlösser, Manfred Schneider, Dr.-Ing. Klaus Seywald und Stefan Storm. Auch meinen langjährigen Bürokollegen Dr.-Ing. Alexander Kolb möchte ich hier natürlich nicht unerwähnt lassen, der mir stets und geduldig ein Ohr lieh, wenn der Regler mal wieder nicht so tat, wie er sollte.
Besonderer Dank geht an Prof. M.Eng. Jianping Li, Dr. Sanchito Banerjee und Miguel Leitão für das finale Durchsehen dieser Arbeit und die vielen, wertvollen Verbesserungsvorschläge.
Natürlich möchte ich mich ebenso bei meinen Studenten bedanken, die durch ihr Engagement auch ihren Teil zum Gelingen dieser Arbeit beigetragen haben. Hier-

bei möchte ich besonders Jens Dodenhöft für seine hervorragende Semesterarbeit hervorheben.
Meinen Eltern Barbara und Jörg möchte ich besonderen Dank aussprechen, die in meiner Kindheit und Jugend so manchen Grundstein setzten, der diese Arbeit erst ermöglicht hat. Bedanken möchte ich mich auch bei meinen Schwiegereltern Christine und Hans-Georg, die uns vor allem durch häufiges und spontanes Einspringen bei der Betreuung unseres Sohnes Anton geholfen haben, um Zeit für meine Dissertation freizuschaufeln. Zu guter Letzt möchte ich meine Frau Katrin erwähnen, die mir trotz ihres eigenen Maschinenbaustudiums stets und bedingungslos den Rücken freigehalten hat und ohne die ein Gelingen dieser Arbeit nicht möglich gewesen wäre. Ich danke Dir herzlich hierfür!

Unterföhring, im Dezember 2017

Fabian Hellmundt

Contents

Acronyms

Notation	Description	Page
ADC	Analogue-to-Digital converter	36
ADS	Air Data System	IX
BIBO	Bounded-Input-Bounded-Output	46
CAS	Control Augmentation System	1
CG	Center of Gravity	X
DPI	Differential PI	G
ESO	Extended State Observer	5
FCS	Flight Control Systems	G
FIR	Finite Impulse Response	67
GM	Gain Margin	116
IRAC	Integrated Resilient Aircaft Control	4
LEF	Leading Edge Flap	VIII
LSB	Least Significant Bit	37
MAC	Mean Aerodynamic Chord	VII
MAV	Micro Aerial Vehicle	4
MIMO	Multiple Input Multiple Output	1
MISO	Multiple Input Single Output	1
MLESO	Modified Linear Extended State Observer	5
MRAC	Model Reference Adaptive Control	3
MSL	Mean Sea Level	XI
NED	North East Down	IX

Notation	Description	Page
RMS	Root Mean Square	XVIII
SAS	Stability Augmentation System	1
SD	Standard Deviation	34
SIMO	Single Input Multiple Output	1
SISO	Single Input Single Output	1
TDM	Time Delay Margin	117
TUM-FSD	TUM Institute of Flight System Dynamics	11
UAV	Unmanned Aerial Vehicle	4
zoh	Zero-Order-Hold	36

Latin Symbols

Notation	Description	Page
$\boldsymbol{A}_{cl}$	Closed-loop system matrix sort	102
$\boldsymbol{A}$	System matrix	23
$\boldsymbol{A}_m$	Model system matrix	46
$\boldsymbol{A}_{m,K}$	Modified model system matrix	81
$\boldsymbol{A}_{m\star}$	Model system matrix, whose dynamics are modifified according to desired eigenvalues	83
a_x	Acceleration in x-direction	17
a_y	Acceleration in y-direction	17
a_z	Acceleration in z-direction	17
$\boldsymbol{B}$	Input matrix	23
b	Wingspan	14
b	Bias	34
$\boldsymbol{B_m}$	Model input matrix	46
$\boldsymbol{b}_m$	Model input vector	74
$\boldsymbol{B}$	Input matrix considering matched and unmatched inputs	100
$\boldsymbol{B}_{um}$	Auxiliary matrix for handling of unmatched uncertainties	46
$\boldsymbol{b}_{um}$	Auxiliary vector for handling of unmatched uncertainties	85
$\boldsymbol{C}$	Output matrix	23
CAP	Control Anticipation Parameter	60
$\bar{c}$	Length of Mean Aerodynamic Chord (MAC)	14
C_i	Transfer function of L1 low-pass filter	51
C_l	Dimensionless aerodynamic moment around x-axis	14
$\boldsymbol{C}_m$	Model output matrix	46
$\boldsymbol{c}_m$	Model output vector	83
C_m	Dimensionless aerodynamic moment around y-axis	14
$C_{m,0}$	Dimensionless aerodynamic zero moment around y-axis	15
$\Delta C_{m,0}$	Multiplicative uncertainty applied to the dimensionless aerodynamic zero moment around y-axis	206

Notation	Description	Page
$C_{m,\Delta}$	Dimensionless additional aerodynamic moment around y-axis	15
$\mathbb{C}_m$	Matrix containing lowpass filters corresponding to matched uncertainties	51
C_m	Lowpass filter corresponding to matched uncertainty	83
$C_{m,LEF}$	Dimensionless aerodynamic moment caused by Leading Edge Flap (LEF) around y-axis	15
$C_{m,q}$	Dimensionless aerodynamic damping coefficient around y-axis	15
$\Delta C_{m,q}$	Multiplicative uncertainty applied to the dimensionless aerodynamic damping coefficient with regard to moment around y-axis	206
$C_{m,q,LEF}$	Dimensionless aerodynamic damping coefficient caused by LEF around y-axis	15
C_n	Dimensionless aerodynamic moment around z-axis	14
$C_\star$	Common dimensionless coefficient	14
$C_{\star,0}$	Common dimensionless zero coefficient	15
$C_{\star,LEF}$	Common dimensionless coefficient caused by LEF	15
$C_{\star,q}$	Common dimensionless damping coefficient	15
$\mathbb{C}_{um}$	Matrix containing lowpass filters corresponding to unmatched uncertainties	51
C_{um}	Lowpass filters corresponding to unmatched uncertainty	83
C_X	Dimensionless aerodynamic force in x-direction	14
$C_{X,0}$	Dimensionless aerodynamic zero force in x-direction	14
$\Delta C_{X,0}$	Multiplicative uncertainty applied to the dimensionless aerodynamic zero force in x-direction	206
$C_{X,LEF}$	Dimensionless aerodynamic force caused by LEF in x-direction	14
$C_{X,q}$	Dimensionless aerodynamic damping coefficient for x-axis	14
$\Delta C_{X,q}$	Multiplicative uncertainty applied to the dimensionless aerodynamic damping coefficient for x-axis	206
$C_{X,q,LEF}$	Dimensionless aerodynamic damping coefficient caused by LEF for x-axis	14
C_Y	Dimensionless aerodynamic force in y-direction	14
C_Z	Dimensionless aerodynamic force in z-direction	14
$C_{Z,0}$	Dimensionless aerodynamic zero force in z-direction	14
$\Delta C_{Z,0}$	Multiplicative uncertainty applied to the dimensionless aerodynamic zero force in z-direction	206
$C_{Z,LEF}$	Dimensionless aerodynamic force caused by LEF in z-direction	14
$C_{Z,q}$	Dimensionless aerodynamic damping coefficient for z-axis	14

Notation	Description	Page
$\Delta C_{Z,q}$	Multiplicative uncertainty applied to the dimensionless aerodynamic damping coefficient for z-axis	206
$C_{Z,q,LEF}$	Dimensionless aerodynamic damping coefficient caused by LEF for z-axis	14
$\boldsymbol{D}$	Feedthrough Matrix	23
d_{gust}	Gust length	30
e_I	Integrated error	59
$\left(\boldsymbol{F}^G\right)_B$	Force given in bodyfixed frame	15
F_0^G	Gravitational force given in North East Down (NED) frame	14
f_s	Sample rate of control law computation	67
$f_{s,sensor}$	Sensor sample rate	34
g	Gravitational acceleration	14
$G_{aa}(s)$	Transfer function of anti aliasing filter	36
$\hat{G}_A$	Estimated transfer function of actuator	60
$\tilde{G}_A$	Error between estimated and real transfer function of actuator	79
G_A	Transfer function of actuator	76
$G_{ADS,lag}(s)$	Transfer function of Air Data System (ADS) lag	36
$G_{d,dt}$	Transfer function representing differentiation	57
$\hat{G}_{D,c}$	Transfer function of estimated delay according to Pade approximation	60
$\tilde{G}_{D,c}$	Error between estimated and real transfer function of delay according to Pade approximation	79
$G_{D,c}$	Transfer function of delay according to Pade approximation	76
G_{FIR}	Finite Impulse Response filter used for upsampling	69
$G_{F,u}$	Transfer function of filter applied to controller output	60
$G_{F,y}$	Transfer function of filter applied to controller inputs	60
$G_{F,y,lp}$	Low pass filter used within $G_{F,y}(s)$	66
G_I	Transfer function of integral portion used for Differential PI control law	59
$G_{\int}$	Transfer function of integrator used for Differential PI controller	57
$G_{f,notch}$	Transfer function of notch filter	66
$G_s(s)$	Transfer function of simple structural mode model	39
h	Altitude	13

Notation	Description	Page
h_{DPI}	Feedforward gain used for the DPI baseline controller	57
H_G	Geopotential height	26
h_{L1}	Feedforward gain used for standalone L1 adaptive controller	103
h_P	Feedforward Gain used for the reference model of the standalone L1 adaptive controller	97
$\boldsymbol{I}$	Identity matrix	25
$\boldsymbol{I}^G$	Inertia tensor	16
k_α	Gain of α feedback	57
$\bar{\boldsymbol{K}}$	Gain matrix used within state predictor of L1 adaptive controller	100
$\bar{\boldsymbol{k}}_m$	Gain matrix used within state predictor of L1 adaptive controller for matched feedback	98
$\bar{\boldsymbol{k}}_{um}$	Gain matrix used within state predictor of of L1 adaptive controller for unmatched feedback	98
$\boldsymbol{k_{DPI}}$	Feedback gain vector of DPI controller	63
$\boldsymbol{K_e}$	Additional error feedback matrix	76
$\boldsymbol{K}$	Feedback gain matrix	42
k_I	Gain of error integration	59
$\boldsymbol{K_{L1}}$	Adaptation gain	49
$\bar{\boldsymbol{k}}_{L1}$	Feedback gains for design model of standalone L1 adaptive controller with Eigenstructure Assignment	107
$\boldsymbol{K}_{L1\star}$	Adaptation gain for L1 Adaptive Control with Eigenstructure Assignment	103
$\boldsymbol{K}_{L1,m\star}$	Adaptation gain for L1 Adaptive Control with Eigenstructure Assignment corresponding to matched uncertainties	103
$\boldsymbol{K}_{L1,um\star}$	Adaptation gain for L1 Adaptive Control with Eigenstructure Assignment corresponding to unmatched uncertainties	103
$\boldsymbol{k}_P$	Feeback gains used for the reference model of the standalone L1 adaptive controller	97
k_q	Gain of q feedback	57
L	Open-Loop transfer function	113
L_A^G	Aerodynamic moment at Center of Gravity (CG) around x-axis given in body-fixed frame	13
L_T^G	Total moment at CG around x-axis given in body-fixed frame	13
$\left(\boldsymbol{M}^G\right)$	Moment at CG given in body-fixed frame	15

Notation	Description	Page
m	Mass	14
m	Scale factor	34
m	Number of system inputs	42
$\boldsymbol{M}_{0B}$	Transformation matrix from bodyfixed to NED frame	20
$\boldsymbol{M}_{B0}$	Transformation matrix from NED to bodyfixed frame	14
M_A^G	Aerodynamic moment at CG around y-axis given in body-fixed frame	13
Ma	Mach number	2
$\boldsymbol{M}_{\bar{K}B}$	Transformation matrix from bodyfixed to kinematic frame	17
$M_{\mathcal{L}_2}$	Performance metric based on $\mathcal{L}_2$ norm	119
$M_{\mathcal{L}_{2,act}}$	Performance metric based on $\mathcal{L}_2$ norm assessing actuator activity	119
$M_{\mathcal{L}_{2,act,rel}}$	Relative change of $\mathcal{L}_2$ norm w.r.t. baseline controller	224
$M_{\mathcal{L}_{2,rel}}$	Relative change of $\mathcal{L}_2$ norm w.r.t. baseline controller	224
$M_{\mathcal{L}_\infty}$	Performance metric based on $\mathcal{L}_\infty$ norm	119
$M_{\mathcal{L}_{\infty,rel}}$	Relative change of $\mathcal{L}_\infty$ norm w.r.t. baseline controller	224
M_T^G	Total moment at CG around y-axis given in body-fixed frame	13
n	Number of system states	42
$N(0,1)$	Normally distributed white noise between 0 and 1	30
N_A^G	Aerodynamic moment at CG around z-axis given in body-fixed frame	13
$\bar{\boldsymbol{N}}$	Null space matrix used for Eigenstructure Assignment	43
$\bar{\boldsymbol{n}}$	Column vectors of null space matrix used for Eigenstructure Assignment	43
$\boldsymbol{N}$	Auxiliary matrix used for Eigenstructure Assignment	43
$\boldsymbol{n}$	Auxiliary vector used for Eigenstructure Assignment	43
$\hat{\boldsymbol{N}}$	Auxiliary matrix used for Eigenstructure Assignment	43
$\hat{\boldsymbol{n}}$	Auxiliary vector used for Eigenstructure Assignment	43
N_T^G	Total moment at CG around z-axis given in body-fixed frame	13
n_{Tr}	Polytropic index for troposphere	26
n_z	Load factor	2
p	Roll rate	16
p	Atmospheric pressure	26
p_s	Reference atmospheric pressure at Mean Sea Level (MSL)	26
$\boldsymbol{P}$	Sorting matrix used for Eigenstructure Assignment	43
q	Pitch rate	X

Notation	Description	Page
$\bar{q}$	Dynamic pressure	2
$\dot{q}$	Pitch acceleration	34
$\Delta\dot{q}$	Deviation between measured and estimated pitch acceleration	91
$\hat{\dot{q}}$	Estimation of pitch acceleration	56
q	Quaternion	20
q_{ref}	Pitch rate of reference model	74
$\boldsymbol{Q}$	Weighting matrix used for Eigenstructure Assignment	44
R	Universal gas constant	26
r	Yaw rate	16
r	Number of system outputs	42
r_E	Earth radius	26
$(\boldsymbol{r})^{GP}$	Position of point P relative to point G	16
S	Wing reference area	14
s	Number of specified eigenvector values	43
T	Temperature	27
T_D	Time delay	66
$T_{D,c}$	Computational (enhanced simulation model) or accumulated (simple simulation model) time delay	32
$T_{D,\alpha}$	Additional delay applied to angle of attack measurement	94
$T_{D,\eta}$	Additional delay applied to elevator deflection measurement	94
$T_{D,FIR}$	Equivalent delay induced by upsampling filter	69
$T_{D,q}$	Additional delay applied to pitch rate measurement	94
$T_{D,\dot{q}}$	Additional delay applied to pitch acceleration measurement	94
T_s	Sample time of control law computation	48
T_s	Reference termperature at MSL	26
$T_{s,sensor}$	Sensor sample time	34
u	Velocity in x-direction given in body-fixed frame	16
$\left(u_W^G\right)_0^0$	Wind velocity at CG relative to the NED frame in x-direction given in the NED frame frame	27
$\left(u_A^G\right)_B^0$	Aerodynamic velocity at CG relative to the NED frame in x-direction given in bodyfixed frame	27
$\left(u_K^G\right)_B^0$	Kinematic velocity at CG relative to the NED frame in x-direction given in bodyfixed frame	16

Notation	Description	Page
$\left(\dot{u}_K^G\right)_B^{0B}$	Kinematic velocity at CG relative to the NED frame in x-direction given in bodyfixed frame derivated w.r.t. the bodyfixed frame	16
u_{ad}	Control signal generated by adaptive controller	70
$u_{ad,1}$	Control signal generated by adaptive augmentation belonging to matched uncertainty	76
$u_{ad,2}$	Control signal generated by adaptive augmentation belonging to matched uncertainty	76
u_{bl}	Control signal generated by baseline controller	70
$\dot{u}_{bl}$	Derivative of control signal generated by baseline controller	78
$\boldsymbol{u}_c$	Feedforward command	42
$u_{cmd,\Delta\dot{q}}$	Control signal generated by $\Delta\dot{q}$ Compensation Law	91
Δu	Hedging signal	76
V	Velocity	14
v	Velocity in y-direction given in body-fixed frame	16
V	Voltage	35
$\boldsymbol{v}$	Eigenvector	42
v	Measurement noise	34
$\left(\boldsymbol{V}_K^G\right)_B^0$	Kinematic velocity at CG relative to the NED frame given in bodyfixed frame	16
$\left(v_K^G\right)_B^0$	Kinematic velocity at CG relative to the NED frame in y-direction given in bodyfixed frame	16
$\left(\dot{\boldsymbol{V}}_K^G\right)_B^{0B}$	Kinematic velocity at CG relative to the NED frame given in bodyfixed frame derivated w.r.t. the bodyfixed frame	16
$\left(\dot{v}_K^G\right)_B^{0B}$	Kinematic velocity at CG relative to the NED frame in y-direction given in bodyfixed frame derivated w.r.t. the bodyfixed frame	16
v_{gust}	Gust velocity	30
w	Velocity in z-direction given in body-fixed frame	16
$\left(w_W^G\right)_0^0$	Wind velocity at CG relative to the NED frame in z-direction given in the NED frame frame	27
$\left(w_A^G\right)_B^0$	Aerodynamic velocity at CG relative to the NED frame in z-direction given in bodyfixed frame	27
$\left(w_K^G\right)_B^0$	Kinematic velocity at CG relative to the NED frame in z-direction given in bodyfixed frame	16

Notation	Description	Page
$\left(\dot{w}_K^G\right)_B^{0B}$	Kinematic velocity at CG relative to the NED frame in z-direction given in bodyfixed frame derivated w.r.t. the bodyfixed frame	16
x	Position relative to reference point in x-direction given in NED-frame	16
$\left(X_A^G\right)_B$	Aerodynamic force at CG in x-direction given in body-fixed frame	13
$x_{CG_{ref},CG}$	Distance between reference CG, at which the aerodynamic moment coefficients are referenced to, and the actual aircraft CG in x-direction in the body-fixed frame	15
$\left(X_G^G\right)_B$	Gravitational force at CG in x-direction given in body-fixed frame	13
x_{gust}	Horizontal position of aircraft within gust (bodyfixed frame)	30
$\hat{\boldsymbol{x}}$	Estimated system state	47
$\left(X_T^G\right)_B$	Total force at CG given in x-direction given in body-fixed frame	13
$\left(X_P^G\right)_B$	Thrust force at CG in x-direction given in body-fixed frame	13
$\tilde{\boldsymbol{x}}$	Estimation error	47
$\left(X_T^G\right)_{\bar{K}}$	Total force at CG given in x-direction given in kinematic frame	17
y	Position relative to reference point in y-direction given in NED-frame	16
$\left(Y_A^G\right)_B$	Aerodynamic force at CG in y-direction given in body-fixed frame	13
$\left(Y_G^G\right)_B$	Gravitational force at CG in y-direction given in body-fixed frame	13
$y_{meas,A}$	Measured, analogue plant output	34
$y_{meas,D}$	Measured, digital plant output	36
y_s	Plant output after processing by structural mode	34
$\left(Y_T^G\right)_B$	Total force at CG given in y-direction given in body-fixed frame	13
$\left(Y_T^G\right)_{\bar{K}}$	Total force at CG given in y-direction given in kinematic frame	17
$\left(Z_A^G\right)_B$	Aerodynamic force at CG in z-direction given in body-fixed frame	13
$\boldsymbol{z}$	Auxiliary vector used for the derivation of Eigenstructure Assignment	42

Notation	Description	Page
$\left(Z_G^G\right)_B$	Gravitational force at CG in z-direction given in body-fixed frame	13
$\left(Z_T^G\right)_B$	Total force at CG given in z-direction given in body-fixed frame	13
$\left(Z_T^G\right)_{\bar{K}}$	Total force at CG given in z-direction given in kinematic frame	17

Greek Symbols

Notation	Description	Page
α	Angle of attack	X
α_0	Angle of attack, which trims the aircraft	56
α_{cmd}	Commanded angle of attack	55
α_{ref}	Angle of attack of reference model	74
β	Side slip angle	16
Δ	Auxiliary transfer function used during derivation of L1 Adaptive Control with Eigenstructure Assignment	105
δ	Dirac impulse	89
$\Delta_{A,D,c}$	Auxiliary transfer function used during derivation of L1 adaptive controller error dynamics	79
$\Delta\alpha$	Difference between commanded and measured α	59
δ_{LEF}	Deflection of LEF	31
$\Delta\omega_{0,act}$	Additive uncertainty applied to natural frequency of actuator dynamics	306
$\delta_{s,lon}$	Longitudinal stick input	56
δ_T	Thrust lever position	13
$\delta_{T,cmd}$	Commanded thrust lever position	32
$\Delta\zeta_{act}$	Additive uncertainty applied to relative damping of actuator dynamics	306
η	Elevator deflection	14
η_0	Elevator trim deflection	65
η_{cmd}	Commanded elevator deflection	1
$\eta_{dead-band}$	Dead-band setting for elevator backlash	33
$\dot{\eta}$	Elevator deflection rate	32
$\dot{\eta}_{cmd}$	Commanded elevator deflection rate	118
η_{meas}	Measured elevator deflection	78
γ	Flight path angle	20

Notation	Description	Page
κ	Isentropic exponent	27
Λ	Control efficiency matrix	46
λ	Eigenvalue	42
Λ_0	Estimated control efficiency matrix	76
λ_I	Eigenvalue corresponding to integrator pole	63
$\lambda_{SP,1}$	First eigenvalue corresponding to short period	63
$\lambda_{SP,2}$	Second eigenvalue corresponding to short period	63
$\boldsymbol{l}$	Parameter vector used for Eigenstructure Assignment	43
L_u	Scale length w.r.t. x-axis for dryden turbulence model	29
L_w	Scale length w.r.t. z-axis for dryden turbulence model	29
Ω	Spatial frequency	28
ω	Frequency	28
ω_0	Natural frequency	36
$\omega_{0,aa}$	Bandwidth of anti aliasing filter	36
$\omega_{0,act}$	Natural frequency of actuator dynamics	31
$\omega_{0,ADS}$	Natural frequency of air data system lag dynamics	36
$\omega_{0,C,m}$	Frequency of low-pass filter for matched uncertainty	84
$\omega_{0,C,um}$	Frequency of low-pass filter for unmatched uncertainty	84
$\omega_{0,F,y,lp,1}$	Natural frequency of low pass filter	66
$\omega_{0,F,y,lp,2}$	Natural frequency of low pass filter	66
$\omega_{0,f,notch}$	Natural frequency of notch filter	66
$\omega_{0,ph}$	Natural frequency of phugoid	26
$\omega_{0,s}$	Natural frequency of structural mode	39
$\omega_{0,sp}$	Natural frequency of short-period	26
$\omega_{0,sp,des}$	Natural frequency of short-period to be established by the controller	62
$\omega_{0,thr}$	Natural frequency of thrust dynamics	32
$\omega_{wb,1}$	Natural frequency of first wing bending mode	116
$\left(\boldsymbol{\omega}^{E0}\right)$	Rotation of NED system relative to the earth-fixed frame	16
ω_{gc}	Gain crossover frequency	66
$\omega_{gc,\Phi}$	Gain crossover frequency, where phase margin is determined	124
$\omega_{gc,TDM}$	Gain crossover frequency, where time delay margin is determined	124
$\left(\boldsymbol{\omega}^{IE}\right)$	Rotation of earth-fixed frame relative to the inertial frame	16
$\left(\boldsymbol{\omega}_K^{OB}\right)_B$	Kinematic rotation of bodyfixed frame relative to NED frame given in bodyfixed frame	16

Notation	Description	Page
$\left(\dot{\omega}_K^{OB}\right)^B$	Kinematic rotation of bodyfixed frame relative to NED frame given in bodyfixed frame derivated w.r.t. the bodyfixed frame	18
Φ	Roll angle	14
Φ	Axiliary matrix used for derivation of L1 Adaptive Control with Eigenstructure Assignment	106
Φ_m	Phase margin	116
Φ	Phase	66
Φ_{q_W}	Dryden spectrum w.r.t. pitch rotation	28
Φ_{u_W}	Dryden spectrum w.r.t. x-axis	28
Φ_{w_W}	Dryden spectrum w.r.t. z-axis	28
Ψ	Yaw angle	14
ρ_s	Reference air density at MSL	27
ρ	Air density	14
$\hat{\sigma}$	Estimated uncertainty	154
$\hat{\sigma}_{m\star}$	Estimated matched uncertainty used to derive L1 Adaptive Control with Eigenstructure Assignment	98
σ_{noise}	Standard deviation of sensor noise	34
$\sigma_{noise,\alpha}$	Standard deviation of sensor noise with regard to angle of attack measurement	276
$\sigma_{noise,\eta}$	Standard deviation of sensor noise with regard to elevator deflection measurement	276
$\sigma_{noise,q}$	Standard deviation of sensor noise with regard to pitch rate measurement	276
σ_u	Root Mean Square (RMS) intensity w.r.t. x-axis for dryden turbulence model	29
$\hat{\sigma}_{um\star}$	Estimated unmatched uncertainty used to derive L1 Adaptive Control with Eigenstructure Assignment	98
σ_w	RMS intensity w.r.t. z-axis for dryden turbulence model	29
Θ	Pitch angle	14
ζ	Relative damping	427
$\zeta_{f,notch,1}$	Relative damping of Notch filter (numerator)	66
ζ_s	Relative damping of structural mode	39
$\zeta_{f,notch,2}$	Relative damping of Notch filter (denumerator)	66
ζ_{act}	Relative damping of actuator dynamics	31
ζ_{ADS}	Relative damping of ADS lag dynamics	36

Notation	Description	Page
$\zeta_{F,y,lp,1}$	Relative damping of 2nd order low pass filter	66
ζ_{ph}	Relative damping of phugoid	26
ζ_{sp}	Relative damping of short-period	26
$\zeta_{sp,des}$	Relative damping of short-period to be established by the controller	60
ζ_{thr}	Relative damping of thrust dynamics	32

1. Introduction

Controllers have for a long time become an integral part of our daily routine. We face them for example while heating our homes, driving our cars, sometimes even while operating a coffee machine. Whenever a physical state of a system is measured in order to determine a suitable actuation command affecting this system, a feedback controller is involved in the process. Controllers can be used, when a physical state should be driven to a desired value and the system should exhibit a particular dynamical behavior during the transient.

Mainly, there are two classes of controllers, which are Single Input Single Output (SISO) [75] and Multiple Input Multiple Output (MIMO) [76] controllers. These can of course also be mixed and result in Single Input Multiple Output (SIMO) and Multiple Input Single Output (MISO) designs, respectively. It is then often distinguished between state-feedback and output-feedback control design approaches. For the latter it is taken into account that certain system states cannot be measured and thus, cannot be used for controller computations. In fact, every real world system contains immeasureable states and would therefore require the application of output-feedback control methods.

The mathematical tools needed to successfully design such controllers are delivered by control theory. In particular, aviation applications played a key role in the progress of control theory, which emerged around the beginning of the 20th century. One of the first applications of control theory within aircraft was the design of pitch dampers [1, p. 305]. Pitch dampers compensate insufficient natural damping of the short-period eigenmode in high altitudes, in order to increase robustness w.r.t turbulence and improve controllability of the aircraft for the pilot. This is achieved by measuring pitch rate q and multiplication of q by an appropriate controller gain k_q, which then yields an elevator deflection η_{cmd} to be provided by the actuator additional to the pilot command. The resulting control law is

$$\eta_{cmd}(t) = k_q \cdot q(t). \tag{1.1}$$

It has to be noted that first implementations of such systems relied on fully mechanical design without digitally computing parts [1, pp. 101-104].

In general, such a pitch damper belongs to the class of Stability Augmentation System (SAS). SASs are applied, whenever eigenmotions of the aircraft exhibit insufficient damping or their natural frequency needs to be adapted [122, pp. 287-303]. Moreover, Control Augmentation System (CAS) addionally offer tracking of selected system states

[122, pp. 303-322]. That means for example the pilot is directly able to command desired angle of attack α, load factor n_z or pitch rate q. These commands are translated to suitable actuator commands by the controller leading to precise tracking of the desired state. This is especially important for fighter aircraft [97, 94] [16, pp. 837-847], which can even inherit unstable dynamics to be stabilized by means of a controller, but is nowadays also quite common for FCS of large transport aircraft [16, pp. 849-865] [50, 125]. These systems can be implemented easiest on FCS based on fly-by-wire. Fly-by-wire means there exists no direct mechanical link between manual flight controls operated by the pilot and the aircraft actuators. Instead, the FCS calculates commands based on the manual flight controls input and sends them digitally to the aircraft actuators [83, pp. 365 ff.]. Autopilots can be designed as an additional cascade around the CAS. Here, for example a pitch rate command CAS can be used as an inner-loop controller, which realizes q_{cmd} demanded by an altitude hold autopilot [122, pp. 303-322].

One challenge in controller design is to select an appropriate architecture, as shown in Eq. (1.1) for the simple pitch damper example. The other challenge is to systematically calculate the associated gains e.g. k_q such that the system dynamics are adjusted according to the desired dynamics. Classical control theory approaches [75, 76] require a precise model of the actual system dynamics, in order to generate controllers, which accurately set up desired dynamics and good command tracking. On the other side, dynamics of a real world system can never be predicted 100% exactly by means of a system model. Thus, the system to be controlled consists of a known part, which can be modeled and uncertainties, which are unknown even considering nominal conditions[1].

If the amount of uncertainties is too high, even a properly designed controller can at worst destabilize the system. In order to provide robustness against destabilization, a controller design is often required to offer certain phase and gain margins [75, pp. 445-448]. Phase and gain margin can be determined by means of analyzing the closed-loop system in the frequency domain [75, pp. 423 ff.]. It is important to note that assessments based on these robust stability properties are also the foundation of aircraft FCS certification w.r.t. robust stability of the control law [111, pp. 25-27].

Known changes of the aircraft dynamics in relation of its flight envelope can be taken into account using gain scheduling during controller design process. In that matter, controller gain computation is processed using many different aircraft models each representing one single point within the flight envelope. These points can be characterized using e.g. Mach number Ma and dynamic pressure $\bar{q}$. Thus, the resulting gains are scheduled and applied suitable to the current envelope point during flight e.g. $k_q\left(Ma, \bar{q}\right)$ for the pitch damper example shown in Eq. (1.1).

Although a certain amount of uncertainties can be handled by classical controllers, these designs often reach their limits, when uncertainties are caused by faults. One

[1] System dynamics behave as expected, no faults occurred

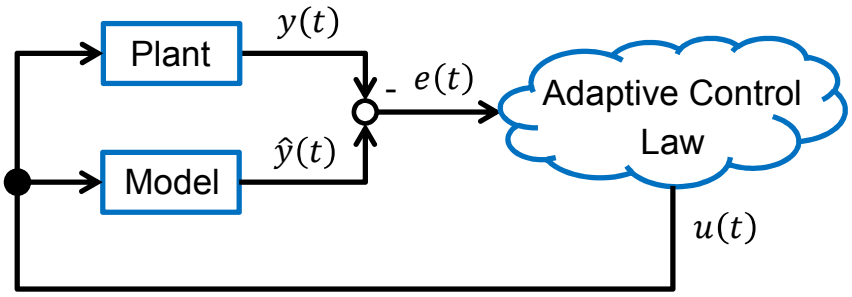

Figure 1.1. – Principle sketch of a closed-loop with adaptive controller

example could be change of aerodynamic properties and/or CG location due to structural disintegration of or cargo dislocation inside the aircraft. In order to increase the span of tolerable uncertainties, adaptive controllers can be used. As most adaptive control approaches are based on reference models of the dynamics to be controlled, these controllers often work according to the principle sketch shown in Fig. 1.1. Plant outputs $y(t)$ are measured and compared to estimated outputs $\hat{y}(t)$ here, which stem from a reference model containing the nominal, desired dynamics of the plant. The adaptive control law uses the resulting error between measurement and estimation $e(t) = \hat{y}(t) - y(t)$ to calculate a suitable control command, in order to shape the plant dynamics according to the reference dynamics. In this way, the controller can react to both expected uncertainties e.g. caused by variance of system dynamics in dependence of the current flight envelope point and unexpected uncertainties e.g. caused by system faults.
It is important to note, that if it is decided to use adaptive controllers, they do not necessarily need to fully replace the controller designed according to classical control methods (baseline controller). The adaptive controller can rather assist the baseline controller using augmentation approaches or can be used as a backup control law, which is activated, if faults are detected. Most of the controller designs presented in this thesis are adaptive augmentations.

1.1. State of the art

One of the most prominent approaches in adaptive control theory is Model Reference Adaptive Control (MRAC) [89, 88, 90]. MRAC directly emerged as an evolution of the *M.I.T rule* [96], which can be considered as one of the origins of adaptive control. The application of MRAC results in a nonlinear controller design, which is quite common for adaptive control approaches. An overview on existing modifications and enhancements of MRAC in a uniform nomenclature can be found in [13].
A well-known problem of classical MRAC is that it produces control signals with comprehensive high-frequency content, whose amount is directly dependent on the choice of adaptation rate. The higher the adaptation rate is chosen, the more amplification

is put on the high-frequency content. Robust stability properties of the closed loop are often decreased drastically due to this high-frequency control signal. Thus, the following can be stated: In order to achieve good robustness against uncertainties within the plant i.e. by setting high adaptation rates, highly reduced robust stability properties have to be accepted.

L1 Adaptive Control has its roots in predictor-based MRAC. It introduces low-pass filtering as an additional key feature, which is applied to the control signal generated by the adaptive controller. Thereby, high frequency content stemming from the adaptation process is prevented from entering the plant or at least damped to a level, at which it is not harmful anymore. Thus, estimation loop and control loop can be decoupled to a certain degree, which allows application of fast adaptation [59] and keeping robust stability properties on an acceptable level at the same time. Moreover, the approach offers guaranteed transient performance through its architecture, as stated in [140].

Furthermore, with the choice of piecewise constant parameter update laws first introduced in [138], the tuning effort can be reduced drastically. This is, because adaptation gains of the piecewise constant parameter update laws are calculated according to a fixed formula using reference system knowledge i.e. matrices of the state-space system and sampling time of the control law computation. As a beneficial side effect, the adaptation process does then not rely on persistency of excitation and the design results in a linear control law [12]. Especially linearity is an advantage w.r.t. certification for aircraft application according to [111], because necessary robustness assessments are based on linear methods, as it is stated above. The rate of adaptation is theoretically only limited by the available CPU power i.e. the smallest available sample time of the embedded controller system. This correlation is also shown in detail in Section 3.2.

It is also worth noting, that the piecewise constant update law was favored over integration-based update laws for flight tests evaluations of the L1 Adaptive Control approach. The first was successful flight testing in the context of the Integrated Resilient Aircaft Control (IRAC) Project on the NASA AirSTAR, which is a turbine powered, subscaled model of a transport aircraft [42, 40, 41, 112, 58]. Only recently L1 Adaptive Control was applied to the manned Calspan's Variable-Stability Learjet of the Edwards Air Force Base in CA, USA, on which several artificial uncertainties were induced during the flight and also effectively tackled by the adaptive controller [2, 22].

Successful applications of L1 Adaptive Control mostly based on simulations can also be found for flight control laws of fighter aircraft [60, 103, 104, 87, 115, 43], large transport aircraft [12, 124, 27, 131], high agility Unmanned Aerial Vehicle (UAV) [99, 71, 136, 38, 119], Micro Aerial Vehicle (MAV) [21], helicopters [11], missiles [101, 130, 17, 31], hypersonic gliders [105, 6], business jets [123] and multicopter UAV [128, 129, 77]. Applications can also be found for gust load alleviation [19] and aerial refueling [136].

Further enhancements on the foundation of L1 Adaptive Control include modifications to achieve Output-Feedback control [65, 10, 20, 18, 17, 66, 64], incorporation of actuator

deflection saturation [72] and usage of nonlinear reference systems [133, 132, 77] amongst others.
An interesting alternative approach tailored to cope with a nonlinear pitch-up phenomenon is shown in [23, 98], where a reference model-based adaptive controller for long range civil aircraft is presented. This approach is well thought out and makes extensive use of aircraft dynamics knowledge rather than following complex control theory.
Also related to MRAC is Adaptive Backstepping [67], which is based on systematic, recursive construction of Lyapunov functions [117, pp. 40 ff.] in order to provide inherent nonlinear stability proof together with the nonlinear controller design. Furthermore, the extension Command Filtered Adaptive Backstepping [28, 36] can be used to reduce the complexity of the controller design process. Aeronautical applications of this approach can be found in [118, 95] for fighter aircraft models or [68, 100, 49] for missile models.
Only recently a notable approach named Modified Linear Extended State Observer (MLESO) Control [46] emerged. Its inherent Extended State Observer (ESO) estimates both system states and disturbances. Similar to L1 Adaptive Control with piecewise constant update laws, the application of MLESO Control also results in a linear control law, which is beneficial in terms of aircraft FCS certification. An application of this approach is shown in [25] and compared to a L1 adaptive controller with piecewise constant update laws. Simulation results show good comparability w.r.t. both performance considering uncertainties and robust stability properties.

1.2. Contributions

The focus of this thesis is to investigate adaptive control strategies with regard to implementation in aircraft FCS. It is not the goal to present a specific controller design suiting one specific aircraft. The dynamics model of a F-16 aircraft is rather utilized exemplarily, in order to demonstrate the principle and potential of the proposed controller designs.
These adaptive control strategies should increase the aircraft performance in case of uncertainties, which could have their origin in failures such as e.g. structural damage. As a result this thesis is focused on the application of L1 Adaptive Control with piecewise constant update laws [59], which is a good candidate in terms of certification for an industrial FCS, because it results in a linear control law. This feature is used for robust stability investigations according to certification specifications [111, pp. 25-27].
In order to increase relevance of the simulation assessments w.r.t. industrial applications further, actuator dynamics, filter dynamics and delays are taken into account throughout the complete controller design process. This also motivates the modeling and application of reality effects like sensor disturbances or discrete-time controller

implementations for the simulations. More specifically, the following points summarize the scientific contribution offered by this thesis:

- **L1 Adaptive Augmentation of DPI Controller [52, 53]**
  L1 Adaptive Control [59] is used to augment a DPI baseline controller in order to increase performance in case of uncertainties. Here, the structure of the DPI controller has to be considered also for the design of the adaptive controller w.r.t. differentiations, integrations as well as rate and deflection saturations. The resulting combination of DPI baseline controller and L1 Adaptive Control offers improved performance properties while being resistant against integrator wind-up caused by actuator saturation.

- **Comparison of different augmentation architectures [52]**
  The aforementioned adaptive augmentation of the DPI baseline controller is designed using two different augmentation strategies. The first one augments plant and baseline controller, which means that the complete baseline controller architecture has to be accounted for during the design of adaptive controller. This approach is often used in literature. For the second approach the open-loop plant is augmented by the adaptive controller first, which is then "augmented" by the baseline controller. It is the goal of this approach that the baseline controller controls a plant, which ideally always behaves like its design model, even in case of uncertainties. It can be shown that the presented augmentation strategies lead to almost identical results w.r.t. both performance and robust stability.

- **Compensation of robust stability degradation w.r.t. actuator cut (bottleneck) for L1 Adaptive Augmentations [52]**
  Although adaptive augmentations increase performance features of a closed-loop, they often degrade robust stability properties. This can also be observed for the L1 Adaptive Augmentations designed in this thesis. L1 Adaptive Control offers a tuning knob to balance this trade-off in terms of the low-pass filter introduced to the control law [59]. Nevertheless, degradation of robust stability properties is still drastic, if good performance in case of uncertainties were to be achieved (c.f. e.g. [71]). Thus, a modification of the state predictor is proposed, which uses actuator deflection measurement and is able to fully restore robust stability properties w.r.t. the actuator cut to the level of the baseline controller. This is especially beneficial, since verification of robust stability considering this cut, which is also called bottleneck, is the most relevant factor in terms of certification [111, p. 25].

- **Augmentation of DPI Controller using $\Delta\dot{q}$ Compensation Law**
  For the sake of comparison, an alternate augmentation is implemented for the DPI Controller, which estimates a deviation in terms of pitch acceleration $\Delta\dot{q}$ between real and design plant and calculates a suitable control command in order

to compensate for this deviation [23, 98]. Introduced as Reference model-based adaptive controller for long range civil aircraft by Delannoy et al. [23], this approach is called $\Delta\dot{q}$ Compensation Law in the course of this thesis.

- **Modification of L1 Adaptive Control approach to allow for adaptive standalone controller in connection with precise pole placement [51]**
  In the course of this thesis L1 Adaptive Control is also investigated for the design of a standalone controller. The standalone controller also needs to handle dynamics shaping in terms of pole placement in this case, in order to ensure excellent handling qualities, besides compensating for uncertainties. It has shown that according to the textbook architecture of L1 Adaptive Control [59] predictable and precise pole placement is not possible without an underlying baseline controller. Thus, a modification is proposed, which introduces feedback of estimated states to both matched and unmatched input of the state predictor. The combination of additional feedback and Eigenstructure Assignment allows for precise pole placement using only the adaptive standalone controller. This way, also actuator dynamics, filter dynamics and delays can be directly incorporated into the design process.

- **Development of enhancements for an aircraft dynamics model comprising reality effects [53]**
  One goal of this thesis is to evaluate the impact of reality effects on the performance of adaptive controllers. Thus, relevant reality effects have to be identified and modeled as addition to the aircraft dynamics model, in order to allow for simulation assessments. The considered reality effects include an actuator model with backlash and sensor models containing variable delay (jitter), measurement noise, sampling as well as anti-aliasing filters and quantization effects. Moreover, the influence of turbulence and gust are taken into account. The comprehensive description of these effects could also serve as a foundation for future investigations of control laws outside of the scope of the thesis at hand.

- **Evaluation of impact caused by reality effects on adaptive controllers [53]**
  The controllers designed in the course of this thesis are investigated in terms of their behavior in presence of reality effects. For this, discrete-time implementations of the control laws are used to incorporate the effect of limited controller sample time. Moreover, an enhanced aircraft model is used, in order to simulate relevant reality effects. The assessments are used to draw comparisons between the different control laws.

Some of the contents presented in this work are already covered in peer-reviewed publications, which were created by the author during the working process of this thesis. A list of these publications is given in the following:

- F. Hellmundt, J. Dodenhöft, and F. Holzapfel. "L1 Adaptive Control with Eigenstructure Assignment for Pole Placement considering Actuator Dynamics and Delays". In: *AIAA Scitech*. American Institute of Aeronautics and Astronautics, Jan. 2016 [51]

- F. Hellmundt, A. Wildschek, R. Maier, R. Osterhuber, and F. Holzapfel. "Comparison of L1 Adaptive Augmentation Strategies for a Differential PI Baseline Controller on a Longitudinal F16 Aircraft Model". In: *Advances in Aerospace Guidance, Navigation and Control*. Ed. by J. Bordeneuve-Guibé, A. Drouin, and C. Roos. Springer International Publishing, 2015, pp. 99–118 [52]

- F. Hellmundt, R. Maier, M. Leitao, C. Heise, and F. Holzapfel. "Performance Assessment of L1 Adaptive Augmentation Strategies for an Enhanced Longitudinal F16 Aircraft Model". In: *Proceedings of the 3rd CEAS EuroGNC, Specialist Conference on Guidance, Navigation & Control*. Toulouse, France, Apr. 2015 [53]

The approach shown in [51] is also described in the semester thesis [25], which was supervised by the author.

1.3. Outline

The longitudinal F-16 aircraft model used to assess the controllers designed in the course of this thesis is presented in Chapter 2. It comprises the steps of introducing its rigid-body dynamics and aerodynamics modeling. This formulation of the dynamics is used to deduce linearized models. Furthermore, reality effects in terms of atmosphere, actuator and sensor models are introduced.
Chapter 3 has its focus on providing theoretical background on control theory, which is necessary to understand the descriptions of the controller designs. It gives an overview on the algorithm of Eigenstructure Assignment, which is used to design controller gains for linear output-feedback in the context of this thesis. Next, the theory of L1 Adaptive Control with piecewise constant update laws is introduced. Here, the adaptation process is described in detail. The last part deals with discrete-time systems and transformations.
Baseline Controller and adaptive controller designs are presented in Chapter 4. At first, an adaptive augmentation is composed utilizing L1 Adaptive Control with piecewise constant update laws and using two different architectures. After that, the $\Delta\dot{q}$ Compensation Law is applied to design an adaptive augmentation. At last, a combination of L1 Adaptive Control and Eigenstructure Assignment is proposed, which offers exact pole placement and robustness against uncertainties at the same time.
Chapter 5 comprises extensive simulation assessments of the deduced controller designs in combination with the nonlinear F-16 aircraft model. The controllers are

analyzed both w.r.t. performance and robust stability. Here, performance is evaluated by means of step responses and one exemplary maneuver considering both nominal and off-nominal conditions of the aircraft. The performance assessments are carried out using both an aircraft model, which is simplified in terms of reality effects, and the same model, where the whole bandwidth of modeled reality effects is applied. Robust stability properties in terms of gain and phase margin are determined using linear methods. In order to further show validity of this method, results are also compared to time delay margin measurements, which are gained through nonlinear simulation of the closed-loop for one controller configuration.
At last, comparisons of the designs are compiled in Chapter 6 highlighting advantages and disadvantages of the individual approaches. Moreover, their sensitivity w.r.t. the individual simulated reality effects is investigated by means of parameter variations.
Conclusions of this thesis are presented in Chapter 7, where particularly the possibility of industrial applications of the proposed controller designs are weighed. Finally, Chapter 8 offers an outlook providing starting points for further research in the field of practical adaptive flight control.

2. Aircraft Model

Figure 2.1. – General Dynamics F-16 Fighting Falcon [135]

In order to assess the controllers, which are designed during the course of this thesis, a simulation model of nonlinear, rigid dynamics of a F-16 aircraft is used. Aerodynamic data and inertia properties are taken from [121], though the model was originally introduced in [91]. Using both references, the model was implemented by the TUM Institute of Flight System Dynamics (TUM-FSD) using MATLAB/Simulink. This thesis concentrates on assessing adaptive control laws in connection with longitudinal aircraft dynamics, thus the aircraft model is simplified in such a manner. Nevertheless, the control methods presented in the course of this thesis are not limited to the application on longitudinal aircraft dynamics, they could also be applied to lateral and directional aircraft dynamics, respectively, or any other use case apart from aerospace applications. For the simulation assessments, two different configurations of the aircraft model are used. The structure of the basic configuration is shown in Fig. 2.2. It contains models of the actuators and a delay besides the rigid-body dynamics of the aircraft, which are described in Section 2.1, and the control law. By means of the delay, which is induced upstream of the actuator, one crucial effect stemming from sensors, filters and computation is modeled. This is also described in detail in Section 2.6. Furthermore, Section 2.1 contains a description of the aerodynamics model and introduces

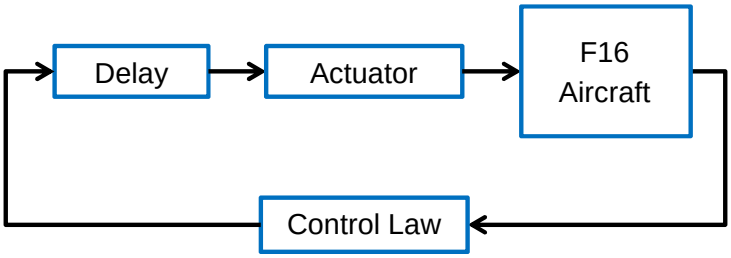

Figure 2.2. – Basic simulation model

linearizations of rigid-body dynamics and the accompanying trim solutions for steady, horizontal flight.
In addition to the configuration of the basic model, for the enhanced simulation model nonlinear backlash is added to the actuator model containing rate and deflection saturations shown in Section 2.5. Furthermore, a sophisticated sensor model comprising sampling, anti-aliasing, quantization, measurement noise, bias, scale-factor errors, variable delay (jitter) and additional lag for ADS measurements is developed in Section 2.6. Atmospheric disturbances are also be applied in terms of turbulence and gust, which are described in Section 2.3 and Section 2.4, respectively. At last, Section 2.7 introduces a very simple model of a structural mode, which serves as unknown, additional dynamics for the controller assessments. It has to be highlighted that this thesis does not aim on modeling all thinkable reality effects influencing an aircraft as precisely as possible. It is rather the goal to model reality effects, which are relevant for assessments of flight control laws, in a depth, that is necessary for such assessments.
Fig.
reality effects, additional signal processing up- and downstream of the control law is required. The description of these filters, which are denoted by Upsampling, Filters and Notch Filter in Fig. 2.3, is covered in Section 4.1.2. This chapter contributes a

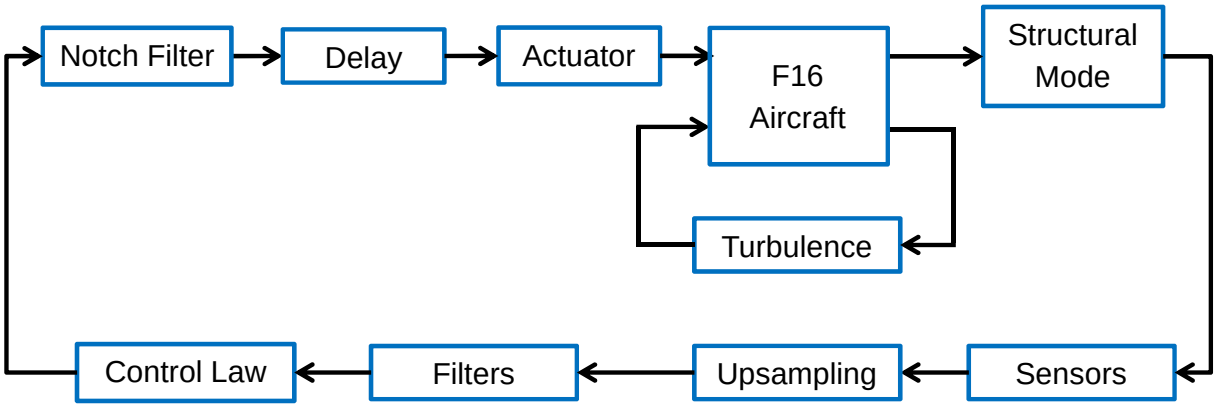

Figure 2.3. – Enhanced simulation model

summary of reality effect models, which are relevant for flight controller assessments, and could also serve as a foundation for further investigations in terms of novel flight control methods.

2.1. Rigid-Body Dynamics

This section contains the mathematical formulation to model the rigid-body dynamics of an aircraft. The equations are shown both for the common case, where the underlying basic structure is derived from [50], and for the condition, where only the longitudinal motion is considered. Detailed derivations containing all intermediate steps and describing all simplifications can be found in [16, 32, 121, 57] among others.

2.1.1. Forces and Moments

Firstly, the external forces and moments are described, which are considered as inputs to the aircraft dynamics. These are split up in contributions of aerodynamics (A), gravity (G) and propulsion (P). For the three body-fixed axes (B), the forces acting at the CG, which is marked by the index G, are summarized as

$$\left(X_T^G\right)_B = \left(X_A^G\right)_B + \left(X_G^G\right)_B + \left(X_P^G\right)_B (\delta_T, h, Ma) \tag{2.1a}$$

$$\left(Y_T^G\right)_B = \left(Y_A^G\right)_B + \left(Y_G^G\right)_B \tag{2.1b}$$

$$\left(Z_T^G\right)_B = \left(Z_A^G\right)_B + \left(Z_G^G\right)_B, \tag{2.1c}$$

and the moments about the body-fixed axes as

$$L_T^G = L_A^G \tag{2.2a}$$

$$M_T^G = M_A^G \tag{2.2b}$$

$$N_T^G = N_A^G. \tag{2.2c}$$

The thrust force $\left(X_P^G\right)_B$ is stored as a lookup-table and is a function of thrust-lever position δ_T, altitude h and Mach number Ma and is illustrated in Figs. A.14 to A.17. It is assumed that the engine only produces a force in body-fixed x-direction. Furthermore, gyroscopic moments stemming from rotating engine parts are not considered here.
The influence of gravity in the body-fixed frame $\left(X_G^G\right)_B$, $\left(Y_G^G\right)_B$ and $\left(Z_G^G\right)_B$ are obtained from the gravity force given in the NED-frame 0

$$\begin{pmatrix} \left(X_G^G\right)_B \\ \left(Y_G^G\right)_B \\ \left(Z_G^G\right)_B \end{pmatrix} = \boldsymbol{M}_{B0} \cdot \underbrace{\begin{pmatrix} 0 \\ 0 \\ m \cdot g \end{pmatrix}_0^G}_{=:F_0^G} \tag{2.3}$$

by means of the transformation matrix [32, p. 117]

$$\boldsymbol{M}_{B0} = \begin{pmatrix} \cos\Psi\cos\Theta & \sin\Psi\cos\Theta & -\sin\Theta \\ \cos\Psi\sin\Theta\sin\Phi - \sin\Psi\cos\Phi & \sin\Psi\sin\Theta\sin\Phi + \cos\Psi\cos\Phi & \cos\Theta\sin\Phi \\ \cos\Psi\sin\Theta\cos\Phi + \sin\Psi\sin\Phi & \sin\Psi\sin\Theta\cos\Phi - \cos\Psi\sin\Phi & \cos\Theta\cos\Phi \end{pmatrix} \tag{2.4}$$

and with the mass $m = 9298.6kg$ considered to be constant. The Euler angles Φ, Θ and Ψ are described in Section 2.1.2.

The aerodynamic forces and moments are calculated from dimensionless coefficients $C_\star$, dynamic pressure $\bar{q}$, wing reference area $S = 27.87m^2$, mean aerodynamic chord $\bar{c} = 3.45m$ and full span of the wing $b = 9.144m$ by means of the following equations:

$$\left(X_A^G\right)_B = \bar{q}S \cdot C_X \tag{2.5a}$$

$$\left(Y_A^G\right)_B = \bar{q}S \cdot C_Y \tag{2.5b}$$

$$\left(Z_A^G\right)_B = \bar{q}S \cdot C_Z \tag{2.5c}$$

$$L_A^G = \bar{q}Sb \cdot C_l \tag{2.5d}$$

$$M_A^G = \bar{q}S\bar{c} \cdot C_m \tag{2.5e}$$

$$N_A^G = \bar{q}Sb \cdot C_n \tag{2.5f}$$

where [122, p. 67]

$$\bar{q} = \frac{1}{2}\rho V_A^2 \tag{2.6}$$

with air density ρ and aerodynamic velocity V_A.

As the lateral motion is neglected for the aircraft model, only $\left(X_A^G\right)_B$, $\left(Z_A^G\right)_B$ and M_A^G are considered with the corresponding coefficients [91, pp. 37-38]

$$C_X = C_{X,0}\left(\alpha_A, \eta\right) + C_{X,LEF}\left(\alpha_A\right) + q \cdot \frac{\bar{c}}{2V_A} \cdot \left[C_{X,q}\left(\alpha_A\right) + C_{X,q,LEF}\left(\alpha_A\right)\right] \tag{2.7a}$$

$$C_Z = C_{Z,0}\left(\alpha_A, \eta\right) + C_{Z,LEF}\left(\alpha_A\right) + q \cdot \frac{\bar{c}}{2V_A} \cdot \left[C_{Z,q}\left(\alpha_A\right) + C_{Z,q,LEF}\left(\alpha_A\right)\right] \tag{2.7b}$$

$$C_m = C_{m,0}\left(\alpha_A, \eta\right) + C_{m,LEF}\left(\alpha_A\right) + q \cdot \frac{\bar{c}}{2V_A} \cdot \left[C_{m,q}\left(\alpha_A\right) + C_{m,q,LEF}\left(\alpha_A\right)\right] + C_Z \cdot x_{CG_{ref},CG} + C_{m,\Delta}\left(\alpha_A, \eta\right), \tag{2.7c}$$

where $x_{CG_{ref},CG}$ is the difference between the CG location, which is the reference for the tabulated aerodynamic moment coefficients, and the actual aircraft CG. The reference CG for the aircraft model lies at $0.35\bar{c}$ [91, p. 40]. For the assessments made in this thesis a forward lying CG of $0.3\bar{c}$ is chosen for the nominal aircraft configuration, in order to be able to investigate the effect of large, aft CG-shifts during flight, which even destabilize the aircraft. This means also that the nominal aircraft behavior is stable in the longitudinal motion for the considered envelope (c.f. Appendix A.3). Thus, for the nominal aircraft $x_{CG_{ref},CG} = 0.1725m$ is set and CG-shifts can be induced by rapid change of $x_{CG_{ref},CG}$.

$C_{\star,0}$ describe the zero forces and momentum containing the influence of the elevator η, $C_{\star,q}$ are damping coefficients, $C_{\star,LEF}$ contain the influence of the Leading Edge Flap (LEF) and $C_{m,\Delta}$ contributes with an additional correctional term as a function of angle of attack α_A and elevator deflection η, especially for high angle of attack. The aerodynamic coefficients used in Eq. (2.7) are stored in lookup-tables, whose values are illustrated in Figs. A.1 to A.13 in the appendix.

The aerodynamic data is valid for low speed up to $Ma \approx 0.6$, since no dependence on Mach number is considered for the aerodynamic coefficients. This correspondes e.g. to $V \approx 204\frac{m}{s}$ at mean sea level MSL or $V \approx 180\frac{m}{s}$ at $h = 10000m$. [91] states the valid range for angle of attack as $-20^\circ \leq \alpha \leq 90^\circ$, whereas [121] claims that only $-10^\circ \leq \alpha \leq 45^\circ$ should be used. That is because on the one hand it can be avoided to dynamically model the post-stall region, on the other hand the aircraft can barely reach angle of attack $\alpha \geq 25^\circ$ due to limitations of the control surfaces.

2.1.2. Equations of Motion

The current state of a rigid-body system model of an aircraft is described according to the state variables contained in Table 2.1. This section summarizes the differential equations in order to obtain the current system state in dependence of the external forces $\sum \left(\boldsymbol{F}^G\right)_B$ and moments $\sum \left(\boldsymbol{M}^G\right)$ stemming from aerodynamics, propulsion and gravity, which act on the aircraft with respect to the CG. In terms of the reference frames, which are required for the formulation of the dynamics, the nomenclature commonly used at TUM-FSD also applies to this work. This nomenclature is derived from the norm LN 9300 [24] and further descriptions can be found in [57, pp. 10-24], [45, pp. 269-273], [68, pp. 177-179] and [128, pp. 167-170].

	Symbol	Description
Translation	$\left(u_K^G\right)_B^E$ or V_K	velocity in x_B direction or absolute velocity
	$\left(v_K^G\right)_B^E$ or β_K	velocity in y_B direction or sideslip angle
	$\left(w_K^G\right)_B^E$ or α_K	velocity in z_B direction or angle of attack
Rotation	p_K	roll rate
	q_K	pitch rate
	r_K	yaw rate
Attitude	Φ	roll angle
	Θ	pitch angle
	Ψ	yaw angle
Position	x	position in x_E direction
	y	position in y_E direction
	h	altitude

Table 2.1. – Rigid-body states of an aircraft

Translation Applying Newton's second law yields the propagation equations for the translational motion [32, p. 149] [57, p. 71]

$$\left(\dot{\boldsymbol{V}}_K^G\right)_B^{0B} = \frac{\sum\left(\boldsymbol{F}^G\right)_B}{m} - \left(\boldsymbol{\omega}_K^{OB}\right)_B \times \left(\boldsymbol{V}_K^G\right)_B^0, \tag{2.8}$$

where the earth is considered as non-rotating ($\left(\boldsymbol{\omega}^{IE}\right) = \mathbf{0}$) and flat ($\left(\boldsymbol{\omega}^{E0}\right) = \mathbf{0}$), mass ($\frac{\mathrm{d}}{\mathrm{dt}}m \approx 0$) and mass distribution ($\frac{\mathrm{d}}{\mathrm{dt}}\boldsymbol{I}^G \approx \mathbf{0}$) are quasi-stationary and the aircraft is considered to be a rigid-body. This means that a vector from CG with the corresponding index G to any arbitrary point of the aircraft P can be assumed to be constant ($\frac{\mathrm{d}}{\mathrm{dt}}\left(\boldsymbol{r}\right)^{GP} = \mathbf{0}$). Eq. (2.8) serves as a differential equation describing the dynamics of $\left(\boldsymbol{V}_K^G\right)_B^0$, which is the kinematic velocity of the aircraft given in the body-fixed frame relative to the NED frame. Solving the cross product the single components can be written as [32, p. 149] [57, p. 70]

$$\left(\dot{u}_K^G\right)_B^{0B} = \frac{1}{m} \cdot \left(X_T^G\right)_B - \left(q_K \cdot \left(w_K^G\right)_B^0 - r_K \cdot \left(v_K^G\right)_B^0\right) \tag{2.9a}$$

$$\left(\dot{v}_K^G\right)_B^{0B} = \frac{1}{m} \cdot \left(Y_T^G\right)_B - \left(r_K \cdot \left(u_K^G\right)_B^0 - p_K \cdot \left(w_K^G\right)_B^0\right) \tag{2.9b}$$

$$\left(\dot{w}_K^G\right)_B^{0B} = \frac{1}{m} \cdot \left(Z_T^G\right)_B - \left(p_K \cdot \left(v_K^G\right)_B^0 - q_K \cdot \left(u_K^G\right)_B^0\right). \tag{2.9c}$$

Here the forces determined according to Eq. (2.1) serve as an input. The dynamics of the translational motion can be transformed to an alternative description using absolute velocity V_K, angle of attack α_K and sideslip angle β_K according to [32, pp. 149-150] [57, p. 73]

$$\dot{V}_K = \frac{\left(X_T^G\right)_{\bar{K}}}{m} \tag{2.10a}$$

$$\dot{\alpha}_K = \frac{\left(Z_T^G\right)_{\bar{K}}}{mV_K \cos\beta_K} + q_K - \tan\beta_K \cdot \left(p_K \cos\alpha_K + r_K \sin\alpha_K\right) \tag{2.10b}$$

$$\dot{\beta}_K = \frac{\left(Y_T^G\right)_{\bar{K}}}{mV_K} + p_K \sin\alpha_K - r_K \cos\alpha_K, \tag{2.10c}$$

by means of a notation in the kinematic frame ($\bar{K}$) and the definitions [32, p. 114] [57, p. 70]

$$V_K := \sqrt{\left(\left(u_K^G\right)_B^0\right)^2 + \left(\left(v_K^G\right)_B^0\right)^2 + \left(\left(w_K^G\right)_B^0\right)^2} \tag{2.11a}$$

$$\alpha_K := \arctan \frac{\left(w_K^G\right)_B^0}{\left(u_K^G\right)_B^0} \tag{2.11b}$$

$$\beta_K := \arctan \frac{\left(v_K^G\right)_B^0}{\sqrt{\left(\left(u_K^G\right)_B^0\right)^2 + \left(\left(w_K^G\right)_B^0\right)^2}}. \tag{2.11c}$$

Note that the description according to Eq. (2.10) also requires a transformation of the forces from body-fixed (B) to kinematic frame ($\bar{K}$) using the transformation matrix [32, p. 117] [57, p. 72]

$$\boldsymbol{M}_{\bar{K}B} = \begin{pmatrix} \cos\alpha_K \cdot \cos\beta_K & \sin\beta_K & \sin\alpha_K \cdot \cos\beta_K \\ -\cos\alpha_K \cdot \sin\beta_K & \sin\beta_K & -\sin\alpha_K \cdot \sin\beta_K \\ -\sin\alpha_K & 0 & \cos\alpha_K \end{pmatrix}. \tag{2.12}$$

Furthermore, the inertial accelerations acting at CG can be derived using Newton's second law once more in the inertial frame [32, p. 135]:

$$\left(\begin{pmatrix} a_x \\ a_y \\ a_z \end{pmatrix}_B^G\right)^{II} = \frac{1}{m} \begin{pmatrix} \left(X_T^G\right)_B \\ \left(Y_T^G\right)_B \\ \left(Z_T^G\right)_B \end{pmatrix}. \tag{2.13}$$

For the next step the lateral and directional dynamics are neglected, thus the following assumptions hold:

- $\left(\dot{v}_K^G\right)_B^{0B}$, which also corresponds to $\dot{\beta}_K = 0$
- $v_K = 0$, which also corresponds to $\beta_K = 0$
- $\dot{p}_K = 0$ and $\dot{r}_K = 0$
- $p_K = 0$ and $r_K = 0$
- $\dot{\Phi} = 0$ and $\dot{\Psi} = 0$
- $\Phi = 0$ and $\Psi = 0$

By means of these assumptions Eq. (2.10) can then be reduced to

$$\dot{V}_K = \frac{\left(X_T^G\right)_{\bar{K}}}{m} \tag{2.14a}$$

$$\dot{\alpha}_K = \frac{\left(Z_T^G\right)_{\bar{K}}}{mV_K \cos\beta_K} + q_K. \tag{2.14b}$$

Likewise, the accelerations according to Eq. (2.13) reduce to

$$\left(\begin{pmatrix} a_x \\ a_z \end{pmatrix}_B^G\right)^{II} = \frac{1}{m}\begin{pmatrix} \left(X_T^G\right)_B \\ \left(Z_T^G\right)_B \end{pmatrix}. \tag{2.15}$$

Rotation The rotational dynamics can be obtained from the law of conservation of angular momentum with respect to CG denoted with the index G and result in [32, p. 144] [57, p. 68]

$$\sum\left(\boldsymbol{M}^G\right) = \boldsymbol{I}^G \cdot \left(\dot{\boldsymbol{\omega}}_K^{OB}\right)^B + \left(\boldsymbol{\omega}_K^{OB}\right)_B \times \boldsymbol{I}^G \cdot \left(\boldsymbol{\omega}_K^{OB}\right)_B, \tag{2.16}$$

where the rigid-body condition, quasi-stationary mass ($\frac{\mathrm{d}}{\mathrm{dt}} m \approx 0$) and quasi-stationary mass distribution $\frac{\mathrm{d}}{\mathrm{dt}} \boldsymbol{I}^G \approx 0$ are assumed. Furthermore, the kinematic angular rates of body-fixed frame (B) relative to NED frame (0) are expressed as [57, p. 69]

$$\left(\boldsymbol{\omega}_K^{OB}\right)_B = \begin{pmatrix} p_K \\ q_K \\ r_K \end{pmatrix} \tag{2.17}$$

given in the body-fixed frame (B) and the inertia tensor is defined according to

$$\boldsymbol{I}^G = \begin{pmatrix} I_{xx} & -I_{xy} & -I_{xz} \\ -I_{yx} & I_{yy} & -I_{yz} \\ -I_{zx} & -I_{zy} & I_{zz} \end{pmatrix}. \tag{2.18}$$

with $I_{xx} = 12875\ kg\,m^2$, $I_{yy} = 75674\ kg\,m^2$, $I_{zz} = 85552\ kg\,m^2$, $I_{xz} = I_{zx} = 1331\ kg\,m^2$ and $I_{xy} = I_{yx} = I_{yz} = I_{zy} = 0\ kg\,m^2$ for the considered F-16 aircraft model.
Solving Eq. (2.16) with respect to the derivatives of the angular rates leads to [57, p. 116]

$$\begin{aligned}\dot{p}_K =& \frac{1}{I_{xx}I_{zz} - I_{xz}^2} \cdot \left[I_{zz} \cdot L_T^G + I_{xz} \cdot N_T^G \right] + \frac{1}{I_{xx}I_{zz} - I_{xz}^2} \\ & \cdot \left[I_{xz} \cdot \left(I_{xx} - I_{yy} + I_{zz} \right) \cdot p_K \cdot q_K - \left(I_{zz}^2 - I_{zz} \cdot I_{yy} + I_{xz}^2 \right) \cdot q_K \cdot r_K \right] \end{aligned} \tag{2.19a}$$

$$\dot{q}_K = \frac{1}{I_{yy}} \cdot M_T^G + \frac{1}{I_{yy}} \cdot \left[I_{xz} \cdot \left(r_K^2 - p_K^2 \right) - \left(I_{xx} - I_{zz} \right) \cdot p_K \cdot r_K \right] \tag{2.19b}$$

$$\begin{aligned}\dot{r}_K =& \frac{1}{I_{xx}I_{zz} - I_{xz}^2} \cdot \left[I_{xz} \cdot L_T^G + I_{xx} \cdot N_T^G \right] + \frac{1}{I_{xx}I_{zz} - I_{xz}^2} \\ & \cdot \left[\left(I_{xz}^2 - I_{xx} \cdot I_{yy} + I_{xx}^2 \right) \cdot p_K \cdot q_K - I_{xz} \cdot \left(I_{xx} - I_{yy} + I_{zz} \right) \cdot q_K \cdot r_K \right]. \end{aligned} \tag{2.19c}$$

For the rotational dynamics the moments according to Eq. (2.2) serve as inputs. Again, considering only the longitudinal motion with the assumptions given above, the dynamics reduce to

$$\dot{q}_K = \frac{1}{I_{yy}} \cdot M_T^G. \tag{2.20}$$

Attitude The angular rates effect a change of the aircraft attitude, which is described by the Euler angles Φ, Θ and Ψ. In general, the attitude is the rotation of the body-fixed frame relative to the NED frame. The relation is derived as [32, p. 126] [57, p. 75]

$$\begin{pmatrix} p_K \\ q_K \\ r_K \end{pmatrix} = \begin{pmatrix} 1 & 0 & -\sin\Theta \\ 0 & \cos\Phi & \sin\Phi\cos\Theta \\ 0 & -sin\Phi & \cos\Phi\cos\Theta \end{pmatrix} \cdot \begin{pmatrix} \dot{\Phi} \\ \dot{\Theta} \\ \dot{\Psi} \end{pmatrix}, \tag{2.21}$$

which can also be inverted, leading to the differential equation for the attitude angles [32, p. 126] [57, p. 76]

$$\begin{pmatrix} \dot{\Phi} \\ \dot{\Theta} \\ \dot{\Psi} \end{pmatrix} = \begin{pmatrix} 1 & \sin\Phi\tan\Theta & \cos\Phi\tan\Theta \\ 0 & \cos\Phi & -\sin\Phi \\ 0 & \frac{sin\Phi}{\cos\Theta} & \frac{\cos\Phi}{\cos\Theta} \end{pmatrix} \cdot \begin{pmatrix} p \\ q \\ r \end{pmatrix}. \tag{2.22}$$

Neglecting the lateral and directional dynamics this equation is simplified to

$$\dot{\Theta} = q_K. \tag{2.23}$$

It should be noted that Eq. (2.22) contains a singularity at $\Theta = \pm 90°$. This singularity can be avoided by means of an alternative approach using quaternions q_0, q_1, q_2 and q_3 to describe the aircraft attitude. Further details can be found in [143, pp. 121-126] [49, pp. 9-10]. Eq. (2.23) shows that the singularity vanishes, if lateral and directional dynamics are neglected. Thus, for the longitudinal aircraft model used within this thesis it is not necessary to consider quaternions.
Considering the longitudinal motion only, one can directly determine the flight path angle γ from pitch angle Θ and angle of attack α using the correlation [16, p. 220]

$$\gamma_K = \Theta - \alpha_K. \tag{2.24}$$

The dynamics of flight path angle γ can be deduced by derivation of Eq. (2.24)

$$\dot{\gamma}_K = \dot{\Theta} - \dot{\alpha}_K = -\frac{\left(Z_T^G\right)_{\bar{K}}}{mV} \tag{2.25}$$

and usage of Eq. (2.14b) and Eq. (2.23).

Position At last, the position is obtained by integration of the kinematic velocities transformed to the NED frame, which can be described as [57, p. 80]

$$\begin{pmatrix} \left(\dot{x}_K^G\right)_0^0 \\ \left(\dot{y}_K^G\right)_0^0 \\ \left(\dot{z}_K^G\right)_0^0 \end{pmatrix} = \boldsymbol{M}_{0B} \cdot \begin{pmatrix} \left(u_K^G\right)_B^0 \\ \left(v_K^G\right)_B^0 \\ \left(w_K^G\right)_B^0 \end{pmatrix} \tag{2.26}$$

with

$$\begin{aligned} \boldsymbol{M}_{0B} &= {\boldsymbol{M}_{B0}}^T = \\ &= \begin{pmatrix} \cos\Psi\cos\Theta & \cos\Psi\sin\Theta\sin\Phi - \sin\Psi\cos\Phi & \cos\Psi\sin\Theta\cos\Phi + \sin\Psi\sin\Phi \\ \sin\Psi\cos\Theta & \sin\Psi\sin\Theta\sin\Phi + \cos\Psi\cos\Phi & \sin\Psi\sin\Theta\cos\Phi - \cos\Psi\sin\Phi \\ -\sin\Theta & \cos\Theta\sin\Phi & \cos\Theta\cos\Phi \end{pmatrix} \end{aligned} \tag{2.27}$$

As the altitude is given in negative z-direction it can be written as

$$h = -\left(z_K^G\right)_0. \tag{2.28}$$

Considering only the longitudinal motion Eq. (2.26) is reduced to

$$\begin{pmatrix} \left(\dot{x}_K^G\right)_0^0 \\ \left(\dot{z}_K^G\right)_0^0 \end{pmatrix} = {\boldsymbol{M}_{0B}}^{lon} \cdot \begin{pmatrix} \left(u_K^G\right)_B^0 \\ \left(w_K^G\right)_B^0 \end{pmatrix} \tag{2.29}$$

with

$$\boldsymbol{M}_{0B}{}^{lon} = \begin{pmatrix} \cos\Theta & \sin\Theta \\ -\sin\Theta & \cos\Theta \end{pmatrix}. \tag{2.30}$$

2.1.3. Trim solution for steady, horizontal flight

In order to initialize the aircraft model properly, it is important to find suitable trim solutions of the dynamics. A trim solution is characterized by the fact that it sets up a stationary equilibrium. In this thesis, mostly the steady, horizontal flight condition is used to find such an equilibrium point. Other examples with respect to the longitudinal motion are steady climb or pull-up and push-down interception maneuvers [57].
The longitudinal aircraft dynamics introduced in the last section are summarized as a system of explicit, nonlinear and coupled differential equations [75, p. 109] [57, p. 292]

$$\dot{\boldsymbol{x}}(t) = \boldsymbol{f}(\boldsymbol{x}(t), \boldsymbol{u}(t)) \tag{2.31a}$$

$$\boldsymbol{y}(t) = \boldsymbol{h}(\boldsymbol{x}(t), \boldsymbol{u}(t)), \tag{2.31b}$$

where the system states $\boldsymbol{x}(t)$ are

$$\boldsymbol{x}(t) = \begin{pmatrix} V_K & \gamma_K & \alpha_K & q_K & x & h \end{pmatrix}^T. \tag{2.32}$$

The system inputs are given as $\boldsymbol{u}(t) = \begin{pmatrix} \eta & \delta_T \end{pmatrix}^T$ and the system outputs $\boldsymbol{y}(t) = \boldsymbol{x}(t)$. For the steady, horizontal flight it is now demanded that the flight path angle vanishes $\gamma_K = 0$. Furthermore, moments acting on the aircraft should be in balance, which is reflected by $q_K = 0$. Velocity V_K and altitude h are set according to the envelope point, at which the trim solution should be computed. The horizontal position x is not relevant in this case, as the aircraft dynamics are mostly decoupled from the horizontal position. By means of the trimming algorithm, the model inputs elevator deflection η_0 and the thrust lever position $\delta_{T,0}$ are determined in accordance to the given flight condition. In this step, also the remaining state angle of attack α_0 is suitable identified. As the considered flight condition is steady, it is also required for all state derivatives apart from $\dot{x}$ to be zero.

1	**2**	**3**	**4**	**5**	**6**	**7**	**8**
102.88	110.32	117.75	125.19	132.63	140.07	147.50	154.94
9	**10**	**11**	**12**	**13**	**14**	**15**	
162.38	169.81	177.25	184.69	192.13	199.56	207.00	

Table 2.2. – Envelope points w.r.t. velocity V in $\left[\frac{m}{s}\right]$

The built-in trim algorithm of *MATLAB* [80] is used to compute a numerical solution to the given optimization problem for Eq. (2.31) and the conditions stated above. Trimming is performed for an altitude of $h = 5000m$ and 15 equally distributed

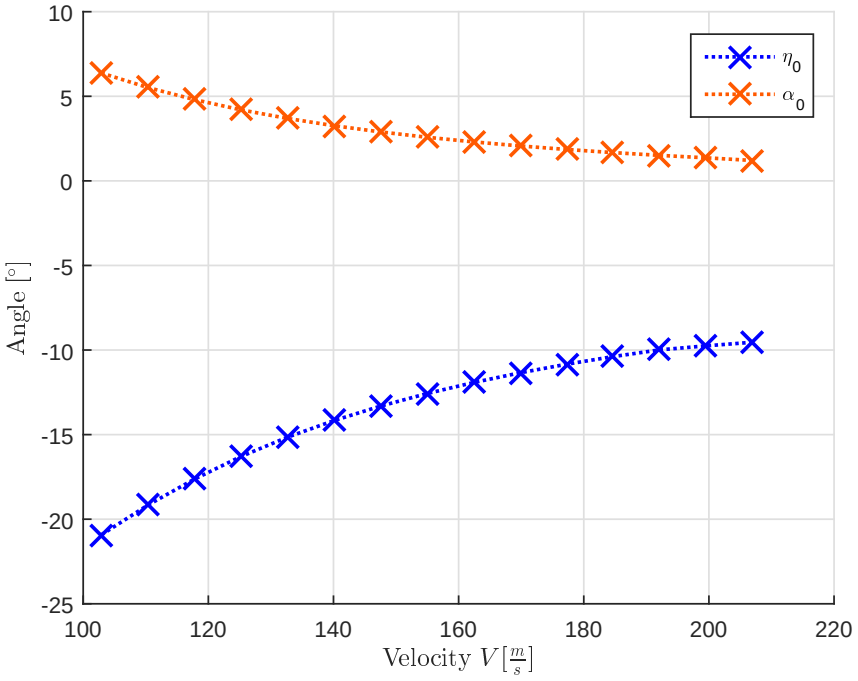

Figure 2.4. – Trim solutions w.r.t. elevator deflection η_0 and angle of attack α_0 for the given velocity range in Table 2.2 and $h = 5000m$

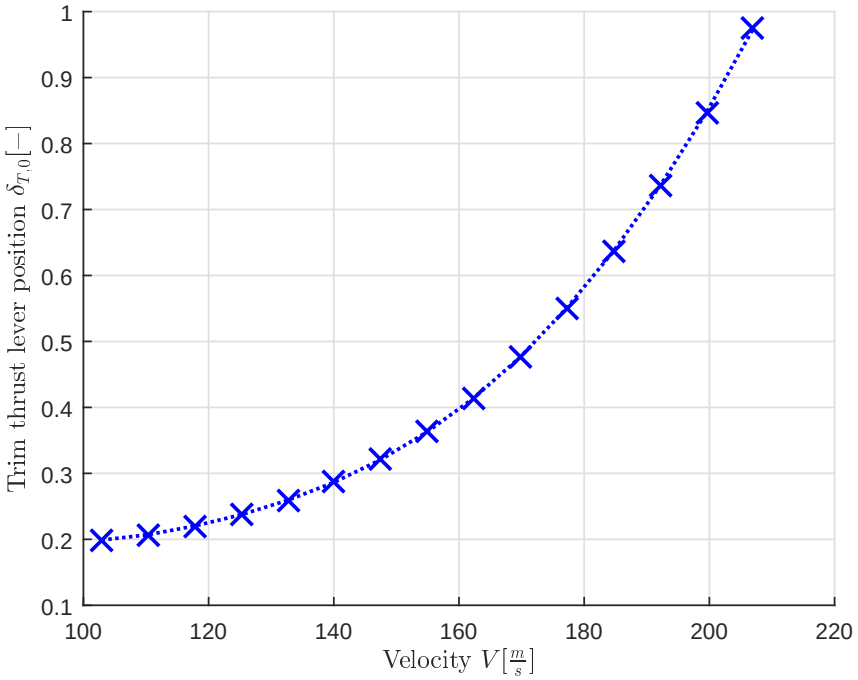

Figure 2.5. – Trim solutions w.r.t. thrust lever position $\delta_{T,0}$ for the given velocity range in Table 2.2 and $h = 5000m$

velocities $102.88\frac{m}{s} \leq V \leq 207\frac{m}{s}$ given in Table 2.2. This also defines the envelope used for assessments in this thesis. The resulting trim elevator deflections η_0 together with the angles of attack α_0 are shown in Fig. 2.4 and the corresponding thrust lever positions are depicted in Fig. 2.5.

2.1.4. Linearization

Symbol	Dimension
$\boldsymbol{A}$	$(n \times n)$
$\boldsymbol{B}$	$(n \times m)$
$\boldsymbol{C}$	$(r \times n)$
$\boldsymbol{D}$	$(r \times m)$
$\boldsymbol{x}$	$(n \times 1)$
$\boldsymbol{u}$	$(m \times 1)$
$\boldsymbol{y}$	$(r \times 1)$

Table 2.3. – Dimensions of matrices and vectors of the state space model [50]

Although the nonlinear dynamics description is important for simulation purposes, for controller design often a linear representation in form of a time invariant state space model is needed. This is also the case for the controller design methods used in this thesis. In general, a state space model can be formulated according to [76, p. 16]

$$\dot{\boldsymbol{x}}(t) = \boldsymbol{A}\boldsymbol{x}(t) + \boldsymbol{B}\boldsymbol{u}(t) \tag{2.33a}$$

$$\boldsymbol{y}(t) = \boldsymbol{C}\boldsymbol{x}(t) + \boldsymbol{D}\boldsymbol{u}(t) \tag{2.33b}$$

$$\boldsymbol{x}(0) = \boldsymbol{x}_0. \tag{2.33c}$$

Here, $\boldsymbol{A}$ is the system matrix, $\boldsymbol{B}$ the input matrix, $\boldsymbol{C}$ the output matrix and $\boldsymbol{D}$ the feed-through matrix. Furthermore, $\boldsymbol{x}$ are the system states, $\boldsymbol{u}$ the system inputs and $\boldsymbol{y}$ the system outputs. The initial state at t_0 is defined through $\boldsymbol{x}_0$. Table 2.3 summarizes the dimensions of the mentioned matrices and vectors.
How to gain such a state space model in Eq. (2.33) from the nonlinear differential equations describing the dynamics given in Eq. (2.31), is deduced in [75, 121, 57, 50] and is also shown in the following. At first, Eq. (2.31a) is reformulated as a Taylor series [107, S. 185] of first order. This leads to [75, p. 110] [57, p. 302]

$$\dot{\boldsymbol{x}} = \boldsymbol{f}(\boldsymbol{x}_0, \boldsymbol{u}_0) + \left.\frac{\partial \boldsymbol{f}(\boldsymbol{x}, \boldsymbol{u})}{\partial \boldsymbol{x}}\right|_{\substack{\boldsymbol{x}=\boldsymbol{x}_0 \\ \boldsymbol{u}=\boldsymbol{u}_0}} \cdot (\boldsymbol{x} - \boldsymbol{x}_0) + \left.\frac{\partial \boldsymbol{f}(\boldsymbol{x}, \boldsymbol{u})}{\partial \boldsymbol{u}}\right|_{\substack{\boldsymbol{x}=\boldsymbol{x}_0 \\ \boldsymbol{u}=\boldsymbol{u}_0}} \cdot (\boldsymbol{u} - \boldsymbol{u}_0) + \mathcal{O}\left(\boldsymbol{x}^2\right) + \mathcal{O}\left(\boldsymbol{u}^2\right), \tag{2.34}$$

where $\mathcal{O}\left(\boldsymbol{x}^2\right)$ and $\mathcal{O}\left(\boldsymbol{u}^2\right)$ are higher order terms. $\boldsymbol{x}_0$ and $\boldsymbol{u}_0$ define the reference state, at which the linearization is performed. This reference state is taken from the trimming solution shown in Section 2.1.3. Likewise, according to Eq. (2.31a) $\dot{\boldsymbol{x}}_0 = \boldsymbol{f}\left(\boldsymbol{x}_0, \boldsymbol{u}_0\right)$ holds. For the next step small deviations from the reference state [75, p. 110]

$$\boldsymbol{x} = \boldsymbol{x}_0 + \delta\boldsymbol{x} \tag{2.35a}$$

$$\boldsymbol{u} = \boldsymbol{u}_0 + \delta\boldsymbol{u} \tag{2.35b}$$

$$\dot{\boldsymbol{x}} = \dot{\boldsymbol{x}}_0 + \delta\dot{\boldsymbol{x}} \tag{2.35c}$$

are formulated. Plugging Eq. (2.35) in Eq. (2.34) yields [75, p. 111] [57, p. 302]

$$\delta\dot{\boldsymbol{x}} = \left.\frac{\partial \boldsymbol{f}\left(\boldsymbol{x}, \boldsymbol{u}\right)}{\partial \boldsymbol{x}}\right|_{\substack{\boldsymbol{x}=\boldsymbol{x}_0 \\ \boldsymbol{u}=\boldsymbol{u}_0}} \cdot \delta\boldsymbol{x} + \left.\frac{\partial \boldsymbol{f}\left(\boldsymbol{x}, \boldsymbol{u}\right)}{\partial \boldsymbol{u}}\right|_{\substack{\boldsymbol{x}=\boldsymbol{x}_0 \\ \boldsymbol{u}=\boldsymbol{u}_0}} \cdot \delta\boldsymbol{u}, \tag{2.36}$$

also neglecting the higher order terms $\mathcal{O}\left(\boldsymbol{x}^2\right)$ and $\mathcal{O}\left(\boldsymbol{u}^2\right)$. The formulation according to Eq. (2.33a) can be directly achieved by means of [75, p. 111] [57, p. 302]

$$\boldsymbol{A} := \left.\frac{\partial \boldsymbol{f}\left(\boldsymbol{x}, \boldsymbol{u}\right)}{\partial \boldsymbol{x}}\right|_{\substack{\boldsymbol{x}=\boldsymbol{x}_0 \\ \boldsymbol{u}=\boldsymbol{u}_0}} \tag{2.37a}$$

$$\boldsymbol{B} := \left.\frac{\partial \boldsymbol{f}\left(\boldsymbol{x}, \boldsymbol{u}\right)}{\partial \boldsymbol{u}}\right|_{\substack{\boldsymbol{x}=\boldsymbol{x}_0 \\ \boldsymbol{u}=\boldsymbol{u}_0}} \tag{2.37b}$$

and crossing out the additional "δ". Although, one has to keep in mind that nevertheless x and u mean deviations from the considered trim state described through x_0 and u_0 and that the linear formulation only holds in the proximity of the trim state.

The same method is also applied to Eq. (2.31b), which results in [57, p. 301]

$$\boldsymbol{y} = \boldsymbol{h}\left(\boldsymbol{x}_0, \boldsymbol{u}_0\right) + \left.\frac{\partial \boldsymbol{h}\left(\boldsymbol{x}, \boldsymbol{u}\right)}{\partial \boldsymbol{x}}\right|_{\substack{\boldsymbol{x}=\boldsymbol{x}_0 \\ \boldsymbol{u}=\boldsymbol{u}_0}} \cdot \left(\boldsymbol{x} - \boldsymbol{x}_0\right) + \left.\frac{\partial \boldsymbol{h}\left(\boldsymbol{x}, \boldsymbol{u}\right)}{\partial \boldsymbol{u}}\right|_{\substack{\boldsymbol{x}=\boldsymbol{x}_0 \\ \boldsymbol{u}=\boldsymbol{u}_0}} \cdot \left(\boldsymbol{u} - \boldsymbol{u}_0\right) + \mathcal{O}\left(\boldsymbol{x}^2\right) + \mathcal{O}\left(\boldsymbol{u}^2\right), \tag{2.38}$$

where $\boldsymbol{y}_0 = \boldsymbol{h}\left(\boldsymbol{x}_0, \boldsymbol{u}_0\right)$. If again Eq. (2.35) is utilized with the additional definition [75, p. 110]

$$\boldsymbol{y} = \boldsymbol{y}_0 + \delta\boldsymbol{y}, \tag{2.39}$$

Eq. (2.38) can be reformulated to [75, p. 111] [57, p. 301]

$$\delta\boldsymbol{y} = \left.\frac{\partial \boldsymbol{h}\left(\boldsymbol{x}, \boldsymbol{u}\right)}{\partial \boldsymbol{x}}\right|_{\substack{\boldsymbol{x}=\boldsymbol{x}_0 \\ \boldsymbol{u}=\boldsymbol{u}_0}} \cdot \delta\boldsymbol{x} + \left.\frac{\partial \boldsymbol{h}\left(\boldsymbol{x}, \boldsymbol{u}\right)}{\partial \boldsymbol{u}}\right|_{\substack{\boldsymbol{x}=\boldsymbol{x}_0 \\ \boldsymbol{u}=\boldsymbol{u}_0}} \cdot \delta\boldsymbol{u}, \tag{2.40}$$

where higher order terms have been neglected. Using the definitions [75, p. 111] [57, p. 301]

$$\boldsymbol{C} := \left.\frac{\partial \boldsymbol{h}\left(\boldsymbol{x},\boldsymbol{u}\right)}{\partial \boldsymbol{x}}\right|_{\substack{\boldsymbol{x}=\boldsymbol{x}_0\\ \boldsymbol{u}=\boldsymbol{u}_0}} \tag{2.41a}$$

$$\boldsymbol{D} := \left.\frac{\partial \boldsymbol{h}\left(\boldsymbol{x},\boldsymbol{u}\right)}{\partial \boldsymbol{u}}\right|_{\substack{\boldsymbol{x}=\boldsymbol{x}_0\\ \boldsymbol{u}=\boldsymbol{u}_0}} \tag{2.41b}$$

directly yields Eq. (2.33b). It has to be noted additionally that the method cannot be applied analytically to the aircraft model presented in this thesis. This is because the dimensionless coefficients $C_\star$ according to Eq. (2.7) shown in Section 2.1.1 describing the aircraft's aerodynamic forces and moments are given as lookup tables and not as analytical functions.

A numerical linearization of the nonlinear dynamics formulated in Eq. (2.31) with the states and outputs defined in Eq. (2.32) results in a state space model with the following structure [55, p. 184]:

$$\underbrace{\begin{pmatrix}\dot{V}\\ \dot{\gamma}\\ \dot{\alpha}\\ \dot{q}\\ \dot{x}\\ \dot{h}\end{pmatrix}}_{=:\dot{\boldsymbol{x}}} = \underbrace{\begin{pmatrix} X_V & -g\cdot\cos\gamma_0 & X_\alpha & X_q & 0 & X_h\\ -Z_V & \frac{g}{V_0}\cdot\sin\gamma_0 & -Z_\alpha & -Z_q & 0 & -Z_h\\ Z_V & -\frac{g}{V_0}\cdot\sin\gamma_0 & Z_\alpha & Z_q+1 & 0 & Z_h\\ M_V & 0 & M_\alpha & M_q & 0 & M_h\\ \cos\gamma_0 & -V_0\sin\gamma_0 & 0 & 0 & 0 & 0\\ \sin\gamma_0 & V_0\cos\gamma_0 & 0 & 0 & 0 & 0\end{pmatrix}}_{=:\boldsymbol{A}} \underbrace{\begin{pmatrix}V\\ \gamma\\ \alpha\\ q\\ x\\ h\end{pmatrix}}_{=:\boldsymbol{x}} + \underbrace{\begin{pmatrix} X_\eta & X_{\delta_T}\\ -Z_\eta & -Z_{\delta_T}\\ Z_\eta & Z_{\delta_T}\\ M_\eta & M_{\delta_T}\\ 0 & 0\\ 0 & 0\end{pmatrix}}_{=:\boldsymbol{B}} \underbrace{\begin{pmatrix}\eta\\ \delta_T\end{pmatrix}}_{=:\boldsymbol{u}} \tag{2.42a}$$

$$\boldsymbol{y} = \boldsymbol{I}_{6\times 6}\cdot\begin{pmatrix}V & \gamma & \alpha & q & x & h\end{pmatrix}^T \tag{2.42b}$$

Here, the subscript K are neglected for the states. The position x has no influence on the other states. Furthermore, the stability derivatives X_h, Z_h and M_h can be considered very small in good approximation. Thus, the states V, γ, α and q are decoupled from x and h. Consequently the state space model can be reduced according to [55, p. 184]

$$\underbrace{\begin{pmatrix}\dot{V}\\ \dot{\gamma}\\ \dot{\alpha}\\ \dot{q}\end{pmatrix}}_{=:\dot{\boldsymbol{x}}} = \underbrace{\begin{pmatrix} X_V & -g\cdot\cos\gamma_0 & X_\alpha & X_q\\ -Z_V & \frac{g}{V_0}\cdot\sin\gamma_0 & -Z_\alpha & -Z_q\\ Z_V & -\frac{g}{V_0}\cdot\sin\gamma_0 & Z_\alpha & Z_q+1\\ M_V & 0 & M_\alpha & M_q\end{pmatrix}}_{=:\boldsymbol{A}} \underbrace{\begin{pmatrix}V\\ \gamma\\ \alpha\\ q\end{pmatrix}}_{=:\boldsymbol{x}} + \underbrace{\begin{pmatrix} X_\eta & X_{\delta_T}\\ -Z_\eta & -Z_{\delta_T}\\ Z_\eta & Z_{\delta_T}\\ M_\eta & M_{\delta_T}\end{pmatrix}}_{=:\boldsymbol{B}} \underbrace{\begin{pmatrix}\eta\\ \delta_T\end{pmatrix}}_{=:\boldsymbol{u}} \tag{2.43a}$$

$$\boldsymbol{y} = \boldsymbol{I}_{4\times 4} \cdot \begin{pmatrix} V \\ \gamma \\ \alpha \\ q \end{pmatrix}. \tag{2.43b}$$

Eqs. (A.1a) to (A.15a) to be found in Appendix A.3 comprise results of linearizations of the longitudinal F-16 dynamics at an altitude of $h = 5000m$ and different velocities according to Table 2.2 using the trim results of Fig. 2.4 and Fig. 2.5.
Appendix A.3 also comprises the resulting eigenvalues of the system matrix $\boldsymbol{A}$ in Eq. (2.43) for the considered envelope i.e. natural frequency and relative damping of short-period and phugoid motion, respectively. As it was already mentioned in Section 2.1.1, the longitudinal dynamics are stable for the chosen CG position of $0.30\bar{c}$. Thus, the natural frequency of the short-period $\omega_{0,sp}$ ranges from $2.33\frac{rad}{s}$ to $4.88\frac{rad}{s}$, where the relative damping ζ_{sp} barely changes and results in values between 0.36 and 0.39. Furthermore, a periodic phugoid mode can be observed, whose natural frequency $\omega_{0,ph}$ lies between $0.06\frac{rad}{s}$ and $0.13\frac{rad}{s}$ and the relative damping ζ_{ph} is 0.13 for low and 0.43 for high velocities.

2.2. Atmospheric Model

The atmospheric model defines, how physical properties like temperature T, barometric pressure p and air density ρ are related to the altitude h of the aircraft. The implementation for the aircraft model used in thesis was performed according to the standard atmosphere given in the standard ISO 2533 [61]. In the following section, the formulas describing the standard atmosphere model are briefly presented and a more detailed summary can be found in [57, pp. 91-92].
The atmosphere is vertically subdivided into three areas, which are the Troposphere ($MSL \leq H_G \leq 11km$), lower Stratosphere ($11km < H_G \leq 20km$) and upper Stratosphere ($20km < H_G \leq 32km$). The geopotential height [57, p. 91]

$$H_G = \frac{r_E \cdot h}{r_E + h} \tag{2.44}$$

with the earth's radius $r_E = 6356.766km$ considers a decrease of gravity with increasing altitude. This effect is neglected[1] for the implemented model, thus it is assumed that $H_G \approx h$. Furthermore, it is concentrated on a description of the Troposphere, as $h = 11km$ are not exceeded for the assessments made in this work. The properties of the Troposphere in dependence of altitude h are obtained from [57, p. 92]

$$p = p_s \cdot \left(1 - \frac{n_{Tr} - 1}{n_{Tr}} \cdot \frac{g}{R \cdot T_s} \cdot h\right)^{\frac{n_{Tr}}{n_{Tr}-1}} \tag{2.45a}$$

[1] For example, the geopotential height corresponding to $h = 5000m$ would be $H_G \approx 4996m$

$$T = T_s \cdot \left(1 - \frac{n_{Tr} - 1}{n_{Tr}} \cdot \frac{g}{R \cdot T_s} \cdot h\right) \tag{2.45b}$$

$$\rho = \rho_s \cdot \left(1 - \frac{n_{Tr} - 1}{n_{Tr}} \cdot \frac{g}{R \cdot T_s} \cdot h\right)^{\frac{1}{n_{Tr}-1}} \tag{2.45c}$$

with

$$p_s = 1.01325 \cdot 10^5 \frac{N}{m^2} \qquad T_s = 288.15K \qquad \rho_s = 1.225 \frac{kg}{m^3} \qquad n_{Tr} = 1.235 \tag{2.46}$$

and with the gas constant $R = 287.05 \frac{J}{kg \cdot K}$ as well as the gravitational acceleration at MSL $g = 9.80665 \frac{m}{s^2}$.
From the atmospheric properties the dynamic pressure $\bar{q}$ according to Eq. (2.6) is obtained, which is needed for the calculation of the absolute aerodynamic forces and moments in Section 2.1.1. Also, the mach number [122, p. 68] [56, p. 2.11]

$$Ma = \frac{V_A}{\sqrt{\kappa \cdot R \cdot T}} \tag{2.47}$$

is calculated additionally considering the isentropic exponent $\kappa = 1.4$.

2.3. Turbulence Model

In general, atmospheric disturbances influence the aerodynamic forces and moments acting on the aircraft. The aircraft model is affected by horizontal $\left(u_W^G\right)_0^0$ and vertical $\left(w_W^G\right)_0^0$ velocity components w.r.t. the NED frame, as well as by the wind-generated pitch rate q_W, as only logitudinal dynamics are considered in this thesis. The resulting velocities and pitch rate of the aircraft relative to the surrounding air can be defined as [16, p. 219]

$$\begin{pmatrix} \left(u_A^G\right)_B^0 \\ \left(w_A^G\right)_B^0 \end{pmatrix} = \begin{pmatrix} \left(u_K^G\right)_B^0 \\ \left(w_K^G\right)_B^0 \end{pmatrix} - \boldsymbol{M}_{B0}{}^{lon} \begin{pmatrix} \left(u_W^G\right)_0^0 \\ \left(w_W^G\right)_0^0 \end{pmatrix} \tag{2.48a}$$

$$q_A = q_K - q_W, \tag{2.48b}$$

where the variables noted with the sub-index K are the kinematic states, which come after integration of the rigid-body equations of motion as described in Section 2.1.2. As the wind velocities are given in the NED frame the transformation matrix

$$\boldsymbol{M}_{B0}{}^{lon} = \begin{pmatrix} \cos\Theta & -\sin\Theta \\ \sin\Theta & \cos\Theta \end{pmatrix} \tag{2.49}$$

is used.
The wind velocities and pitch rate are obtained from a turbulence model. It is stated in [16] that in most applications one of two possible approximations is used, which utilize the Dryden or the van Kármán spectrum. The van Kármán spectrum is rather used for assessments in the frequency domain e.g. load calculations, whereas the Dryden spectrum is prefered for flight mechanical assessments within the time domain due to its simplicity. As the focus of this thesis lies on the latter, the Dryden spectrum is used for further investigations. It should be additionally noted that [82] recommends usage of the van Kármán spectrum in case comparable structural analysis is performed, in order to achieve comparability of the assessments.
For the simulation model of this thesis, the continuous Dryden turbulence implementation is used, which is included in the *MATLAB* Aerospace Blockset toolbox [78]. It follows the specifications given in the adequate MIL-spec [81]. The underlying principle of this model is that turbulence is assumed to be a random process with a normal (Gaussian) distribution. This showed to be sufficient for flying quality assessments. But it has to be kept in mind that actual turbulence is widely understood as being non-Gaussian, which has to be considered e.g. for research regarding meterological phenomena [85].
The Dryden spectra are defined according to [81, p. 47]

$$\Phi_{u_W}(\omega) = {\sigma_u}^2 \cdot \frac{2L_u}{\pi V_K} \cdot \frac{1}{1 + \left(\frac{L_u}{V_K} \cdot \omega\right)^2} \tag{2.50a}$$

$$\Phi_{w_W}(\omega) = {\sigma_w}^2 \cdot \frac{L_w}{\pi V_K} \cdot \frac{1 + 3\left(\frac{L_w}{V_K} \cdot \omega\right)^2}{\left[1 + \left(\frac{L_w}{V_K} \cdot \omega\right)^2\right]^2} \tag{2.50b}$$

$$\Phi_{q_W}(\omega) = \frac{\left(\frac{\omega}{V_K}\right)^2}{1 + \left(\frac{4b}{\pi V_K} \cdot \omega\right)^2} \cdot \Phi_{w_W}(\omega) \tag{2.50c}$$

as a function of frequency ω, velocity V_K and wingspan $b = 9.144m$. [81] specifies the spectra as functions of the spatial frequency Ω. Assuming that turbulence is frozen during the aircraft transition, it can be considered a stationary process. Thus, the spectra can be expressed by means of the circular frequency $\omega = \Omega \cdot V_K$ using the aircraft velocity V_K rather than the spatial frequency Ω [35]. The scale lengths L_u and L_w, as well as the RMS intensities σ_u and σ_w are defined in Table 2.4 for different altitude h ranges. For altitudes below $1000ft$ an additional parameter u_{20} is needed, which represents the wind speed at $20ft$ above the ground. Suitable values for u_{20} can be found in Table 2.5 for probabilities of exceedance. The probability of exceedance, as it also appears in Fig. 2.6, defines the turbulence intensity. Here, 10^{-2} correspondes to

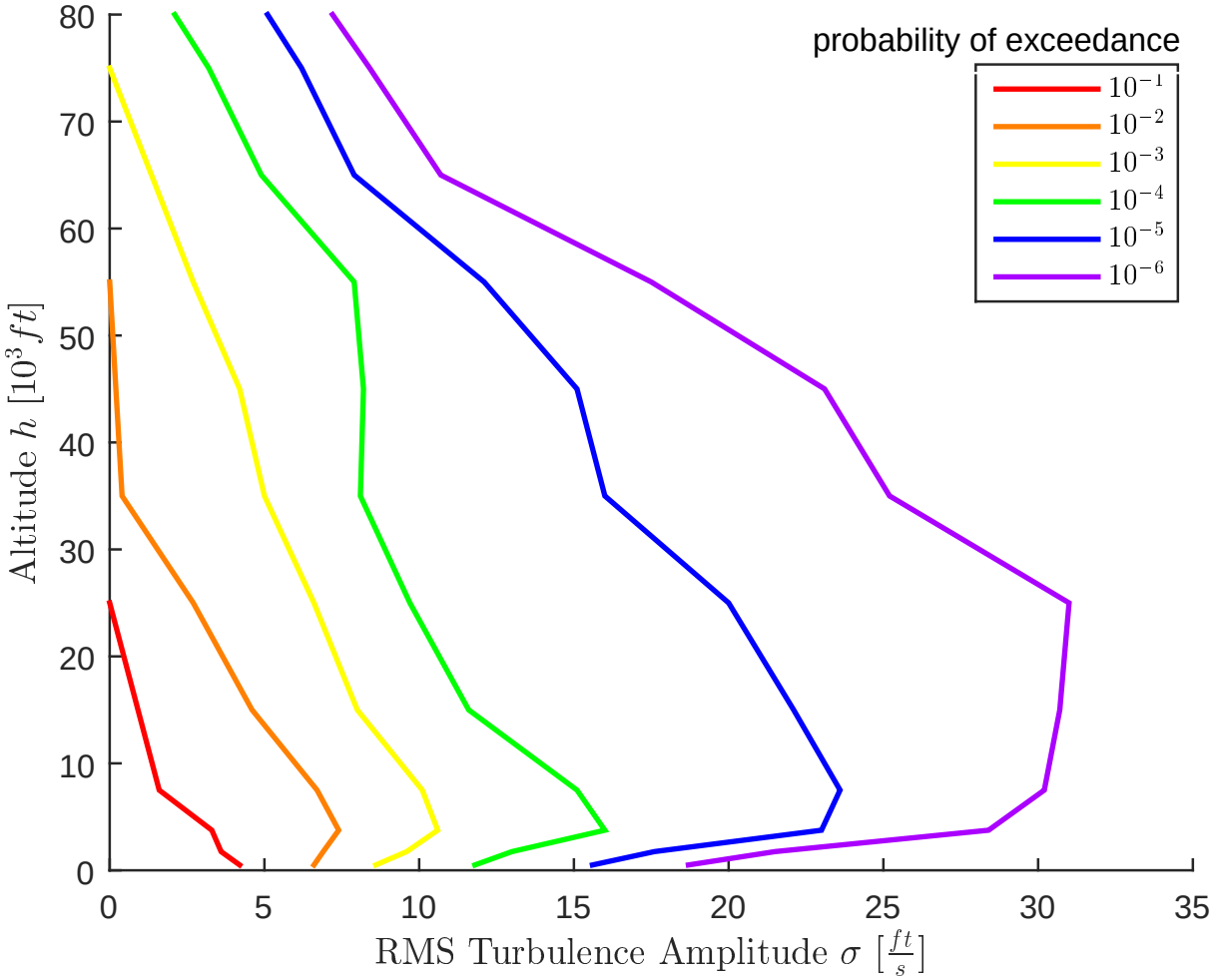

Figure 2.6. – Turbulence exceedance probability (data extracted from [80, 78])

Condition	**RMS Intensities** $\left[\frac{ft}{s}\right]$ (σ_u, σ_w)	**Scale Lengths in** $[ft]$ (L_u, L_w)
$h > 1000ft$	$\sigma_u = \sigma_w$ choose according to Fig. 2.6	$L_u = L_w = 1750$
$h \leq 1000ft$	$\sigma_w = 0.1 \cdot u_{20}$ $\sigma_u = \frac{\sigma_w}{(0.177+0.000823 \cdot h)^{0.4}}$ choose u_{20} according to Table 2.5	$L_u = \frac{h}{(0.177+0.000823 \cdot h)^{1.2}}$ $L_w = h$

Table 2.4. – Turbulence model parameters [81, p. 48] [137, p. 120]

Probability of exceedance	u_{20} $[kts]$
10^{-1}	16
10^{-2} (light)	23
10^{-3} (moderate)	30
10^{-4}	38
10^{-5} (severe)	45

Table 2.5. – Wind speed at $20ft$ above the ground u_{20} (data extracted from [81, p. 52])

light, 10^{-3} to moderate and 10^{-5} to severe turbulence [81]. Note additionally that the formulation for the spectrum of the angular velocity disturbance q_W is only valid, if structural modes are not significant [81, p. 58].
In order to achieve the required spectra in Eq. (2.50) for the turbulence signals, normally distributed white noise $N(0,1)$ is led through suitable forming filter functions resulting in [137, p. 118]

$$\left(u_W^G\right)_0^0 = \sigma_u \cdot \sqrt{\frac{2L_u}{V_K}} \cdot \frac{1}{1+\frac{L_u}{V_K}\cdot s} \cdot N(0,1) \tag{2.51a}$$

$$\left(w_W^G\right)_0^0 = \sigma_w \cdot \sqrt{\frac{L_w}{V_K}} \cdot \frac{1+\sqrt{3}\frac{L_w}{V_K}s}{\left(1+\frac{L_w}{V_K}\cdot s\right)^2} \cdot N(0,1) \tag{2.51b}$$

$$q_W = \frac{\frac{1}{V_K}s}{1+\frac{4b}{\pi V_K}\cdot s} \cdot \left(w_W^G\right)_0^0. \tag{2.51c}$$

2.4. Gust Model

In addition to the turbulence model described in Section 2.3, a wind gust model is implemented. In this case, the aircraft is affected by wind components according to a specific shape, which is time-dependent. The so-called *1-cosine* shape is well established for aircraft analyses and is also used for the assessments made within this thesis[2]. Its resulting wind velocity is formulated as [81, p. 48]

$$\left(w_W^G\right)_0^0 = \begin{cases} 0 & \text{if } x_{gust} < 0 \\ \frac{v_{gust}}{2}\cdot\left(1-\cos\frac{\pi\cdot x_{gust}}{d_{gust}}\right) & \text{if } 0 < x_{gust} < d_{gust} \\ v_{gust} & \text{if } x > d_{gust} \end{cases}, \tag{2.52}$$

[2]More specifically, an implementation included in the *MATLAB* Aerospace Blockset toolbox is used [79]

where x_{gust} denotes the horizontal position of the aircraft in body-fixed x-direction within the gust. It is calculated by means of integrating the kinematic velocity V_K over time starting at $t_{0,gust}$. The gust length can be defined in d_{gust} and the resulting wind velocity is described by v_{gust}. Fig. 2.7 gives an example on the shape of the resulting wind velocity. In the same way, the *1-cosine* gust can also be formulated for $\left(u_W^G\right)_0^0$ analogously to Eq. (2.52).

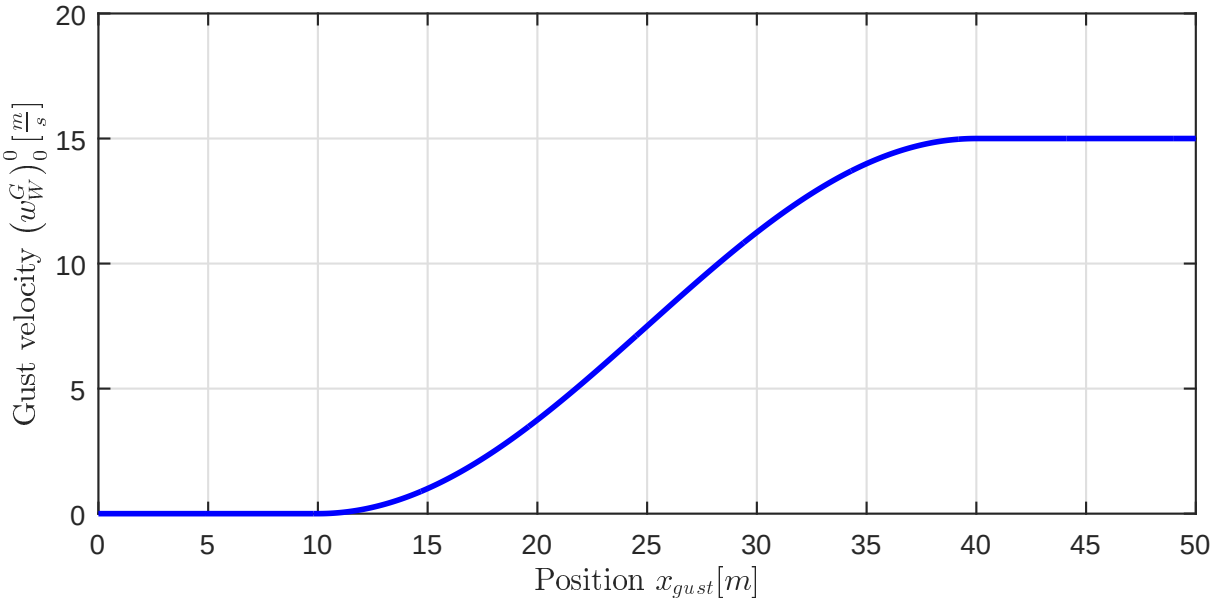

Figure 2.7. – Resulting wind velocity $\left(w_W^G\right)_0^0$ for *1-cosine* gust starting $10m$ in front of the aircraft with $d_{gust} = 30m$ and $v_m = 15\frac{m}{s}$

2.5. Actuator Model

The original aircraft uses mainly two aerodynamic control surfaces for the longitudinal motion, namely the elevator and the LEF. Their position with respect to the airframe can be seen in Fig. 2.8. The deflection of the LEF δ_{LEF} is determined as a function of α and Ma. As the Ma-dependence is very low for the considered valid envelope and neglecting the actuator dynamics, the control of the LEF was merged into the aerodynamic coefficients [121]. Thus, the elevator deflection η is left as only aerodynamic control input with respect to the longitudinal motion.
The elevator is modeled as a 2nd order transfer function with a natural frequency $\omega_{0,act} = 40\frac{rad}{s}$ and relative damping $\zeta_{act} = 0.71$. The system can generally be written as

$$\begin{pmatrix} \dot{x}_{1,act} \\ \dot{x}_{2,act} \end{pmatrix} = \begin{pmatrix} 0 & 1 \\ -{\omega_{0,act}}^2 & -2\zeta_{act}\omega_{0,act} \end{pmatrix} \begin{pmatrix} x_{1,act} \\ x_{2,act} \end{pmatrix} + \begin{pmatrix} 0 \\ {\omega_{0,act}}^2 \end{pmatrix} \eta_{cmd} \tag{2.53a}$$

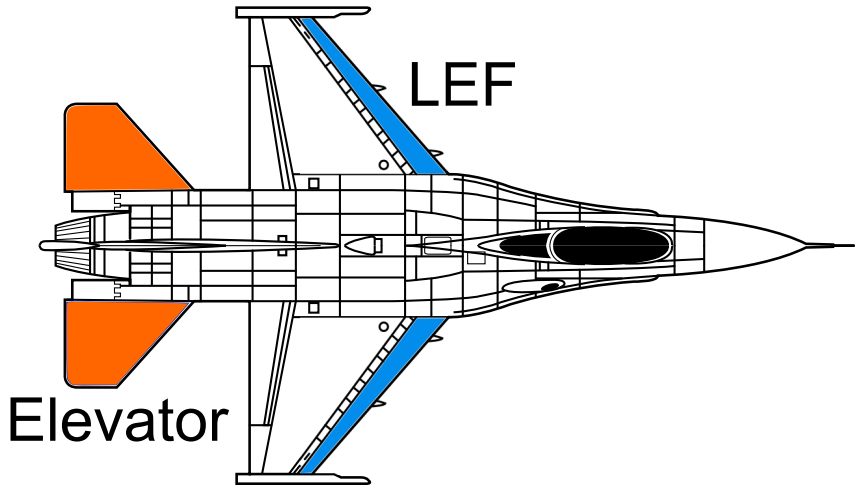

Figure 2.8. – Control surfaces of F-16 aircraft used to control the longitudinal motion [134]

$$\eta = \begin{pmatrix} 1 & 0 \end{pmatrix} \begin{pmatrix} x_{1,act} \\ x_{2,act} \end{pmatrix} \tag{2.53b}$$

in state space representation. Furthermore, the structure is also shown in Fig. 2.9. η_{cmd} is the signal commanded by the controller and η the signal, that actually affects the plant. The absolute deflection of the elevator η is limited to $|\eta| \leq 25°$ with a rate limit of $|\dot{\eta}| \leq 60\frac{°}{s}$.
The engine dynamics are modeled in the same way, as the commanded thrust lever position $0 \leq \delta_{T,cmd} \leq 1$ is retarded using an analogous model as given in Eq. (2.53). The natural frequency is set to $\omega_{0,thr} = 1\frac{rad}{s}$ with a relative damping of $\zeta_{thr} = 0.95$.

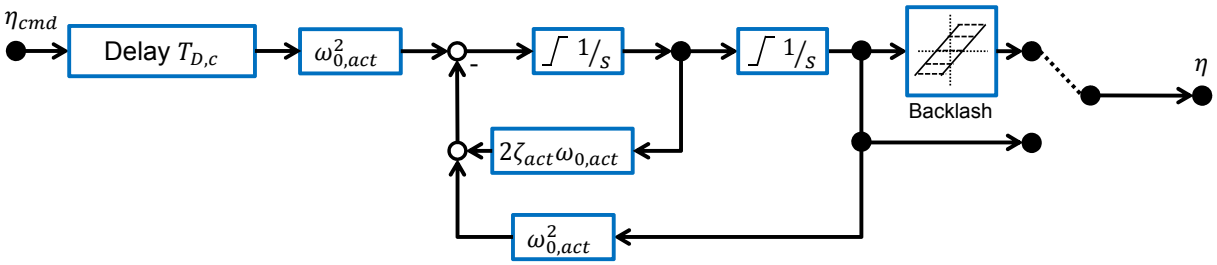

Figure 2.9. – Structure of the actuator model

In order to consider reality effects, some additions are made to the basic actuator model shown in Eq. (2.53). At first, a continuous delay is inserted upstream of the integrator, through which both the effect of computational time delay and delays resulting from filtering can be taken into account. For the assessments using the simple aircraft model, the delay is set to $T_{D,c} = 0.055s$ considering one accumulated delay resulting from various sources. If the enhanced model is used, for which the more sophisticated

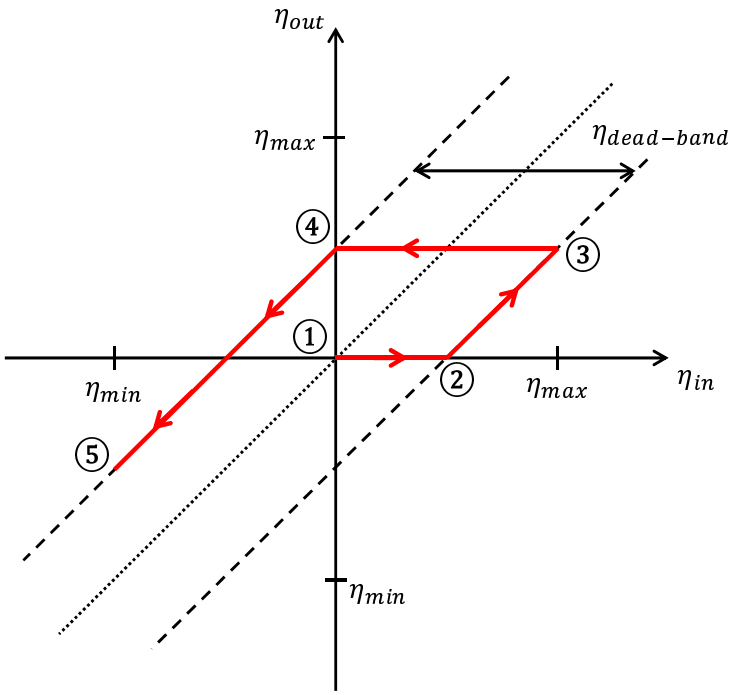

Figure 2.10. – Example for actuator backlash

sensor models described in Section 2.6 and the filters are active, the delay is set to $T_{D,c} = 0.015s$. This represents delay resulting from computation only.
One can also activate the option that the actuators receive commands with a limited sample rate. This is achieved through additional sample rate conversion. For this work, the sample rates of the receivers corresponding to the command signals η_{cmd} and $\delta_{T,cmd}$ are set to $50Hz$. In order to avoid aliasing effects, low-pass filtering is applied upstream of the sample rate conversion, as it is also described in the next section.
It is additionally possible to consider backlash[3] for the actuator. Backlash within the actuator means that the actuator position has a certain amount of play e.g. due to wear of mechanical components like bearings. This has mainly two effects. On the one hand the actuator movement has to pass a certain dead-band first, before the control surface actually changes its position. On the other hand, movement of the control surface within this dead-band can be induced by the surrounding air e.g. through turbulence. For the model at hand only the first effect is modeled by means of an optional dead-band implementation within the actuator model shown in Fig. 2.9. The dead-band for the elevator is set to $\eta_{dead-band} = 0.13°$. According to [74] this is the maximum value tolerable for trailing edge actuators for the TORNADO aircraft. Fig. 2.10 gives a simple example for the effect of backlash, where η_{in} is the signal before and η_{out} is the signal after the backlash block shown in Fig. 2.9. The actuator command is initialized in zero position and is first driven to the maximum η_{max} and

[3]The effect of backlash is also often to be found in literature described by the term freeplay

then to the minimum position η_{min}. But instead of resulting in an actuator deflection instantaneously, at first the dead-band $\eta_{dead-band}$ has to be passed between ① and ②, before the actuator moves to ③. Vice versa when changing the direction of actuator movement, which results in a change of sign in $\dot{\eta}$, the dead-band $\eta_{dead-band}$ has to be passed again between ③ and ④, before ⑤ is reached. Thus, the effect of backlash can be compared to a combination of time-delay and loss of positional accuracy.

2.6. Sensor Model

A more sophisticated sensor model is applied for the measurement of angle of attack α, load factor n_z, pitch rate q, pitch acceleration $\dot{q}$, elevator deflection η and the dynamic pressure $\bar{q}$, which is configured according to Table 2.6 for the standard assessment test case. Various sources of errors during the measurement and the associated processing are taken into account.
The basic structure is depicted in Fig. 2.11. At first, the analog plant output signal y_s is perturbed by use of the relation

$$y_{meas,A} = b + m \cdot y_s + v, \tag{2.54}$$

where b introduces a bias, m a scale factor and v measurement noise [69]. For the following experiments, only constant b and m are used representing average values. The generation of noise v is implemented as a Gaussian (normally) distributed random number around a mean value of 0. The amount can be configured by means of the Standard Deviation (SD) σ_{noise}, which also directly gives the noise variance [107, p. 464]

$$\mathrm{Var}\,(v) = {\sigma_{noise}}^2 \tag{2.55}$$

with respect to the sensor noise v.
Furthermore, before being processed by Eq. (2.54), the clean system output y_s can be delayed by $T_{D,sensor}$. This creates the possibility to consider e.g. computational delay or additional delay induced by a failure. Additionally, the amount of the delay can be configured to vary with the inverse sample rate of the sensor $T_{s,sensor} = \frac{1}{f_{s,sensor}}$ with a definable probability. This way, the effect of random jitter can be applied on the signal,

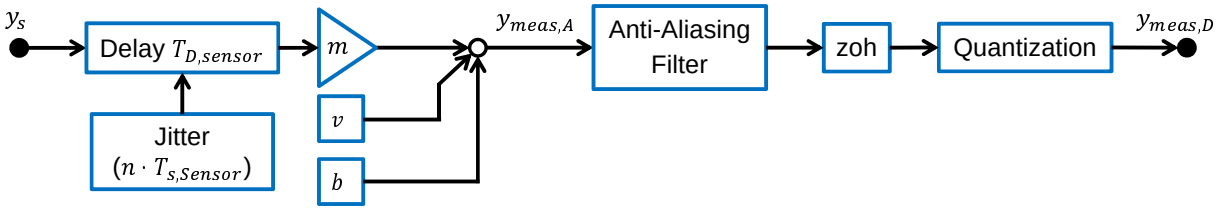

Figure 2.11. – Structure of the sensor model

Table 2.6. – Sensor model configuration for the standard test case

	α	n_z	q	$\dot{q}$	η	$\bar{q}$
Sample Rate $f_{s,sensor}$	100 Hz	200 Hz	200 Hz	200 Hz	50 Hz	100 Hz
Bias b	0.2°	0.03	$0\frac{^\circ}{s}$	$0\frac{^\circ}{s^2}$	0.1°	$0\frac{N}{m^2}$
Scale Factor m	1.01	1.02	0.99	0.99	1.01	0.98
Noise SD σ_{noise} [137]	0.2°	0.1524	$0.08\frac{^\circ}{s}$	$0.1\frac{^\circ}{s^2}$	0.1°	$478.81\frac{N}{m^2}$
Delay T_D	0s	0s	0s	0s	0s	0s
Signal length n_{Bit}	12 bit	12 bit	12 bit	12 bit	12 bit	12 bit
Voltage $[V_{min}; V_{max}]$	$[0V; 5V]$	$[0V; 5V]$	$[0V; 5V]$	$[0V; 5V]$	$[0V; 5V]$	$[0V; 5V]$
Limits	$\pm 20^\circ$	± 10	$\pm 30\frac{^\circ}{s}$	$\pm 1000\frac{^\circ}{s}$	$\pm 30^\circ$	$[0;\ 3 \cdot 10^4]\ \frac{N}{m^2}$

as it could appear due to errors within the signal transfer between sensor and FCS e.g. due to wrong time stamp assignment. For the simulation assessments within this thesis, jitter is configured to appear as a decrease of the delay by one time step $T_{s,sensor}$ with a probability of 5% each simulation step. Likewise, the delay can be increased with the same probability, but in this case the amount can be $n_{jitter} \cdot T_{s,sensor}$, where $n_{jitter} \in [1 \dots 3]$ is a random integer.

For measurements performed by the ADS, which are angle of attack α and dynamic pressure $\bar{q}$ in this case, additional lag is introduced. This is done by application of a second order low-pass filter [75, pp. 295-306]

$$G_{ADS,lag}(s) = \frac{{\omega_{0,ADS}}^2}{s^2 + 2\zeta_{ADS}\omega_{0,ADS} \cdot s + {\omega_{0,ADS}}^2}, \tag{2.56}$$

where $\omega_{0,ADS} = 4.8Hz$ and $\zeta_{ADS} = \frac{\sqrt{2}}{2}$ [9], on the signal y_s, before it enters the sensor model shown in Fig. 2.11. Note that the value for $\omega_{0,ADS}$ might be conservative for a fighter aircraft, because [9] deals with the controller design for a business jet class aircraft.

In the next step, the analog, continuous signal $y_{meas,A}$ is converted to a digital, discrete signal $y_{meas,D}$ having the sample rate $f_{s,sensor}$. For this purpose, a Analogue-to-Digital converter (ADC) model is implemented. In order to take account of the Sampling Theorem by Nyquist and Shannon [106, p. 28], the signal is low-pass filtered by means of a 2nd order butterworth filter [106, p. 717-719]

$$G_{aa}(s) = \frac{{\omega_{0,aa}}^2}{s^2 + \sqrt{2}\omega_{0,aa} \cdot s + {\omega_{0,aa}}^2} \tag{2.57}$$

at first, before the actual conversion takes place. The filter bandwidth is set to $\omega_{0,aa} = \frac{1}{3} f_{s,sensor} \cdot 2\pi$, where the conversion from Hz to $\frac{rad}{s}$ is considered by means of the factor 2π. Consequently, signal content above the Nyquist frequency $\omega_0 > 0.5 f_{s,sensor}$ gets sufficiently attenuated in order to avoid aliasing, in this case the attenuation is around $-7.5dB$ at the Nyquist frequency.

$y_{meas,A}$ is then discretized by means of an ideal sampler. It consists of a Zero-Order-Hold (zoh) element, which operates with the sample rate $f_{s,sensor}$ [127]. $y_{meas,D}$ is set to the value of $y_{meas,A}$ at every discrete time-step of the measurement processing, while it is held constant for the remaining time $T_{s,sensor}$. This is considered as a quantization of the signal with respect to the time axis.

Furthermore, ADC causes a quantization with respect to the actual value of the signal, too [33]. This is due to a finite digital resolution applied during sampling of the analogue signal, which is usually physically defined by a certain voltage $V \in [V_{min}; V_{max}]$. The digital resolution is defined in terms of the bit length n_{Bit} in Bit, therefore $2^{n_{Bit}}$ possible digital output codes exist. The following steps show the modelling of the described sensor effect based on an approach integrated in [80],

where the block utilized for the implementation of the digital quantizing effect is called "Idealized ADC quantizer".
At first, the signal obtained from the zoh-processing y is converted to a suitable voltage V considering both bounds on the signal y_{max}, y_{min} and voltage V_{max}, V_{min}:

$$V = V_{max}\frac{y - y_{min}}{y_{max} - y_{min}} + V_{min} \tag{2.58}$$

Now, the range between V_{min} and V_{max} is subdivided into $2^{n_{Bit}} - 1$ intervals of equal size [80]

$$LSB = \frac{V_{max} - V_{min}}{2^{n_{Bit}}}, \tag{2.59}$$

where the Least Significant Bit (LSB) is the smallest change in signal to be detected by the ADC in dependence of the chosen signal length n_{Bit}. A change in signal is detected, if the signal crosses the center of one of this intervals. This algorithm is expressed by means of the formula [80]

$$V_{bit} = \text{floor}\left\{\frac{1}{LSB} \cdot [\text{sat}\,(V) - V_{min}] + 0.5\right\} \tag{2.60}$$

using the limiting function

$$\text{sat}\,(u) = \begin{cases} u & \text{if } u_{min} < u < u_{max} \\ u_{max} & \text{if } u \geq u_{max} \\ u_{min} & \text{if } u \leq u_{min} \end{cases} \tag{2.61}$$

with the lower limit $u_{min} = V_{min}$ and the upper limit $u_{max} = V_{max} - \frac{3}{2} \cdot LSB$. Here, the round function floor (x) is used, which rounds x down to the next integer value. While Eq. (2.60) translates V_{min} to 0, V_{max} on the other hand cannot be exactly mapped to an integer within the defined range, because the upper bound of the integer value V_{bit} is $2^{n_{Bit}} - 1$. This is the reason, why the upper limit of $u_{max} = V_{max} - \frac{3}{2} \cdot LSB$ has to be applied for the saturation function included in Eq. (2.60), where the threshold 0.5 is additionally taken into account.
Using the integer V_{bit}, which is calculated according to Eq. (2.60), the quantized measurement $y_{meas,D}$ can be obtained from

$$y_{meas,D} = \frac{y_{max} - y_{min}}{2^{n_{Bit}}} \cdot V_{bit} + y_{min}. \tag{2.62}$$

Fig. 2.12 contains the simulation plot of an exemplary signal $u_{original}$, in order to illustrate the effect of quantization. Two quantizations $y_{quant,2bit}$ and $y_{quant,12bit}$ are shown, which differ in terms of the applied bit length n_{Bit}. In particular, the $n_{Bit} = 2Bit$ case reveals that the quantized signal never reaches y_{max}. This is due to the fact that

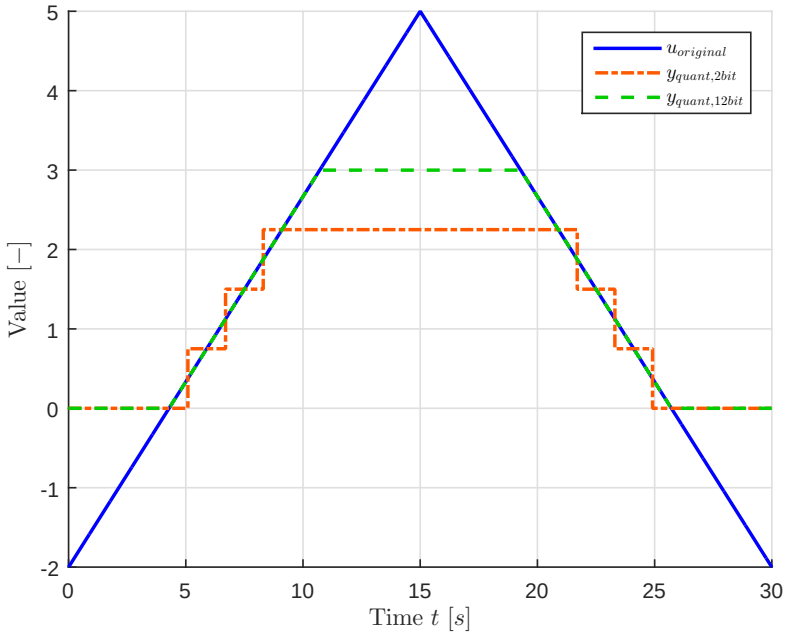

Figure 2.12. – Example for signal quantizations with $V_{min} = 0$, $V_{max} = 4$, $y_{min} = 0$ and $y_{max} = 3$ considering the bit lengths $n_{Bit} = 2Bit$ and $n_{Bit} = 12Bit$,

there exists no corresponding integer V_{bit} for the maximum voltage V_{max}, as it was discussed above. Furthermore, the maximum value of V_{bit} is $2^{n_{Bit}} - 1$. The maximum achievable measurement value can then be calculated according to Eq. (2.62) and results in

$$\begin{aligned} y_{meas,D,max} &= \frac{y_{max} - y_{min}}{2^{n_{Bit}}} \cdot (2^{n_{Bit}} - 1) + y_{min} \\ &= y_{max} \underbrace{- \frac{y_{max} - y_{min}}{2^{n_{Bit}}}}_{=:\Delta y_{max}} . \end{aligned} \tag{2.63}$$

Thus, the error $|\Delta y_{max}|$ decreases with increasing bit length, which can also be seen in Fig. 2.12. For the $n_{Bit} = 2Bit$ case, Δy_{max} results in -0.75, whereas for $n_{Bit} = 12Bit$ a difference of $\Delta y_{max} = -7.32 \cdot 10^{-4}$ can be achieved. It should be noted that $n_{Bit} = 12Bit$ is used for the sensor measurements delivered by the enhanced aircraft model.

2.7. Structural Mode

With the intention to induce another physically motivated, dynamical disturbance to the aircraft model, the simplified effect of the first structural wing bending mode is taken into account. An approach as presented in [139] is used for the implementation. The mode is modeled as an additional low-damped 2nd order low-pass filter applied to the system output signal. Thus, the plant output signal with additional dynamics y_s is expressed as

$$y_s = [1 - G_s(s)] \cdot y \tag{2.64}$$

with the unprocessed plant output y and the transfer function $G_s(s)$ being defined as

$$G_s(s) = \frac{s^2 + 2\zeta_s\omega_{0,s} \cdot s}{s^2 + 2\zeta_s\omega_{0,s} \cdot s + {\omega_{0,s}}^2}. \tag{2.65}$$

The implementation can also be seen in Fig. 2.14. For the structural mode a natural frequency $\omega_{0,s} = 6.05Hz \equiv 38.01\frac{rad}{s}$ is chosen[4] and the relative damping is set to $\zeta_s = 0.05$. This leads to an amplification of the area around $\omega_{0,s}$ and phase-loss, which can be clearly seen in the corresponding bode plot [14] [75, pp. 246-248] Fig. 2.13. The dynamical disturbance is applied to the system outputs angle of attack α, load factor n_z, pitch rate q and pitch acceleration $\dot{q}$.

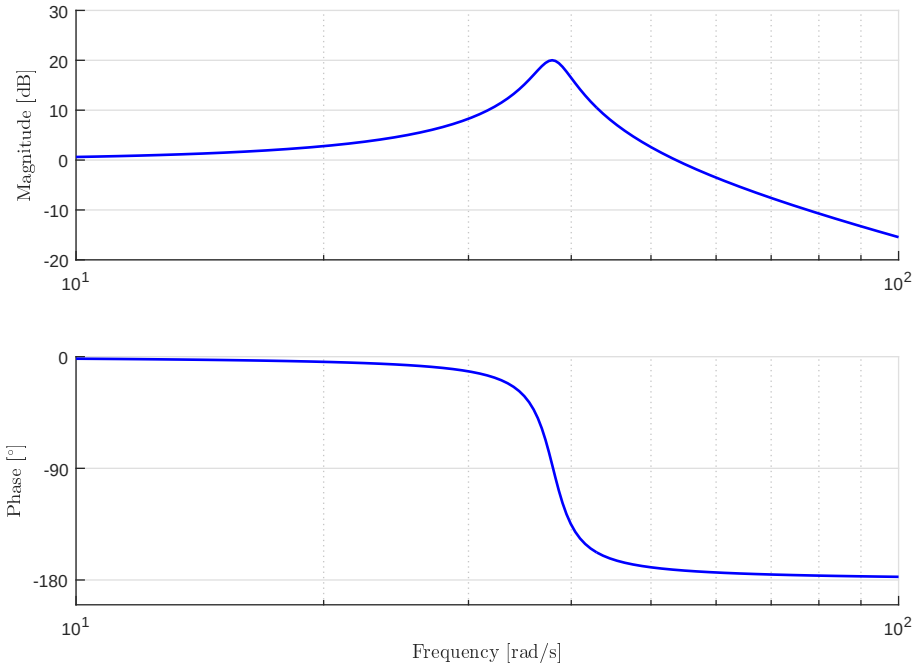

Figure 2.13. – Bode plot of transfer function $1 - G_s(s)$

[4]For the sake of comparison: the short-period frequency of the closed-loop system is $\omega_{0,sp} \leq 2Hz$

It must be noted that it is not claimed that this approach represents a proper modeling of aircraft aeroelastics. On the one hand, an aircraft inherits an infinite number of structural modes, of which usually more than one are to be considered w.r.t. the controller design. On the other hand, the calculation of additional forces and moments, depending on the aircraft states, would be required to implement an aeroelastic model. This leads to coupling of rigid and flexible aircraft modes [32]. It is not straight forward to gain those relations from a structural model of the aircraft and to integrate them into the aircraft model, see e.g. [113, 126, 5, 44]. An exemplary approximation of the lateral dynamics of an aircraft coupled with four structural modes can be found in [30, pp. 182-188].

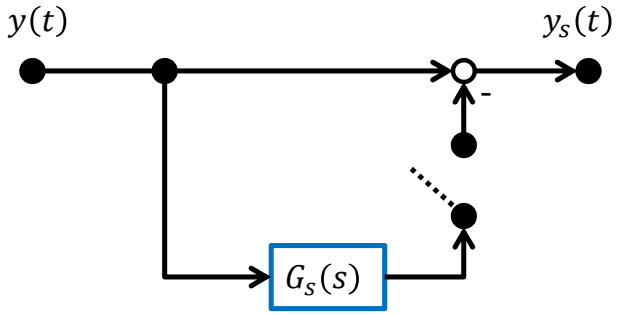

Figure 2.14. – Implementation of simple structural mode model according to Eq. (2.64)

3. Control Theory

This chapter presents the theoretical foundation underlying the control laws, which are designed in Chapter 4. This includes first a description of the Eigenstructure Assignment algorithm. Eigenstructure Assignment is a systemic gain design approach for linear, MIMO output feedback controllers with the goal to precisely adjust the eigendynamics of the system to be controlled. The second part of this chapter shows the elements of a L1 adaptive controller. Here, the idea of piecewise constant update laws for uncertainty estimation, as well as the connection between controller sample time and adaptation performance is explained visually. The last section briefly introduces discrete-time systems by means of the z-transformation and presents two methods, how to transform continuous-time systems into a discrete-time representation.

3.1. Eigenstructure Assignment

From the 1970ies until the mid-1980ies, Eigenstructure Assignment was developed as an enhancement of Pole Placement for MIMO systems [16, p. 545]. It can be read in [16] that it has its roots in investigations made by Moore in [84]. Specifically in aircraft applications, it is often used for the design of the lateral controller due to its capability to systematically and automatically calculate gains suiting the requirements on eigenvalues and to ensure decoupling of eigenmotions for MIMO systems. Successful applications can be found in [37, 54, 47, 110, 70] amongst others.
In this section, the theory of Eigenstructure Assignment is explained in terms of sketching the general idea and summarizing all necessary steps for a practical application following the comprehensions made in [54, 47, 50]. A more detailed description of the theory can be found e.g. in [34, pp. 49-87] [122, pp. 387-397].
Generally, the design model can be written as a linear state space model without feedthrough[1] [76, p. 16]

$$\dot{\boldsymbol{x}}(t) = \boldsymbol{A}\boldsymbol{x}(t) + \boldsymbol{B}\boldsymbol{u}(t) \tag{3.1a}$$

$$\boldsymbol{y}(t) = \boldsymbol{C}\boldsymbol{x}(t). \tag{3.1b}$$

[1] For a linear state-space model a feedthrough exists, if the input has a direct impact on the output of the system without having to pass an integrator. The output equation with feedthrough would read $\boldsymbol{y}(t) = \boldsymbol{C}\boldsymbol{x}(t) + \boldsymbol{D}\boldsymbol{u}(t)$. [76, p. 16]

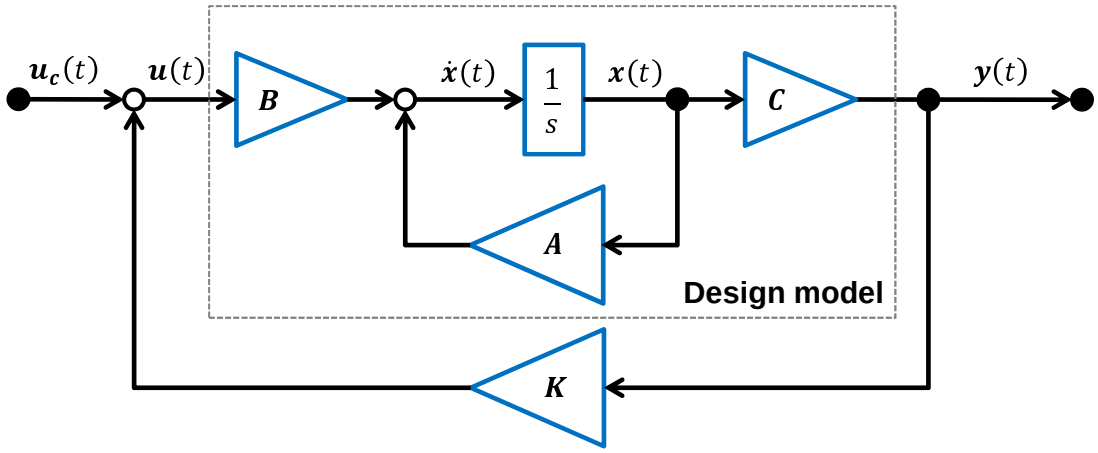

Figure 3.1. – Structural overview of the closed-loop considered for the Eigenstructure Assignment

The system matrix $\boldsymbol{A}$ is of dimension $(n \times n)$, the dimension of the full rank input matrix $\boldsymbol{B}$ is set as $(n \times m)$ and the output matrix $\boldsymbol{C}$ has the dimension $(r \times n)$. That means the system has n states, m linear independent inputs and r measurable outputs. The control law is conducted as [54]

$$\boldsymbol{u} = -\boldsymbol{K}\boldsymbol{y} + \boldsymbol{u}_c\,(t) \tag{3.2}$$

with an output feedback and a feedforward path $\boldsymbol{u}_c\,(t)$. Plugging the control law Eq. (3.2) into the model Eq. (3.1) results in the closed-loop [54]

$$\dot{\boldsymbol{x}}\,(t) = \underbrace{(\boldsymbol{A} - \boldsymbol{B}\boldsymbol{K}\boldsymbol{C})}_{\boldsymbol{A}^*}\boldsymbol{x}\,(t) + \boldsymbol{B}\boldsymbol{u}_c\,(t)\,, \tag{3.3}$$

where $\boldsymbol{A}^*$ is the closed-loop system matrix. This is also illustrated in Fig. 3.1. The task is now to determine the feedback matrix $\boldsymbol{K}$ in such a way that $\boldsymbol{A}^*$ has desired eigenvalues λ^* and eigenvectors $\boldsymbol{v}^*$. Considering one pair consisting of eigenvalue and corresponding eigenvector, it can be stated according to their definition that [107, p. 95]

$$\lambda_i^* \boldsymbol{v}_i^* = \boldsymbol{A}^* \boldsymbol{v}_i^*. \tag{3.4}$$

Using the definition of $\boldsymbol{A}^*$ from Eq. (3.3) results in the intermediate step

$$(\lambda_i^* \boldsymbol{I}_{n\times n} - \boldsymbol{A} + \boldsymbol{B}\boldsymbol{K}\boldsymbol{C})\,\boldsymbol{v}_i^* = \boldsymbol{0}, \tag{3.5}$$

which can be further rearranged to [54]

$$\begin{pmatrix}\lambda_i^* \boldsymbol{I}_{n\times n} - \boldsymbol{A} & \boldsymbol{B}\end{pmatrix}\begin{pmatrix}\boldsymbol{v}_i^* \\ \boldsymbol{z}_i^*\end{pmatrix} = \boldsymbol{0} \tag{3.6}$$

with

$$\boldsymbol{z}_i^* = \boldsymbol{K}\boldsymbol{C}\boldsymbol{v}_i^*. \tag{3.7}$$

The matrix $\begin{pmatrix}\lambda_i^*\boldsymbol{I}_{n\times n} - \boldsymbol{A} & \boldsymbol{B}\end{pmatrix}$ is of dimension $(n \times (n+m))$ and has a maximum of n linear independent column vectors. If λ_i^* is not an eigenvalue of $\boldsymbol{A}$ and $\boldsymbol{A}$ has full rank, then exactly n linear independent column vectors exist and thus, the span of the matrix is n-dimensional. This means that m vectors exist, which define the m-dimensional kernel of the matrix. The kernel of a matrix is a space that contains all vectors, whose linear combinations are projected onto the null-vector by this matrix. Exactly such a solution is required for Eq. (3.6), therefore $\begin{pmatrix}\boldsymbol{v}^* \\ \boldsymbol{z}^*\end{pmatrix}$ has to lie in the null space of the matrix $\begin{pmatrix}\lambda_i^*\boldsymbol{I}_{n\times n} - \boldsymbol{A} & \boldsymbol{B}\end{pmatrix}$, in order to produce a non-zero, i.e. nontrivial, solution of Eq. (3.6).
The basis vectors $\bar{\boldsymbol{n}}_i$ of the null space belonging to the matrix $\begin{pmatrix}\lambda_i^*\boldsymbol{I}_{n\times n} - \boldsymbol{A} & \boldsymbol{B}\end{pmatrix}$ can be summarized in

$$\bar{\boldsymbol{N}} = \begin{pmatrix}\bar{\boldsymbol{n}}_1 & \cdots & \bar{\boldsymbol{n}}_m\end{pmatrix}, \tag{3.8}$$

which is of dimension $((n+m) \times m)$ and can be further subdivided into [54]

$$\bar{\boldsymbol{N}} = \begin{pmatrix}\boldsymbol{N} \\ \hat{\boldsymbol{N}}\end{pmatrix} = \begin{pmatrix}\boldsymbol{n}_1 & \cdots & \boldsymbol{n}_m \\ \hat{\boldsymbol{n}}_1 & \cdots & \hat{\boldsymbol{n}}_m\end{pmatrix}, \tag{3.9}$$

where $\boldsymbol{n}_i$ has the dimension $(n \times 1)$ and $\hat{\boldsymbol{n}}_i$ the dimension $(m \times 1)$, respectively. As it was stated above, any achievable solution $\begin{pmatrix}\boldsymbol{v}_i^* \\ \boldsymbol{z}_i^*\end{pmatrix}$ can be generally described as linear combination of these basis vectors of the null space [54]:

$$\begin{pmatrix}\boldsymbol{v}_i^* \\ \boldsymbol{z}_i^*\end{pmatrix} = \bar{\boldsymbol{N}} \cdot \boldsymbol{l}_i = \begin{pmatrix}\boldsymbol{N} \\ \hat{\boldsymbol{N}}\end{pmatrix} \boldsymbol{l}_i \tag{3.10}$$

Here, $\boldsymbol{l}_i$ is a parameter vector, which has to be determined in such a way, that

$$\boldsymbol{v}_i^* = \boldsymbol{N} \cdot \boldsymbol{l}_i \tag{3.11}$$

equals to the desired eigenvector.
In general $s \leq n$ values of the eigenvector are relevant to be set by the controller designer. For that reason, one prioritizes the choice of vector elements. This is done by means of a sorting matrix $\boldsymbol{P}_i$, which shifts s entries of the eigenvector to be specified $\boldsymbol{v}_i^s$ to the top and the remaining ones $\boldsymbol{v}_i^u$ to the bottom of the vector [54]:

$$\begin{pmatrix}\boldsymbol{v}_i^s \\ \boldsymbol{v}_i^u\end{pmatrix} = \boldsymbol{P}_i \cdot \boldsymbol{v}_i^* = \begin{pmatrix}\boldsymbol{P}_i^s \\ \boldsymbol{P}_i^u\end{pmatrix} \boldsymbol{v}_i^* \tag{3.12}$$

For the next step Eq. (3.11) is plugged into the equation for $\boldsymbol{v}_i^s$ contained in Eq. (3.12):

$$\boldsymbol{v}_i^s = \boldsymbol{P}_i^s \cdot \boldsymbol{N} \cdot \boldsymbol{l}_i \tag{3.13}$$

The goal is to determine $\boldsymbol{l}_i$ such, that in the end $\boldsymbol{v}_i^s$ contains the desired, specifiable eigenvector values. Since the eigenvector $\boldsymbol{v}_i^*$ has n components of which s are chosen via inclusion in $\boldsymbol{v}_i^s$, the matrix $\boldsymbol{P}_i^s$ has to be of dimension $(s \times n)$. From Eq. (3.9) it is clear that $\boldsymbol{N}$ has the dimension $(n \times m)$. Thus, the product [54]

$$\boldsymbol{N}^s = \boldsymbol{P}_i^s \cdot \boldsymbol{N} \tag{3.14}$$

has a dimension of $(s \times m)$. That means $\boldsymbol{N}^s$ is only invertible in case the number of specified eigenvector values s equals the number of linearly independent system inputs m. Therefore, Eq. (3.13) can only be solved directly with respect to the parameter vector $\boldsymbol{l}_i$, if $s = m$ holds [54]:

$$\boldsymbol{l}_i = \underbrace{\left(\boldsymbol{P}_i^s \cdot \boldsymbol{N}\right)^{-1}}_{\left(\boldsymbol{N}^s\right)^{-1}} \cdot \boldsymbol{v}_i^s. \tag{3.15}$$

In case $s > m$ is required for the controller design, one has to calculate the pseudoinverse $\left(\boldsymbol{N}^s\right)^+$ of $\boldsymbol{N}^s$ in order to obtain suitable $\boldsymbol{l}_i$. This can be derived by multiplying the hermitian adjoint $\left(\boldsymbol{N}^s\right)^H$ $(m \times s)$ to the left side of Eq. (3.13). In combination with Eq. (3.14), the result reads

$$\left(\boldsymbol{N}^s\right)^H \boldsymbol{v}_i^s = \left(\boldsymbol{N}^s\right)^H \boldsymbol{N}^s \boldsymbol{l}_i. \tag{3.16}$$

Now Eq. (3.16) can be solved with respect to

$$\boldsymbol{l}_i = \underbrace{\left(\left(\boldsymbol{N}^s\right)^H \boldsymbol{N}^s\right)^{-1} \left(\boldsymbol{N}^s\right)^H}_{\left(\boldsymbol{N}^s\right)^+} \cdot \boldsymbol{v}_i^s, \tag{3.17}$$

where

$$\left(\boldsymbol{N}^s\right)^+ = \left(\left(\boldsymbol{N}^s\right)^H \boldsymbol{N}^s\right)^{-1} \left(\boldsymbol{N}^s\right)^H \tag{3.18}$$

is the definition of the pseudoinverse of $\boldsymbol{N}^s$ [107, p. 98]. The drawback of a choice $s > m$ is loss of preciseness due to application of the pseudoinverse [3]. In consequence it is not possible to specify every single entry of this vector e.g. for aircraft applications exactly, where usually $n > m$ holds. In order to balance this problem, one can add a diagonal matrix $\boldsymbol{Q}_i^s$ $(s \times s)$ to Eq. (3.16) to be able to weight certain values of the specified part of the eigenvector [54]:

$$\left(\boldsymbol{N}^s\right)^H \boldsymbol{Q}_i^s \boldsymbol{v}_i^s = \left(\boldsymbol{N}^s\right)^H \boldsymbol{Q}_i^s \boldsymbol{N}^s \boldsymbol{l}_i \tag{3.19}$$

The solution for the parameter vector is then given by [54]

$$\boldsymbol{l}_i = \left(\left(\boldsymbol{N}^s\right)^H \boldsymbol{Q}_i^s \boldsymbol{N}^s \right)^{-1} \left(\boldsymbol{N}^s\right)^H \boldsymbol{Q}_i^s \cdot \boldsymbol{v}_i^s. \tag{3.20}$$

In a nutshell, during the controller design process the following steps have to be performed for every single eigenvalue λ_i^* and eigenvector $\boldsymbol{v}_i^*$ with $i = 1...r$ to be assigned. The number of assignable eigenvalues and eigenvectors is determined by the number r of available plant outputs.
At first, $\boldsymbol{l}_i$ is determined according to Eq. (3.15), Eq. (3.17) or Eq. (3.20) depending on the choice of s. Furthermore, the null space has also to be determined individually for every λ_i^* according to Eq. (3.8) and Eq. (3.9). Then $\boldsymbol{v}_i^*$ and $\boldsymbol{z}_i^*$ can be calculated by means of Eq. (3.10).
Using the solutions $\boldsymbol{v}_i^*$ and $\boldsymbol{z}_i^*$ with $i = 1...r$ finally $\boldsymbol{K}$ can be determined. For this, Eq. (3.7) is evaluated for every $\boldsymbol{v}_i^*$ and $\boldsymbol{z}_i^*$, which yields

$$\begin{aligned} \boldsymbol{z}_1^* &= \boldsymbol{K}\boldsymbol{C}\boldsymbol{v}_1^* \\ \boldsymbol{z}_2^* &= \boldsymbol{K}\boldsymbol{C}\boldsymbol{v}_2^* \\ &\vdots \\ \boldsymbol{z}_r^* &= \boldsymbol{K}\boldsymbol{C}\boldsymbol{v}_r^*. \end{aligned} \tag{3.21}$$

These equations can be summarized to one single matrix equation [54]

$$\begin{pmatrix} \boldsymbol{z}_1^* & \dots & \boldsymbol{z}_r^* \end{pmatrix} = \boldsymbol{K} \cdot \boldsymbol{C} \cdot \begin{pmatrix} \boldsymbol{v}_1^* & \dots & \boldsymbol{v}_r^* \end{pmatrix}, \tag{3.22}$$

where $\boldsymbol{C}$ has the dimension $(r \times n)$ and $\begin{pmatrix} \boldsymbol{v}_1^* & \dots & \boldsymbol{v}_r^* \end{pmatrix}$ is $(n \times r)$, since r eigenvectors have been assigned. In consequence, the product of these two matrices is also invertible, thus the gain matrix $\boldsymbol{K}$ can be directly calculated as [54]

$$\boldsymbol{K} = \begin{pmatrix} \boldsymbol{z}_1^* & \dots & \boldsymbol{z}_r^* \end{pmatrix} \left[\boldsymbol{C} \cdot \begin{pmatrix} \boldsymbol{v}_1^* & \dots & \boldsymbol{v}_r^* \end{pmatrix} \right]^{-1}. \tag{3.23}$$

3.2. L1 Adaptive Control with piecewise constant update laws

This section describes L1 Adaptive Control [59] with piecewise constant update laws. In order to highlight the necessary steps in terms of an implementation of the presented control methodology, the accompaying mathematical proofs with respect to theoretical error bounds are omitted in this thesis. Nevertheless, the interested reader may be referred to [59] in this matter.
Furthermore, this section concentrates on L1 Adaptive Control with piecewise constant update laws, as no integration-based update laws are used for the assessments within this thesis. Utilizing piecewise constant update laws the design results in a linear

control law [12]. An architectural overview is given in Fig. 3.2 and all main elements will be summarized subsequently.

Plant The plant dynamics to be controlled by the L1 adaptive controller can be modeled as [59, p. 159]

$$\dot{\boldsymbol{x}}(t) = \boldsymbol{A}_m \boldsymbol{x}(t) + \boldsymbol{B}_m \left[\boldsymbol{\Lambda} \cdot \boldsymbol{u}(t) + \boldsymbol{f}_m\left(t, \boldsymbol{x}(t), \boldsymbol{y}_z(t)\right)\right] + \boldsymbol{B}_{um} \boldsymbol{f}_{um}\left(t, \boldsymbol{x}(t), \boldsymbol{y}_z(t)\right) \tag{3.24a}$$

$$\dot{\boldsymbol{x}}_z(t) = \boldsymbol{f}_z\left(t, \boldsymbol{x}_z(t), \boldsymbol{x}(t)\right) \tag{3.24b}$$

$$\boldsymbol{y}_z(t) = \boldsymbol{g}_z\left(t, \boldsymbol{x}_z(t)\right) \tag{3.24c}$$

$$\boldsymbol{y}(t) = \boldsymbol{C}_m \boldsymbol{x}(t), \tag{3.24d}$$

where $\boldsymbol{A}_m$ $(n \times n)$, $\boldsymbol{B}_m$ $(n \times m)$ with $m \leq n$ and $\boldsymbol{C}_m$ $(r \times n)$ are known matrices describing the system dynamics by means of the system state $\boldsymbol{x}(t)$. $\boldsymbol{A}_m$ is Hurwitz and $\boldsymbol{C}_m$ only generates the r outputs to be tracked by the controller from the states $\boldsymbol{x}$. Additionally, no direct feedthrough exists from input to output. The system according to Eq. (3.24a) is both controllable and observable and its transmission zeros feature a negative real part i.e. the system is minimum phase[2]. The internal, unmodeled dynamics, which are Bounded-Input-Bounded-Output (BIBO) stable, are described by their state $\dot{\boldsymbol{x}}_z(t)$ and output $\boldsymbol{y}_z(t)$ vectors, as well as the nonlinear functions $\boldsymbol{f}_z$ and $\boldsymbol{g}_z$. A deviation of the known dynamics is taken into account through the unknown matched $\boldsymbol{f}_m\left(t, \boldsymbol{x}(t), \boldsymbol{y}_z(t)\right)$ and unmatched uncertainties $\boldsymbol{f}_{um}\left(t, \boldsymbol{x}(t), \boldsymbol{y}_z(t)\right)$, respectively. $\boldsymbol{f}_{um}\left(t, \boldsymbol{x}(t), \boldsymbol{y}_z(t)\right)$ enters the system through the unmatched input matrix $\boldsymbol{B}_{um}$, which is constructed such that $\boldsymbol{B}_m{}^T \boldsymbol{B}_{um} = 0$ holds and $\boldsymbol{B} = \begin{pmatrix}\boldsymbol{B}_m & \boldsymbol{B}_{um}\end{pmatrix}$ has maximal

[2] [6] features a solution to control non-minimum phase systems without neglecting compensation of unmatched uncertainties

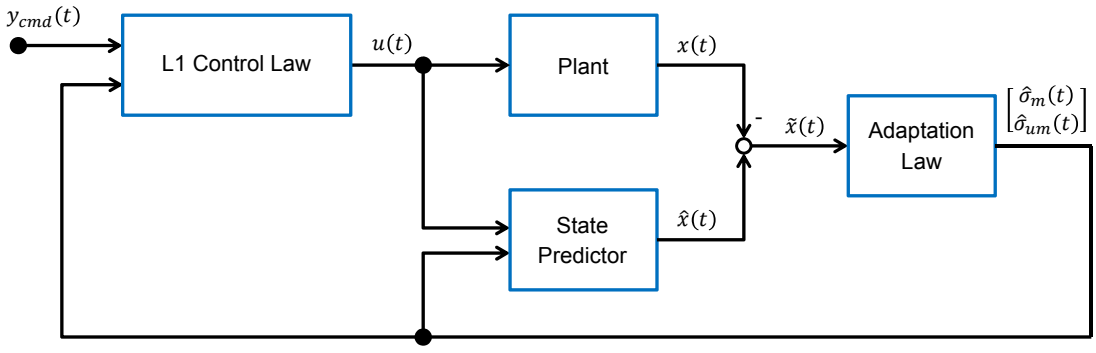

Figure 3.2. – Structural overview of a L1 adaptive controller with piecewise constant update laws

rank of n. The control signal $\boldsymbol{u}(t)$ is fed into the system with an unknown control efficiency $\boldsymbol{\Lambda}$, of which at least the sign has to be known.

State Predictor The desired dynamics to be reached by the closed-loop consisting of plant and L1 adaptive controller are reflected in the matrices $\boldsymbol{A}_m$ and $\boldsymbol{B}_m$. The State Predictor [59, p. 163]

$$\dot{\hat{\boldsymbol{x}}}(t) = \boldsymbol{A}_m \hat{\boldsymbol{x}}(t) + \boldsymbol{B}_m \left[\boldsymbol{\Lambda}_0 \cdot \boldsymbol{u}(t) + \hat{\boldsymbol{\sigma}}_m(t)\right] + \boldsymbol{B}_{um} \hat{\boldsymbol{\sigma}}_{um}(t) \tag{3.25a}$$

$$\hat{\boldsymbol{y}}(t) = \boldsymbol{C}_m \hat{\boldsymbol{x}}(t) \tag{3.25b}$$

parametrizes this desired behavior and via $\hat{\boldsymbol{\sigma}}_m(t)$ and $\hat{\boldsymbol{\sigma}}_{um}(t)$ the difference between desired and estimated, real dynamics. It has exactly the same structure as the formulation of the plant, but contains a constant, initial guess of the control effectiveness $\boldsymbol{\Lambda}_0$ and estimations of both the matched $\hat{\boldsymbol{\sigma}}_m(t)$ and the unmatched uncertainties $\hat{\boldsymbol{\sigma}}_{um}(t)$. The update laws for these estimated values are derived from the dynamics of the estimation error

$$\tilde{\boldsymbol{x}}(t) = \hat{\boldsymbol{x}}(t) - \boldsymbol{x}(t). \tag{3.26}$$

Note that $\boldsymbol{\Lambda}_0$ is not adapted in the applications shown in this thesis, thus an initial guess is used, which is usually $\boldsymbol{I}_{m\times m}$. The L1 Adaptive Control framework in general contains the possibility to adapt $\boldsymbol{\Lambda}_0$, but for this an integral update law has to be applied [59, pp. 37-60]. In order to keep the linear character of the control law, this is avoided here.

Error Dynamics A differential equation for the estimation error can be deduced by differentiation of $\tilde{\boldsymbol{x}}(t)$ in Eq. (3.26). Inserting plant Eq. (3.24a) and state predictor dynamics Eq. (3.25a) leads to [12, p. 285]

$$\begin{aligned}\dot{\tilde{\boldsymbol{x}}}(t) &= \dot{\hat{\boldsymbol{x}}}(t) - \dot{\boldsymbol{x}}(t) = \\ &= \boldsymbol{A}_m \tilde{\boldsymbol{x}} + \boldsymbol{B}_m \left[\hat{\boldsymbol{\sigma}}_m - \left(\boldsymbol{f}_m - \left(\boldsymbol{\Lambda}_0 - \boldsymbol{\Lambda}\right) \cdot \boldsymbol{u}\right)\right] + \boldsymbol{B}_{um}\left(\hat{\boldsymbol{\sigma}}_{um} - \boldsymbol{f}_{um}\right).\end{aligned} \tag{3.27}$$

The uncertainties stemming from a deviation of the real control effectiveness $\boldsymbol{\Lambda}$ and its initial guess $\boldsymbol{\Lambda}_0$ are lumped into

$$\boldsymbol{\sigma}_m := \left(\boldsymbol{f}_m - \left(\boldsymbol{\Lambda}_0 - \boldsymbol{\Lambda}\right) \cdot \boldsymbol{u}\right) \tag{3.28}$$

together with $\boldsymbol{f}_m$. Likewise, it holds that

$$\boldsymbol{\sigma}_{um} := \boldsymbol{f}_{um} \tag{3.29}$$

for the sake of consistent notation. The estimation errors, which quantify the difference between estimated and real uncertainties, can be defined as

$$\tilde{\boldsymbol{\sigma}}_{\boldsymbol{m}} = \hat{\boldsymbol{\sigma}}_{\boldsymbol{m}} - \boldsymbol{\sigma}_{\boldsymbol{m}} \tag{3.30a}$$

$$\tilde{\boldsymbol{\sigma}}_{\boldsymbol{um}} = \hat{\boldsymbol{\sigma}}_{\boldsymbol{um}} - \boldsymbol{\sigma}_{\boldsymbol{um}}. \tag{3.30b}$$

The definitions from Eqs. (3.28), (3.29), (3.30a) and (3.30b) can be used to simplify Eq. (3.27), which results in

$$\begin{aligned}\dot{\tilde{\boldsymbol{x}}}(t) &= \boldsymbol{A}_m\tilde{\boldsymbol{x}} + \boldsymbol{B}_{\boldsymbol{m}}\left(\hat{\boldsymbol{\sigma}}_{\boldsymbol{m}} - \boldsymbol{\sigma}_{\boldsymbol{m}}\right) + \boldsymbol{B}_{um}\left(\hat{\boldsymbol{\sigma}}_{\boldsymbol{um}} - \boldsymbol{\sigma}_{\boldsymbol{um}}\right) = \\ &= \boldsymbol{A}_m\tilde{\boldsymbol{x}} + \boldsymbol{B}_{\boldsymbol{m}}\tilde{\boldsymbol{\sigma}}_{\boldsymbol{m}} + \boldsymbol{B}_{um}\tilde{\boldsymbol{\sigma}}_{\boldsymbol{um}} \\ &= \boldsymbol{A}_m\tilde{\boldsymbol{x}} + \begin{pmatrix}\boldsymbol{B}_{\boldsymbol{m}} & \boldsymbol{B}_{um}\end{pmatrix}\begin{pmatrix}\tilde{\boldsymbol{\sigma}}_{\boldsymbol{m}} \\ \tilde{\boldsymbol{\sigma}}_{\boldsymbol{um}}\end{pmatrix}.\end{aligned} \tag{3.31}$$

Solving the ODE Eq. (3.31) for an arbitrary starting time t_0 leads to

$$\tilde{\boldsymbol{x}}(t_0 + t) = e^{\boldsymbol{A}_m t}\cdot\tilde{\boldsymbol{x}}(t_0) + \int_{t_0}^{t_0+t} e^{\boldsymbol{A}_m(t_0+t-\xi)}\boldsymbol{B}\begin{pmatrix}\tilde{\boldsymbol{\sigma}}_{\boldsymbol{m}}(\xi) \\ \tilde{\boldsymbol{\sigma}}_{\boldsymbol{um}}(\xi)\end{pmatrix}\,\mathrm{d}\xi \tag{3.32}$$

with $\boldsymbol{B} := \begin{pmatrix}\boldsymbol{B}_{\boldsymbol{m}} & \boldsymbol{B}_{um}\end{pmatrix}$. If the solution is considered for one discrete time step with sampling time T_s and the integral is transformed with $\epsilon = \xi - iT_s$, the equation becomes [12, p. 285]

$$\begin{aligned}\tilde{\boldsymbol{x}}(iT_s + T_s) = e^{\boldsymbol{A}_m T_s}\cdot\tilde{\boldsymbol{x}}(iT_s) &+ \int_0^{T_s} e^{\boldsymbol{A}_m(T_s-\epsilon)}\boldsymbol{B}\begin{pmatrix}\hat{\boldsymbol{\sigma}}_{\boldsymbol{m}}(iT_s+\epsilon) \\ \hat{\boldsymbol{\sigma}}_{\boldsymbol{um}}(iT_s+\epsilon)\end{pmatrix}\,\mathrm{d}\epsilon \\ &- \int_0^{T_s} e^{\boldsymbol{A}_m(T_s-\epsilon)}\boldsymbol{B}\begin{pmatrix}\boldsymbol{\sigma}_{\boldsymbol{m}}(iT_s+\epsilon) \\ \boldsymbol{\sigma}_{\boldsymbol{um}}(iT_s+\epsilon)\end{pmatrix}\,\mathrm{d}\epsilon,\end{aligned} \tag{3.33}$$

where Eq. (3.30a) and Eq. (3.30b) are plugged in and $i \in \mathbb{N}_0$. The idea of the piecewise constant update law is to define the estimations $\hat{\boldsymbol{\sigma}}_{\boldsymbol{m}}$ and $\hat{\boldsymbol{\sigma}}_{\boldsymbol{um}}$ as constant between two discrete time steps and to use them, in order to fully cancel the propagation of the previous error $e^{\boldsymbol{A}_m T_s}\cdot\tilde{\boldsymbol{x}}(iT_s)$ at every discrete time step. Thus, the uncertainty estimations must satisfy [12, p. 286]

$$e^{\boldsymbol{A}_m T_s}\cdot\tilde{\boldsymbol{x}}(iT_s) + \int_0^{T_s} e^{\boldsymbol{A}_m(T_s-\epsilon)}\boldsymbol{B}\begin{pmatrix}\hat{\boldsymbol{\sigma}}_{\boldsymbol{m}}(iT_s) \\ \hat{\boldsymbol{\sigma}}_{\boldsymbol{um}}(iT_s)\end{pmatrix}\,\mathrm{d}\epsilon \overset{!}{=} 0. \tag{3.34}$$

Nevertheless, Eq. (3.33) indicates that uncertainties accumulate further between two discrete time steps despite this cancellation. The residual error is discussed in the remainder of this section and can be found in Eq. (3.40).
Because of the constant matrix $\boldsymbol{A}_m$ and the piecewise constant definition of $\hat{\boldsymbol{\sigma}}_{\boldsymbol{m}}$ and $\hat{\boldsymbol{\sigma}}_{\boldsymbol{um}}$ the integral in Eq. (3.34) has the solution [12, p. 286]

$$\int_0^{T_s} e^{\boldsymbol{A}_m(T_s-\epsilon)}\boldsymbol{B}\begin{pmatrix}\hat{\boldsymbol{\sigma}}_{\boldsymbol{m}}\left(iT_s\right)\\ \hat{\boldsymbol{\sigma}}_{\boldsymbol{um}}\left(iT_s\right)\end{pmatrix}\,\mathrm{d}\epsilon = \left[-{\boldsymbol{A}_m}^{-1}e^{\boldsymbol{A}_m(T_s-\epsilon)}\boldsymbol{B}\begin{pmatrix}\hat{\boldsymbol{\sigma}}_{\boldsymbol{m}}\left(iT_s\right)\\ \hat{\boldsymbol{\sigma}}_{\boldsymbol{um}}\left(iT_s\right)\end{pmatrix}\right]_0^{T_s}. \tag{3.35}$$

Thus, Eq. (3.34) can be formulated according to

$$e^{\boldsymbol{A}_m T_s}\cdot\tilde{\boldsymbol{x}}\left(iT_s\right) - {\boldsymbol{A}_m}^{-1}\boldsymbol{B}\begin{pmatrix}\hat{\boldsymbol{\sigma}}_{\boldsymbol{m}}\left(iT_s\right)\\ \hat{\boldsymbol{\sigma}}_{\boldsymbol{um}}\left(iT_s\right)\end{pmatrix} + {\boldsymbol{A}_m}^{-1}e^{\boldsymbol{A}_m T_s}\boldsymbol{B}\begin{pmatrix}\hat{\boldsymbol{\sigma}}_{\boldsymbol{m}}\left(iT_s\right)\\ \hat{\boldsymbol{\sigma}}_{\boldsymbol{um}}\left(iT_s\right)\end{pmatrix} \stackrel{!}{=} 0, \tag{3.36}$$

which can be further rearranged resulting in [12, p. 286]

$$e^{\boldsymbol{A}_m T_s}\cdot\tilde{\boldsymbol{x}}\left(iT_s\right) + {\boldsymbol{A}_m}^{-1}\left(e^{\boldsymbol{A}_m T_s} - \boldsymbol{I}_{n\times n}\right)\boldsymbol{B}\begin{pmatrix}\hat{\boldsymbol{\sigma}}_{\boldsymbol{m}}\left(iT_s\right)\\ \hat{\boldsymbol{\sigma}}_{\boldsymbol{um}}\left(iT_s\right)\end{pmatrix} \stackrel{!}{=} 0. \tag{3.37}$$

Parameter Update Law In order to finally obtain the parameter update Law, Eq. (3.37) has to be solved w.r.t. $\hat{\sigma}_m$ and $\hat{\sigma}_{um}$. This leads to [59, pp. 162-163]

$$\begin{pmatrix}\hat{\boldsymbol{\sigma}}_{\boldsymbol{m}}\left(t\right)\\ \hat{\boldsymbol{\sigma}}_{\boldsymbol{um}}\left(t\right)\end{pmatrix} = \boldsymbol{K_{L1}}\left(T_s\right)\tilde{\boldsymbol{x}}\left(iT_s\right) \quad \forall t\in\left[iT_s,\left(i+1\right)T_s\right], \tag{3.38}$$

where

$$\boldsymbol{K_{L1}}\left(T_s\right) = -\boldsymbol{B}^{-1}\left(e^{\boldsymbol{A}_m T_s} - \boldsymbol{I}_{n\times n}\right)^{-1}\boldsymbol{A}_m e^{\boldsymbol{A}_m T_s} \tag{3.39}$$

only depends on the sampling time T_s besides the known desired system dynamics. As T_s is constant, the parameter update law results in a linear feedback of the sampled estimation error $\tilde{\boldsymbol{x}}\left(t\right)$ via the gain $\boldsymbol{K_{L1}}$.
Applying the parameter update law Eq. (3.38), the estimation error $\tilde{\boldsymbol{x}}\left(iT_s+T_s\right)$ according to Eq. (3.33) yields [12, p. 286]

$$\tilde{\boldsymbol{x}}\left(iT_s+T_s\right) = -\int_0^{T_s} e^{\boldsymbol{A}_m(T_s-\epsilon)}\boldsymbol{B}\begin{pmatrix}\sigma_{\boldsymbol{m}}\left(iT_s+\epsilon\right)\\ \sigma_{\boldsymbol{um}}\left(iT_s+\epsilon\right)\end{pmatrix}\,\mathrm{d}\epsilon. \tag{3.40}$$

Thus, the remaining estimation error only consists of uncertainties accumulated between two discrete computational steps. The basic idea underlying the piecewise constant update law and its effect on the evolution of the estimation error is also qualitatively illustrated in Fig. 3.3. The red dashed-dotted lines mark the effect of the update law. It generates parameter estimations that would drive the estimation error to zero within two sample points. But during this time span new uncertainties appear, which leads to an increase of the estimation error marked by the green dashed lines. These two effects sum up to the total estimation error shown in blue. It should be noticed that the functional progressions are chosen to be linear only for the sake of simplified depiction.
Having this mechanism in mind it becomes clear, why a decrease in sampling time T_s leads to a decrease of the maximum estimation error. This is shown in Fig. 3.4,

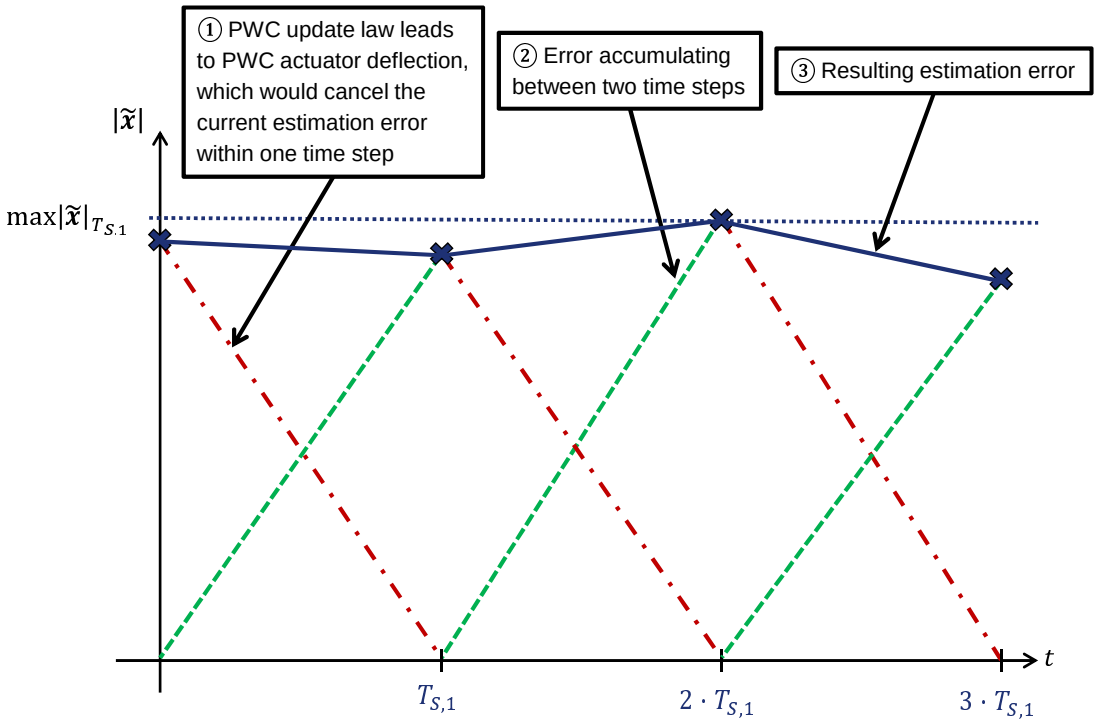

Figure 3.3. – Qualitative illustration of the estimation error $\tilde{x}(t)$ development due to applications of piecewise constant parameter update law

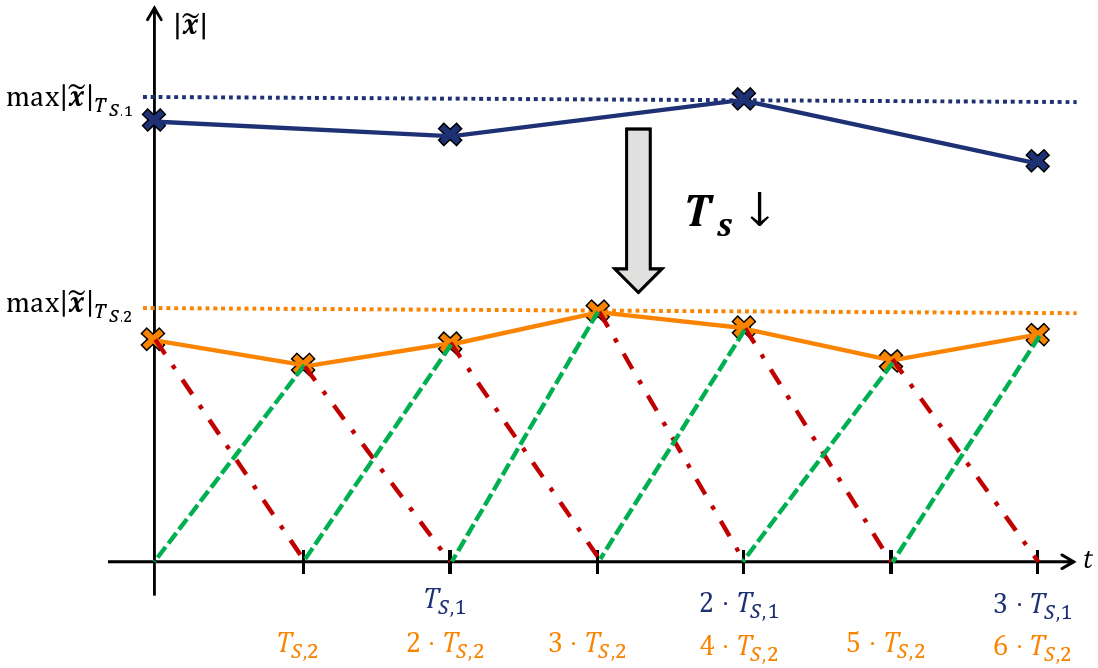

Figure 3.4. – Qualitative illustration of the estimation error $\tilde{x}(t)$ development for two different sample times $T_{s,1}$ and $T_{s,2}$

where $T_{s,2} = 0.5 \cdot T_{s,1}$. The shorter the update intervals are, i.e. the smaller T_s is, the less estimation error can accumulate during two time steps. On the other hand, the determined estimation error also has to be compensated in a shorter time interval, which reveals an increase of the adaptation gain $\boldsymbol{K_{L1}}(T_s)$. This can also be shown by means of

$$\lim_{T_s \to 0} \boldsymbol{K_{L1}}(T_s) = \lim_{T_s \to 0} -\boldsymbol{B}^{-1} \left(e^{\boldsymbol{A}_m T_s} - I_{n \times n} \right)^{-1} \boldsymbol{A}_m e^{\boldsymbol{A}_m T_s} = \boldsymbol{\infty}_{n \times n} \tag{3.41}$$

taken from Eq. (3.39) with [107, p. 87]

$$\lim_{T_s \to 0} e^{\boldsymbol{A}_m T_s} = \lim_{T_s \to 0} \sum_{i=0}^{\infty} \frac{1}{i!} \left(\boldsymbol{A}_m T_s \right)^i = I_{n \times n}. \tag{3.42}$$

Control Law Finally, the control law is constructed as [42]

$$\boldsymbol{u}(s) = -\boldsymbol{\Lambda}_0^{-1} \left[\mathbb{C}_m(s)\, \hat{\boldsymbol{\sigma}}_{\boldsymbol{m}}(s) + \mathbb{C}_{um}(s)\, \boldsymbol{H_m}^{-1}(s)\, \boldsymbol{H_{um}}(s)\, \hat{\boldsymbol{\sigma}}_{\boldsymbol{um}}(s) + \boldsymbol{h} \cdot \boldsymbol{y_{cmd}}(s) \right], \tag{3.43}$$

where $\mathbb{C}_m(s)$ and $\mathbb{C}_{um}(s)$ are low-pass filters defined as

$$\mathbb{C}_m(s) = \operatorname{diag}\left(C_1(s), \cdots, C_m(s) \right) \tag{3.44a}$$

$$\mathbb{C}_{um}(s) = \operatorname{diag}\left(C_{m+1}(s), \cdots, C_{2m}(s) \right). \tag{3.44b}$$

The purpose of the filters is to prevent high frequency content resulting from the adaptation process within $\hat{\boldsymbol{\sigma}}_{\boldsymbol{m}}$ and $\hat{\boldsymbol{\sigma}}_{\boldsymbol{um}}$ from entering the plant dynamics. PT1 transfer functions according to

$$C_i(s) = \frac{\omega_{C,i}}{s + \omega_{C,i}} \quad \forall i \in [1; n] \tag{3.45}$$

are the most straightforward choices for the low-pass filters $C_i(s)$, which have a unity DC-gain and a bandwidth of $\omega_{C,i}$. Moreover, $\mathbb{C}_{um}(s)$ can be used to render the transfer function $\mathbb{C}_{um}(s)\, \boldsymbol{H_m}^{-1}(s)\, \boldsymbol{H_{um}}(s)$ proper, which could be necessary due to the inversion of $\boldsymbol{H_m}(s)$. In this matter and also to shape the resulting frequency response of the closed loop even further, filters of higher order are possible, too (see e.g. [2, 38, 104, 140]).

$$\boldsymbol{H_m}(s) = \boldsymbol{C}_m \left(s I_{n \times n} - \boldsymbol{A}_m \right)^{-1} \boldsymbol{B_m} \tag{3.46a}$$

$$\boldsymbol{H_{um}}(s) = \boldsymbol{C}_m \left(s I_{n \times n} - \boldsymbol{A}_m \right)^{-1} \boldsymbol{B}_{um} \tag{3.46b}$$

are the transfer functions from the plant inputs and unmatched uncertainties to the outputs, respectively [59, p. 160].

The first term of the control law in Eq. (3.43) $-\boldsymbol{\Lambda}_0^{-1}\mathbb{C}_m(s)\,\hat{\boldsymbol{\sigma}}_{\boldsymbol{m}}(s)$ is composed such that it cancels the effect of matched uncertainties within the bandwidth set by means of $\mathbb{C}_m(s)$. The second term $-\boldsymbol{\Lambda}_0^{-1}\mathbb{C}_{um}(s)\,\boldsymbol{H_m}^{-1}(s)\,\boldsymbol{H_{um}}(s)\,\hat{\boldsymbol{\sigma}}_{\boldsymbol{um}}(s)$ serves the same purpose for the unmatched uncertainties. But these cannot be directly canceled as the plant inherits no "physical" unmatched input. Thus, a matched control input $\boldsymbol{u}_m(s)$ is estimated, which cancels the effect of unmatched uncertainties on the plant output. For this purpose, it is utilized that the transfer functions $\boldsymbol{H_m}(s)$ and $\boldsymbol{H_{um}}(s)$ map $\boldsymbol{u}_m(s)$ and $\hat{\boldsymbol{\sigma}}_{\boldsymbol{um}}(s)$ to the same outputs to be tracked, respectively. Assuming that $\boldsymbol{\Lambda} = \boldsymbol{\Lambda}_0$ the estimation $\boldsymbol{u}_m(s)$ can be gained from

$$\boldsymbol{H_m}(s)\,\boldsymbol{\Lambda}_0\boldsymbol{u}_m(s) = \boldsymbol{H_{um}}(s)\,\hat{\boldsymbol{\sigma}}_{\boldsymbol{um}}(s)\,, \tag{3.47}$$

which can be directly transformed to

$$\boldsymbol{u}_m(s) = \boldsymbol{\Lambda}_0^{-1}\boldsymbol{H_m}^{-1}(s)\,\boldsymbol{H_{um}}(s)\,\hat{\boldsymbol{\sigma}}_{\boldsymbol{um}}(s)\,. \tag{3.48}$$

If the introduced cancellation of unmatched uncertainties should be included in the control law Eq. (3.43), it is important to consider that the number of outputs to be tracked matches the number of linearly independent inputs i.e. $r = m$. Otherwise, the inversion $\boldsymbol{H_m}^{-1}(s)$ in Eq. (3.48) cannot be applied. Moreover, all transmission zeros of $\boldsymbol{H_m}(s)$ have to lie in the open left half plane in order to generate a stable inversion $\boldsymbol{H_m}^{-1}(s)$ [59, p. 160]. Analogous to the matched portion of the control law, low-pass filtering via $\mathbb{C}_{um}$ is applied to $\boldsymbol{u}_m(s)$ before it is fed to the plant input.
Finally, the feedforward portion of the control law with the gain $\boldsymbol{h}$ calculated according to [59, pp. 164]

$$\boldsymbol{h} = -\left(\boldsymbol{C}_m\boldsymbol{A}_m{}^{-1}\boldsymbol{B_m}\right)^{-1} \tag{3.49}$$

is added to the control law, in order to achieve stationary tracking of $\boldsymbol{y_{cmd}}$ for the plant outputs $\boldsymbol{y}$. Note that Eq. (3.49) can only be used, if the number of outputs to be tracked r equals the number of system inputs m, which is also the case for a SISO system.

3.3. Discrete-time systems and transformation

Hardware controllers require discrete-time implementations of the control law and one goal of this thesis is to consider the most important reality effects w.r.t. control law design. This is why the implementations of the controllers, which are designed and evaluated in the remainder of this thesis, are also chosen to be discrete-time.
Except for the piecewise constant update law of the L1 adaptive controller shown in Section 3.2, all transfer functions are designed as continuous-time functions. Thus, these functions need to be transformed to discrete-time. Considerations of discrete-

time systems $G(z)$ in the frequency domain are based on the z-transformation [76, p. 486], which is defined according to

$$z := e^{sT_s}. \tag{3.50}$$

Hence, z^{-1} can be interpreted as a delay of one discrete time step T_s [75, p. 255]. For implementation purposes this transformation needs to be further approximated, because for a transformation of a continuous-time system $G(s)$ the inverse of Eq. (3.50) is needed, which results in

$$s = \frac{\ln z}{T_s}. \tag{3.51}$$

Using this transformation does not lead to a rational expression $G(z)$ and is thus not implementable. To solve this issue, the definition of the exponential function as a power series [107, p. 513]

$$e(x) := \sum_{n=0}^{\infty} \frac{x^n}{n!} \tag{3.52}$$

is used to gain its first order approximation, which reads

$$e(x) \approx \sum_{n=0}^{1} \frac{x^n}{n!} = 1 + x. \tag{3.53}$$

Applying Eq. (3.53) to the z-transformation shown in Eq. (3.50) results in Euler's Method [4, p. 294]

$$z \approx 1 + sT_s, \tag{3.54}$$

which can be applied by plugging its inverse

$$s \approx \frac{z-1}{T_s}. \tag{3.55}$$

into the transfer function, which should be transformed. A disadvantage of this approach is the possibility that a stable continuous-time system transforms to a discrete-time system, which is unstable. Another disadvantage is distortion of the frequency scale, whose manifestation depends on the choice of the sample time T_s (the smaller, the better). This directly corresponds to an uncertainty w.r.t. the system poles after transformation and is a major problem e.g. for notch filters. One solution to this problem is the bilinear transformation, also known as Tustin's approximation, which solves the first problem [4, pp. 294-299] and gives some remedy for the second. It can be deduced by using Eq. (3.50) again and splitting the term e^{sT_s} according to

$$z = e^{sT_s} = e^{s\frac{T_s}{2} - \left(-s\frac{T_s}{2}\right)} = \frac{e^{s\frac{T_s}{2}}}{e^{-s\frac{T_s}{2}}}, \tag{3.56}$$

which by means of the approximation Eq. (3.53) results in the transformation

$$z \approx \frac{1 + s\frac{T_s}{2}}{1 - s\frac{T_s}{2}}. \tag{3.57}$$

Its inverse can be used to transform continuous-time transfer functions [4, pp. 295]:

$$s \approx \frac{2}{T_s} \cdot \frac{z-1}{z+1} \tag{3.58}$$

[4, pp. 294-299] also mentions an enhancement to the bilinear transformation, which is called frequency prewarping. By means of frequency prewarping it is possible to reduce the effect of frequency scale distortion even further in an area around a certain, definable frequency. This is not discussed further here, as the bilinear transformation without prewarping has shown to be sufficient for the implementations made for this thesis, because the considered dynamics are slow enough compared to the chosen sample time T_s.
At last, it has to be noted that continuous-time systems without feedthrough can inherit a feedthrough after application of bilinear transformation. That is especially important for implementations, because feedthrough can lead to algebraic loops.

4. Control Law Design

Using the techniques shown in Chapter 3 this chapter focuses on the design of adaptive control laws. Because particular emphasis is placed on adaptive augmentations, at first a conventional, linear baseline controller architecture is introduced in Section 4.1. This baseline controller is designed using the DPI approach [97, 94, 16], which is explained in detail. The controller shapes the short-period dynamics by means of angle of attack α and q feedback and offers steady-state tracking of α_{cmd}. An appropriate filter chain is described in Section 4.1.2, which should cope with turbulent, noisy and discrete-time measurements and thus consists of an upsampling algorithm and filter transfer functions upstream (before) and a notch filter downstream (after) the controller. The consideration of these filter dynamics, as well as actuator dynamics and delay for the controller design leads to an output-feedback problem w.r.t. feedback gain choice. This issue can be handled by means of Eigenstructure Assignment, which is used to design the resulting MISO controller feedback gains in Section 4.1.1.

In the next step, an adaptive augmentation for the baseline controller is developed in Section 4.2. L1 Adaptive Control is used to augment the DPI baseline controller. Here, two different augmentation strategies are considered, where the first one is very common in literature (see e.g. [43, 71]). Here, the adaptive controller augments the closed-loop connection of plant and baseline controller. Not as widely used is the second option, at which the adaptive controller augments the open-loop plant first. The resulting inter-connection is then "augmented" by the baseline controller. Both the combination of L1 Adaptive Control and DPI, as well as a extensive comparison between the two augmentation strategies, cannot be found in literature to the best knowledge of the author, yet.

As it is very common for adaptive augmentations, also the L1 adaptive augmentations in their basic configuration decrease robust stability properties of the baseline controller w.r.t the actuator cut. In general, this is a major counterargument to the application of adaptive augmentations. In order to solve this issue, this thesis contributes a modification of the state predictor within the L1 adaptive controller, which uses actuator position measurement. The modification is described in Section 4.2.2 and Section 4.2.3, respectively. This way, the robust stability properties w.r.t. the actuator cut are fully restored. The restoring effect can be particularly observed in Fig. 5.30 and Fig. 5.31 introduced in Section 5.2.2.1.

The authors of [23, 98] proposed an alternate approach to design a Reference model-based adaptive controller for long range civil aircraft, which is referred to as $\Delta\dot{q}$

Compensation Law in the course of this thesis. For this control law, a deviation $\Delta\dot{q}$ between a linear estimation $\hat{\dot{q}}$ and the pitch acceleration $\dot{q}$ acting on the aircraft is calculated, which is then used to generate a compensating actuator deflection. For the sake of comparison to the L1 Adaptive Control approach, this thesis contributes a combination of the described $\Delta\dot{q}$ Compensation Law and the DPI baseline controller, which is shown in Section 4.3.
At last, Section 4.4 contributes with a novel combination of L1 Adaptive Control and Eigenstructure Assignment. This approach also implies a modification of the state predictor in terms of feedback of estimated states to both matched and unmatched inputs. In a nutshell, this combination allows for an adaptive standalone controller, which is able to precisely place desired poles for nominal plant conditions, even considering actuator dynamics, filter dynamics and delay. Moreover, this approach can be further modified in terms of utilizing actuator position measurement, which, as shown above, has a beneficial effect on the robust stability properties w.r.t. the actuator cut. This modification is also presented in the course of this chapter.
As it was already stated, this thesis has not the goal to present a specific controller design for a specific aircraft. It is rather the focus to develop and evaluate methods for the design of practice-oriented adaptive controllers, which are then exemplarily applied to a longitudinal F-16 aircraft model.

4.1. Baseline Controller

It is the task of the baseline controller to ensure Level 1 handling qualities in terms of aircraft short-period frequency and damping [81, pp. 13-16] for the nominal case, where no failure occurs. The pole locations of the short-period are shaped by means of angle of attack α and q feedback. Furthermore, it ensures steady-state tracking of the angle of attack command α_{cmd}.
α_{cmd} is determined from the stick input $\delta_{s,lon} \in [-1, 1]$, where -1 translates to $\alpha_{min} = -10^\circ$ and $+1$ to $\alpha_{max} = 7^\circ$, respectively. The limits α_{min} and α_{max} are chosen such that they can be achieved without reaching the actuator deflection limit in nominal conditions for the considered aircraft presented in Chapter 2. Additionally, stick input $\delta_{s,lon}$ is processed by rate limitation with a maximum slope of $\pm 5\frac{1}{s}$. At neutral stick position α_0 is commanded. Here, α_0 is fixed to the trim angle of attack value corresponding to the initial envelope point of the simulation. This shows to be sufficient for the assessments made within this thesis, because it is focused on the short-time dynamics of the aircraft. A pilot would of course require automatic trimming functionality for the actual envelope point in a real FCS, which is not considered here. In case the enhanced simulation model is used, α_{cmd} is additionally quantized using the same algorithm applied to the measured angle of attack α as shown in Section 2.6. This way, α_{cmd} has the same resolution as α and artificial steady-state errors can be avoided [33].

For this work, the DPI approach was chosen for the design of the baseline controller [97, 94] [16, pp. 837-847]. It is very similar to the well-known PI controller, but distinguishes slightly from that, because of the introduction of differentiation operators at every input (i.e. sensor signals and command inputs) and an integrator at the output. Thus, it is possible to limit both absolute value and rate of the control signal at the integrator according to the properties of the actuator, without having to deal with integrator windup. Another advantage of this control structure is the possibility to use fast states, such as angle of attack α, as scheduling parameters for the gains within the controller without generating hidden feedback (cf. also [109]). The integrator also has a smoothing effect on the control signal when using noisy measurements as scheduling parameters. Furthermore, the smoothing behavior is beneficial, when gains have to be rapidly changed due to fast aircraft configuration changes. Finally, proportional state feedback does not generate a steady-state signal, because the constant portion of the feedback signal is removed by means of the differentiations.

The structure of the controller is depicted in Fig. 4.1. For shaping of the closed-loop dynamics w.r.t. the short-period, feedback of the states α and q is used. The signals are differentiated before they are fed in the gains k_α and k_q, respectively. Differentiations are modeled by means of the transfer function

$$G_{d,dt}(s) = \frac{s}{cs+1}. \tag{4.1}$$

In order to be proper and thus implementable, $G_{d,dt}$ features a fast pole at $\lambda_{d,dt} = -\frac{1}{c}$ besides the zero causing the differentiation. $\lambda_{d,dt}$ is chosen such that it is sufficiently below the Nyquist frequency $0.5 \cdot \frac{1}{T_s}$ [106, p. 28], where T_s is the controller sample time. Therefore, for the implementation

$$\lambda_{d,dt} = -\frac{1}{3} \cdot \frac{1}{T_s} \cdot 2\pi \tag{4.2}$$

is used, which leads to

$$c = 3 \cdot \frac{T_s}{2\pi} \tag{4.3}$$

considering also conversion from Hz to $\frac{rad}{s}$ by means of the factor 2π. $G_{d,dt}(s)$ is as well used to differentiate the feedforward path α_{cmd} via h_{DPI}.

Although $\lambda_{d,dt}$ is chosen very fast, it induces additional, unwanted dynamics. Thus, the transfer function of the integrator at the controller output

$$G_{\int}(s) = \frac{cs+1}{s} \tag{4.4}$$

is constructed such that these additional dynamics are canceled again by means of an additional zero.

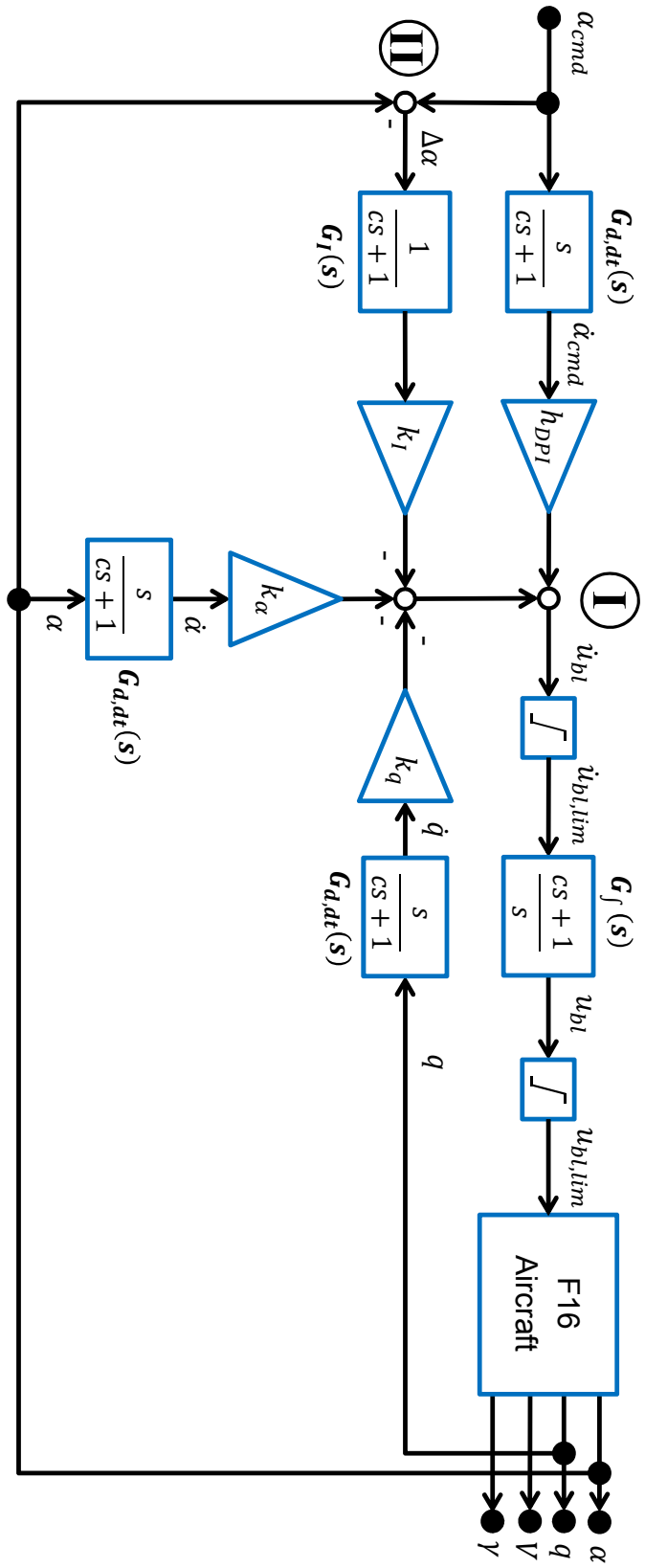

Figure 4.1. – Structure of the DPI baseline controller

In consequence, $G_{\int}(s)$ and $G_{d,dt}(s)$ cancel out each other perfectly, if rate saturation is not reached.
The last path to be analyzed is the integral feedback of the control error

$$\Delta\alpha = \alpha_{cmd} - \alpha, \tag{4.5}$$

which ensures zero steady-state error. In order to achieve pure integral feedback via gain k_I and transfer function $G_{\int}(s)$ according to Eq. (4.4), one has again to consider the additional zero of $G_{\int}(s)$. Thus, it is canceled by means of an additional pole set by the transfer function

$$G_I(s) = \frac{1}{cs+1}, \tag{4.6}$$

which is placed in the integral error feedback path. In conclusion, though all controller input signals are differentiated to gain the advantages mentioned above, the transfer functions cancel out each other except for an integration in the error feedback path, when a strictly linear analysis of the structure is performed. Thus, the structure equals an ordinary PI controller in this case.
For the baseline controller implementation, the transfer functions are transformed to discrete-time using bilinear transformation introduced in Section 3.3. The control law is processed at a sample time of $T_s = 0.01s$, which equals a sample rate of $100Hz$.

4.1.1. Gain Design

The circumstance that the DPI controller structure equals the one of a PI controller, if saturations are neglected, is utilized for the gain design process. One could use the whole spectrum of linear control theory, in order to design the gains k_α, k_q, k_I and h_{DPI} according to desired handling qualities. Within this work, Eigenstructure Assignment is chosen for this task, as it is described in Section 3.1. In case of a SIMO system presented here, Eigenstructure Assignment allows systematic pole placement using output feedback [50], whereas most other pole placement approaches require state feedback. This is an advantage, because transfer functions of actuator model, delays and filters can be directly incorporated in the design process for the sake of a more accurate representation of the actual plant dynamics within the controller design model. This cannot be done using state feedback approaches, because all the mentioned elements contribute additional states to the design model, which are not available as measurements of the actual plant. Thus, the outputs of the controller design model are angle of attack α, pitch rate q besides the integral $\int -\alpha(\tau)\,dt$, in order to be able to shape the poles corresponding to the short-period dynamics and the integral error feedback $e_I = \int [\alpha_{cmd}(\tau) - \alpha(\tau)]\,dt$.
Fig. 4.2 gives an overview on the structure of the controller design model, which defines the state space matrices $\boldsymbol{A}$, $\boldsymbol{B}$ and $\boldsymbol{C}$ to be used in Eq. (3.1) for the Eigenstructure

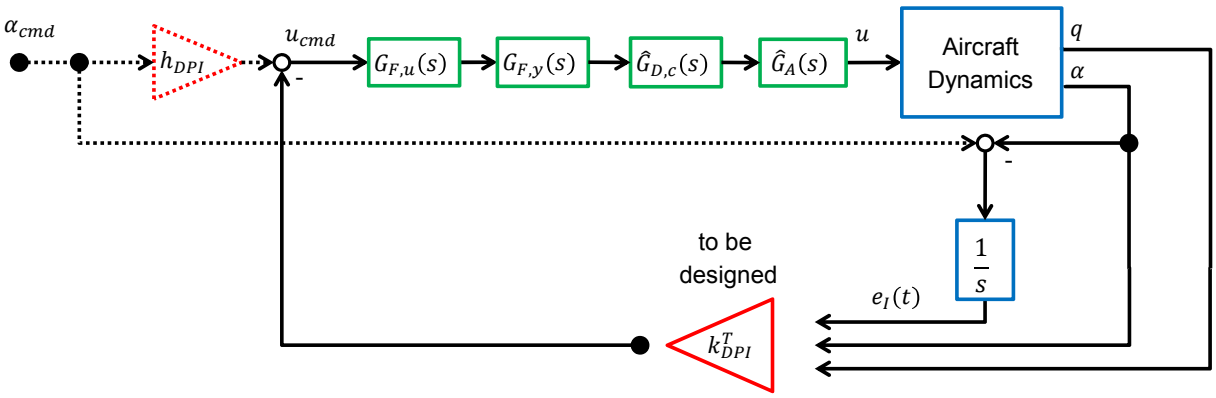

Figure 4.2. – Model structure for gain design

Assignment algorithm according to Section 3.1. The linear, longitudinal aircraft dynamics shown in Eq. (2.43) are used here, which are deduced in Section 2.1.3. Furthermore, the actuator model of Section 2.5 in Eq. (2.53) represented by the transfer function

$$\hat{G}_A(s) = \frac{{\omega_{0,act}}^2}{s^2 + 2\zeta_{act}\omega_{0,act} \cdot s + {\omega_{0,act}}^2} \tag{4.7}$$

is incorporated in the structure, along with delay of $T_{D,c}$ represented by a Padé approximation [39, pp. 572-574] of second order

$$\hat{G}_{D,c}(s) = \frac{1 - \frac{1}{2}T_{D,c}s + \frac{1}{12}{T_{D,c}}^2 s^2}{1 + \frac{1}{2}T_{D,c}s + \frac{1}{12}{T_{D,c}}^2 s^2}. \tag{4.8}$$

It was mentioned before in Chapter 2 that two configurations of the simulation model are used in this thesis, which are the simple and the enhanced version. Thus, also two different controller designs have to be considered. The first difference lies in the amount of delay $T_{D,c}$ (c.f. Section 2.5), which is $0.055s$ for the simple and $0.015s$ for the enhanced aircraft model. In case of the simple aircraft model, $T_{D,c}$ represents all delays contained in the control loop. For the enhanced aircraft model, $T_{D,c}$ contains only computational delay (c.f. Section 2.5), because additional delay is generated though measurement sampling and filtering. This is why the filter transfer functions $G_{F,u}(s)$ and $G_{F,y}(s)$ are also taken into account for the controller design, in case they are activated. The filter transfer functions are introduced and described in Section 4.1.2. Note, that although the filter transfer function $G_{F,y}(s)$ is applied to the plant output signals, it can be shifted to the plant input channel considering linear short-period dynamics for the design model [12, p. 94].
The requirement set up to the Eigenstructure Assignment algorithm in both cases is that it shapes the short-period such that a CAP of 0.7 and relative damping $\zeta_{sp,des} = 0.95$ are achieved. This corresponds to Level 1 handling qualities [81, pp. 13-16]. The CAP

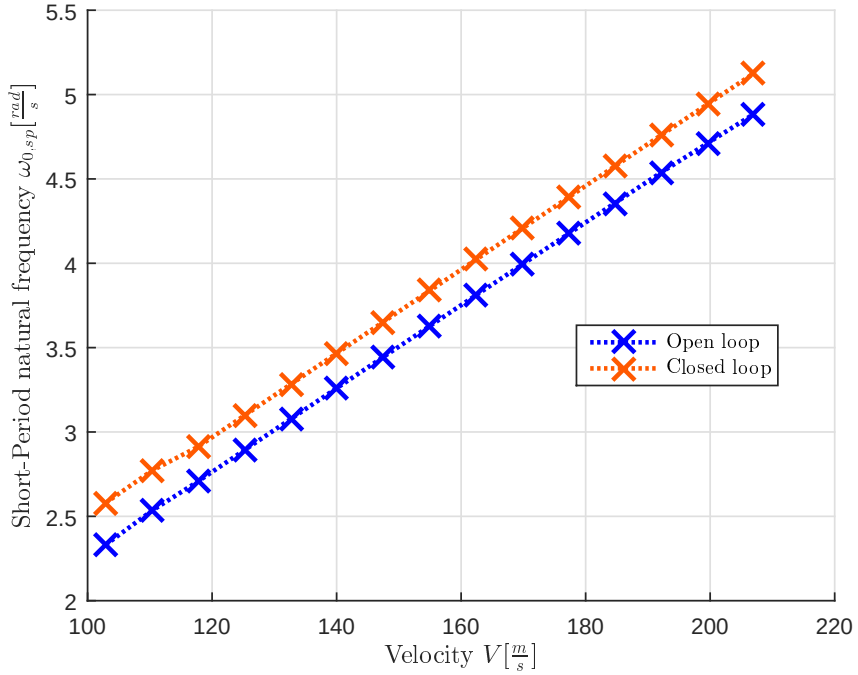

Figure 4.3. – Natural frequency of the short-period $\omega_{0,SP}$ in dependence of V

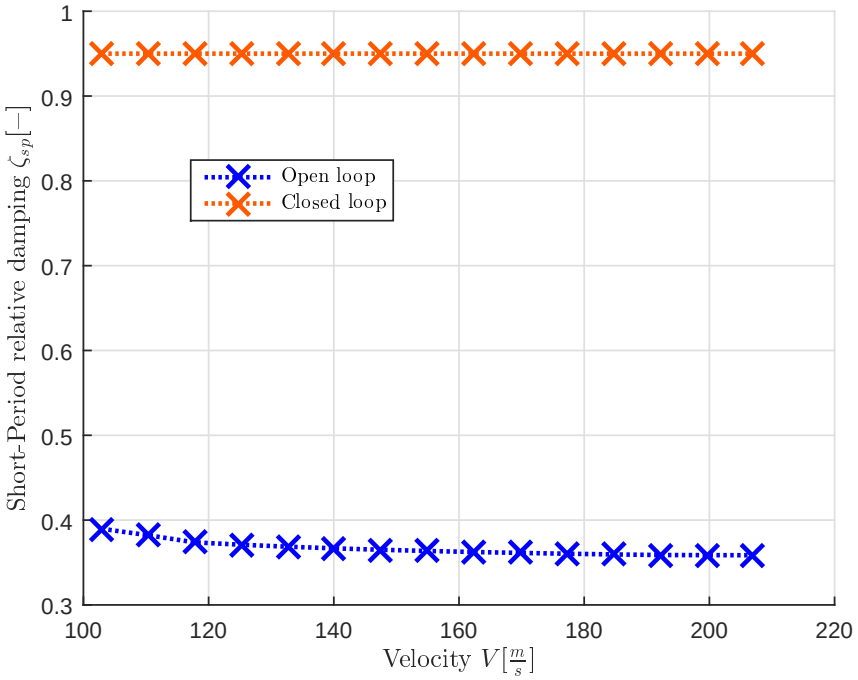

Figure 4.4. – Relative damping of the short-period ζ_{SP} in dependence of V

is defined as the ratio between the initial angular acceleration $\dot{q}_0$ and the resulting steady state load factor $n_{z,s}$

Velocity V $\left[\frac{m}{s}\right]$	Open-loop $\omega_{0,sp}$ $\left[\frac{rad}{s}\right]$	Closed-loop $\omega_{0,sp,des}$ $\left[\frac{rad}{s}\right]$
102.88	2.33	2.58
110.32	2.53	2.77
117.75	2.71	2.91
125.19	2.89	3.10
132.63	3.08	3.28
140.07	3.26	3.47
147.50	3.44	3.65
154.94	3.63	3.84
162.38	3.81	4.02
169.81	3.99	4.21
177.25	4.17	4.39
184.69	4.36	4.58
192.13	4.54	4.76
199.56	4.71	4.94
207.00	4.88	5.13

Table 4.1. – Natural frequency of the short-period $\omega_{0,SP}$ for the open-loop aircraft and the desired natural frequency $\omega_{0,SP,des}$ to be established by the controller considering different envelope points

$$CAP := \frac{\dot{q}_0}{n_{z,s}} = -{\omega_{0,sp}}^2 \frac{g}{Z_\alpha} \tag{4.9}$$

and can be seen as a measure for longitudinal control sensitivity [16, p. 463]. The corresponding, desired short-period frequency $\omega_{0,sp,des}$ can be calculated using

$$\omega_{0,sp,des} = \sqrt{-CAP \cdot \frac{Z_\alpha}{g}}. \tag{4.10}$$

in dependence of the stability derivative Z_α. This dependence results in individual values of $\omega_{0,sp,des}$ for the single envelope points. Considering velocities V according to Table 2.2 and altitude $h = 5000m$ the resulting $\omega_{0,sp,des}$ for $CAP = 0.7$ can be found in Fig. 4.3 and Table 4.1, where also $\omega_{0,sp}$ of the open loop aircraft is shown for the sake of comparison. Likewise, the open loop relative damping ζ_{sp} is plotted in Fig. 4.4

besides the desired damping $\zeta_{sp,des}$. The desired short-period can also be characterized by means of its complex conjugated pole pair according to [75, p. 298]

$$\lambda_{SP,1} = -\zeta_{sp,des}\omega_{0,sp,des} + i \cdot \omega_{0,sp,des}\sqrt{1-\zeta_{sp,des}} \tag{4.11a}$$

$$\lambda_{SP,2} = -\zeta_{sp,des}\omega_{0,sp,des} - i \cdot \omega_{0,sp,des}\sqrt{1-\zeta_{sp,des}}. \tag{4.11b}$$

Besides the short-period, the pole $\lambda_I = -1$ corresponding to the integral error feedback e_I should also be placed.
The following steps of the Eigenstructure Assignment algorithm are performed three times $i \in \{1,2,3\}$, from which two are for placement of both complex conjugated short-period poles and the last for the error feedback pole. At first, the basis vectors of the null space $\bar{\boldsymbol{N}}$ belonging to the matrix $\begin{pmatrix}\lambda_i^* \boldsymbol{I}_{n\times n} - \boldsymbol{A} & \boldsymbol{B}\end{pmatrix}$ are computed, where the specifications mentioned in the last paragraph are used to define λ_i^*. Section 3.1 offers three different possibilities to define the auxiliary parameter vector $\boldsymbol{l}_i$. Here, the first option is chosen, where the number of definable eigenvector elements equals the number of linear independent system inputs. As only elevator η is available to the controller, one eigenvector value can be specified. A reasonable choice in this case is to demand 1 for the eigenvector value corresponding to the state q for both short-period poles and also 1 for the value belonging to the state e_I for the integral error feedback pole. This information is used to suitably construct the matrix $\boldsymbol{P}_i^s$. Next, $\boldsymbol{l}_i$ can be calculated according to Eq. (3.15). By means of this result and the matrix $\bar{\boldsymbol{N}}$, the vectors $\boldsymbol{v}_i^*$ and $\boldsymbol{z}_i^*$ can be computed using Eq. (3.10). After performing these steps for the three poles, the gains $\boldsymbol{k_{DPI}} = \begin{pmatrix}k_\alpha & k_q & k_I\end{pmatrix}$ can be obtained from Eq. (3.23).
Finally, the feed-forward gain h_{DPI} is calculated such that it cancels the pole of the error integration with respect to the transfer function from α_{cmd} to α [54]. It can be calculated according to

$$h_{DPI} = \frac{k_I}{\lambda_I}. \tag{4.12}$$

The gain design algorithm shown in this section is applied to the linear aircraft models given in Eqs. (A.1a) to (A.15a), which represent the longitudinal aircraft dynamics at an altitude of $h = 5000m$ and velocities in Table 2.2 ranging from $V_{min} = 102.88\frac{m}{s}$ to $V_{max} = 207\frac{m}{s}$. Using these models, a gain-scheduling can be established, where the gains used within the controller computations are interpolated utilizing the calculated gains as fixed points. In order to be able to additionally consider slight changes in altitude h, besides changes in velocity V, dynamic pressure $\bar{q}$ is chosen as scheduling variable. This is convenient, since $\bar{q}$ contains both information about velocity and altitude, the latter indirectly through air density ρ (c.f. Eq. (2.6)). Note that Ma is also used fairly often for gain scheduling purposes in practical FCS applications. This is not necessary here, because the aerodynamic data used within the aircraft model does not incorporate any dependence on Ma (c.f. Section 2.1.1). In general, the controller

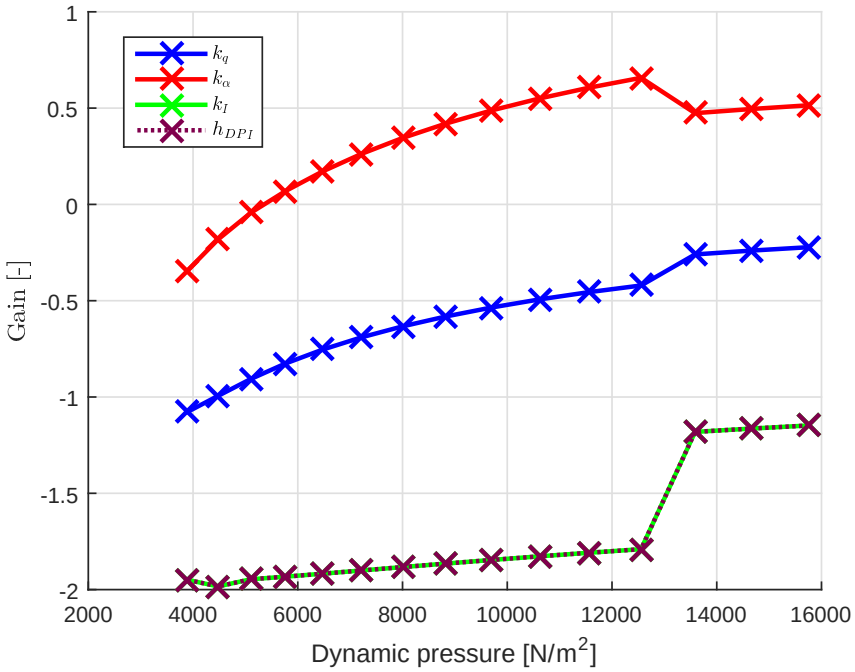

Figure 4.5. – Baseline controller gains in dependence of $\bar{q}$ for simple aircraft model and $T_D = 0.055s$

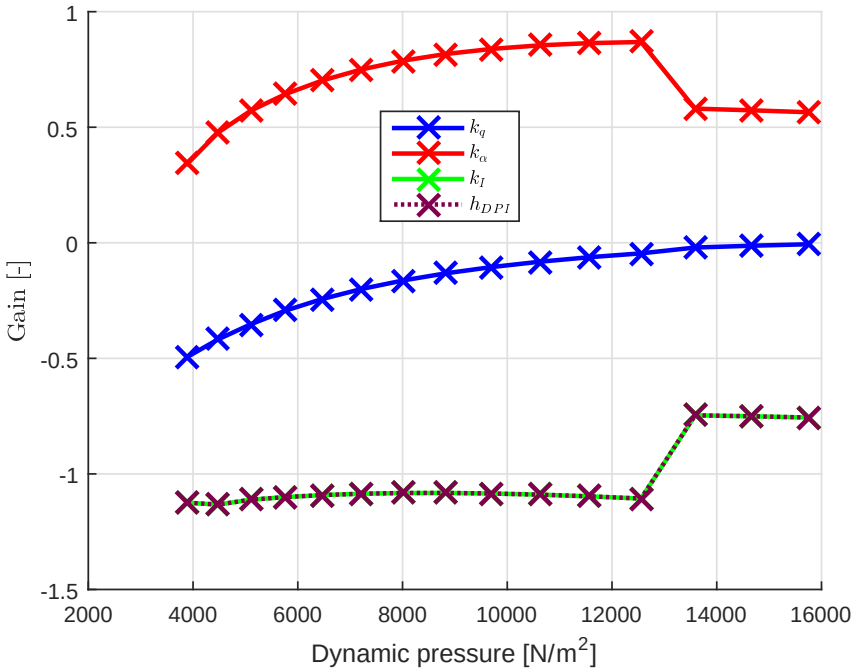

Figure 4.6. – Baseline controller gains in dependence of $\bar{q}$ for enhanced aircraft model

designs shown in this section are not limited to the application of only one scheduling variable.
The resulting gains are illustrated in Fig. 4.5 in dependence of dynamic pressure $\bar{q}$ for the simple aircraft model and in Fig. 4.6 considering the enhanced model. One can notice a rapid change with respect to the gain progression around $\bar{q} \approx 13000\frac{N}{m^2}$ for both design cases. This rapid change stems from the nonlinear aerodynamic data set included in the aircraft model. The rapid change appears between the 12th and the 13th design point, which correspond to the velocities $V_{0,12} = 184.69\frac{m}{s}$ and $V_{0,13} = 192.13\frac{m}{s}$ according to Table 2.2 introduced in Section 2.1.3. In the same section, the corresponding elevator deflections η_0, that trim the aircraft, can be found in Fig. 2.4. The figure reveals that the trim elevator deflection η_0 crosses $-10°$ between the 12th and 13th design point i.e. $\eta_{0,12} = -10.39°$ and $\eta_{0,13} = -9.99°$. $-10°$ is one of the breakpoints $\eta \in \{-25°; -10°; 0°; 10°; 25°\}$, at which discrete data points are available for the aerodynamic coefficients $C_{X,0}$, $C_{Z,0}$ and $C_{m,0}$. This can also be seen in Fig. A.1, Fig. A.5 and Fig. A.9 in Appendix A. Moving left and right from breakpoint $-10°$ with respect to the η-axis results in different slopes of the resulting aerodynamic coefficients. The change in slope has an impact the corresponding linearized models, which can be found in Eq. (A.12a) and Eq. (A.13a). A relatively big change of their input matrices $\boldsymbol{B}$ with respect to the column belonging to η can be observed, especially when the change with respect to other linear models is considered. As these models are used for the controller design, the changes with respect to the control effectiveness are the reason for the rapid change observed at the gain progression in Fig. 4.5 and Fig. 4.6. It has to be noted also that only one of these rapid changes appears for the entire envelope, because $\eta_0 \in [-20.93; -9.54]$ (c.f. Fig. 2.4) crosses the breakpoints $\eta \in \{-25°; -10°; 0°; 10°; 25°\}$ with regard to η only once. Furthermore, one could assume that a more detailed aerodynamic data grid i.e. a grid containing more breakpoints in η would also lead to a smoother progression.
Since Eigenstructure Assignment without modifications inherits no robustness assessment, it has to be validated afterwards, that the robust stability margins are ensured by the controller design. This is shown in Section 5.2.1.1.

4.1.2. Filter Design

The illustration of the enhanced closed-loop simulation model Fig. 2.3 in Chapter 2 contains three blocks apart from the Control Law which are not yet described. These are *Filters*, *Notch Filter* and *Upsampling*, which are rather related to the FCS than to the aircraft model. Thus, they are further examined in this section.
In aircraft applications, one the major sources for phase lags, and thus delays within the closed-loop system, are filters. Besides of considering the impact of these lags on the controller performance, the filters serve three purposes in the context of this thesis. First, to reject high frequency content from the measurements in order to attenuate the influence of turbulence and sensor noise on the controller. Second, to avoid excitation

of the simple structural mode, which is described in Section 2.7. Finally, the third part of the filtering chain is measurement upsampling.
Rejection of high frequency content is achieved by means of a lowpass filter chain applied to the sensor measurements angle of attack α and pitch rate q, before they enter the controller. The chain consists of a 2nd order and a 1st order low-pass filter connected in series according to

$$G_{F,y,lp}(s) = \frac{{\omega_{0,F,y,lp,1}}^2}{s^2 + 2\zeta_{F,y,lp,1}\omega_{0,F,y,lp,1} \cdot s + {\omega_{0,F,y,lp,1}}^2} \cdot \frac{\omega_{0,F,y,lp,2}}{s + \omega_{0,F,y,lp,2}}, \tag{4.13}$$

where the filter parameters are chosen as $\omega_{0,F,y,lp,1} = 14\frac{rad}{s}$, $\zeta_{F,y,lp,1} = \frac{\sqrt{2}}{2}$ and $\omega_{0,F,y,lp,2} = 14.2\frac{rad}{s}$ after some manual tuning.
The second objective, which is avoidance of structural mode excitation, is achieved through application of notch filters both on the measurements angle of attack α, pitch rate q and elevator deflection η and on the command η_{cmd} generated by the controller. The notch filters are defined through

$$G_{f,notch}(s) = \frac{s^2 + 2\zeta_{f,notch,1}\omega_{0,f,notch} \cdot s + {\omega_{0,f,notch}}^2}{s^2 + 2\zeta_{f,notch,2}\omega_{0,f,notch} \cdot s + {\omega_{0,f,notch}}^2}. \tag{4.14}$$

It is considered that both the natural frequency and the relative damping of the structural mode are not exactly known. Therefore, the parameters of the notch filters are set up as $\omega_{0,f,notch} = 6Hz$, $\zeta_{f,notch,1} = 0.07$ and $\zeta_{f,notch,2} = 0.2$ to account for uncertainty in the knowledge of the exact properties.
The filter transfer function applied to the measurements angle of attack α, pitch rate q and elevator deflection η can be summarized as

$$G_{F,y}(s) = G_{F,y,lp}(s) \cdot G_{f,notch}(s) \tag{4.15}$$

and the filter applied to the controller command η_{cmd} is

$$G_{F,u}(s) = G_{f,notch}(s). \tag{4.16}$$

Bode diagrams [75, pp. 246-248] of both filter transfer functions can be found in Fig. 4.7, where especially the significant phase lag caused by $G_{F,y}(s)$ can be observed. The relative loss in phase Φ can be translated to a time delay T_D by means of the gain crossover frequency ω_{gc} and

$$T_D = \frac{\Phi}{\omega_{gc}} \tag{4.17}$$

according to [8, p. 32]. For the control problem at hand the gain crossover frequency to be used for the formula is the short-period frequency set up by the controller (c.f. Section 4.1.1). Utilizing Eq. (4.17) leads to a range of equivalent time delays

$T_{D,f,y} = 0.179s \ldots 0.18s$ for $G_{F,y}(s)$ and $T_{D,f,u} = 0.0069s \ldots 0.007s$ for $G_{F,u}$ depending on the short-period frequencies over the whole envelope. Thus, in good approximation the time delays can be considered independent from the envelope point as $T_{D,f,y} = 0.18s$ and $T_{D,f,u} = 0.007s$. The filter transfer functions $G_{F,y}(s)$ and $G_{F,u}(s)$ are implemented by means of their discrete-time representations $G_{F,y}(z)$ and $G_{F,u}(z)$, which are gained utilizing bilinear transformation introduced in Section 3.3.

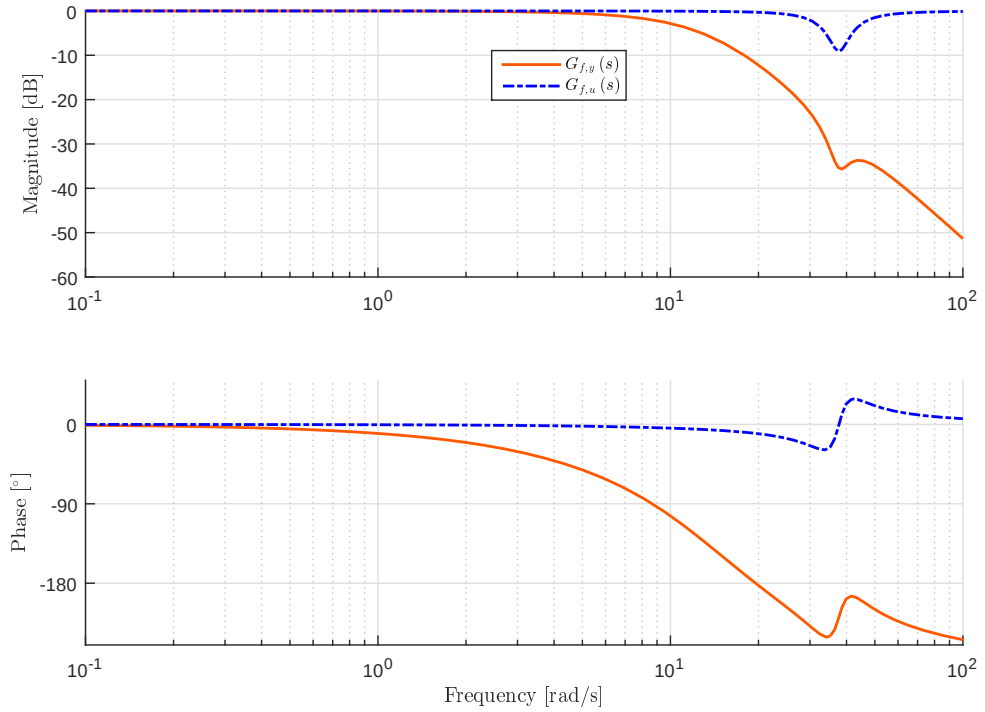

Figure 4.7. – Bode plot of filters applied to the measurements $G_{f,y}(s)$ and to the controller command $G_{F,u}(s)$

The last part of the filtering chain is the measurement upsampling, which was already mentioned above. It turned out that an L1 adaptive controller is very sensitive with respect to measurement signals, which have a lower sample rate $f_{s,sensor} = \frac{1}{T_{s,sensor}}$ than the sample rate of control law computation $f_s = \frac{1}{T_s}$, i.e. the control law computation is faster than the sensor can deliver a new measurement point. This circumstance can lead to high frequency oscillation for the parameter estimation (c.f. Eq. (3.38) in Section 3.2) resulting in a destabilizing controller. Thus, two options are available to solve the problem. The first one is to choose the control law computation rate according to the slowest sensor measurement. An alternative solution, which is also used within this thesis, is to artificially increase the measurement sample rate to the value of the controller sample rate, in case of $f_{s,sensor} < f_s$ or $T_{s,sensor} > T_s$. This is achieved by means of a Finite Impulse Response (FIR) filter [106, pp. 563-582], which

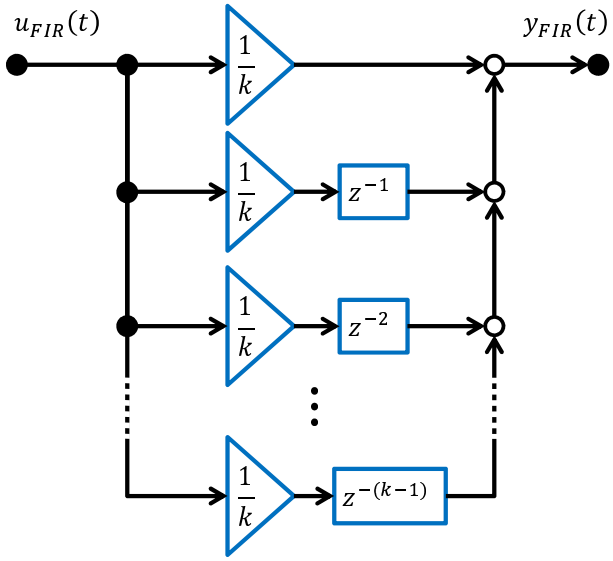

Figure 4.8. – Structure of upsampling FIR filter

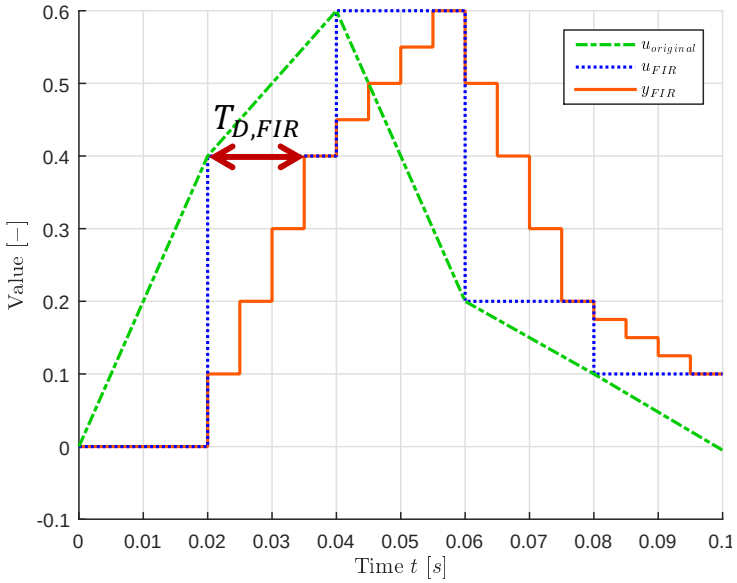

Figure 4.9. – Example for measurement upsampling with $T_{s,Sensor} = 0.02s$ and $T_s = 0.005s$ ($k = 4$)

linearily interpolates "missing" values between two discrete time steps. In this way, a signal results, which has the same sample rate as the control law computation.

The algorithm for upsampling presented here can only be applied, if the controller sample time T_s can be scaled by means of an integer k with respect to $T_{s,sensor}$, i.e. $T_{s,sensor} = k \cdot T_s$ and $k \in \mathbb{N}$. It can be described by means of a discrete filter transfer function

$$G_{FIR}(z) = \sum_{j=0}^{k-1} \frac{1}{k} \cdot z^{-j}, \tag{4.18}$$

where z^{-j} denotes a time delay of $j \cdot T_s$ and with

$$k = \frac{T_{s,sensor}}{T_s}. \tag{4.19}$$

The filter structure is also depicted in Fig. 4.8. The filter is applied to the measurement using the same sample time T_s as the controller is operated with. In this way, $(k-1)$ interpolation points are generated, before the filter output equals its input again i.e. the filter output is the actual measurement signal acquired $(k-1)$ discrete sample time steps ago. Thus, the filter gives a linear interpolation on the upside, but generates additional delay of

$$T_{D,FIR} = (k-1) \cdot T_s \tag{4.20}$$

on the downside. This is, because the filter has to be causal in order to be implementable and thus can only work in a retrospective way. In order to illustrate this mechanism, an example is shown in Fig. 4.9, where the measurement sample time is chosen to be $T_{s,sensor} = 0.02s$ and the controller sample time is set to $T_s = 0.005s$. The original signal $u_{original}$ is first sampled by means of a zoh with the sample time $T_{s,sensor}$, which results in u_{FIR}. y_{FIR} denotes the output of the upsampling filter $G_{FIR}(z)$, which processes the measurement u_{FIR}. It can be calculated by means of Eq. (4.19) and Eq. (4.20) that for the presented example, the scaling factor is $k = 4$ and the time delay results in $T_{D,FIR} = 0.015s$. This can also be observed in Fig. 4.9.

Finally, one has to care also for the opposite case, where the measurement sample rate is faster than the control law computation, i.e. $f_{s,sensor} > f_s$ or $T_{s,sensor} < T_s$. In this case aliasing could occur as it was already described in Section 2.6, which should be avoided. In order to tackle this issue, no additional filter is introduced, but the anti aliasing filter included in the sensor model Eq. (2.57) is used to attenuate critical signal content. Thus, the filter bandwidth is set to $\omega_{0,aa} = \frac{1}{3} f_s$ instead of $\omega_{0,aa} = \frac{1}{3} f_{s,sensor}$ if $f_{s,sensor} > f_s$ holds for the specific measurement.

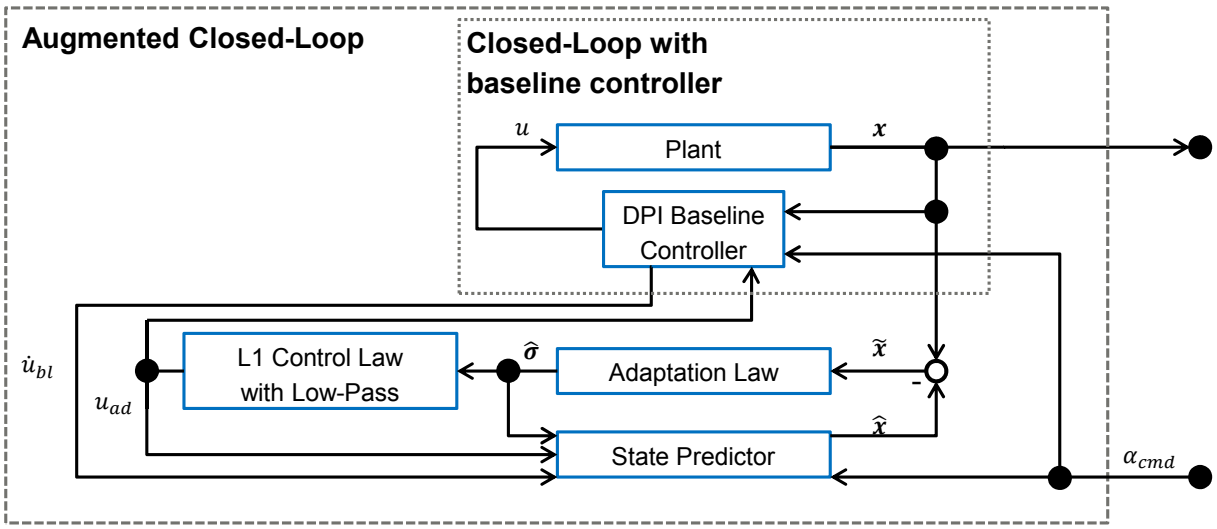

Figure 4.10. – Interconnection for DPI Augmentation

4.2. L1 Adaptive Augmentation

In order to increase the robust performance of the controller in case of uncertainty, this thesis proposes to augment the DPI baseline controller using L1 Adaptive Control with piecewise constant update laws [59], which was introduced in Section 3.2. Simultaneously to the performance increase in case of uncertainty, the augmentation should neither degenerate the performance for the nominal case, nor should it significantly decrease robust stability of the closed-loop. As an additional requirement it should be ensured, that the control law

$$\eta_{cmd} = u_{bl} + u_{ad}, \tag{4.21}$$

where u_{bl} is the control signal portion generated by the baseline controller and u_{ad} the one produced by the L1 adaptive controller, respectively, does not exceed given saturation and rate limits for the actuator (c.f. Section 2.5). Thus, a convenient solution is to feed in u_{ad} at summation Ⓘ of the baseline controller depicted in Fig. 4.1. This summation point is upstream of the limiting structure of the DPI controller. It has to be kept in mind that, due to the baseline controller structure, u_{ad} has to be differentiated e.g. by means of the transfer function Eq. (4.1), before being inserted.
Two different approaches to augment the interconnection of aircraft and baseline controller and to generate the adaptive control signal u_{ad} are presented in this section. The first would be the most obvious choice and can be found quite often in literature (see e.g. [43, 71]). The basic structure is illustrated in Fig. 4.10. In that case, the L1 adaptive controller with its elements *State Predictor*, *Adaptation Law* and *L1 Control Law with Low-Pass* tries to maintain the dynamics of the closed-loop aircraft with the baseline controller. For this reason the reference model to be used for the setup of the

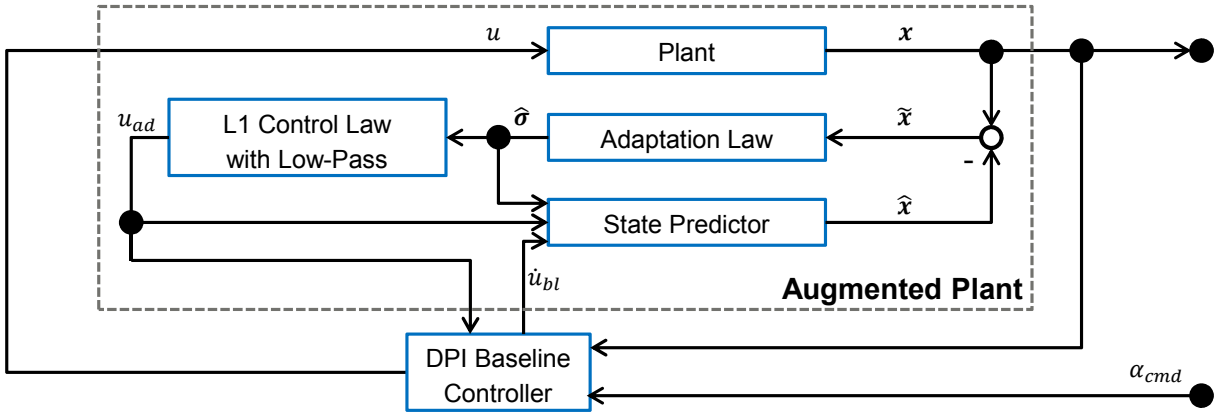

Figure 4.11. – Interconnection for L1 Plant Augmentation

controller is the nominal closed-loop aircraft. This also requires consideration of the baseline controller within the adaptive controller structure, i.e. in the State Predictor. Thus, it is called *DPI Augmentation* or *Closed-Loop Augmentation* here and is further described in Section 4.2.2.

An alternative augmentation method was developed at the TUM-FSD and is depicted in Fig. 4.11. For this approach, the baseline controller is wrapped around a unit consisting of aircraft and L1 adaptive controller. In contrast to the *DPI Augmentation* it is now task of the adaptive augmentation to ensure that the baseline controller always "sees" its design model. Hence, the state predictor of the L1 adaptive controller can be reduced to the open-loop aircraft model in this case. This approach is called *Plant Augmentation* in the context of this thesis and is explained in Section 4.2.3.

This thesis offers an extensive comparison of both augmentation approaches considering the mathematical foundation on the one hand in this section, which also comprises results of [52] gained by the author. Comparisons w.r.t. robust stability and performance aspects on the other hand are presented in Section 5.2.2 and throughout Chapter 6.

4.2.1. Reference Dynamics

Although the approaches differ from each other from a structural point of view, the desired aircraft dynamics to be achieved by the combination of adaptive augmentation and baseline controller in terms of the transfer function $\alpha_{cmd} \rightarrow \alpha$ remains the same. In comparison to the baseline controller design model, a short-period approximation

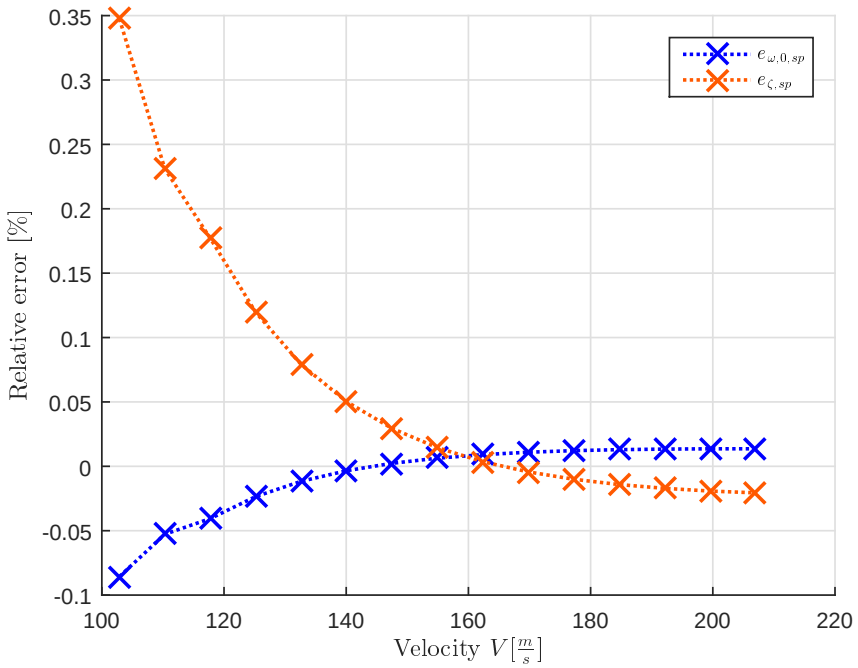

Figure 4.12. – Relative errors $e_{\omega,0,sp}$ and $e_{\zeta,sp}$ for short-period natural frequency $\omega_{0,sp}$ and relative damping ζ_{sp}, if states velocity V and flight path angle γ are neglected in the linear state space model (short-period approximation)

of the linear, longitudinal dynamics in Eq. (2.43) is considered for this reference model. It comes from neglecting states velocity V and γ and results in

$$\underbrace{\begin{pmatrix}\dot{\alpha}\\ \dot{q}\end{pmatrix}}_{=:\dot{\boldsymbol{x}}} = \underbrace{\begin{pmatrix}Z_\alpha & Z_q+1\\ M_\alpha & M_q\end{pmatrix}}_{=:\boldsymbol{A}} \underbrace{\begin{pmatrix}\alpha\\ q\end{pmatrix}}_{=:\boldsymbol{x}} + \underbrace{\begin{pmatrix}Z_\eta\\ M_\eta\end{pmatrix}}_{=:\boldsymbol{B}} \underbrace{\eta}_{=:\boldsymbol{u}} \tag{4.22a}$$

$$\boldsymbol{y} = \boldsymbol{I}_{2\times 2} \cdot \begin{pmatrix}\alpha\\ q\end{pmatrix}. \tag{4.22b}$$

This is a valid representation of the fast-time longitudinal dynamics, if the coupling of the phugoid in the short-period motion can be approximately neglected. Exactly that can be observed in Eqs. (A.1a) to (A.15a), where the lower-left values of the $\boldsymbol{A}$ matrix are near 0. Fig. 4.12 gives further evidence on the validity of the approximation. It shows the relative errors $e_{\omega,0,sp}$ and $e_{\zeta,sp}$ of short-period natural frequency $\omega_{0,sp}$ and relative damping ζ_{sp}, respectively, between short-period approximation and reduced, longitudinal aircraft model considering the states velocity V and flight path angle γ. The errors are well below 0.1% for most velocities, only the damping reaches higher values up to 0.35% for very low velocity.

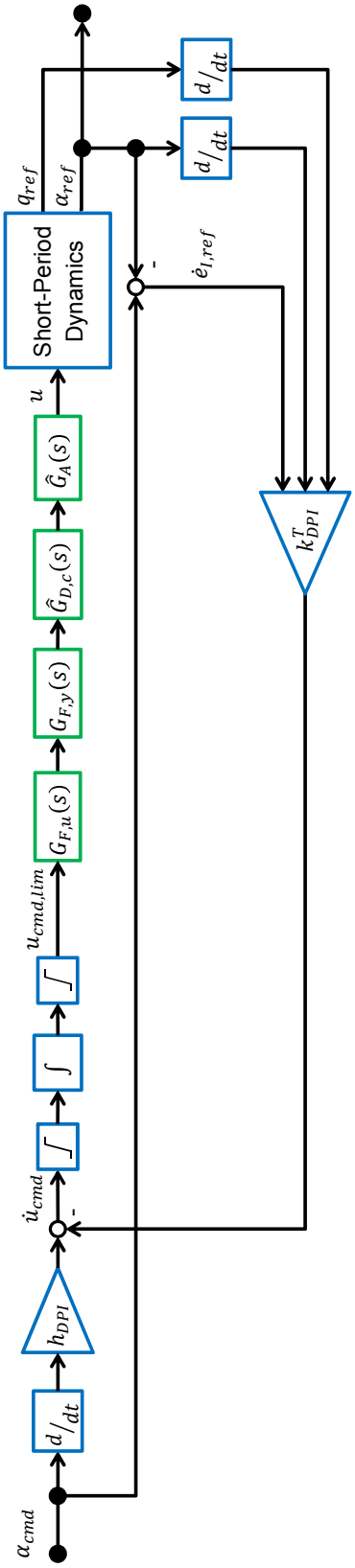

Figure 4.13. – Closed-loop reference dynamics to be maintained by the L1 Adaptive Control augmentations

The short-period approximation is used to design a reference model, as it is shown in Fig. 4.13. Here, the aircraft dynamics are interconnected with a representation of the baseline controller. In order to reflect the combination of baseline controller and aircraft model as precise as possible, it is important to also consider the specific structure of the DPI controller. For that matter, derivations, the integrator and saturation functions according to Eq. (2.61) are included. The saturation functions represent both rate (upstream of the integration) and deflection (downstream of the integration) limits of the actuator. The closed-loop can also be formulated according to

$$\begin{aligned}\dot{\boldsymbol{x}}_{ref}(t) = \boldsymbol{A}_m \boldsymbol{x}_{\boldsymbol{ref}}(t) + \boldsymbol{b}_m \cdot G_{F,u}(t) * G_{F,y}(t) * \hat{G}_{D,c}(t) * \hat{G}_A(t) \\ * \operatorname{sat}\left\{ \int_{t_0}^{t} \operatorname{sat}\left[-\boldsymbol{k_{DPI}}^T \cdot \frac{d}{d\tau}\boldsymbol{x}_{ref}(\tau) + h_{DPI} \cdot \frac{d}{d\tau}\alpha_{cmd}(\tau) \right] d\tau \right\} \\ + \begin{pmatrix} 0 \\ 0 \\ 1 \end{pmatrix} \alpha_{cmd}(t)\,,\end{aligned} \tag{4.23}$$

where

$$\boldsymbol{x}_{ref}(t) = \begin{pmatrix} \alpha_{ref} \\ q_{ref} \\ e_{I,ref} \end{pmatrix}. \tag{4.24}$$

Here, the convolution operator "$*$" [107, p. 302] is utilized, in order to connect the different transfer functions in the time-domain. The nominal open-loop aircraft is described by the short-period approximation discussed above, which is enhanced by the integration $e_{I,ref} = \int \left[\alpha_{cmd}(\tau) - \alpha_{ref}(\tau)\right] dt$. Hence, the system and input matrices are defined as

$$\boldsymbol{A}_m = \begin{pmatrix} Z_\alpha & Z_q + 1 & 0 \\ M_\alpha & M_q & 0 \\ -1 & 0 & 0 \end{pmatrix} \tag{4.25a}$$

$$\boldsymbol{b}_m = \begin{pmatrix} Z_\eta \\ M_\eta \\ 0 \end{pmatrix}. \tag{4.25b}$$

The dynamics are shaped by means of the feedback gains $\boldsymbol{k_{DPI}}^T$, as they are determined in Section 4.1.1, while the feed-forward contribution of α_{cmd} is scaled with the gain h_{DPI}. In this thesis, the philosophy is to use as much physical knowledge as possible while describing reference dynamics. This knowledge is also used for the construction of suitable state predictor architectures of the adaptive controllers in the same way. Thus, actuator dynamics, delay and filter transfer functions are considered by means of $\hat{G}_A(t)$ shown in Eq. (4.7), $\hat{G}_{D,c}(t)$ introduced in Eq. (4.8) and $G_{F,u}(t)$ as well as

$G_{F,y}(t)$, which are described in Section 4.1.2. $G_{F,y}(t)$ is shifted to the input channel exploiting the linear character of the short-period dynamics (c.f. also Section 4.1.1). The filters $G_{F,u}(t)$ and $G_{F,y}(t)$ are only applied for the controller design, when the enhanced aircraft model is used for the simulations and neglected for the basic aircraft model case. This is done in accordance with the baseline controller gain design shown in Section 4.1.1. Note additionally that the saturation functions are the reason, why the reference dynamics cannot be summarized into one single $\boldsymbol{A}_m$ matrix and the feedback $\boldsymbol{k_{DPI}}^T$ has to be considered separately in Eq. (4.23). Thus, $\boldsymbol{A}_m$ could also contain eigenvalues with positive real part value i.e. the poles of $\boldsymbol{A}_m$ indicate an unstable open-loop system, which is stabilized by means of the baseline controller. This case is not considered for the work at hand.

The aircraft dynamic behavior in terms of short-period frequency $\omega_{0,sp}$ and damping ζ_{sp} is not homogeneous across the envelope, which can be seen in Eqs. (A.1c) to (A.15c). The same statement can be made for the targeted $\omega_{0,sp,des}$, which should be achieved by the controller as shown in Fig. 4.3. Thus, it would make no sense to demand that the adaptive controller adjusts the dynamics according to a reference model determined on one single envelope point. Instead, $\boldsymbol{A}_m$ and $\boldsymbol{b}_m$, as well as the gains of the modeled controller h_{DPI} and $\boldsymbol{k_{DPI}}$, are scheduled with the dynamic pressure $\bar{q}$, which is the same scheduling as applied to the baseline controller shown in Section 4.1. This way, the reference dynamics always represent the nominal aircraft dynamics in combination with the baseline controller in dependence of the current envelope point.

4.2.2. DPI Augmentation

This section further describes the application of the classical closed-loop augmentation approach on the DPI baseline controller using L1 Adaptive Control with piecewise constant update laws. The basic structure of the approach shown in Section 3.2 is adapted in order to suit the specific control problem. First, the plant dynamics to be controlled are formulated. The next step shows an appropriate state predictor design matching the assumed structure of the plant. On this basis, the resulting estimation error dynamics can be derived, which result in the piecewise constant parameter update law and the accompanying control law.

Plant The plant dynamics to be controlled by the L1 adaptive controller applied as *DPI Augmentation* (*Closed-Loop Augmentation*) consist of aircraft short-period dynamics, baseline controller, actuator and filter dynamics, as well as delay. Thus, the structure heavily builds up on the reference dynamics given in Eq. (4.23). This equation is extended by the formulation of uncertainties according to Eq. (3.24a), which results in

$$\begin{aligned}\dot{\boldsymbol{x}}(t) &= \boldsymbol{A}_m \boldsymbol{x}(t) + \boldsymbol{b}_m \cdot \Lambda(t) * G_{F,u}(t) * G_{F,y}(t) * G_{D,c}(t) * G_A(t) \\ &\quad * \operatorname{sat}\left\{ \int_{t_0}^{t} \operatorname{sat}\left[-\boldsymbol{k_{DPI}}^T \cdot \frac{d}{d\tau} x(\tau) + h_{DPI} \cdot \frac{d}{d\tau} \alpha_{cmd}(\tau) + \frac{d}{d\tau} u_{ad,1}(\tau) \right] d\tau \right\} \\ &\quad + \boldsymbol{b}_m f_m(t, \boldsymbol{x}(t), \boldsymbol{y_z}(t)) + \boldsymbol{B}_{um} \boldsymbol{f_{um}}(t, \boldsymbol{x}(t), \boldsymbol{y_z}(t)) \\ &\quad + \begin{pmatrix} 0 \\ 0 \\ 1 \end{pmatrix} \left[u_{ad,2}(t) + \alpha_{cmd}(t) \right], \end{aligned} \tag{4.26}$$

where $\boldsymbol{A}_m$ and $\boldsymbol{b}_m$ are defined in Eq. (4.25a) and Eq. (4.25b), respectively. The adaptive control law is subdivided into two portions representing the matched uncertainty compensation $u_{ad,1}(t)$ and $u_{ad,2}(t)$, which compensates for unmatched uncertainties. The uncertainties $\boldsymbol{f_m}$ and $\boldsymbol{f_{um}}$ both depend on time t, the system states $\boldsymbol{x}(t)$ and unknown internal dynamics represented by their output $\boldsymbol{y_z}(t)$ (c.f. also Section 3.2).

$$\boldsymbol{B}_{um} = \begin{pmatrix} b_{um,11} & b_{um,12} \\ b_{um,21} & b_{um,22} \\ b_{um,31} & b_{um,32} \end{pmatrix} \tag{4.27}$$

is a matrix chosen such that $\boldsymbol{b_m}^T \boldsymbol{B}_{um} = 0$ is satisfied.
The already mentioned subdivison of the adaptive control signal has the purpose that $u_{ad,2}(t)$ can be directly inserted into the integrator of the DPI Controller. This way, additional integral error feedback can be avoided [12, pp. 189-190]. A detailed explanation can be found following the introduction of the control law in the remainder of this section. Thus, the insertion point for $u_{ad,2}(t)$ in Fig. 4.1 is summation point ⑪. Note that in contrast to the statement made in Section 4.2, $u_{ad,2}(t)$ does not need to be differentiated in this case.

State Predictor Analogous to the plant dynamics described in Eq. (4.26), the state predictor is constructed according to

$$\begin{aligned}\dot{\hat{\boldsymbol{x}}}(t) &= \boldsymbol{A}_m \hat{\boldsymbol{x}}(t) + \boldsymbol{b}_m \cdot \Lambda_0 \cdot G_{F,u}(t) * G_{F,y}(t) * \hat{G}_{D,c}(t) * \hat{G}_A(t) \\ &\quad * \operatorname{sat}\left\{ \int_{t_0}^{t} \operatorname{sat}\left[-\boldsymbol{k_{DPI}}^T \cdot \frac{d}{d\tau} \hat{\boldsymbol{x}}(\tau) + h_{DPI} \cdot \frac{d}{d\tau} \alpha_{cmd}(\tau) + \frac{d}{d\tau} u_{ad,1}(\tau) \right] d\tau \right\} \\ &\quad + \boldsymbol{b}_m \hat{\sigma}_m(t) + \boldsymbol{B}_{um} \hat{\boldsymbol{\sigma}}_{\boldsymbol{um}}(t) + \begin{pmatrix} 0 \\ 0 \\ 1 \end{pmatrix} \left[u_{ad,2}(t) + \alpha_{cmd}(t) \right] \\ &\quad + \boldsymbol{b}_m \cdot \Delta u(t) + \boldsymbol{K}_e \tilde{\boldsymbol{x}}(t) \end{aligned} \tag{4.28}$$

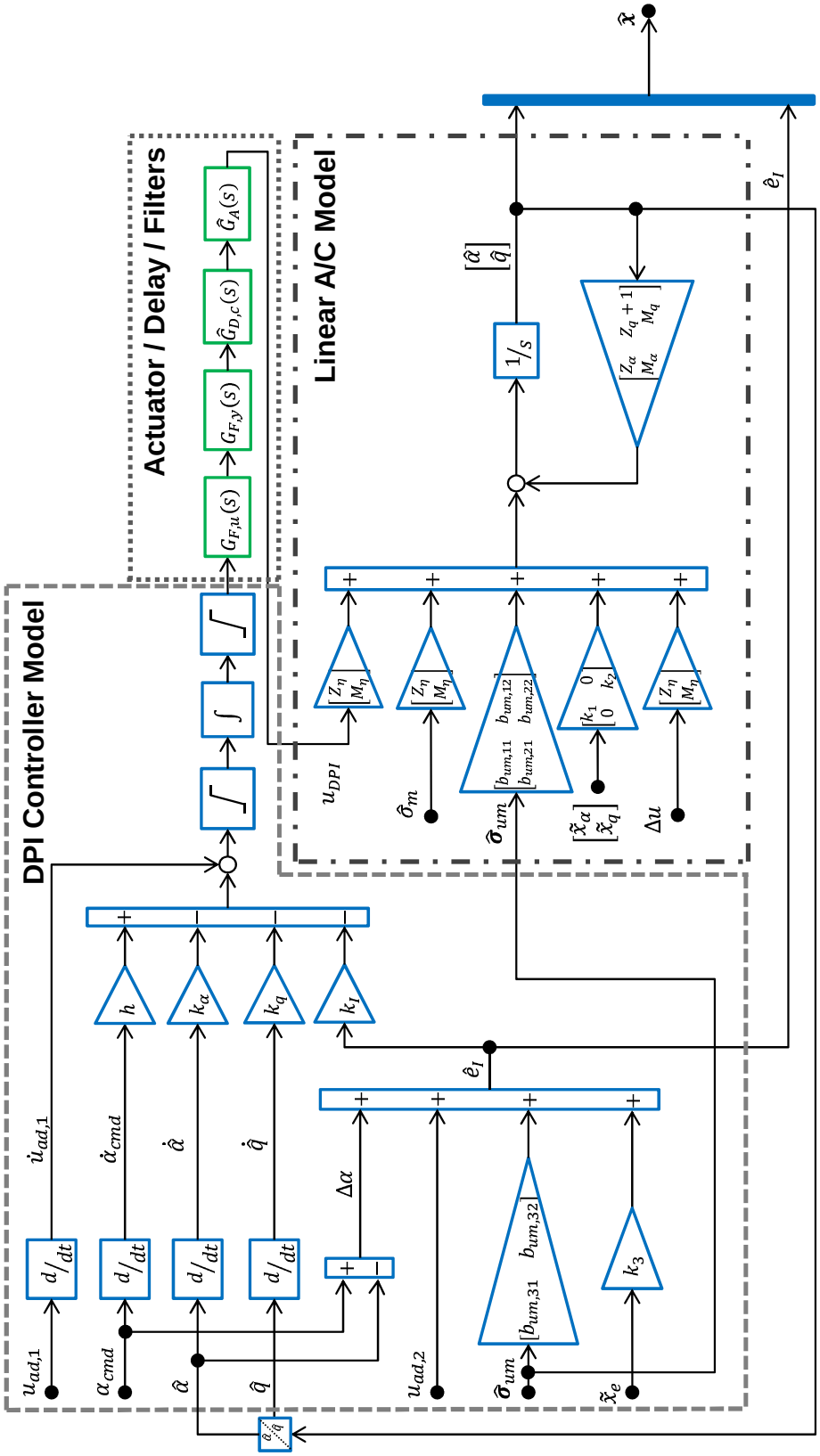

Figure 4.14. – DPI Augmentation - State predictor

with estimations of the matched $\hat{\sigma}_m$ and unmatched $\hat{\boldsymbol{\sigma}}_{\boldsymbol{um}}$ uncertainties. The state predictor structure is also compiled in Fig. 4.14. Λ_0 is an initial guess of the control effectiveness and is set to $\Lambda_0 = 1$. The state predictor contains a replication of the baseline controller structure. This way, it is ensured that the adaptive control signal does not "fight" the baseline controller signal, in case of nominal plant conditions [43]. Additional feedback of the estimation error

$$\tilde{\boldsymbol{x}}(t) = \hat{\boldsymbol{x}}(t) - \boldsymbol{x}(t) \tag{4.29}$$

can be used to further tune the performance with respect to the error dynamics by adjusting the gain matrix $\boldsymbol{K_e}$ [138, 59]. In [26, pp. 45-46] it is shown how this term can be used to adjust the error dynamics using pole placement. In this thesis, $\boldsymbol{K_e}$ is not used to extensively modify the error dynamics, but serves the purpose to enable the inversion of the error dynamics system matrix, which is required to build up the parameter update law. Without this modification, the matrix $\boldsymbol{A}_m$ in Eq. (4.25a) defines the error dynamics, which cannot be inverted as it does not have full rank. This is due to the consideration of the integrator state.
In contrast to the L1 Adaptive Control with piecewise constant update laws according to the textbook approach presented in Section 3.2, another modifications is proposed in this thesis [52]. This modification accounts for additional unmodeled dynamics at the plant input channel and is performed by means of the term

$$\begin{aligned}\Delta u(t) = \eta_{meas}(t) - \Lambda_0 \cdot G_{F,u}(t) * G_{F,y}(t) * \hat{G}_{D,c}(t) * \hat{G}_A(t) \\ * \operatorname{sat}\left\{ \int_{t_0}^{t} \operatorname{sat}\left[\dot{u}_{bl}(\tau) + \frac{d}{d\tau} u_{ad,1}(\tau) \right] d\tau \right\}\end{aligned} \tag{4.30}$$

with

$$\dot{u}_{bl}(\tau) = -\boldsymbol{k_{DPI}}^T \cdot \frac{d}{d\tau} x(\tau) + h_{DPI} \cdot \frac{d}{d\tau} \alpha_{cmd}(\tau) \tag{4.31}$$

at the state predictor input, which is also shown in Fig. 4.15. This term is constructed utilizing the idea of Pseudo-Control Hedging [62]. $\Delta u(t)$ is the difference between the measured actuator deflection $\eta_{meas}(t)$ and the control signal, which is expected to enter the aircraft dynamics on a system level. Thus, the last term consists of the complete control law command including the baseline controller command. This command is led through models of all additional dynamics, which are also considered within the state predictor. As shown in Fig. 5.30 and Fig. 5.31 in Section 5.2.2.1, this term has a significant role in preserving the robust stability properties w.r.t. the actuator cut of the closed-loop system.
Analogous to the reference dynamics shown in Section 4.2.1, the state predictor uses scheduled versions of $\boldsymbol{A}_m$, $\boldsymbol{b}_m$, $\boldsymbol{k_{DPI}}$ and h_{DPI}. It has to be noted that state predictor scheduling for the L1 adaptive controller was also utilized during the NASA AirSTAR

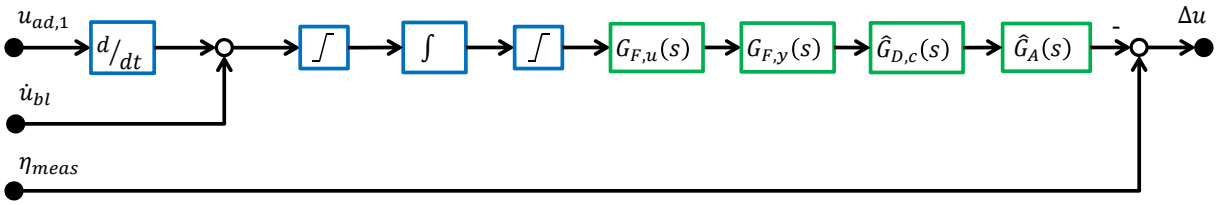

Figure 4.15. – DPI Augmentation - Hedging

flight tests [58, pp. 254-255]. In contrast to this application, here scheduling is also applied to the matrices and transfer functions used within the parameter update law and the control law shown below as well as for the matrix $\boldsymbol{B}_{um}$.

Error Dynamics The error dynamics can be derived from derivation of Eq. (4.29) and usage of the plant Eq. (4.26) and state predictor definition Eq. (4.28), which leads to

$$\begin{aligned}\dot{\tilde{\boldsymbol{x}}}(t) &= \dot{\hat{\boldsymbol{x}}}(t) - \dot{\boldsymbol{x}}(t)\\ &= (\boldsymbol{A}_m + \boldsymbol{K}_{\boldsymbol{e}})\,\tilde{\boldsymbol{x}}(t)\\ &+ \boldsymbol{b}_m \cdot \Lambda_0 \cdot G_{F,u}(t) * G_{F,y}(t) * \hat{G}_{D,c}(t) * \hat{G}_A(t) * \hat{u}(t)\\ &- \boldsymbol{b}_m \cdot \Lambda(t) * G_{F,u}(t) * G_{F,y}(t) * \left(\hat{G}_{D,c}(t) - \tilde{G}_{D,c}(t)\right) * \left(\hat{G}_A(t) - \tilde{G}_A(t)\right) * u(t)\\ &+ \boldsymbol{b}_m \left[\hat{\sigma}_m(t) - f_m\left(t, \boldsymbol{x}(t), \boldsymbol{y}_z(t)\right)\right] + \boldsymbol{B}_{um}\left[\hat{\boldsymbol{\sigma}}_{\boldsymbol{um}}(t) - \boldsymbol{f}_{\boldsymbol{um}}\left(t, \boldsymbol{x}(t), \boldsymbol{y}_z(t)\right)\right]\\ &+ \boldsymbol{b}_m \cdot \Delta u(t)\end{aligned} \tag{4.32}$$

in a first step. Here, the definitions

$$u(t) = \text{sat}\left\{\int_{t_0}^{t} \text{sat}\left[-\boldsymbol{k}_{\boldsymbol{DPI}}{}^T \cdot \frac{d}{d\tau}\boldsymbol{x}(\tau) + h_{DPI} \cdot \frac{d}{d\tau}\alpha_{cmd}(\tau) + \frac{d}{d\tau}u_{ad,1}(\tau)\right] d\tau\right\} \tag{4.33a}$$

$$\hat{u}(t) = \text{sat}\left\{\int_{t_0}^{t} \text{sat}\left[-\boldsymbol{k}_{\boldsymbol{DPI}}{}^T \cdot \frac{d}{d\tau}\hat{\boldsymbol{x}}(\tau) + h_{DPI} \cdot \frac{d}{d\tau}\alpha_{cmd}(\tau) + \frac{d}{d\tau}u_{ad,1}(\tau)\right] d\tau\right\} \tag{4.33b}$$

$$\tilde{G}_{D,c}(t) = \hat{G}_{D,c}(t) - G_{D,c}(t) \tag{4.33c}$$

$$\tilde{G}_A(t) = \hat{G}_A(t) - G_A(t) \tag{4.33d}$$

are used. An intermediate step shows that

$$\left(\hat{G}_{D,c}(t) - \tilde{G}_{D,c}(t)\right) * \left(\hat{G}_A(t) - \tilde{G}_A(t)\right) = \hat{G}_{D,c}(t) * \hat{G}_A(t) + \Delta_{A,D,c}(t) \tag{4.34}$$

with

$$\begin{aligned}\Delta_{A,D,c}(t) &= -\hat{G}_{D,c}(t) * \tilde{G}_A(t) - \tilde{G}_{D,c}(t) * \hat{G}_A(t) + \tilde{G}_{D,c}(t) * \tilde{G}_A(t) \\ &= -\hat{G}_{D,c}(t) * \hat{G}_A(t) + \hat{G}_{D,c}(t) * G_A(t) - \hat{G}_{D,c}(t) * \hat{G}_A(t) \\ &+ G_{D,c}(t) * \hat{G}_A(t) + \left[\hat{G}_{D,c}(t) - G_{D,c}(t)\right] * \left[\hat{G}_A(t) - G_A(t)\right] \\ &= -2 \cdot \hat{G}_{D,c}(t) * \hat{G}_A(t) + \hat{G}_{D,c}(t) * G_A(t) + G_{D,c}(t) * \hat{G}_A(t) \\ &+ \hat{G}_{D,c}(t) * \hat{G}_A(t) - \hat{G}_{D,c}(t) * G_A(t) - G_{D,c}(t) * \hat{G}_A(t) \\ &+ G_{D,c}(t) * G_A(t) \\ &= G_{D,c}(t) * G_A(t) - \hat{G}_{D,c}(t) * \hat{G}_A(t). \end{aligned} \tag{4.35}$$

Using this relation, Eq. (4.32) can be further rearranged to

$$\begin{aligned}\dot{\tilde{\boldsymbol{x}}}(t) &= (\boldsymbol{A}_m + \boldsymbol{K}_e)\,\tilde{\boldsymbol{x}}(t) \\ &+ \boldsymbol{b}_m\{\hat{\sigma}_m(t) - f_m(t, \boldsymbol{x}(t), \boldsymbol{y}_z(t)) - \Lambda(t) * G_{F,u}(t) * G_{F,y}(t) * \Delta_{A,D,c}(t) * u(t) \\ &+ G_{F,u}(t) * G_{F,y}(t) * \hat{G}_{D,c}(t) * \hat{G}_A(t) * [\Lambda_0 \cdot \hat{u}(t) - \Lambda(t) * u(t)]\} \\ &+ \boldsymbol{B}_{um}\left[\hat{\boldsymbol{\sigma}}_{\boldsymbol{um}}(t) - \boldsymbol{f}_{\boldsymbol{um}}(t, \boldsymbol{x}(t), \boldsymbol{y}_z(t))\right] + \boldsymbol{b}_m \cdot \Delta u(t). \end{aligned} \tag{4.36}$$

Note that the commutative law is also valid for the convolution operator [107, p. 302]. Based on this equation, two different cases have to be considered, where hedging is whether applied or not. In the first case, hedging is used, thus plugging Eq. (4.30) in Eq. (4.36) under consideration of the definition Eq. (4.33a) yields

$$\begin{aligned}\dot{\tilde{\boldsymbol{x}}}(t) &= (\boldsymbol{A}_m + \boldsymbol{K}_e)\,\tilde{\boldsymbol{x}}(t) \\ &+ \boldsymbol{b}_m\{\hat{\sigma}_m(t) - f_m(t, \boldsymbol{x}(t), \boldsymbol{y}_z(t)) - \Lambda(t) * G_{F,u}(t) * G_{F,y}(t) * \Delta_{A,D,c}(t) * u(t) \\ &+ \eta_{meas}(t) - \Lambda(t) * G_{F,u}(t) * G_{F,y}(t) * \hat{G}_{D,c}(t) * \hat{G}_A(t) * u(t) \\ &+ G_{F,u}(t) * G_{F,y}(t) * \hat{G}_{D,c}(t) * \hat{G}_A(t) * [\Lambda_0 \cdot (\hat{u}(t) - u(t))]\} \\ &+ \boldsymbol{B}_{um}\left[\hat{\boldsymbol{\sigma}}_{\boldsymbol{um}}(t) - \boldsymbol{f}_{\boldsymbol{um}}(t, \boldsymbol{x}(t), \boldsymbol{y}_z(t))\right] \end{aligned} \tag{4.37}$$

after some rearrangement. Now defining the lumped matched and unmatched uncertainties as

$$\begin{aligned}\sigma_m(t) &= f_m(t, \boldsymbol{x}(t), \boldsymbol{y}_z(t)) + \Lambda(t) * G_{F,u}(t) * G_{F,y}(t) * \Delta_{A,D,c}(t) * u(t) \\ &+ \Lambda(t) * G_{F,u}(t) * G_{F,y}(t) * \hat{G}_{D,c}(t) * \hat{G}_A(t) * u(t) - \eta_{meas}(t) \\ &- G_{F,u}(t) * G_{F,y}(t) * \hat{G}_{D,c}(t) * \hat{G}_A(t) * [\Lambda_0 \cdot (\hat{u}(t) - u(t))] \end{aligned} \tag{4.38a}$$

$$\boldsymbol{\sigma}_{\boldsymbol{um}}(t) = \boldsymbol{f}_{\boldsymbol{um}}(t, \boldsymbol{x}(t), \boldsymbol{y}_z(t)) \tag{4.38b}$$

and using the definition

$$\boldsymbol{A}_{m,K} = \boldsymbol{A}_m + \boldsymbol{K_e}, \tag{4.39}$$

Eq. (4.37) results in

$$\dot{\tilde{\boldsymbol{x}}}(t) = \boldsymbol{A}_{m,K}\tilde{\boldsymbol{x}}(t) + \boldsymbol{b}_m\left[\hat{\sigma}_m(t) - \sigma_m(t)\right] + \boldsymbol{B}_{um}\left[\hat{\boldsymbol{\sigma}}_{\boldsymbol{um}}(t) - \boldsymbol{\sigma}_{\boldsymbol{um}}(t)\right], \tag{4.40}$$

which has the same shape as Eq. (3.27), from which the parameter update law is deduced in Section 3.2. Considering Eq. (4.40) in combination with Eq. (4.39) another advantage of the introduced additional error feedback via $\boldsymbol{K_e}$ becomes obvious. In case the open-loop system has unstable dynamics, i.e. $\boldsymbol{A}_m$ has eigenvalues with positive real part, $\boldsymbol{K_e}$ can be used to stabilize the error dynamics Eq. (4.40). This way, it can be made sure that all eigenvalues of $\boldsymbol{A}_{m,K}$ lie in the left half-plane.
In case hedging is not used, $\Delta u(t) = 0$ is plugged into Eq. (4.36). This also results in Eq. (4.40), but the lumped matched uncertainty

$$\begin{aligned}\sigma_m(t) = {} & f_m\left(t, \boldsymbol{x}(t), \boldsymbol{y_z}(t)\right) + \Lambda(t) * G_{F,u}(t) * G_{F,y}(t) * \Delta_{A,D,c}(t) * u(t) \\ & - G_{F,u}(t) * G_{F,y}(t) * \hat{G}_{D,c}(t) * \hat{G}_A(t) * \left[\Lambda_0 \cdot \hat{u}(t) - \Lambda(t) * u(t)\right]\end{aligned} \tag{4.41}$$

is slightly different to the one shown in Eq. (4.38a). Table 4.2 highlights these differences and it can be seen that the additional information of the actuator deflection due to hedging also reflects in the structure of the lumped matched uncertainty.

Parameter Update Law Using Eq. (4.40) the piecewise constant update law for the matched and unmatched uncertainty estimations can be deduced analogously to Eq. (3.38) in Section 3.2 and results in

$$\begin{pmatrix}\hat{\sigma}_m(t) \\ \hat{\boldsymbol{\sigma}}_{\boldsymbol{um}}(t)\end{pmatrix} = \boldsymbol{K_{L1}}(T_s)\,\tilde{\boldsymbol{x}}(iT_s) \quad \forall t \in [iT_s, (i+1)T_s] \tag{4.42}$$

where

$$\boldsymbol{K_{L1}}(T_s) = -\begin{pmatrix}\boldsymbol{b}_m & \boldsymbol{B}_{um}\end{pmatrix}^{-1}\left[\boldsymbol{A}_{m,K}{}^{-1}\left(e^{\boldsymbol{A}_{m,K}T_s} - \boldsymbol{I}_{n\times n}\right)\right]^{-1} e^{\boldsymbol{A}_{m,K}T_s}. \tag{4.43}$$

This parameter update law is valid independent of the choice, if hedging is applied or not. It was mentioned before that the additional error feedback matrix $\boldsymbol{K_e}$ is used to gain an invertible system matrix $\boldsymbol{A}_{m,K}$ for the error dynamics. This is exactly needed for the computation of Eq. (4.43). In the context of this thesis

Table 4.2. – Comparison of components of lumped matched uncertainty for *DPI Augmentation* considering the cases with and without hedging

***DPI Augmentation* with Hedging**	
Component	**Description**
$f_m\left(t, \boldsymbol{x}\left(t\right), \boldsymbol{y_z}\left(t\right)\right)$	Uncertainties concerning the system matrix $\boldsymbol{A}_m$
$\Lambda\left(t\right) * G_{F,u}\left(t\right) * G_{F,y} * \Delta_{A,D,c}\left(t\right) * u\left(t\right)$	Uncertainties due to deficiencies between actuator / delay model and reality
$-G_{F,u}\left(t\right) * G_{F,y}\left(t\right) * \hat{G}_{D,c}\left(t\right) * \hat{G}_A\left(t\right) * \left[\Lambda_0 \cdot \left(\hat{u}\left(t\right) - u\left(t\right)\right)\right]$	Uncertainties due to difference between modeled $\hat{u}\left(t\right)$ and real control command $u\left(t\right)$
$\Lambda\left(t\right) * G_{F,u}\left(t\right) * G_{F,y}\left(t\right) * \hat{G}_{D,c}\left(t\right) * \hat{G}_A\left(t\right) * u\left(t\right) - \eta_{meas}$	Uncertainties due to deviation between expected and measured control deflection
***DPI Augmentation* without Hedging**	
Component	**Description**
$f_m\left(t, \boldsymbol{x}\left(t\right), \boldsymbol{y_z}\left(t\right)\right)$	Uncertainties concerning the system matrix $\boldsymbol{A}_m$
$\Lambda\left(t\right) * G_{F,u}\left(t\right) * G_{F,y} * \Delta_{A,D,c}\left(t\right) * u\left(t\right)$	Uncertainties due to deficiencies between actuator / delay model and reality
$-G_{F,u}\left(t\right) * G_{F,y}\left(t\right) * \hat{G}_{D,c}\left(t\right) * \hat{G}_A\left(t\right) * \left[\Lambda_0 \cdot \hat{u}\left(t\right) - \Lambda\left(t\right) * u\left(t\right)\right]$	Uncertainties due to difference between modeled $\hat{u}\left(t\right)$ and real control command considering also modeled Λ_0 and real $\Lambda\left(t\right)$ control effectiveness

$$\boldsymbol{K_e} = \begin{pmatrix} 0 & 0 & 0 \\ 0 & 0 & 0 \\ 0 & 0 & -0.1 \end{pmatrix} \tag{4.44}$$

is used for this purpose.

Control Law The control law from Eq. (3.43) in Section 3.2 is subdivided in portions for matched and unmatched uncertainties, respectively. They are defined as

$$u_{ad,1}(s) = -C_m(s)\,\hat{\sigma}_m(s) \tag{4.45a}$$

$$u_{ad,2}(s) = -C_{um}(s)\,{H_m}^{-1}(s)\,\boldsymbol{H_{um}}(s)\,\underbrace{\begin{pmatrix} \hat{\sigma}_{um,1}(s) \\ \hat{\sigma}_{um,2}(s) \end{pmatrix}}_{\hat{\sigma}_{\boldsymbol{um}}(s)}, \tag{4.45b}$$

where the transfer functions

$$H_m(s) = \boldsymbol{c}_m\left(s\boldsymbol{I}_{n\times n} - \boldsymbol{A}_{m\star}\right)^{-1}\begin{pmatrix} 0 \\ 0 \\ 1 \end{pmatrix} \tag{4.46}$$

$$\boldsymbol{H_{um}}(s) = \boldsymbol{c}_m\left(s\boldsymbol{I}_{n\times n} - \boldsymbol{A}_{m\star}\right)^{-1}\boldsymbol{B}_{um} \tag{4.47}$$

with $\boldsymbol{c}_m = \begin{pmatrix} 1 & 0 & 0 \end{pmatrix}$ are used. The system matrix used for the transfer functions is conducted as

$$\boldsymbol{A}_{m\star} = \boldsymbol{A}_m - \boldsymbol{b}_m k_\star^T, \tag{4.48}$$

where the gains $k_\star^T$ are designed such that $\boldsymbol{A}_{m\star}$ inherits the desired dynamics with respect to short-period and integrator pole, as they are described in Section 4.2.1. Note that, in this context, the idealizing assumption is used that the plant dynamics can be characterized by short-period and error integration, solely. Another reason to use $\boldsymbol{A}_{m\star}$ instead of $\boldsymbol{A}_m$ here is the already mentioned possibility of an unstable open-loop system. This is, because the baseline controller, which is stabilizing in this case, is not represented in $\boldsymbol{A}_m$ and is considered separately in the state predictor structure due to the nonlinear limitations.
It is also considered in Eq. (4.46) that $u_{ad,2}$ is fed into the integrator of the baseline controller as mentioned above. For that reason, the input vector $\begin{pmatrix} 0 & 0 & 1 \end{pmatrix}^T$ is used instead of $\boldsymbol{b}_m$, as it is shown in [12, pp. 189-190]. ${H_m}^{-1}(s)\,\boldsymbol{H_{um}}(s)$ consists of two transfer functions, one related to uncertainties in α (i.e. $\hat{\sigma}_{um,1}(s)$) and the other related to uncertainties in e_I (i.e. $\hat{\sigma}_{um,2}(s)$) assuming $\boldsymbol{b}_m \approx \begin{pmatrix} 0 & M_\eta & 0 \end{pmatrix}^T$ and $Z_\eta \approx 0$. If $\boldsymbol{b}_m$ was used for the generation of $H_m(s)$ in this case, the second transfer function

would be a pure integration. This is not desired, since $\hat{\sigma}_{um,2}(s)$ is proportional to the estimation error $\tilde{\boldsymbol{x}}(t)$ and thus, this configuration would result in additional integral error feedback. With the choice of $H_m(s)$ shown in Eq. (4.46) the first transfer function results equally, but contains an additional zero in the origin. The second transfer function is then a constant gain. Thus, feeding $u_{ad,2}$ in the integrator of the baseline controller leads to the same transfer behavior as shown above, but in contrast to that, no additional integration is generated.
At last, the Low-Pass Filters of the control law are chosen to be first order filter transfer functions [75, pp. 291-295]

$$C_m(s) = \frac{\omega_{0,C,m}}{s + \omega_{0,C,m}} \tag{4.49a}$$

$$C_{um}(s) = \frac{\omega_{0,C,um}}{s + \omega_{0,C,um}}, \tag{4.49b}$$

where the bandwidths are set to $\omega_{0,C,m} = 15\frac{rad}{s}$ and $\omega_{0,C,um} = 7\frac{rad}{s}$. This values stem from a tuning process considering maneuver simulations using the enhanced aircraft model in a sever turbulence case without parametric uncertainties (e.g. Fig. 6.20). The goal was to narrow the bandwidths to a point, where the performance using the adaptive augmentation in this use-case is comparable to the performance achieved by the baseline controller. The reason why the adaptive controller is much more sensitive to sensor signals, which are affected by turbulence, is that the parameter update law Eq. (4.42) leads to high gain feedback of these sensor signals in combination with Eq. (4.45). Thus, appropriate low-pass filtering of the resulting control commands using $C_m(s)$ and $C_{um}(s)$, in addition to the filter chain introduced in Section 4.1.2, gives remedy here. This filter configuration is used for assessments with both the simple and the enhanced aircraft model.
The adaptive augmentation is processed with the same sampling time of $T_s = 0.01s$ as the baseline controller. All transfer functions contained in the adaptive control law are transformed to discrete-time by means of bilinear transformation introduced in Section 3.3. The only exception is the implementation of the short-period dynamics within the state predictor, where Euler's method is applied. This is done in order to avoid an algebraic loop. The application of bilinear transformation, which would increase accuracy here, results in a state space model with direct feedthrough, whereas its continuous-time representation does not have a feedthrough portion.

4.2.3. Plant Augmentation

Next, the architecture of the *Plant Augmentation* approach is described. In contrast to *DPI Augmentation* shown in the last section, the idea of *Plant Augmentation* is to augment the open-loop aircraft using an adaptive controller first. Afterwards, the baseline controller is applied to the resulting closed loop. This modified perspective on

the augmentation architecture leads to slight differences with respect to the elements of the adaptive controller, especially the state predictor. These differences are highlighted in this section.

Plant It was already mentioned that the adaptive controller is applied to the open-loop aircraft, which also reflects in the structure of the plant to be considered for the controller design:

$$\begin{aligned}\dot{\boldsymbol{x}}(t) = {} & \boldsymbol{A}_m \boldsymbol{x}(t) + \boldsymbol{b}_m \cdot \Lambda(t) * G_{F,u}(t) * G_{F,y}(t) * G_{D,c}(t) * G_A(t) \\ & * \operatorname{sat}\left\{ \int_{t_0}^{t} \operatorname{sat}\left[\dot{u}_{bl}(\tau) + \frac{d}{d\tau} u_{ad}(\tau) \right] d\tau \right\} \\ & + \boldsymbol{b}_m f_m\left(t, \boldsymbol{x}(t), \boldsymbol{y_z}(t)\right) + \boldsymbol{b}_{um} f_{um}\left(t, \boldsymbol{x}(t), \boldsymbol{y_z}(t)\right)\end{aligned} \tag{4.50}$$

The system matrix reduces to the 2×2 short-period approximation

$$\boldsymbol{A}_m = \begin{pmatrix} Z_\alpha & Z_q + 1 \\ M_\alpha & M_q \end{pmatrix}, \tag{4.51}$$

where the integrator state is neglected and with the input vector

$$\boldsymbol{b}_m = \begin{pmatrix} Z_\eta \\ M_\eta \end{pmatrix} \tag{4.52}$$

chosen accordingly. Nevertheless, the limitation structure of the DPI baseline should be used for the adaptive control command also for this type of augmentation. This means that the adaptive control command $u_{ad}(t)$ is inserted at summation point Ⓘ of the baseline controller in Fig. 4.1. This is reflected in the plant representation in Eq. (4.50). On the other side, one has to consider also the contribution of the baseline controller $\dot{u}_{bl}(t)$ according to Eq. (4.31) to the total commanded actuator deflection rate. But in contrast to the *DPI Augmentation* approach, the exact structure of the signal generation, and thus the baseline controller, does not need to be known in this case, except for the limitation structure in this particular application. This is an advantage, because the baseline controller can then be widely considered as a black box from the point of view of the adaptive control designer.
Furthermore, $\boldsymbol{b}_{um}$ is chosen such that ${\boldsymbol{b}_m}^T \boldsymbol{b}_{um} = \boldsymbol{0}$ holds. Transfer functions of actuator, filters and delay are included analogously to the approach shown in the last section.

State Predictor The state predictor is again constructed according to the plant dynamics. It can be stated as

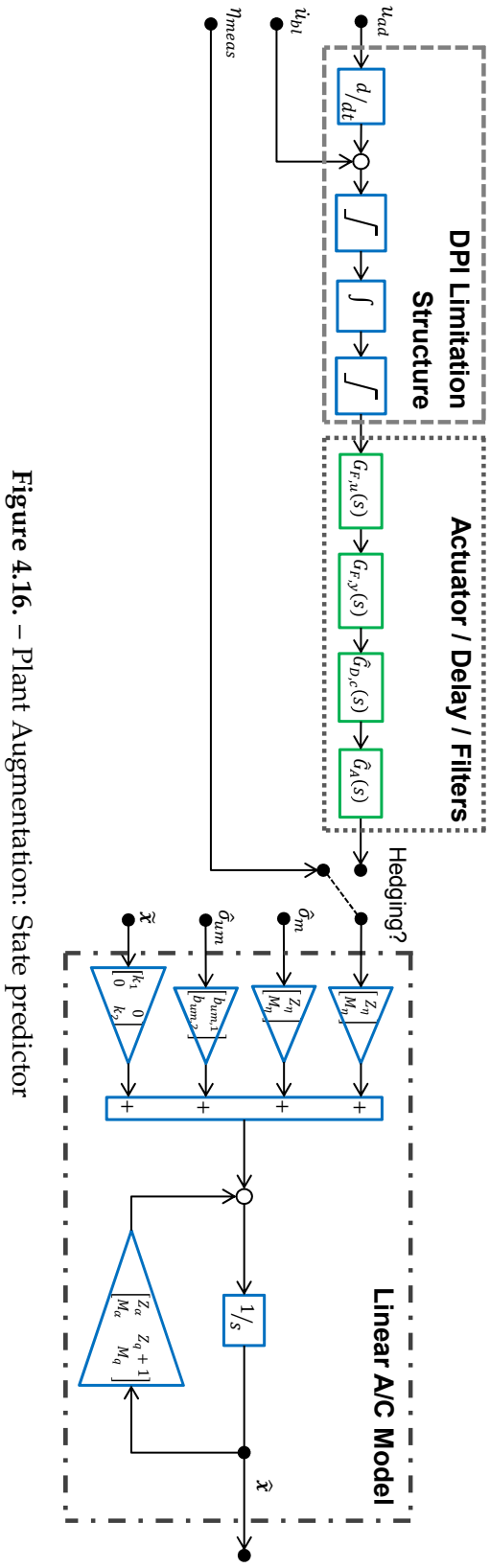

Figure 4.16. – Plant Augmentation: State predictor

$$\begin{aligned}\dot{\hat{\boldsymbol{x}}}(t) = \boldsymbol{A}_m\hat{\boldsymbol{x}}(t) + \boldsymbol{b}_m \cdot \Lambda_0 \cdot G_{F,u}(t) * G_{F,y}(t) * \hat{G}_{D,c}(t) * \hat{G}_A(t) \\ * \operatorname{sat}\left\{\int_{t_0}^{t} \operatorname{sat}\left[\dot{u}_{bl}(\tau) + \frac{d}{d\tau}u_{ad}(\tau)\right] d\tau\right\} \\ + \boldsymbol{b}_m\hat{\sigma}_m(t) + \boldsymbol{b}_{um}\hat{\sigma}_{um}(t) + \boldsymbol{b}_m \cdot \Delta u(t) + \boldsymbol{K_e}\tilde{\boldsymbol{x}}(t)\end{aligned} \tag{4.53}$$

with $\boldsymbol{b}_m{}^T\boldsymbol{b}_{um} = \boldsymbol{0}$. Compared to the state predictor used for the *DPI Augmentation*, it neglects the integrator state and the structure of the baseline controller, except for the command signal limitation structure. The control signal contributed by the baseline controller is denoted with $\dot{u}_{bl}(\tau)$. In order to be able to predict the plant dynamics correctly, the state predictor needs the same control command as an input, as it is sent to the actual plant. Thus, the baseline controller contribution $\dot{u}_{bl}(\tau)$ is summed up with the adaptive controller command $\frac{d}{d\tau}u_{ad}(\tau)$.
As for the *DPI Augmentation*, the gain matrix $\boldsymbol{K_e}$ can be used to control the error dynamics. This is not used for the assessments made in this thesis, thus $\boldsymbol{K_e} = \boldsymbol{0}$ is set.
Analogous to Eq. (4.30), the hedging modification proposed by this thesis

$$\begin{aligned}\Delta u(t) = \eta_{meas}(t) - \Lambda_0 \cdot G_{F,u}(t) * G_{F,y}(t) * \hat{G}_{D,c}(t) * \hat{G}_A(t) \\ * \operatorname{sat}\left\{\int_{t_0}^{t} \operatorname{sat}\left[\dot{u}_{bl} + \frac{d}{d\tau}u_{ad}(\tau)\right] d\tau\right\}\end{aligned} \tag{4.54}$$

can be used to increase the robust stability properties of the resulting closed loop, as it was already described in Section 4.2.2. In case hedging is used, i.e. when Eq. (4.54) is plugged into Eq. (4.53), the state predictor dynamics reduce to

$$\dot{\hat{\boldsymbol{x}}}(t) = \boldsymbol{A}_m\hat{\boldsymbol{x}}(t) + \boldsymbol{b}_m\eta_{meas} + \boldsymbol{b}_m\hat{\sigma}_m(t) + \boldsymbol{b}_{um}\hat{\sigma}_{um}(t) + \boldsymbol{K_e}\tilde{\boldsymbol{x}}(t). \tag{4.55}$$

Both state predictor configurations with respect to hedging are also depicted in Fig. 4.16. Comparing this to the state predictor structure of the *DPI Augmentation* shown in Eq. (4.28), one can clearly see a decrease in complexity, which is achieved by means of *Plant Augmentation*, in particular, if hedging is used.

Error Dynamics Also fully analogously to the last section, the error dynamics can be derived from derivation of

$$\tilde{\boldsymbol{x}}(t) = \hat{\boldsymbol{x}}(t) - \boldsymbol{x}(t) \tag{4.56}$$

and usage of the plant Eq. (4.50) and state predictor definition Eq. (4.53), which leads to

$$\begin{aligned}\dot{\tilde{\boldsymbol{x}}}(t) &= \dot{\hat{\boldsymbol{x}}}(t) - \dot{\boldsymbol{x}}(t)\\ &= (\boldsymbol{A}_m + \boldsymbol{K}_e)\,\tilde{\boldsymbol{x}}(t)\\ &+ \boldsymbol{b}_m \cdot \Lambda_0 \cdot G_{F,u}(t) * G_{F,y}(t) * \hat{G}_{D,c}(t) * \hat{G}_A(t) * u(t)\\ &- \boldsymbol{b}_m \cdot \Lambda(t) * G_{F,u}(t) * G_{F,y}(t) * \left(\hat{G}_{D,c}(t) - \tilde{G}_{D,c}(t)\right) * \left(\hat{G}_A(t) - \tilde{G}_A(t)\right) * u(t)\\ &+ \boldsymbol{b}_m\left[\hat{\sigma}_m(t) - f_m\left(t, \boldsymbol{x}(t), \boldsymbol{y}_z(t)\right)\right] + \boldsymbol{b}_{um}\left[\hat{\sigma}_{um}(t) - f_{um}\left(t, \boldsymbol{x}(t), \boldsymbol{y}_z(t)\right)\right]\\ &+ \boldsymbol{b}_m \cdot \Delta u(t).\end{aligned} \tag{4.57}$$

Here, the definitions

$$u(t) = \text{sat}\left\{\int_{t_0}^{t} \text{sat}\left[\dot{u}_{bl}(\tau) + \frac{d}{d\tau}u_{ad}(\tau)\right] d\tau\right\}, \tag{4.58}$$

$\tilde{G}_{D,c}(t)$ in Eq. (4.33c) and $\tilde{G}_A(t)$ in Eq. (4.33d) are used.
Applying the definition of $\Delta_{A,D,c}(t)$ introduced in Eq. (4.35) one can rearrange Eq. (4.57) to

$$\begin{aligned}\dot{\tilde{\boldsymbol{x}}}(t) &= (\boldsymbol{A}_m + \boldsymbol{K}_e)\,\tilde{\boldsymbol{x}}(t)\\ &+ \boldsymbol{b}_m\{\hat{\sigma}_m(t) - f_m\left(t, \boldsymbol{x}(t), \boldsymbol{y}_z(t)\right) - \Lambda(t) * G_{F,u}(t) * G_{F,y}(t) * \Delta_{A,D,c}(t) * u(t)\\ &- \Lambda(t) * G_{F,u}(t) * G_{F,y}(t) * \hat{G}_{D,c}(t) * \hat{G}_A(t) * \cdot u(t)\\ &+ \Lambda_0 \cdot G_{F,u}(t) * G_{F,y}(t) * \hat{G}_{D,c}(t) * \hat{G}_A(t) * u(t)\}\\ &+ \boldsymbol{b}_{um}\left[\hat{\sigma}_{um}(t) - f_{um}\left(t, \boldsymbol{x}(t), \boldsymbol{y}_z(t)\right)\right] + \boldsymbol{b}_m \cdot \Delta u(t)\end{aligned} \tag{4.59}$$

Finally, the error dynamics can be reformulated as

$$\dot{\tilde{\boldsymbol{x}}}(t) = \boldsymbol{A}_{m,K}\tilde{\boldsymbol{x}}(t) + \boldsymbol{b}_m\left[\hat{\sigma}_m(t) - \sigma_m(t)\right] + \boldsymbol{b}_{um}\left[\hat{\sigma}_{um}(t) - \sigma_{um}(t)\right], \tag{4.60}$$

with the definition of $\boldsymbol{A}_{m,K}$ in Eq. (4.39). As it was already mentioned in Section 4.2.2, the additional error feedback via $\boldsymbol{K}_e$ can be used to prevent unstable error dynamics, in case the open-loop system is unstable.
The lumped matched uncertainty results in

$$\begin{aligned}\sigma_m(t) &= f_m\left(t, \boldsymbol{x}(t), \boldsymbol{y}_z(t)\right) + \Lambda(t) * G_{F,u}(t) * G_{F,y}(t) * \Delta_{A,D,c}(t) * u(t)\\ &+ \Lambda(t) * G_{F,u}(t) * G_{F,y}(t) * \hat{G}_{D,c}(t) * \hat{G}_A(t) * u(t) - \eta_{meas},\end{aligned} \tag{4.61}$$

if hedging is used i.e. Eq. (4.54) is plugged into Eq. (4.59). In case hedging is not activated, i.e. $\Delta u(t) = 0$, the lumped matched uncertainty reads

Table 4.3. – Comparison of components of lumped matched uncertainty for *Plant Augmentation* considering the cases with and without hedging

***Plant Augmentation* with Hedging**	
Component	**Description**
$f_m\left(t, \boldsymbol{x}\left(t\right), \boldsymbol{y_z}\left(t\right)\right)$	Uncertainties concerning the system matrix $\boldsymbol{A}_m$
$\Lambda\left(t\right) * G_{F,u}\left(t\right) * G_{F,y} * \Delta_{A,D,c}\left(t\right) * u\left(t\right)$	Uncertainties due to deficiencies between actuator / delay model and reality
$\Lambda\left(t\right) * G_{F,u}\left(t\right) * G_{F,y}\left(t\right) * \hat{G}_{D,c}\left(t\right) * \hat{G}_A\left(t\right) * u\left(t\right) - \eta_{meas}$	Uncertainties due to deviation between expected and measured control deflection
***Plant Augmentation* without Hedging**	
Component	**Description**
$f_m\left(t, \boldsymbol{x}\left(t\right), \boldsymbol{y_z}\left(t\right)\right)$	Uncertainties concerning the system matrix $\boldsymbol{A}_m$
$\Lambda\left(t\right) * G_{F,u}\left(t\right) * G_{F,y} * \Delta_{A,D,c}\left(t\right) * u\left(t\right)$	Uncertainties due to deficiencies between actuator / delay model and reality
$\left[\delta\left(t\right) \cdot \Lambda_0 - \Lambda\left(t\right)\right] * G_{F,u}\left(t\right) * G_{F,y} * \hat{G}_{D,c}\left(t\right) * \hat{G}_A\left(t\right) * u\left(t\right)$	Uncertainties due to difference between modeled Λ_0 and real $\Lambda\left(t\right)$ control effectiveness

$$\begin{aligned}\sigma_m(t) = {} & f_m(t, \boldsymbol{x}(t), \boldsymbol{y_z}(t)) + \Lambda(t) * G_{F,u}(t) * G_{F,y}(t) * \Delta_{A,D,c}(t) * u(t) \\ & - [\delta(t) \cdot \Lambda_0 - \Lambda(t)] * G_{F,u}(t) * G_{F,y}(t) * \hat{G}_{D,c}(t) * \hat{G}_A(t) * u(t), \end{aligned} \tag{4.62}$$

where $\delta(t)$ denotes the Dirac impulse. The Dirac impulse is defined according to [107, p. 293]

$$\delta(t) = \begin{cases} \infty & \text{if } t = 0 \\ 0 & \text{if } t \neq 0 \end{cases}. \tag{4.63}$$

Independent from the choice of hedging activation, the definition of the lumped unmatched uncertainty reads

$$\sigma_{um}(t) = f_{um}(t, \boldsymbol{x}(t), \boldsymbol{y_z}(t)). \tag{4.64}$$

The components of the lumped matched uncertainties are summarized in Table 4.3 for both hedging cases. A comparison with Table 4.2 corresponding to the *DPI Augmentation* shows that the components are mostly matching. The only exception is that the *DPI Augmentation* features an additional component, which considers an uncertainty based on the difference between modeled and real baseline controller command. Thus, it can be summarized that by means of the *Plant Augmentation* approach one source for uncertainty can be removed.

Parameter Update Law The resulting error dynamics in Eq. (4.60) can be used to generate the parameter update law for the estimated uncertainties following the approach shown in Section 3.2. Thus, the update law reads

$$\begin{pmatrix} \hat{\sigma}_m(t) \\ \hat{\sigma}_{um}(t) \end{pmatrix} = \boldsymbol{K_{L1}}(T_s)\, \tilde{\boldsymbol{x}}(iT_s) \quad \forall t \in [iT_s, (i+1)T_s] \tag{4.65}$$

where

$$\boldsymbol{K_{L1}}(T_s) = -\begin{pmatrix} \boldsymbol{b}_m & \boldsymbol{b}_{um} \end{pmatrix}^{-1} \left[{\boldsymbol{A}_{m,K}}^{-1} \left(e^{\boldsymbol{A}_{m,K} T_s} - \boldsymbol{I}_{n\times n} \right) \right]^{-1} e^{\boldsymbol{A}_{m,K} T_s} \tag{4.66}$$

with $\boldsymbol{A}_{m,K} = \boldsymbol{A}_m + \boldsymbol{K_e}$. As shown for the *DPI Augmentation*, the formulation of the parameter update law is independent from the circumstance, if hedging is applied or not.

Control Law At last the control law can be described through

$$u_{ad}(s) = -C_m(s)\, \hat{\sigma}_m(s) - C_{um}(s)\, {H_m}^{-1}(s)\, H_{um}(s)\, \hat{\sigma}_{um}(s) \tag{4.67}$$

where

$$H_m(s) = \boldsymbol{c}_m \left(s\boldsymbol{I}_{n\times n} - \boldsymbol{A}_{m\star}\right)^{-1} \boldsymbol{b}_{m,\star} \tag{4.68a}$$

$$H_{um}(s) = \boldsymbol{c}_m \left(s\boldsymbol{I}_{n\times n} - \boldsymbol{A}_{m\star}\right)^{-1} \boldsymbol{b}_{um,\star} \tag{4.68b}$$

with $\boldsymbol{A}_{m\star}$ introduced in Eq. (4.48), which is defined in Section 4.2.2. The input vectors are chosen according to $\boldsymbol{b}_{m,\star} = \begin{pmatrix} Z_\eta & M_\eta & 0 \end{pmatrix}^T$ and

$$\boldsymbol{b}_{um,\star} = \begin{pmatrix} b_{um,11} \\ b_{um,21} \\ b_{um,31} \end{pmatrix}, \tag{4.69}$$

which is the first column of $\boldsymbol{B}_{um}$ shown in Eq. (4.27). At last, the output vector is set to $\boldsymbol{c}_m = \begin{pmatrix} 1 & 0 & 0 \end{pmatrix}$. It was chosen to use the simplified closed-loop dynamics represented by $\boldsymbol{A}_{m\star}$ here instead of the open-loop system matrix $\boldsymbol{A}_m$, because this way the unmatched uncertainty compensation works even in case of an unstable open-loop system, i.e. $\boldsymbol{A}_m$ has eigenvalues with negative real part. Using $\boldsymbol{A}_m$ would then lead to an unstable transfer function $-C_{um}(s)\, {H_m}^{-1}(s)\, H_{um}(s)$, which is highly undesirable. The low-pass filters are defined according to Eq. (4.49a) and Eq. (4.49b) and are set up with the same bandwidth as used for the *DPI Augmentation*. The controller also uses a sampling time of $T_s = 0.01s$ and the same methods of discrete-time transformation are applied as they were described in Section 4.2.2.

4.3. $\Delta\dot{q}$ Compensation Law

Apart from L1 Adaptive Control, one alternate adaptive augmentation approach is also presented in this thesis for the sake of comparison. This approach is introduced in [23, 98] and is rather well thought out than following complex theory. Furthermore, it is tailored for compensation of uncertainties appearing in the aircraft short-period dynamics. This thesis contributes a combination of this adaptive method with a DPI baseline controller.

The general idea of [23, 98] is to online calculate an estimated pitch acceleration $\hat{\dot{q}}(t)$ using knowledge about the kinematic aircraft behavior and measurements first. $\hat{\dot{q}}(t)$ is then compared to the actual measured or calculated pitch acceleration $\dot{q}(t)$ resulting in a deviation $\Delta\dot{q}(t)$, which corresponds to an unwanted pitch moment. In order to compensate for this unwanted pitch moment, the resulting $\Delta\dot{q}(t)$ can be used to directly determine a suitable control surface deflection $u_{cmd,\Delta\dot{q}}(t)$, while again kinematic knowledge about the aircraft is utilized.

The authors of [23] named this approach Reference model-based adaptive controller. In the context of this thesis, the control law is referred to as $\Delta\dot{q}$ Compensation Law, in order to avoid possible misunderstandings during control law comparisons in Chapter 6.

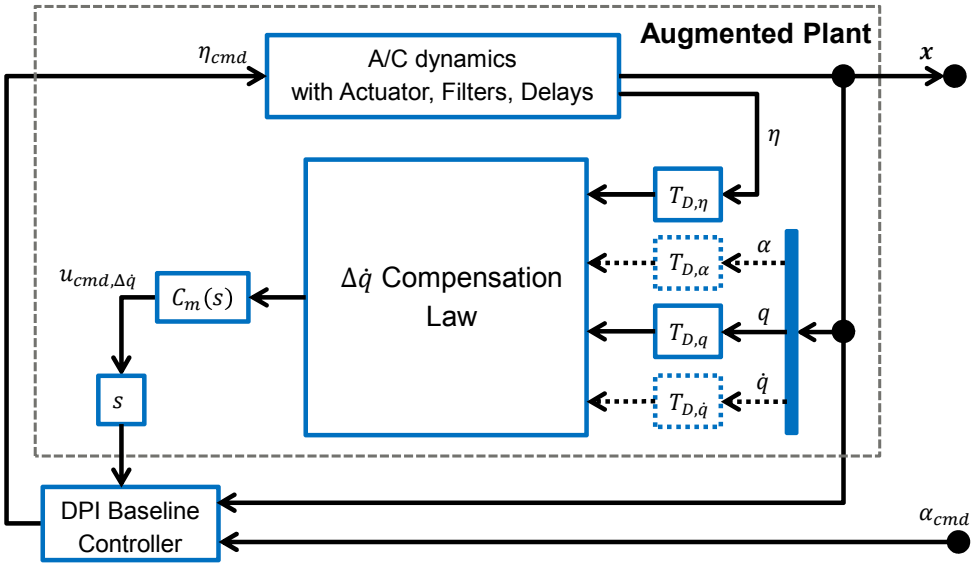

Figure 4.17. – Closed-loop for $\Delta\dot{q}$ Compensator Augmentation

The underlying reference dynamics stem directly from the linear open-loop aircraft dynamics defined in

$$\begin{pmatrix} \dot{\alpha}(t) \\ \dot{q}(t) \end{pmatrix} = \begin{pmatrix} Z_\alpha & Z_q + 1 \\ M_\alpha & M_q \end{pmatrix} \begin{pmatrix} \alpha(t) \\ q(t) \end{pmatrix} + \begin{pmatrix} Z_\eta \\ M_\eta \end{pmatrix} \eta(t) . \tag{4.70}$$

The $\Delta\dot{q}$ Compensation Law does not account for any shift of the aircraft eigendynamics resulting from application of a baseline controller in terms of this reference model. Thus, the $\Delta\dot{q}$ Compensation Law can also be considered to be a Plant Augmentation in combination with a baseline controller. The basic structure of this augmentation for the DPI baseline controller is illustrated in Fig. 4.17, where the control law $u_{cmd,\Delta\dot{q}}(t)$ is inserted at summation ① of the baseline controller shown in Fig. 4.1. In order to satisfy the baseline controller structure, $u_{cmd,\Delta\dot{q}}(t)$ has to be differentiated upstream of the insertion point, as it is also done in Section 4.2 for the L1 Adaptive Control Law. For this purpose, the differentiating filter according to Eq. (4.1) is used.

Eq. (4.70) can be directly used to deduce a linear estimation for the pitch rate acceleration considering the second equation contained in the matrix equation Eq. (4.70) [23]

$$\hat{\dot{q}}(t) = M_\alpha \cdot \Delta\alpha(t) + M_q \cdot q_{meas}(t) + M_\eta \cdot \Delta\eta(t) . \tag{4.71}$$

As it was stated before, measurements are used to calculate $\hat{\dot{q}}(t)$ rather than estimated states stemming from a reference model. This is one major difference to any model reference control approach, which includes also L1 Adaptive Control. [23] describes that angle of attack α is not measured, but gained from suitable filtering of pitch rate

$q(t)$. This filter can be gained from solving the first equation of Eq. (4.70) with respect to $\alpha(t)$ in the Laplace space:

$$\Delta\alpha(s) = \frac{Z_q + 1}{s - Z_\alpha} \cdot q(s) + \frac{Z_\eta}{s - Z_\alpha} \cdot \Delta\eta(s) \tag{4.72}$$

Furthermore, [23] uses the simplifications that $Z_q \approx 0$ and $Z_\eta \approx 0$ i.e. control surface deflection results in a pitch moment and induces approximately no direct lift. This results in [23]

$$\Delta\alpha(s) \approx \frac{1}{s - Z_\alpha} \cdot q(s). \tag{4.73}$$

An alternative solution to calculate $\Delta\alpha(s)$ uses measurement of angle of attack $\alpha(t)$. In this case, it holds that

$$\Delta\alpha(t) = \alpha_{meas}(t) - \alpha_0(t), \tag{4.74}$$

which is used for the assessments made in this thesis. In order to solve Eq. (4.71), at last the deviation of the control surface deflection from its trim value $\Delta\eta(t)$ is required. [23] proposes to use a high-passed version of the measured control deflection according to

$$\Delta\eta(s) = \frac{T_\eta}{T_\eta s + 1} \cdot \eta_{meas}(s), \tag{4.75}$$

whereas also usage of tabulated $\eta_0(t)$ values is possible resulting in

$$\Delta\eta(t) = \eta_{meas}(t) - \eta_0(t). \tag{4.76}$$

Eq. (4.76) is used for the controller implementation of this thesis.
Using $\dot{\hat{q}}(t)$ from Eq. (4.71) the unwanted deviation between the real aircraft pitch acceleration and the estimated one can be directly calculated according to

$$\Delta\dot{q}(t) = \dot{\hat{q}}(t) - \dot{q}(t), \tag{4.77}$$

where $\dot{q}(t)$ can be either used directly, if it is available as a measurement, or be determined through differentiation of the pitch rate $q_{meas}(t)$ as it is described in [23]. Last but not least, using the linear relationship between pitch rate acceleration and control surface deflection from Eq. (4.70) a compensating control deflection $u_{cmd,\Delta\dot{q}}(t)$ can be simply calculated according to [23]

$$u_{cmd,\Delta\dot{q}}(t) = \frac{\Delta\dot{q}(t)}{M_\eta} = \frac{M_\alpha}{M_\eta} \cdot \Delta\alpha(t) + \frac{M_q}{M_\eta} \cdot q_{meas}(t) + \Delta\eta(t) - \frac{\dot{q}(t)}{M_\eta}. \tag{4.78}$$

In order to increase performance during severe turbulence (c.f. Fig. 5.74 and Fig. 5.75 in Section 5.2.3.2) and to gain better comparability to the L1 Augmentation approaches,

it was decided to add a low-pass filter to the control law. Thus, the control law finally reads

$$u_{cmd,\Delta\dot{q}}(s) = C_m(s)\left(\frac{M_\alpha}{M_\eta}\cdot\Delta\alpha(s) + \frac{M_q}{M_\eta}\cdot q_{meas}(s) + \Delta\eta(s) - \frac{\dot{q}(s)}{M_\eta}\right) \tag{4.79}$$

with $C_m(s)$ defined according to Eq. (4.49a), the filter bandwidth is set to $\omega_{0,C,m} = 15\frac{rad}{s}$, as it is also defined for the L1 Adaptive Augmentations in Section 4.2.

Additionally, Fig. 4.17 indicates that the sensor signals $\eta(t)$, $\alpha(t)$, $q(t)$ and $\dot{q}(t)$ are led through time delays $T_{D,\eta}$, $T_{D,\alpha}$, $T_{D,q}$ and $T_{D,\dot{q}}$, respectively. [23] emphasizes the importance of equally phased signals to be fed into the controller, in order to achieve satisfying robust stability. This means all signals should approximately represent the same point in time with respect to the physical state of the aircraft. This does not necessarily have to be case in a real world application. For example, [23] mentions heavily filtered pitch rate q measurement for their application, which requires elevator deflection η measurement to be delayed artificially. Generally, first it is determined, which signal inherits the largest time delay $T_{D,max}$. For the other signals, the single time delay blocks can then be used to delay the signal, in order to also achieve $T_{D,max}$ for the individual signal.

For the application of this thesis, the same filter chain is applied to all sensor signals using the enhanced aircraft model, as it was described in Section 4.1.2. But, nevertheless, differences in signal phasing appear due to different sample rates of the individual signals. Different sample rates require upsampling in case the sensor rate is lower than the controller computation rate. The upsampling algorithm causes additional delay, which is also explained in Section 4.1.2. For the sensor configuration shown in Table 2.6 in Section 2.6, this is the case for the measurement of the elevator deflection η, where upsampling causes a delay of $T_{D,FIR,\eta} = 0.01s$ according to Eq. (4.20) for the enhanced aircraft model. Here, a controller sample time of $T_s = 0.01s$ is used. Thus, one could choose $T_{D,\alpha} = T_{D,q} = 0.01s$ to synchronize angle of attack α and pitch rate q measurements to the one of elevator deflection η. Nevertheless, the additional time delays are deactivated for the assessments made in this thesis, i.e. $T_{D,\alpha} = T_{D,q} = T_{D,\eta} = T_{D,\dot{q}} = 0s$, because artificially delaying angle of attack α and pitch rate q measurement turns out to affect robustness stability rather adverse (c.f. Fig. 5.65, Fig. 5.66 and Fig. 5.67 in Section 5.2.3.1).

The transfer functions contained in the controller implementation are transformed to discrete-time utilizing bilinear transformation, which was introduced in Section 3.3.

4.4. L1 Adaptive Control with Eigenstructure Assignment

In the sections above, several ways were demonstrated, how the DPI baseline controller can be augmented by an adaptive controller. In this case, the baseline controller is responsible for shaping the short-period in terms of desired handling qualities and the adaptive augmentation has the task of maintaining them, even in case of uncertainty.

This changes in case a standalone adaptive controller is considered. Without a baseline controller, the adaptive controller should be able to place the poles defining the dynamics to be controlled with sufficient preciseness by itself. It was found that by means of a standalone L1 adaptive controller implemented according to [59], the poles could be shifted to the proximity of the desired pole locations, but the deviation of desired and resulting pole location was not predictable. In this case, the system matrix A_m of the state predictor (c.f. Eq. (3.25a)) directly incorporates the desired dynamics instead of the open-loop plant dynamics.

In order to increase the precision of achieving desired dynamics, a novel combination of L1 Adaptive Control and Eigenstructure Assignment was developed and introduced in [51] by the author. This combination leads to modifications on the state predictor architecture and allows exact pole placement, while offering all advantages of L1 Adaptive Control with piecewise constant update laws on the other hand.

The approach is further described in this section. First, the reference dynamics to be achieved by the controller are introduced. They differ from the ones shown in Section 4.2.1, because of the missing baseline controller. Next, the idea of the controller architecture is explained. This architecture is also formulated mathematically following the structuring also used for the description of the adaptive augmentations. In particular, the error dynamics of the resulting closed-loop give further insight into the operation of the controller. At last, additional implementation guidelines are provided.

4.4.1. Reference Dynamics

First of all, the reference model is described, which defines the reference dynamics, that the adaptive controller should establish in connection with the plant. As it can be seen in Fig. 4.18, this reference model is similar to the one introduced for the augmentation approaches in Section 4.2.1, which can be found in Fig. 4.13. Differences are due to neglecting the integrator state, the derivations, as well as the integration all corresponding to the DPI baseline controller.

The reference model can then be formulated as

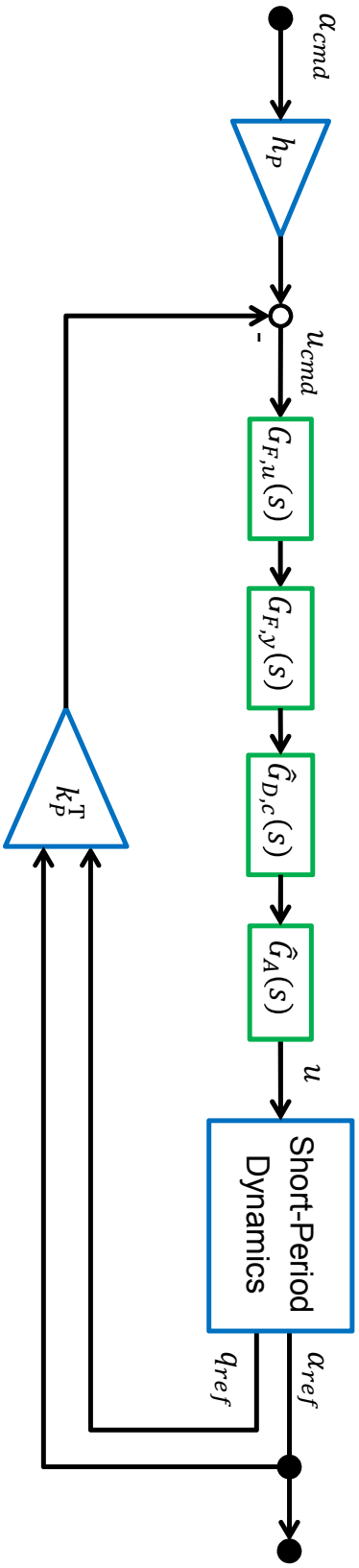

Figure 4.18. – Linear reference model for standalone L1 adaptive controller

$$\dot{\boldsymbol{x}}_{ref}(t) = \boldsymbol{A}_m \boldsymbol{x}_{ref}(t) + \boldsymbol{b}_m \cdot G_{F,u}(t) * G_{F,y}(t) * \hat{G}_{D,c}(t) * \hat{G}_A(t) * \left(-\boldsymbol{k}_P{}^T \boldsymbol{x}_{ref}(t) + h_P \cdot \alpha_{cmd}(t)\right) \tag{4.80}$$

with

$$\boldsymbol{x}_{ref} = \begin{pmatrix} \alpha_{ref} \\ q_{ref} \end{pmatrix} \tag{4.81}$$

and the matrices defining the short-period dynamics

$$\boldsymbol{A}_m = \begin{pmatrix} Z_\alpha & Z_q + 1 \\ M_\alpha & M_q \end{pmatrix} \qquad \boldsymbol{b}_m = \begin{pmatrix} Z_\eta \\ M_\eta \end{pmatrix}, \tag{4.82}$$

which are also shown in Eq. (4.22). The formulation of the reference dynamics also includes dynamics of the filter chain $G_{F,u}(t)$ and $G_{F,y}(t)$ as well as transfer functions representing actuator dynamics $\hat{G}_A(t)$ and delay $\hat{G}_{D,c}(t)$. It has to be noted that rate and deflection limitations according to actuator specifications are included in the implementation of $\hat{G}_A(t)$. The filters $G_{F,u}(t)$ and $G_{F,y}(t)$ are only considered for the controller design, when the enhanced aircraft model is used for the simulations. Likewise, they are neglected for the basic aircraft model case.

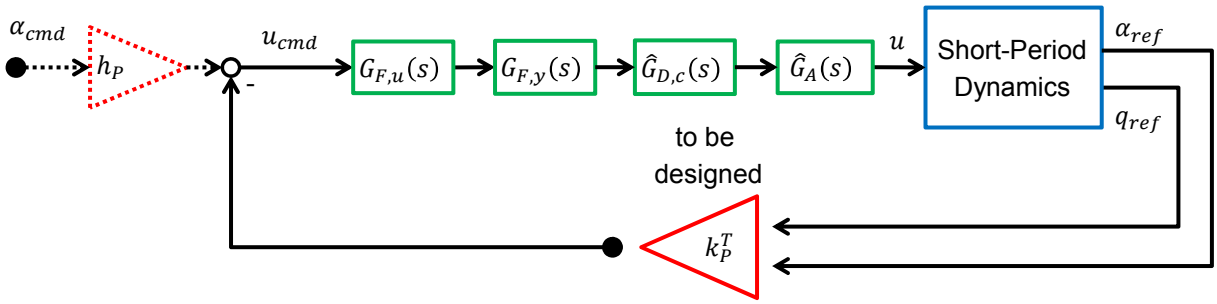

Figure 4.19. – Gain design model for reference model of the standalone L1 adaptive controller

Making use of the Eigenstructure Assignment algorithm shown in Section 3.1, the gains $\boldsymbol{k}_P{}^T$ and h_P can be designed analogously to the method shown in Section 4.1.1 utilizing the design model illustrated in Fig. 4.19. The same requirements were set for natural frequency and damping of the short-period, as they were also chosen for the baseline controller and the adaptive augmentations. Thus, the desired properties are $\omega_{0,sp,des}$ according to $CAP = 0.7$, whose values can be found in Fig. 4.3, and $\zeta_{sp,des} = 0.95$.

4.4.2. Controller Architecture

The controller architecture is described in this section by means of first introducing the plant dynamics to be controlled, followed by the modified state predictor structure. The error dynamics between measured and estimated states are analyzed and result in the parameter update law. At last, the control law is presented.

Plant The dynamics of the physical plant are formulated according to

$$\begin{aligned}\dot{\boldsymbol{x}}(t) = \boldsymbol{A}_m \boldsymbol{x}(t) + \boldsymbol{b}_m \cdot \Lambda(t) * G_{F,u}(t) * G_{F,y}(t) * G_{D,c}(t) * G_A(t) * u_{ad}(t) \\ + \boldsymbol{b}_m f_m\left(t, \boldsymbol{x}(t), \boldsymbol{y}_z(t)\right) + \boldsymbol{b}_{um} f_{um}\left(t, \boldsymbol{x}(t), \boldsymbol{y}_z(t)\right),\end{aligned} \tag{4.83}$$

which is very similar to the description shown for the *Plant Augmentation* approach in Eq. (4.50), apart from the missing baseline control command and the saturation functions. As it was already stated, the adaptive control command $u_{ad}(t)$ is the only controller command in this case. Actuator dynamics, delay and filter transfer functions are considered by means of $G_A(t)$ shown in Eq. (4.7), $G_{D,c}(t)$ introduced in Eq. (4.8) and $G_{F,u}(t)$ as well as $G_{F,y}(t)$, which are described in Section 4.1.2. Here, actuator deflection and rate saturations are incorporated in $G_A(t)$ according to Fig. 2.9. Matched and unmatched uncertainties are described by f_m and f_{um}, respectively.

State Predictor The structure of the state predictor shown in Fig. 4.20 is chosen in accordance to the plant structure and can be expressed as

$$\begin{aligned}\dot{\hat{\boldsymbol{x}}}_\star(t) = \boldsymbol{A}_m \hat{\boldsymbol{x}}_\star(t) - \boldsymbol{b}_m \bar{\boldsymbol{k}}_m{}^T \hat{\boldsymbol{x}}_\star(t) - \boldsymbol{b}_{um} \bar{\boldsymbol{k}}_{um}{}^T \hat{\boldsymbol{x}}_\star(t) \\ + \boldsymbol{b}_m \cdot \Lambda_0 \cdot G_{F,u}(t) * G_{F,y}(t) * \hat{G}_{D,c}(t) * \hat{G}_A(t) * u_{ad}(t) \\ + \boldsymbol{b}_m \hat{\sigma}_{m\star}(t) + \boldsymbol{b}_{um} \hat{\sigma}_{um\star}(t) + \boldsymbol{b}_m \cdot \Delta u(t) + \boldsymbol{K}_e \tilde{\boldsymbol{x}}_\star(t)\end{aligned} \tag{4.84}$$

where the transfer functions $\hat{G}_{D,c}(t)$ and $\hat{G}_A(t)$ are estimations of the delay and actuator dynamics. The notation $(\cdot)_\star$ is used to distinguish between the modified and the textbook state predictor. This especially matters for the assessments made in Section 4.4.3.
Again, rate and absolute saturation are considered for the implementation of $\hat{G}_A(t)$ within the controller. $\hat{\sigma}_{m\star}(t)$ and $\hat{\sigma}_{um\star}(t)$ denote estimations of the matched and unmatched uncertainties, respectively. Compared to the standard architecture shown in Section 3.2, two modifications are proposed.
The first one is that $\hat{\boldsymbol{x}}_\star(t)$ is fed back via gains $\bar{\boldsymbol{k}}_m{}^T$ and $\bar{\boldsymbol{k}}_{um}{}^T$ to both matched and unmatched input channel of the state predictor. It is important to note that the feedback to the matched input is inserted *downstream* of the actuator model. By means of a

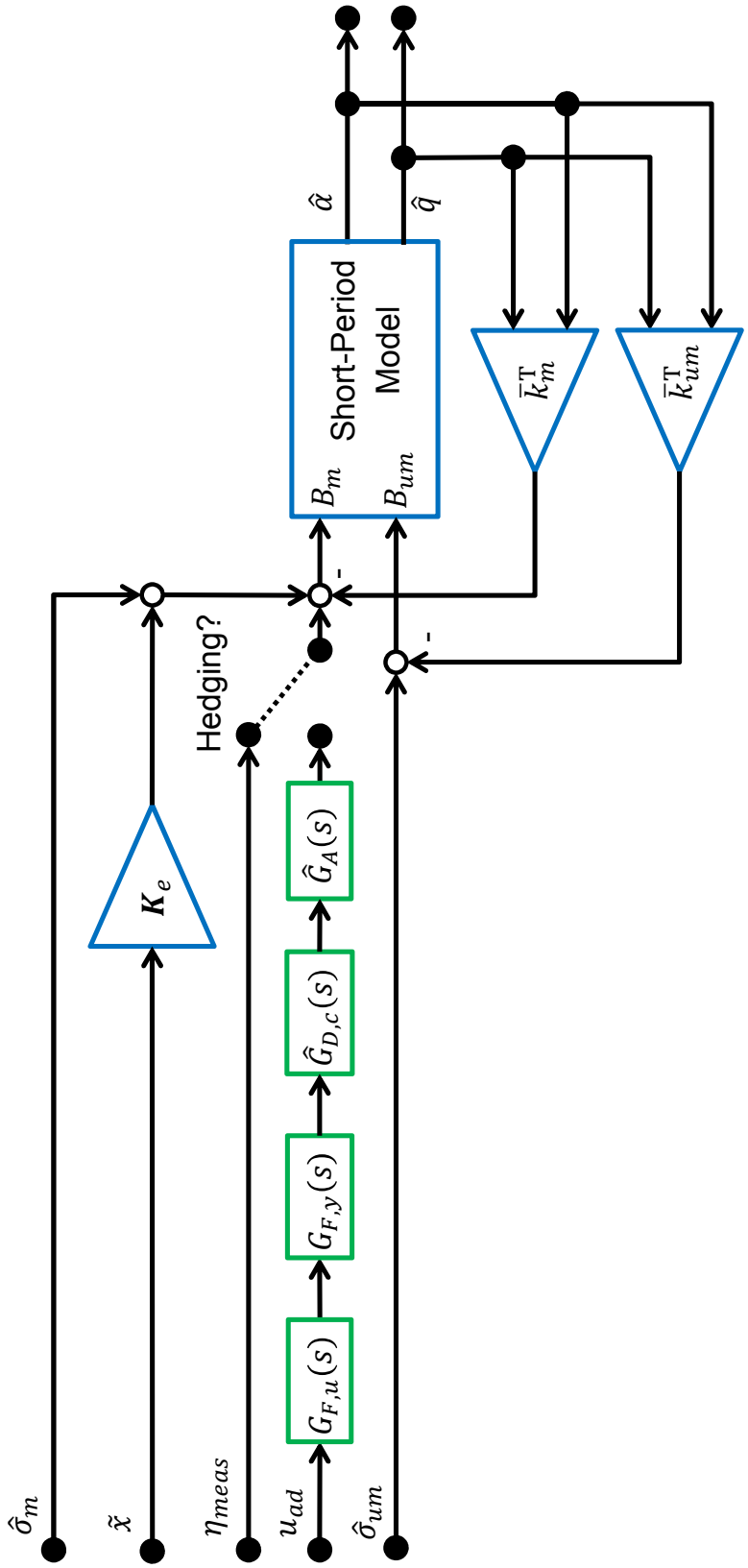

Figure 4.20. – State predictor architecture of standalone L1 adaptive controller

smart choice of the feedback gains $\bar{\boldsymbol{k}}_m{}^T$ and $\bar{\boldsymbol{k}}_{um}{}^T$, one is able to exactly[1] shape the dynamics of the resulting closed-loop. A suitable method to achieve this is shown in Section 4.4.3.
The second modification is the introduction of an additional hedging term $\Delta u\,(t)$ to the dynamic model, as it is also used for the adaptive augmentations explained in Section 4.2. As it is shown in Section 5.2.4.1, particularly in Fig. 5.78 and Fig. 5.79, this modification contributed by this thesis turns out to have a beneficial effect on robust stability properties w.r.t. the actuator cut.
The hedging term $\Delta u\,(t)$ reads

$$\Delta u\,(t) = \eta_{meas}\,(t) - \Lambda_0 \cdot G_{F,u}\,(t) * G_{F,y}\,(t) * \hat{G}_{D,c}\,(t) * \hat{G}_A\,(t) * u_{ad}\,(t) \tag{4.85}$$

and uses the measured actuator deflection η_{meas} to compare the control signal, which is expected to enter the aircraft dynamics on a system level. Plugging the hedging term Eq. (4.85) into the state predictor Eq. (4.84) shows that the state predictor implementation can be simplified according to

$$\dot{\hat{\boldsymbol{x}}}_\star\,(t) = \boldsymbol{A}_m\hat{\boldsymbol{x}}_\star\,(t) - \boldsymbol{B}\bar{\boldsymbol{K}}\hat{\boldsymbol{x}}_\star\,(t) + \boldsymbol{b}_m\left[\eta_{meas}\,(t) + \hat{\sigma}_{m\star}\,(t)\right] + \boldsymbol{b}_{um}\hat{\sigma}_{um\star}\,(t) + \boldsymbol{K}_{\boldsymbol{e}}\tilde{\boldsymbol{x}}_\star\,(t)\,, \tag{4.86}$$

with

$$\boldsymbol{B} := \begin{pmatrix}\boldsymbol{b}_m & \boldsymbol{b}_{um}\end{pmatrix} \tag{4.87a}$$

$$\bar{\boldsymbol{K}} := \begin{pmatrix}\bar{\boldsymbol{k}}_m{}^T \\ \bar{\boldsymbol{k}}_{um}{}^T\end{pmatrix}, \tag{4.87b}$$

which does not require modeling of the actuator, delay and filters, because it uses the measured actuator deflection $\eta_{meas}\,(t)$. Both options with respect to hedging are depicted in Fig. 4.20.
At last, feedback of the estimation error via $\boldsymbol{K}_{\boldsymbol{e}}$ can be applied within the state predictor, as it was also already introduced for the adaptive augmentations in Section 4.2. As for the *Plant Augmentation*, the gain matrix $\boldsymbol{K}_{\boldsymbol{e}}$ is set to $\boldsymbol{K}_{\boldsymbol{e}} = \boldsymbol{0}$ for the assessments made in this thesis.

Error Dynamics The prediction error is defined according to

$$\tilde{\boldsymbol{x}}_\star\,(t) = \hat{\boldsymbol{x}}_\star\,(t) - \boldsymbol{x}\,(t) \tag{4.88}$$

for plant and state predictor introduced in Eq. (4.83) and Eq. (4.84), respectively. A differential equation for its temporal development is given by

[1] In case of nominal conditions i.e. no uncertainties, failures, additional dynamics etc. The same condition holds also for any classical control design.

$$\begin{aligned}\dot{\tilde{\boldsymbol{x}}}_\star(t) &= \dot{\hat{\boldsymbol{x}}}_\star(t) - \dot{\boldsymbol{x}}_\star(t)\\ &= (\boldsymbol{A}_m + \boldsymbol{K_e})\,\tilde{\boldsymbol{x}}_\star(t) - \boldsymbol{B}\bar{\boldsymbol{K}}\hat{\boldsymbol{x}}_\star(t)\\ &+ \boldsymbol{b}_m \cdot \Lambda_0 \cdot G_{F,u}(t) * G_{F,y}(t) * \hat{G}_{D,c}(t) * \hat{G}_A(t) * u_{ad}(t)\\ &- \boldsymbol{b}_m \cdot \Lambda(t) * G_{F,u}(t) * G_{F,y}(t) * \left(\hat{G}_{D,c}(t) - \tilde{G}_{D,c}(t)\right) * \left(\hat{G}_A(t) - \tilde{G}_A(t)\right) * u_{ad}(t)\\ &+ \boldsymbol{b}_m\left[\hat{\sigma}_{m\star}(t) - f_m\left(t, \boldsymbol{x}(t), \boldsymbol{y_z}(t)\right)\right] + \boldsymbol{b}_{um}\left[\hat{\sigma}_{um\star}(t) - f_{um}\left(t, \boldsymbol{x}(t), \boldsymbol{y_z}(t)\right)\right]\\ &+ \boldsymbol{b}_m \cdot \Delta u(t),\end{aligned} \tag{4.89}$$

where $\tilde{G}_{D,c}(t)$ and $\tilde{G}_A(t)$ are defined according to Eq. (4.33c) and Eq. (4.33d), respectively. Applying the definition of $\Delta_{A,D,c}(t)$ introduced in Eq. (4.35) one can rearrange Eq. (4.89) to

$$\begin{aligned}\dot{\tilde{\boldsymbol{x}}}_\star(t) &= (\boldsymbol{A}_m + \boldsymbol{K_e})\,\tilde{\boldsymbol{x}}_\star(t) - \boldsymbol{B}\bar{\boldsymbol{K}}\hat{\boldsymbol{x}}_\star(t)\\ &+ \boldsymbol{b}_m\{\hat{\sigma}_{m\star}(t) - f_m\left(t, \boldsymbol{x}(t), \boldsymbol{y_z}(t)\right) - \Lambda(t) * G_{F,u}(t) * G_{F,y}(t) * \Delta_{A,D,c}(t) * u_{ad}(t)\\ &- \Lambda(t) * G_{F,u}(t) * G_{F,y}(t) * \hat{G}_{D,c}(t) * \hat{G}_A(t) * u_{ad}(t)\\ &+ \Lambda_0 \cdot G_{F,u}(t) * G_{F,y}(t) * \hat{G}_{D,c}(t) * \hat{G}_A(t) * u_{ad}(t)\}\\ &+ \boldsymbol{b}_{um}\left[\hat{\sigma}_{um\star}(t) - f_{um}\left(t, \boldsymbol{x}(t), \boldsymbol{y_z}(t)\right)\right] + \boldsymbol{b}_m \cdot \Delta u(t).\end{aligned} \tag{4.90}$$

Now the error dynamics can be reformulated as

$$\dot{\tilde{\boldsymbol{x}}}_\star(t) = \boldsymbol{A}_{m,K}\tilde{\boldsymbol{x}}_\star(t) - \boldsymbol{B}\bar{\boldsymbol{K}}\hat{\boldsymbol{x}}_\star(t) + \boldsymbol{b}_m\left[\hat{\sigma}_{m\star}(t) - \sigma_m(t)\right] + \boldsymbol{b}_{um}\left[\hat{\sigma}_{um\star}(t) - \sigma_{um}(t)\right], \tag{4.91}$$

with the definition of $\boldsymbol{A}_{m,K}$ in Eq. (4.39) and the lumped matched uncertainty

$$\begin{aligned}\sigma_m(t) &= f_m\left(t, \boldsymbol{x}(t), \boldsymbol{y_z}(t)\right) + \Lambda(t) * G_{F,u}(t) * G_{F,y}(t) * \Delta_{A,D,c}(t) * u_{ad}(t)\\ &+ \Lambda(t) * G_{F,u}(t) * G_{F,y}(t) * \hat{G}_{D,c}(t) * \hat{G}_A(t) * u_{ad}(t) - \eta_{meas}(t),\end{aligned} \tag{4.92}$$

where hedging is used, i.e. Eq. (4.85) is plugged into Eq. (4.90). In case hedging $\Delta u(t) = 0$ is deactivated, the lumped matched uncertainty is defined according to

$$\begin{aligned}\sigma_m(t) &= f_m\left(t, \boldsymbol{x}(t), \boldsymbol{y_z}(t)\right) + \Lambda(t) * G_{F,u}(t) * G_{F,y}(t) * \Delta_{A,D,c}(t) * u_{ad}(t)\\ &- \left[\delta(t) \cdot \Lambda_0 - \Lambda(t)\right] * G_{F,u}(t) * G_{F,y}(t) * \hat{G}_{D,c}(t) * \hat{G}_A(t) * u_{ad}(t).\end{aligned} \tag{4.93}$$

For both cases, the definition of the lumped unmatched uncertainty

$$\sigma_{um}(t) = f_{um}(t, \boldsymbol{x}(t), \boldsymbol{y}_z(t)) \tag{4.94}$$

holds. Note that, apart from the additional term due to the state feedback within the state predictor and the missing baseline control command, this result is identical to the one for the *Plant Augmentation* approach shown in Eqs. (4.60) to (4.64) in Section 4.2.3. This is why the comparison of the lumped matched uncertainties with and without hedging shown in Table 4.3 is also valid for the standalone L1 adaptive controller presented in this section.

Eq. (4.91) is reordered in the next step. Furthermore, $-\boldsymbol{B}\bar{\boldsymbol{K}}\boldsymbol{x}(t) + \boldsymbol{B}\bar{\boldsymbol{K}}\boldsymbol{x}(t) = 0$ is added on the right-hand side of the equation. This results in

$$\begin{aligned}\dot{\tilde{\boldsymbol{x}}}_\star(t) &= \boldsymbol{A}_{m,K}\tilde{\boldsymbol{x}}_\star(t) - \boldsymbol{B}\bar{\boldsymbol{K}}\hat{\boldsymbol{x}}_\star(t) - \boldsymbol{B}\bar{\boldsymbol{K}}\boldsymbol{x}(t) + \boldsymbol{B}\bar{\boldsymbol{K}}\boldsymbol{x}(t) + \boldsymbol{b}_m\left[\hat{\sigma}_{m\star}(t) - \sigma_m(t)\right] \\ &\quad + \boldsymbol{b}_{um}\left[\hat{\sigma}_{um\star}(t) - \sigma_{um}(t)\right] \\ &= \left[\underbrace{\boldsymbol{A}_{m,K} - \boldsymbol{B}\bar{\boldsymbol{K}}}_{=:\boldsymbol{A}_{cl}}\right]\tilde{\boldsymbol{x}}_\star(t) - \boldsymbol{B}\bar{\boldsymbol{K}}\boldsymbol{x}(t) + \boldsymbol{b}_m\tilde{\sigma}_m(t) + \boldsymbol{b}_{um}\tilde{\sigma}_{um}(t).\end{aligned} \tag{4.95}$$

Eq. (4.95) is an ordinary, first order differential equation. The solution between two discrete timesteps with step size T_s reads

$$\begin{aligned}\tilde{\boldsymbol{x}}_\star(iT_s + T_s) &= e^{\boldsymbol{A}_{cl}T_s}\cdot\tilde{\boldsymbol{x}}_\star(iT_s) + \int_0^{T_s} e^{\boldsymbol{A}_{cl}(T_s-\epsilon)}\boldsymbol{B}\begin{pmatrix}\hat{\sigma}_{m\star}(iT_s+\epsilon)\\ \hat{\sigma}_{um\star}(iT_s+\epsilon)\end{pmatrix}\,\mathrm{d}\epsilon \\ &\quad - \int_0^{T_s} e^{\boldsymbol{A}_{cl}(T_s-\epsilon)}\boldsymbol{B}\bar{\boldsymbol{K}}\boldsymbol{x}(iT_s+\epsilon)\,\mathrm{d}\epsilon \\ &\quad - \int_0^{T_s} e^{\boldsymbol{A}_{cl}(T_s-\epsilon)}\boldsymbol{B}\begin{pmatrix}\sigma_m(iT_s+\epsilon)\\ \sigma_{um}(iT_s+\epsilon)\end{pmatrix}\,\mathrm{d}\epsilon.\end{aligned} \tag{4.96}$$

This intermediate result is compared to the unmodified error dynamics shown in Eq. (3.33). It shows that the introduction of the feedback gain matrix $\bar{\boldsymbol{K}}$ yields an additional term

$$\Delta\tilde{\boldsymbol{x}}_\star(iT_s + T_s) = -\int_0^{T_s} e^{\boldsymbol{A}_{cl}(T_s-\epsilon)}\boldsymbol{B}\bar{\boldsymbol{K}}\boldsymbol{x}(iT_s+\epsilon)\,\mathrm{d}\epsilon, \tag{4.97}$$

which also excites the error dynamics. Furthermore, the error dynamics are shifted from $\boldsymbol{A}_m$ to $\boldsymbol{A}_{cl} = \boldsymbol{A}_{m,K} - \boldsymbol{B}\bar{\boldsymbol{K}}$. Thus, one has to verify that $\boldsymbol{A}_{cl}$ has negative eigenvalues, in order to achieve stable error dynamics. At this point it should be stressed that the poles of $\boldsymbol{A}_{cl}$ do not correspond to the desired closed-loop poles.

Parameter Update Law Following the approach shown in Eq. (3.34) in Section 3.2, the estimated uncertainties $\hat{\sigma}_{m\star}(iT_s)$ and $\hat{\sigma}_{um\star}(iT_s)$ are considered to be piecewise constant between two discrete processing time steps. They are chosen such that they cancel the prediction error accumulation. This results in

$$\begin{pmatrix} \hat{\sigma}_{m\star}(t) \\ \hat{\sigma}_{um\star}(t) \end{pmatrix} = \boldsymbol{K}_{L1\star}(T_s)\,\tilde{\boldsymbol{x}}_\star(iT_s) \quad \forall t \in [iT_s, (i+1)\,T_s[\,, \tag{4.98}$$

where

$$\boldsymbol{K}_{L1\star}(T_s) = \begin{pmatrix} \boldsymbol{K}_{L1,m\star}{}^T(T_s) \\ \boldsymbol{K}_{L1,um\star}{}^T(T_s) \end{pmatrix} = -\boldsymbol{B}^{-1}\left(e^{\boldsymbol{A}_{cl}T_s} - \boldsymbol{I}_{n\times n}\right)^{-1}\boldsymbol{A}_{cl}e^{\boldsymbol{A}_{cl}T_s}. \tag{4.99}$$

The resulting update law is fully equivalent to the one derived in Eq. (3.38), but it has to be noticed that the additional gain $\bar{\boldsymbol{K}}$ influences the way, how $\tilde{\boldsymbol{x}}_\star(t)$ is composed. It was shown above that the introduction of $\bar{\boldsymbol{K}}$ causes an additional term $\Delta\tilde{\boldsymbol{x}}_\star(iT_s + T_s)$ within the error dynamics. Section 4.4.3 shows, how this additional term including the gain $\bar{\boldsymbol{K}}$ can be used to achieve exact pole placement.

Control Law The control law is compiled analogous to the one introduced for the *Plant Augmentation* in Eq. (4.67) with the difference that it also includes a feedforward portion with the purpose of ensuring α_{cmd} tracking. Thus, the control law is compiled as

$$u_{ad}(s) = -C_m(s)\,\hat{\sigma}_{m\star}(s) - C_{um}(s)\,{H_m}^{-1}(s)\,H_{um}(s)\,\hat{\sigma}_{um\star}(s) + h_{L1}\cdot\alpha_{cmd}(s)\,, \tag{4.100}$$

where

$$H_m(s) = \boldsymbol{c}_m\left(s\boldsymbol{I}_{n\times n} - \boldsymbol{A}_m\right)^{-1}\boldsymbol{b}_m \tag{4.101a}$$

$$H_{um}(s) = \boldsymbol{c}_m\left(s\boldsymbol{I}_{n\times n} - \boldsymbol{A}_m\right)^{-1}\boldsymbol{b}_{um} \tag{4.101b}$$

with the open-loop system matrix $\boldsymbol{A}_m$, the input matrices $\boldsymbol{b}_m$, $\boldsymbol{b}_{um}$ and the output vector chosen as $\boldsymbol{c}_m = \begin{pmatrix} 1 & 0 \end{pmatrix}$.
The calculation of the feedforward gain h_{L1} indirectly requires information about the content of $\bar{\boldsymbol{K}}$. This is why its derivation is shown in the next section.
The low-pass filters are defined according to Eq. (4.49a) and Eq. (4.49b) and set up with the same bandwidth as used for both the *Closed-Loop Augmentation* and the *Plant Augmentation*. The resulting closed-loop structure using the architecture shown in this section is illustrated in Fig. 4.21.
For the implementation of the control law, which is processed at a sample time of $T_s = 0.01s$, discrete-time representations of the necessary transfer functions are used. The techniques introduced in Section 3.3 are applied analogously to the adaptive augmentations presented in Section 4.2.2 with one exception. In case hedging is not

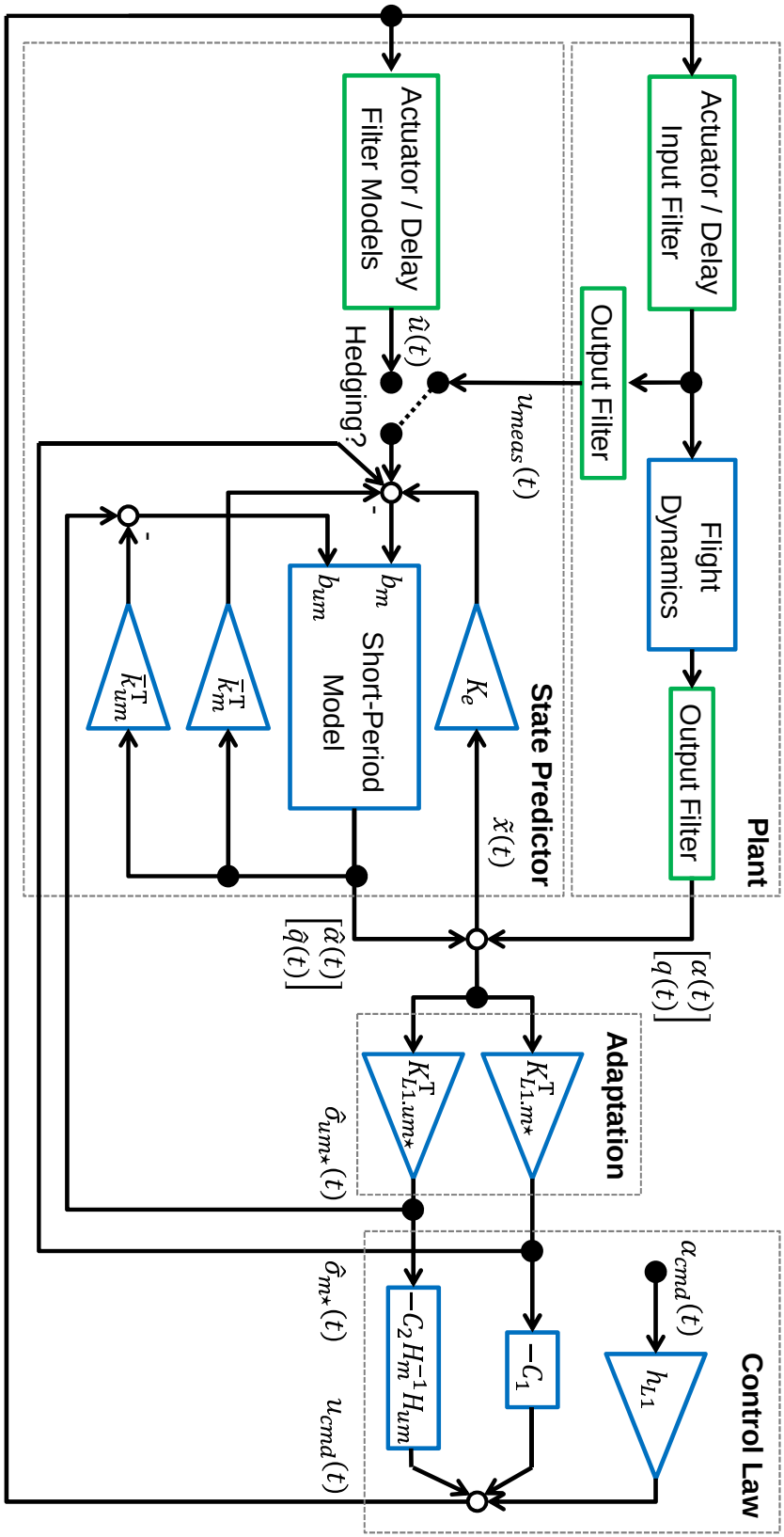

Figure 4.21. – Resulting closed-loop with standalone L1 adaptive controller containing the state predictor architecture shown in Fig. 4.20

activated for the L1 adaptive controller with Eigenstructure Assignment, the necessary actuator model within the state predictor is transformed using Euler's Transformation, in order to be able to apply rate and absolute saturations.

4.4.3. Feedback Gain Design

In order to gain better understanding of the effect of the introduced feedback gains $\bar{\boldsymbol{k}}_m{}^T$ and $\bar{\boldsymbol{k}}_{um}{}^T$ on the closed loop dynamics, the resulting error between plant and estimated dynamics is investigated further. Thus, a correlation between the introduced feedback within the state predictor $-\bar{\boldsymbol{K}}\hat{\boldsymbol{x}}(t)$ and its effect on the closed-loop behavior should be derived. Using this knowledge, a method can be shown, which utilizes $\bar{\boldsymbol{k}}_m{}^T$ and $\bar{\boldsymbol{k}}_{um}{}^T$ to achieve precise pole placement.
It was stated before that the estimated uncertainties in Eq. (4.98) are chosen such that the first two summands in Eq. (4.96) cancel each other. Thus, the remaining error at the end of each discrete time step is

$$\tilde{\boldsymbol{x}}_\star(iT_s+T_s) = \underbrace{-\int_0^{T_s} e^{\boldsymbol{A}_{cl}(T_s-\epsilon)}\boldsymbol{B}\begin{pmatrix}\sigma_m(iT_s+\epsilon)\\ \sigma_{um}(iT_s+\epsilon)\end{pmatrix}\,\mathrm{d}\epsilon}_{=\tilde{\boldsymbol{x}}(iT_s+T_s)} - \int_0^{T_s} e^{\boldsymbol{A}_{cl}(T_s-\epsilon)}\boldsymbol{B}\bar{\boldsymbol{K}}\boldsymbol{x}(iT_s+\epsilon)\,\mathrm{d}\epsilon, \tag{4.102}$$

which can also be expressed for the point in time iT_s as

$$\tilde{\boldsymbol{x}}_\star(iT_s) = \tilde{\boldsymbol{x}}(iT_s) - \int_0^{T_s} e^{\boldsymbol{A}_{cl}(T_s-\epsilon)}\boldsymbol{B}\bar{\boldsymbol{K}}\boldsymbol{x}((i-1)T_s+\epsilon)\,\mathrm{d}\epsilon, \tag{4.103}$$

where $\tilde{\boldsymbol{x}}(iT_s)$ is the remaining prediction error in a conventional state predictor architecture presented in Eq. (3.25a) in Section 3.2. After setting Eq. (4.103) back into the update law Eq. (4.98), one can conclude that the proposed state predictor modification, which introduces the feedback of $-\bar{\boldsymbol{K}}\hat{\boldsymbol{x}}(t)$, leads to a Δ-term within the estimated uncertainties according to

$$\begin{aligned}\begin{pmatrix}\hat{\sigma}_{m\star}(t)\\ \hat{\sigma}_{um\star}(t)\end{pmatrix} &= \boldsymbol{K}_{L1\star}(T_s)\,\tilde{\boldsymbol{x}}_\star(iT_s)\\ &= \boldsymbol{K}_{L1\star}(T_s)\,\tilde{\boldsymbol{x}}(iT_s)\underbrace{-\boldsymbol{K}_{L1\star}(T_s)\int_0^{T_s} e^{\boldsymbol{A}_{cl}(T_s-\epsilon)}\boldsymbol{B}\bar{\boldsymbol{K}}\boldsymbol{x}((i-1)T_s+\epsilon)\,\mathrm{d}\epsilon}_{=:\Delta(t)}\\ &= \begin{pmatrix}\hat{\sigma}_m(t)\\ \hat{\sigma}_{um}(t)\end{pmatrix} + \Delta(t) \qquad \forall t\in[iT_s,(i+1)T_s[\end{aligned} \tag{4.104}$$

compared to the standard uncertainty estimation in Eq. (3.38).
In the following paragraphs, the additional contribution

$$\Delta(t) = -\boldsymbol{K}_{L1\star}(T_s) \int_0^{T_s} e^{\boldsymbol{A}_{cl}(T_s-\epsilon)} \boldsymbol{B}\bar{\boldsymbol{K}}\boldsymbol{x}((i-1)T_s+\epsilon)\ \mathrm{d}\epsilon \tag{4.105}$$

to the parameter update law is investigated further. The sampling of the controller is assumed to be much faster than the dynamics to be controlled, which is the case for most real word control applications. Consequently, one can consider the states $\boldsymbol{x}(iT_s)$ to be piecewise constant also. Thus, Eq. (4.105) can be rearranged to

$$\Delta(t) = -\boldsymbol{K}_{L1\star}(T_s) \int_0^{T_s} e^{\boldsymbol{A}_{cl}(T_s-\epsilon)}\ \mathrm{d}\epsilon \cdot \boldsymbol{B}\bar{\boldsymbol{K}}\boldsymbol{x}((i-1)T_s). \tag{4.106}$$

In the next step the integral is solved

$$\Delta(t) = -\boldsymbol{K}_{L1\star}(T_s)\, {\boldsymbol{A}_{cl}}^{-1} \left(e^{\boldsymbol{A}_{cl}T_s} - \boldsymbol{I}_{n\times n}\right) \boldsymbol{B}\bar{\boldsymbol{K}}\boldsymbol{x}((i-1)T_s) \tag{4.107}$$

and the definition of $\boldsymbol{K}_{L1\star}$ from Eq. (4.99) is reinserted

$$\Delta(t) = \boldsymbol{B}^{-1}\left(e^{\boldsymbol{A}_{cl}T_s} - \boldsymbol{I}_{n\times n}\right)^{-1} \boldsymbol{A}_{cl} \cdot e^{\boldsymbol{A}_{cl}T_s} \cdot {\boldsymbol{A}_{cl}}^{-1} \left(e^{\boldsymbol{A}_{cl}T_s} - \boldsymbol{I}_{n\times n}\right) \boldsymbol{B}\bar{\boldsymbol{K}}\boldsymbol{x}((i-1)T_s). \tag{4.108}$$

The Δ-term can then be transformed to the Laplace space, which results in

$$\Delta(t) = \Phi(\bar{\boldsymbol{K}}) \cdot \boldsymbol{x}((i-1)T_s) \quad \circ\!\!-\!\!\bullet \quad \Delta(s) = \Phi(\bar{\boldsymbol{K}}) \cdot e^{-sT_s}\boldsymbol{x}(s) \qquad \forall t \in [iT_s, (i+1)T_s[\tag{4.109}$$

with

$$\begin{aligned}\Phi(\bar{\boldsymbol{K}}) = {} & \boldsymbol{B}^{-1}\left(e^{\boldsymbol{A}_{cl}T_s} - \boldsymbol{I}_{n\times n}\right)^{-1} \boldsymbol{A}_{cl} \cdot e^{\boldsymbol{A}_{cl}T_s} \cdot {\boldsymbol{A}_{cl}}^{-1} \left(e^{\boldsymbol{A}_{cl}T_s} - \boldsymbol{I}_{n\times n}\right) \boldsymbol{B} \cdot \bar{\boldsymbol{K}} = \\ = {} & \boldsymbol{B}^{-1}\left(e^{(\boldsymbol{A}_{m,K}-\boldsymbol{B}\bar{\boldsymbol{K}})T_s} - \boldsymbol{I}_{n\times n}\right)^{-1} (\boldsymbol{A}_{m,K} - \boldsymbol{B}\bar{\boldsymbol{K}}) \\ & \cdot e^{(\boldsymbol{A}_{m,K}-\boldsymbol{B}\bar{\boldsymbol{K}})T_s} \cdot (\boldsymbol{A}_{m,K} - \boldsymbol{B}\bar{\boldsymbol{K}})^{-1} \left(e^{(\boldsymbol{A}_{m,K}-\boldsymbol{B}\bar{\boldsymbol{K}})T_s} - \boldsymbol{I}_{n\times n}\right) \boldsymbol{B} \cdot \bar{\boldsymbol{K}},\end{aligned} \tag{4.110}$$

where $\boldsymbol{A}_{cl} = \boldsymbol{A}_{m,K} - \boldsymbol{B}\bar{\boldsymbol{K}}$ is reinserted. Interestingly, Eq. (4.110) can be simplified drastically, if very small sampling times T_s are considered. In this case, $\Phi(\bar{\boldsymbol{K}})$ can be expressed by means of

$$\lim_{T_s\to 0} \Phi(\bar{\boldsymbol{K}}) = \bar{\boldsymbol{K}}. \tag{4.111}$$

Despite this simplification, in this work Eq. (4.110) is used for the feedback gain design, because it achieves increased preciseness in terms of pole placement.

Finally, the effect of the Δ-term stemming from the feedbacks within the state predictor via $\bar{\boldsymbol{K}} = \left(\bar{\boldsymbol{k}}_m{}^T \quad \bar{\boldsymbol{k}}_{um}{}^T\right)^T$ becomes clear, when the two portions of the parameter update law Eq. (4.104) are plugged into the control law according to Eq. (4.100)

$$\begin{aligned} u_{ad}(s) &= -C_m(s)\,\hat{\sigma}_{m\star}(s) - C_{um}(s)\,H_m{}^{-1}(s)\,H_{um}(s)\,\hat{\sigma}_{um\star}(s) + h_{L1}\cdot y_{cmd}(s) \\ &= -C_m(s)\,\hat{\sigma}_m(s) - C_{um}(s)\,H_m{}^{-1}(s)\,H_{um}(s)\,\hat{\sigma}_{um}(s) + h_{L1}\cdot y_{cmd}(s) \\ &\quad - \begin{pmatrix} C_m(s) \\ C_{um}(s)\,H_m{}^{-1}(s)\,H_{um}(s) \end{pmatrix}^T \Delta(s)\,. \end{aligned} \tag{4.112}$$

Moreover, Eq. (4.109) is plugged into the control law

$$\begin{aligned} u_{ad}(s) &= -C_m(s)\,\hat{\sigma}_{m\star}(s) - C_{um}(s)\,H_m{}^{-1}(s)\,H_{um}(s)\,\hat{\sigma}_{um\star}(s) + h_{L1}\cdot y_{cmd}(s) \\ &= -C_m(s)\,\hat{\sigma}_m(s) - C_{um}(s)\,H_m{}^{-1}(s)\,H_{um}(s)\,\hat{\sigma}_{um}(s) + h_{L1}\cdot y_{cmd}(s) \\ &\quad - \begin{pmatrix} C_m(s) \\ C_{um}(s)\,H_m{}^{-1}(s)\,H_{um}(s) \end{pmatrix}^T \cdot \Phi(\bar{\boldsymbol{K}})\cdot e^{-sT_s}\boldsymbol{x}(s)\,, \end{aligned} \tag{4.113}$$

in order to show that the Δ-term appears as a feedback of the measured states $\boldsymbol{x}(t)$, which are delayed by one time step (e^{-sT_s}) within the control law. The gain for the feedback is determined by the choice of Φ, which is a degree of freedom, because $\bar{\boldsymbol{K}}$ has not been defined, yet.
The matrix Φ can be designed such that the feedback generates no unmatched portion[2] and that the matched portion is utilized for pole placement. A suitable method for pole placement in this case is again Eigenstructure Assignment according to the approach used for baseline controller gain design in Section 4.1.1. The algorithm is applied to a design model according to Fig. 4.22 to determine a gain-set $\bar{\boldsymbol{k}}_{L1}{}^T$, which satisfies the design conditions set for the short-period dynamics defined in Section 4.4.1. Note that, in contrast to Section 4.1.1, a short-period approximation of the longitudinal aircraft dynamics is used here instead of the linear model shown in Eq. (2.42). In order to model the exact path of the feedback, besides actuator and delay, also the low-pass filter $C_m(s)$ for the matched uncertainties and the time step delay T_s are accounted for in the design model. In particular, the influence of $C_m(s)$ and the time step delay T_s on the feedback can be seen in the control law Eq. (4.113). For the implementation of the gain design model, the additional time delay T_s is added to the time delay $T_{D,c}$ and is thus considered in the Padé approximation $\hat{G}_{D,c}(s)$.
These two design conditions for Φ can be formulated as

$$\Phi(\bar{\boldsymbol{K}}) \stackrel{!}{=} \begin{pmatrix} \bar{\boldsymbol{k}}_{L1}{}^T \\ 0_{1\times 2} \end{pmatrix}, \tag{4.114}$$

[2] i.e. a signal led through $C_{um}(s)\,H_m{}^{-1}(s)\,H_{um}(s)$

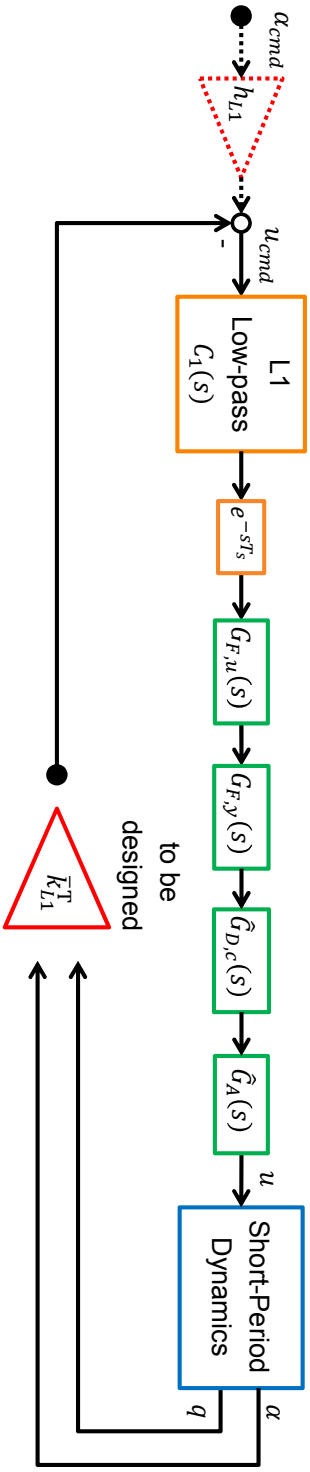

Figure 4.22. – Design model for state predictor feedback gain computation

which can be solved w.r.t. $\bar{\boldsymbol{K}}$ using a numerical solver. This yields a solution for the feedback gains for the state predictor $\bar{\boldsymbol{k}}_m{}^T$ and $\bar{\boldsymbol{k}}_{um}{}^T$ to finally achieve

$$\begin{aligned} u_{ad}(s) = &-C_m(s)\,\hat{\sigma}_m(s) - C_{um}(s)\,H_m{}^{-1}(s)\,H_{um}(s)\,\hat{\sigma}_{um}(s) + h_{L1}\cdot y_{cmd}(s) \\ &- C_m(s)\cdot e^{-sT_s}\bar{\boldsymbol{k}}_{L1}{}^T\cdot\boldsymbol{x}(s)\,. \end{aligned} \tag{4.115}$$

Note that the state feedback of $\boldsymbol{x}(t)$ is not explicitly implemented at the control law, but induced by the feedback via $\bar{\boldsymbol{K}}$ within the state predictor. It is not necessary to modify the structure of both adaptation law and control law, which can also be seen in Fig. 4.21.
In the last step, the feedforward gain h_{L1} is calculated suitable to the targeted eigendynamics of the plant. These targeted dynamics are already introduced in Fig. 4.22, where the designed gain-set $\bar{\boldsymbol{k}}_{L1}{}^T$ is now set in. The resulting system $\boldsymbol{A}_m$ and input $\boldsymbol{B_m}$ matrices are used to calculate h_{L1} according to Eq. (3.49). Here, the output matrix $\boldsymbol{C}_m$ is formulated such that the system only outputs the state α.

5. Controller Assessments

The goal of this chapter is to assess the control laws designed in Chapter 4 by means of simulation results. More specifically, baseline controller, adaptive DPI and Plant Augmentations, the $\Delta\dot{q}$ Compensation Law and the standalone L1 adaptive controller with Eigenstructure Assignment are considered.

With this regard, Section 5.1 introduces the methodology of the assessments in general. This includes the description of linear methods to determine robust stability properties of the closed-loop. Furthermore, the example maneuver used for performance assessments is characterized and the accompanying performance metrics are formulated. At last, the linearizations are described, which are used to assess the closed-loop poles resulting from the combination of controller and aircraft.

In the next step, the assessments are performed for the individual controller configurations in Section 5.2. The results of the baseline controller configuration serve as a reference for the adaptive controller assessments with regards to both robust stability and performance. This also allows for first comparisons, although a detailed comparison considering all controller configurations is in the focus of Chapter 6. Nevertheless, the approximate equivalence of the adaptive DPI and Plant Augmentation approaches w.r.t. simulation results is also worked out in this chapter.

In particular, the effect of the state predictor modifications proposed in Chapter 4 for the L1 adaptive controllers is shown. More specifically, this includes the hedging modification, where actuator measurement is used on the one hand. The beneficial effect on the robust stability properties w.r.t. the actuator cut can be clearly observed by means of the examples shown in this chapter (c.f. Section 5.2.2.1 and Section 5.2.4.1). Moreover, it is shown that this modification has neglectable influence on the controller performance. On the other hand, it is demonstrated in Section 5.2.4 that L1 Adaptive Control with Eigenstructure Assignment is able to precisely set up desired dynamics and to offer robust performance at the same time.

The assessments also include results gained using the enhanced aircraft model. In this chapter an exemplary configuration of the reality effects induced by the enhanced model is used. Detailed analyses of the single effects on the controller performance and variations of the model parameters are in the scope of Chapter 6.

5.1. Methodology of assessments

In this section a general description of the methodologies can be found, which are used to analyze the controller designs. The determination and specification of robust stability properties is shown in terms of linear methods in Section 5.1.1. Section 5.1.2 introduces the example maneuver to be simulated and performance metrics to be evaluated in order to be able to rank the controllers' performances.

5.1.1. Robust stability

As it was already stated before, assessments determining robust stability properties of the closed-loop are one important foundation of aircraft FCS certification [111, pp. 25-27]. For this reason they are also analyzed for the controller designs conducted in this thesis.

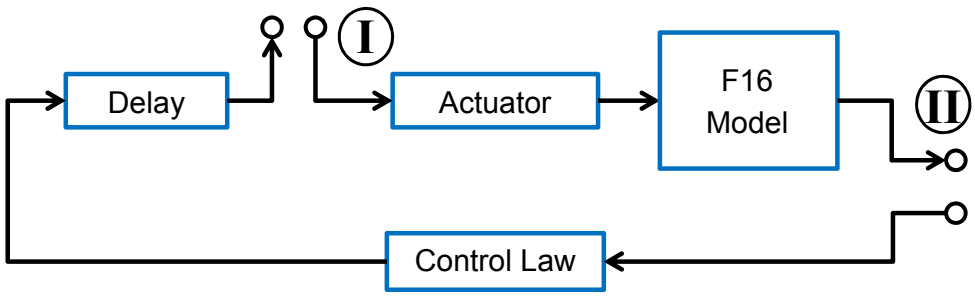

Figure 5.1. – Model utilized to determine transfer functions for robust stability assessments for the basic aircraft model

For the linear assessments specific open-loop transfer functions have to be determined first. Thus, the closed-loop consisting of aircraft, controller and additional dynamics is cut either upstream the actuator or for the single sensor measurements. This is shown in Fig. 5.1 for the basic and in Fig. 5.2 for the enhanced aircraft model. The first cut Ⓘ is called actuator cut, also known as bottleneck cut, the second one Ⓘ describes the sensor cuts. In this thesis, the investigations include the actuator cut for elevator command η_{cmd} and the sensor cuts for angle of attack α as well as pitch rate q. Additionally, the cut for pitch acceleration $\dot{q}$ is considered for the $\Delta\dot{q}$ Compensation Law, in case $\dot{q}$ measurement is available. It can be read in [111, pp. 25-27] that the bottleneck cut is the most relevant in terms of FCS certification and that the sensor cuts play a secondary role.
The transfer functions required for robust stability assessments can be obtained by means of linearization of the closed-loops shown in Fig. 5.1 and Fig. 5.2, which are cut up at one position at a time. The transfer functions then represent the linear dynamics of the cut up closed-loop at one certain envelope point. It is important that the considered closed-loops are in a trimmed state before linearization, i.e. in this case the initial controller command is the trimming elevator deflection $\eta_{cmd} = \eta_0$.

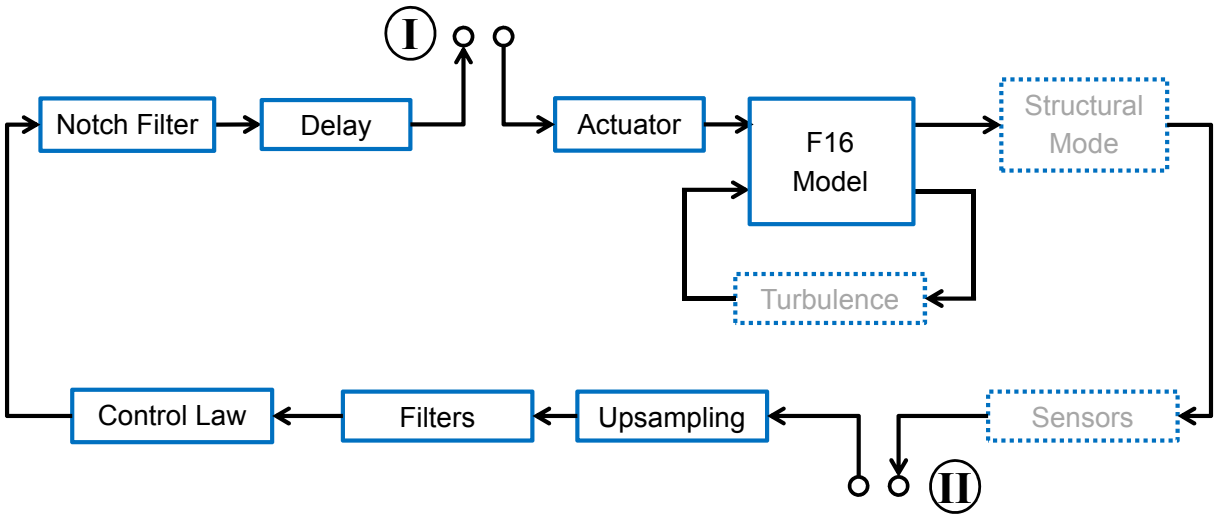

Figure 5.2. – Model utilized to determine transfer functions for robust stability assessments for the enhanced aircraft model

Note also that the linear robust stability assessments are performed separately using both the basic and the enhanced aircraft model configuration for all controllers. It is indicated in Fig. 5.2 that certain elements are left out for linearization. These are turbulence and gust models, sensor models and the simple structural mode model. Atmospheric disturbance are not considered during linear robust stability assessments. Furthermore, most effects contributed by the sensor model cannot be mapped to a linear model. At last, the structural mode is considered as unknown dynamics and is thus not considered for these assessments.
Now that the transfer functions of the cut up closed-loops are obtained, they can be analyzed in the frequency domain. Let $L(s)$ be one of these transfer functions. Note that the following statements hold independent from the position of the loop cut and the aircraft model configuration used for the assessment.

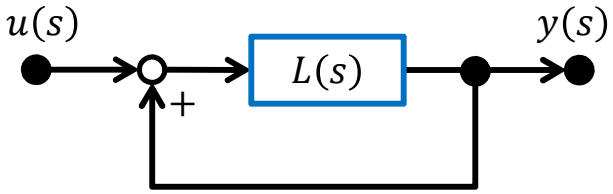

Figure 5.3. – Original closed-loop obtained by putting $L(s)$ in a positive feedback loop

The frequency response $L(j\omega)$ of the transfer function with $\omega \in [-\infty;\infty[$ [75, p. 240] can be plotted in the complex plane. The resulting diagram is called Nyquist plot [93, 102]. In addition to the frequency response, the closed-loop poles of the system to be analyzed are also represented in the Nyquist plot. Their position can be obtained by application of the following considerations. First, the original loop is closed again,

which in general can be achieved by putting $L(s)$ in a positive feedback loop. This is also shown in Fig. 5.3. After that, the closed-loop transfer function can be calculated and results in

$$y = \frac{L(s)}{1 - L(s)} u. \tag{5.1}$$

It is now obvious that the closed-loop poles λ_i satisfy the relation

$$1 - L(\lambda_i) = 0. \tag{5.2}$$

Thus, the closed-loop poles are mapped onto the point $L(\lambda_i) = +1 + 0 \cdot j$ in the corresponding Nyquist plot. An example showing such a plot can be found in Fig. 5.4a. Here, the dotted line indicates the part of the frequency response corresponding to $\omega \in [-\infty; 0[$.

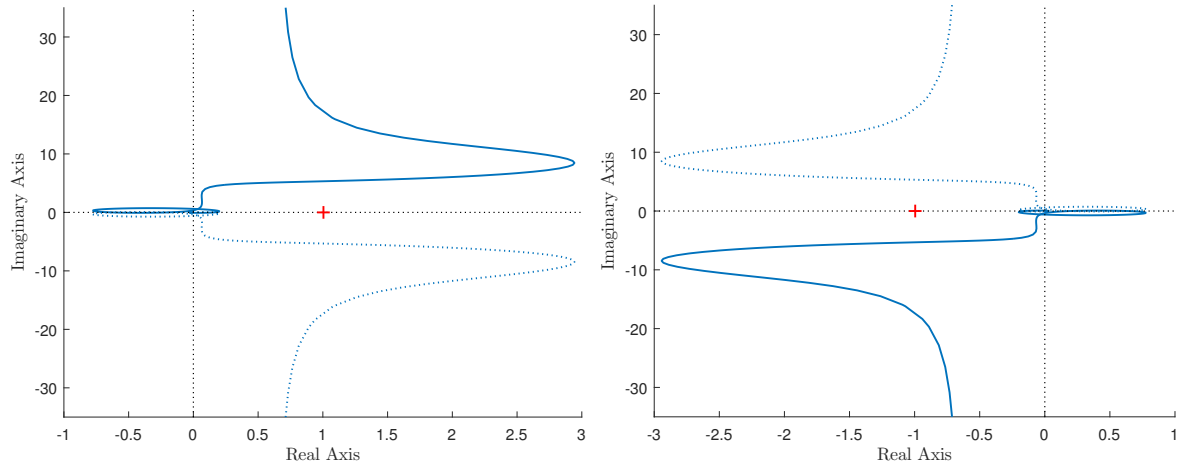

(a) Critical point defined at $+1 + 0 \cdot j$ **(b)** Critical point defined at $-1 + 0 \cdot j$

Figure 5.4. – Example for a nyquist plot

At this point, the Nyquist criterion can be utilized in order to determine, whether the closed-loop is stable or unstable. The criterion states that, if the curve $L(j\omega)$ is plotted for $\omega \in [-\infty; \infty[$ and if the critical point $+1 + 0 \cdot j$ "lies completely outside this curve[,] the system is stable; if not[,] it is unstable" [93, p. 136]. A more thorough treatise on this criterion can e.g. be found in [75, pp. 433-434]. Application of the Nyquist criterion on the example plot shown in Fig. 5.4a indicates that the closed loop is stable. While the considerations of Nyquist et. al. in [93] define the critical point at $+1 + 0 \cdot j$, it can be often found in literature that the critical point lies at $-1 + 0 \cdot j$ (c.f. e.g. [75, pp. 433-434], [16, p. 302]). Though, a few exceptions (e.g. [23]) can be found, which use the definition $+1 + 0 \cdot j$. The reason for this is that often negative feedback is assumed for the closed-loop shown in Fig. 5.3. This changes Eq. (5.1) to

$$y = \frac{L(s)}{1 + L(s)} u, \tag{5.3}$$

which directly leads to

$$1 + L(\lambda_i) = 0 \tag{5.4}$$

for the closed-loop poles λ_i. Thus, the critical point lies at $-1 + 0 \cdot j$ in this case.
In order to suit the nomenclature commonly used in literature, the assessments in this thesis also use the definition of the critical point located at $-1 + 0 \cdot j$. As the feedback is still positive, if the cut up loop is closed again (c.f. Fig. 5.3), the frequency response of $\tilde{L}(j\omega) = -L(j\omega)$ is plotted for $\omega \in [-\infty; \infty[$. Thus, $\tilde{L}(j\omega)$ corresponds to a point reflection of $L(j\omega)$ with respect to the origin. This can be also seen in Fig. 5.4b. The statement of Fig. 5.4a and Fig. 5.4b remains the same despite of the point reflection. It is interesting to note that Bode also used the definition of the critical point at $-1 + 0 \cdot j$ for his specific application in [15], which he achieved by rotating the Nyquist plot "through 180° from its normal position so that the critical point occurs at -1, 0 rather than +1, 0." [15, p. 431].

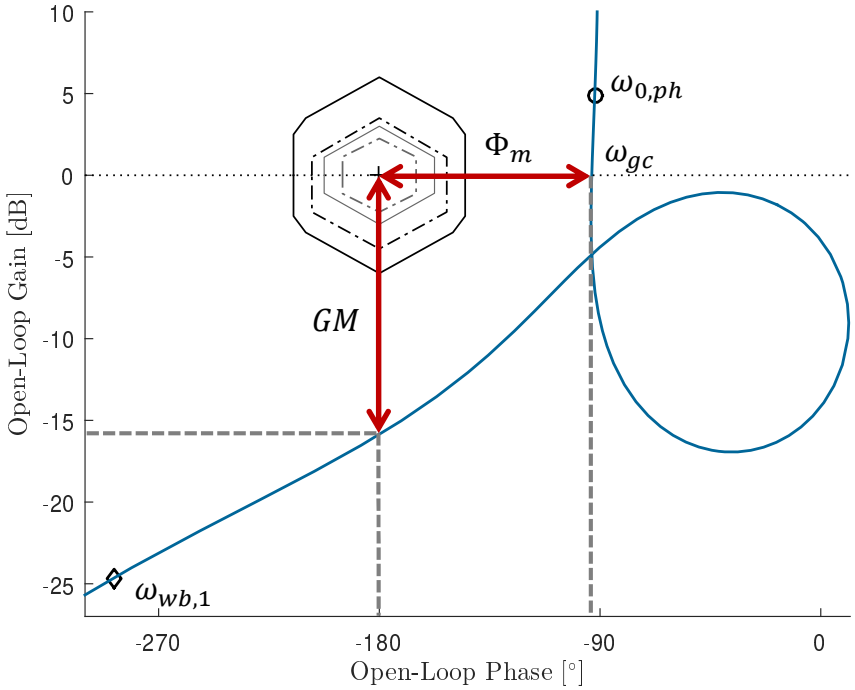

Figure 5.5. – Example for a nichols plot with nichols diamonds for robust stability assessment

Although robust stability margins in terms of gain and phase margin can generally also be obtained from Nyquist plots [75, pp. 445-448], Nichols plots [92, pp. 179-186]

of $\tilde{L}(j\omega)$ offer a more intuitive illustration in that matter. For that reason Nichols plots are used for the robust stability assessments of the different controller configurations in the remainder of this chapter.
In order to generate a Nichols plot, the frequency response $\tilde{L}(j\omega)$ with $\omega \in [0;\infty[$ is plotted into a diagram showing magnitude versus phase. This corresponds to a mapping of the frequency response $\tilde{L}(j\omega)$ of the Nyquist plot to polar coordinates in combination with logarithmic scaling of magnitude. Therefore, Nichols plots are also closely related to Bode plots [14] [75, pp. 246-248].
The nichols plot obtained from the frequency response shown in Fig. 5.4b can be found in Fig. 5.5. Note also, that the critical point $-1+0\cdot j$ is mapped to $[-180^\circ \;\; 0dB]$[1]. The phugoid frequency $\omega_{0,ph}$ is marked by means of a black circle on the frequency response curve and a black diamond indicates the estimated frequency of first wing-bending mode $\omega_{wb,1}$. Phase margin Φ_m and gain margin Gain Margin (GM) can be directly obtained from the plot as shown in Fig. 5.5.

	GM $[dB]$	Φ_m $[^\circ]$	**Appearance**
$\omega \geq \omega_{0,ph}$ Nominal conditions	$[-6;6]$	$[-35;35]$	black, solid
$\omega < \omega_{0,ph}$ Nominal conditions	$[-4.5;3.5]$	$[-27.5;27.5]$	black, dashed-dotted
$\omega \geq \omega_{0,ph}$ aerodynamic uncertainty assessment	$[-3;3]$	$[-22.5;22.5]$	grey, solid
$\omega < \omega_{0,ph}$ aerodynamic uncertainty assessment	$[-2.25;2.25]$	$[-15;15]$	grey, dashed-dotted

Table 5.1. – Definition of the edges defining the nichols diamonds in dependence of considered frequency ω and type of assessment

Furthermore, Nichols plots offer a illustrative way to define exclusion regions around the critical point, which indicate weak robust stability of the closed-loop [8, p. 35]. These exclusion regions are defined by means of so called Nichols diamonds, which can also be found in Fig. 5.5. For a certain controller configuration it applies that the frequency response $\tilde{L}(j\omega)$ should not cross the exclusion area as an acceptance criterion. Different nichols diamonds are considered in dependence of considered frequency ω and type of assessment. These are summarized in Table 5.1. For the assessments made in this thesis mainly the robustness margins according to [86] are used. Missing values are suitable interpolated using the definitions in [111, p. 26]. Thus, it can be seen in Fig. 5.5 that the exemplary controller configuration offers sufficient robust stability margins. For the robustness assessments in the remainder of

[1]The critical point $+1+0\cdot j$ would be mapped to $[0^\circ \;\; 0dB]$

this chapter it is required that the margins defined by means of the nichols diamond are not violated considering the bottleneck cut. Note also that for informational purposes the nichols diamond is also included in analyzes considering sensor cuts, although it is not required by [111, pp. 25-27] that certain margins have to be fulfilled here.
Moreover, it is demanded in [111, p. 27] that flexible modes of the aircraft offer a minimum gain margin of $8dB$ and a minimum phase margin of $60°$. It was already mentioned above that the structural mode model according to Section 2.7 is not considered for the robust stability assessments in this thesis. Although, in order to provide a preliminary assessment with regard to robust stability of flexible modes, for every controller configuration the bottleneck cut is also investigated utilizing the enhanced aircraft model, where the structural mode is activated. These assessments are carried out for one exemplary envelope point.
Besides gain margin GM and phase margin Φ_m, also Time Delay Margin (TDM) is determined for the controller assessments made in this thesis. Being closely related to the phase margin Φ_m, TDM directly indicates, how much delay is tolerable at the considered cut position before the closed-loop is rendered unstable. As already stated, TDM is calculated from phase margin Φ_m in combination with gain crossover frequency ω_{gc}, which is also marked in Fig. 5.5. This results in [8, p. 32]

$$TDM = \frac{\Phi_m}{\omega_{gc}}. \tag{5.5}$$

5.1.2. Performance

Robust stability assessments represent one important pillar of the investigations on the controller designs made in this thesis. The other pillar is analysis of the controller performance by means of linear and nonlinear simulations.
At first, step responses of the controllers are assessed using both the basic (linear and nonlinear) and the enhanced aircraft model (nonlinear). Fig. 5.6 shows a step in command angle of attack α_{cmd} at $t = 1s$. Furthermore, the desired responses α_{ref} for both the standalone L1 adaptive controller and the remaining controllers are depicted.

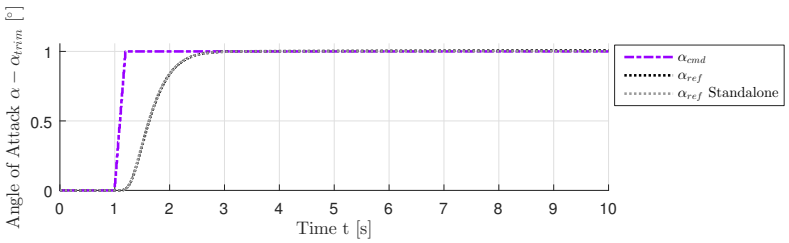

Figure 5.6. – Step maneuver used for performance assessments containing angle of attack command α_{cmd}, reference angle of attack α_{ref} to be tracked by the controllers

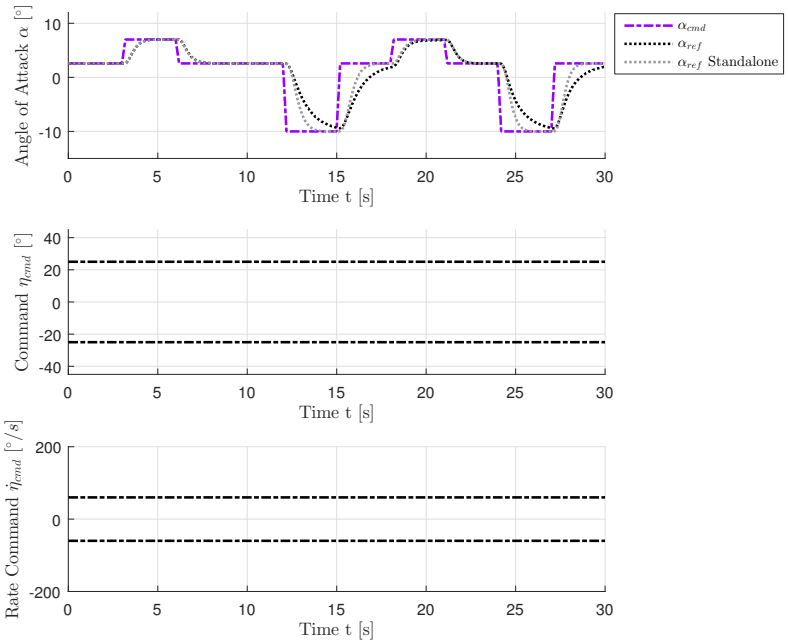

Figure 5.7. – Example maneuver used for performance assessments containing angle of attack command α_{cmd}, reference angle of attack α_{ref} to be tracked by the controllers and resulting angle of attack α, elevator command η_{cmd} and elevator command rate $\dot{\eta}_{cmd}$

The reason for using two different reference signals becomes obvious when considering a more complex maneuver. This is shown in Fig. 5.7. In addition to angle of attack α, also the controller command η_{cmd} and the accompanying first derivation $\dot{\eta}_{cmd}$, i.e. commanded elevator rate, are presented. The limits of the actuator are also marked thereby. It can be seen that, especially in case $\alpha_{cmd} = -10°$, the reference signals α_{ref} differ from each other. The reason for this is the rate limiting, which is part of the DPI baseline controller included in the reference model. Rate limiting within the control law is not present for the standalone L1 adaptive controller and its reference model. This assumption would appear to be confirmed by Fig. 5.8, in which the inherent rate limiting is deactivated for the DPI baseline controller and both α_{ref} are practically matching.

In order to assure comparability throughout this thesis and also in order to not exceed the limits of this work, one exemplary maneuver is considered for all controller configurations. This maneuver is performed using nonlinear simulations in this chapter at first considering the basic and the enhanced aircraft model set up with light and severe turbulence under nominal conditions. Thereby, the sensor models are adjusted according to Table 2.6. After that, performance considering a CG-shift of 5% for the basic and 2% for the enhanced aircraft model is investigated. Furthermore, this maneuver is also used for the assessments shown in Chapter 6.

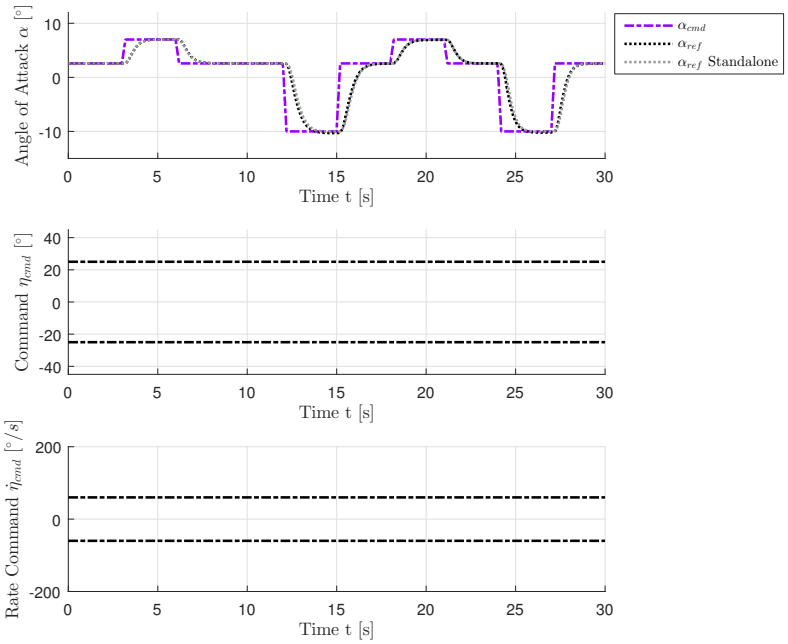

Figure 5.8. – Example maneuver used for performance assessments containing angle of attack command α_{cmd}, reference angle of attack α_{ref} (DPI rate limit deactivated) to be tracked by the controllers and resulting angle of attack α, elevator command η_{cmd} and elevator command rate $\dot{\eta}_{cmd}$

With the objective of quantifying the controller performances, certain metrics are calculated additionally. This further enhances comparability of the results. In order to assess tracking with regard to the reference model, angle of attack α is compared to α_{ref} utilizing the $\mathcal{L}_2$ and $\mathcal{L}_\infty$ norms according to [120]

$$M_{\mathcal{L}_2} = \left\| \alpha\left(t\right) - \alpha_{ref}\left(t\right) \right\|_{\mathcal{L}_2} = \sqrt{\int_{t_0}^{t_f} \left(\alpha\left(t\right) - \alpha_{ref}\right)^2 dt} \tag{5.6a}$$

$$M_{\mathcal{L}_\infty} = \left\| \alpha\left(t\right) - \alpha_{ref}\left(t\right) \right\|_{\mathcal{L}_\infty} = \max_{t \in \left[t_0, t_f\right]} \left| \alpha\left(t\right) - \alpha_{ref}\left(t\right) \right|. \tag{5.6b}$$

$M_{\mathcal{L}_\infty}$ thereby measures the maximum value of the control error, whereas $M_{\mathcal{L}_2}$ is a measure for its energy. The $\mathcal{L}_2$ norm is also utilized to assess the demanded actuator activity by means of

$$M_{\mathcal{L}_{2,act}} = \left\| \dot{\eta}_{cmd} \right\|_{\mathcal{L}_2} = \sqrt{\int_{t_0}^{t_f} \dot{\eta}_{cmd}{}^2 \, dt}, \tag{5.7}$$

where $\dot{\eta}_{cmd}$ is the commanded elevator deflection rate. It holds for all metrics during comparisons that the performance is better, if the metric value is smaller. The metrics

are mainly used in Section 6.2, where comparisons between the proposed control laws presented in Chapter 4 are drawn.

5.1.3. Closed-loop poles

Besides performance and robust stability investigations, it has to be verified initially that the desired dynamic behavior of the aircraft is set up by the controller. This can be assessed by means of closed-loop linearizations and the corresponding poles of the closed-loop transfer functions of commanded angle of attack α_{cmd} to measurement α.

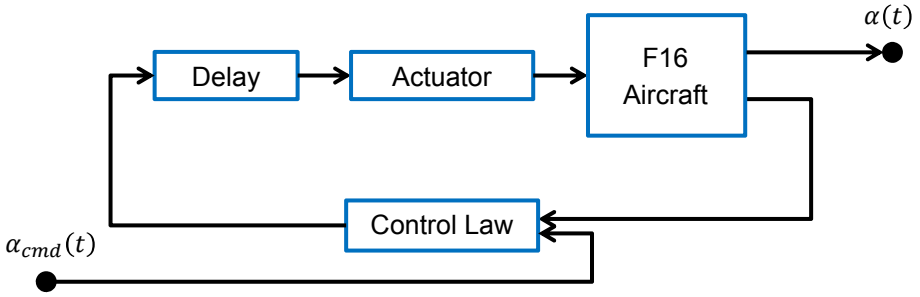

Figure 5.9. – Model utilized to determine transfer function of $\alpha_{cmd} \rightarrow \alpha$ for the basic aircraft model

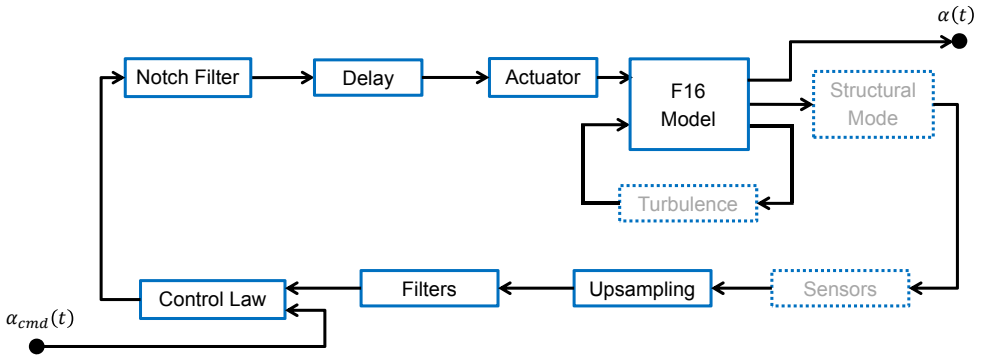

Figure 5.10. – Model utilized to determine transfer function of $\alpha_{cmd} \rightarrow \alpha$ for the enhanced aircraft model

In this regard, numerical linearizations are performed using the closed-loops Fig. 5.9 for the basic and Fig. 5.10 for the enhanced aircraft. It has to be noted that turbulence, structural mode and sensor models are left out for this evaluation as it was already shown in Section 5.1.1 for the robustness assessments.
During the process of linearization, the discrete-time transfer functions of controller and filters are implicitly converted to their continuous-time representations using the bilinear transformation, which was introduced in Section 3.3. That is, because the investigation with regard to system poles are chosen to be performed in the

frequency domain. In order to be able to analyze the transfer function without considering the uncertainty stemming from the discrete-time implementation and the necessary conversions to continuous-time, also continuous-time implementations of the controllers were generated.
Thus, four different linearizations are calculated for every controller utilizing basic and enhanced aircraft model with accompanying filters on the one hand, discrete-time and continuous-time implementations of controller and filters on the other hand. The resulting poles are presented for one exemplary envelope point, which is $V_0 = 154.94\frac{m}{s}$ and $h_0 = 5000m$, in order to not exceed the frame of this work. Furthermore, the system poles are summarized in tables rather than complex plane diagrams due to the number of system poles and the broad range of their frequencies.

5.2. Analyses of control laws

After the methodology of assessments was introduced in the last section, the remainder of this chapter focuses on the analyses of the control laws designed in Chapter 4 with regard to performance, robust stability and closed-loop system poles. The simulation results for the DPI baseline controller are summarized in Section 5.2.1.
Section 5.2.2 features the L1 Adaptive Augmentations, which includes both the DPI (Closed-Loop) and the Plant Augmentation architectures. Robust stability assessments here prove the beneficial effect of the hedging technique, which was proposed in Section 4.2, on gain and phase margin with regard to the bottleneck cut.
Next to that, simulation results of the $\Delta\dot{q}$ Compensation Law are summarized and discussed in Section 5.2.3. At last, Section 5.2.4 shows investigations using the standalone L1 adaptive controller with Eigenstructure Assignment, at which the closed-loop poles gained at an exemplary envelope point show its ability to precisely place system poles.

5.2.1. Baseline controller

In order to serve as a reference for the evaluations of the adaptive control laws, the DPI baseline controller is analyzed first.
The dynamic behavior of the aircraft is initially analyzed by means of linearizations of the closed-loop containing both aircraft and baseline controller. For the basic aircraft configuration the results are shown in Table A.1 for the discrete-time and in Table A.2 for the continuous-time controller implementation.
As it was stated before, the linearizations are performed exemplarily for the envelope point defined by $V_0 = 154.94\frac{m}{s}$ and $h_0 = 5000m$. The corresponding desired natural frequency for the short-period at this envelope point can be determined as $\omega_{0,sp,des} = 3.84\frac{rad}{s}$ using Table 4.1. The relative damping is uniformly chosen as $\zeta_{sp,des} = 0.95$. Exactly these values can be found in both Table A.1 and Table A.2 for the complex

conjugate pole pair 5 and 6. This confirms that the gain design methodology introduced in Section 4.1.1 works properly for the control problem at hand.
Likewise, the system poles are determined for the enhanced aircraft configuration. The results can be found in Table A.3 for the discrete-time and in Table A.4 for the continuous-time controller implementation. Exact matching of the desired location of the short-period can be determined considering again the complex conjugate pole pair 5 and 6 for the continuous-time implementation, whereas slight deviations can be detected considering the discrete-time controller. The resulting short-period here lies at $\omega_{0,sp} = 3.09\frac{rad}{s}$ with a relative damping of $\zeta_{sp} = 0.84$. In this case, the differences stem from inaccuracies caused by the conversion of the discrete-time filter transfer functions back to continuous-time.

5.2.1.1. Linear robust stability

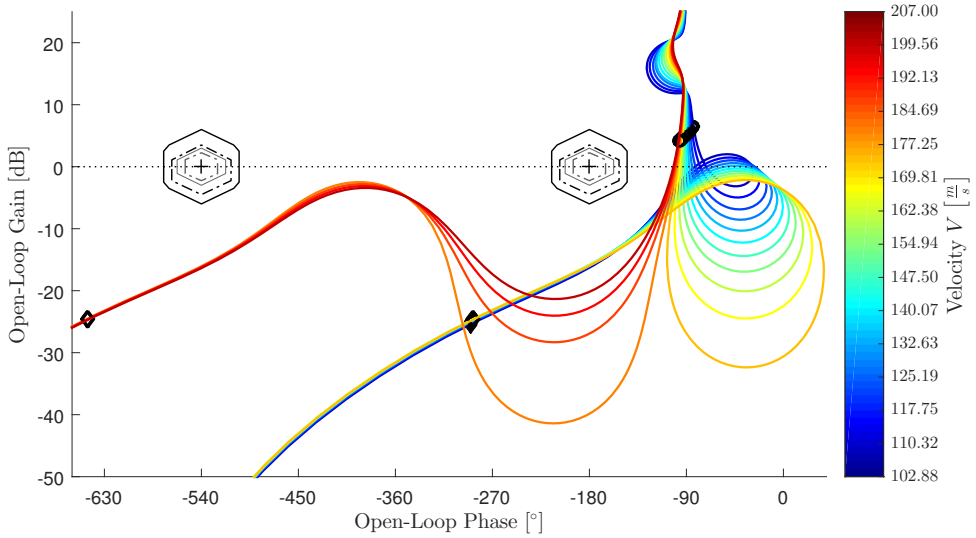

Figure 5.11. – Nichols plot for robust stability assessment of baseline controller at envelope points according to Table 2.2 generated for η_{cmd} (bottleneck) loop cut (basic aircraft model)

As it was shown in Section 5.1.1, the robust stability properties of the DPI baseline control law can be analyzed by means of nichols plots of open-loop transfer functions determined at different cuts of the closed-loop. These are the bottleneck cut at the commanded elevator deflection η_{cmd} upstream the actuator ① and the sensor cuts for angle of attack α and pitch rate q ⑪ both pictured in Fig. 5.1 and Fig. 5.2 for basic and enhanced aircraft model, respectively. In terms of flight control certification, the most important robustness assessment is the one performed for the bottleneck cut [111, pp. 25-27]. Although, investigations w.r.t. sensor cuts are also provided as additional information in this thesis.

Table 5.2. – Robust stability properties gain margin (GM), phase margin Φ_m, time delay margins (TDM) and corresponding gain-crossover frequencies $\omega_{gc,\Phi}$ and $\omega_{gc,TDM}$ for robust stability assessment of baseline controller at envelope points according to Table 2.2 generated for η_{cmd} (bottleneck) loop cut (basic aircraft model)

Velocity $V\ \left[\frac{m}{s}\right]$	**GM** $[dB]$	$\Phi_m\ [^\circ]$	$\omega_{gc,\Phi}\ \left[\frac{rad}{s}\right]$	**TDM** $[s]$	$\omega_{gc,TDM}\ \left[\frac{rad}{s}\right]$
102.88	16.28	98.00	3.31	0.517	3.31
	$-\infty$	-209.53	1.83	-1.383	3.31
110.32	16.12	102.75	0.72	0.527	3.42
	$-\infty$	-207.41	2.12	-1.312	3.42
117.75	16.07	98.34	0.68	0.544	3.49
	$-\infty$	-206.57	2.39	-1.256	3.49
125.19	15.97	95.37	0.66	0.571	3.54
	$-\infty$	-209.07	2.69	-1.206	3.54
132.63	15.90	92.78	0.65	0.628	3.50
	$-\infty$	-215.31	3.06	-1.167	3.50
140.07	15.86	90.47	0.64	2.464	0.64
	$-\infty$	-269.53	0.64	-7.341	0.64
147.50	15.84	88.44	0.63	2.445	0.63
	$-\infty$	-271.56	0.63	-7.508	0.63
154.94	15.85	86.63	0.62	2.424	0.62
	$-\infty$	-273.37	0.62	-7.650	0.62
162.38	15.87	84.99	0.62	2.406	0.62
	$-\infty$	-275.01	0.62	-7.786	0.62
169.81	15.91	83.49	0.61	2.389	0.61
	$-\infty$	-276.51	0.61	-7.913	0.61
177.25	15.97	82.11	0.60	2.373	0.60
	$-\infty$	-277.89	0.60	-8.031	0.60
184.69	16.05	80.85	0.60	2.358	0.60
	$-\infty$	-279.15	0.60	-8.142	0.60
192.13	16.15	79.77	0.59	2.350	0.59
	$-\infty$	-280.23	0.59	-8.255	0.59
199.56	16.25	78.81	0.59	2.335	0.59
	$-\infty$	-281.19	0.59	-8.333	0.59
207.00	16.36	77.91	0.59	2.322	0.59
	$-\infty$	-282.09	0.59	-8.409	0.59

Fig. 5.11 contains nichols plots generated for different envelope points according to Table 2.2 for the combination of DPI controller and basic aircraft model. The frequency responses clearly indicate sufficient stability margins, i.e. none of curves is crossing the nichols diamond, where the black dashed-dotted diamond corresponds to frequencies $\omega < \omega_{0,ph}$ and the outermost black solid diamond is valid for $\omega \geq \omega_{0,ph}$ (c.f. Table 5.1). This is also confirmed by Table 5.2, which contains gain margins GM, besides phase margins Φ_m and time-delay margins TDM with their corresponding crossover frequencies $\omega_{gc,\Phi}$ and $\omega_{gc,TDM}$ for the different envelope points. It can be seen that the gain margin remains approximately constant at $\approx 16db$ and the phase margin Φ_m results between 77.91° and 98°. According to Table 5.1 a phase margin of 35° and a gain margin of $6dB$ are required here.
With regard to the determined TDM a rapid increase can be detected between the envelope points corresponding to $V_{0,5} = 132.63\frac{m}{s}$ and $V_{0,6} = 140.07\frac{m}{s}$, where TDM changes from $0.628s$ to $2.464s$. The reason for this is the loop contained in the frequency response, which can clearly be seen in Fig. 5.11 for the envelope points $V_{0,1} = 102.88\frac{m}{s}$ to $V_{0,11} = 177.25\frac{m}{s}$. For low velocities up to $V_{0,5} = 132.63\frac{m}{s}$ this loop is crossed by the $0dB$-line. This results in three different phase values, which have to be considered for the determination of TDM according to Eq. (5.5) in dependence of the three corresponding gain crossover frequencies $\omega_{gc,TDM}$. The smallest result is then the critical TDM value. It should be noted that this minimum TDM value does not necessarily correspond to the crossing point of the $0dB$-line, where the phase margin is determined, i.e. the crossing point having the shortest distance to the critical point. This can be seen for example at $V_{0,5} = 132.63\frac{m}{s}$ in Table 5.2, where $\omega_{gc,TDM} \neq \omega_{gc,\Phi}$. For $V_{0,6} = 140.07\frac{m}{s}$ the $0dB$-line crossing around $\omega_{gc} \approx 3.5\frac{rad}{s}$, at which the minimum TDM is detected for lower velocities, does not exist, because the $0dB$-line does not cross the loop here. Thus, only one gain crossover point exists, at which the frequency is $\omega_{gc} = 0.64\frac{rad}{s}$. As the gain crossover frequency ω_{gc} appears as divisor in Eq. (5.5), smaller values of ω_{gc} lead to higher TDM values. This explains the rapid increase of TDM between the envelope points corresponding to $V_{0,5} = 132.63\frac{m}{s}$ and $V_{0,6} = 140.07\frac{m}{s}$.
Moreover, Table 5.2 also includes the opposite margins. Especially for unstable aircraft configurations (c.f. [86]) it is important to consider the opposite gain margin, because the frequency response also crosses the $-180°$-line on the upper side of the nichols diamond in this case. Thus, an additional gain margin exists, which has a negative dB-value, i.e. its magnitude lies between 0 and 1. For informational purposes, such additional margins are also determined for phase and time delay of the open-loop frequency response, which indicate, how much delay can be removed from the closed-loop, until the system response becomes unstable. It should be noted that these are rather theoretical values, in particular, if they are higher than the actual, total delay contained in the closed-loop.
The corresponding assessment for the enhanced aircraft model configuration can be found in Fig. 5.12 for the nichols plot and in Table 5.3 for the robust stability properties, respectively. Still, the required robust stability margins are fulfilled, although gain and

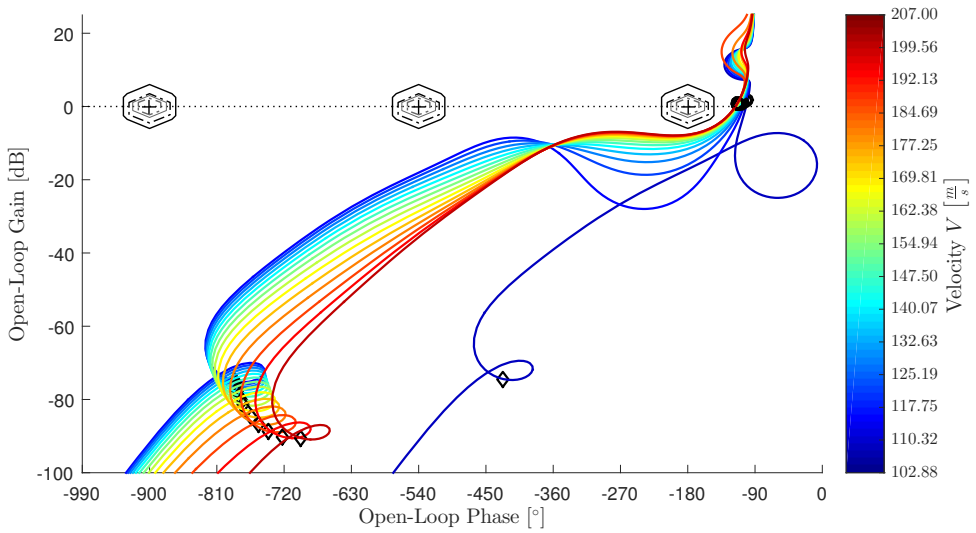

Figure 5.12. – Nichols plot for robust stability assessment of baseline controller at envelope points according to Table 2.2 generated for η_{cmd} (bottleneck) loop cut (enhanced aircraft model)

phase margins are decreased in comparison to the basic aircraft configuration. This is mainly due to the introduced filters for the enhanced configuration, which cause phase loss. Furthermore, Fig. 5.13 shows the same assessment for the exemplary envelope point of $V_0 = 154.94\frac{m}{s}$ and $h_0 = 5000m$, where the structural mode model according to Section 2.7 is activated. It can be clearly seen that for the frequency range upwards of the first wing bending mode, which is modeled at $\omega_{0,s} = 6.05Hz \equiv 38.01\frac{rad}{s}$ and is marked by the small diamond, a margin of $\approx 65dB$ can be detected. Thus, the closed-loop offers sufficient robust stability margins with regard to the flexible mode, where $8dB$ margin are demanded.
Besides bottleneck cut, also the sensor cuts are investigated for the DPI baseline controller. For both aircraft model configurations sufficient stability margins can be observed for the sensor cuts, where the resulting nichols plots can be found in Fig. 5.14 and Fig. 5.15 for the α-cut and in Fig. 5.16 and Fig. 5.17 for the q-cut, respectively. The corresponding tabulated values can be found in Table A.25, Table A.59 for the α-cut and in Table A.26, Table A.60 for the q-cut. The tables can be found in Appendix A.5.2 and Appendix A.6.

Table 5.3. – Robust stability properties gain margin (GM), phase margin Φ_m, time delay margins (TDM) and corresponding gain-crossover frequencies $\omega_{gc,\Phi}$ and $\omega_{gc,TDM}$ for robust stability assessment of baseline controller at envelope points according to Table 2.2 generated for η_{cmd} (bottleneck) loop cut (enhanced aircraft model)

Velocity $V\ \left[\frac{m}{s}\right]$	**GM** $[dB]$	$\Phi_m\ [^\circ]$	$\omega_{gc,\Phi}\ \left[\frac{rad}{s}\right]$	**TDM** $[s]$	$\omega_{gc,TDM}\ \left[\frac{rad}{s}\right]$
102.88	17.15	77.99	0.45	3.031	0.45
	$-\infty$	-282.01	0.45	-10.960	0.45
110.32	18.06	75.01	0.43	3.014	0.43
	$-\infty$	-284.99	0.43	-11.450	0.43
117.75	15.88	72.63	0.42	3.003	0.42
	$-\infty$	-287.37	0.42	-11.881	0.42
125.19	13.15	70.85	0.42	2.971	0.42
	$-\infty$	-289.15	0.42	-12.124	0.42
132.63	11.55	69.35	0.41	2.937	0.41
	$-\infty$	-290.65	0.41	-12.308	0.41
140.07	10.46	68.07	0.41	2.900	0.41
	$-\infty$	-291.93	0.41	-12.435	0.41
147.50	9.68	67.00	0.41	2.863	0.41
	$-\infty$	-293.00	0.41	-12.520	0.41
154.94	9.13	66.12	0.41	2.827	0.41
	$-\infty$	-293.88	0.41	-12.565	0.41
162.38	8.69	65.41	0.41	2.792	0.41
	$-\infty$	-294.59	0.41	-12.575	0.41
169.81	8.36	64.82	0.41	2.758	0.41
	$-\infty$	-295.18	0.41	-12.561	0.41
177.25	8.12	64.39	0.41	2.724	0.41
	$-\infty$	-295.61	0.41	-12.505	0.41
184.69	7.94	63.94	0.41	2.697	0.41
	$-\infty$	-296.06	0.41	-12.488	0.41
192.13	7.82	63.99	0.41	2.704	0.41
	$-\infty$	-296.01	0.41	-12.508	0.41
199.56	7.74	63.75	0.42	2.628	0.42
	$-\infty$	-296.25	0.42	-12.212	0.42
207.00	7.69	63.66	0.43	2.588	0.43
	$-\infty$	-296.34	0.43	-12.049	0.43

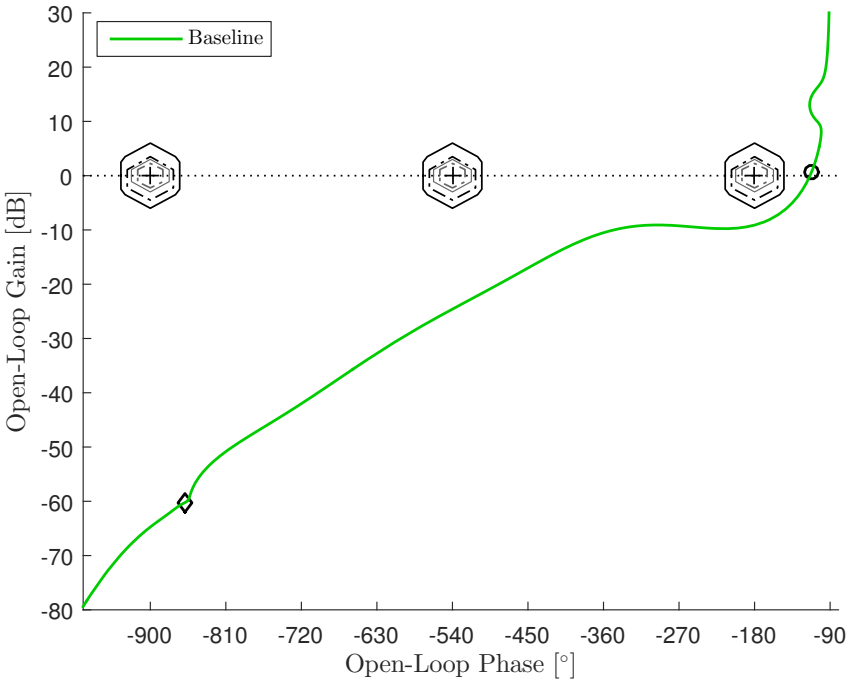

Figure 5.13. – Nichols plot for robust stability assessment of baseline controller at $V = 154.94 \frac{m}{s}$ generated for η_{cmd} (bottleneck) loop cut (enhanced aircraft model, activated structural mode)

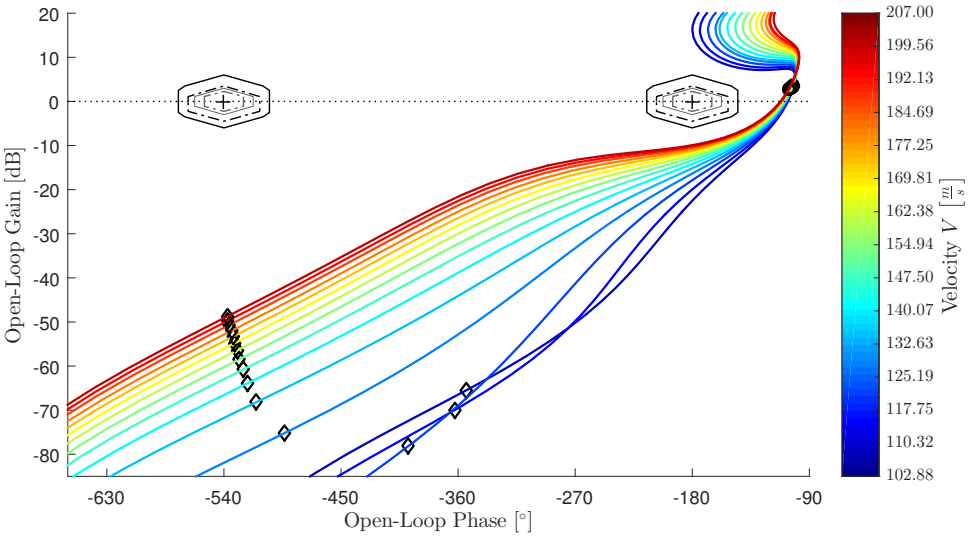

Figure 5.14. – Nichols plot for robust stability assessment of baseline controller at envelope points according to Table 2.2 generated for α loop cut (basic aircraft model)

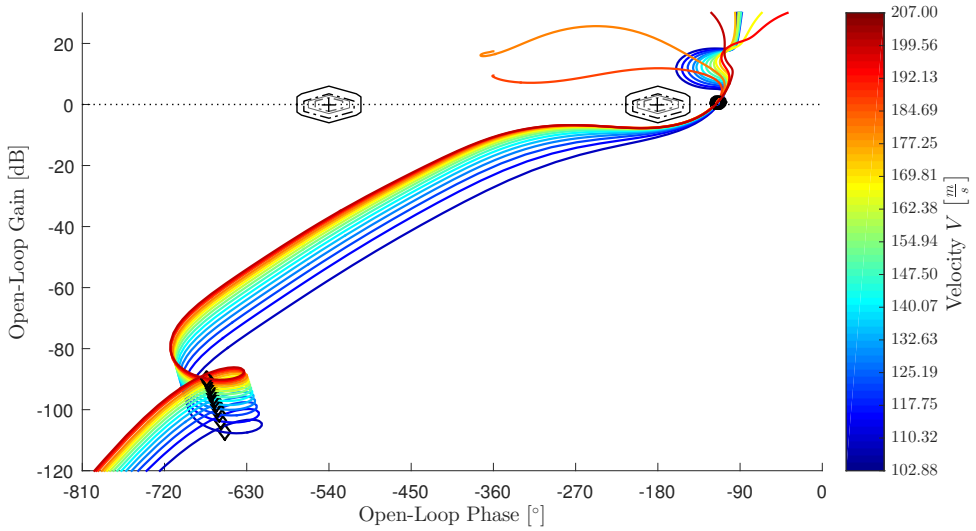

Figure 5.15. – Nichols plot for robust stability assessment of baseline controller at envelope points according to Table 2.2 generated for α loop cut (enhanced aircraft model)

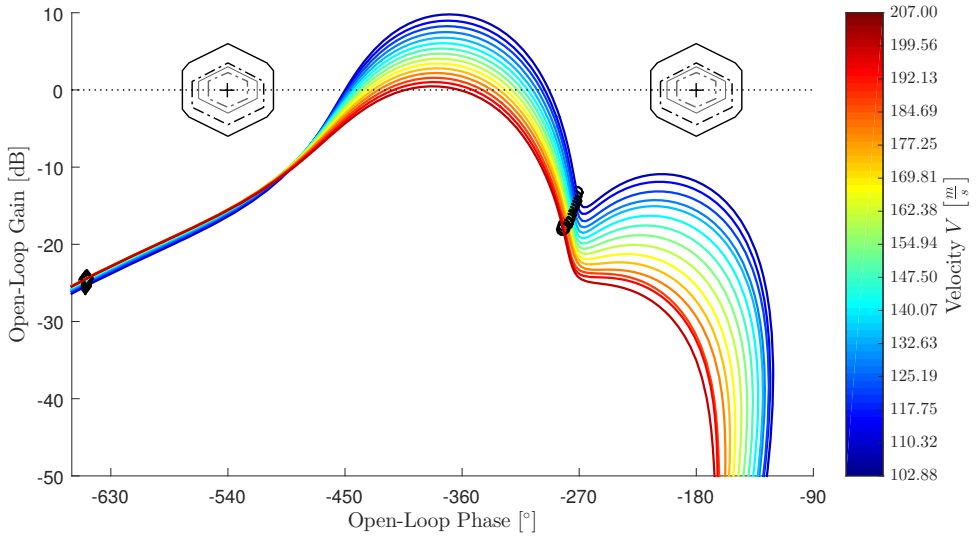

Figure 5.16. – Nichols plot for robust stability assessment of baseline controller at envelope points according to Table 2.2 generated for q loop cut (basic aircraft model)

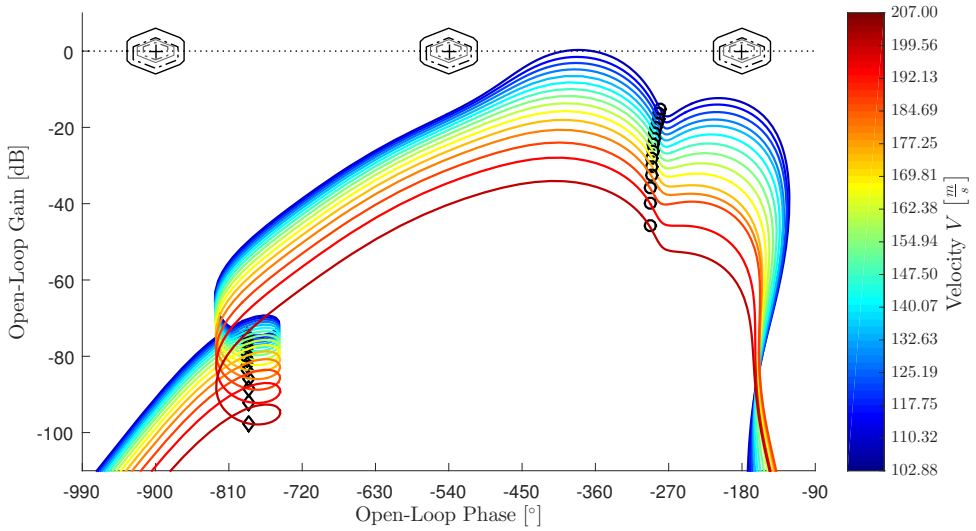

Figure 5.17. – Nichols plot for robust stability assessment of baseline controller at envelope points according to Table 2.2 generated for q loop cut (enhanced aircraft model)

5.2.1.2. Performance

In the next step, the performance of the DPI baseline controller is investigated by means of step responses and the simulation of an exemplary maneuver.
The first step response is shown in Fig. 5.18 for all envelope points according to Table 2.2, where the controller is simulated in combination with the basic aircraft model. In this case, the flight dynamics within the basic aircraft model are described by the linear short-period approximation, which can be found in Eq. (4.23). Although, delay and actuator dynamics are still included. The response shows good performance and precise tracking of the commanded angle of attack α_{cmd}. One can also observe that the control effectiveness changes rapidly between the envelope points corresponding to $V_{0,12} = 184.69\frac{m}{s}$ and $V_{0,13} = 192.13\frac{m}{s}$, which results in a difference of demanded elevator deflection η_{cmd} of more than 1°. The reason for this was already discussed in Section 4.1.1.
In addition to that, Fig. 5.19 shows a long-term response of the closed-loop, where the short-period approximation is replaced by the linear "4x4" aircraft model, which can be found in Eq. (2.42). Again, delay and actuator dynamics are included as well. It can be seen that the phugoid slightly disturbs the control task, nevertheless tracking of the commanded angle of attack α_{cmd} is still achieved considering large time scale. The same system response for short time scale is shown in Fig. A.73, which is included in Appendix A.7.2.
Fig. 5.20 shows the step response, where the nonlinear, basic aircraft model is applied. Good tracking performance is achieved for the envelope points up to $V_{0,12} = 184.69\frac{m}{s}$, whereas the nonlinear character of the aircraft model can clearly be observed between

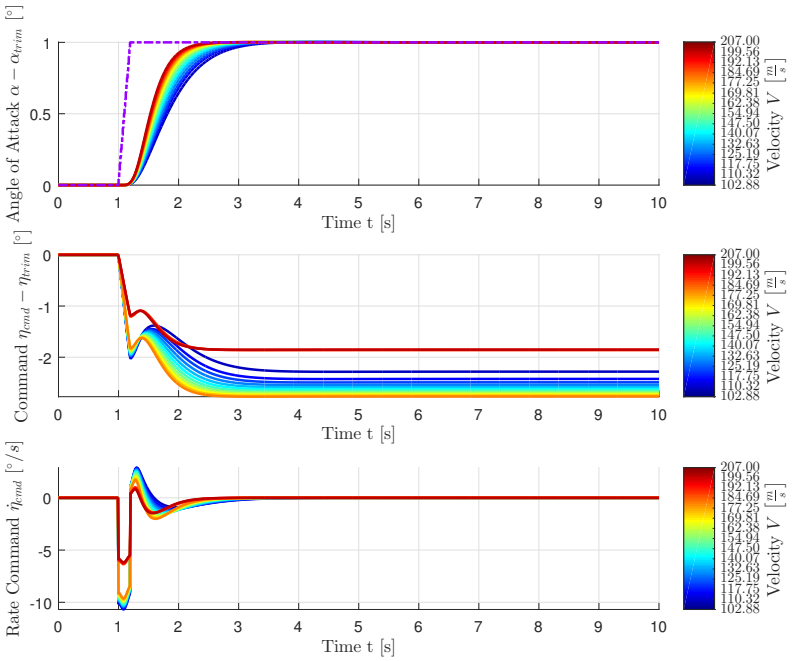

Figure 5.18. – α_{cmd} step responses of basic, linear aircraft model containing only the short-period approximation and baseline controller at envelope points according to Table 2.2

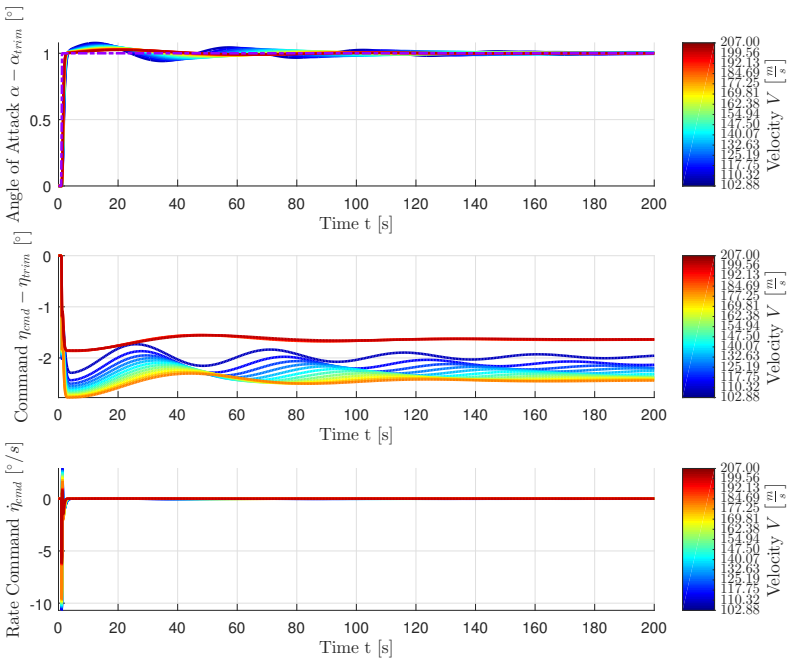

Figure 5.19. – α_{cmd} step responses of basic, linear aircraft model and baseline controller at envelope points according to Table 2.2 for large timescale

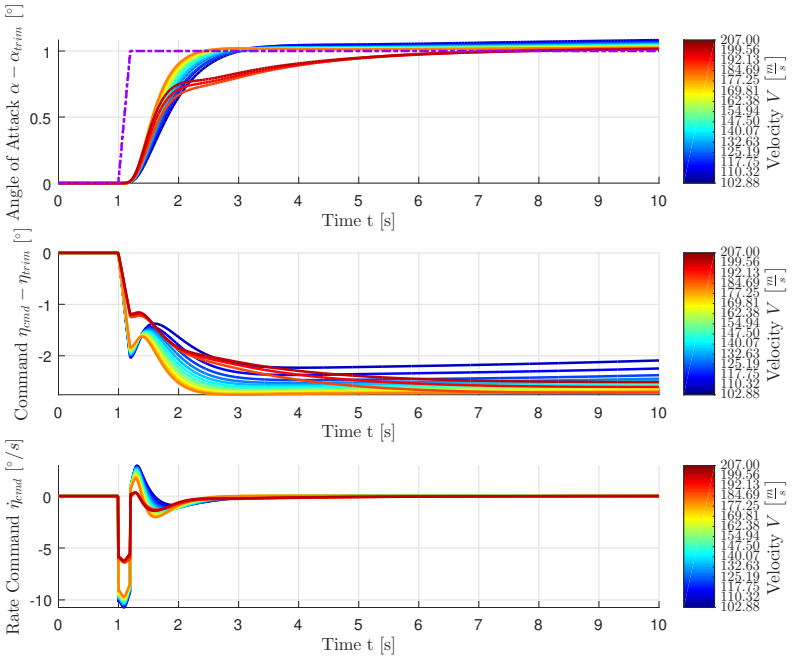

Figure 5.20. – α_{cmd} step responses of basic, nonlinear aircraft model and baseline controller at envelope points according to Table 2.2

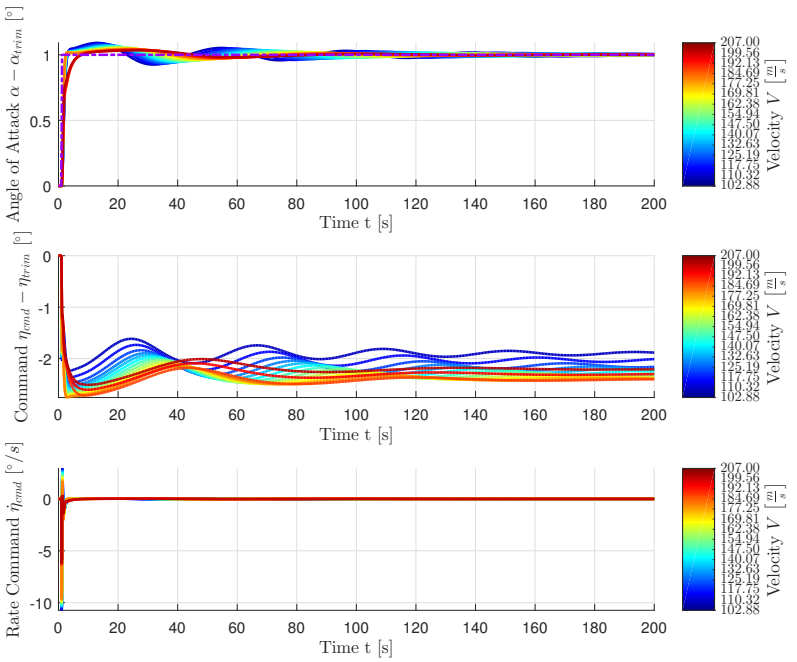

Figure 5.21. – α_{cmd} step responses of basic, nonlinear aircraft model and baseline controller at envelope points according to Table 2.2 for large timescale

the envelope points $V_{0,13} = 192.13\frac{m}{s}$ and $V_{0,15} = 207\frac{m}{s}$. Here, the amplification of the feedforward gain $|h_{DPI}|$ is smaller than required, which stems from the rapid change of control effectiveness in the linear aircraft models starting at $V_{0,13} = 192.13\frac{m}{s}$, which was already shown in the step response Fig. 5.18. This leads to undershoot. The resulting control error is then compensated by the integral portion of the control law. Thus, this issue can also be considered as potential for improvement to be addressed by the adaptive control methods investigated in the remainder of this chapter.
The corresponding step response to Fig. 5.20 for large time scale can be found in Fig. 5.21, where the effect of the phugoid can be observed. Furthermore, the nonlinear step responses of the DPI baseline controller in combination with the enhanced aircraft model configuration can be found in Fig. A.74 and Fig. A.75 in Appendix A.7.2.

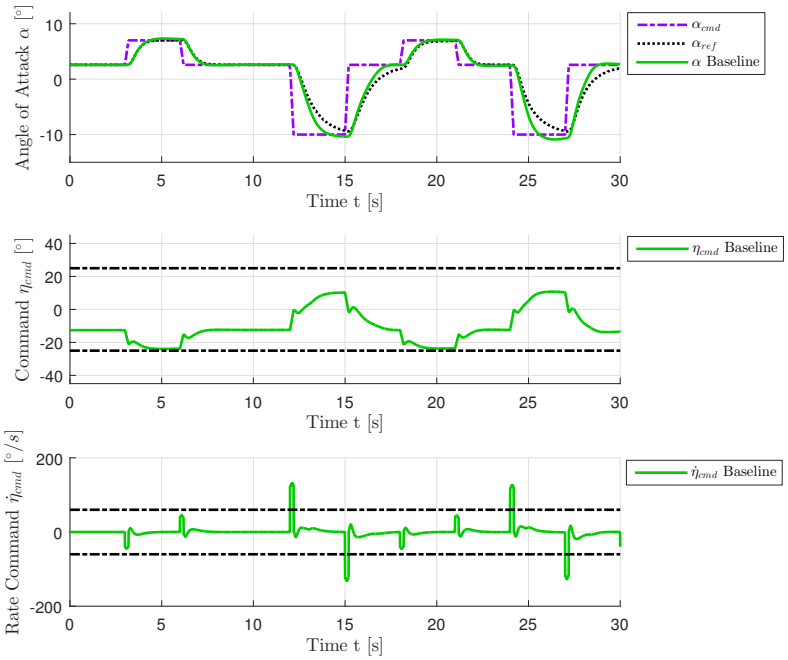

Figure 5.22. – Angle of attack α, elevator command η_{cmd} and elevator command rate $\dot{\eta}_{cmd}$ for example maneuver performed by basic, nonlinear aircraft model with baseline controller starting at $V_0 = 154.94\frac{m}{s}$ and $h_0 = 5000m$

After investigations based on step responses, an exemplary maneuver is assessed in the next step. Starting with the nonlinear, basic aircraft model, Fig. 5.22 contains the resulting angle of attack α, demanded elevator deflection η_{cmd} and rate $\dot{\eta}_{cmd}$, as it was already described in Section 5.1.2. The accompanying diagram Fig. 5.23 contains the corresponding velocity V and altitude h resulting from the maneuver, where a broad range of design envelope points according to Table 2.2 is covered. One can see in Fig. 5.22 that angle of attack α approximately matches the one of the reference model α_{ref}, when $\alpha_{max} = 7°$ is commanded. For the $\alpha_{min} = -10°$ sections, a slight deviation can be observed. This difference stems from the nonlinear character of the

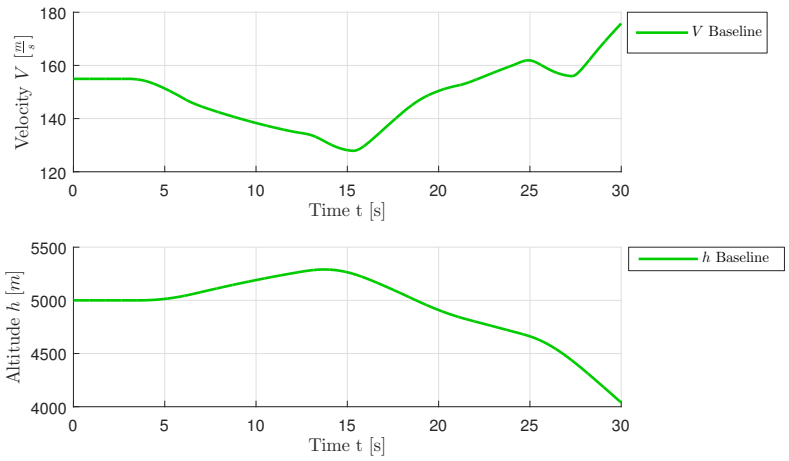

Figure 5.23. – Velocity V and altitude h for example maneuver performed by basic, nonlinear aircraft model with baseline controller starting at $V_0 = 154.94\frac{m}{s}$ and $h_0 = 5000m$

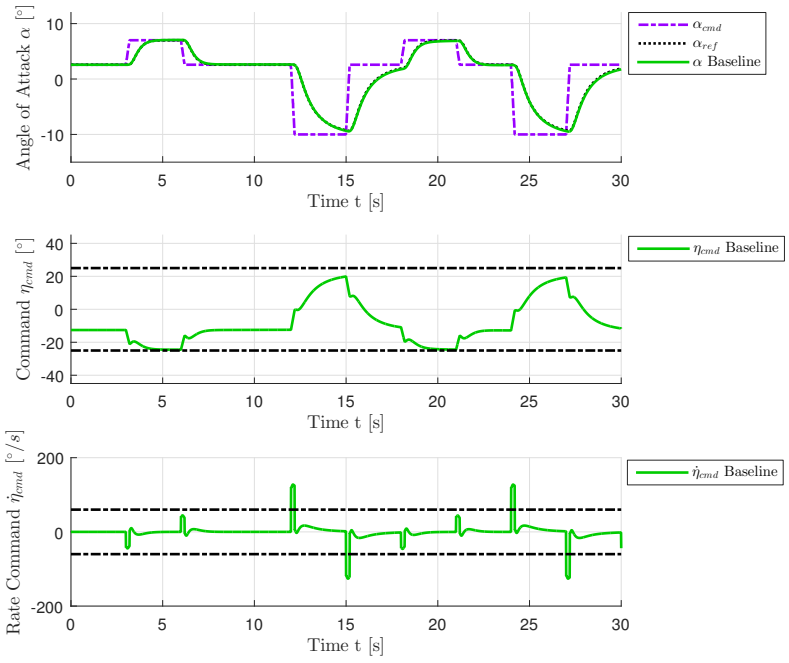

Figure 5.24. – Angle of attack α, elevator command η_{cmd} and elevator command rate $\dot{\eta}_{cmd}$ for example maneuver performed by basic, linear aircraft model with baseline controller starting at $V_0 = 154.94\frac{m}{s}$ and $h_0 = 5000m$

aircraft model, which can be verified by means of the same maneuver performed by the controller in combination with a linear model of the aircraft dynamics according to Eq. (2.42). In this case perfect matching of α and α_{ref} is achieved, which is shown in Fig. 5.24.

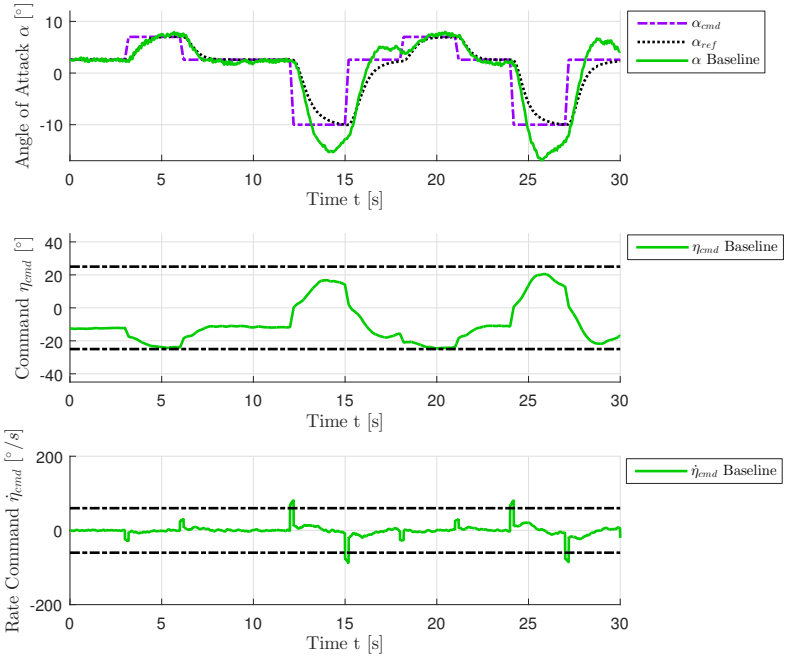

Figure 5.25. – Angle of attack α, elevator command η_{cmd} and elevator command rate $\dot{\eta}_{cmd}$ for example maneuver performed by enhanced, nonlinear aircraft model with baseline controller starting at $V_0 = 154.94\frac{m}{s}$ and $h_0 = 5000m$

The same maneuver is simulated utilizing the enhanced aircraft model, where light turbulence (probability of exceedance 10^{-2}) is applied and the sensor models are configured according to Table 2.6. In addition to turbulence and the more realistic sensor models, also actuator backlash and the simple model of a structural mode are added to the plant dynamics. Moreover, the filter chain, which is discussed in Section 4.1.2, is now included in the controller. The result can be found in Fig. 5.25 for angle of attack α, demanded elevator deflection η_{cmd} and rate $\dot{\eta}_{cmd}$. Fig. 5.26 additionally shows velocity V and altitude h. Again, good matching with the reference model can be detected for the sections, where $\alpha_{max} = 7°$ is commanded. In contrast to that, the nonlinearity appearing for $\alpha_{min} = -10°$ generates large overshoot within the system response. In comparison to the assessments using the basic aircraft model shown in Fig. 5.22 this performance degradation can be explained with the increased delay within the closed-loop induced by the filter chain (c.f. Section 4.1.2).

Furthermore, Fig. 5.27 shows a simulation result, where severe turbulence (probability of exceedance 10^{-5}) is applied. Despite the already discussed overshoot for the

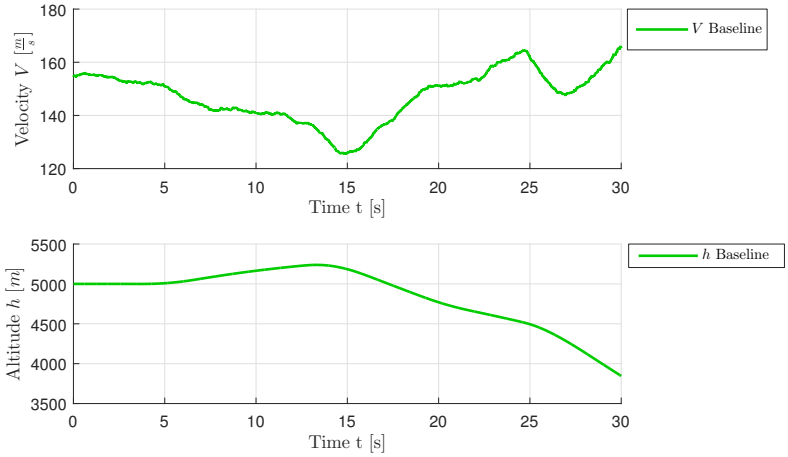

Figure 5.26. – Velocity V and altitude h for example maneuver performed by enhanced, nonlinear aircraft model with baseline controller starting at $V_0 = 154.94\frac{m}{s}$ and $h_0 = 5000m$

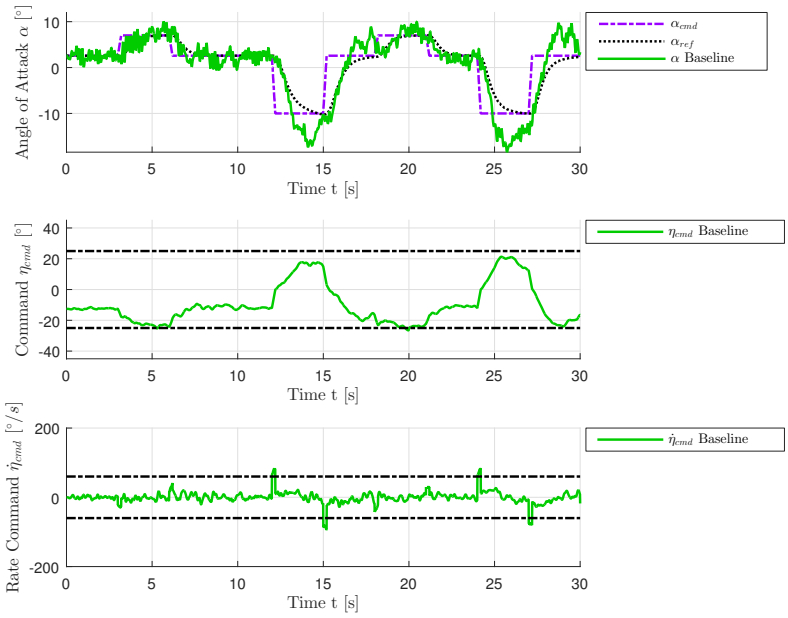

Figure 5.27. – Angle of attack α, elevator command η_{cmd} and elevator command rate $\dot{\eta}_{cmd}$ for example maneuver performed by enhanced, nonlinear aircraft model with baseline controller starting at $V_0 = 154.94\frac{m}{s}$ and $h_0 = 5000m$ considering severe turbulence

$\alpha_{min} = -10°$ sections, the DPI baseline controller achieves good performance also considering heavy turbulence.

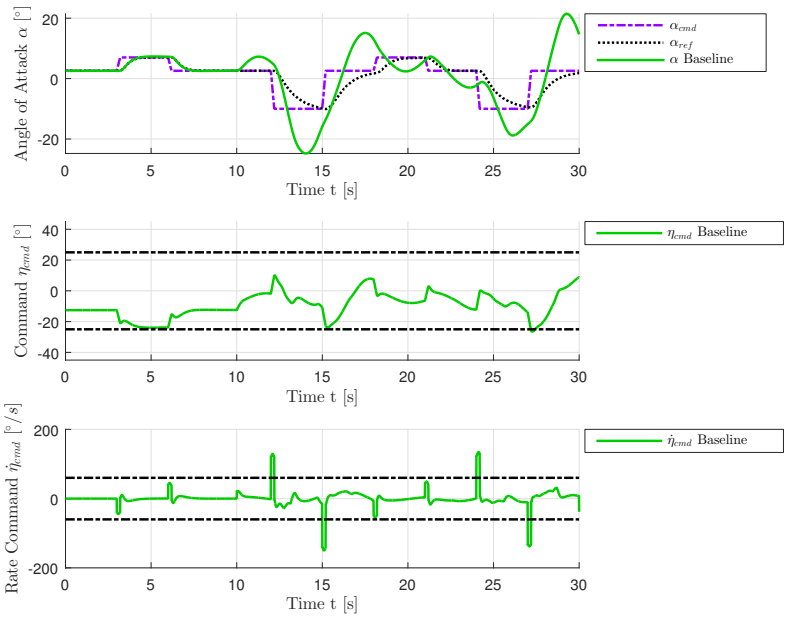

Figure 5.28. – Angle of attack α, elevator command η_{cmd} and elevator command rate $\dot{\eta}_{cmd}$ for example maneuver performed by basic, nonlinear aircraft model with baseline controller starting at $V_0 = 154.94\frac{m}{s}$ and $h_0 = 5000m$ considering CG-shift of 5% at $t = 10s$

At last, the controller performance is assessed considering rapid CG-shifts appearing at $t = 10s$ during the maneuver. The simulation results are compiled in Fig. 5.28 for the basic aircraft model and in Fig. 5.29 for the enhanced aircraft model, where CG-shifts of 5% ($x_{CG_{ref},CG} = 0m$) and 2% ($x_{CG_{ref},CG} = 0.1035m$) are applied, respectively. Note that the nominal CG position is $0.3\bar{c}$ ($x_{CG_{ref},CG} = 0.1725m$), which was also discussed in Section 2.1.1. It can be stated for both cases that the aircraft response exhibits large overshoots and would not have satisfactory handling qualities anymore. Although, one can observe that the oscillations are still stable for the considered CG-shifts. Thus, the exemplary failure case of a rapid CG-shift leaves room for improvement with regard to the controller performance. This issue is also addressed in the following sections, where the adaptive control laws are investigated.

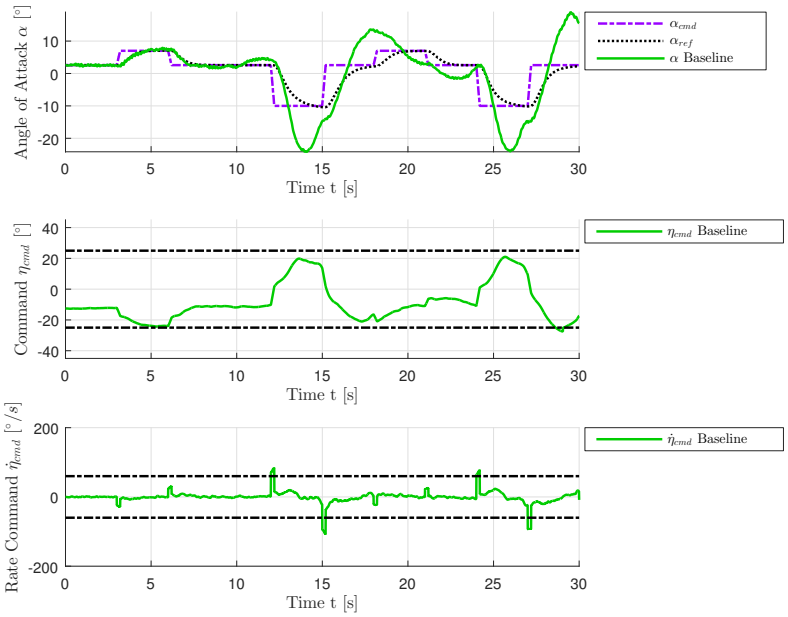

Figure 5.29. – Angle of attack α, elevator command η_{cmd} and elevator command rate $\dot{\eta}_{cmd}$ for example maneuver performed by enhanced, nonlinear aircraft model with baseline controller starting at $V_0 = 154.94\frac{m}{s}$ and $h_0 = 5000m$ considering CG-shift of 2% at $t = 10s$

5.2.2. L1 Adaptive Closed-Loop and Plant Augmentations

This section provides simulation assessments of the L1 Adaptive Augmentations introduced in Section 4.2, which include both DPI Augmentation (Closed-Loop Augmentation) and Plant Augmentation. It is one goal to present the performance benefit gained though an augmentation of the DPI baseline controller, but also to highlight the similarities of the results, which are obtained for both augmentation architectures.

Firstly, the closed-loop poles are analyzed considering an application of the DPI Augmentation approach. The hedging term introduced in Section 4.2.2 is applied here. Again, the linearizations are calculated for the envelope point corresponding to $V_0 = 154.94\frac{m}{s}$ and $h_0 = 5000m$. The expected natural frequency at this envelope point is $\omega_{0,sp,des} = 3.84\frac{rad}{s}$, where the relative damping should be $\zeta_{sp,des} = 0.95$. Table A.5 and Table A.8 summarize the system poles resulting from a combination of basic aircraft model and closed-loop augmented DPI controller, where the former uses the discrete-time and the latter the continuous-time implementation of the controller. For the continuous-time case, the short-period can be detected almost exactly at the desired pole location, whereas for the linearization of the discrete-time implementation the short-period poles are shifted onto the real axis, and thus generate two aperiodic eigenmotions with $\lambda_{SP,1} = -3.49$ and $\lambda_{SP,2} = -6.86$. This deviation can be explained through the fact that Euler's method (c.f. Section 3.3) is applied to transform the

short-period approximation within the state predictor to discrete-time. The application of bilinear transformation would increase accuracy here, but leads to an algebraic loop within the control law, because the resulting state space model contains a direct feedthrough, which is not apparent in its continuous-time representation. This fact was also already mentioned in Section 4.2.2. Note that one other possibility would be to insert a delay of one discrete time step to resolve the algebraic loop. However, that would mean that an additional $10ms$ time delay would have to be added within the controller, which decreases accuracy with regard to closed-loop poles even further.

Moreover, it should be noted that Table A.5 contains a positive pole at $1.2 \cdot 10^{-12}$, which is assumed to be a numerical disturbance of an integrator pole lying in the origin of the complex plane. In order to show that this pole is not relevant in terms of robust stability, i.e. the magnitude of this pole is not growing, when inducing disturbances at the bottleneck cut position, Table A.6 and Table A.7 contain the closed-loop poles for the cases, where destabilizing, artificial gain and delay, which corresponds to phase loss, are induced at η_{cmd}, respectively. It can be stated for both cases that the fast poles (11/12 and 7/8) are moving across the imaginary axis leading to unstable system dynamics. However, the real part of the pole $1.2 \cdot 10^{-12}$ even decreases in both cases.

For the enhanced aircraft model configuration the resulting poles are summarized in Table A.9 for the discrete-time and in Table A.10 for the continuous-time implementation of the L1 Augmented DPI controller. For the continuous-time case, the short-period has a natural frequency of $\omega_{0,sp} = 3.79\frac{rad}{s}$ with a relative damping of $\zeta_{sp} = 0.946$, the discrete-time implementation results in $\omega_{0,sp} = 3.86\frac{rad}{s}$ with a relative damping of $\zeta_{sp} = 0.796$.

In the next step the closed-loop poles are analyzed for the Plant Augmentation approach. Also in this case, hedging as introduced in Section 4.2.3 is activated. Table A.11 and Table A.12 comprise the results gained utilizing the basic aircraft model for the discrete-time and the continuous-time controller implementation, respectively. Again, it can be observed for the discrete-time case that the short-period becomes aperiodic with $\lambda_{SP,1} = -3.82$ and $\lambda_{SP,2} = -6.9$. The continuous-time implementation results in $\omega_{0,sp} = 3.91\frac{rad}{s}$ with a relative damping of $\zeta_{sp} = 0.949$, which points out good matching in comparison to the desired values. It should also be highlighted that the total number of system poles is lower for the Plant Augmentation approach compared to the DPI Augmentation architecture. The reason for this is first, that it is not required to rebuild the baseline controller within the state predictor for the Plant Augmentation approach and second, that the state predictor can be further reduced by means of applied hedging, which is also shown in Section 4.2.3.

At last, the closed-loop poles resulting from a combination of enhanced aircraft model, L1 Plant Augmentation and DPI baseline controller can be found in Table A.13 for the discrete-time and in Table A.14 for the continuous-time implementation of the controller. It can be seen that the short-period has the properties $\omega_{0,sp} = 3.85\frac{rad}{s}$ and

$\zeta_{sp} = 0.794$ for the discrete-time implementation, the continuous-time implementation results in $\omega_{0,sp} = 3.91\frac{rad}{s}$ and $\zeta_{sp} = 0.949$.

5.2.2.1. Linear robust stability

It was stated before that the hedging terms introduced in Section 4.2.2 and Section 4.2.3 have a significant impact on the resulting robustness properties of the closed-loop, where one of the L1 Adaptive Augmentations is applied. Thus, this section concentrates on assessments with regard to the effect of the proposed hedging term, but also provides comparisons between the DPI and Plant Augmentation architectures.
In order to highlight these comparisons, the robust stability assessments are firstly performed considering the exemplary envelope point belonging to $V_0 = 154.94\frac{m}{s}$ and $h_0 = 5000m$. In Fig. 5.30 nichols plots of DPI and Plant Augmentation in combination with baseline controller and basic aircraft model can be found for the bottleneck cut, whereby in each case the plots are generated with and without hedging activated. In addition to that, the nichols plot of the baseline controller at the same envelope point is shown for the purpose of comparison. At first, it can be seen that the curves of DPI and Plant Augmentation are approximately matching for the case with hedging. Although, without hedging slight deviations can be detected for lower frequencies. Furthermore, it can be observed that both augmentation approaches strongly benefit from hedging, because the resulting curves with hedging have a larger distance to the nichols diamond and the critical point compared to the cases without hedging. More precisely, the frequency responses of the adaptive augmentations approximately match the frequency response of the baseline controller for the case, where hedging is activated. This also reflects in the robust stability properties shown in Table 5.4. Both gain and phase margin of the adaptive augmentations decrease drastically in comparison to the baseline controller, where hedging is not applied. With hedging the phase margins are determined in the same range compared to the baseline controller, whereas the gain margins can even be increased. It should also be noted that the TDM significantly decreases without hedging, which is due to a considerable increase of gain crossover frequency $\omega_{gc,TDM}$ from $0.62\frac{rad}{s}$ to $8.16\frac{rad}{s}$.
A similar comparison can be drawn for the case, where the enhanced aircraft model configuration is utilized. The accompanying nichols plot can be found in Fig. 5.31 and it can be seen that also in this case the frequency responses of the adaptive augmentations approximately match the one of the baseline controller, when hedging is used. Although, the robust stability properties in Table 5.5 indicate that the difference generated by the application of hedging is not as large as for the basic aircraft model configuration. In this case, the phase margin without hedging is even higher compared to the baseline controller. As for the basic aircraft model case, TDM drops without hedging, since the gain crossover frequency $\omega_{gc,TDM}$ increases.
The same assessment is carried out again in Fig. 5.32 with the difference that the structural mode according to Section 2.7 is activated in this case. It can be seen that

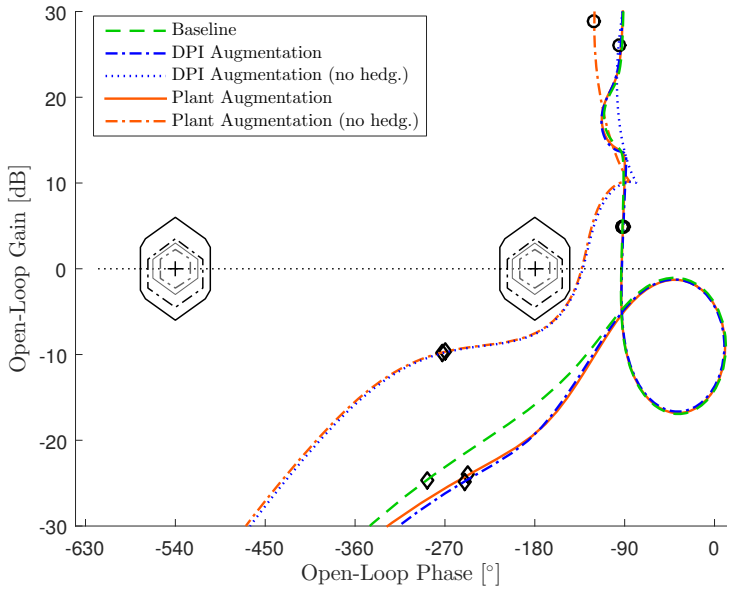

Figure 5.30. – Nichols plot for robust stability comparison of DPI and Plant Augmentation with and without hedging at $V = 154.94\frac{m}{s}$ generated for η_{cmd} (bottleneck) loop cut (basic aircraft model)

Table 5.4. – Robust stability properties gain margin (GM), phase margin Φ_m, time delay margins (TDM) and corresponding gain-crossover frequencies $\omega_{gc,\Phi}$ and $\omega_{gc,TDM}$ for robust stability comparison of DPI and Plant Augmentation with and without hedging at $V = 154.94\frac{m}{s}$ generated for η_{cmd} (bottleneck) loop cut (basic aircraft model)

Controller	**GM** $[dB]$	Φ_m $[°]$	$\omega_{gc,\Phi}$ $\left[\frac{rad}{s}\right]$	**TDM** $[s]$	$\omega_{gc,TDM}$ $\left[\frac{rad}{s}\right]$
Baseline	15.85	86.63	0.62	2.424	0.62
	$-\infty$	-273.37	0.62	-7.650	0.62
DPI Augmentation	19.27	87.23	0.62	2.451	0.62
	$-\infty$	-272.77	0.62	-7.664	0.62
DPI Augmentation (no hedg.)	7.62	48.03	8.16	0.103	8.16
	$-\infty$	-311.97	8.16	-0.667	8.16
Plant Augmentation	19.23	86.95	0.62	2.439	0.62
	$-\infty$	-273.05	0.62	-7.659	0.62
Plant Augmentation (no hedg.)	7.53	46.95	8.24	0.099	8.24
	$-\infty$	-313.05	8.24	-0.663	8.24

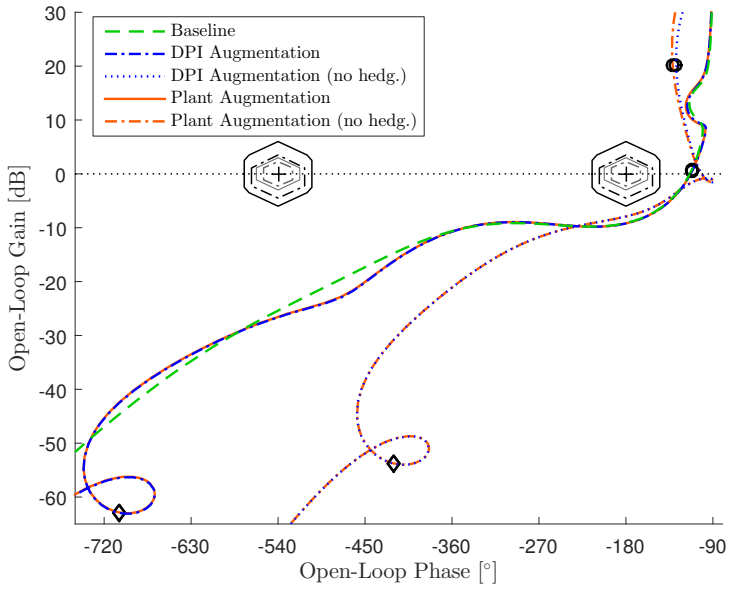

Figure 5.31. – Nichols plot for robust stability comparison of DPI and Plant Augmentation with and without hedging at $V = 154.94\frac{m}{s}$ generated for η_{cmd} (bottleneck) loop cut (enhanced aircraft model)

Table 5.5. – Robust stability properties gain margin (GM), phase margin Φ_m, time delay margins (TDM) and corresponding gain-crossover frequencies $\omega_{gc,\Phi}$ and $\omega_{gc,TDM}$ for robust stability comparison of DPI and Plant Augmentation with and without hedging at $V = 154.94\frac{m}{s}$ generated for η_{cmd} (bottleneck) loop cut (enhanced aircraft model)

Controller	**GM** $[dB]$	Φ_m $[°]$	$\omega_{gc,\Phi}$ $\left[\frac{rad}{s}\right]$	**TDM** $[s]$	$\omega_{gc,TDM}$ $\left[\frac{rad}{s}\right]$
Baseline	9.13	66.12	0.41	2.827	0.41
	$-\infty$	-293.88	0.41	-12.565	0.41
DPI Augmentation	9.21	67.00	0.40	2.896	0.40
	$-\infty$	-293.00	0.40	-12.663	0.40
DPI Augmentation (no hedg.)	7.91	78.66	2.04	0.672	2.04
	$-\infty$	-281.34	2.04	-2.403	2.04
Plant Augmentation	9.20	66.94	0.40	2.893	0.40
	$-\infty$	-293.06	0.40	-12.666	0.40
Plant Augmentation (no hedg.)	7.91	77.97	2.05	0.664	2.05
	$-\infty$	-282.03	2.05	-2.401	2.05

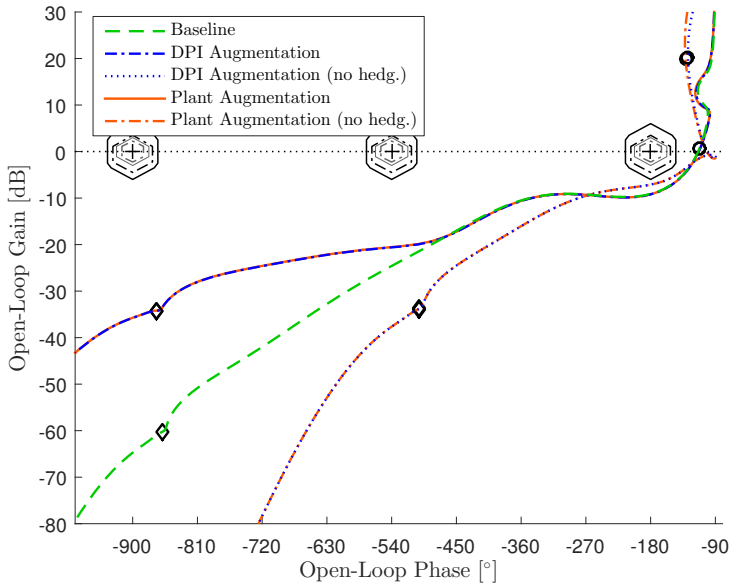

Figure 5.32. – Nichols plot for robust stability comparison of DPI and Plant Augmentation with and without hedging at $V = 154.94\frac{m}{s}$ generated for η_{cmd} (bottleneck) loop cut (enhanced aircraft model, activated structural mode)

the margins for frequencies upwards the first wing bending mode, which is marked by the small diamond, are $\approx 38dB$ without and $\approx 36dB$ with hedging, respectively. That means, the margins are reduced in comparison to the baseline controller configuration, where $\approx 65dB$ can be measured. In any case, the required margin of $8dB$ for flexible modes according to [111, p. 27] is fulfilled.

In order to consider the entire envelope according to Table 2.2, Table 5.6 contains a summary of nichols plots and associated tables containing robust stability properties for all combinations of adaptive augmentations, hedging activation cases and aircraft models. Considering the DPI Augmentation approach, it can be seen in Fig. A.18 and Fig. A.19 included in Appendix A.5.3 for the basic aircraft model that the robustness margins are fulfilled for the entire envelope regardless of the hedging activation case. The same observation can be made for the enhanced aircraft model configuration, as it is shown in Fig. A.43 and Fig. A.44, which can be found in Appendix A.6.3. These statements can be fully analogously applied to the Plant Augmentation, the robustness assessments can also be extracted from Table 5.6.

In addition to the important bottleneck cut, this section also investigates robust stability with regard to the sensor cuts. Starting with angle of attack α, the resulting frequency responses for the adaptive augmentation and the baseline controller can be found in Fig. 5.33 for the basic aircraft model. Tabulated results with regard to margins can be found in Table A.23, which is included in Appendix A.5.1. One can observe that the curves for both augmentations are closer to the critical point, whereby the one belonging to the DPI Augmentation is slightly closer. On the other hand hedging

Table 5.6. – Summary of robust stability assessments of L1 Adaptive Augmentations with regard to the η_{cmd} bottleneck cut for the entire envelope according to Table 2.2

	Basic aircraft model	**Enhanced aircraft model**
DPI Augmentation		
Hedging	Fig. A.18 Table A.27	Fig. A.43 Table A.61
No Hedging	Fig. A.19 Table A.28	Fig. A.44 Table A.62
Plant Augmentation		
Hedging	Fig. A.24 Table A.33	Fig. A.49 Table A.67
No Hedging	Fig. A.25 Table A.34	Fig. A.50 Table A.68

does not have any effect on the frequency response here, the curves are matching for both hedging cases. A similar statement can be made for the enhanced aircraft configuration, where the results are shown in Fig. 5.34 and Table A.57. As for the bottleneck cut, the results covering the entire envelope are summarized in Table 5.7. Note that the nichols diamond is only included for informational purposes here and does not state any requirements with regard to stability margins.
At last the pitch rate q sensor cut is investigated. For both aircraft models the results can be found in Fig. 5.35 and Fig. 5.36, where the tabulated values are to be found in Table A.24 and Table A.58. As it was already shown for the α sensor cut, the frequency responses of the adaptive augmentation are closer to the critical point compared to the baseline controller. Furthermore, both frequency responses form a loop around the critical point, which is not the case for the baseline controller configuration. In case of a loop around the critical point it can be stated that the closed-loop would destabilize, if the concerned sensor fails completely. Thus, the pitch rate sensor would have to be fail-safe for an L1 augmented DPI controller here. Although, in case of an open-loop unstable aircraft configuration, fail-safety of sensor measurements would also be a requirement without any adaptive augmentation. The statements formulated for the robust stability assessments at the pitch rate q cut hold for the entire envelope, the results can be found in Table 5.8.
One can conclude that the L1 Adaptive Augmentations can fulfill the required robust stability margins with regard to the bottleneck cut. Moreover, the robustness properties are, thanks to the proposed hedging term, on the same level as for the baseline controller. This holds for both adaptive augmentation approaches. On the downside, the adaptive augmentations are more demanding with regard to sensor precision, which is directly connected to the gain margin, and fail-safety. Furthermore, the controllers are much more sensitive to unexpected delays within the sensor channels.

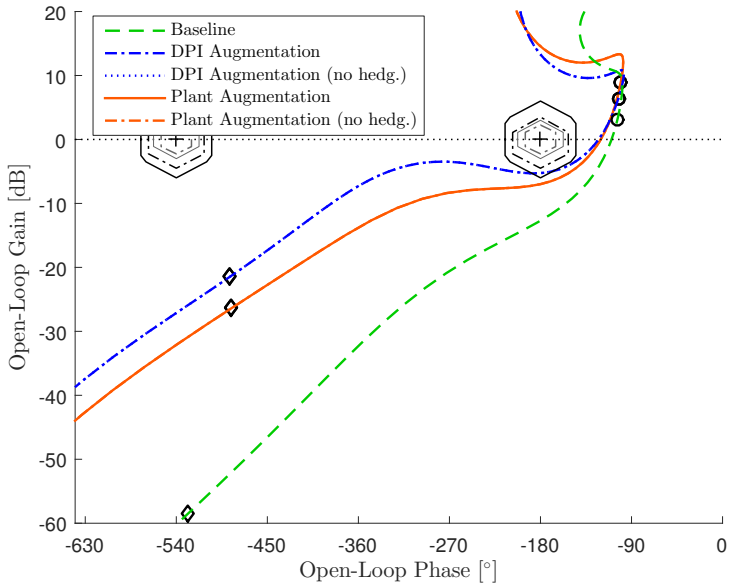

Figure 5.33. – Nichols plot for robust stability comparison of DPI and Plant Augmentation with and without hedging at $V = 154.94\frac{m}{s}$ generated for α loop cut (basic aircraft model)

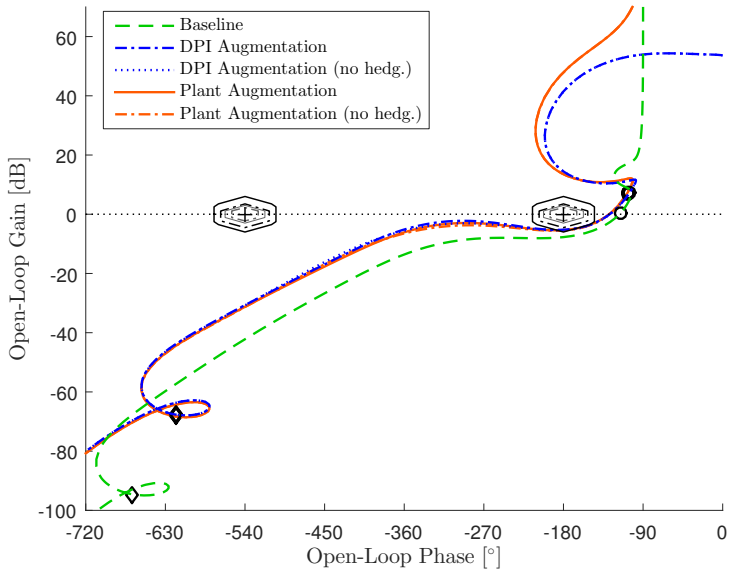

Figure 5.34. – Nichols plot for robust stability comparison of DPI and Plant Augmentation with and without hedging at $V = 154.94\frac{m}{s}$ generated for α loop cut (enhanced aircraft model)

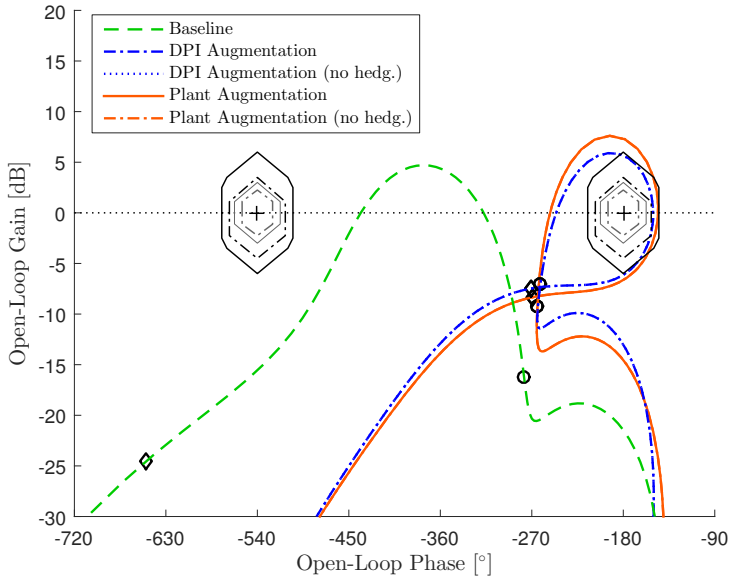

Figure 5.35. – Nichols plot for robust stability comparison of DPI and Plant Augmentation with and without hedging at $V = 154.94 \frac{m}{s}$ generated for q loop cut (basic aircraft model)

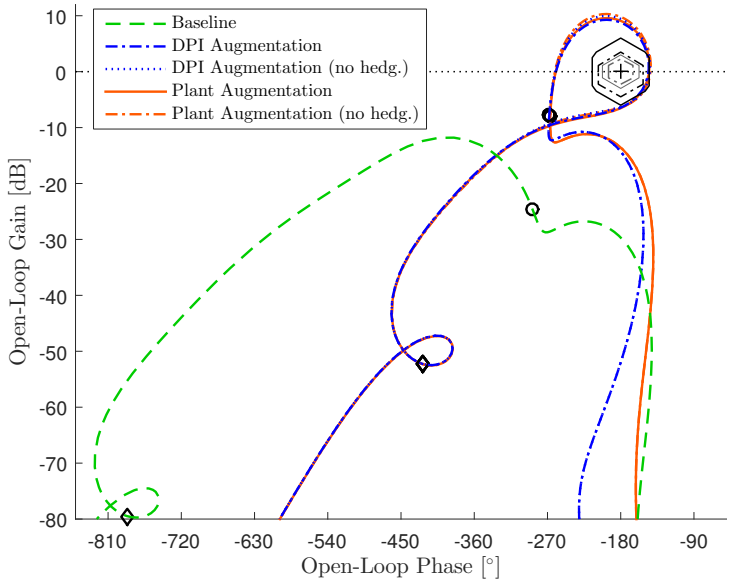

Figure 5.36. – Nichols plot for robust stability comparison of DPI and Plant Augmentation with and without hedging at $V = 154.94 \frac{m}{s}$ generated for q loop cut (enhanced aircraft model)

Table 5.7. – Summary of robust stability assessments of L1 Adaptive Augmentations with regard to the angle of attack α sensor cut for the entire envelope according to Table 2.2

	Basic aircraft model	**Enhanced aircraft model**
DPI Augmentation		
Hedging	Fig. A.20 Table A.29	Fig. A.45 Table A.63
No Hedging	Fig. A.21 Table A.30	Fig. A.46 Table A.64
Plant Augmentation		
Hedging	Fig. A.26 Table A.35	Fig. A.51 Table A.69
No Hedging	Fig. A.27 Table A.36	Fig. A.52 Table A.70

Table 5.8. – Summary of robust stability assessments of L1 Adaptive Augmentations with regard to the pitch rate q sensor cut for the entire envelope according to Table 2.2

	Basic aircraft model	**Enhanced aircraft model**
DPI Augmentation		
Hedging	Fig. A.22 Table A.31	Fig. A.47 Table A.65
No Hedging	Fig. A.23 Table A.32	Fig. A.48 Table A.66
Plant Augmentation		
Hedging	Fig. A.28 Table A.37	Fig. A.53 Table A.71
No Hedging	Fig. A.29 Table A.38	Fig. A.54 Table A.72

5.2.2.2. Simulation based robust stability assessment

The section above presented an assessment of the proposed L1 Adaptive Augmentations, where linearized open-loop transfer functions were utilized to investigate the robust stability properties of the resulting closed-loops. Thus, the analyzes were carried out in the frequency-domain. Robust stability is also the main topic of this section, however, the assessments are based on simulations of the closed-loops (time-domain) containing the nonlinear aircraft model besides baseline controller and adaptive augmentation. This method can also be used to assess nonlinear control laws [136]. To the best knowledge of the author, there is yet no generic way found to calculate robust stability properties of nonlinear, complex systems like TDM or gain margin in a general way, as it can be done for linear representations of the systems (c.f. Section 5.1.1).

In order to determine TDM in the time-domain, artificial time delay is inserted into the closed-loop. For example, if robust stability with regard to the bottleneck should be investigated, the delay is placed upstream the actuator (η_{cmd}). The closed-loop is initialized in a trimmed state and a slight deviation (1%) from the elevator trim deflection η_0 is commanded by means of η_{cmd} during simulation. In the next step, the artificial time delay is increased systematically, until the system response with regard to angle of attack α exhibits undamped oscillations. The determined time delay is then equal to the TDM. This idea is also described in [140]. A drawback of this method is, that it leads to a significant simulation effort, whereas for the frequency-domain assessment only one linearization has to be calculated.

The gain margin can be determined fully analogously by inserting an artificial gain instead of a time delay at the desired position within the closed-loop. The trim state of the closed-loop is then also perturbed and the gain margin can be determined by systematic increase of the artificial gain, until undamped oscillations in the angle of attack response are detected.

The described simulation based assessment is exemplarily applied to the bottleneck (upstream the actuator) for the closed-loop containing basic aircraft model, DPI baseline controller and DPI Augmentation. Here, the envelope point defined by $V_0 = 132.63\frac{m}{s}$ and $h_0 = 5000m$ is considered. Furthermore, both cases with and without the hedging term within the DPI Augmentation are shown. The results can be found in Table 5.9. For the sake of comparison, the results of the corresponding frequency-domain analyzes are included as well. It can be seen that the determined gain margins of both assessments approximately match for the different controller configurations, although the values are slightly more conservative. The same observation can be made with regard to the TDM. In addition to that, also the gain crossover frequency $\omega_{gc,TDM}$ can be determined in the time-domain, because it directly corresponds to the natural frequency of the undamped oscillation, which appears in the angle of attack α system response during the TDM determination. Also for $\omega_{gc,TDM}$ good matching can be observed to the results gained from the frequency-domain assessments. By means of a

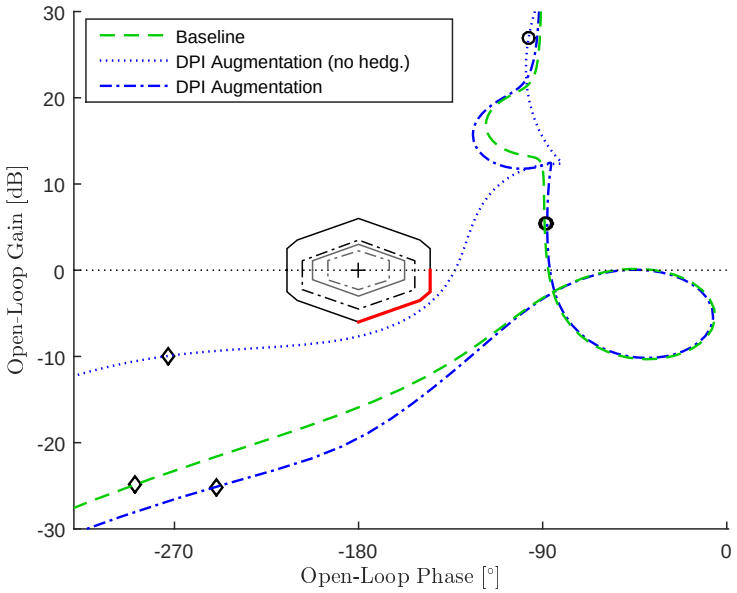

Figure 5.37. – Nichols plot for robust stability assessment of DPI Augmentation with and without hedging at $V = 132.63\frac{m}{s}$ in comparison to baseline controller generated for η_{cmd} (bottleneck) loop cut (basic aircraft model)

Table 5.9. – Robust stability properties gain margin (GM), phase margin Φ_m, time delay margins (TDM) and corresponding gain-crossover frequencies $\omega_{gc,\Phi}$ and $\omega_{gc,TDM}$ determined through linear and nonlinear methods for robust stability comparison of DPI Augmentation with and without hedging and baseline controller at $V = 132.63\frac{m}{s}$ generated for η_{cmd} (bottleneck) loop cut (basic aircraft model)

	GM $[dB]$	Φ_m $[°]$	$\omega_{gc,\Phi}$ $\left[\frac{rad}{s}\right]$	**TDM** $[s]$	$\omega_{gc,TDM}$ $\left[\frac{rad}{s}\right]$
Frequency-domain					
Baseline	15.90 $-\infty$	92.78 -215.31	0.65 3.06	0.628 -1.167	3.50 3.50
DPI Augmentation	19.45 $-\infty$	93.60 -220.09	0.65 3.14	0.672 -1.191	3.37 3.37
DPI Augmentation (no hedg.)	7.67 $-\infty$	47.14 -312.86	7.94 7.94	0.104 -0.688	7.94 7.94
Time-domain					
Baseline	15.02 -	122.1 -	3.49 -	0.61 -	3.49 -
DPI Augmentation	19.62 -	125.56 -	3.37 -	0.65 -	3.37 -
DPI Augmentation (no hedg.)	6.98 -	40.08 -	7.77 -	0.09 -	7.77 -

rearrangement of Eq. (5.5) shown in Section 5.1.1, it is possible to calculate a phase margin using the results from the time-domain simulations:

$$\Phi_m = TDM \cdot \omega_{gc} \tag{5.8}$$

The resulting phase margins Φ_m can also be found in Table 5.9. For the DPI Augmentation without hedging, the phase margin can be determined as $\Phi_m = 40.08^\circ$ by means of Eq. (5.8). Compared to $\Phi_m = 47.14^\circ$ from the frequency-domain assessments, this result corresponds to an estimation error of $\approx 15\%$ and is more conservative. However, for baseline controller and DPI Augmentation with hedging, this estimation indicates a much larger phase margin than expected considering the frequency-domain results. The reason for this that three different gain crossover frequencies ω_{gc} exist for these cases, which can be seen in Fig. 5.37. This is due to a loop within the frequency response, which is also discussed in Section 5.2.2.1. Thus, $\omega_{gc,TDM}$ and $\omega_{gc,\Phi}$ do not match for baseline controller and DPI Augmentation with hedging in the frequency-domain, as it can be seen in Table 5.9. On the other hand, only the phase margin corresponding to the minimum TDM value can be found utilizing time-domain methods. For example, for the baseline controller, the corresponding TDM to the phase margin $\Phi_m = 92.78^\circ$ results in $TDM = 2.49s$ according to Eq. (5.5) and considering $\omega_{gc,\Phi} = 0.65\frac{rad}{s}$, which is much higher than the minimum $TDM = 0.628s$. In a nutshell, it can be stated that it is not guaranteed to detect the minimum phase margin using the discussed time-domain assessment, although it is possible to estimate the minimum TDM.

In the time-domain assessments shown above, either the artificial gain or the artificial delay were varied, in order to determine the robust stability properties of the closed-loop. However, it is also possible to vary both values at the same time. This way, the critical combinations of gain and time delay can be determined. With regard to the implementation, the artificial gain is firstly set to a fixed value and the TDM is determined by means of the method described above. Figuratively speaking this corresponds to a shift of the frequency response upwards in the nichols plot Fig. 5.37 by means of the artificial gain first, then the artificial time delay is steadily increased shifting the frequency response to the left, until it crosses the critical point. The resulting TDMs can be plotted as a function of gain, which generates a curve defining the boundary between stability and instability for the considered closed-loop in the space spanned by time delay and gain.

Such diagrams can be found in Fig. 5.38 and Fig. 5.39 for baseline controller and DPI Augmentation, where both hedging cases are considered. Here, the aircraft is also trimmed according to the envelope point defined by $V_0 = 132.63\frac{m}{s}$ and $h_0 = 5000m$. Again, it can be seen that the resulting curves for baseline controller and DPI controller with hedging are approximately matching, which confirms the results of the nichols plots shown in Fig. 5.37. With regard to the corner points, the determined TDMs match

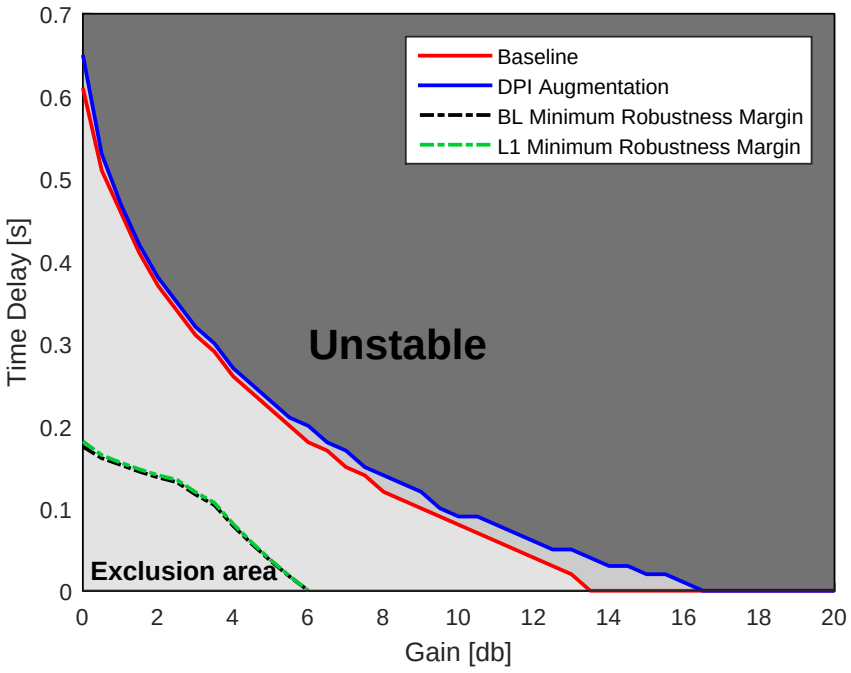

Figure 5.38. – Plot of TDM over gain for nonlinear robust stability comparison of DPI Augmentation with hedging and baseline controller at $V = 132.63\frac{m}{s}$ generated for η_{cmd} (bottleneck) loop cut (basic aircraft model)

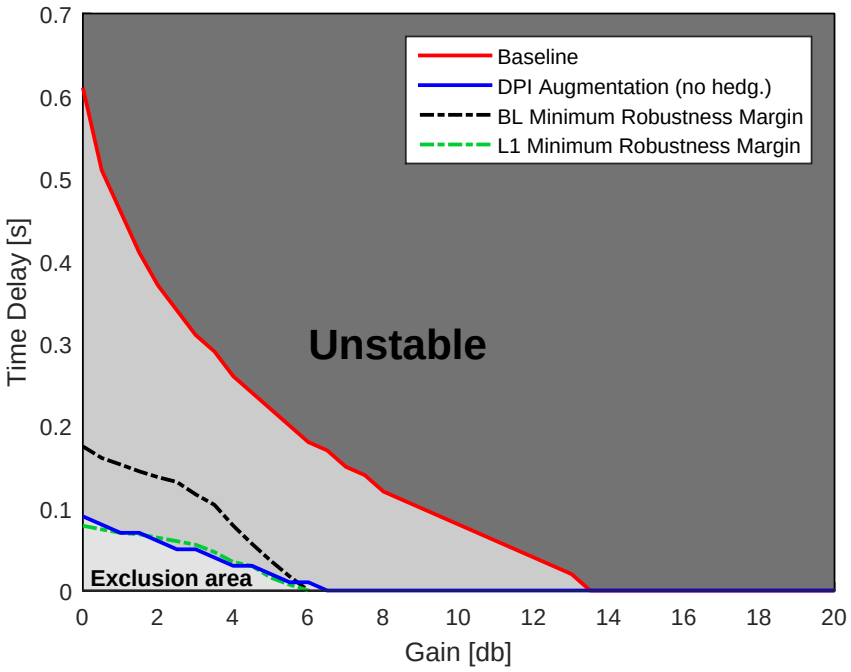

Figure 5.39. – Plot of TDM over gain for nonlinear robust stability comparison of DPI Augmentation without hedging and baseline controller at $V = 132.63\frac{m}{s}$ generated for η_{cmd} (bottleneck) loop cut (basic aircraft model)

the ones shown in Table 5.9, however the resulting gain margin is more conservative in the diagrams.
Another advantage of the proposed visualization is that combined, minimum robustness margins can be directly taken into account. These minimum robustness margins mark an exclusion area, which should not be crossed by the resulting curves. In that matter this exclusion area is then very similar to a nichols diamond. Thus, the bottom right quarter of the outermost nichols diamond, which is marked in red in Fig. 5.37, is projected into the diagram utilizing Eq. (5.5) for this purpose. For this calculation the gain crossover frequency ω_{gc} is used, which is detected during the determination of the TDM for a specific value of the artificial gain. Thus, for every controller results a specific contour of the exclusion area border. In particular, this can be observed for the DPI Augmentation without hedging, where the gain crossover frequencies ω_{gc} are higher compared to the baseline controller, which can also be seen in Table 5.9. Thus, significantly smaller TDMs result for the border of the exclusion area. It can also be observed that DPI Augmentation without hedging violates the robustness requirements in Fig. 5.39, which underlines the conservative calculations underlying the proposed diagrams.

5.2.2.3. Performance

After analyzing the L1 Adaptive Augmentations with regard to robust stability, they are assessed in terms of performance in this section. As it was done for the baseline controller, step responses are investigated firstly, which are followed by evaluations of an exemplary maneuver case.
Fig. 5.40 shows step responses for all envelope points according to Table 2.2 considering the closed-loop containing basic aircraft model, DPI baseline controller and adaptive DPI Augmentation. Here, the flight dynamics within the basic aircraft model are replaced by the linear short-period approximation, which can be found in Eq. (4.23). The system response shows good tracking of the commanded angle of attack α_{cmd} and no degradation in comparison to the baseline controller step response, as it is depicted in Fig. 5.18.
Furthermore, the step response to be found in Fig. 5.41 features the linear "4x4" aircraft model instead of the short-period approximation, as it is shown in Eq. (2.42). The phugoid motion can clearly be observed in the system response, although it slowly decays considering a large time scale. The diagram considering a shorter time scale can be found in Fig. A.76, which is included in Appendix A.7.3.
The linear aircraft dynamics model is replaced by the nonlinear dynamics model for the step responses shown in Fig. 5.42 for short time scale and in Fig. 5.43 for long time scale, respectively. One can clearly see in Fig. 5.42 that the adaptive augmentation manages to "repair" the system responses for the high velocity envelope points $V_{0,13} = 192.13\frac{m}{s}$ up to $V_{0,15} = 207\frac{m}{s}$, which were an issue during the performance assessment of the baseline controller (c.f. Fig. 5.20). The same observation can be made for the enhanced

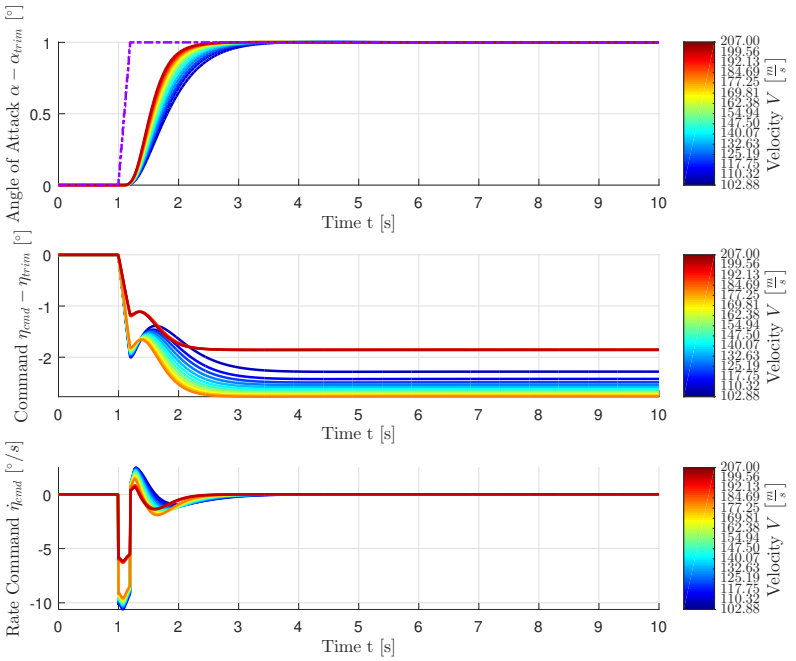

Figure 5.40. – α_{cmd} step responses of basic, linear aircraft model containing only the short-period approximation and DPI Augmentation at envelope points according to Table 2.2

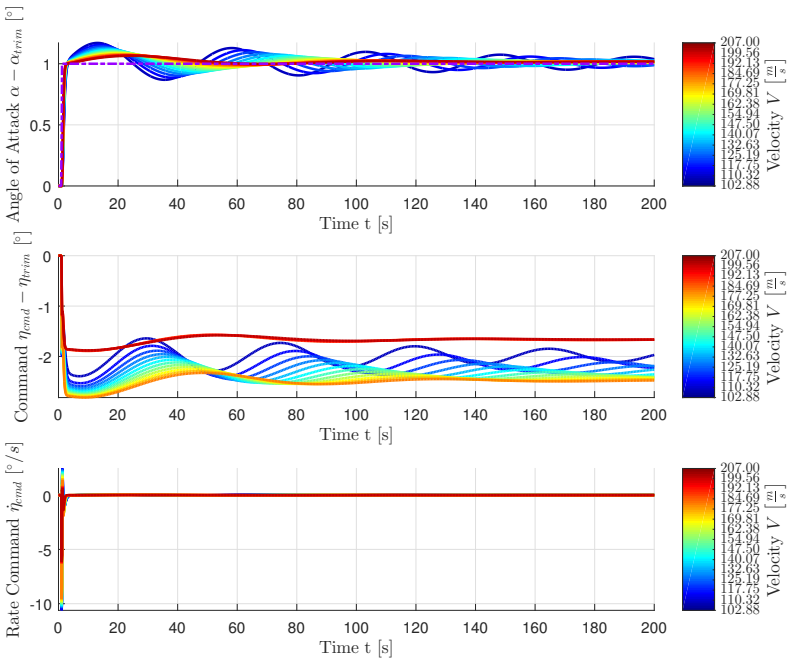

Figure 5.41. – α_{cmd} step responses of basic, linear aircraft model and DPI Augmentation at envelope points according to Table 2.2 for large timescale

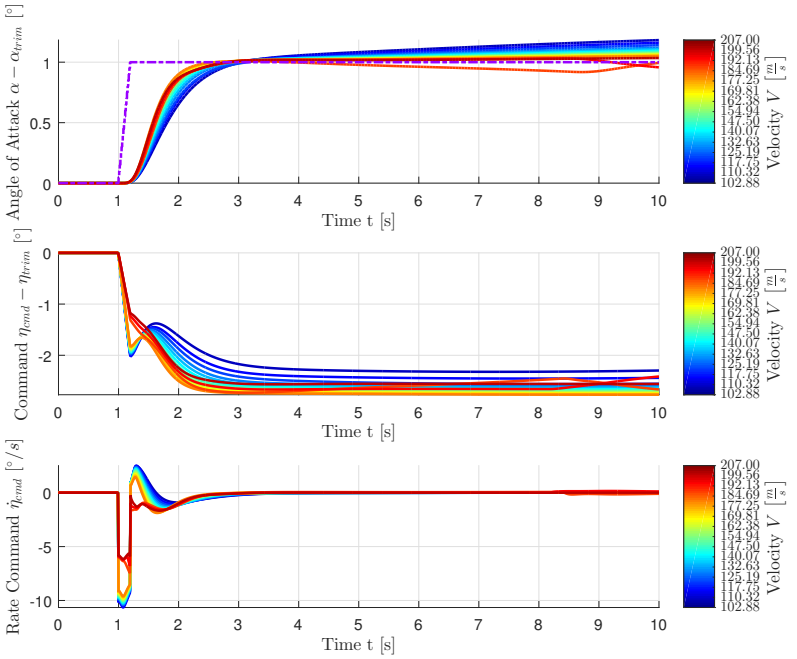

Figure 5.42. – α_{cmd} step responses of basic, nonlinear aircraft model and DPI Augmentation at envelope points according to Table 2.2

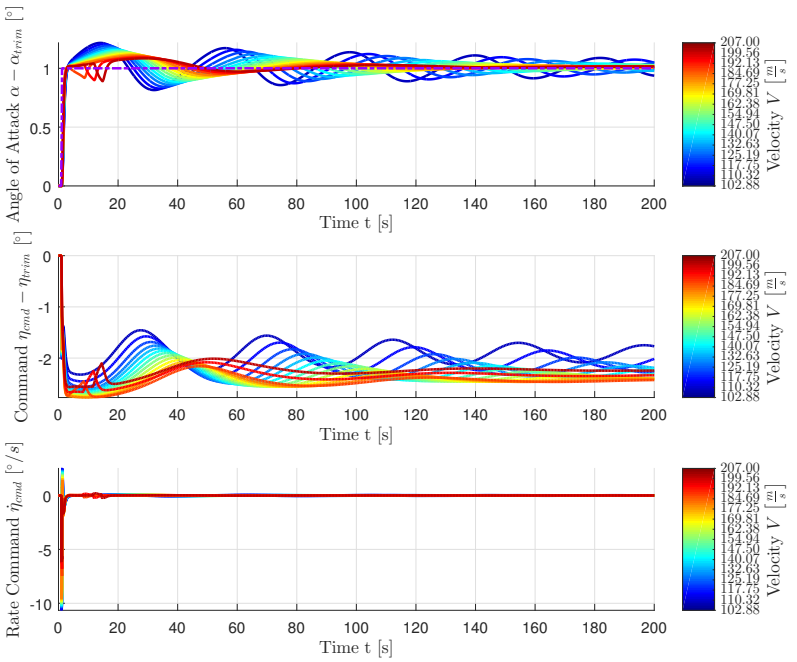

Figure 5.43. – α_{cmd} step responses of basic, nonlinear aircraft model and DPI Augmentation at envelope points according to Table 2.2 for large timescale

aircraft configuration, whose step response in combination with baseline controller and DPI Augmentation can be found in Fig. A.77 and Fig. A.78.
Moreover, the corresponding step responses for the Plant Augmentation can be found in Fig. A.80, Fig. A.81, Fig. A.82, Fig. A.83, Fig. A.84, Fig. A.85 and Fig. A.86, which are included in Appendix A.7.4. As they are very similar to the results gained for the DPI Augmentation, basically the same statements as shown above can also be made here.

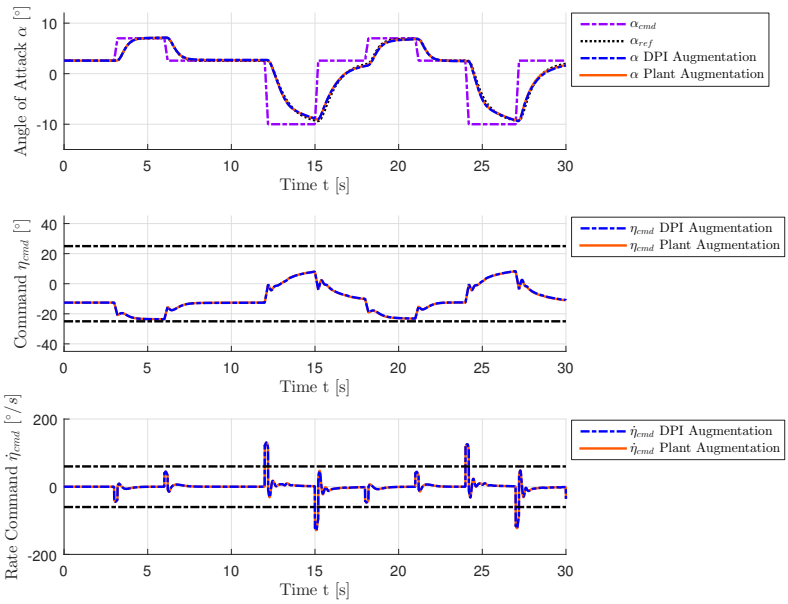

Figure 5.44. – Angle of attack α, elevator command η_{cmd} and elevator command rate $\dot{\eta}_{cmd}$ for example maneuver performed by basic, nonlinear aircraft model in combination with DPI and Plant Augmentation starting at $V_0 = 154.94\frac{m}{s}$ and $h_0 = 5000m$

The performance benefits contributed by the adaptive augmentations of the DPI baseline controller can also be identified considering the exemplary maneuver Fig. 5.44. One can notice that the resulting angle of attack α responses almost perfectly match the reference model α_{cmd}. This is also the case for the $\alpha_{min} = -10°$ sections, where the baseline controller exhibits deviations in the transient (c.f. Fig. 5.22). Thus, the adaptive part of the controller takes action in this sections. This is also reflected in the values of the estimation parameters $\hat{\sigma}$ of the L1 adaptive controller, which are depicted in Fig. 5.45. The uncertainties within the aircraft dynamics during the $\alpha_{min} = -10°$ sections can mostly be compensated by means of the matched parameter estimations $\hat{\sigma}_m$, which reach values up to 0.2. Here, the matched estimation parameters show a slight difference comparing the two different augmentation approaches, whereas the unmatched estimation parameters are matching for both cases. Note also that $\hat{\sigma}_{um,2}$ belonging to the DPI Augmentation remains near zero, because this parameter is mainly driven by uncertainties within the dynamics of the integral state of the baseline

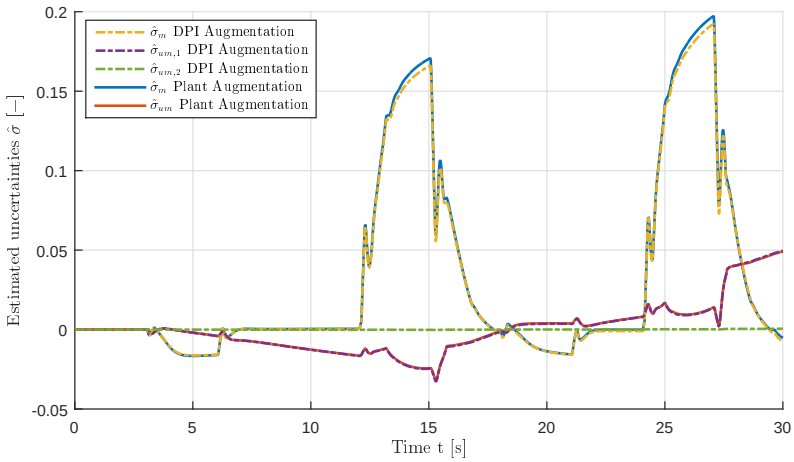

Figure 5.45. – Estimated parameters $\hat{\sigma}$ for example maneuver performed by basic, nonlinear aircraft model in combination with DPI and Plant Augmentation starting at $V_0 = 154.94\frac{m}{s}$ and $h_0 = 5000m$

controller. One can discern this relationship from the parameter update law Eq. (4.42) of the DPI Augmentation, where $\boldsymbol{K_{L1}}(T_s)$ is exemplarily solved for the envelope point belonging to $V_0 = 154.94\frac{m}{s}$ and $h_0 = 5000m$ considering $T_s = 0.01s$:

$$\begin{pmatrix} \hat{\sigma}_m(t) \\ \hat{\sigma}_{um,1}(t) \\ \hat{\sigma}_{um,2}(t) \end{pmatrix} = \begin{pmatrix} -0.9387 & 19.4031 & 0 \\ 99.3931 & -0.7579 & 0 \\ -0.4988 & -0.0001 & -99.95 \end{pmatrix} \begin{pmatrix} \tilde{\alpha}(iT_s) \\ \tilde{q}(iT_s) \\ \tilde{e}_I(iT_s) \end{pmatrix} \quad \forall t \in [iT_s, (i+1)T_s] \quad (5.9)$$

Here, the estimation errors are denoted as $\tilde{\alpha}$, $\tilde{q}$ and $\tilde{e}_I$ belonging to angle of attack, pitch rate and integrator state, respectively. However, there exists no uncertainty between the real baseline controller and its model within the state predictor by design, i.e. $\tilde{e}_I(iT_s) = 0$, which leads to very small $\hat{\sigma}_{um,2}$.
Utilizing the enhanced aircraft model, the performance of the adaptive augmentations is investigated considering more realistic conditions. The system responses for both augmentations can be found in Fig. 5.46 for the exemplary maneuver. In comparison to the baseline controller response in Fig. 5.25 it can be observed that the overshoots appearing in the $\alpha_{min} = -10°$ sections can be compensated by means of the L1 Adaptive Augmentations. In essence, the system responses exhibit good matching with the reference model α_{cmd} response, despite application of the reality effects. However, it can also be seen that the disturbance stemming from light turbulence (probability of exceedance 10^{-2}) is amplified to a higher degree by the control law compared to the baseline controller response in Fig. 5.25. In particular, this is obvious considering the commanded elevator rate $\dot{\eta}_{cmd}$. The effect of turbulence is also clearly visible in the values of the estimation parameters in Fig. 5.47. This can be explained by again considering the parameter update law of the DPI Augmentation shown in Eq. (5.9).

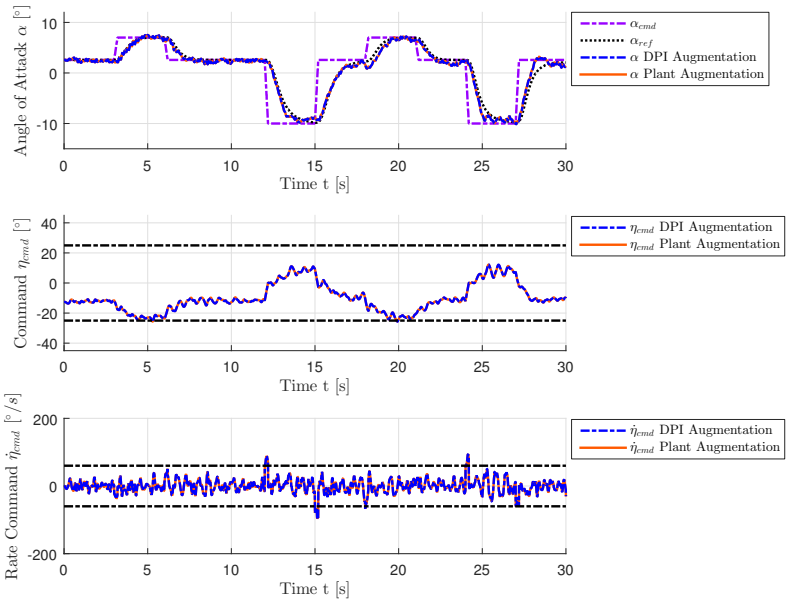

Figure 5.46. – Angle of attack α, elevator command η_{cmd} and elevator command rate $\dot{\eta}_{cmd}$ for example maneuver performed by enhanced, nonlinear aircraft model in combination with DPI and Plant Augmentation starting at $V_0 = 154.94\frac{m}{s}$ and $h_0 = 5000m$

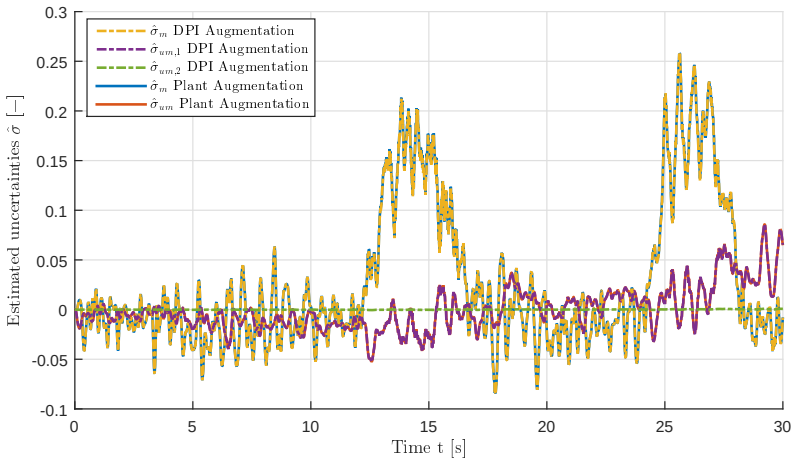

Figure 5.47. – Estimated parameters $\hat{\sigma}$ for example maneuver performed by enhanced, nonlinear aircraft model in combination with DPI and Plant Augmentation starting at $V_0 = 154.94\frac{m}{s}$ and $h_0 = 5000m$

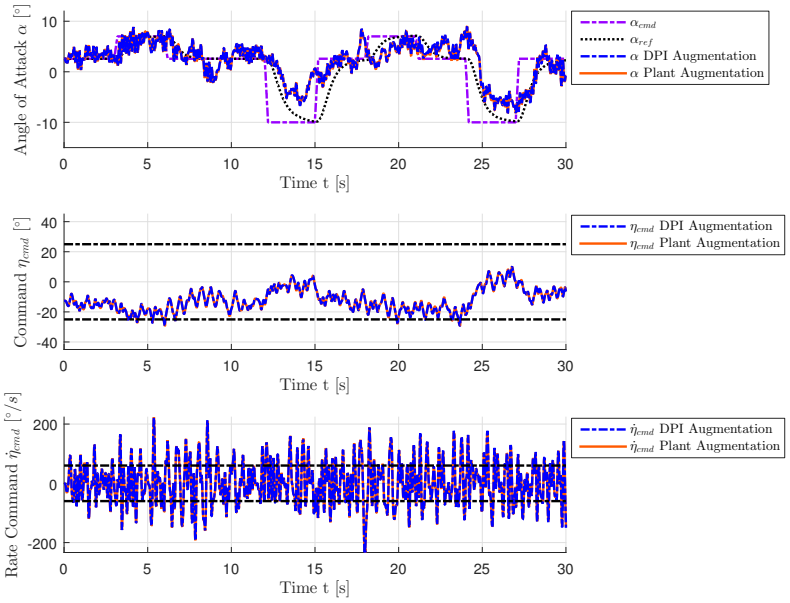

Figure 5.48. – Angle of attack α, elevator command η_{cmd} and elevator command rate $\dot{\eta}_{cmd}$ for example maneuver performed by enhanced, nonlinear aircraft model in combination with DPI and Plant Augmentation starting at $V_0 = 154.94\frac{m}{s}$ and $h_0 = 5000m$ considering severe turbulence

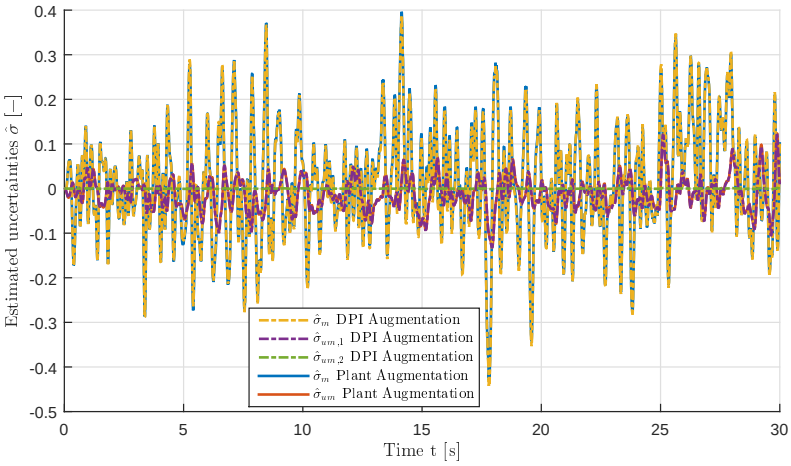

Figure 5.49. – Estimated parameters $\hat{\sigma}$ for example maneuver performed by enhanced, nonlinear aircraft model in combination with DPI and Plant Augmentation starting at $V_0 = 154.94\frac{m}{s}$ and $h_0 = 5000m$ considering severe turbulence

The measurements, which are afflicted by turbulence, enter the parameter update law via the estimation errors $\tilde{\alpha}$ and $\tilde{q}$. These estimation errors are then amplified by a high gain resulting in the parameter estimations $\hat{\sigma}_m(t)$, $\hat{\sigma}_{um,1}(t)$ and $\hat{\sigma}_{um,2}(t)$. In the end, the parameter estimations are directly used to calculate the desired elevator deflection η_{cmd} by means of Eq. (4.45), which is then also affected by amplified content stemming from turbulence. The same observation can be made for the Plant Augmentation. For the sake of completeness, its parameter update law Eq. (4.65) considering the envelope point $V_0 = 154.94\frac{m}{s}$ and $h_0 = 5000m$ can be found in

$$\begin{pmatrix} \hat{\sigma}_m(t) \\ \hat{\sigma}_{um}(t) \end{pmatrix} = \begin{pmatrix} -0.9387 & 19.4031 \\ 99.3931 & -0.7579 \end{pmatrix} \begin{pmatrix} \tilde{\alpha}(iT_s) \\ \tilde{q}(iT_s) \end{pmatrix} \quad \forall t \in [iT_s, (i+1)T_s], \tag{5.10}$$

where $T_s = 0.01s$.
The amplification becomes even more obvious, when severe turbulence (probability of exceedance 10^{-5}) is considered. Fig. 5.48 and Fig. 5.49 show the results for this case. The effect of turbulence on the adaptive controllers is further examined in the course of the controller comparisons in Section 6.2.1 and also in more detail in Section 6.2.17 and Section 6.2.18.
In the next step, rapid CG-shifts are induced at $t = 10s$ during the maneuver. Considering the basic aircraft model with a CG-shift of 5% firstly, the results are depicted in Fig. 5.50. Again, the system responses match for both augmentation architectures. One can observe that the aircraft is quickly brought back into trim position after the induction of the CG-shift and that the controller is still able to track the reference model response α_{cmd} with light overshoots, despite the extensive change of the aircraft dynamics. Fig. 5.53 shows the parameter estimations for this case. The amount of the matched estimations σ_m indicates as expected that the CG-shift mostly causes matched uncertainties, because a CG-shift mainly affects the moments acting on the aircraft. The beneficial effect of the adaptive augmentations is also demonstrated in Fig. 5.52 and Fig. 5.53, where the enhanced aircraft model is utilized considering a 2% CG-shift. At last, the effect of the proposed hedging term on the controller performance is investigated. It can be seen in Fig. 5.54 and Fig. 5.55 that the system responses considering the basic aircraft model are matching for the cases with and without hedging for both augmentation architectures. The same statement can also be made utilizing the enhanced aircraft model. The accompanying results can be found in Fig. A.79 and Fig. A.87., included in Appendix A.7.3 and Appendix A.7.4, respectively.

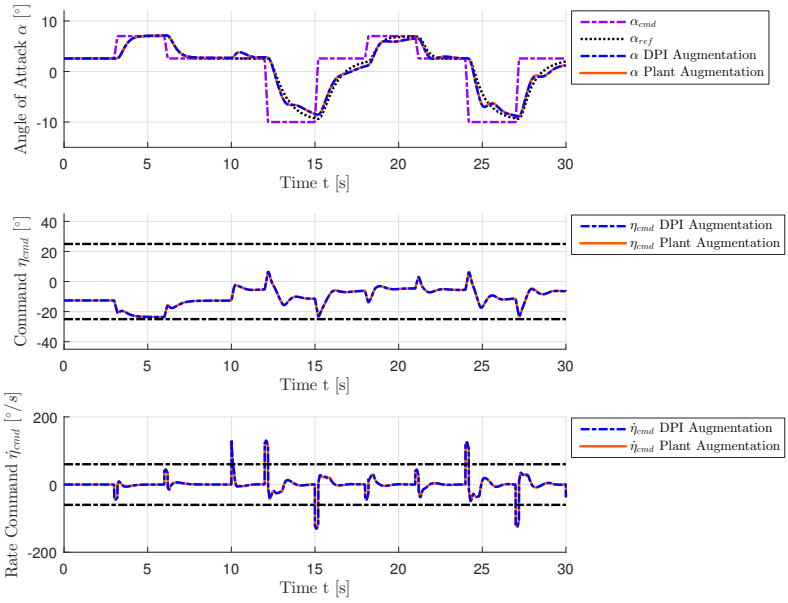

Figure 5.50. – Angle of attack α, elevator command η_{cmd} and elevator command rate $\dot{\eta}_{cmd}$ for example maneuver performed by basic, nonlinear aircraft model in combination with DPI and Plant Augmentation starting at $V_0 = 154.94\frac{m}{s}$ and $h_0 = 5000m$ considering CG-shift of 5% at $t = 10s$

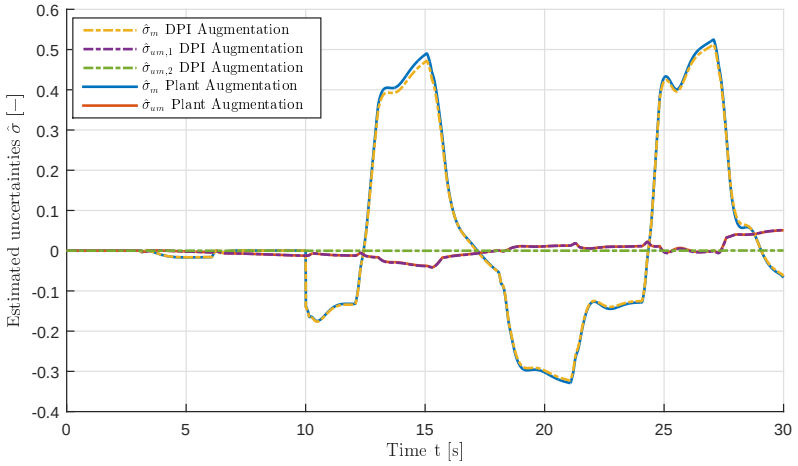

Figure 5.51. – Estimated parameters $\hat{\sigma}$ for example maneuver performed by basic, nonlinear aircraft model in combination with DPI and Plant Augmentation starting at $V_0 = 154.94\frac{m}{s}$ and $h_0 = 5000m$ considering CG-shift of 5% at $t = 10s$

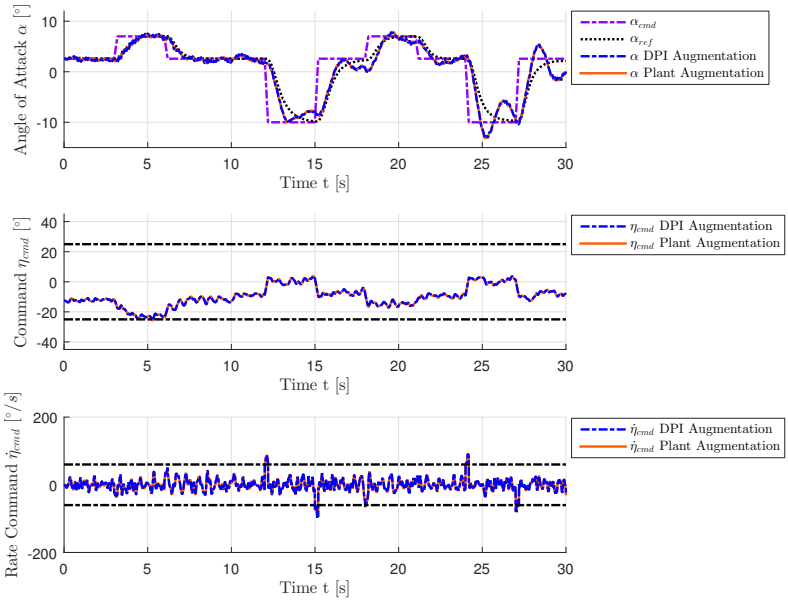

Figure 5.52. – Angle of attack α, elevator command η_{cmd} and elevator command rate $\dot{\eta}_{cmd}$ for example maneuver performed by enhanced, nonlinear aircraft model in combination with DPI and Plant Augmentation starting at $V_0 = 154.94\frac{m}{s}$ and $h_0 = 5000m$ considering CG-shift of 2% at $t = 10s$

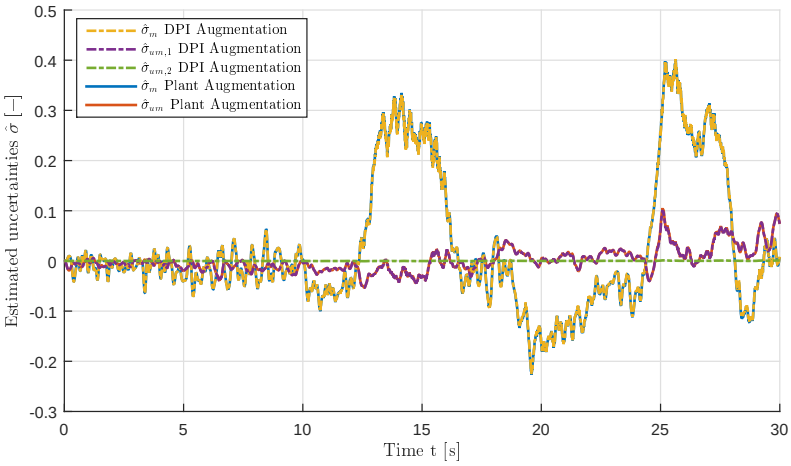

Figure 5.53. – Estimated parameters $\hat{\sigma}$ for example maneuver performed by enhanced, nonlinear aircraft model in combination with DPI and Plant Augmentation starting at $V_0 = 154.94\frac{m}{s}$ and $h_0 = 5000m$ considering CG-shift of 2% at $t = 10s$

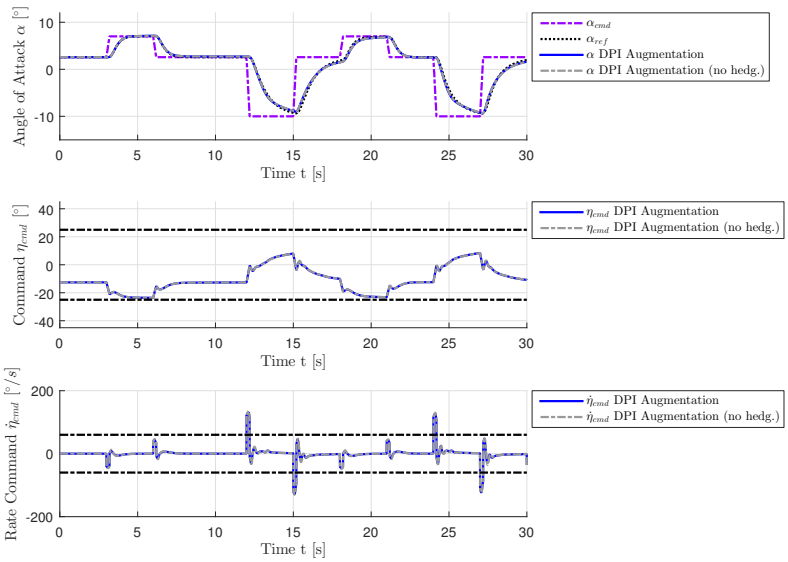

Figure 5.54. – Angle of attack α, elevator command η_{cmd} and elevator command rate $\dot{\eta}_{cmd}$ for example maneuver performed by basic, nonlinear aircraft model with DPI Augmentation with and without hedging applied at $V_0 = 154.94\frac{m}{s}$ and $h_0 = 5000m$

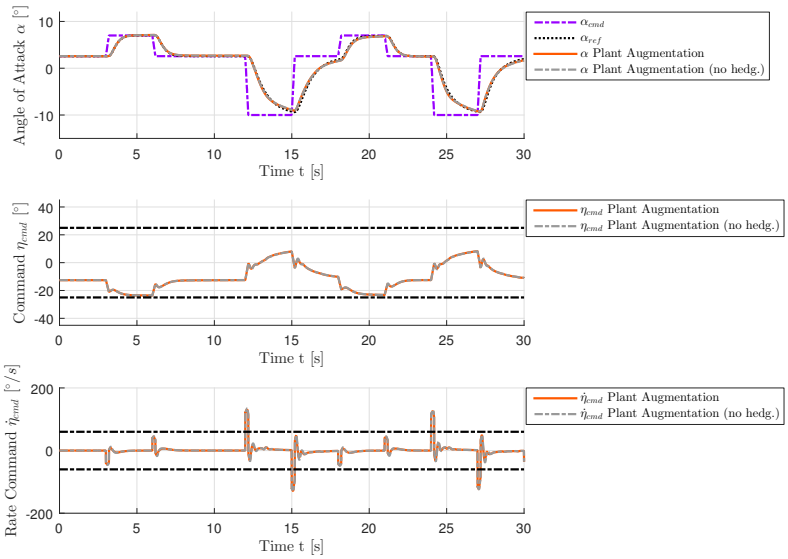

Figure 5.55. – Angle of attack α, elevator command η_{cmd} and elevator command rate $\dot{\eta}_{cmd}$ for example maneuver performed by basic, nonlinear aircraft model with Plant Augmentation with and without hedging applied at $V_0 = 154.94\frac{m}{s}$ and $h_0 = 5000m$

5.2.3. $\Delta\dot{q}$ Compensation Law

After the presentation of the L1 Adaptive Augmentations, this section concentrates on the $\Delta\dot{q}$ Compensation Law, which was introduced by Delannoy et. al. in [23] and was adapted to suit as an augmentation for the DPI baseline controller explained in Section 4.3.
First of all, the poles of the closed-loops consisting of aircraft model, baseline controller and $\Delta\dot{q}$ Compensation Law are discussed. Furthermore, an assessment on robust stability is given in the following section. At last, the performance of the control law is investigated by means of simulations.
As it was also shown for the other control laws, the closed-loop poles are examined considering an exemplary envelope point, which is defined by $V_0 = 154.94\frac{m}{s}$ and $h_0 = 5000m$. The corresponding desired natural frequency for the short-period at this envelope point is specified according to Table 4.1. The short-period should have a natural frequency of $\omega_{0,sp,des} = 3.84\frac{rad}{s}$, while the relative damping should be $\zeta_{sp,des} = 0.95$.
The resulting system poles considering the closed-loop including basic aircraft model, DPI baseline controller and $\Delta\dot{q}$ Compensation Law can be found in Table A.15 for the discrete-time and in Table A.16 for the continuous-time implementation of the controller, respectively. It can be seen that both implementations result in the same closed-loop poles. With regard to the relative damping $\zeta_{sp} = 0.936$ the requirements are approximately met considering poles 5 and 6. For the natural frequency $\omega_{0,sp} = 3.63\frac{rad}{s}$ a slight deviation of $\approx 0.2\frac{rad}{s}$ occurs.
The enhanced aircraft model configuration is taken into account for the system poles shown in Table A.17 for the discrete-time and in Table A.18 for the continuous-time implementation of the controller. In this case, slight deviations from the desired values can be detected considering the short-period poles, which are denoted by 5 and 6. For the continuous-time implementation, the short-period is characterized by $\omega_{0,sp} = 3.13\frac{rad}{s}$ and $\zeta_{sp} = 0.935$ and for the discrete-time implementation natural frequency and relative damping result in $\omega_{0,sp} = 3.14\frac{rad}{s}$ and $\zeta_{sp} = 0.882$.
With respect to the controller configuration it is assumed first that angle of attack α measurement is available, second that the current trim elevator deflection η_0 is known and third that the pitch acceleration $\dot{q}$ has to be estimated using the pitch rate q (c.f. Section 4.3). Although, the robust stability assessments are also performed considering the case, where $\dot{q}$ can be measured for the sake of comparison.

5.2.3.1. Linear robust stability

In this section, the $\Delta\dot{q}$ Compensation Law is investigated with regard to robust stability. The methods presented in Section 5.1.1 are utilized here. Again, the assessments are carried out firstly considering the exemplary envelope point $V_0 = 154.94\frac{m}{s}$ and $h_0 = 5000m$.

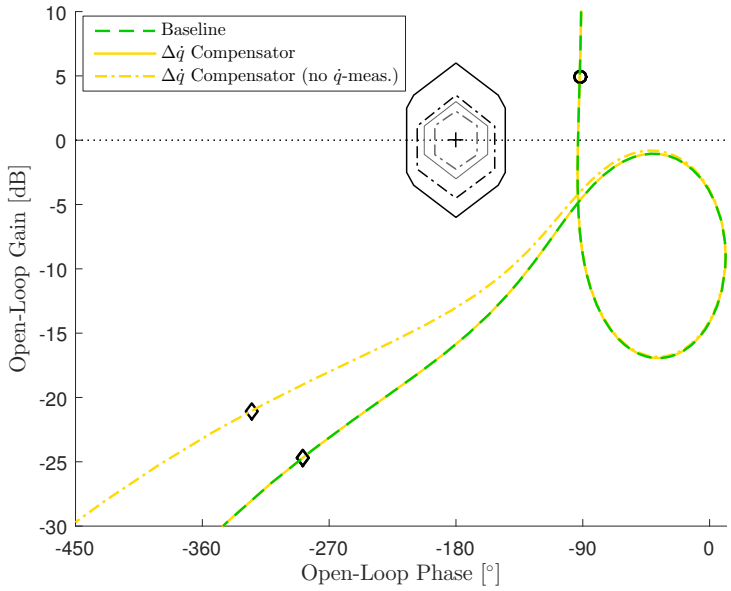

Figure 5.56. – Nichols plot for robust stability comparison of $\Delta\dot{q}$ Compensation Law with and without $\dot{q}$ measurement at $V = 154.94\frac{m}{s}$ generated for η_{cmd} (bottleneck) loop cut (basic aircraft model)

Table 5.10. – Robust stability properties gain margin (GM), phase margin Φ_m, time delay margins (TDM) and corresponding gain-crossover frequencies $\omega_{gc,\Phi}$ and $\omega_{gc,TDM}$ for robust stability comparison of $\Delta\dot{q}$ Compensation Law with and without $\dot{q}$ measurement at $V = 154.94\frac{m}{s}$ generated for η_{cmd} (bottleneck) loop cut (basic aircraft model)

Controller	**GM** $[dB]$	Φ_m $[°]$	$\omega_{gc,\Phi}$ $\left[\frac{rad}{s}\right]$	**TDM** $[s]$	$\omega_{gc,TDM}$ $\left[\frac{rad}{s}\right]$
Baseline	15.85	86.63	0.62	2.424	0.62
	$-\infty$	-273.37	0.62	-7.650	0.62
$\Delta\dot{q}$ Compensator	15.85	86.63	0.62	2.424	0.62
	$-\infty$	-273.37	0.62	-7.650	0.62
$\Delta\dot{q}$ Compensator (no $\dot{q}$-meas.)	13.01	86.64	0.62	2.425	0.62
	$-\infty$	-273.36	0.62	-7.650	0.62

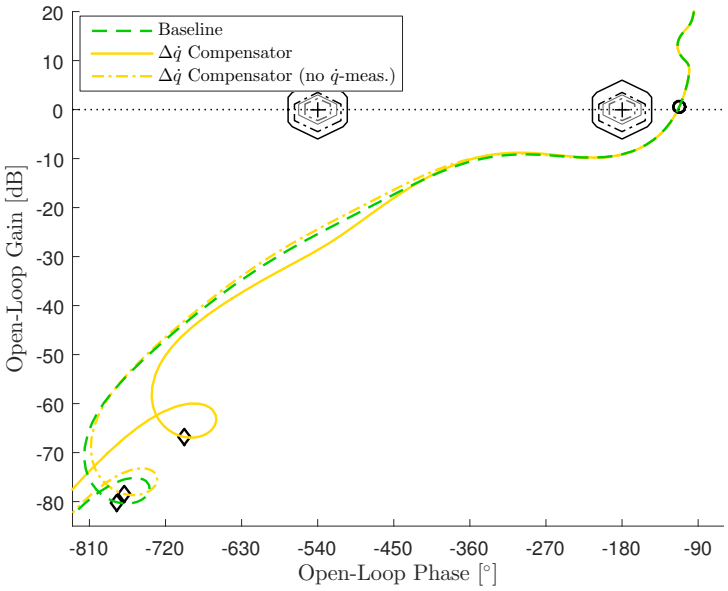

Figure 5.57. – Nichols plot for robust stability comparison of $\Delta\dot{q}$ Compensation Law with and without $\dot{q}$ measurement at $V = 154.94\frac{m}{s}$ generated for η_{cmd} (bottleneck) loop cut (enhanced aircraft model)

Table 5.11. – Robust stability properties gain margin (GM), phase margin Φ_m, time delay margins (TDM) and corresponding gain-crossover frequencies $\omega_{gc,\Phi}$ and $\omega_{gc,TDM}$ for robust stability comparison of $\Delta\dot{q}$ Compensation Law with and without $\dot{q}$ measurement at $V = 154.94\frac{m}{s}$ generated for η_{cmd} (bottleneck) loop cut (enhanced aircraft model)

Controller	**GM** $[dB]$	Φ_m $[°]$	$\omega_{gc,\Phi}$ $\left[\frac{rad}{s}\right]$	**TDM** $[s]$	$\omega_{gc,TDM}$ $\left[\frac{rad}{s}\right]$
Baseline	9.13	66.12	0.41	2.827	0.41
	$-\infty$	-293.88	0.41	-12.565	0.41
$\Delta\dot{q}$ Compensator	9.16	66.13	0.41	2.833	0.41
	$-\infty$	-293.87	0.41	-12.588	0.41
$\Delta\dot{q}$ Compensator (no $\dot{q}$-meas.)	9.20	66.14	0.41	2.833	0.41
	$-\infty$	-293.86	0.41	-12.589	0.41

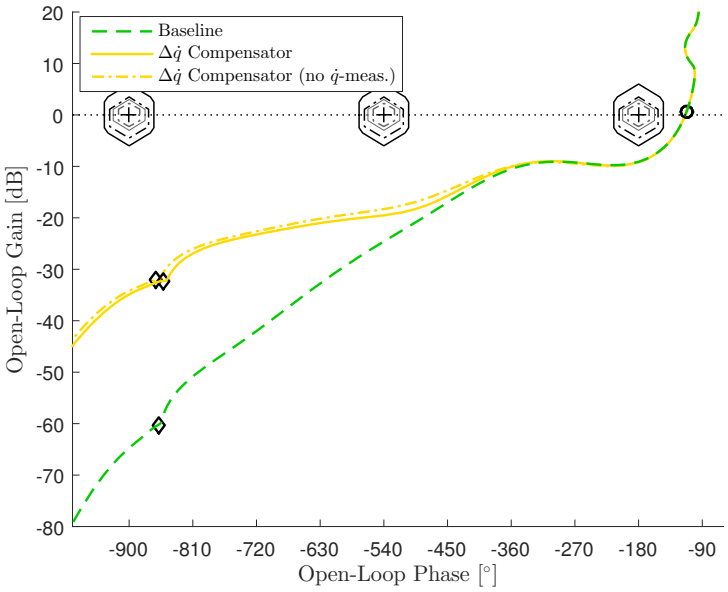

Figure 5.58. – Nichols plot for robust stability comparison of $\Delta\dot{q}$ Compensation Law with and without $\dot{q}$ measurement at $V = 154.94\frac{m}{s}$ generated for η_{cmd} (bottleneck) loop cut (enhanced aircraft model, activated structural mode)

Considering the nichols plot generated for the bottleneck cut of the closed-loop consisting of basic aircraft model, DPI baseline controller and $\Delta\dot{q}$ Compensation Law in Fig. 5.56, one can see that the augmentation with $\dot{q}$ measurement does not degrade robust stability, which is offered by the baseline controller. In this case the frequency responses of DPI baseline controller and $\Delta\dot{q}$ Compensation Law are exactly matching in the considered frequency range. This is also confirmed by Table 5.10, which shows that gain margin, phase margin and TDM are identical. In case $\dot{q}$ cannot be measured, the phase margin barely changes, whereas the gain margin drops by $\approx 2.8dB$.
For the enhanced aircraft configuration it can be observed in Fig. 5.57 that the frequency responses only differ for higher frequencies. Thus, the robustness properties shown in Table 5.11 match almost exactly regardless whether $\dot{q}$ measurement is available or not. Moreover, considering the nichols plot Fig. 5.58, where the structural mode according to Section 2.7 is activated, one can observe that the margins for frequencies upwards the first wing bending mode, which is marked by the small diamond, result in $\approx 38dB$ without and in $\approx 36dB$ with $\dot{q}$ measurement. As it was already shown for the L1 Adaptive Augmentations in Section 5.2.2.1, the margins decrease in a similar way compared to the baseline controller. Although, the required margin of $8dB$ is still fulfilled.
Robustness assessments with regard to the bottleneck cut for the entire envelope according to Table 4.1 are collected in Table 5.12, for which a distinction is made between the applied aircraft model and availability of $\dot{q}$ measurement. The robustness requirements are fulfilled for all cases and envelope points. Furthermore, application

Table 5.12. – Summary of robust stability assessments of $\Delta\dot{q}$ Compensation Law with regard to the η_{cmd} bottleneck cut for the entire envelope according to Table 2.2

	Basic aircraft model	**Enhanced aircraft model**
No $\dot{q}$ measurement	Fig. A.30 Table A.43	Fig. A.56 Table A.77
$\dot{q}$ measurement	Fig. A.31 Table A.42	Fig. A.55 Table A.76

of the $\Delta\dot{q}$ Compensation Law does barely change both frequency responses and robust stability properties for all envelope points, in case $\dot{q}$ can be measured.

Robust stability with regard to the sensor cuts is assessed next. The nichols plots generated for the angle of attack α sensor cut considering the basic aircraft model are shown in Fig. 5.59. Firstly, one can see that the distance of the frequency response to the critical point is very comparable to the one of the baseline controller. This is also reflected in phase and gain margin, which can be taken from Table A.39 included in Appendix A.5.5. Secondly, the frequency responses barely differ between the cases, where $\dot{q}$ measurement is available or not. Thirdly, in contrast to the baseline controller frequency response, the curve belonging to the $\Delta\dot{q}$ Compensation Law also crosses the $-180°$-line above the $0dB$-line. This results in an additional, negative gain margin, which is also included in Table A.39. The same statements also hold for the enhanced aircraft configuration, where the robust stability assessments can be found in Fig. 5.60 and Table A.73 . Results covering the entire envelope are compiled in Table 5.13, where it is distinguished between aircraft configuration and availability of $\dot{q}$ measurement.

In the next step, the pitch rate q sensor cut is examined. The resulting nichols plots are depicted in Fig. 5.61 and Fig. 5.62 for basic and enhanced aircraft configuration, respectively. One can observe a clear difference between the frequency responses corresponding to the $\dot{q}$ measurement availability cases. In case $\dot{q}$ measurement is available, the distance to the critical point is slightly reduced. This is confirmed by the robust stability properties presented in Table A.40 and Table A.74. While pitch

Table 5.13. – Summary of robust stability assessments of $\Delta\dot{q}$ Compensation Law with regard to the angle of attack α sensor cut for the entire envelope according to Table 2.2

	Basic aircraft model	**Enhanced aircraft model**
No $\dot{q}$ measurement	Fig. A.32 Table A.44	Fig. A.58 Table A.79
$\dot{q}$ measurement	Fig. A.33 Table A.45	Fig. A.57 Table A.78

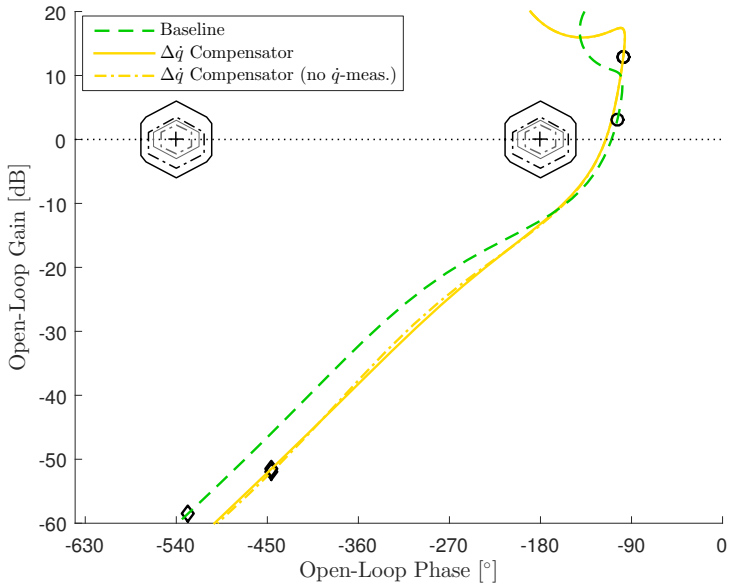

Figure 5.59. – Nichols plot for robust stability comparison of $\Delta\dot{q}$ Compensation Law with and without $\dot{q}$ measurement at $V = 154.94\frac{m}{s}$ generated for α loop cut (basic aircraft model)

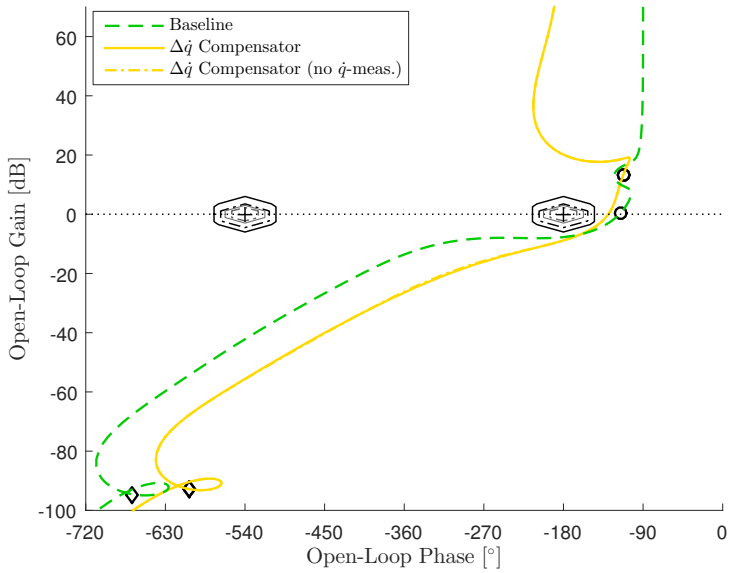

Figure 5.60. – Nichols plot for robust stability comparison of $\Delta\dot{q}$ Compensation Law with and without $\dot{q}$ measurement at $V = 154.94\frac{m}{s}$ generated for α loop cut (enhanced aircraft model)

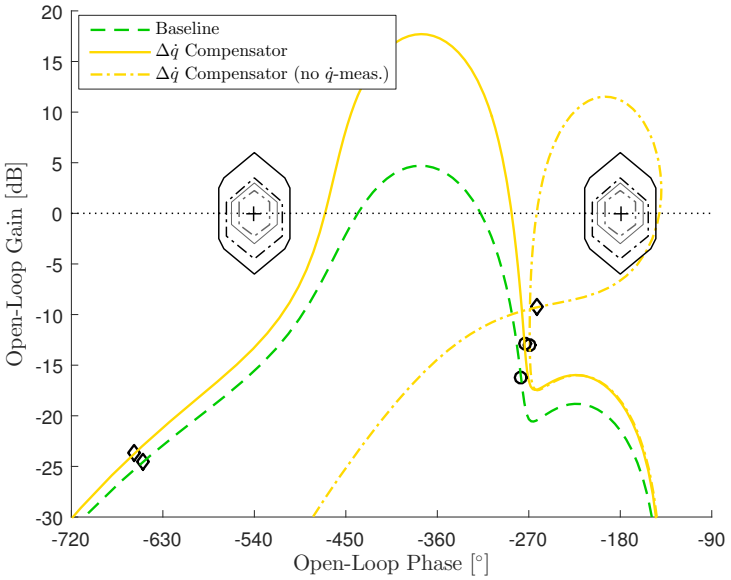

Figure 5.61. – Nichols plot for robust stability comparison of $\Delta\dot{q}$ Compensation Law with and without $\dot{q}$ measurement at $V = 154.94\frac{m}{s}$ generated for q loop cut (basic aircraft model)

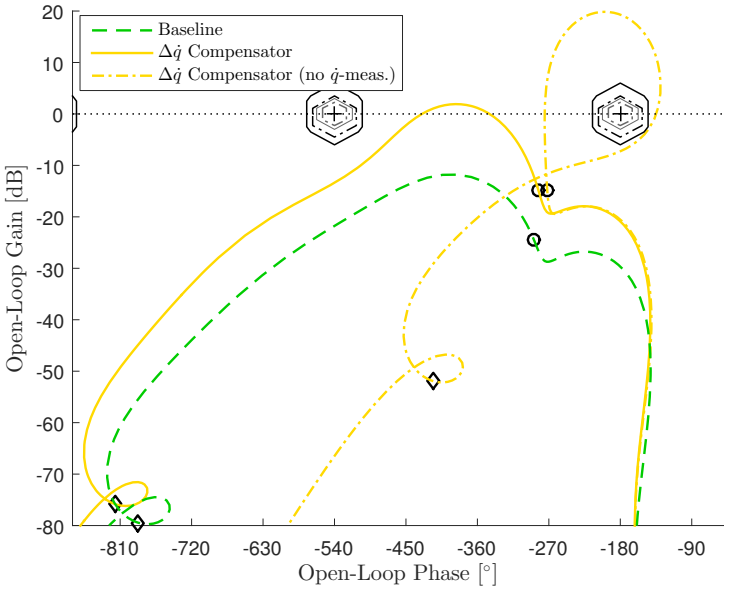

Figure 5.62. – Nichols plot for robust stability comparison of $\Delta\dot{q}$ Compensation Law with and without $\dot{q}$ measurement at $V = 154.94\frac{m}{s}$ generated for q loop cut (enhanced aircraft model)

Table 5.14. – Summary of robust stability assessments of $\Delta\dot{q}$ Compensation Law with regard to the pitch rate q sensor cut for the entire envelope according to Table 2.2

	Basic aircraft model	**Enhanced aircraft model**
No $\dot{q}$ measurement	Fig. A.34 Table A.46	Fig. A.60 Table A.81
$\dot{q}$ measurement	Fig. A.35 Table A.47	Fig. A.59 Table A.80

acceleration $\dot{q}$ is not available as measurement, the frequency response generates a circle around the critical points resulting in reduced robust stability properties. Thus, the closed-loop would destabilize, if the pitch rate measurement fails. This was also discussed for the L1 Adaptive Augmentations in Section 5.2.2.1. Similar observations can be made for other envelope points, where the results are collected in Table 5.14.
In contrast to the other control laws considered in this thesis, a third sensor cut has to be examined with regard to the robust stability assessment, which is the one belonging to the pitch acceleration $\dot{q}$ sensor. Both nichols plots shown in Fig. 5.63 and Fig. 5.64 for the two aircraft configurations exhibit a loop around the critical point generated by the frequency response. Thus, fail-safety would have to be provided for the pitch acceleration $\dot{q}$ measurement in this case. The accompanying tabulated gain margin, phase margin and TDM can be found in Table A.41 and Table A.75. The robust stability assessment comprising the entire envelope can be found in Fig. A.36 and Fig. A.61, where the tabulated robust stability properties are summarized in Table A.48 and Table A.82.
At last, the effect of the additional time delays on the robust stability of the closed-loop is investigated, which are incorporated in the $\Delta\dot{q}$ Compensation Law and can be utilized to synchronize the phase of the measurement signals. These time delays are also discussed in Section 4.3. In this case, time delay having the amount of $T_{D,\alpha} = T_{D,q} = 0.01s$ is applied to angle of attack α and pitch rate q measurements. Here, only the case is considered, where pitch rate acceleration $\dot{q}$ measurement is not available. The resulting nichols plots for bottleneck cut and sensor cuts can be found in Fig. 5.65, Fig. 5.66 and Fig. 5.67. One can observe that the time delays rather harm for this specific use case considering the frequency responses, although the difference is not very large. Thus, the additional time delays are not used for further assessments made in this thesis.

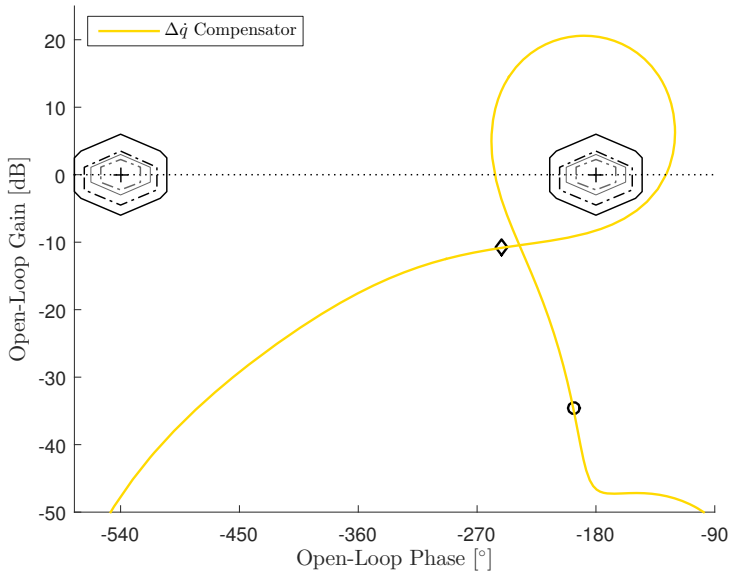

Figure 5.63. – Nichols plot for robust stability assessment of $\Delta\dot{q}$ Compensation Law with $\dot{q}$ measurement at $V = 154.94\frac{m}{s}$ generated for $\dot{q}$ loop cut (basic aircraft model)

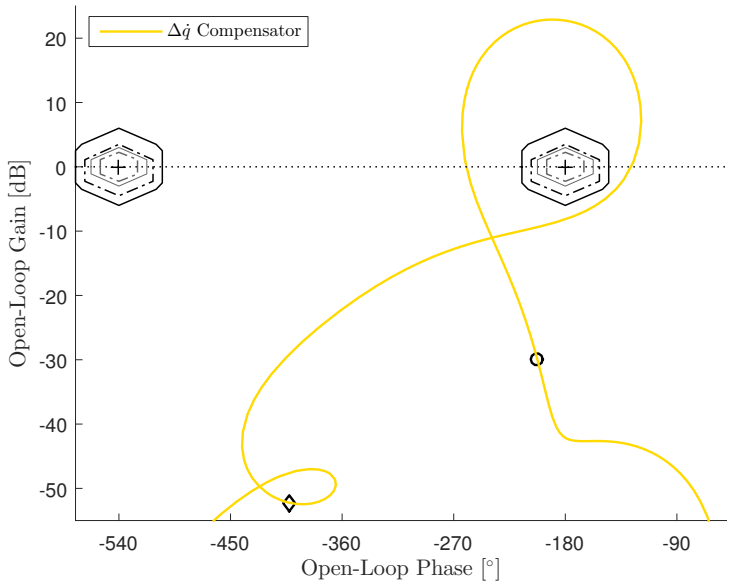

Figure 5.64. – Nichols plot for robust stability assessment of $\Delta\dot{q}$ Compensation Law with $\dot{q}$ measurement at $V = 154.94\frac{m}{s}$ generated for $\dot{q}$ loop cut (enhanced aircraft model)

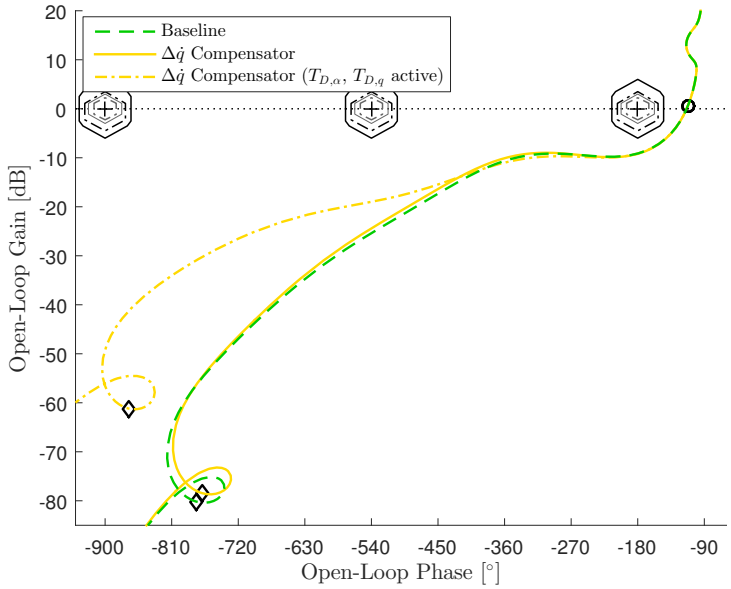

Figure 5.65. – Nichols plot for robust stability comparison of $\Delta\dot{q}$ Compensation Law with and without additional delays $T_{D,\alpha}$, $T_{D,q}$ at $V = 154.94\frac{m}{s}$ generated for η_{cmd} (bottleneck) loop cut (enhanced aircraft model)

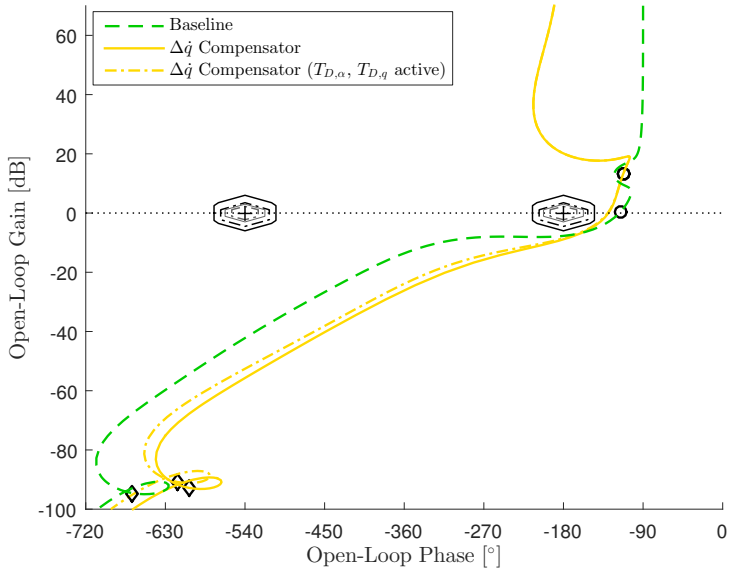

Figure 5.66. – Nichols plot for robust stability comparison of $\Delta\dot{q}$ Compensation Law with and without additional delays $T_{D,\alpha}$, $T_{D,q}$ at $V = 154.94\frac{m}{s}$ generated for α loop cut (enhanced aircraft model)

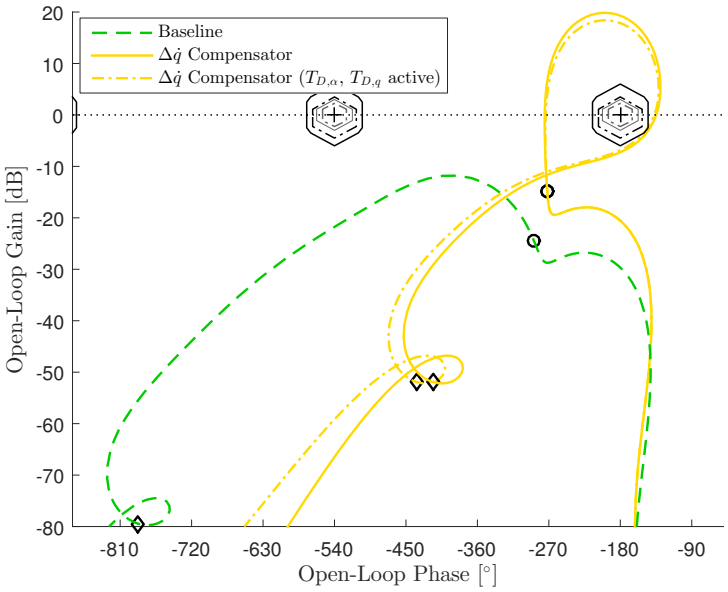

Figure 5.67. – Nichols plot for robust stability comparison of $\Delta\dot{q}$ Compensation Law with and without additional delays $T_{D,\alpha}$, $T_{D,q}$ at $V = 154.94\frac{m}{s}$ generated for q loop cut (enhanced aircraft model)

5.2.3.2. Performance

In the following section, a closer look is taken on the performance of the $\Delta\dot{q}$ Compensation Law. As shown for the other control laws, both step responses and an exemplary maneuver are considered for these assessments.

Step responses of the combination of basic aircraft model, where the nonlinear longitudinal dynamics are replaced by the linear short-period approximation according to Eq. (4.23), baseline controller and $\Delta\dot{q}$ Compensation Law are shown in Fig. 5.68 for the envelope points summarized in Table 2.2. In comparison to the baseline controller step response to be found in Fig. 5.18 no degradation can be detected stemming from the $\Delta\dot{q}$ Compensation Law and the commanded angle of attack is α_{cmd} perfectly tracked.

The assessment is repeated utilizing the linear "4x4" aircraft model shown in Eq. (2.42), which results in Fig. 5.69. The decaying influence of the phugoid can be observed, nevertheless α_{cmd} is tracked considering large time scale. The same step response for short time scale is depicted in Fig. A.88, which can be found in Appendix A.7.5.

Considering the nonlinear, basic aircraft model it can be seen in the corresponding step responses shown in Fig. 5.70 that the desired system response can be restored for the high velocity cases. These exhibited insufficient performance for the baseline controller step response shown in Fig. 5.20. The same step responses are depicted in Fig. 5.71 for a large time scale. The same observation can be made for the enhanced aircraft model configuration, where the step responses are shown in Fig. A.89 and Fig. A.90.

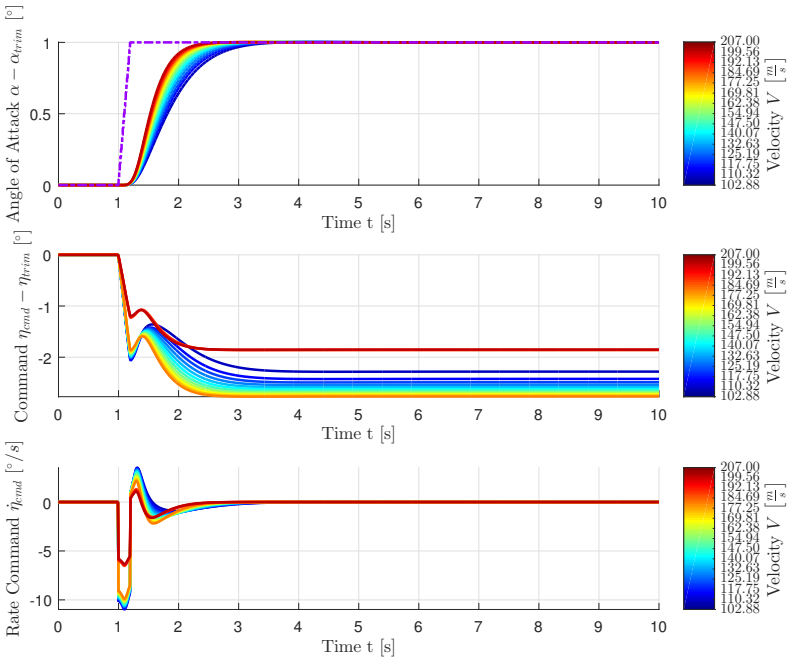

Figure 5.68. – α_{cmd} step responses of basic, linear aircraft model containing only the short-period approximation and $\Delta\dot{q}$ Compensation Law at envelope points according to Table 2.2

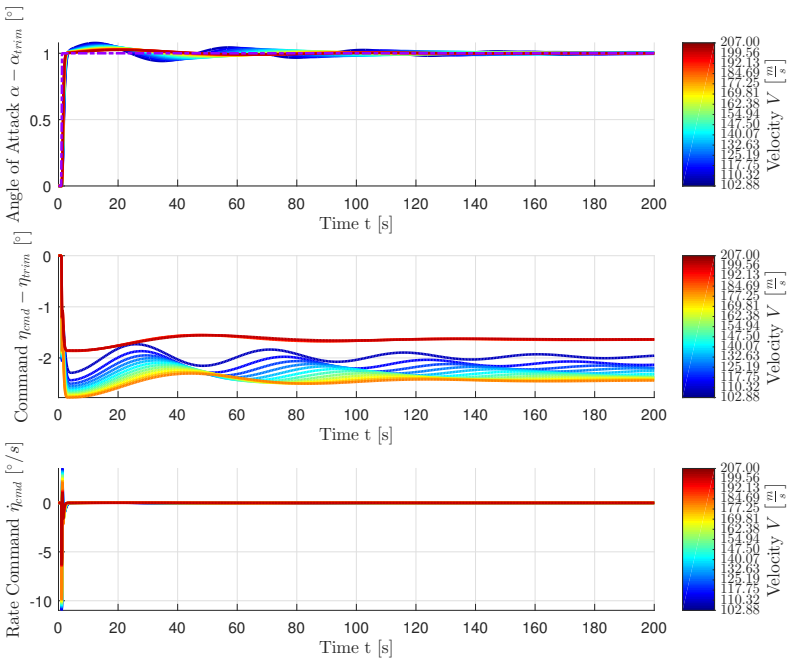

Figure 5.69. – α_{cmd} step responses of basic, linear aircraft model and $\Delta\dot{q}$ Compensation Law at envelope points according to Table 2.2 for large timescale

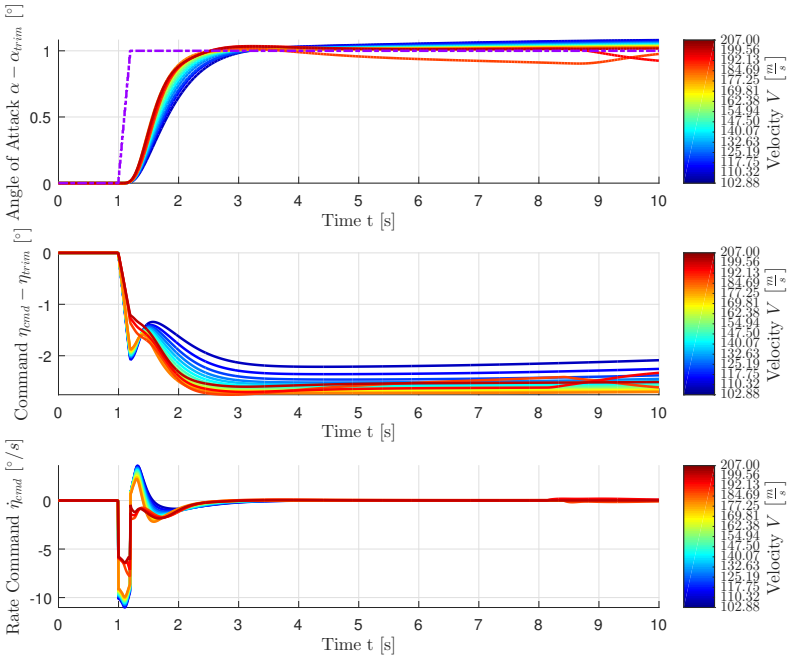

Figure 5.70. – α_{cmd} step responses of basic, nonlinear aircraft model and $\Delta\dot{q}$ Compensation Law at envelope points according to Table 2.2

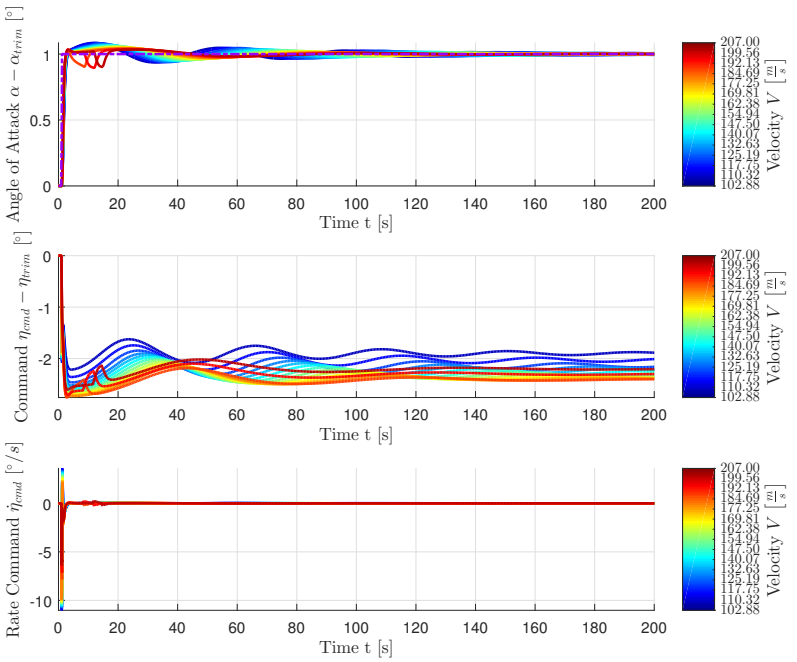

Figure 5.71. – α_{cmd} step responses of basic, nonlinear aircraft model and $\Delta\dot{q}$ Compensation Law at envelope points according to Table 2.2 for large timescale

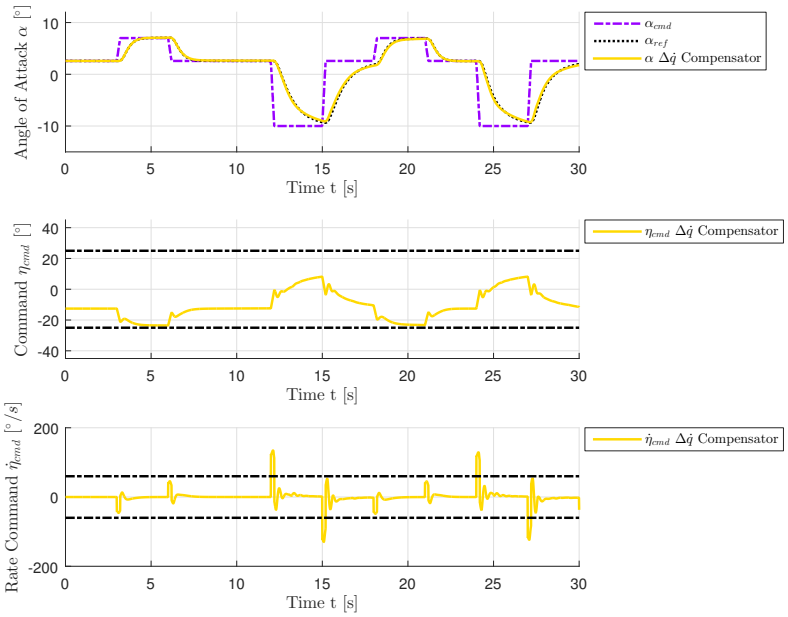

Figure 5.72. – Angle of attack α, elevator command η_{cmd} and elevator command rate $\dot{\eta}_{cmd}$ for example maneuver performed by basic, nonlinear aircraft model with $\Delta\dot{q}$ Compensation Law starting at $V_0 = 154.94\frac{m}{s}$ and $h_0 = 5000m$

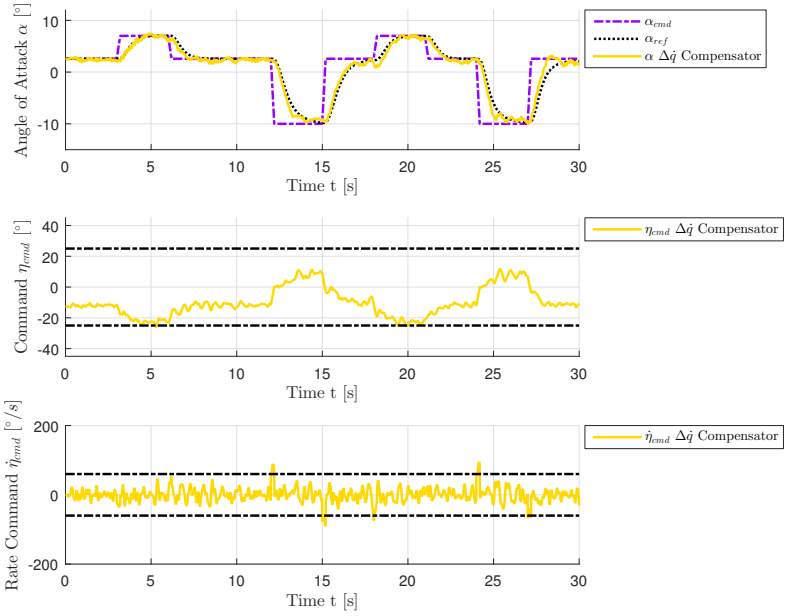

Figure 5.73. – Angle of attack α, elevator command η_{cmd} and elevator command rate $\dot{\eta}_{cmd}$ for example maneuver performed by enhanced, nonlinear aircraft model with $\Delta\dot{q}$ Compensation Law starting at $V_0 = 154.94\frac{m}{s}$ and $h_0 = 5000m$

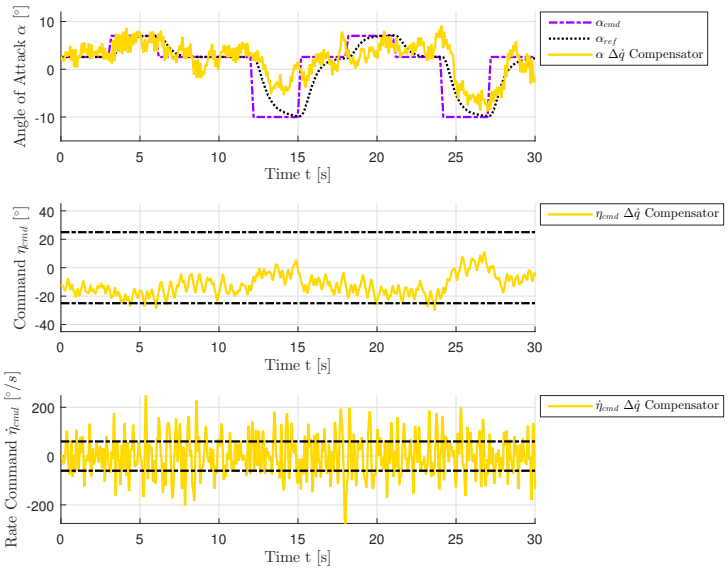

Figure 5.74. – Angle of attack α, elevator command η_{cmd} and elevator command rate $\dot{\eta}_{cmd}$ for example maneuver performed by enhanced, nonlinear aircraft model with $\Delta\dot{q}$ Compensation Law starting at $V_0 = 154.94\frac{m}{s}$ and $h_0 = 5000m$ considering severe turbulence

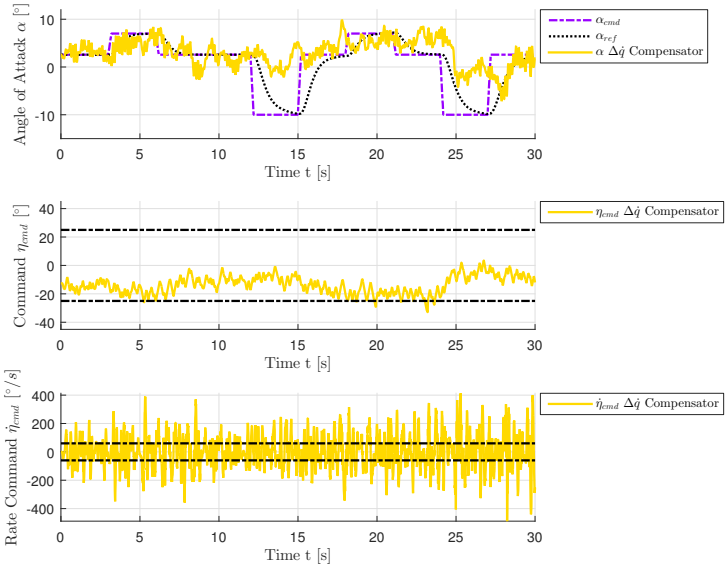

Figure 5.75. – Angle of attack α, elevator command η_{cmd} and elevator command rate $\dot{\eta}_{cmd}$ for example maneuver performed by enhanced, nonlinear aircraft model with $\Delta\dot{q}$ Compensation Law starting at $V_0 = 154.94\frac{m}{s}$ and $h_0 = 5000m$ considering severe turbulence without additional low-pass filter applied to η_{cmd}

In the next step, the simulation of the exemplary maneuver for the basic aircraft configuration is investigated. The results can be found in Fig. 5.72. It can be seen that the system response with regard to angle of attack α accurately matches the reference model response α_{cmd}. This is also true for the $\alpha_{min} = -10^{\circ}$ sections, where a nonlinearity was detected, which led to overshoot using only the baseline controller (c.f. Fig. 5.22). A similar picture emerges, when assessing the same maneuver with the enhanced aircraft configuration, which is shown in Fig. 5.73. The matching with the reference model dynamics is still good, although compared to the baseline controller configuration, higher amplification of the light turbulence (probability of exceedance 10^{-2}) can be detected. This was also observed for the L1 Adaptive Augmentations (c.f. Fig. 5.46). In this case, the amplification can be explained through the derivation of the pitch rate q measurement, which is directly afflicted by turbulence. This derivation amplifies the turbulence content. However the derivation is necessary, in order to estimate the pitch acceleration $\dot{q}$ (c.f. Section 4.3). Note also that even in case, $\dot{q}$ could directly be measured, the measurement would also contain the "physically derived" turbulence content and would thus require heavy filtering.
The described phenomenon of turbulence amplification appears in an even higher degree for severe turbulence (probability of exceedance 10^{-5}), which is shown in Fig. 5.74. Also in this case the system response is very comparable to the one gained with the L1 Adaptive Augmentations (c.f. Fig. 5.48). The necessity of the additional low-pass filter, which is proposed in Section 4.3, becomes clear when considering the system response without this filter in Fig. 5.75. In this case, the commanded maneuver cannot be realized anymore.
Furthermore, the effects of rapid CG-shifts are also investigated for the $\Delta\dot{q}$ Compensation Law. Fig. 5.76 shows the result considering the basic aircraft configuration and a CG-shift of 5%. The response is again very similar to the one achieved by means of the L1 Adaptive Augmentations shown in Fig. 5.50. Still, the controller accomplishes to follow the reference model dynamics depicted by α_{ref}. The same observation can be made for the enhanced aircraft configuration in Fig. 5.77, where a CG-shift of 2% is applied.

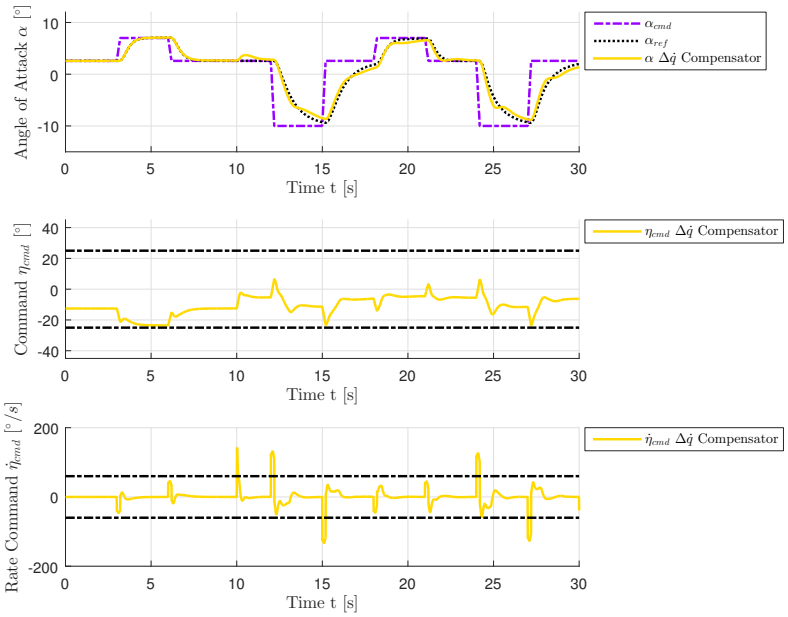

Figure 5.76. – Angle of attack α, elevator command η_{cmd} and elevator command rate $\dot{\eta}_{cmd}$ for example maneuver performed by basic, nonlinear aircraft model with $\Delta\dot{q}$ Compensation Law starting at $V_0 = 154.94\frac{m}{s}$ and $h_0 = 5000m$ considering CG-shift of 5% at $t = 10s$

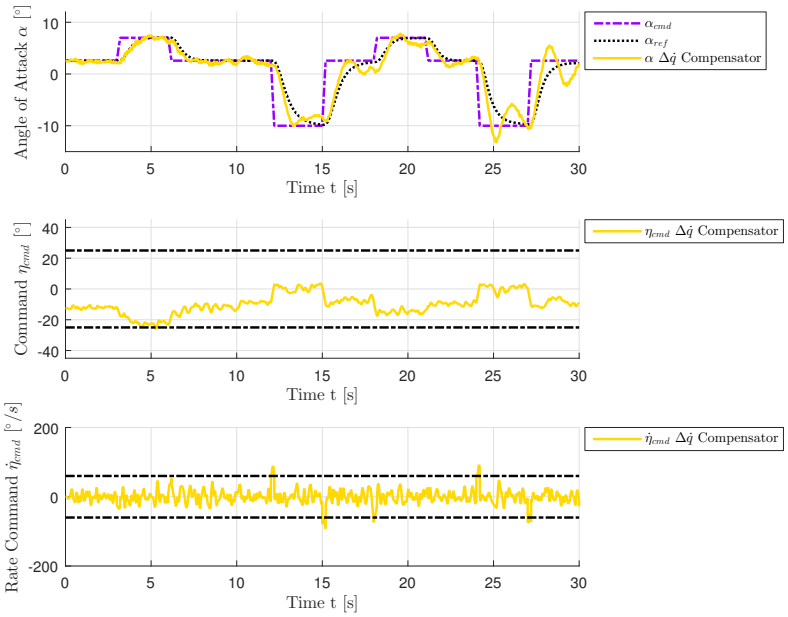

Figure 5.77. – Angle of attack α, elevator command η_{cmd} and elevator command rate $\dot{\eta}_{cmd}$ for example maneuver performed by enhanced, nonlinear aircraft model with $\Delta\dot{q}$ Compensation Law starting at $V_0 = 154.94\frac{m}{s}$ and $h_0 = 5000m$ considering CG-shift of 2% at $t = 10s$

5.2.4. L1 adaptive controller with Eigenstructure Assignment

The last controller to be evaluated in this chapter in terms of closed-loop dynamics, robust stability and performance is the L1 adaptive controller with Eigenstructure Assignment, whose architecture is presented in Section 4.4.
At first, the resulting poles of the closed-loop consisting of basic aircraft and L1 adaptive controller are examined. Note that no baseline controller is involved in this setup. The linearization is performed considering the envelope point $V_0 = 154.94\frac{m}{s}$ and $h_0 = 5000m$. At this envelope point, the properties of the short period dynamics should result in $\omega_{0,sp,des} = 3.84\frac{rad}{s}$ and $\zeta_{sp,des} = 0.95$. It can be seen in Table A.20 that this values are almost perfectly matched for the continuous-time controller implementation, where the pair of complex conjugate poles 4 and 5 indicate that the short-period has a frequency of $\omega_{0,sp} = 3.81\frac{rad}{s}$ with a relative damping of $\zeta_{sp} = 0.949$. Thus, it can be confirmed that precise pole placement is possible by means of the proposed modification of the state predictor, which was introduced in Section 4.4.2.
Considering the discrete-time implementation in Table A.19, the poles belonging to the short-period can be detected in pole 4 and in the pole pair 5/6, which forms from a merge of two poles stemming from the pole pairs 4/5 and 6/7 in the continuous-time representation. This deviation from the desired values can again be explained through the fact that Euler's transformation has to be used for the short-period approximation within the state predictor of the L1 adaptive controller (c.f. Section 5.2.2).
Similar observations can be made for the closed-loop poles considering the combination of enhanced aircraft model and L1 adaptive controller. Again, the poles of the short-period are placed as desired and result in $\omega_{0,sp} = 3.79\frac{rad}{s}$ and $\zeta_{sp} = 0.95$, as it can be seen in Table A.22. For the discrete-time implementation a deviation occurs, which was also detected for the basic aircraft model. The results can be found in Table A.22.

5.2.4.1. Linear robust stability

Robust stability of the proposed L1 adaptive controller with Eigenstructure Assignment is investigated in the following section. For this purpose, the assessments are carried out in detail considering the exemplary envelope point $V_0 = 154.94\frac{m}{s}$ and $h_0 = 5000m$, whereby results covering the entire envelope are also provided.
Nichols plots for the bottleneck cut considering the combination of basic aircraft model and L1 adaptive controller and generated at the exemplary envelope point are depicted in Fig. 5.78. For the sake of comparison, the frequency response of the baseline controller is provided as well. The robustness margins are fulfilled for both cases, where hedging according to Section 4.4.2 is activated and where no hedging is used. The beneficial effect of hedging, which was also discussed for the adaptive augmentations in Section 5.2.2.1, can also be observed for the standalone L1 adaptive controller. In case hedging is used, the frequency response does not cross the $0dB$-line, which means that the phase margin is infinite. This is also confirmed by Table 5.15.

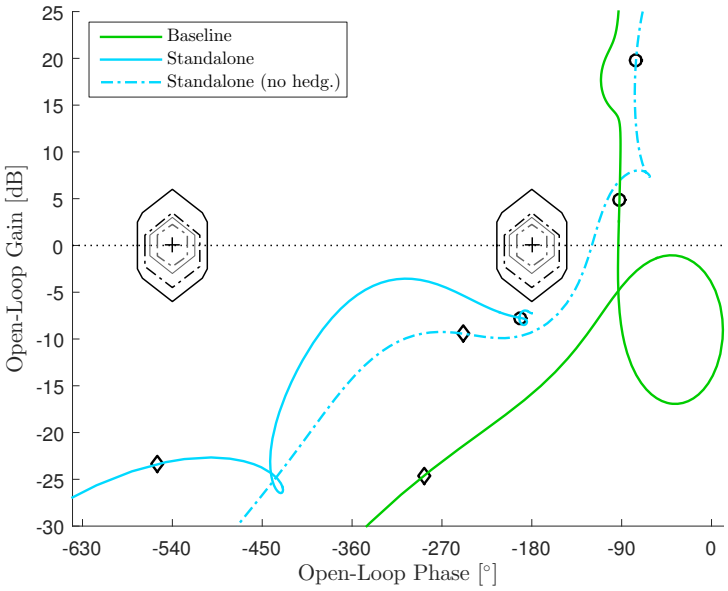

Figure 5.78. – Nichols plot for robust stability comparison of L1 adaptive controller with Eigenstructure Assignment with and without hedging at $V = 154.94\frac{m}{s}$ generated for η_{cmd} (bottleneck) loop cut (basic aircraft model)

Table 5.15. – Robust stability properties gain margin (GM), phase margin Φ_m, time delay margins (TDM) and corresponding gain-crossover frequencies $\omega_{gc,\Phi}$ and $\omega_{gc,TDM}$ for robust stability comparison of L1 adaptive controller with Eigenstructure Assignment with and without hedging at $V = 154.94\frac{m}{s}$ generated for η_{cmd} (bottleneck) loop cut (basic aircraft model)

Controller	**GM** $[dB]$	Φ_m $[°]$	$\omega_{gc,\Phi}$ $\left[\frac{rad}{s}\right]$	**TDM** $[s]$	$\omega_{gc,TDM}$ $\left[\frac{rad}{s}\right]$
Baseline	15.85	86.63	0.62	2.424	0.62
	$-\infty$	-273.37	0.62	-7.650	0.62
L1 Standalone	23.05	∞	0.00	∞	0.00
	$-\infty$	$-\infty$	0.00	$-\infty$	0.00
L1 Standalone (no hedg.)	9.27	60.19	7.37	0.142	7.37
	$-\infty$	-299.81	7.37	-0.710	7.37

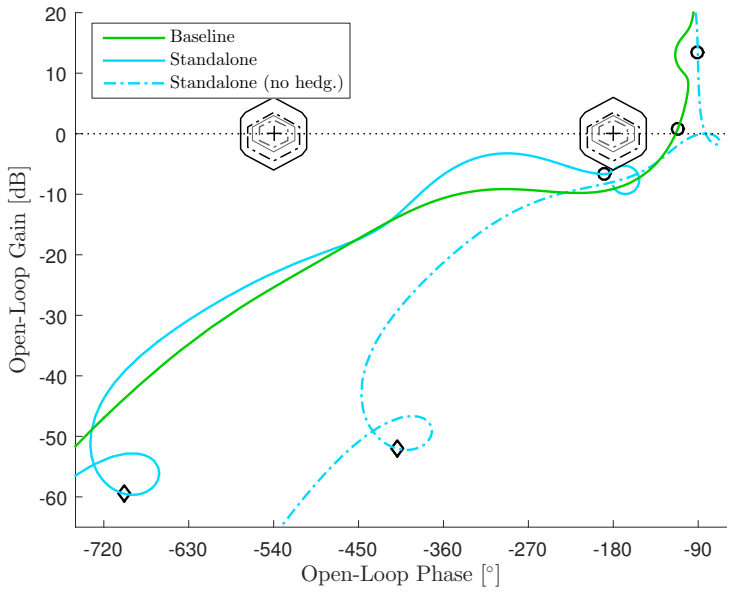

Figure 5.79. – Nichols plot for robust stability comparison of L1 adaptive controller with Eigenstructure Assignment with and without hedging at $V = 154.94\frac{m}{s}$ generated for η_{cmd} (bottleneck) loop cut (enhanced aircraft model)

Table 5.16. – Robust stability properties gain margin (GM), phase margin Φ_m, time delay margins (TDM) and corresponding gain-crossover frequencies $\omega_{gc,\Phi}$ and $\omega_{gc,TDM}$ for robust stability comparison of L1 adaptive controller with Eigenstructure Assignment with and without hedging at $V = 154.94\frac{m}{s}$ generated for η_{cmd} (bottleneck) loop cut (enhanced aircraft model)

Controller	**GM** $[dB]$	Φ_m $[°]$	$\omega_{gc,\Phi}$ $\left[\frac{rad}{s}\right]$	**TDM** $[s]$	$\omega_{gc,TDM}$ $\left[\frac{rad}{s}\right]$
Baseline	9.13	66.12	0.41	2.827	0.41
	$-\infty$	-293.88	0.41	-12.565	0.41
L1 Standalone	5.98	∞	0.00	∞	0.00
	$-\infty$	$-\infty$	0.00	$-\infty$	0.00
L1 Standalone (no hedg.)	7.97	96.64	3.80	0.444	3.80
	$-\infty$	-261.65	3.73	-1.211	3.80

Table 5.17. – Summary of robust stability assessments of L1 adaptive controller with Eigenstructure Assignment with regard to the η_{cmd} bottleneck cut for the entire envelope according to Table 2.2

	Basic aircraft model	**Enhanced aircraft model**
Hedging	Fig. A.37 Table A.51	Fig. A.62 Table A.85
No Hedging	Fig. A.38 Table A.52	Fig. A.63 Table A.86

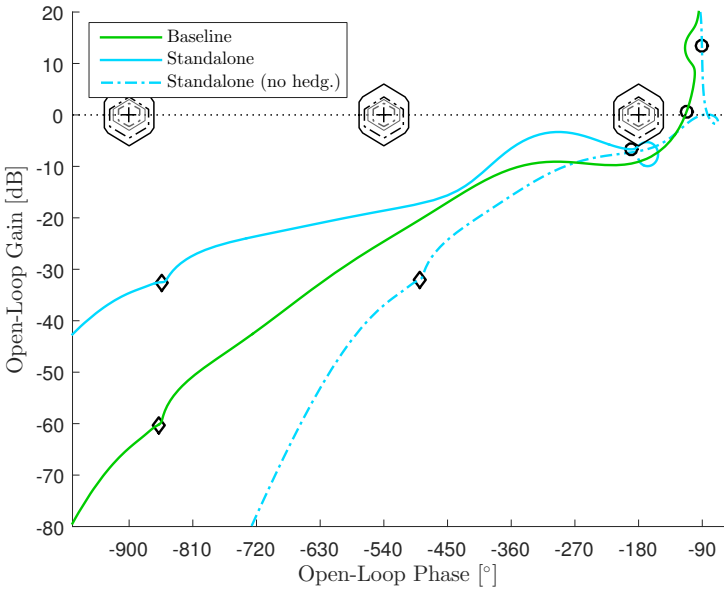

Figure 5.80. – Nichols plot for robust stability comparison of L1 adaptive controller with Eigenstructure Assignment with and without hedging at $V = 154.94\frac{m}{s}$ generated for η_{cmd} (bottleneck) loop cut (enhanced aircraft model, activated structural mode)

Although the plot indicates that the curve of the frequency response is exactly starting at a phase of $-180°$, the starting point is in fact slightly below $-180°$. Thus, a gain margin of $23.05dB$ with respect to the critical point at $-540°$ results instead of $\approx 7.2dB$. A similar statement can be made for the closed-loop of the enhanced aircraft configuration. The corresponding nichols plots are shown in Fig. 5.79. Furthermore, it can be seen that the frequency response is crossing the outermost diamond. However, this happens for small frequencies $\omega < \omega_{0,ph}$. For these frequencies the black, dashed-dotted diamond constitutes the required robustness margin according to Table 5.1. Thus, the requirements with regard to robust stability are still fulfilled. The accompanying robust stability properties can be found in Table 5.16.
In addition to the setup shown above, the structural mode according to Section 2.7 is activated for the nichols plot shown in Fig. 5.80. It can be seen that the margins for frequencies upwards the first wing bending mode, which is marked by the small diamond, result in $\approx 37dB$ without and $\approx 35dB$ with hedging. As for the adaptive augmentations, also for the standalone L1 adaptive controller a decrease in this margin can be detected with regard to the baseline controller. Although, the required margin of $8dB$ is still fulfilled.
References to nichols plots covering the entire envelope as well as to tables summarizing the corresponding gain margins, phase margins and TDM are collected in Table 5.17. Sufficient stability margins can be detected for the entire envelope for both configurations with and without hedging.

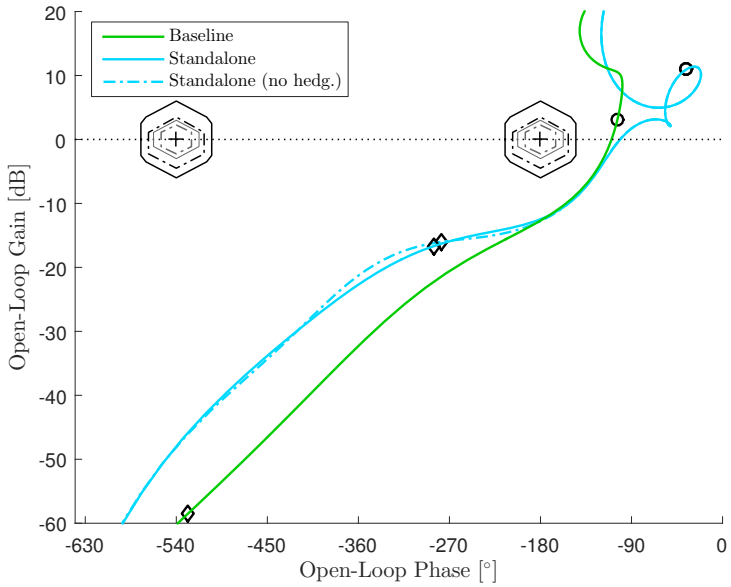

Figure 5.81. – Nichols plot for robust stability comparison of L1 adaptive controller with Eigenstructure Assignment with and without hedging at $V = 154.94\frac{m}{s}$ generated for α loop cut (basic aircraft model)

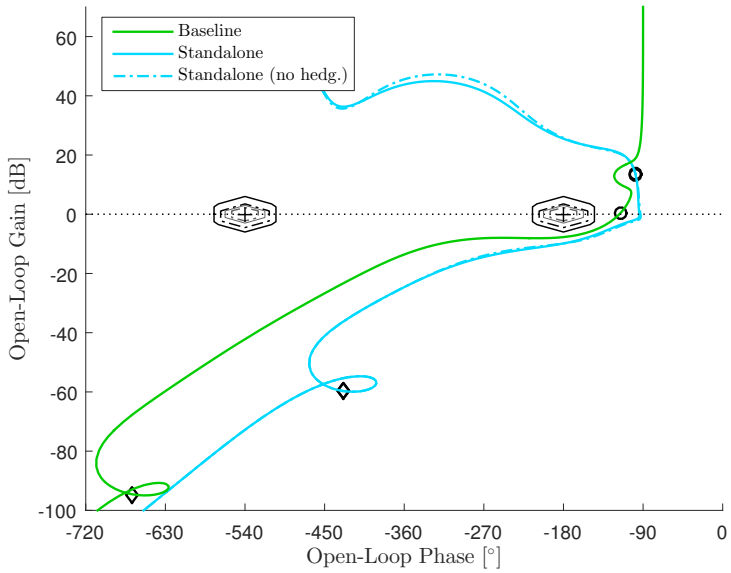

Figure 5.82. – Nichols plot for robust stability comparison of L1 adaptive controller with Eigenstructure Assignment with and without hedging at $V = 154.94\frac{m}{s}$ generated for α loop cut (enhanced aircraft model)

Table 5.18. – Summary of robust stability assessments of L1 adaptive controller with Eigenstructure Assignment with regard to the angle of attack α sensor cut for the entire envelope according to Table 2.2

	Basic aircraft model	**Enhanced aircraft model**
Hedging	Fig. A.39 Table A.53	Fig. A.64 Table A.87
No Hedging	Fig. A.40 Table A.54	Fig. A.65 Table A.88

Robust stability with regard to the angle of attack α sensor cut is examined in the next step. In Fig. 5.81 the assessments for the basic aircraft configuration are shown. It can be seen that the distance of the frequency response corresponding to the standalone L1 adaptive controller to the critical point is comparable to the one belonging to the baseline controller. This is also reflected in gain and phase margins, which can be found in Table A.49 included in Appendix A.5.6. Furthermore, the frequency response barely changes between the two hedging cases. For the enhanced aircraft configuration the robust stability margins even increase compared to the baseline controller, which can be seen in Fig. 5.82 and Table A.83. A summary of assessments with regard to the entire envelope according to Table 2.2 can be found in Table 5.18.

Moreover, the pitch rate q sensor cut is investigated in Fig. 5.83 and Table A.50 for the basic aircraft configuration. One can observe that the phase margin is ∞ in contrast to the DPI baseline controller frequency response, although the gain margin is lower for the standalone L1 adaptive controller in this case. For the enhanced aircraft configuration shown in Fig. 5.84 and Table A.84 both controllers have a phase margin of ∞ and again it can be observed that the standalone L1 adaptive controller has less gain margin than the DPI baseline controller. The results for the entire envelope can be found in Table 5.19.

In a nutshell, it can be stated that the L1 adaptive controller with Eigenstructure Assignment offers good properties with regard to robust stability. For the important bottleneck cut an infinite phase margin can be detected for both basic and enhanced

Table 5.19. – Summary of robust stability assessments of L1 adaptive controller with Eigenstructure Assignment with regard to the angle of attack q sensor cut for the entire envelope according to Table 2.2

	Basic aircraft model	**Enhanced aircraft model**
Hedging	Fig. A.41 Table A.55	Fig. A.66 Table A.89
No Hedging	Fig. A.42 Table A.56	Fig. A.67 Table A.90

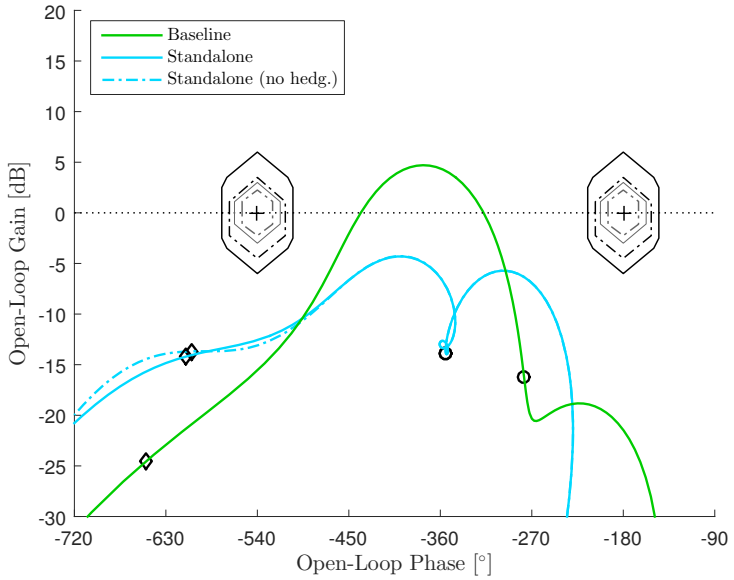

Figure 5.83. – Nichols plot for robust stability comparison of L1 adaptive controller with Eigenstructure Assignment with and without hedging at $V = 154.94\frac{m}{s}$ generated for q loop cut (basic aircraft model)

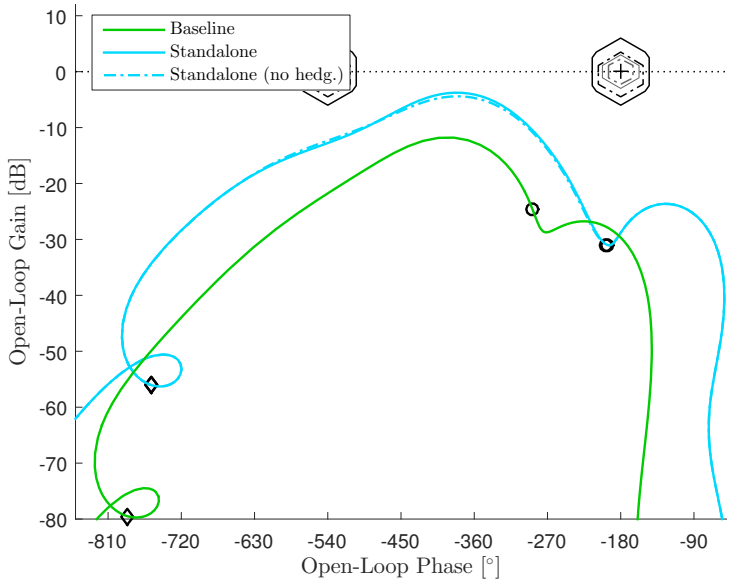

Figure 5.84. – Nichols plot for robust stability comparison of L1 adaptive controller with Eigenstructure Assignment with and without hedging at $V = 154.94\frac{m}{s}$ generated for q loop cut (enhanced aircraft model)

aircraft model configuration. The proposed hedging technique has a beneficial effect here as well. Furthermore, the closed-loop does not destabilize in case of a failing sensor, which could be observed for the adaptive augmentations assessed in Section 5.2.2.1 and the $\Delta\dot{q}$ Compensation Law investigated in Section 5.2.3.1.

5.2.4.2. Performance

This section investigates the L1 adaptive controller with Eigenstructure Assignment in terms of performance. For this purpose, both step responses and an exemplary maneuver are assessed, as it was done already for the other control laws in this chapter. Fig. 5.85 presents step responses for the entire envelope according to Table 2.2. For this, the combination of basic aircraft model, where the nonlinear flight dynamics are replaced by the linear short-period approximation shown in Eq. (4.23), and the standalone L1 adaptive controller is considered. The step responses exhibit good tracking of the commanded angle of attack α_{cmd} and a proper transient.
In the next step, the linear "4x4" aircraft model according to Eq. (2.42) is utilized instead of the short-period approximation. Although good tracking of α_{cmd} can still be observed considering short time scale in Fig. 5.86, a larger time in Fig. 5.87 reveals that a residual steady-state error between commanded α_{cmd} and measured angle of attack α remains. For the lowest velocity case this steady-state error results in $\alpha_{cmd} - \alpha = \approx -0.3^\circ$. The reason for this is that the control law does not contain an integral portion, as it is for example provided by the baseline controller for the adaptive augmentations shown in Section 4.2 and Section 4.3. Thus, due to the missing integral portion within the control law, a residual steady-state error remains.
A similar statement can be made, when the nonlinear, basic aircraft model is considered. The step responses are shown in Fig. 5.88 for short and in Fig. 5.89 for large time scale, respectively. Despite the already discussed steady-state error, it can also be observed that the standalone L1 adaptive controller is able to compensate the undersized feedforward gain h_{L1} for the high velocity envelope cases, as it was already shown for the adaptive augmentations (c.f. Fig. 5.42 and Fig. 5.70). The corresponding step responses considering the enhanced aircraft model configuration can be found in Fig. A.91 and Fig. A.92, which are both included in Appendix A.7.6. Here, the steady-state error results in maximum of -0.2° for the lowest velocity case.
After the presentation of the step response investigations, the performance of the L1 adaptive controller with Eigenstructure Assignment considering the exemplary maneuver is considered in the next step. The corresponding plot for the combination of basic aircraft model and L1 adaptive controller can be found in Fig. 5.90. One can observe in the system response with regard to angle of attack α that the standalone adaptive controller is precisely able to shape the plant dynamics in accordance to the reference model, which is represented by α_{ref}. In particular, this applies to the $\alpha_{min} = -10^\circ$ sections, which exhibit a nonlinearity within the aircraft dynamics, as it was already discussed in Section 5.2.1.2. This confirms, once again, the ability of the

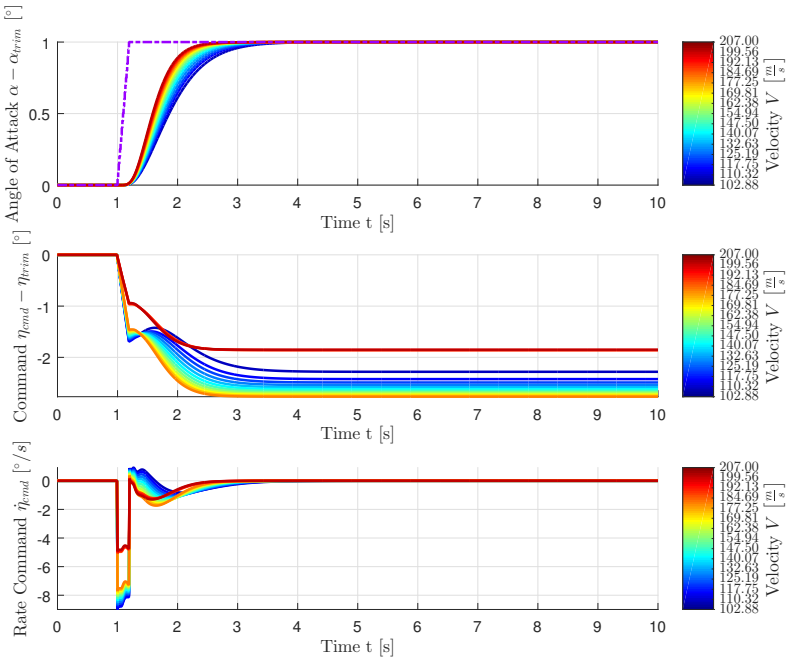

Figure 5.85. – α_{cmd} step responses of basic, linear aircraft model containing only the short-period approximation and L1 adaptive controller with Eigenstructure Assignment at envelope points according to Table 2.2

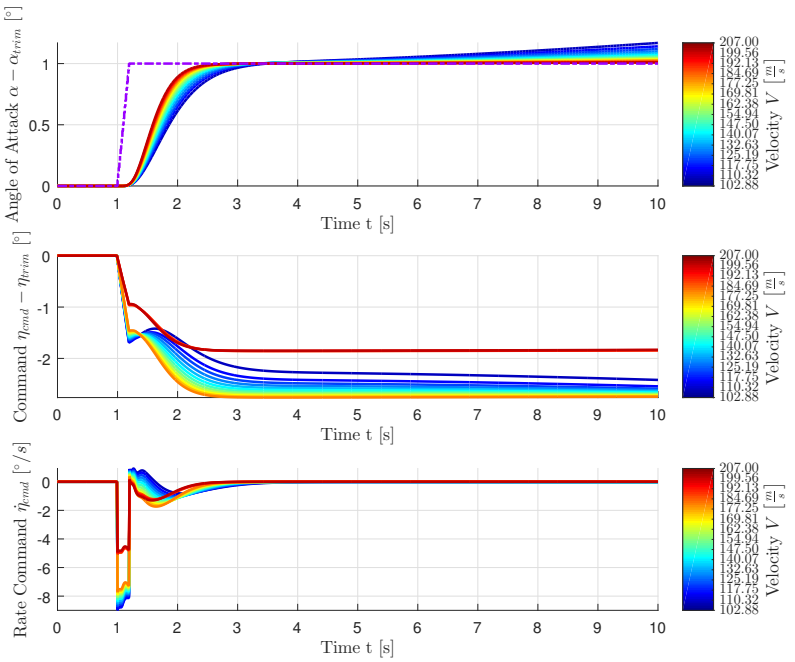

Figure 5.86. – α_{cmd} step responses of basic, linear aircraft model and L1 adaptive controller with Eigenstructure Assignment at envelope points according to Table 2.2

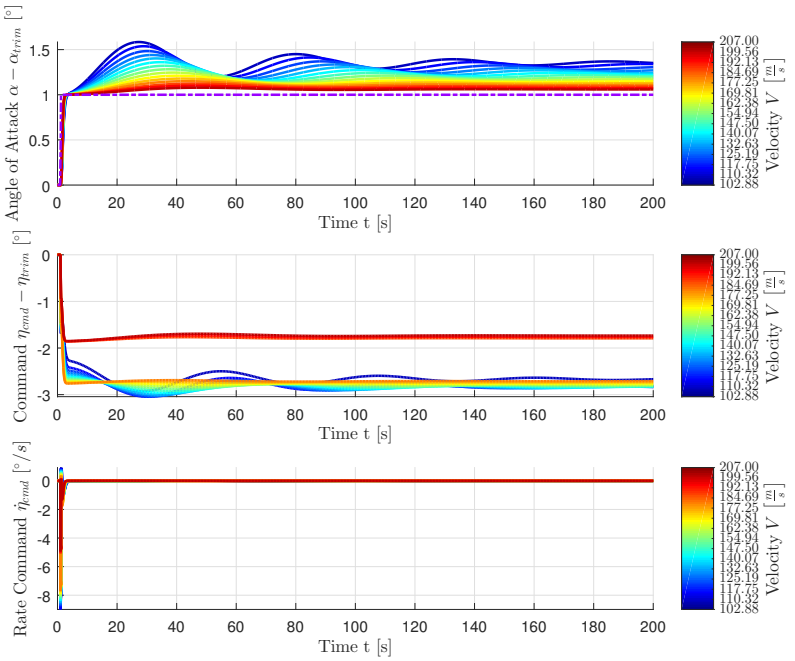

Figure 5.87. – α_{cmd} step responses of basic, linear aircraft model and L1 adaptive controller with Eigenstructure Assignment at envelope points according to Table 2.2 for large timescale

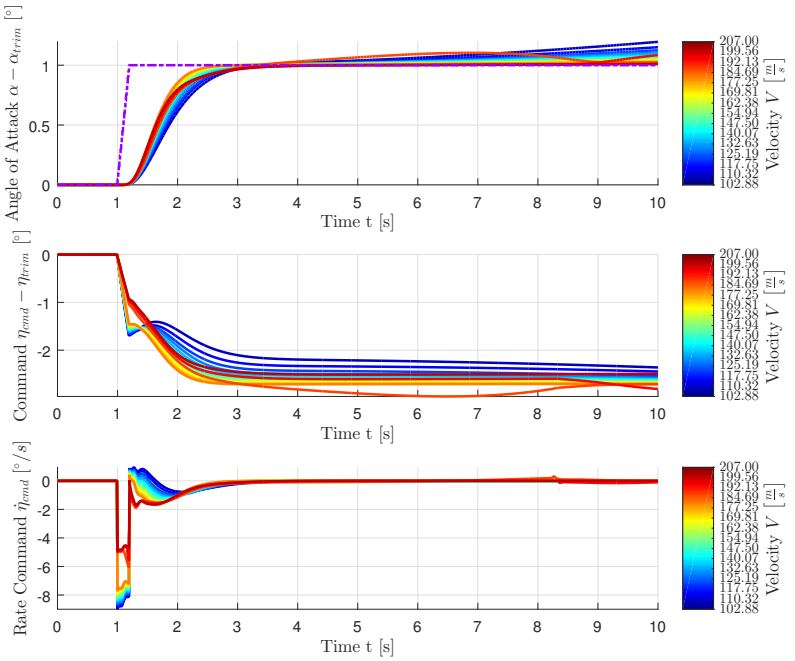

Figure 5.88. – α_{cmd} step responses of basic, nonlinear aircraft model and L1 adaptive controller with Eigenstructure Assignment at envelope points according to Table 2.2

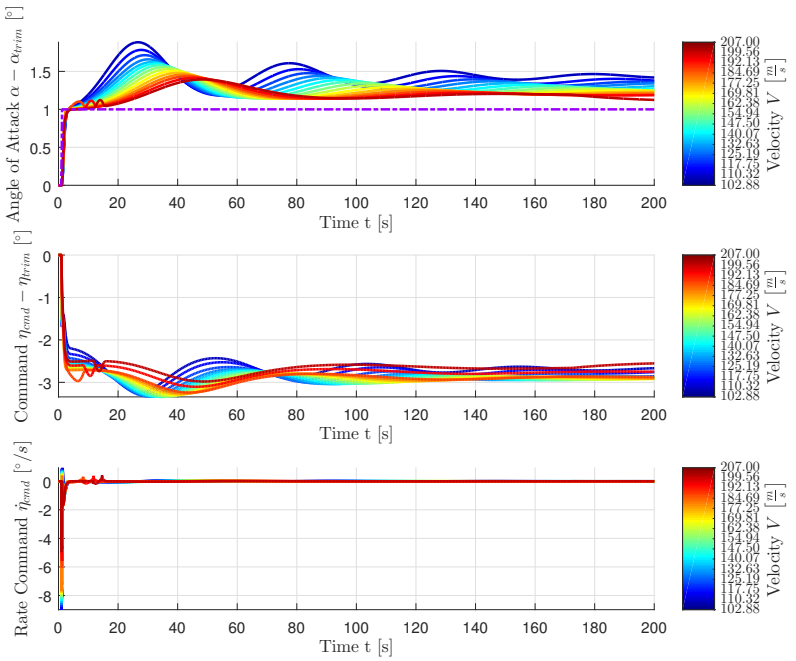

Figure 5.89. – α_{cmd} step responses of basic, nonlinear aircraft model and L1 adaptive controller with Eigenstructure Assignment at envelope points according to Table 2.2 for large timescale

standalone adaptive controller to exactly place closed-loop system poles by means of the proposed modification of the state predictor. The steady-state error is $\approx -0.05°$ for the $\alpha_{max} = 7°$ sections and $\approx -0.25°$ for the $\alpha_{min} = -10°$ sections. Moreover, it can be seen considering the commanded elevator deflection η_{cmd} that the control law provides a clean, almost oscillation free control signal. Compared to the adaptive augmentations one can observe in Fig. 5.91 that the controller workload in terms of adaptation is higher (c.f. Fig. 5.45). This is not surprising, because in this case the shaping of the plant dynamics in directly incorporated into the adaptation process, which is discussed in Section 4.4.3.

Results considering the same maneuver, but utilizing the enhanced aircraft model configuration, are compiled in Fig. 5.92. As it was already observed for the adaptive augmentations in Fig. 5.46 and the $\Delta\dot{q}$ Compensation Law in Fig. 5.73, the applied light turbulence (probability of exceedance 10^{-2}) is stronger amplified compared to the baseline controller results shown in Fig. 5.25. This can especially been observed considering the commanded elevator rate $\dot{\eta}_{cmd}$ in Fig. 5.92 and the parameters $\hat{\sigma}$ in Fig. 5.93. The reason for this can be found in the high-gain adaptation law, as it was already described in Section 5.2.2.3. Nevertheless, the standalone adaptive controller is still able to precisely apply the desired dynamic behavior on the plant, which leads to good matching of the system response with regard to angle of attack α and the reference model output α_{ref}.

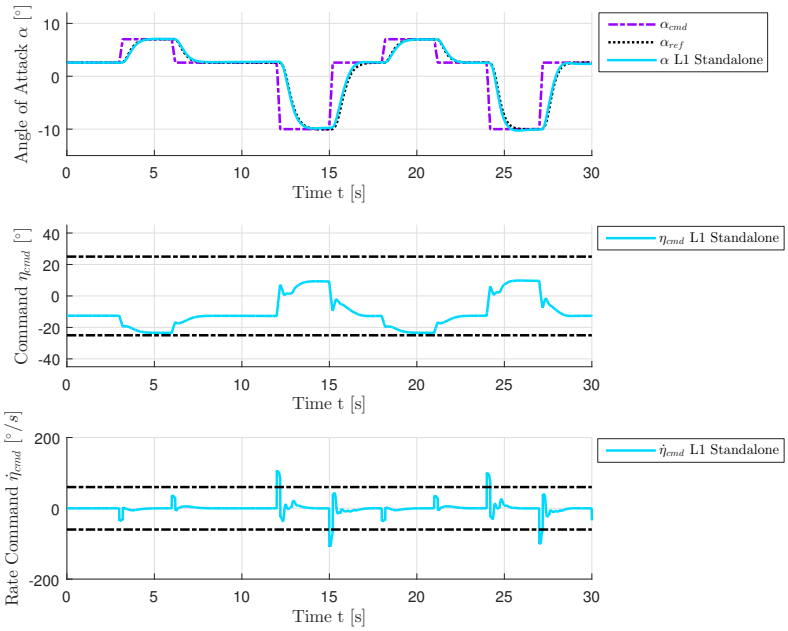

Figure 5.90. – Angle of attack α, elevator command η_{cmd} and elevator command rate $\dot{\eta}_{cmd}$ for example maneuver performed by basic, nonlinear aircraft model with L1 adaptive controller with Eigenstructure Assignment starting at $V_0 = 154.94\frac{m}{s}$ and $h_0 = 5000m$

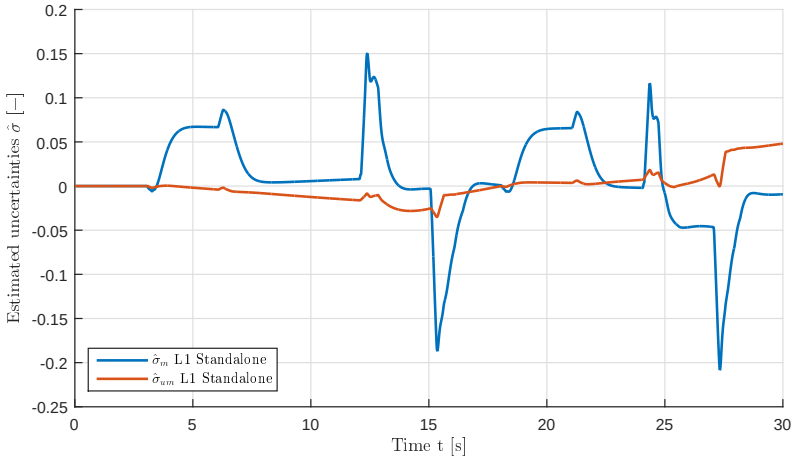

Figure 5.91. – Estimated parameters $\hat{\sigma}$ for example maneuver performed by basic, nonlinear aircraft model with L1 adaptive controller with Eigenstructure Assignment starting at $V_0 = 154.94\frac{m}{s}$ and $h_0 = 5000m$

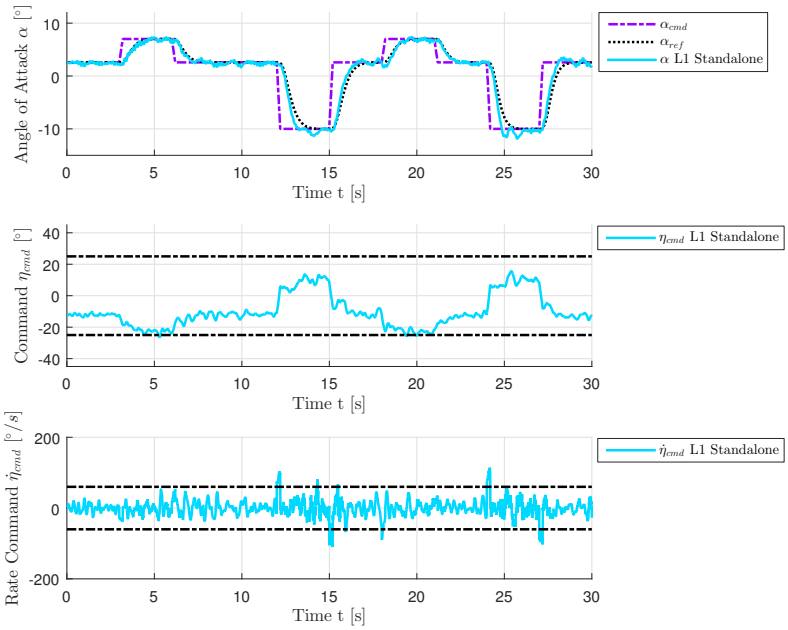

Figure 5.92. – Angle of attack α, elevator command η_{cmd} and elevator command rate $\dot{\eta}_{cmd}$ for example maneuver performed by enhanced, nonlinear aircraft model with L1 adaptive controller with Eigenstructure Assignment starting at $V_0 = 154.94\frac{m}{s}$ and $h_0 = 5000m$

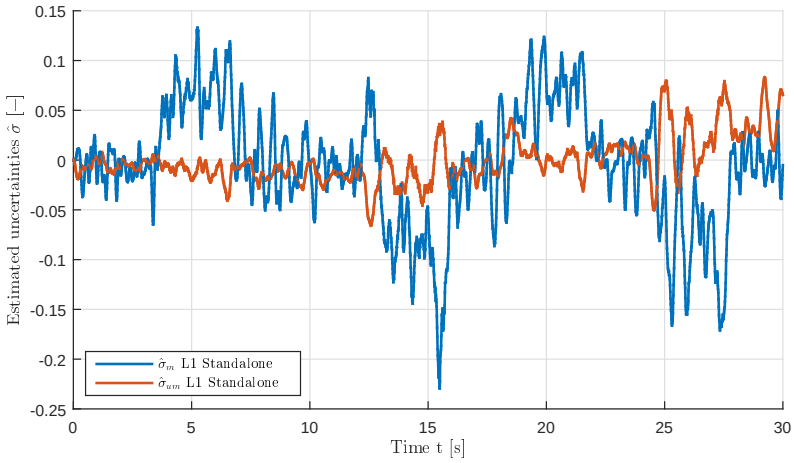

Figure 5.93. – Estimated parameters $\hat{\sigma}$ for example maneuver performed by enhanced, nonlinear aircraft model with L1 adaptive controller with Eigenstructure Assignment starting at $V_0 = 154.94\frac{m}{s}$ and $h_0 = 5000m$

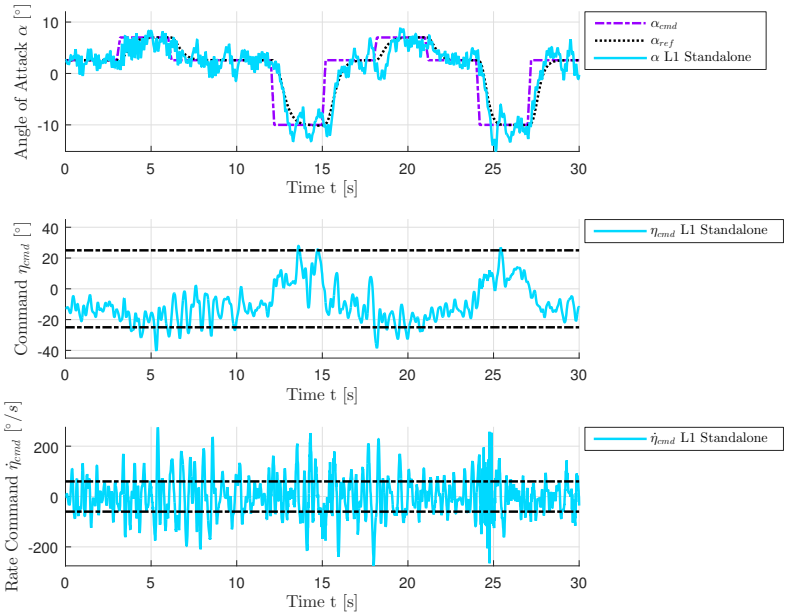

Figure 5.94. – Angle of attack α, elevator command η_{cmd} and elevator command rate $\dot{\eta}_{cmd}$ for example maneuver performed by enhanced, nonlinear aircraft model with L1 adaptive controller with Eigenstructure Assignment starting at $V_0 = 154.94\frac{m}{s}$ and $h_0 = 5000m$ considering severe turbulence

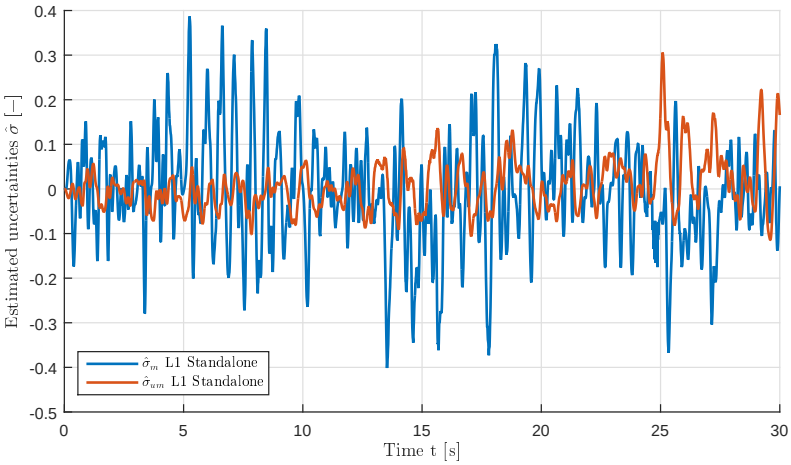

Figure 5.95. – Estimated parameters $\hat{\sigma}$ for example maneuver performed by enhanced, nonlinear aircraft model with L1 adaptive controller with Eigenstructure Assignment starting at $V_0 = 154.94\frac{m}{s}$ and $h_0 = 5000m$ considering severe turbulence

This can even be observed, when considering sever turbulence (probability of exceedance 10^{-5}). The controller is still able to implement the commanded angle of attack α_{cmd}, despite the control signal hits the limits of the actuator considering both rate $\dot{\eta}_{cmd}$ and absolute command η_{cmd}. Although, the system response and the adaptive parameters in Fig. 5.95 indicate that the filtering applied to the sensor signals still leaves room for improvement considering severe turbulence.
The next assessment considers a rapid CG-shift of 5%, which is induced at $t = 10s$ during the maneuver. The system response of basic aircraft model and standalone adaptive controller can be found in Fig. 5.96. One can see that the controller is able to handle this off-nominal situation and follows the reference model response α_{ref}, although overshoots arise in the system response. The accompanying parameter estimations $\hat{\sigma}$ can be found in Fig. 5.97. A similar statement can be made, when a CG-shift of 2% is considered for the enhanced aircraft configuration. This is shown in Fig. 5.98 and Fig. 5.99. Despite the applied reality effects, the controller is still able to compensate for the off-nominal CG-shift.
At last, the impact of hedging on the controller performance is investigated. Fig. 5.100 shows the exemplary maneuver considering the basic aircraft model configuration, where both hedging cases are presented. It can be seen that the two system responses barely differ. In contrast to that, a deviation can be detected considering the enhanced aircraft model configuration in Fig. 5.101. This deviation stems from the fact that the actuator model within the state predictor, which is only active, if hedging is not used, is transformed to discrete-time utilizing Euler's method in order to be able to incorporate rate and absolute saturations of the actuator. This was already addressed in Section 4.4.2. Using Euler's method instead of bilinear transformation generates a larger deviation with regard to dynamics of the originating continuous-time system. Thus, also in terms of performance it shows to be beneficial to apply the hedging term.
In summary, it can be shown that the combination of L1 Adaptive Control and Eigenstructure Assignment is able to precisely shape the plant dynamics, while offering all advantages of an adaptive control law at the same time. This can especially been seen considering the maneuver cases, where a rapid CG-shift is applied. Although, the missing integral portion of the proposed control law leads to a slight residual steady-state error with regard to angle of attack α. This could be subject to future research and a possible solution is highlighted in Chapter 8.

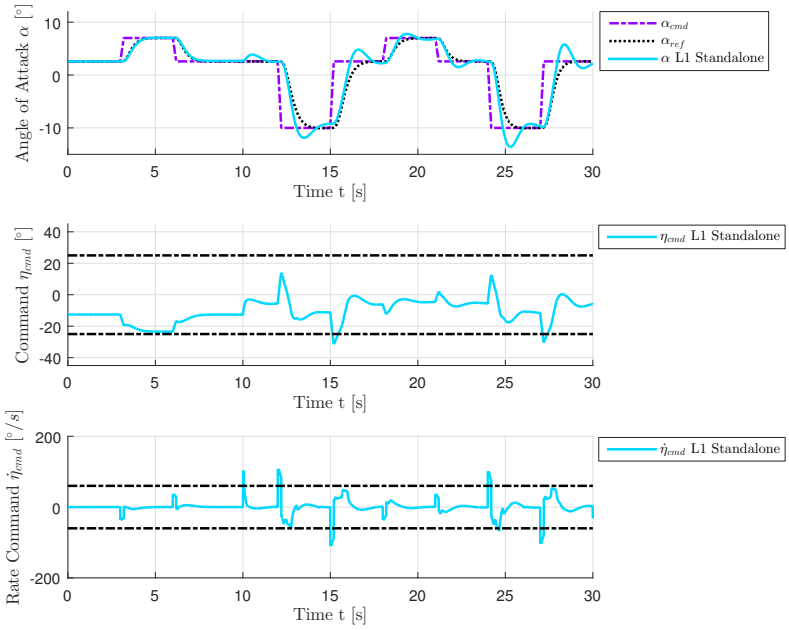

Figure 5.96. – Angle of attack α, elevator command η_{cmd} and elevator command rate $\dot{\eta}_{cmd}$ for example maneuver performed by basic, nonlinear aircraft model with L1 adaptive controller with Eigenstructure Assignment starting at $V_0 = 154.94\frac{m}{s}$ and $h_0 = 5000m$ considering CG-shift of 5% at $t = 10s$

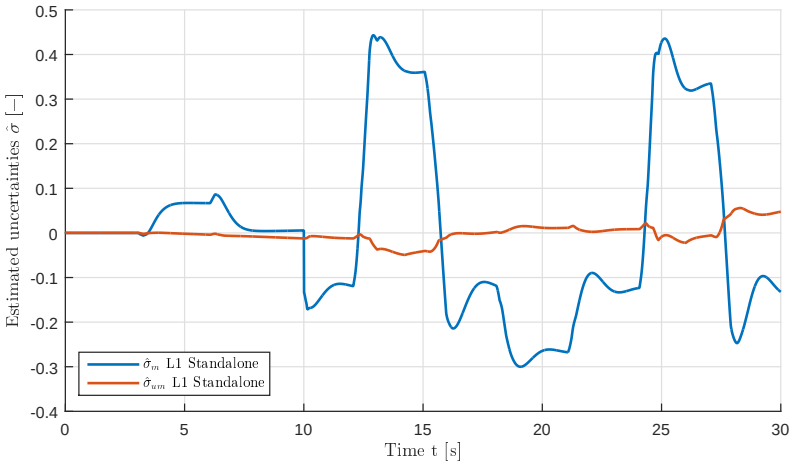

Figure 5.97. – Estimated parameters $\hat{\sigma}$ for example maneuver performed by basic, nonlinear aircraft model with L1 adaptive controller with Eigenstructure Assignment starting at $V_0 = 154.94\frac{m}{s}$ and $h_0 = 5000m$ considering CG-shift of 5% at $t = 10s$

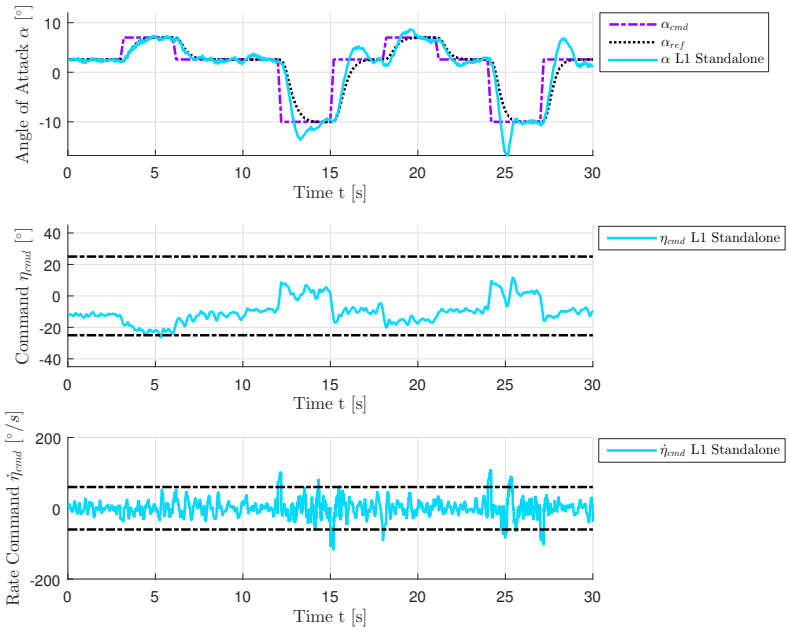

Figure 5.98. – Angle of attack α, elevator command η_{cmd} and elevator command rate $\dot{\eta}_{cmd}$ for example maneuver performed by enhanced, nonlinear aircraft model with L1 adaptive controller with Eigenstructure Assignment starting at $V_0 = 154.94\frac{m}{s}$ and $h_0 = 5000m$ considering CG-shift of 2% at $t = 10s$

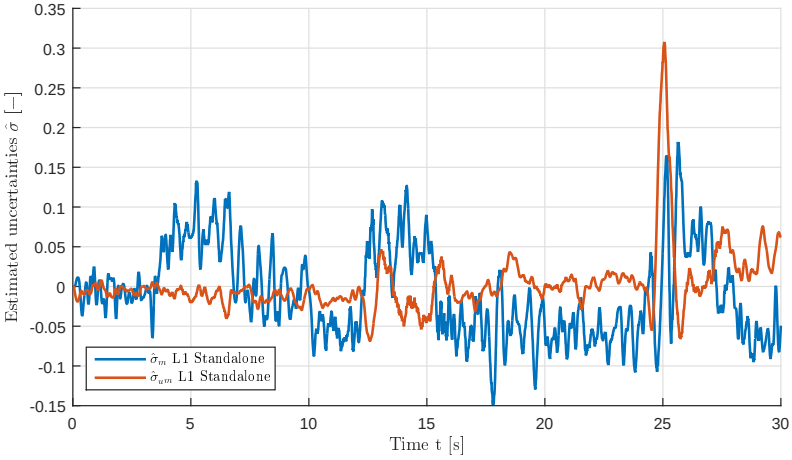

Figure 5.99. – Estimated parameters $\hat{\sigma}$ for example maneuver performed by enhanced, nonlinear aircraft model with L1 adaptive controller with Eigenstructure Assignment starting at $V_0 = 154.94\frac{m}{s}$ and $h_0 = 5000m$ considering CG-shift of 2% at $t = 10s$

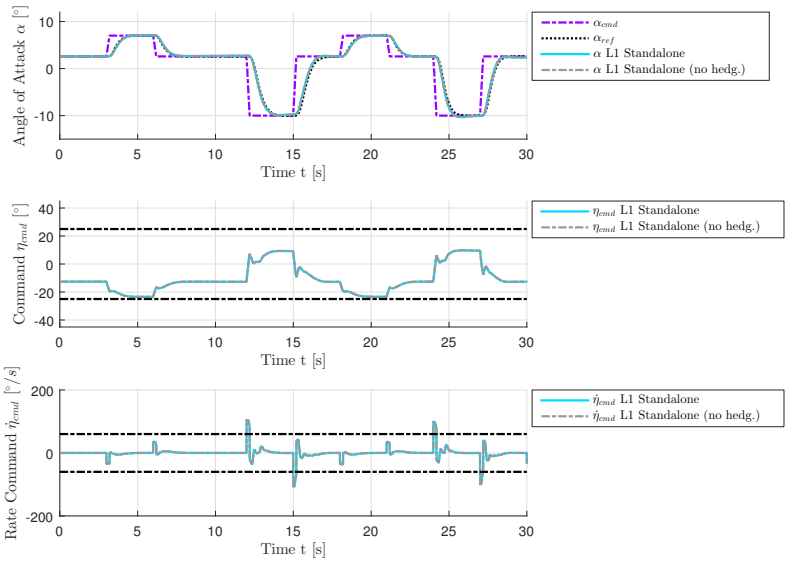

Figure 5.100. – Angle of attack α, elevator command η_{cmd} and elevator command rate $\dot{\eta}_{cmd}$ for example maneuver performed by basic, nonlinear aircraft model with L1 adaptive controller with Eigenstructure Assignment with and without hedging applied at $V_0 = 154.94\frac{m}{s}$ and $h_0 = 5000m$

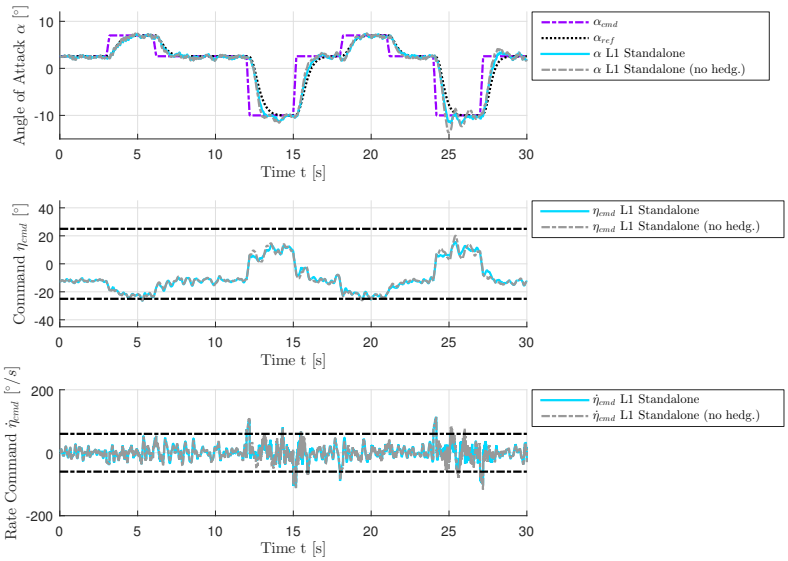

Figure 5.101. – Angle of attack α, elevator command η_{cmd} and elevator command rate $\dot{\eta}_{cmd}$ for example maneuver performed by enhanced, nonlinear aircraft model with L1 adaptive controller with Eigenstructure Assignment with and without hedging applied at $V_0 = 154.94\frac{m}{s}$ and $h_0 = 5000m$

6. Comparison of control laws

This chapter continues to investigate the control laws, which were designed in Chapter 4. This contains the DPI baseline controller, its adaptive augmentations (DPI and Plant Augmentation), $\Delta\dot{q}$ Compensation Law and the standalone L1 adaptive controller. Although preliminary comparisons were already drawn in the last chapter, this part of the thesis profoundly compares performance and robust stability properties of the proposed controller architectures. In particular, the effect of the individual reality effects on the controller performance is investigated, whereat also parameter variations are considered. This includes variations applied to aerodynamic coefficients, CG-shifts, sensor delays, sensor noise, the structural mode model, the actuator model, gust and turbulence. A short summary on the results is provided at the end of this chapter.

6.1. Linear robust stability

Firstly, the control laws are compared with regard to their robust stability properties. For this purpose, the results considering nominal conditions, which were gained in the course of Chapter 5, are again summarized, in order to allow for useful comparisons. After that, robust stability is investigated considering variations on aerodynamic coefficients of the aircraft model.

6.1.1. Nominal conditions

This section provides comparisons of the robust stability assessments made in Chapter 5. These assessments consider nominal conditions, i.e. no variations or uncertainties with respect to the aircraft model are applied. Furthermore, both the actuator (bottleneck) cut and sensor cuts are examined (c.f. Section 5.1.1). The comparisons are carried out for both basic and enhanced aircraft configuration considering the envelope point corresponding to $V_0 = 154.94\frac{m}{s}$ and $h_0 = 5000m$.
Nichols plots for the different control laws with regard to the bottleneck cut are shown in Fig. 6.1 for the basic aircraft configuration. Hedging is activated here for the L1 Adaptive Control based approaches, whereas pitch rate acceleration $\dot{q}$ measurement is not available for the $\Delta\dot{q}$ Compensation Law. It can be seen that the three augmentation approaches match quite good for low frequencies with respect to their frequency response. As it was stated before, the L1 Adaptive Augmentations exhibit larger gain

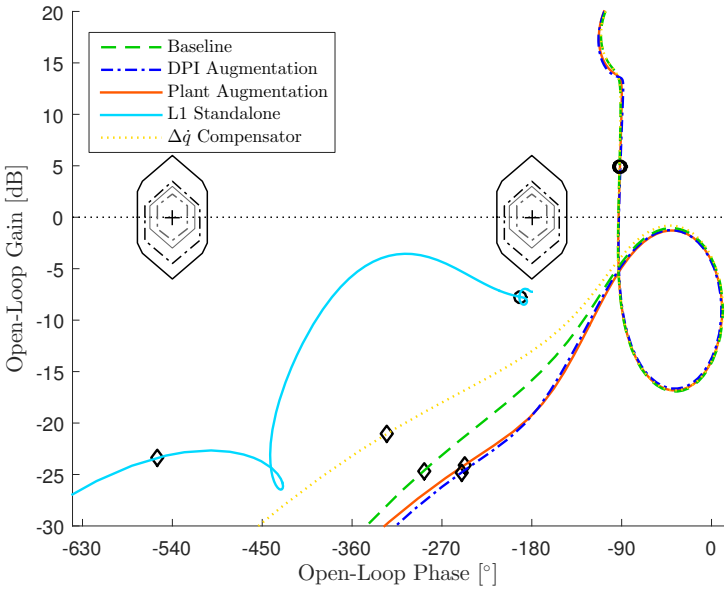

Figure 6.1. – Nichols plot for robust stability comparison of baseline controller, L1 Adaptive Augmentations, $\Delta\dot{q}$ Compensation Law and L1 adaptive controller with Eigenstructure Assignment at $V = 154.94\frac{m}{s}$ generated for η_{cmd} (bottleneck) loop cut (basic aircraft model)

Table 6.1. – Robust stability properties gain margin (GM), phase margin Φ_m, time delay margins (TDM) and corresponding gain-crossover frequencies $\omega_{gc,\Phi}$ and $\omega_{gc,TDM}$ for robust stability comparison of baseline controller, L1 Adaptive Augmentations, $\Delta\dot{q}$ Compensation Law and L1 adaptive controller with Eigenstructure Assignment at $V = 154.94\frac{m}{s}$ generated for η_{cmd} (bottleneck) loop cut (basic aircraft model)

Controller	**GM** $[dB]$	Φ_m $[°]$	$\omega_{gc,\Phi}$ $\left[\frac{rad}{s}\right]$	**TDM** $[s]$	$\omega_{gc,TDM}$ $\left[\frac{rad}{s}\right]$
Baseline	15.85	86.63	0.62	2.424	0.62
	$-\infty$	-273.37	0.62	-7.650	0.62
DPI Augmentation	19.27	87.23	0.62	2.451	0.62
	$-\infty$	-272.77	0.62	-7.664	0.62
Plant Augmentation	19.23	86.95	0.62	2.439	0.62
	$-\infty$	-273.05	0.62	-7.659	0.62
L1 Standalone	23.05	∞	0.00	∞	0.00
	$-\infty$	$-\infty$	0.00	$-\infty$	0.00
$\Delta\dot{q}$ Compensator	13.01	86.64	0.62	2.425	0.62
	$-\infty$	-273.36	0.62	-7.650	0.62

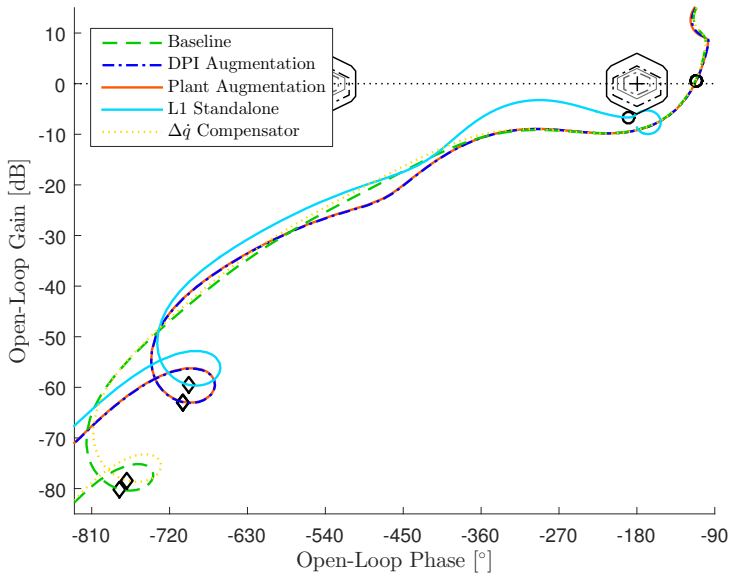

Figure 6.2. – Nichols plot for robust stability comparison of baseline controller, L1 Adaptive Augmentations, $\Delta\dot{q}$ Compensation Law and L1 adaptive controller with Eigenstructure Assignment at $V = 154.94\frac{m}{s}$ generated for η_{cmd} (bottleneck) loop cut (enhanced aircraft model)

Table 6.2. – Robust stability properties gain margin (GM), phase margin Φ_m, time delay margins (TDM) and corresponding gain-crossover frequencies $\omega_{gc,\Phi}$ and $\omega_{gc,TDM}$ for robust stability comparison of baseline controller, L1 Adaptive Augmentations, $\Delta\dot{q}$ Compensation Law and L1 adaptive controller with Eigenstructure Assignment at $V = 154.94\frac{m}{s}$ generated for η_{cmd} (bottleneck) loop cut (enhanced aircraft model)

Controller	**GM** $[dB]$	Φ_m $[°]$	$\omega_{gc,\Phi}$ $\left[\frac{rad}{s}\right]$	**TDM** $[s]$	$\omega_{gc,TDM}$ $\left[\frac{rad}{s}\right]$
Baseline	9.13	66.12	0.41	2.827	0.41
	$-\infty$	-293.88	0.41	-12.565	0.41
DPI Augmentation	9.21	67.00	0.40	2.896	0.40
	$-\infty$	-293.00	0.40	-12.663	0.40
Plant Augmentation	9.20	66.94	0.40	2.893	0.40
	$-\infty$	-293.06	0.40	-12.666	0.40
L1 Standalone	5.98	∞	0.00	∞	0.00
	$-\infty$	$-\infty$	0.00	$-\infty$	0.00
$\Delta\dot{q}$ Compensator	9.20	66.14	0.41	2.833	0.41
	$-\infty$	-293.86	0.41	-12.589	0.41

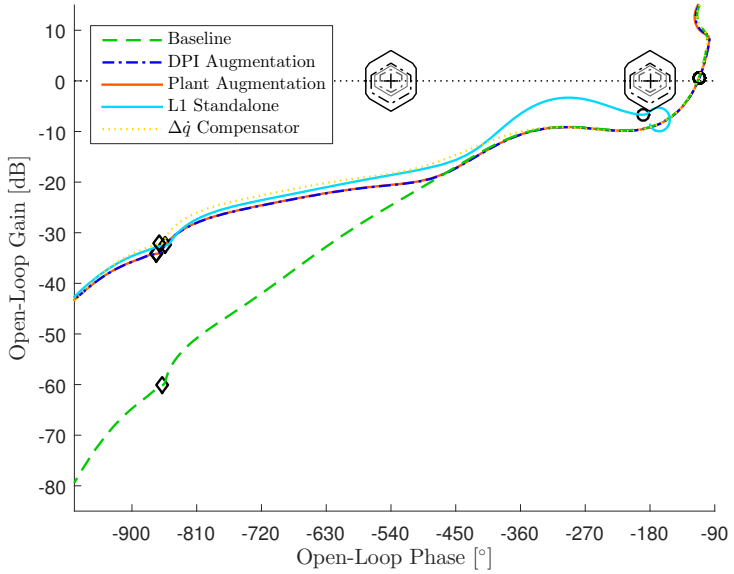

Figure 6.3. – Nichols plot for robust stability comparison of baseline controller, L1 Adaptive Augmentations, $\Delta\dot{q}$ Compensation Law and L1 adaptive controller with Eigenstructure Assignment at $V = 154.94\frac{m}{s}$ generated for η_{cmd} (bottleneck) loop cut (enhanced aircraft model, activated structural mode)

margin compared to the baseline controller, which is slightly reduced considering the $\Delta\dot{q}$ Compensation Law. This observation is confirmed by Table 6.1, where the gain margins, phase margins and TDMs are summarized. It should be emphasized again that the standalone L1 adaptive controller inherits infinite phase margin with regard to the bottleneck cut. These statements also hold for the enhanced aircraft configuration. The accompanying nichols plots can be found in Table 6.2, where the robust stability properties are summarized in Fig. 6.3. In addition to that, the same assessment is also shown in Fig. 6.3, where the simple structural mode model is active. As it was shown in Chapter 5, all control laws fulfill the robust stability margins with regard to frequencies above the first wing bending mode, which is marked by the small diamond. The minimum gain margin in this case is $8dB$.

In the following, also nichols plots are compared, which are generated considering the sensor cuts. Utilizing the basic aircraft model configuration, results with regard to the angle of attack α cut are shown in Fig. 6.4. Compared to the baseline controller, reduced robustness margins can be observed for the L1 Adaptive Augumentations. This is not the case considering the $\Delta\dot{q}$ Compensation Law and the standalone L1 adaptive controller. The corresponding margin calculations can be found in Table 6.3. Considering the enhanced aircraft configuration it can be observed additionally that the standalone L1 adaptive controller exhibits the largest distance from the critical point. This is also confirmed by Table 6.4.

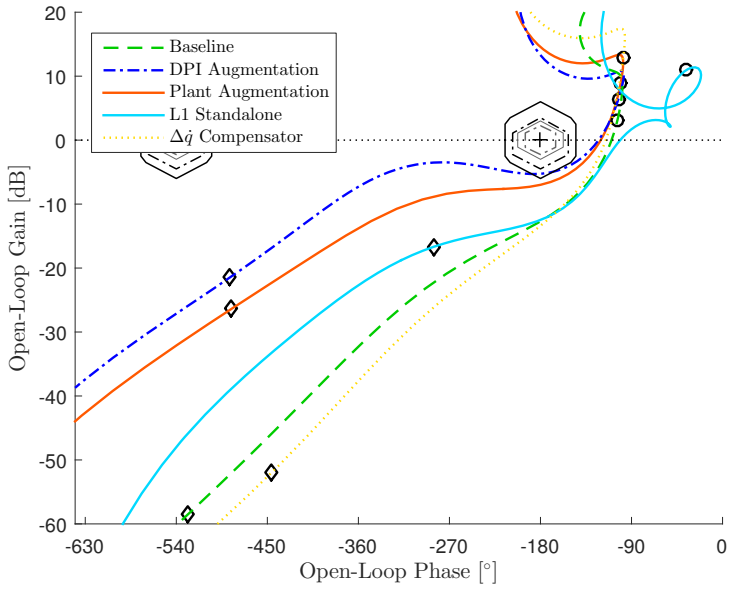

Figure 6.4. – Nichols plot for robust stability comparison of baseline controller, L1 Adaptive Augmentations, $\Delta\dot{q}$ Compensation Law and L1 adaptive controller with Eigenstructure Assignment at $V = 154.94\frac{m}{s}$ generated for α loop cut (basic aircraft model)

Table 6.3. – Robust stability properties gain margin (GM), phase margin Φ_m, time delay margins (TDM) and corresponding gain-crossover frequencies $\omega_{gc,\Phi}$ and $\omega_{gc,TDM}$ for robust stability comparison of baseline controller, L1 Adaptive Augmentations, $\Delta\dot{q}$ Compensation Law and L1 adaptive controller with Eigenstructure Assignment at $V = 154.94\frac{m}{s}$ generated for α loop cut (basic aircraft model)

Controller	**GM** $[dB]$	Φ_m $[°]$	$\omega_{gc,\Phi}$ $\left[\frac{rad}{s}\right]$	**TDM** $[s]$	$\omega_{gc,TDM}$ $\left[\frac{rad}{s}\right]$
Baseline	12.69	70.24	0.55	2.239	0.55
	$-\infty$	-289.76	0.55	-9.235	0.55
DPI Augmentation	5.25	57.43	0.92	1.091	0.92
	-13.29	-302.57	0.92	-5.749	0.92
Plant Augmentation	6.99	59.52	1.16	0.898	1.16
	-14.58	-300.48	1.16	-4.533	1.16
L1 Standalone	12.47	78.84	5.27	0.261	5.27
	$-\infty$	-281.16	5.27	-0.932	5.27
$\Delta\dot{q}$ Compensator	13.38	64.56	1.62	0.696	1.62
	-18.41	-295.44	1.62	-3.183	1.62

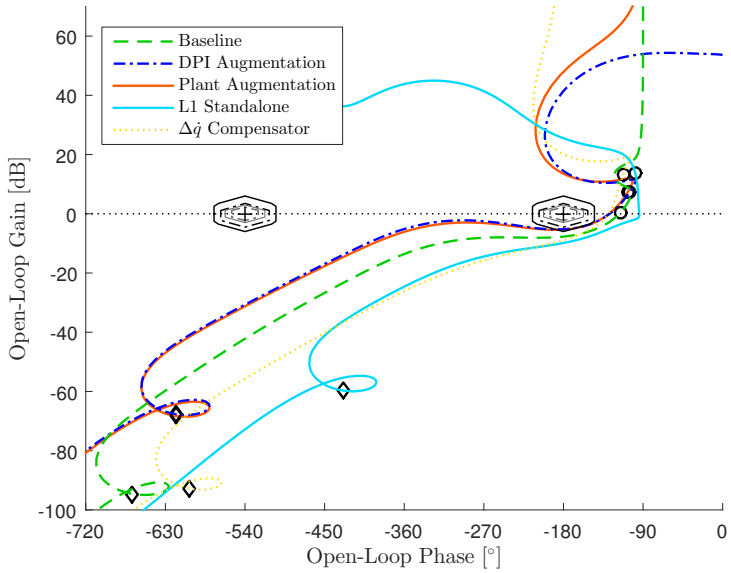

Figure 6.5. – Nichols plot for robust stability comparison of baseline controller, L1 Adaptive Augmentations, $\Delta\dot{q}$ Compensation Law and L1 adaptive controller with Eigenstructure Assignment at $V = 154.94\frac{m}{s}$ generated for α loop cut (enhanced aircraft model)

Table 6.4. – Robust stability properties gain margin (GM), phase margin Φ_m, time delay margins (TDM) and corresponding gain-crossover frequencies $\omega_{gc,\Phi}$ and $\omega_{gc,TDM}$ for robust stability comparison of baseline controller, L1 Adaptive Augmentations, $\Delta\dot{q}$ Compensation Law and L1 adaptive controller with Eigenstructure Assignment at $V = 154.94\frac{m}{s}$ generated for α loop cut (enhanced aircraft model)

Controller	**GM** $[dB]$	Φ_m $[°]$	$\omega_{gc,\Phi}$ $\left[\frac{rad}{s}\right]$	**TDM** $[s]$	$\omega_{gc,TDM}$ $\left[\frac{rad}{s}\right]$
Baseline	7.72	63.12	0.40	2.777	0.40
	$-\infty$	-296.88	0.40	-13.063	0.40
DPI Augmentation	5.21	52.22	0.93	0.981	0.93
	-14.47	-307.78	0.93	-5.781	0.93
Plant Augmentation	5.34	51.43	0.96	0.935	0.96
	-13.54	-308.57	0.96	-5.609	0.96
L1 Standalone	9.85	85.76	1.99	0.754	1.99
	-25.51	-274.24	1.99	-2.411	1.99
$\Delta\dot{q}$ Compensator	8.87	50.79	1.41	0.628	1.41
	-20.15	-309.21	1.41	-3.823	1.41

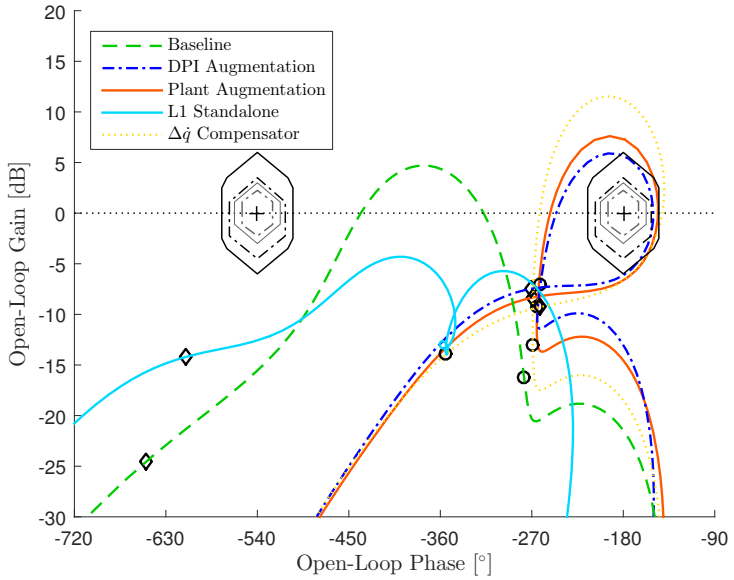

Figure 6.6. – Nichols plot for robust stability comparison of baseline controller, L1 Adaptive Augmentations, $\Delta\dot{q}$ Compensation Law and L1 adaptive controller with Eigenstructure Assignment at $V = 154.94\frac{m}{s}$ generated for q loop cut (basic aircraft model)

Table 6.5. – Robust stability properties gain margin (GM), phase margin Φ_m, time delay margins (TDM) and corresponding gain-crossover frequencies $\omega_{gc,\Phi}$ and $\omega_{gc,TDM}$ for robust stability comparison of baseline controller, L1 Adaptive Augmentations, $\Delta\dot{q}$ Compensation Law and L1 adaptive controller with Eigenstructure Assignment at $V = 154.94\frac{m}{s}$ generated for q loop cut (basic aircraft model)

Controller	**GM** $[dB]$	Φ_m $[°]$	$\omega_{gc,\Phi}$ $\left[\frac{rad}{s}\right]$	**TDM** $[s]$	$\omega_{gc,TDM}$ $\left[\frac{rad}{s}\right]$
Baseline	15.54	101.74	4.39	0.404	4.39
	$-\infty$	-137.46	1.92	-1.026	4.39
DPI Augmentation	6.13	29.35	8.20	0.062	8.20
	-5.62	-65.95	0.93	-0.704	8.20
Plant Augmentation	6.62	34.07	8.41	0.071	8.41
	-7.30	-71.97	1.14	-0.676	8.41
L1 Standalone	12.56	∞	0.00	∞	0.00
	$-\infty$	$-\infty$	0.00	$-\infty$	0.00
$\Delta\dot{q}$ Compensator	6.63	38.43	9.56	0.070	9.56
	-11.17	-82.27	1.63	-0.587	9.56

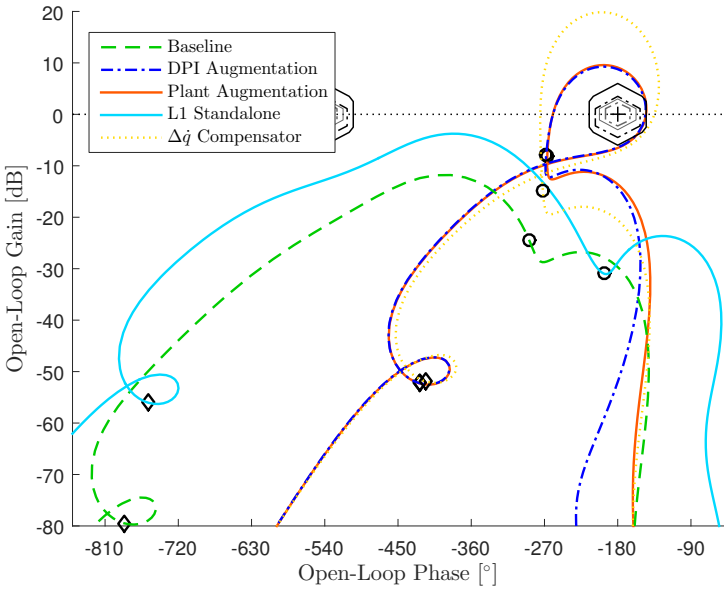

Figure 6.7. – Nichols plot for robust stability comparison of baseline controller, L1 Adaptive Augmentations, $\Delta\dot{q}$ Compensation Law and L1 adaptive controller with Eigenstructure Assignment at $V = 154.94\frac{m}{s}$ generated for q loop cut (enhanced aircraft model)

Table 6.6. – Robust stability properties gain margin (GM), phase margin Φ_m, time delay margins (TDM) and corresponding gain-crossover frequencies $\omega_{gc,\Phi}$ and $\omega_{gc,TDM}$ for robust stability comparison of baseline controller, L1 Adaptive Augmentations, $\Delta\dot{q}$ Compensation Law and L1 adaptive controller with Eigenstructure Assignment at $V = 154.94\frac{m}{s}$ generated for q loop cut (enhanced aircraft model)

Controller	**GM** $[dB]$	Φ_m $[°]$	$\omega_{gc,\Phi}$ $\left[\frac{rad}{s}\right]$	**TDM** $[s]$	$\omega_{gc,TDM}$ $\left[\frac{rad}{s}\right]$
Baseline	21.76	∞	0.00	∞	0.00
	$-\infty$	$-\infty$	0.00	$-\infty$	0.00
DPI Augmentation	6.44	33.97	4.69	0.126	4.69
	-8.77	-79.55	0.88	-1.213	4.69
Plant Augmentation	6.53	34.77	4.70	0.129	4.70
	-9.09	-79.69	0.90	-1.208	4.70
L1 Standalone	12.77	∞	0.00	∞	0.00
	$-\infty$	$-\infty$	0.00	$-\infty$	0.00
$\Delta\dot{q}$ Compensator	7.26	44.99	5.36	0.146	5.36
	-19.28	-95.20	1.60	-1.025	5.36

The next sensor cut, which the pitch rate q cut, is examined in Fig. 6.6 and Table 6.5 considering the basic aircraft model. As it was discussed before in Chapter 5, the frequency responses of the L1 Adaptive Augmentations as well as the $\Delta\dot{q}$ Compensation Law generate a loop around the critical point. This shows that a loss of the pitch rate q measurement would lead to an unstable closed-loop in this cases. Fig. 6.7 reveals that the loops are also generated in case of the enhanced aircraft configuration. The accompanying robust stability margins can be found in Table 6.6. It has to be noted again that according to [111, pp. 25-27] compliance with the required robust stability margins has to be proven only with regard to the bottleneck cut.

6.1.2. Uncertainty w.r.t. aerodynamic coefficients

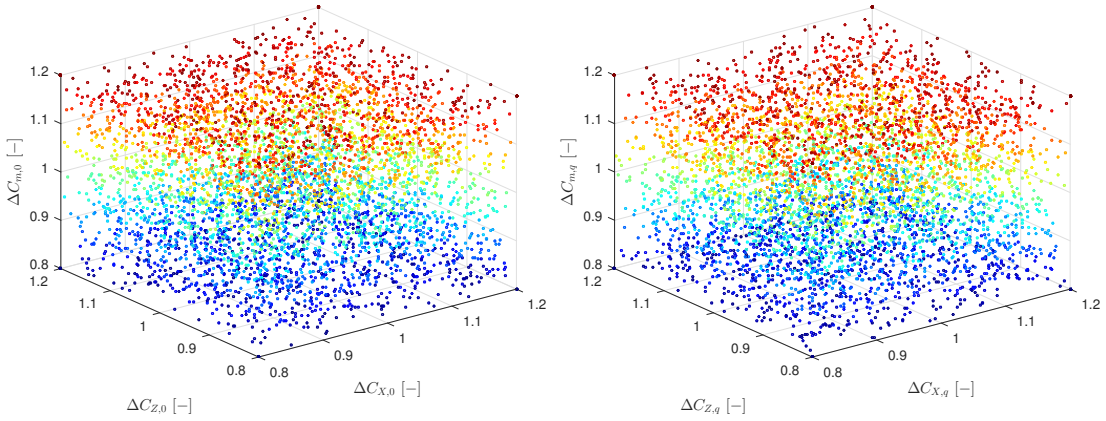

(a) Variation of $\Delta C_{X,0}$, $\Delta C_{Z,0}$, $\Delta C_{M,0}$ **(b)** Variation of $\Delta C_{X,q}$, $\Delta C_{Z,q}$, $\Delta C_{M,q}$

Figure 6.8. – Variation of multiplicative uncertainties applied to aerodynamic coefficients $C_{X,0}$, $C_{X,q}$, $C_{Z,0}$, $C_{Z,q}$, $C_{m,0}$ and $C_{m,q}$

In the next step, the robust stability assessment is carried out under consideration of uncertainties with regard to the aerodynamic coefficients of the aircraft model. According to [111, p. 27] this investigation is required in terms of aircraft certification. It should be shown that the closed-loop still inherits specified minimum stability margins, although 20% variation on critical aerodynamic coefficients is induced [111, p. 27]. The reduced stability margins applied here can be found in Table 5.1, which is introduced in Section 5.1.1. More specifically, in this section the grey diamonds should be interpreted as minimum robustness margins, while nichols plots are considered.
For the robust stability assessment, the bottleneck cut and the exemplary envelope point corresponding to $V_0 = 154.94\frac{m}{s}$ and $h_0 = 5000m$ are considered. Furthermore, the results are generated utilizing the enhanced aircraft configuration. In order to suit to the requirements shown above, the assessments feature multiplicative uncertainties simultaneously applied to the force coefficients $C_{X,0}$, $C_{Z,0}$, $C_{X,q}$ and $C_{Z,q}$, as well as to the moment coefficients $C_{m,0}$ and $C_{m,q}$ (c.f. Section 2.1.1). The corresponding factors

are denoted with an additional "Δ". Thus, in case of the zero moment coefficient, the value applied to the aircraft dynamics would result in

$$C_{m,0,perturb} = C_{m,0} \cdot \Delta C_{m,0}. \tag{6.1}$$

In total 5064 variations of the factors $\Delta C_{X,0}$, $\Delta C_{Z,0}$, $\Delta C_{X,q}$, $\Delta C_{Z,q}$, $\Delta C_{m,0}$ and $\Delta C_{m,q}$ are randomly generated considering a value range of $[0.8; 1.2]$ [111, p. 27] and taking the edges of the resulting hypercube into account. The resulting factors are depicted in Fig. 6.8.

Fig. 6.9 shows the resulting frequency responses for the baseline controller considering the bottleneck cut, where the introduced variations of the aerodynamic coefficients are applied to the enhanced aircraft model. Thereby, the frequency of the nominal configuration is plotted by means of the black, dashed-dotted line. As it was stated before, for these assessments the grey diamonds mark the required robustness margins. It can be seen that the DPI baseline controller fulfills the robust stability requirements with regard to aerodynamic uncertainty. The scattering of the results can be observed in Table 6.7, where minimum and maximum values of gain margin, phase margin and TDM can be found. In addition, the corresponding mean values and standard deviations are calculated.

In comparison to the baseline controller, one can see in Fig. 6.10 that the scattering is higher with regard to the gain margin, when the DPI Augmentation is utilized. Nevertheless, the requirements with regard to both margins are met. Furthermore, the distance of the most critical frequency response to the critical point is larger than the most critical frequency response of the baseline controller. This also reflects in Table 6.8, where it can be seen that the minimum gain and phase margins increase by means of the DPI Augmentation. In order to further increase comparability, also the percentage of the values with respect to the corresponding values belonging to the baseline controller results are given in the table. Basically the same statement can also be made for the Plant Augmentation, whose results are shown in Fig. 6.11 and Table 6.9

The resulting frequency responses belonging to the $\Delta\dot{q}$ Compensation Law are presented in Fig. 6.12. It can be observed from this diagram and from Table 6.10 that the scattering with regard to the maximum gain margin increases. On the other hand, the minimum gain margin is slightly smaller than for the L1 Adaptive Augmentations. Nevertheless, the $\Delta\dot{q}$ Compensation Law still offers an advantage compared to the baseline controller here. This holds also for the phase margin. In order to summarize, the required robustness margins are fulfilled also for this control law.

The last control law considered in this section is the L1 adaptive controller with Eigenstructure Assignment. The frequency responses and the resulting margins are shown in Fig. 6.13 and Table 6.11, respectively. In this case it can be stated that the scattering with regard to the nominal frequency response is reduced in comparison to the adaptive augmentations. Although, three uncertainty cases exist, where the

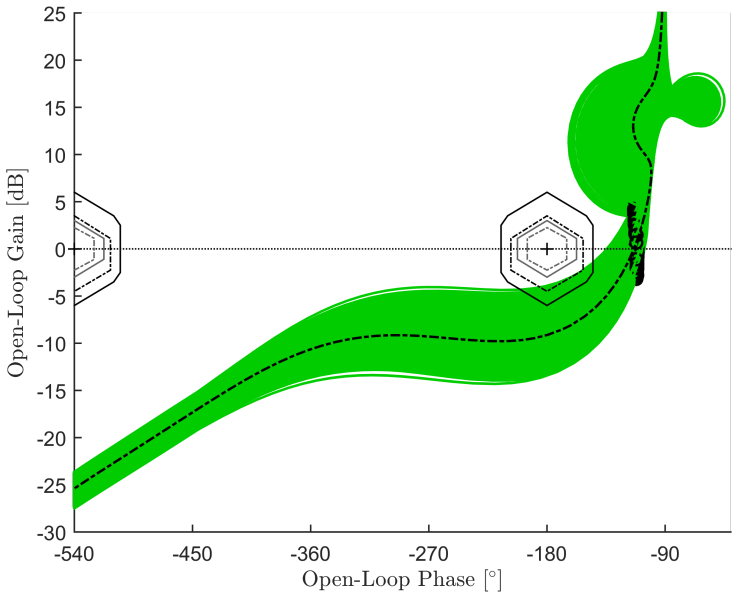

Figure 6.9. – Nichols plot for robust stability assessment of baseline controller at $V = 154.94\frac{m}{s}$ generated for η_{cmd} (bottleneck) loop cut considering uncertainty w.r.t aerodynamic coefficients (enhanced aircraft model)

Table 6.7. – Robust stability properties gain margin (GM), phase margin Φ_m, time delay margins (TDM) and corresponding gain-crossover frequencies $\omega_{gc,\Phi}$ and $\omega_{gc,TDM}$ for robust stability assessment of baseline controller at $V = 154.94\frac{m}{s}$ generated for η_{cmd} (bottleneck) loop cut considering uncertainty w.r.t aerodynamic coefficients (enhanced aircraft model)

	GM $[dB]$	Φ_m $[°]$	**TDM** $[s]$
max	13.42	74.273	5.22
min	3.90	45.412	1.10
$\varnothing$	9.06	65.202	2.88
σ	1.861	5.5126	0.791

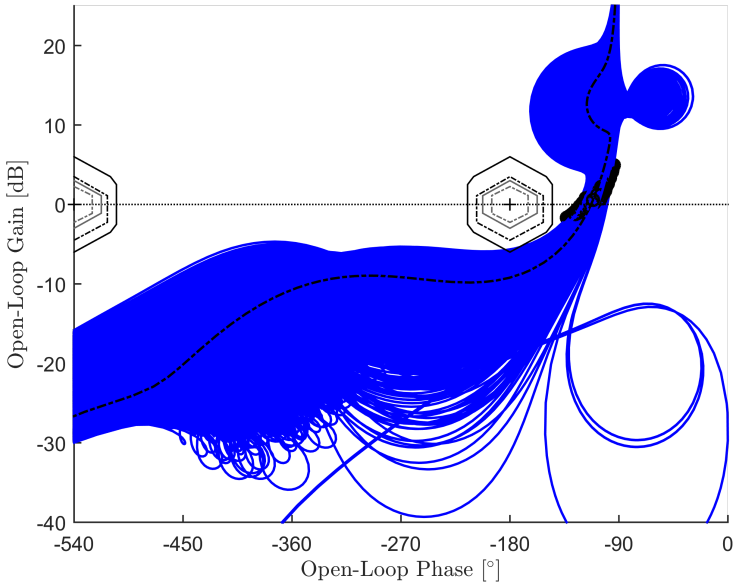

Figure 6.10. – Nichols plot for robust stability assessment of DPI Augmentation at $V = 154.94\frac{m}{s}$ generated for η_{cmd} (bottleneck) loop cut considering uncertainty w.r.t aerodynamic coefficients (enhanced aircraft model)

Table 6.8. – Robust stability properties gain margin (GM), phase margin Φ_m, time delay margins (TDM) and corresponding gain-crossover frequencies $\omega_{gc,\Phi}$ and $\omega_{gc,TDM}$ for robust stability assessment of DPI Augmentation and comparison to baseline controller at $V = 154.94\frac{m}{s}$ generated for η_{cmd} (bottleneck) loop cut considering uncertainty w.r.t aerodynamic coefficients (enhanced aircraft model)

	GM $[dB]$	Φ_m $[^\circ]$	**TDM** $[s]$	$\mathbf{GM}_{rel}$ $[\%]$	$\Phi_{m,rel}$ $[\%]$	$\mathbf{TDM}_{rel}$ $[\%]$
max	20.44	80.383	3.43	152.3%	108.2%	65.7%
min	5.65	55.219	2.14	144.8%	121.6%	195.2%
$\varnothing$	9.71	67.043	2.88	107.1%	102.8%	100.1%
σ	2.593	5.1221	0.299	139.3%	92.9%	37.7%

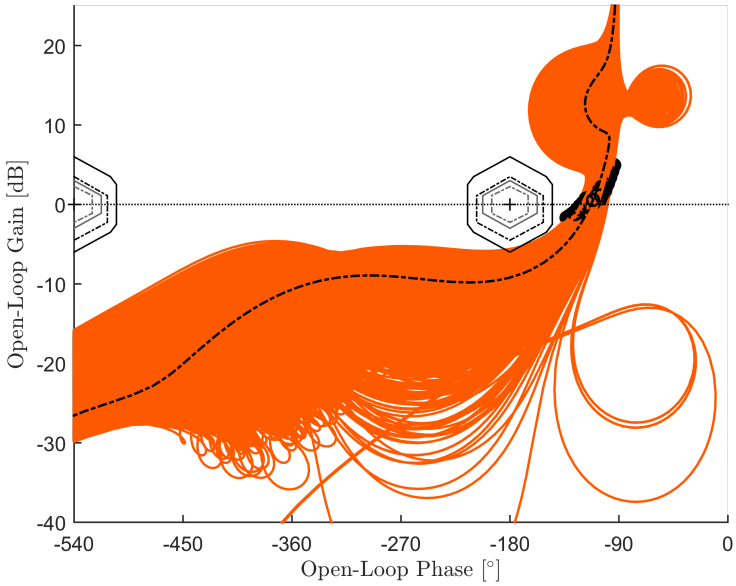

Figure 6.11. – Nichols plot for robust stability assessment of Plant Augmentation at $V = 154.94\frac{m}{s}$ generated for η_{cmd} (bottleneck) loop cut considering uncertainty w.r.t aerodynamic coefficients (enhanced aircraft model)

Table 6.9. – Robust stability properties gain margin (GM), phase margin Φ_m, time delay margins (TDM) and corresponding gain-crossover frequencies $\omega_{gc,\Phi}$ and $\omega_{gc,TDM}$ for robust stability assessment of Plant Augmentation and comparison to baseline controller at $V = 154.94\frac{m}{s}$ generated for η_{cmd} (bottleneck) loop cut considering uncertainty w.r.t aerodynamic coefficients (enhanced aircraft model)

	GM $[dB]$	Φ_m $[^\circ]$	**TDM** $[s]$	$\mathbf{GM}_{rel}$ $[\%]$	$\Phi_{m,rel}$ $[\%]$	$\mathbf{TDM}_{rel}$ $[\%]$
max	20.72	80.763	3.41	154.4%	108.7%	65.4%
min	5.59	54.851	2.15	143.3%	120.8%	195.5%
∅	9.72	66.988	2.88	107.3%	102.7%	100.0%
σ	2.644	5.2183	0.295	142.1%	94.7%	37.2%

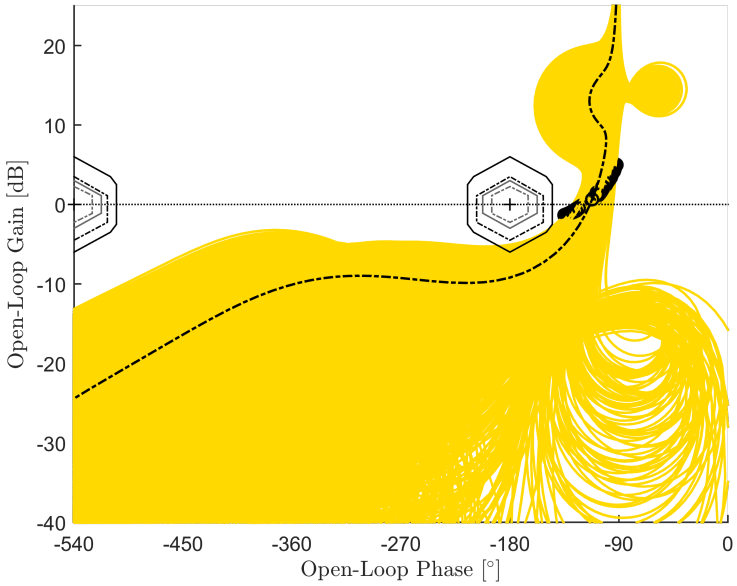

Figure 6.12. – Nichols plot for robust stability assessment of $\Delta\dot{q}$ Compensation Law at $V = 154.94\frac{m}{s}$ generated for η_{cmd} (bottleneck) loop cut considering uncertainty w.r.t aerodynamic coefficients (enhanced aircraft model)

Table 6.10. – Robust stability properties gain margin (GM), phase margin Φ_m, time delay margins (TDM) and corresponding gain-crossover frequencies $\omega_{gc,\Phi}$ and $\omega_{gc,TDM}$ for robust stability assessment of $\Delta\dot{q}$ Compensation Law and comparison to baseline controller at $V = 154.94\frac{m}{s}$ generated for η_{cmd} (bottleneck) loop cut considering uncertainty w.r.t aerodynamic coefficients (enhanced aircraft model)

	GM $[dB]$	Φ_m $[°]$	**TDM** $[s]$	$\mathbf{GM}_{rel}$ $[\%]$	$\Phi_{m,rel}$ $[\%]$	$\mathbf{TDM}_{rel}$ $[\%]$
max	53.08	85.126	3.09	395.6%	114.6%	59.1%
min	5.06	51.711	2.24	129.7%	113.9%	204.0%
$\varnothing$	15.18	66.345	2.80	167.5%	101.8%	97.4%
σ	10.566	6.2098	0.183	567.8%	112.6%	23.1%

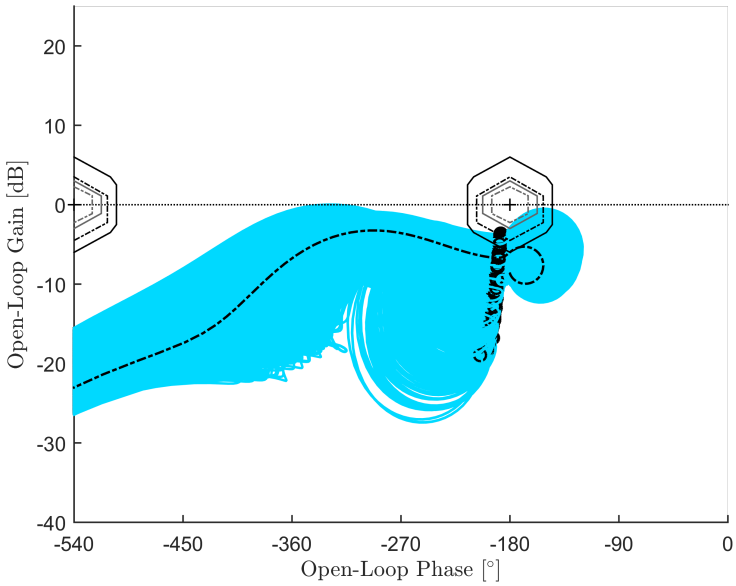

Figure 6.13. – Nichols plot for robust stability assessment of L1 adaptive controller with Eigenstructure Assignment at $V = 154.94\frac{m}{s}$ generated for η_{cmd} (bottleneck) loop cut considering uncertainty w.r.t aerodynamic coefficients (enhanced aircraft model)

Table 6.11. – Robust stability properties gain margin (GM), phase margin Φ_m, time delay margins (TDM) and corresponding gain-crossover frequencies $\omega_{gc,\Phi}$ and $\omega_{gc,TDM}$ for robust stability assessment of L1 adaptive controller with Eigenstructure Assignment and comparison to baseline controller at $V = 154.94\frac{m}{s}$ generated for η_{cmd} (bottleneck) loop cut considering uncertainty w.r.t aerodynamic coefficients (enhanced aircraft model)

	GM $[dB]$	Φ_m $[°]$	**TDM** $[s]$	$\mathbf{GM}_{rel}$ $[\%]$	$\Phi_{m,rel}$ $[\%]$	$\mathbf{TDM}_{rel}$ $[\%]$
max	26.45	∞	∞	197.1%	-	-
min	2.87	206.128	0.93	73.6%	453.9%	85.1%
$\varnothing$	8.86	-	-	97.7%	-	-
σ	6.758	-	-	363.2%	-	-

Table 6.12. – Critical variations for robust stability assessment of L1 adaptive controller with Eigenstructure Assignment and comparison to baseline controller at $V = 154.94\frac{m}{s}$ generated for η_{cmd} (bottleneck) loop cut considering uncertainty w.r.t aerodynamic coefficients (enhanced aircraft model)

	$\Delta C_{X,0}$	$\Delta C_{X,q}$	$\Delta C_{Z,0}$	$\Delta C_{Z,q}$	$\Delta C_{m,0}$	$\Delta C_{m,q}$
1	0.8	1.2	1.2	1.2	0.8	1.2
2	0.8	0.8	1.2	1.2	0.8	1.2
3	0.8	1.2	1.2	0.8	1.2	1.2

robust stability margins are harmed. This can be observed in a zoomed version of the nichols plot in Fig. 6.14. In this case the innermost diamond, which belongs to frequencies $\omega < \omega_{0,ph}$, is slightly crossed by three of the 5065 frequency responses. The concerning variations are summarized in Table 6.12. It can be observed that all variations represent corner cases here. Thus, in case of a real aircraft FCS certification attempt, this controller would need further tuning to avoid this. Note also that this would also require the consideration of a fine grid of different envelope points, whereas only one exemplary envelope point is examined here.

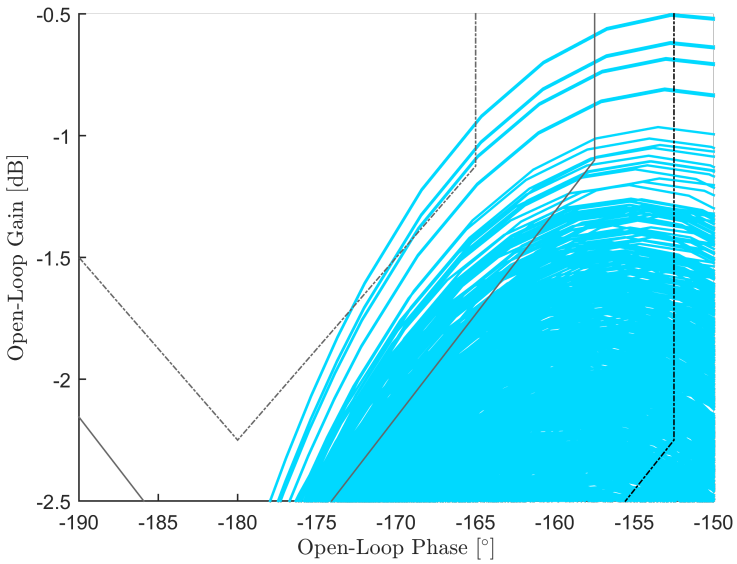

Figure 6.14. – Nichols plot for robust stability assessment of L1 adaptive controller with Eigenstructure Assignment at $V = 154.94\frac{m}{s}$ generated for η_{cmd} (bottleneck) loop cut considering uncertainty w.r.t aerodynamic coefficients (enhanced aircraft model, zoom for critical uncertainty cases)

6.2. Performance

After comparisons with regard to robust stability were drawn in the last section, the remainder of this chapter concentrates on performance assessments. Firstly, the performances of the controllers presented in Chapter 4 are compared by means of the assessments made in Chapter 5, which include step responses and the exemplary maneuver. Nominal conditions are applied here, i.e. no uncertainty is induced except for turbulence considering the enhanced aircraft model.
In the next step, the effect of individual uncertainties on the controller performance is thoroughly investigated. For this purpose, uncertainties are firstly applied on aerodynamic coefficients, as it was already shown in Section 6.1.2. Here, uncertainties are also induced individually on force and moment coefficients. After that, CG-shifts are applied to the aircraft model. For the sake of comparison, results gained in Chapter 5 are summarized and can also be compared by means of performance metrics. Furthermore, variations on the point in time, where the CG-shift is induced, are examined. The next assessments feature variations on sensor delay and noise. These are also individually investigated for the particular sensor measurements, which include angle of attack α, pitch rate q and elevator deflection η. Moreover, variations with regard to the dynamics of the simple structural mode model and the actuator dynamics are considered. The last assessments focus on atmospheric disturbance, where the effect of gust and turbulence on the controller performance is examined.

6.2.1. Nominal conditions

In this section, results gained in Chapter 5, in particular Section 5.2.1.2, Section 5.2.2.3, Section 5.2.3.2 and Section 5.2.4.2, are revisited in order to increase comparability of the control laws designed in the course of this thesis. Thus, step responses considering one envelope point and performance assessments using the exemplary maneuver are investigated. In addition to simulation plots, also the corresponding performance metrics $M_{\mathcal{L}_2}$, $M_{\mathcal{L}_\infty}$ and $M_{\mathcal{L}_{2,act}}$, which were introduced in Eq. (5.6a), Eq. (5.6b) and Eq. (5.7), are provided. It holds for all metrics that a smaller value indicates better performance. The definition of the metrics can be found in Section 5.1.2.
At first, the step responses of the different control laws combined with the basic aircraft model are investigated considering the envelope point corresponding to $V_0 = 154.94\frac{m}{s}$ and $h_0 = 5000m$. Although, the step responses only marginally differ considering a short time scale in Fig. 6.15 and Table 6.13, differences can be observed considering a large time scale in Fig. 6.16 and Table 6.14. The residual steady-state error, which was already discussed in Section 5.2.4.2, can be observed for the standalone L1 adaptive controller. Furthermore, the phugoid has a larger impact on the response considering the L1 Adaptive Augmentations compared to DPI baseline controller and $\Delta\dot{q}$ Compensation Law. Moreover, it can be seen in Table 6.14 that the metrics belonging to DPI baseline controller and $\Delta\dot{q}$ Compensation Law barely differ. Resulting step

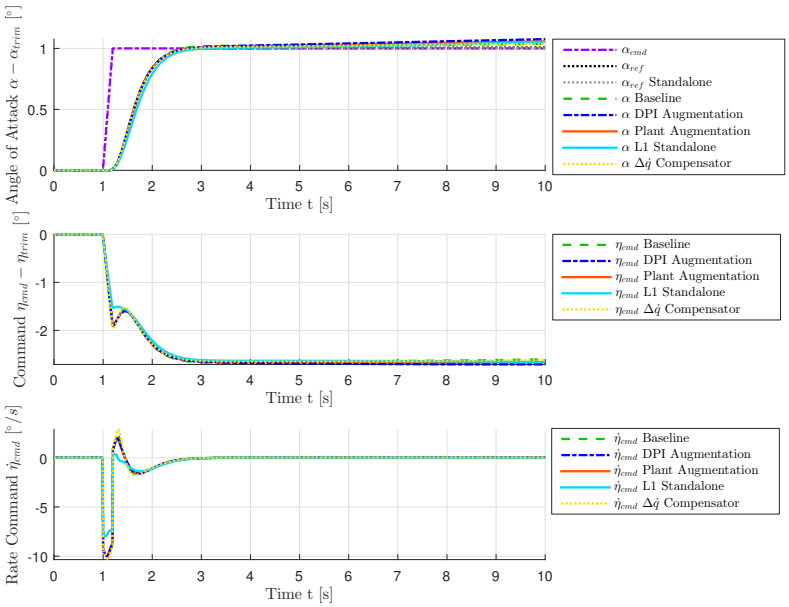

Figure 6.15. – Comparison of α_{cmd} step responses of basic, nonlinear aircraft model in combination with baseline controller, L1 Adaptive Augmentations, $\Delta\dot{q}$ Compensation Law and L1 adaptive controller with Eigenstructure Assignment at $V_0 = 154.94\frac{m}{s}$

Table 6.13. – Comparison of performance metrics $M_{\mathcal{L}_2}$, $M_{\mathcal{L}_\infty}$ and $M_{\mathcal{L}_{2,act}}$ generated from step responses of basic, nonlinear aircraft model in combination with baseline controller, L1 Adaptive Augmentations, $\Delta\dot{q}$ Compensation Law and L1 adaptive controller with Eigenstructure Assignment at $V_0 = 154.94\frac{m}{s}$

Controller	$M_{\mathcal{L}_2}$ $[-]$	$M_{\mathcal{L}_\infty}$ $[-]$	$M_{\mathcal{L}_{2,act}}$ $[-]$
Baseline	0.032	0.0005	0.788
DPI Augmentation	0.064	0.0012	0.777
Plant Augmentation	0.049	0.0009	0.774
L1 Standalone	0.050	0.0014	0.628
$\Delta\dot{q}$ Compensator	0.031	0.0006	0.808

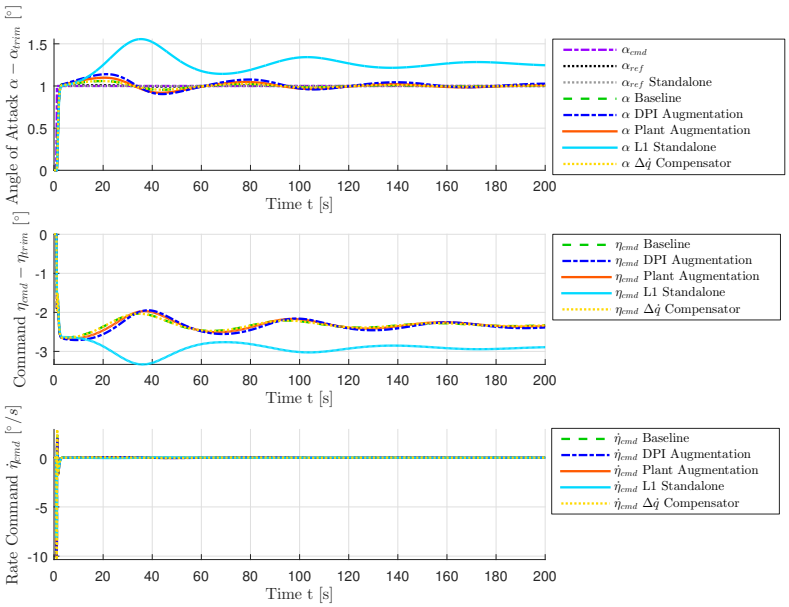

Figure 6.16. – Comparison of α_{cmd} step responses of basic, nonlinear aircraft model in combination with baseline controller, L1 Adaptive Augmentations, $\Delta\dot{q}$ Compensation Law and L1 adaptive controller with Eigenstructure Assignment at $V_0 = 154.94\frac{m}{s}$ for large timescale

Table 6.14. – Comparison of performance metrics $M_{\mathcal{L}_2}$, $M_{\mathcal{L}_\infty}$ and $M_{\mathcal{L}_{2,act}}$ generated from step responses of basic, nonlinear aircraft model in combination with baseline controller, L1 Adaptive Augmentations, $\Delta\dot{q}$ Compensation Law and L1 adaptive controller with Eigenstructure Assignment at $V_0 = 154.94\frac{m}{s}$ for large timescale

Controller	$M_{\mathcal{L}_2}$ $[-]$	$M_{\mathcal{L}_\infty}$ $[-]$	$M_{\mathcal{L}_{2,act}}$ $[-]$
Baseline	0.143	0.0008	0.789
DPI Augmentation	0.387	0.0023	0.778
Plant Augmentation	0.269	0.0015	0.775
L1 Standalone	2.234	0.0097	0.629
$\Delta\dot{q}$ Compensator	0.143	0.0008	0.808

responses and performance metrics, where the linear aircraft dynamics are utilized, can additionally be found in Fig. A.68, Table A.91, Fig. A.69, Table A.92, Fig. A.70, and Table A.93, which are included in Appendix A.7.1.
Utilizing the enhanced aircraft model, where the reality effects turbulence (probability of exceedance 10^{-2}), sensor noise, jitter and quantization are activated, results in very similar step responses, as it can be seen in Fig. 6.17. Although, the commanded actuator activity is significantly higher for all adaptive controllers compared to the baseline controller. This is also confirmed by the metrics, in particular by means of $M_{\mathcal{L}_{2,act}}$, in Table 6.15. The reason for this is the high gain update law with respect to the L1 Adaptive Control approach on the on hand and on the other hand the derivation of the pitch rate q, as it is needed for the $\Delta\dot{q}$ Compensation Law. This was also already discussed in Chapter 5. Corresponding step responses considering the enhanced aircraft model, where turbulence and actuator backlash as well as noise, jitter, scale factor, bias and quantization within the sensor are deactivated, can be found in Fig. A.71, Table A.94, Fig. A.72 and Table A.95.
The exemplary maneuver is considered in the next step. Fig. 6.18 shows the system responses of the different controllers combined with the basic aircraft model. It can be seen that the adaptive controllers manage to compensate the nonlinearity, which appears for the $\alpha_{min} = -10^{\circ}$ sections. Thus, also the metrics in Table 6.16 indicate an increase in performance by means of the adaptive control laws in comparison to the baseline controller configuration.
The results of the same maneuver are depicted in Fig. 6.19, where the enhanced aircraft model is used. It can be seen that the adaptive controllers are still able to increase the performance. Although, as it was already shown for the step responses, the amplification of noisy measurements increases according to $M_{\mathcal{L}_{2,act}}$ in Table 6.17. Thus, the commanded actuator activity increases, which is especially due to turbulence. This can also be observed in Fig. 6.20, where severe instead of light turbulence is applied. In this case, the metrics $M_{\mathcal{L}_2}$ and $M_{\mathcal{L}_\infty}$ in Table 6.18 indicate similar performance in terms of the error between measured angle of attack α and reference model α_{ref}, although the commanded actuator activity increases drastically for the adaptive controllers (c.f. $M_{\mathcal{L}_2}$).

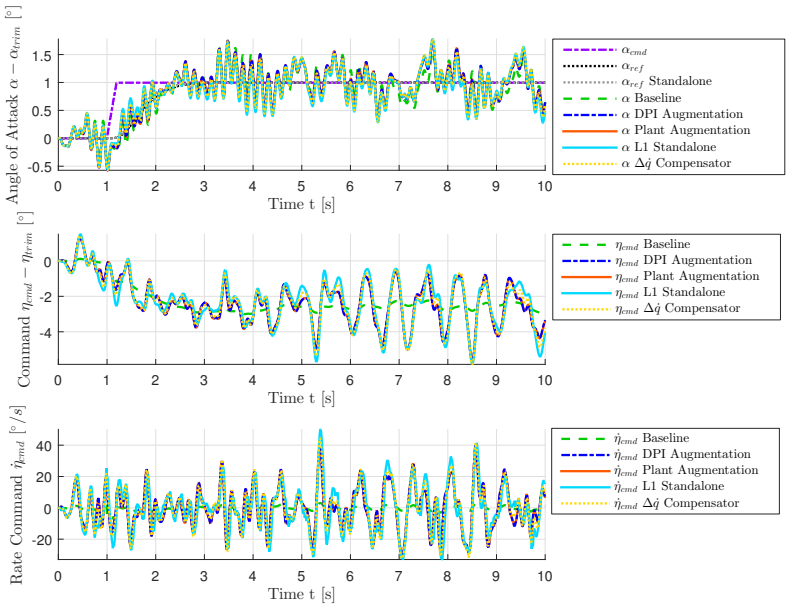

Figure 6.17. – Comparison of α_{cmd} step responses of enhanced, nonlinear aircraft model in combination with baseline controller, L1 Adaptive Augmentations, $\Delta\dot{q}$ Compensation Law and L1 adaptive controller with Eigenstructure Assignment at $V_0 = 154.94\frac{m}{s}$ with light turbulence, sensor noise, jitter and quantization effects

Table 6.15. – Comparison of performance metrics $M_{\mathcal{L}_2}$, $M_{\mathcal{L}_\infty}$ and $M_{\mathcal{L}_{2,act}}$ generated from step responses of enhanced, nonlinear aircraft model in combination with baseline controller, L1 Adaptive Augmentations, $\Delta\dot{q}$ Compensation Law and L1 adaptive controller with Eigenstructure Assignment at $V_0 = 154.94\frac{m}{s}$ with light turbulence, sensor noise, jitter and quantization effects

Controller	$M_{\mathcal{L}_2}$ $[-]$	$M_{\mathcal{L}_\infty}$ $[-]$	$M_{\mathcal{L}_{2,act}}$ $[-]$
Baseline	0.438	0.0129	0.758
DPI Augmentation	0.460	0.0130	7.110
Plant Augmentation	0.461	0.0130	7.081
L1 Standalone	0.488	0.0136	7.937
$\Delta\dot{q}$ Compensator	0.479	0.0135	7.586

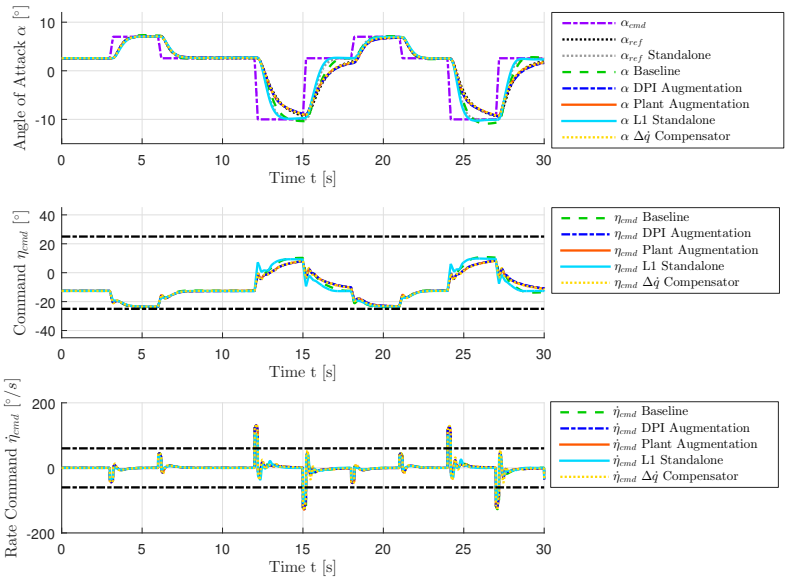

Figure 6.18. – Comparison of angle of attack α, elevator command η_{cmd} and elevator command rate $\dot{\eta}_{cmd}$ for example maneuver performed by basic, nonlinear aircraft model in combination with baseline controller, L1 Adaptive Augmentations, $\Delta\dot{q}$ Compensation Law and L1 adaptive controller with Eigenstructure Assignment starting at $V_0 = 154.94\frac{m}{s}$ and $h_0 = 5000m$

Table 6.16. – Comparison of performance metrics $M_{\mathcal{L}_2}$, $M_{\mathcal{L}_\infty}$ and $M_{\mathcal{L}_{2,act}}$ generated from example maneuver performed by basic, nonlinear aircraft model in combination with baseline controller, L1 Adaptive Augmentations, $\Delta\dot{q}$ Compensation Law and L1 adaptive controller with Eigenstructure Assignment starting at $V_0 = 154.94\frac{m}{s}$ and $h_0 = 5000m$

Controller	$M_{\mathcal{L}_2}$ $[-]$	$M_{\mathcal{L}_\infty}$ $[-]$	$M_{\mathcal{L}_{2,act}}$ $[-]$
Baseline	3.04	0.052	21.26
DPI Augmentation	0.81	0.018	20.74
Plant Augmentation	0.75	0.017	20.71
L1 Standalone	0.95	0.023	16.77
$\Delta\dot{q}$ Compensator	0.62	0.016	21.30

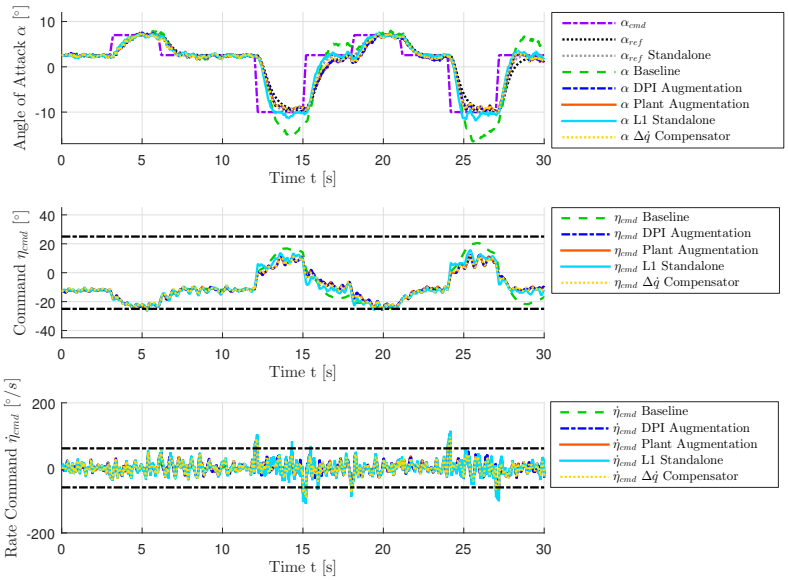

Figure 6.19. – Comparison of angle of attack α, elevator command η_{cmd} and elevator command rate $\dot{\eta}_{cmd}$ for example maneuver performed by enhanced, nonlinear aircraft model in combination with baseline controller, L1 Adaptive Augmentations, $\Delta\dot{q}$ Compensation Law and L1 adaptive controller with Eigenstructure Assignment starting at $V_0 = 154.94\frac{m}{s}$ and $h_0 = 5000m$

Table 6.17. – Comparison of performance metrics $M_{\mathcal{L}_2}$, $M_{\mathcal{L}_\infty}$ and $M_{\mathcal{L}_{2,act}}$ generated from example maneuver performed by enhanced, nonlinear aircraft model in combination with baseline controller, L1 Adaptive Augmentations, $\Delta\dot{q}$ Compensation Law and L1 adaptive controller with Eigenstructure Assignment starting at $V_0 = 154.94\frac{m}{s}$ and $h_0 = 5000m$

Controller	$M_{\mathcal{L}_2}$ $[-]$	$M_{\mathcal{L}_\infty}$ $[-]$	$M_{\mathcal{L}_{2,act}}$ $[-]$
Baseline	7.79	0.142	14.45
DPI Augmentation	2.29	0.047	19.48
Plant Augmentation	2.31	0.047	19.33
L1 Standalone	2.61	0.071	22.18
$\Delta\dot{q}$ Compensator	2.40	0.050	19.03

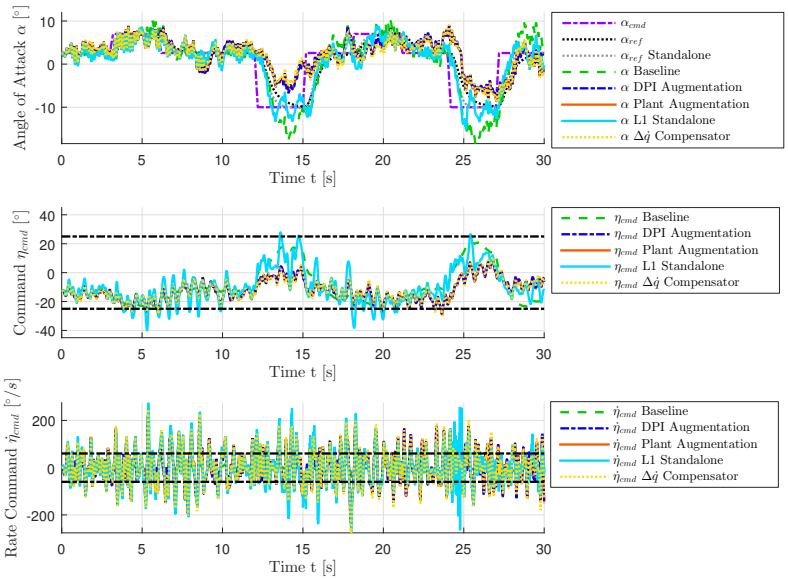

Figure 6.20. – Comparison of angle of attack α, elevator command η_{cmd} and elevator command rate $\dot{\eta}_{cmd}$ for example maneuver performed by enhanced, nonlinear aircraft model in combination with baseline controller, L1 Adaptive Augmentations, $\Delta\dot{q}$ Compensation Law and L1 adaptive controller with Eigenstructure Assignment starting at $V_0 = 154.94\frac{m}{s}$ and $h_0 = 5000m$ considering severe turbulence

Table 6.18. – Comparison of performance metrics $M_{\mathcal{L}_2}$, $M_{\mathcal{L}_\infty}$ and $M_{\mathcal{L}_{2,act}}$ generated from example maneuver performed by enhanced, nonlinear aircraft model in combination with baseline controller, L1 Adaptive Augmentations, $\Delta\dot{q}$ Compensation Law and L1 adaptive controller with Eigenstructure Assignment starting at $V_0 = 154.94\frac{m}{s}$ and $h_0 = 5000m$ considering severe turbulence

Controller	$M_{\mathcal{L}_2}$ $[-]$	$M_{\mathcal{L}_\infty}$ $[-]$	$M_{\mathcal{L}_{2,act}}$ $[-]$
Baseline	8.85	0.164	15.85
DPI Augmentation	8.78	0.184	67.19
Plant Augmentation	8.77	0.184	66.89
L1 Standalone	5.39	0.102	74.04
$\Delta\dot{q}$ Compensator	9.15	0.196	73.78

6.2.2. Uncertainty w.r.t. aerodynamic coefficients (only pitch moment)

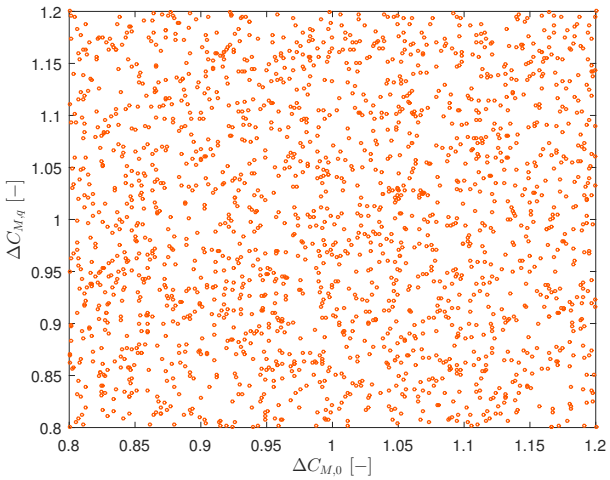

Figure 6.21. – Variation of multiplicative uncertainties applied to aerodynamic coefficients $C_{M,0}$ and $C_{M,q}$

The next three sections investigate the effect of uncertainties concerning the aerodynamic coefficients on the controller performances. Firstly, uncertainties are only induced to the moment coefficients in this section. After that, the same assessment is made considering uncertainties applied to the forces. At last, the effect of combined uncertainties is examined.
As it was already presented for the robust stability assessments in Section 6.1.2, multiplicative uncertainties are applied to the aerodynamics coefficients, in this case only to the moment coefficients $C_{m,0}$ and $C_{m,q}$ (c.f. Section 2.1.1). The corresponding factors $\Delta C_{m,0}$ and $\Delta C_{m,q}$ are randomly varied in a range of $[0.8; 1.2]$. Including the corner cases, in total 2000 variation combinations are generated, which are shown in Fig. 6.21. The performance is again investigated by means of the exemplary maneuver, which was introduced in Section 5.1.2. For this purpose, the enhanced aircraft configuration is utilized. Note also that for all simulations the same seed is used, in order to generate the random numbers needed for the dryden turbulence model. In this case, light turbulence is applied.
The system responses as well as the performance metrics are presented for every controller configuration. In terms of the performance metrics, the minimum and maximum values are summarized together with their mean values and the standard deviations. For the adaptive controllers, also relative percentages of the metrics are given which are calculated with respect to the baseline controller configuration. The results can be found in Fig. 6.22 and Table 6.19 for the baseline controller, in Fig. 6.23 and Table 6.20 for the DPI Augmentation, in Fig. 6.24 and Table 6.21 for the Plant Augmentation, in Fig. 6.25 and Table 6.22 for the $\Delta\dot{q}$ Compensation Law and in Fig. 6.26 and Table 6.23

for the standalone L1 adaptive controller with Eigenstructure Assignment. It can be observed that the adaptive augmentations increase the performance considering uncertainty with regard to the pitch moment coefficients. In particular, this can be seen for the $\alpha_{min} = -10^{\circ}$ sections, where, additional to the uncertainty, also a nonlinearity within the aircraft dynamics is present. The L1 Adaptive Augmentations manage to decrease the standard deviation of the $M_{\mathcal{L}_2}$ metric, which is a good measure for the scattering of the responses, by approximately 90% in comparison to the configuration, where only the baseline controller is used. This can be seen in Table 6.20 and Table 6.21. In Table 6.22 one can also see that the performance of the $\Delta\dot{q}$ Compensation Law is very similar to the one of the L1 Adaptive Augmentations. Also the standalone L1 adaptive controller is able to cope with this type of uncertainty, which is confirmed by Table 6.23. Although, its performance is slighty worse in comparison to the adaptive augmentations. Note that the increase in commanded actuator activity (c.f. $M_{\mathcal{L}_{2,act}}$) stems from the amplification of turbulence in case of the adaptive controllers.

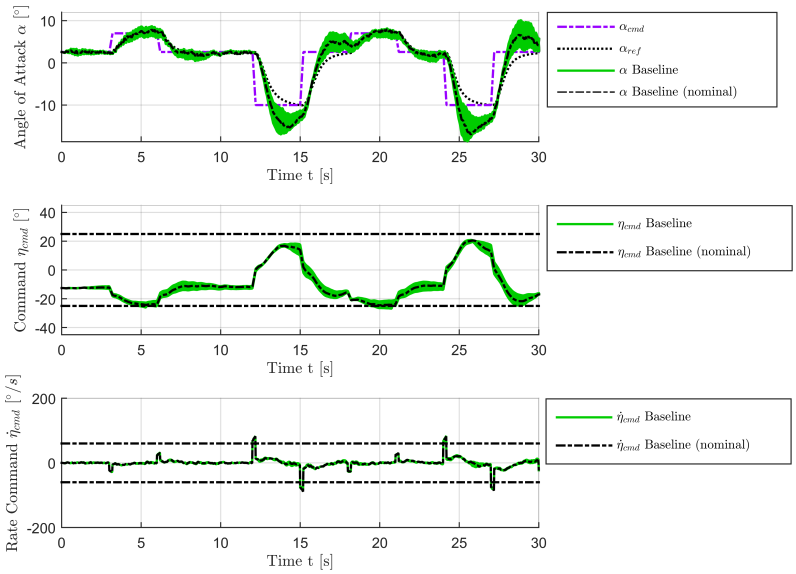

Figure 6.22. – Angle of attack α, elevator command η_{cmd} and elevator command rate $\dot{\eta}_{cmd}$ for example maneuver performed by enhanced, nonlinear aircraft model with baseline controller starting at $V_0 = 154.94\frac{m}{s}$ and $h_0 = 5000m$ considering variation of aerodynamic forces

Table 6.19. – Performance metrics $M_{\mathcal{L}_2}$, $M_{\mathcal{L}_\infty}$ and $M_{\mathcal{L}_{2,act}}$ (maximum, minimum, mean value and standard deviation) generated from example maneuver performed by enhanced, nonlinear aircraft model with baseline controller starting at $V_0 = 154.94\frac{m}{s}$ and $h_0 = 5000m$ considering variation of aerodynamic forces

	$M_{\mathcal{L}_2}$ $[-]$	$M_{\mathcal{L}_\infty}$ $[-]$	$M_{\mathcal{L}_{2,act}}$ $[-]$
max	11.30	0.190	14.51
min	3.72	0.067	14.26
$\varnothing$	7.64	0.137	14.42
σ	2.036	0.0321	0.057

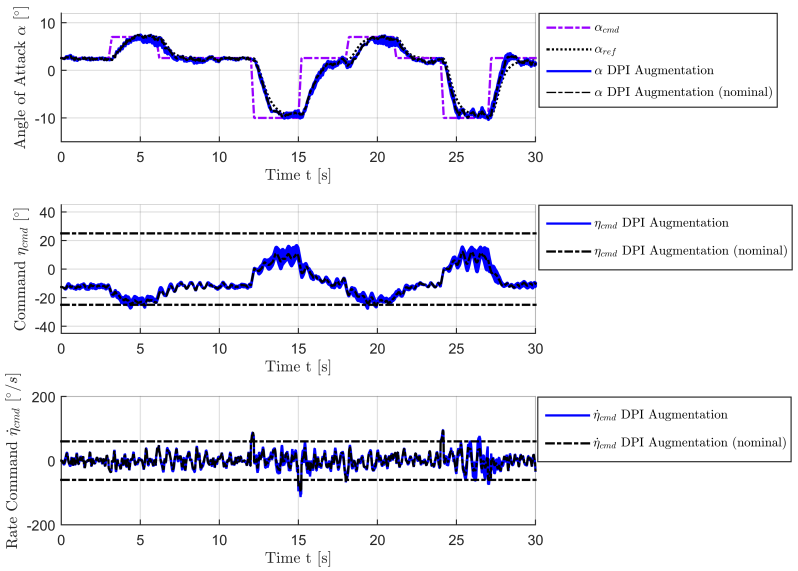

Figure 6.23. – Angle of attack α, elevator command η_{cmd} and elevator command rate $\dot{\eta}_{cmd}$ for example maneuver performed by enhanced, nonlinear aircraft model with DPI Augmentation starting at $V_0 = 154.94\frac{m}{s}$ and $h_0 = 5000m$ considering variation of aerodynamic moment

Table 6.20. – Performance metrics $M_{\mathcal{L}_2}$, $M_{\mathcal{L}_\infty}$ and $M_{\mathcal{L}_{2,act}}$ (maximum, minimum, mean value and standard deviation) generated from example maneuver performed by enhanced, nonlinear aircraft model with DPI Augmentation and comparison to baseline controller starting at $V_0 = 154.94\frac{m}{s}$ and $h_0 = 5000m$ considering variation of aerodynamic moment

	$M_{\mathcal{L}_2}$ [−]	$M_{\mathcal{L}_\infty}$ [−]	$M_{\mathcal{L}_{2,act}}$ [−]	$M_{\mathcal{L}_{2,rel}}$ [%]	$M_{\mathcal{L}_{\infty,rel}}$ [%]	$M_{\mathcal{L}_{2,act,rel}}$ [%]
max	3.04	0.064	22.37	26.9%	33.6%	154.2%
min	2.15	0.035	18.21	57.9%	52.2%	127.7%
∅	2.40	0.046	19.70	31.4%	33.8%	136.6%
σ	0.223	0.0075	1.181	11.0%	23.4%	2069.3%

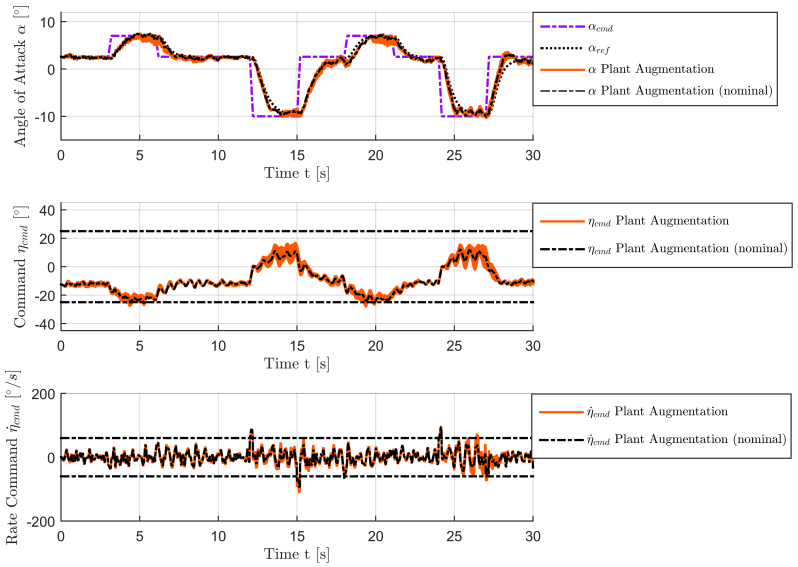

Figure 6.24. – Angle of attack α, elevator command η_{cmd} and elevator command rate $\dot{\eta}_{cmd}$ for example maneuver performed by enhanced, nonlinear aircraft model with Plant Augmentation starting at $V_0 = 154.94\frac{m}{s}$ and $h_0 = 5000m$ considering variation of aerodynamic moment

Table 6.21. – Performance metrics $M_{\mathcal{L}_2}$, $M_{\mathcal{L}_\infty}$ and $M_{\mathcal{L}_{2,act}}$ (maximum, minimum, mean value and standard deviation) generated from example maneuver performed by enhanced, nonlinear aircraft model with Plant Augmentation and comparison to baseline controller starting at $V_0 = 154.94\frac{m}{s}$ and $h_0 = 5000m$ considering variation of aerodynamic moment

	$M_{\mathcal{L}_2}$ [−]	$M_{\mathcal{L}_\infty}$ [−]	$M_{\mathcal{L}_{2,act}}$ [−]	$M_{\mathcal{L}_{2,rel}}$ [%]	$M_{\mathcal{L}_{\infty,rel}}$ [%]	$M_{\mathcal{L}_{2,act,rel}}$ [%]
max	3.03	0.064	21.93	26.8%	33.8%	151.2%
min	2.16	0.035	18.15	58.1%	52.6%	127.3%
∅	2.41	0.047	19.51	31.5%	34.1%	135.3%
σ	0.216	0.0077	1.079	10.6%	23.9%	1889.5%

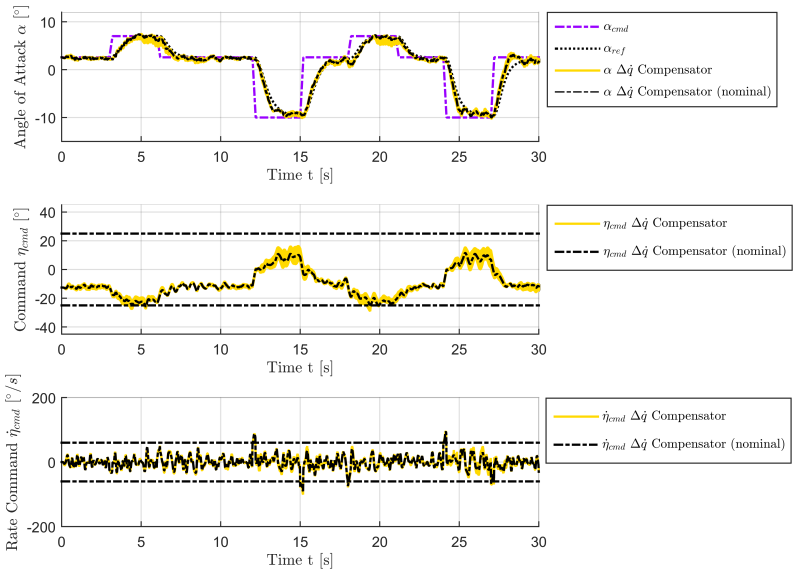

Figure 6.25. – Angle of attack α, elevator command η_{cmd} and elevator command rate $\dot{\eta}_{cmd}$ for example maneuver performed by enhanced, nonlinear aircraft model with $\Delta\dot{q}$ Compensation Law starting at $V_0 = 154.94\frac{m}{s}$ and $h_0 = 5000m$ considering variation of aerodynamic moment

Table 6.22. – Performance metrics $M_{\mathcal{L}_2}$, $M_{\mathcal{L}_\infty}$ and $M_{\mathcal{L}_{2,act}}$ (maximum, minimum, mean value and standard deviation) generated from example maneuver performed by enhanced, nonlinear aircraft model with $\Delta\dot{q}$ Compensation Law and comparison to baseline controller starting at $V_0 = 154.94\frac{m}{s}$ and $h_0 = 5000m$ considering variation of aerodynamic moment

	$M_{\mathcal{L}_2}$ $[-]$	$M_{\mathcal{L}_\infty}$ $[-]$	$M_{\mathcal{L}_{2,act}}$ $[-]$	$M_{\mathcal{L}_{2,rel}}$ $[\%]$	$M_{\mathcal{L}_{\infty,rel}}$ $[\%]$	$M_{\mathcal{L}_{2,act,rel}}$ $[\%]$
max	2.98	0.065	20.19	26.3%	34.5%	139.1%
min	2.30	0.037	18.28	62.0%	55.6%	128.2%
$\varnothing$	2.51	0.050	19.08	32.9%	36.8%	132.3%
σ	0.183	0.0087	0.577	9.0%	27.2%	1010.3%

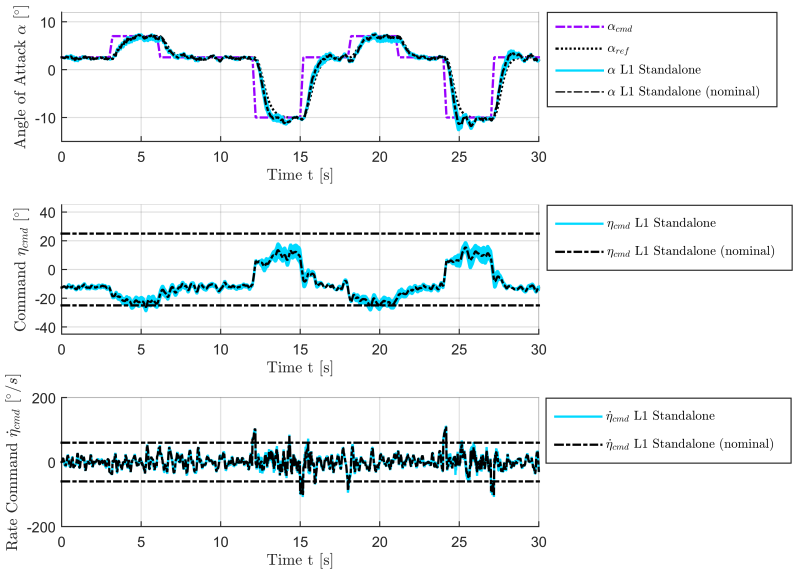

Figure 6.26. – Angle of attack α, elevator command η_{cmd} and elevator command rate $\dot{\eta}_{cmd}$ for example maneuver performed by enhanced, nonlinear aircraft model with L1 adaptive controller with Eigenstructure Assignment starting at $V_0 = 154.94\frac{m}{s}$ and $h_0 = 5000m$ considering variation of aerodynamic moment

Table 6.23. – Performance metrics $M_{\mathcal{L}_2}$, $M_{\mathcal{L}_\infty}$ and $M_{\mathcal{L}_{2,act}}$ (maximum, minimum, mean value and standard deviation) generated from example maneuver performed by enhanced, nonlinear aircraft model with L1 adaptive controller with Eigenstructure Assignment and comparison to baseline controller starting at $V_0 = 154.94\frac{m}{s}$ and $h_0 = 5000m$ considering variation of aerodynamic moment

	$M_{\mathcal{L}_2}$ $[-]$	$M_{\mathcal{L}_\infty}$ $[-]$	$M_{\mathcal{L}_{2,act}}$ $[-]$	$M_{\mathcal{L}_{2,rel}}$ $[\%]$	$M_{\mathcal{L}_{\infty,rel}}$ $[\%]$	$M_{\mathcal{L}_{2,act,rel}}$ $[\%]$
max	3.66	0.098	23.40	32.4%	51.8%	161.2%
min	1.88	0.044	21.56	50.7%	66.4%	151.2%
$\varnothing$	2.63	0.071	22.26	34.5%	51.8%	154.3%
σ	0.515	0.0141	0.477	25.3%	43.9%	835.5%

6.2.3. Uncertainty w.r.t. aerodynamic coefficients (only forces)

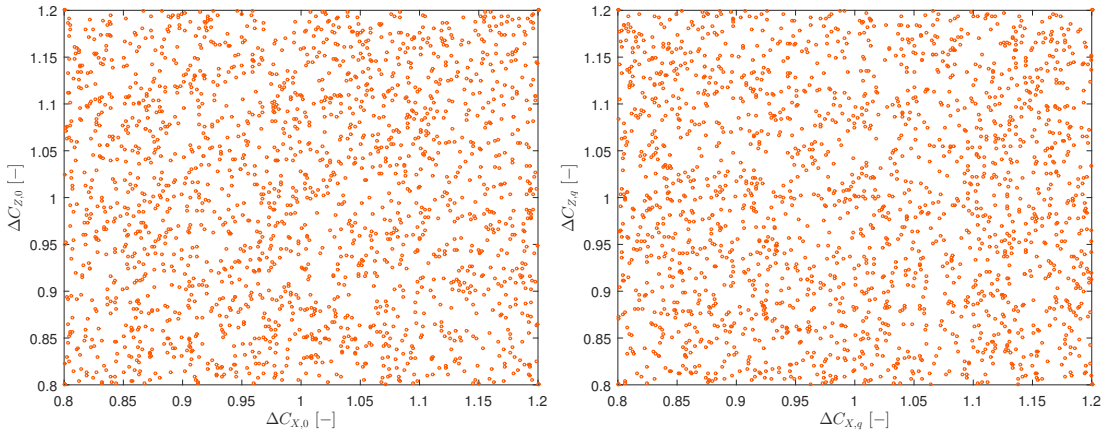

(a) Variation of $\Delta C_{X,0}$ and $\Delta C_{Z,0}$ **(b)** Variation of $\Delta C_{X,q}$ and $\Delta C_{Z,q}$

Figure 6.27. – Variation of multiplicative uncertainties applied to aerodynamic coefficients $C_{X,0}$, $C_{X,q}$, $C_{Z,0}$ and $C_{Z,q}$

In the next step, the performance is investigated considering uncertainties with regard to aerodynamic forces. Thus, variations in the range of $[0.8; 1.2]$ are randomly generated for the factors $\Delta C_{X,0}$, $\Delta C_{Z,0}$, $\Delta C_{X,q}$ and $\Delta C_{Z,q}$. The results are depicted in Fig. 6.27. As for the pitch moment uncertainty assessments, also in this case 2000 variations are created, which include the corner cases. The results of the simulations are summarized in Fig. 6.28 and Table 6.24 for the baseline controller, in Fig. 6.29 and Table 6.25 for the DPI Augmentation, in Fig. 6.30 and Table 6.26 for the Plant Augmentation, in Fig. 6.31 and Table 6.27 for the $\Delta\dot{q}$ Compensation Law and in Fig. 6.32 and Table 6.28 for the standalone L1 adaptive controller with Eigenstructure Assignment. In this respect again, the adaptive augmentations increase the performance in comparison to the baseline controller. In particular, the standard deviation of $M_{\mathcal{L}_2}$ considering the L1 Adaptive Augmentations can be decreased by approximately 80%, in case of the $\Delta\dot{q}$ Compensation Law even by 84%. Although, some uncertainty combinations lead to oscillations within the system response in the second $\alpha_{min} = -10°$ section. This issue is not apparent for the first $\alpha_{min} = -10°$ section, because the velocity of the aircraft (below $140\frac{m}{s}$) is lower here compared to the second section (around $170\frac{m}{s}$). Thus, this assessment indicates that the adaptive augmentations face problems at this envelope point, while compensating the combination of aerodynamic nonlinearity and uncertainty within the aerodynamic forces. This issue can also be observed for the standalone L1 adaptive controller, where the commanded actuator activity is drastically increased for some uncertainty cases during the second $\alpha_{min} = -10°$ section. Nevertheless, also the standalone adaptive controller offers a performance increase with regard to the considered uncertainty case.

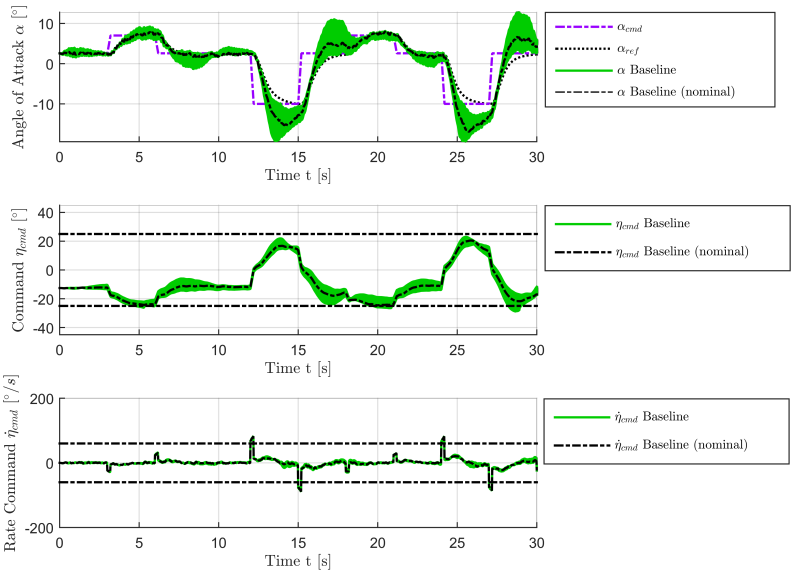

Figure 6.28. – Angle of attack α, elevator command η_{cmd} and elevator command rate $\dot{\eta}_{cmd}$ for example maneuver performed by enhanced, nonlinear aircraft model with baseline controller starting at $V_0 = 154.94\frac{m}{s}$ and $h_0 = 5000m$ considering variation of aerodynamic forces

Table 6.24. – Performance metrics $M_{\mathcal{L}_2}$, $M_{\mathcal{L}_\infty}$ and $M_{\mathcal{L}_{2,act}}$ (maximum, minimum, mean value and standard deviation) generated from example maneuver performed by enhanced, nonlinear aircraft model with baseline controller starting at $V_0 = 154.94\frac{m}{s}$ and $h_0 = 5000m$ considering variation of aerodynamic forces

	$M_{\mathcal{L}_2}$ $[-]$	$M_{\mathcal{L}_\infty}$ $[-]$	$M_{\mathcal{L}_{2,act}}$ $[-]$
max	13.98	0.201	15.29
min	3.49	0.065	13.97
$\varnothing$	7.93	0.137	14.47
σ	2.912	0.0403	0.318

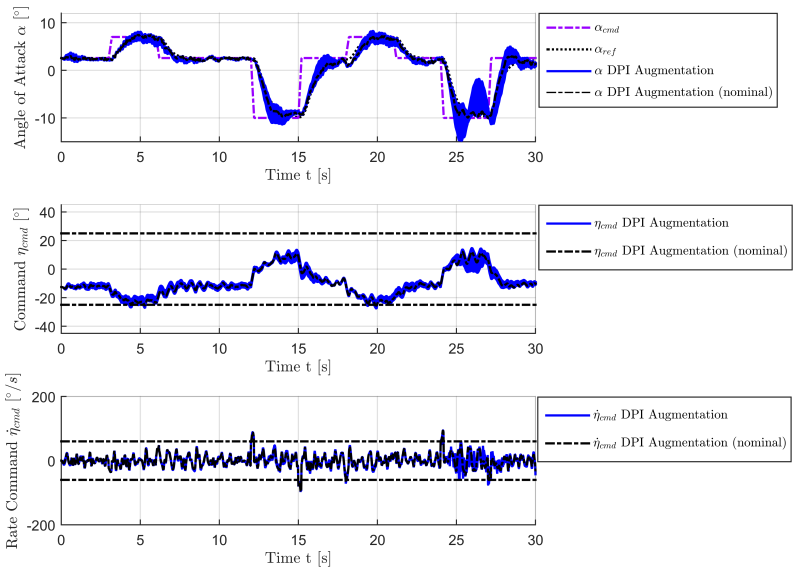

Figure 6.29. – Angle of attack α, elevator command η_{cmd} and elevator command rate $\dot{\eta}_{cmd}$ for example maneuver performed by enhanced, nonlinear aircraft model with DPI Augmentation starting at $V_0 = 154.94\frac{m}{s}$ and $h_0 = 5000m$ considering variation of aerodynamic forces

Table 6.25. – Performance metrics $M_{\mathcal{L}_2}$, $M_{\mathcal{L}_\infty}$ and $M_{\mathcal{L}_{2,act}}$ (maximum, minimum, mean value and standard deviation) generated from example maneuver performed by enhanced, nonlinear aircraft model with DPI Augmentation and comparison to baseline controller starting at $V_0 = 154.94\frac{m}{s}$ and $h_0 = 5000m$ considering variation of aerodynamic forces

	$M_{\mathcal{L}_2}$ $[-]$	$M_{\mathcal{L}_\infty}$ $[-]$	$M_{\mathcal{L}_{2,act}}$ $[-]$	$M_{\mathcal{L}_{2,rel}}$ $[\%]$	$M_{\mathcal{L}_{\infty,rel}}$ $[\%]$	$M_{\mathcal{L}_{2,act,rel}}$ $[\%]$
max	4.44	0.101	20.55	31.8%	50.5%	134.4%
min	2.15	0.034	16.96	61.6%	51.6%	121.4%
$\varnothing$	2.67	0.052	19.24	33.7%	37.9%	132.9%
σ	0.571	0.0173	0.828	19.6%	43.0%	260.3%

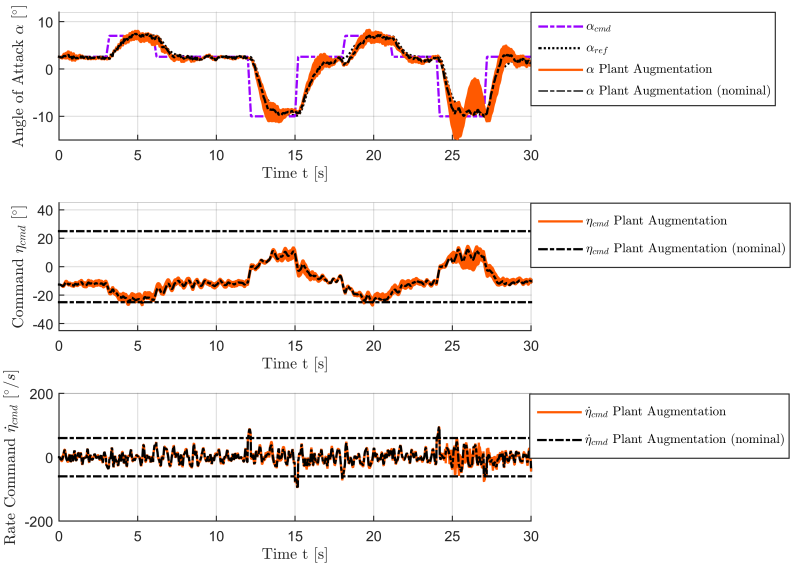

Figure 6.30. – Angle of attack α, elevator command η_{cmd} and elevator command rate $\dot{\eta}_{cmd}$ for example maneuver performed by enhanced, nonlinear aircraft model with Plant Augmentation starting at $V_0 = 154.94\frac{m}{s}$ and $h_0 = 5000m$ considering variation of aerodynamic forces

Table 6.26. – Performance metrics $M_{\mathcal{L}_2}$, $M_{\mathcal{L}_\infty}$ and $M_{\mathcal{L}_{2,act}}$ (maximum, minimum, mean value and standard deviation) generated from example maneuver performed by enhanced, nonlinear aircraft model with Plant Augmentation and comparison to baseline controller starting at $V_0 = 154.94\frac{m}{s}$ and $h_0 = 5000m$ considering variation of aerodynamic forces

	$M_{\mathcal{L}_2}$ $[-]$	$M_{\mathcal{L}_\infty}$ $[-]$	$M_{\mathcal{L}_{2,act}}$ $[-]$	$M_{\mathcal{L}_{2,rel}}$ $[\%]$	$M_{\mathcal{L}_{\infty,rel}}$ $[\%]$	$M_{\mathcal{L}_{2,act,rel}}$ $[\%]$
max	4.36	0.101	20.42	31.2%	50.5%	133.6%
min	2.15	0.034	16.85	61.7%	51.9%	120.6%
$\varnothing$	2.67	0.052	19.09	33.7%	38.2%	131.9%
σ	0.567	0.0173	0.814	19.5%	42.9%	255.9%

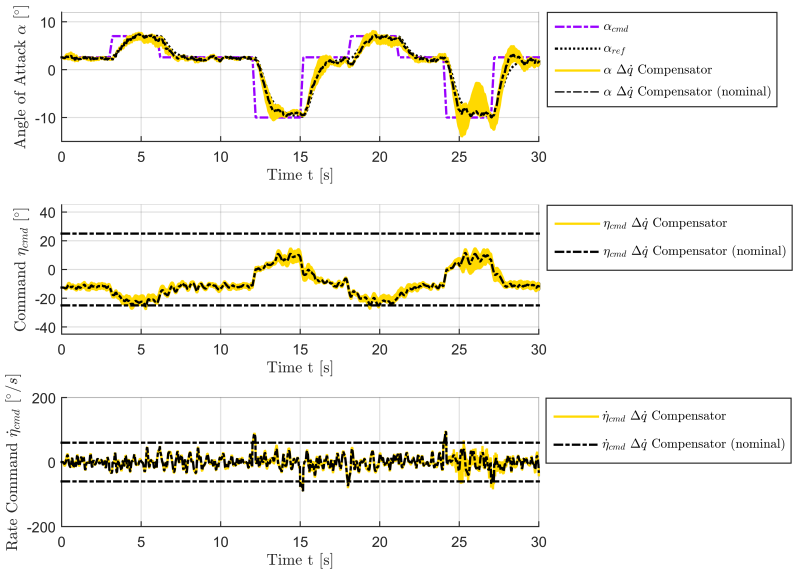

Figure 6.31. – Angle of attack α, elevator command η_{cmd} and elevator command rate $\dot{\eta}_{cmd}$ for example maneuver performed by enhanced, nonlinear aircraft model with $\Delta\dot{q}$ Compensation Law starting at $V_0 = 154.94\frac{m}{s}$ and $h_0 = 5000m$ considering variation of aerodynamic forces

Table 6.27. – Performance metrics $M_{\mathcal{L}_2}$, $M_{\mathcal{L}_\infty}$ and $M_{\mathcal{L}_{2,act}}$ (maximum, minimum, mean value and standard deviation) generated from example maneuver performed by enhanced, nonlinear aircraft model with $\Delta\dot{q}$ Compensation Law and comparison to baseline controller starting at $V_0 = 154.94\frac{m}{s}$ and $h_0 = 5000m$ considering variation of aerodynamic forces

	$M_{\mathcal{L}_2}$ $[-]$	$M_{\mathcal{L}_\infty}$ $[-]$	$M_{\mathcal{L}_{2,act}}$ $[-]$	$M_{\mathcal{L}_{2,rel}}$ $[\%]$	$M_{\mathcal{L}_{\infty,rel}}$ $[\%]$	$M_{\mathcal{L}_{2,act,rel}}$ $[\%]$
max	4.04	0.091	20.41	28.9%	45.1%	133.5%
min	2.24	0.036	16.58	64.2%	56.1%	118.7%
$\varnothing$	2.67	0.054	18.91	33.7%	39.3%	130.7%
σ	0.454	0.0142	0.786	15.6%	35.2%	247.1%

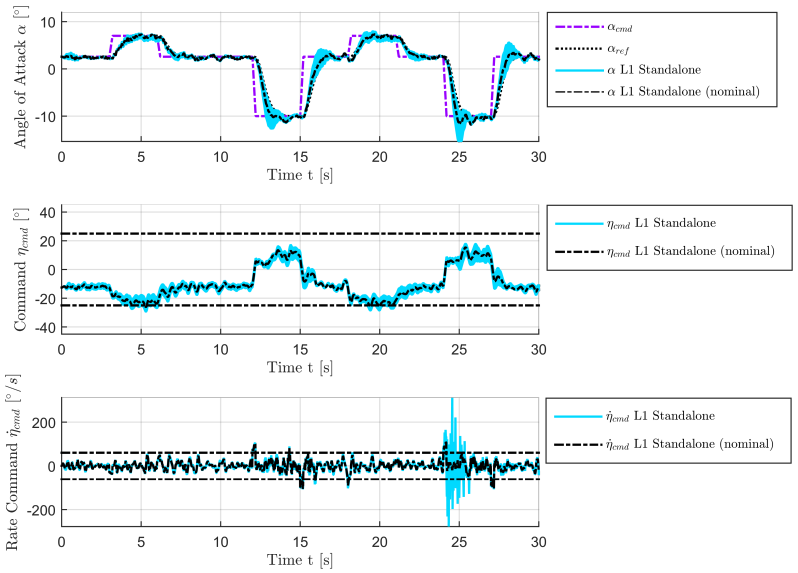

Figure 6.32. – Angle of attack α, elevator command η_{cmd} and elevator command rate $\dot{\eta}_{cmd}$ for example maneuver performed by enhanced, nonlinear aircraft model with L1 adaptive controller with Eigenstructure Assignment starting at $V_0 = 154.94\frac{m}{s}$ and $h_0 = 5000m$ considering variation of aerodynamic forces

Table 6.28. – Performance metrics $M_{\mathcal{L}_2}$, $M_{\mathcal{L}_\infty}$ and $M_{\mathcal{L}_{2,act}}$ (maximum, minimum, mean value and standard deviation) generated from example maneuver performed by enhanced, nonlinear aircraft model with L1 adaptive controller with Eigenstructure Assignment and comparison to baseline controller starting at $V_0 = 154.94\frac{m}{s}$ and $h_0 = 5000m$ considering variation of aerodynamic forces

	$M_{\mathcal{L}_2}$ [−]	$M_{\mathcal{L}_\infty}$ [−]	$M_{\mathcal{L}_{2,act}}$ [−]	$M_{\mathcal{L}_{2,rel}}$ [%]	$M_{\mathcal{L}_{\infty,rel}}$ [%]	$M_{\mathcal{L}_{2,act,rel}}$ [%]
max	4.51	0.127	27.55	32.3%	63.1%	180.2%
min	1.91	0.038	21.31	54.6%	57.8%	152.5%
∅	2.80	0.075	22.75	35.3%	54.7%	157.3%
σ	0.782	0.0255	1.238	26.9%	63.2%	389.4%

6.2.4. Uncertainty w.r.t. aerodynamic coefficients (forces and pitch-moment)

After the individual assessments of uncertainties with regard to aerodynamic forces and moments, this section investigates combined uncertainty cases. For this purpose, the same variations on the aerodynamic coefficients according to Fig. 6.8 are utilized, as they were presented for the robust stability assessment in Section 6.1.2. Thus, a total amount of 5065 simulations is performed for every controller in combination with the enhanced aircraft model including the nominal configuration with regard to the aerodynamic coefficients.
The simulation results can be found in Fig. 6.33 and Table 6.29 for the baseline controller, in Fig. 6.34 and Table 6.30 for the DPI Augmentation, in Fig. 6.35 and Table 6.31 for the Plant Augmentation, in Fig. 6.36 and Table 6.32 for the $\Delta\dot{q}$ Compensation Law and in Fig. 6.37 and Table 6.33 for the standalone L1 adaptive controller with Eigenstructure Assignment. Also for combined uncertainties with regard to both aerodynamic forces and moments, the adaptive augmentations achieve an increase with regard to the performance metrics in comparison to the baseline controller. This holds also in case of the standalone L1 adaptive controller. On the other hand it can also be seen for the adaptive augmentations that the amplitudes of the oscillations in the second $\alpha_{min} = -10^\circ$ section are larger compared to the force-only uncertainty cases in Section 6.2.3. This can also be seen considering the commanded actuator activity of the standalone adaptive controller.

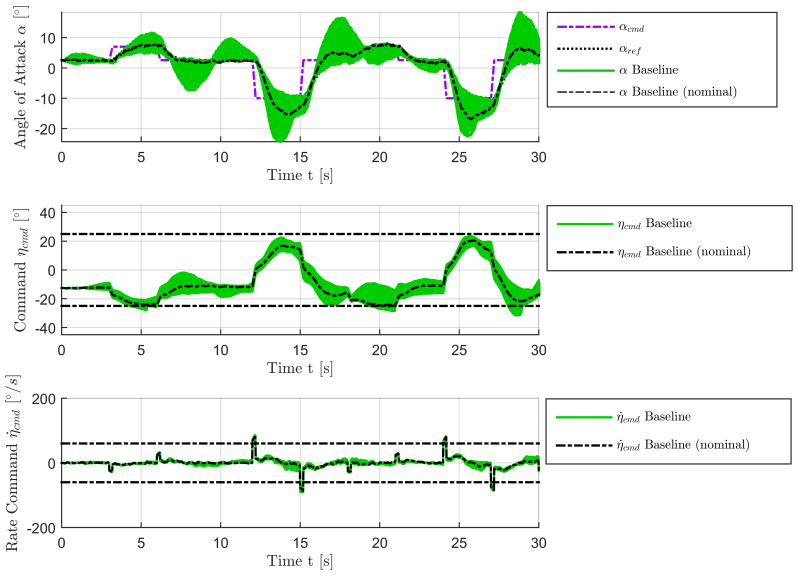

Figure 6.33. – Angle of attack α, elevator command η_{cmd} and elevator command rate $\dot{\eta}_{cmd}$ for example maneuver performed by enhanced, nonlinear aircraft model with baseline controller starting at $V_0 = 154.94\frac{m}{s}$ and $h_0 = 5000m$ considering variation of aerodynamic forces and moment

Table 6.29. – Performance metrics $M_{\mathcal{L}_2}$, $M_{\mathcal{L}_\infty}$ and $M_{\mathcal{L}_{2,act}}$ (maximum, minimum, mean value and standard deviation) generated from example maneuver performed by enhanced, nonlinear aircraft model with baseline controller starting at $V_0 = 154.94\frac{m}{s}$ and $h_0 = 5000m$ considering variation of aerodynamic forces and moment

	$M_{\mathcal{L}_2}$ $[-]$	$M_{\mathcal{L}_\infty}$ $[-]$	$M_{\mathcal{L}_{2,act}}$ $[-]$
max	21.39	0.297	16.06
min	2.58	0.036	13.79
$\varnothing$	8.01	0.136	14.47
σ	3.585	0.0507	0.364

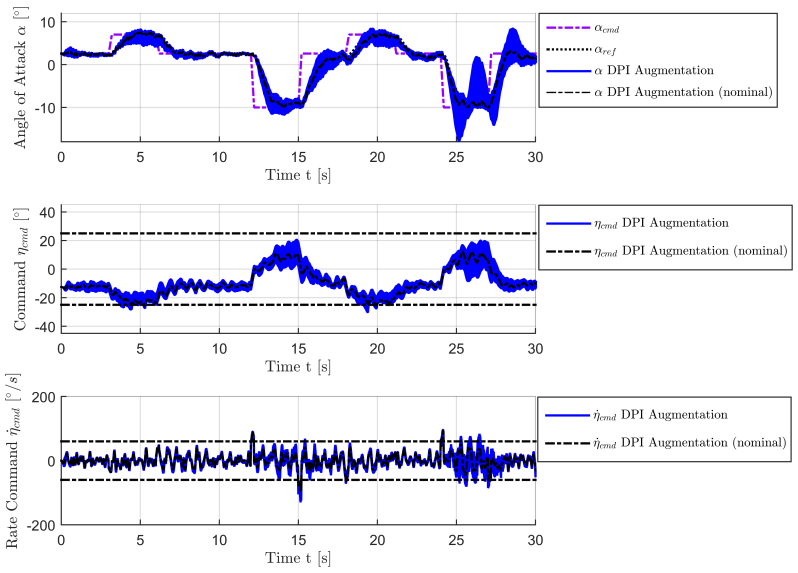

Figure 6.34. – Angle of attack α, elevator command η_{cmd} and elevator command rate $\dot{\eta}_{cmd}$ for example maneuver performed by enhanced, nonlinear aircraft model with DPI Augmentation starting at $V_0 = 154.94\frac{m}{s}$ and $h_0 = 5000m$ considering variation of aerodynamic forces and moment

Table 6.30. – Performance metrics $M_{\mathcal{L}_2}$, $M_{\mathcal{L}_\infty}$ and $M_{\mathcal{L}_{2,act}}$ (maximum, minimum, mean value and standard deviation) generated from example maneuver performed by enhanced, nonlinear aircraft model with DPI Augmentation and comparison to baseline controller starting at $V_0 = 154.94\frac{m}{s}$ and $h_0 = 5000m$ considering variation of aerodynamic forces and moment

	$M_{\mathcal{L}_2}$ [−]	$M_{\mathcal{L}_\infty}$ [−]	$M_{\mathcal{L}_{2,act}}$ [−]	$M_{\mathcal{L}_{2,rel}}$ [%]	$M_{\mathcal{L}_{\infty,rel}}$ [%]	$M_{\mathcal{L}_{2,act,rel}}$ [%]
max	6.71	0.169	25.15	31.4%	56.9%	156.6%
min	2.11	0.033	16.40	81.8%	92.1%	118.9%
∅	2.79	0.054	19.57	34.8%	39.8%	135.2%
σ	0.647	0.0199	1.589	18.0%	39.3%	437.0%

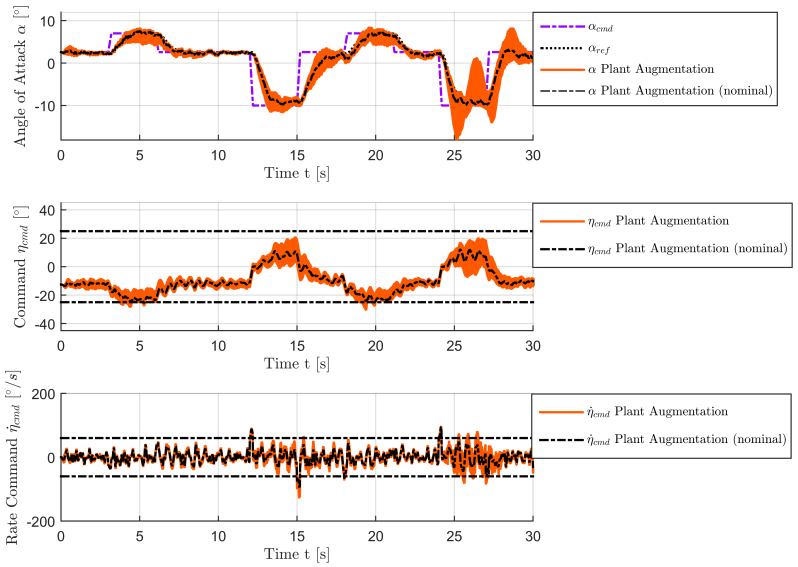

Figure 6.35. – Angle of attack α, elevator command η_{cmd} and elevator command rate $\dot{\eta}_{cmd}$ for example maneuver performed by enhanced, nonlinear aircraft model with Plant Augmentation starting at $V_0 = 154.94\frac{m}{s}$ and $h_0 = 5000m$ considering variation of aerodynamic forces and moment

Table 6.31. – Performance metrics $M_{\mathcal{L}_2}$, $M_{\mathcal{L}_\infty}$ and $M_{\mathcal{L}_{2,act}}$ (maximum, minimum, mean value and standard deviation) generated from example maneuver performed by enhanced, nonlinear aircraft model with Plant Augmentation and comparison to baseline controller starting at $V_0 = 154.94\frac{m}{s}$ and $h_0 = 5000m$ considering variation of aerodynamic forces and moment

	$M_{\mathcal{L}_2}$ [−]	$M_{\mathcal{L}_\infty}$ [−]	$M_{\mathcal{L}_{2,act}}$ [−]	$M_{\mathcal{L}_{2,rel}}$ [%]	$M_{\mathcal{L}_{\infty,rel}}$ [%]	$M_{\mathcal{L}_{2,act,rel}}$ [%]
max	6.50	0.169	24.76	30.4%	57.0%	154.2%
min	2.12	0.033	16.36	82.4%	93.1%	118.7%
∅	2.79	0.055	19.40	34.8%	40.1%	134.0%
σ	0.641	0.0201	1.508	17.9%	39.6%	414.8%

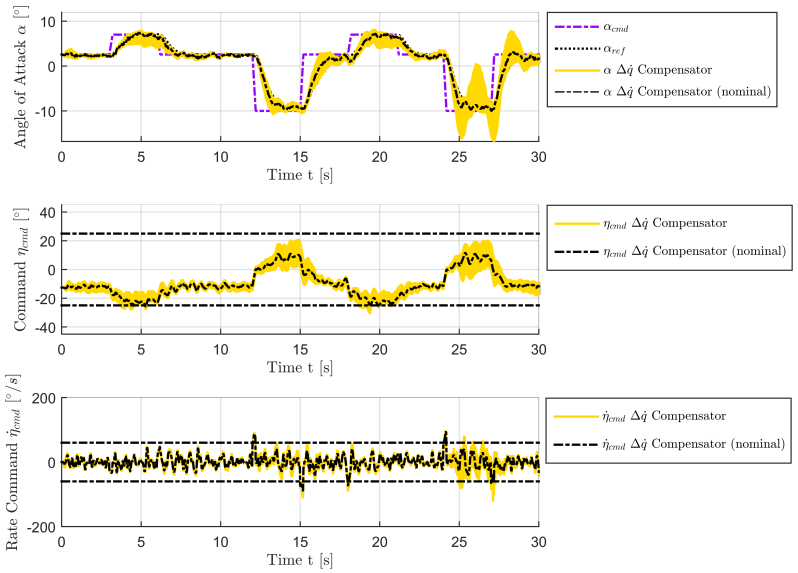

Figure 6.36. – Angle of attack α, elevator command η_{cmd} and elevator command rate $\dot{\eta}_{cmd}$ for example maneuver performed by enhanced, nonlinear aircraft model with $\Delta\dot{q}$ Compensation Law starting at $V_0 = 154.94\frac{m}{s}$ and $h_0 = 5000m$ considering variation of aerodynamic forces and moment

Table 6.32. – Performance metrics $M_{\mathcal{L}_2}$, $M_{\mathcal{L}_\infty}$ and $M_{\mathcal{L}_{2,act}}$ (maximum, minimum, mean value and standard deviation) generated from example maneuver performed by enhanced, nonlinear aircraft model with $\Delta\dot{q}$ Compensation Law and comparison to baseline controller starting at $V_0 = 154.94\frac{m}{s}$ and $h_0 = 5000m$ considering variation of aerodynamic forces and moment

	$M_{\mathcal{L}_2}$ $[-]$	$M_{\mathcal{L}_\infty}$ $[-]$	$M_{\mathcal{L}_{2,act}}$ $[-]$	$M_{\mathcal{L}_{2,rel}}$ $[\%]$	$M_{\mathcal{L}_{\infty,rel}}$ $[\%]$	$M_{\mathcal{L}_{2,act,rel}}$ $[\%]$
max	5.49	0.133	23.36	25.7%	44.7%	145.5%
min	2.15	0.037	16.27	83.2%	101.7%	118.0%
$\varnothing$	2.76	0.056	19.08	34.4%	41.1%	131.8%
σ	0.534	0.0160	1.120	14.9%	31.7%	308.0%

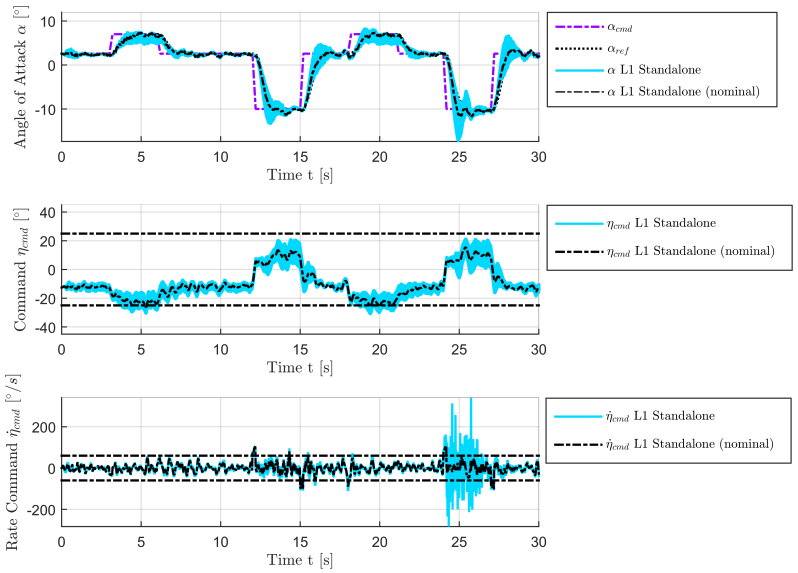

Figure 6.37. – Angle of attack α, elevator command η_{cmd} and elevator command rate $\dot{\eta}_{cmd}$ for example maneuver performed by enhanced, nonlinear aircraft model with L1 adaptive controller with Eigenstructure Assignment starting at $V_0 = 154.94\frac{m}{s}$ and $h_0 = 5000m$ considering variation of aerodynamic forces and moment

Table 6.33. – Performance metrics $M_{\mathcal{L}_2}$, $M_{\mathcal{L}_\infty}$ and $M_{\mathcal{L}_{2,act}}$ (maximum, minimum, mean value and standard deviation) generated from example maneuver performed by enhanced, nonlinear aircraft model with L1 adaptive controller with Eigenstructure Assignment and comparison to baseline controller starting at $V_0 = 154.94\frac{m}{s}$ and $h_0 = 5000m$ considering variation of aerodynamic forces and moment

	$M_{\mathcal{L}_2}$ $[-]$	$M_{\mathcal{L}_\infty}$ $[-]$	$M_{\mathcal{L}_{2,act}}$ $[-]$	$M_{\mathcal{L}_{2,rel}}$ $[\%]$	$M_{\mathcal{L}_{\infty,rel}}$ $[\%]$	$M_{\mathcal{L}_{2,act,rel}}$ $[\%]$
max	5.90	0.169	30.75	27.6%	56.9%	191.5%
min	1.87	0.033	20.90	72.7%	91.6%	151.6%
$\varnothing$	2.86	0.075	22.88	35.8%	55.0%	158.1%
σ	0.875	0.0293	1.394	24.4%	57.8%	383.3%

6.2.5. Uncertainty w.r.t. CG location

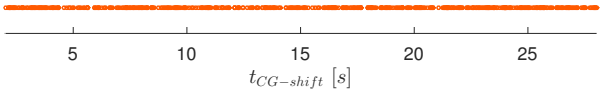

Figure 6.38. – Variation of point in time $t_{CG-shift}$, at which sudden CG-shift of 3% is applied

In this section, the performance of the proposed controller designs is investigated by means of rapid CG-shifts. For this purpose, also results gained in Chapter 5 are compiled here, in order to increase comparability between the control laws. This includes assessments of CG-shifts, which appear at $t_{CG-shift} = 10s$ during the exemplary maneuver. Furthermore, a 3% CG-shift case is examined utilizing the enhanced aircraft model, where the incidence of the CG-shift with respect to time is varied. In this case, 500 random variations of $t_{CG-shift}$ are generated in a range of $[2s; 28s]$, which are shown in Fig. 6.38.
In the first experiment, the 5% CG-shift case is revisited considering the basic aircraft model and $t_{CG-shift} = 10s$. The results for all controllers are depicted in Fig. 6.39, where the accompanying performance metrics can be found in Table 6.34. By means of the plots and the metrics, the statements made in Chapter 5 are confirmed that the adaptive controllers are capable of compensating this rapid CG-shift, whereas the performance of the baseline controller would lead to unacceptable handling qualities. Note also that in case of the missing influence of turbulence and sensor noise, this performance increase is achieved without an increase in commanded actuator activity (c.f. $M_{\mathcal{L}_{2,act}}$). The performance increase can even be observed in case of a 7% CG-shift for the adaptive augmentations, which include both L1 Adaptive Augmentations as well as the $\Delta\dot{q}$ Compensation Law. Although, the standalone L1 adaptive controller is not able to stabilize this configuration anymore. A reason for this could be the limitation of the controller command and its rate, which is directly incorporated into the design of the DPI baseline controller and is also considered for the design of the augmentations (c.f. Section 4.2 and Section 4.3). It can also be observed that the controller command reaches the limit with respect of the actuator deflection around $t \approx 15s$, $t \approx 25s$ and $t \approx 27s$. Despite these saturations, the adaptive augmentations are still able to stabilize the aircraft, which is also due to the DPI approach.
The beneficial effect of the adaptive controllers can also be observed, when the enhanced aircraft model is considered. In this case, CG-shifts of 2% and 3% are applied. The results can be found in Fig. 6.41 and Table 6.36 for the 2% CG-shift and in Fig. 6.42 and Table 6.37 for the 3% CG-shift case. Despite the introduction of several reality effects, the adaptive controllers still significantly increase the performance of the aircraft in comparison to the baseline controller configuration. Similar to the assessment with respect to aerodynamic uncertainty in Section 6.2.4 oscillations can be detected

in the second $\alpha_{min} = -10^{\circ}$ section for the 3% CG-shift case. This indicates that the potentialities of the adaptive controllers are nearly exploited also for this uncertainty case.
In the next step, variations of $t_{CG-shift}$ according to Fig. 6.38 are considered. The simulation results are summarized in Fig. 6.43 and Table 6.38 for the baseline controller, in Fig. 6.44 and Table 6.39 for the DPI Augmentation, in Fig. 6.45 and Table 6.40 for the Plant Augmentation, in Fig. 6.46 and Table 6.41 for the $\Delta\dot{q}$ Compensation Law and in Fig. 6.47 and Table 6.42 for the standalone L1 adaptive controller with Eigenstructure Assignment. It can still be observed that the adaptive controllers are able to stabilize the aircraft independent from the point in time $t_{CG-shift}$, where the CG-shift appears, in contrast to the baseline controller configuration. Thus, the adaptive augmentations achieve a performance increase of approximately 81% with regard to the mean values of the $M_{\mathcal{L}_2}$ metric. For the standalone adaptive controller this value even increases to nearly 85%.

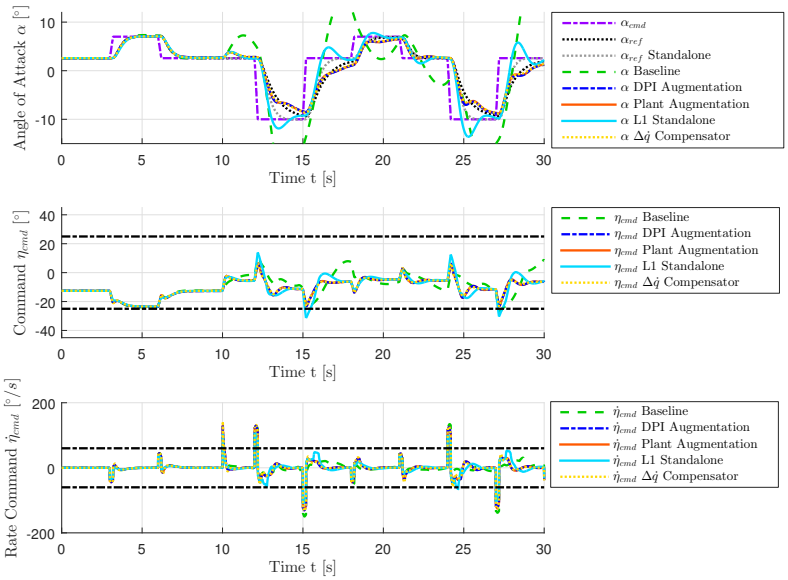

Figure 6.39. – Comparison of angle of attack α, elevator command η_{cmd} and elevator command rate $\dot{\eta}_{cmd}$ for example maneuver performed by basic, nonlinear aircraft model in combination with baseline controller, L1 Adaptive Augmentations, $\Delta\dot{q}$ Compensation Law and L1 adaptive controller with Eigenstructure Assignment starting at $V_0 = 154.94\frac{m}{s}$ and $h_0 = 5000m$ considering CG-shift of 5% at $t = 10s$

Table 6.34. – Comparison of performance metrics $M_{\mathcal{L}_2}$, $M_{\mathcal{L}_\infty}$ and $M_{\mathcal{L}_{2,act}}$ generated from example maneuver performed by basic, nonlinear aircraft model in combination with baseline controller, L1 Adaptive Augmentations, $\Delta\dot{q}$ Compensation Law and L1 adaptive controller with Eigenstructure Assignment starting at $V_0 = 154.94\frac{m}{s}$ and $h_0 = 5000m$ considering CG-shift of 5% at $t = 10s$

Controller	$M_{\mathcal{L}_2}$ $[-]$	$M_{\mathcal{L}_\infty}$ $[-]$	$M_{\mathcal{L}_{2,act}}$ $[-]$
Baseline	21.00	0.357	23.59
DPI Augmentation	2.03	0.044	22.96
Plant Augmentation	2.04	0.042	22.91
L1 Standalone	3.95	0.084	20.66
$\Delta\dot{q}$ Compensator	1.75	0.033	23.11

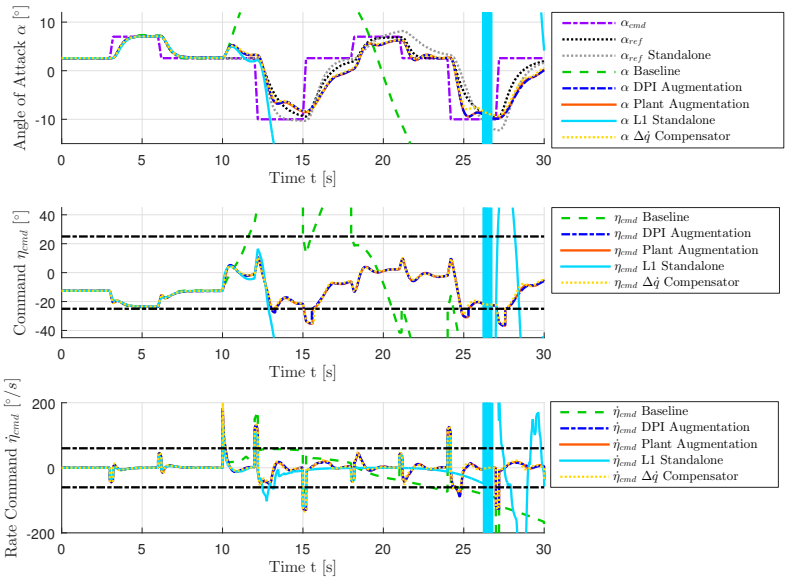

Figure 6.40. – Comparison of angle of attack α, elevator command η_{cmd} and elevator command rate $\dot{\eta}_{cmd}$ for example maneuver performed by basic, nonlinear aircraft model in combination with baseline controller, L1 Adaptive Augmentations, $\Delta\dot{q}$ Compensation Law and L1 adaptive controller with Eigenstructure Assignment starting at $V_0 = 154.94\frac{m}{s}$ and $h_0 = 5000m$ considering CG-shift of 7% at $t = 10s$

Table 6.35. – Comparison of performance metrics $M_{\mathcal{L}_2}$, $M_{\mathcal{L}_\infty}$ and $M_{\mathcal{L}_{2,act}}$ generated from example maneuver performed by basic, nonlinear aircraft model in combination with baseline controller, L1 Adaptive Augmentations, $\Delta\dot{q}$ Compensation Law and L1 adaptive controller with Eigenstructure Assignment starting at $V_0 = 154.94\frac{m}{s}$ and $h_0 = 5000m$ considering CG-shift of 7% at $t = 10s$

Controller	$M_{\mathcal{L}_2}$ $[-]$	$M_{\mathcal{L}_\infty}$ $[-]$	$M_{\mathcal{L}_{2,act}}$ $[-]$
Baseline	86.47	1.559	58.24
DPI Augmentation	3.96	0.072	26.16
Plant Augmentation	3.85	0.071	26.05
L1 Standalone	251.74	3.348	152485.73
$\Delta\dot{q}$ Compensator	3.20	0.054	26.00

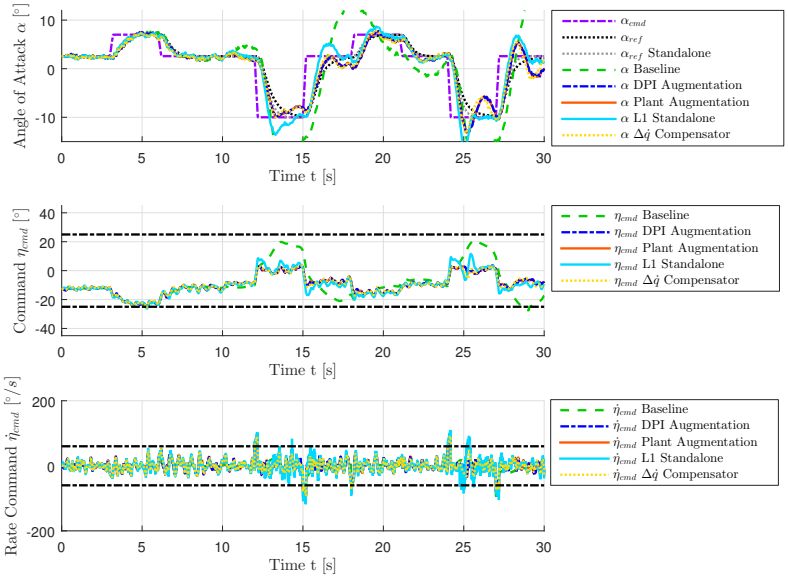

Figure 6.41. – Comparison of angle of attack α, elevator command η_{cmd} and elevator command rate $\dot{\eta}_{cmd}$ for example maneuver performed by enhanced, nonlinear aircraft model in combination with baseline controller, L1 Adaptive Augmentations, $\Delta\dot{q}$ Compensation Law and L1 adaptive controller with Eigenstructure Assignment starting at $V_0 = 154.94\frac{m}{s}$ and $h_0 = 5000m$ considering CG-shift of 2% at $t = 10s$

Table 6.36. – Comparison of performance metrics $M_{\mathcal{L}_2}$, $M_{\mathcal{L}_\infty}$ and $M_{\mathcal{L}_{2,act}}$ generated from example maneuver performed by enhanced, nonlinear aircraft model in combination with baseline controller, L1 Adaptive Augmentations, $\Delta\dot{q}$ Compensation Law and L1 adaptive controller with Eigenstructure Assignment starting at $V_0 = 154.94\frac{m}{s}$ and $h_0 = 5000m$ considering CG-shift of 2% at $t = 10s$

Controller	$M_{\mathcal{L}_2}$ $[-]$	$M_{\mathcal{L}_\infty}$ $[-]$	$M_{\mathcal{L}_{2,act}}$ $[-]$
Baseline	18.41	0.295	15.89
DPI Augmentation	4.72	0.106	18.00
Plant Augmentation	4.80	0.108	17.94
L1 Standalone	5.52	0.150	23.35
$\Delta\dot{q}$ Compensator	4.90	0.110	18.54

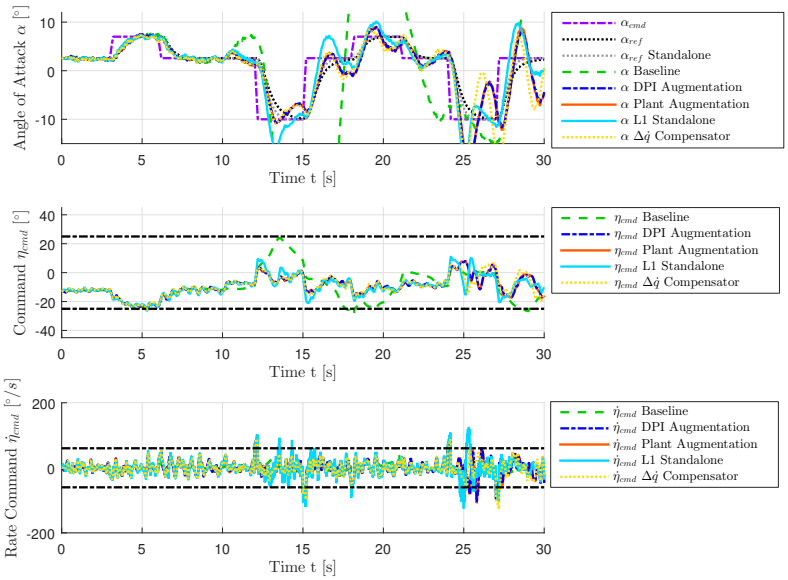

Figure 6.42. – Comparison of angle of attack α, elevator command η_{cmd} and elevator command rate $\dot{\eta}_{cmd}$ for example maneuver performed by enhanced, nonlinear aircraft model in combination with baseline controller, L1 Adaptive Augmentations, $\Delta\dot{q}$ Compensation Law and L1 adaptive controller with Eigenstructure Assignment starting at $V_0 = 154.94\frac{m}{s}$ and $h_0 = 5000m$ considering CG-shift of 3% at $t = 10s$

Table 6.37. – Comparison of performance metrics $M_{\mathcal{L}_2}$, $M_{\mathcal{L}_\infty}$ and $M_{\mathcal{L}_{2,act}}$ generated from example maneuver performed by enhanced, nonlinear aircraft model in combination with baseline controller, L1 Adaptive Augmentations, $\Delta\dot{q}$ Compensation Law and L1 adaptive controller with Eigenstructure Assignment starting at $V_0 = 154.94\frac{m}{s}$ and $h_0 = 5000m$ considering CG-shift of 3% at $t = 10s$

Controller	$M_{\mathcal{L}_2}$ $[-]$	$M_{\mathcal{L}_\infty}$ $[-]$	$M_{\mathcal{L}_{2,act}}$ $[-]$
Baseline	56.04	1.042	14.57
DPI Augmentation	8.71	0.224	21.13
Plant Augmentation	9.00	0.227	21.16
L1 Standalone	7.94	0.204	25.57
$\Delta\dot{q}$ Compensator	9.39	0.200	22.10

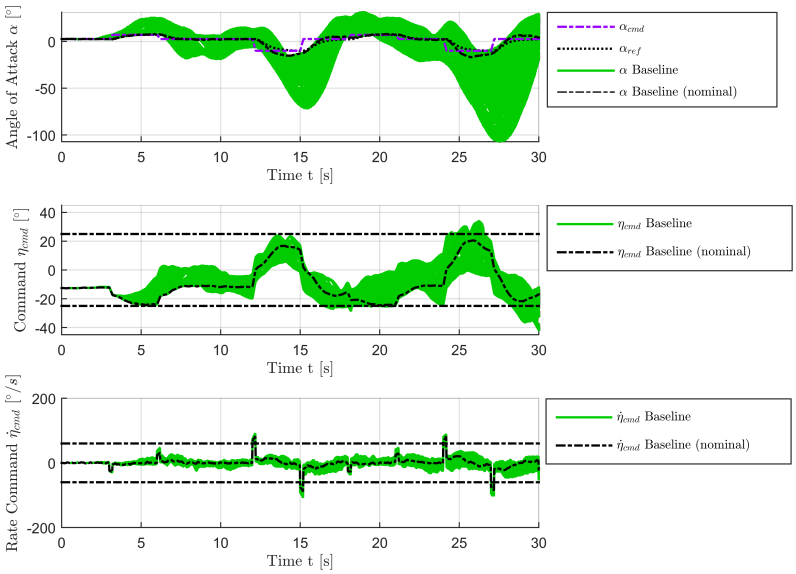

Figure 6.43. – Angle of attack α, elevator command η_{cmd} and elevator command rate $\dot{\eta}_{cmd}$ for example maneuver performed by enhanced, nonlinear aircraft model with baseline controller starting at $V_0 = 154.94\frac{m}{s}$ and $h_0 = 5000m$ considering variation of $t_{CG-shift}$

Table 6.38. – Performance metrics $M_{\mathcal{L}_2}$, $M_{\mathcal{L}_\infty}$ and $M_{\mathcal{L}_{2,act}}$ (maximum, minimum, mean value and standard deviation) generated from example maneuver performed by enhanced, nonlinear aircraft model with baseline controller starting at $V_0 = 154.94\frac{m}{s}$ and $h_0 = 5000m$ considering variation of $t_{CG-shift}$

	$M_{\mathcal{L}_2}$ $[-]$	$M_{\mathcal{L}_\infty}$ $[-]$	$M_{\mathcal{L}_{2,act}}$ $[-]$
max	86.71	1.693	16.69
min	7.79	0.142	13.81
$\varnothing$	45.16	0.890	15.17
σ	20.256	0.4041	0.611

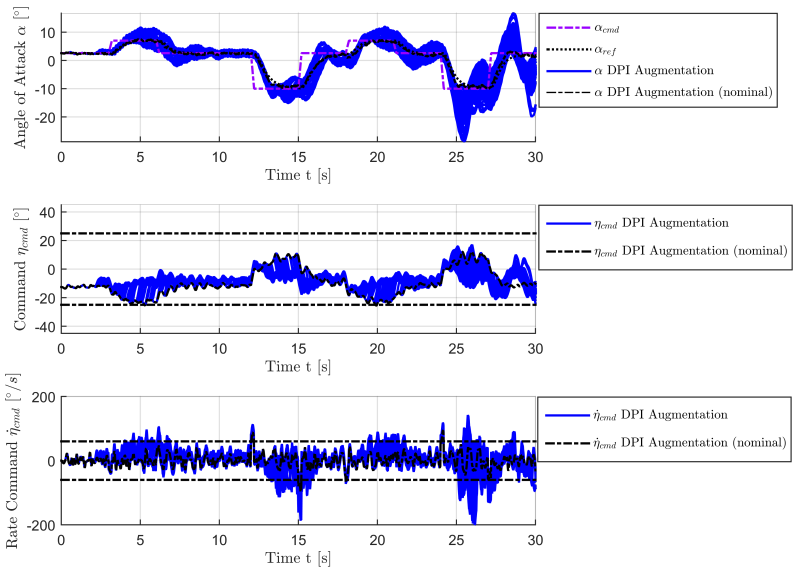

Figure 6.44. – Angle of attack α, elevator command η_{cmd} and elevator command rate $\dot{\eta}_{cmd}$ for example maneuver performed by enhanced, nonlinear aircraft model with DPI Augmentation starting at $V_0 = 154.94\frac{m}{s}$ and $h_0 = 5000m$ considering variation of $t_{CG-shift}$

Table 6.39. – Performance metrics $M_{\mathcal{L}_2}$, $M_{\mathcal{L}_\infty}$ and $M_{\mathcal{L}_{2,act}}$ (maximum, minimum, mean value and standard deviation) generated from example maneuver performed by enhanced, nonlinear aircraft model with DPI Augmentation and comparison to baseline controller starting at $V_0 = 154.94\frac{m}{s}$ and $h_0 = 5000m$ considering variation of $t_{CG-shift}$

	$M_{\mathcal{L}_2}$ [−]	$M_{\mathcal{L}_\infty}$ [−]	$M_{\mathcal{L}_{2,act}}$ [−]	$M_{\mathcal{L}_{2,rel}}$ [%]	$M_{\mathcal{L}_{\infty,rel}}$ [%]	$M_{\mathcal{L}_{2,act,rel}}$ [%]
max	11.41	0.387	28.81	13.2%	22.9%	172.6%
min	2.29	0.047	19.35	29.4%	32.8%	140.1%
∅	8.19	0.205	21.23	18.1%	23.0%	139.9%
σ	1.406	0.0420	1.309	6.9%	10.4%	214.3%

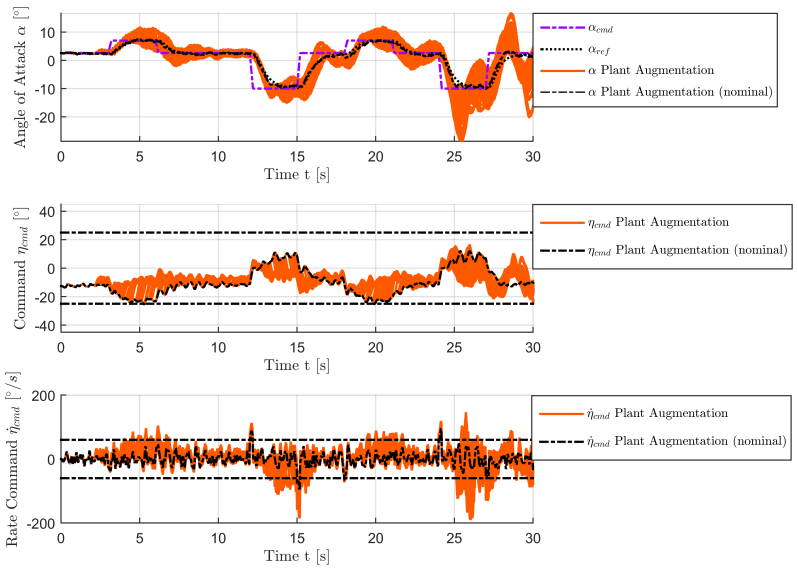

Figure 6.45. – Angle of attack α, elevator command η_{cmd} and elevator command rate $\dot{\eta}_{cmd}$ for example maneuver performed by enhanced, nonlinear aircraft model with Plant Augmentation starting at $V_0 = 154.94\frac{m}{s}$ and $h_0 = 5000m$ considering variation of $t_{CG-shift}$

Table 6.40. – Performance metrics $M_{\mathcal{L}_2}$, $M_{\mathcal{L}_\infty}$ and $M_{\mathcal{L}_{2,act}}$ (maximum, minimum, mean value and standard deviation) generated from example maneuver performed by enhanced, nonlinear aircraft model with Plant Augmentation and comparison to baseline controller starting at $V_0 = 154.94\frac{m}{s}$ and $h_0 = 5000m$ considering variation of $t_{CG-shift}$

	$M_{\mathcal{L}_2}$ [−]	$M_{\mathcal{L}_\infty}$ [−]	$M_{\mathcal{L}_{2,act}}$ [−]	$M_{\mathcal{L}_{2,rel}}$ [%]	$M_{\mathcal{L}_{\infty,rel}}$ [%]	$M_{\mathcal{L}_{2,act,rel}}$ [%]
max	11.38	0.393	28.02	13.1%	23.2%	167.9%
min	2.31	0.047	19.22	29.6%	33.3%	139.2%
∅	8.40	0.208	21.22	18.6%	23.3%	139.9%
σ	1.471	0.0427	1.235	7.3%	10.6%	202.1%

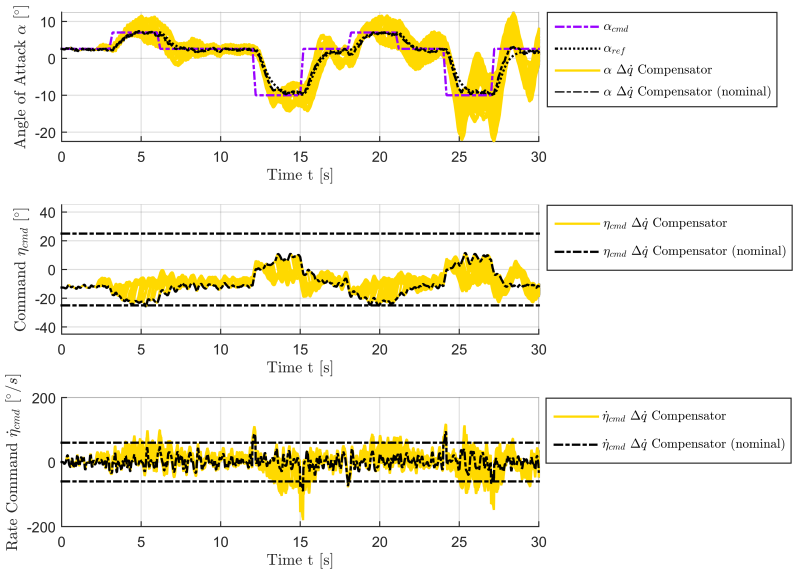

Figure 6.46. – Angle of attack α, elevator command η_{cmd} and elevator command rate $\dot{\eta}_{cmd}$ for example maneuver performed by enhanced, nonlinear aircraft model with $\Delta\dot{q}$ Compensation Law starting at $V_0 = 154.94\frac{m}{s}$ and $h_0 = 5000m$ considering variation of $t_{CG-shift}$

Table 6.41. – Performance metrics $M_{\mathcal{L}_2}$, $M_{\mathcal{L}_\infty}$ and $M_{\mathcal{L}_{2,act}}$ (maximum, minimum, mean value and standard deviation) generated from example maneuver performed by enhanced, nonlinear aircraft model with $\Delta\dot{q}$ Compensation Law and comparison to baseline controller starting at $V_0 = 154.94\frac{m}{s}$ and $h_0 = 5000m$ considering variation of $t_{CG-shift}$

	$M_{\mathcal{L}_2}$ $[-]$	$M_{\mathcal{L}_\infty}$ $[-]$	$M_{\mathcal{L}_{2,act}}$ $[-]$	$M_{\mathcal{L}_{2,rel}}$ $[\%]$	$M_{\mathcal{L}_{\infty,rel}}$ $[\%]$	$M_{\mathcal{L}_{2,act,rel}}$ $[\%]$
max	10.81	0.266	26.24	12.5%	15.7%	157.2%
min	2.40	0.050	19.03	30.8%	35.5%	137.9%
$\varnothing$	8.59	0.191	21.90	19.0%	21.4%	144.4%
σ	1.530	0.0308	1.012	7.6%	7.6%	165.7%

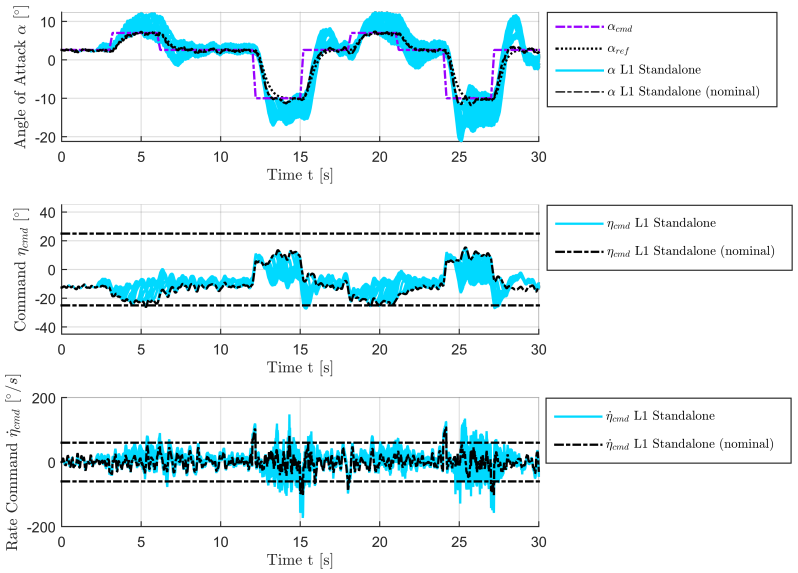

Figure 6.47. – Angle of attack α, elevator command η_{cmd} and elevator command rate $\dot{\eta}_{cmd}$ for example maneuver performed by enhanced, nonlinear aircraft model with L1 adaptive controller with Eigenstructure Assignment starting at $V_0 = 154.94\frac{m}{s}$ and $h_0 = 5000m$ considering variation of $t_{CG-shift}$

Table 6.42. – Performance metrics $M_{\mathcal{L}_2}$, $M_{\mathcal{L}_\infty}$ and $M_{\mathcal{L}_{2,act}}$ (maximum, minimum, mean value and standard deviation) generated from example maneuver performed by enhanced, nonlinear aircraft model with L1 adaptive controller with Eigenstructure Assignment and comparison to baseline controller starting at $V_0 = 154.94\frac{m}{s}$ and $h_0 = 5000m$ considering variation of $t_{CG-shift}$

	$M_{\mathcal{L}_2}$ [−]	$M_{\mathcal{L}_\infty}$ [−]	$M_{\mathcal{L}_{2,act}}$ [−]	$M_{\mathcal{L}_{2,rel}}$ [%]	$M_{\mathcal{L}_{\infty,rel}}$ [%]	$M_{\mathcal{L}_{2,act,rel}}$ [%]
max	8.25	0.228	26.71	9.5%	13.5%	160.0%
min	2.61	0.071	22.07	33.5%	50.2%	159.9%
∅	6.97	0.193	24.91	15.4%	21.7%	164.2%
σ	1.108	0.0290	1.061	5.5%	7.2%	173.5%

6.2.6. Uncertainty w.r.t. sensor delay

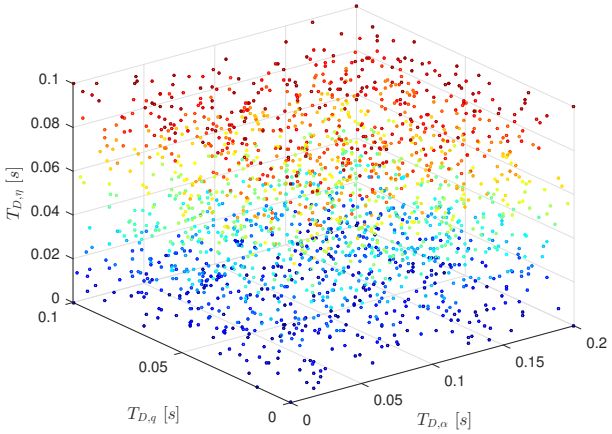

Figure 6.48. – Variation of additional time delays $T_{D,\alpha}$, $T_{D,q}$ and $T_{D,\eta}$ applied to sensor measurements of angle of attack α, pitch rate q and elevator deflection η

The following four sections focus on assessments of the controller performances with regard to additional delay, which is applied to the sensor measurements. For this purpose, this section investigates combined uncertainty cases, where additional delays are inserted in all relevant sensor signals, which are angle of attack α, pitch rate q and elevator deflection η. In the following sections Section 6.2.7, Section 6.2.8 and Section 6.2.9, delay is separately applied to the individual sensor measurements.
Therefore, the additional sensor delays $T_{D,\alpha}$, $T_{D,q}$ and $T_{D,\eta}$ are randomly varied within the limits $[0s; 0.1s]$ for pitch rate and elevator deflector as well as $[0s; 0.2s]$ for angle of attack measurement, where the corner cases are also considered. The resulting parameter space is depicted in Fig. 6.48. It includes a total amount of 2000 variations. These variations are applied to the sensor models of the enhanced aircraft model and the model is simulated in combination with the controllers, which were designed in the course of this thesis. The results can be found in Fig. 6.49 and Table 6.43 for the baseline controller, in Fig. 6.50 and Table 6.44 for the DPI Augmentation, in Fig. 6.51 and Table 6.45 for the Plant Augmentation, in Fig. 6.52 and Table 6.46 for the $\Delta\dot{q}$ Compensation Law and in Fig. 6.53 and Table 6.47 for the standalone L1 adaptive controller with Eigenstructure Assignment. It can be observed from the scattering shown in the plots and from the standard deviation of $M_{\mathcal{L}_2}$ that the adaptive controllers are much more sensitive to sensor delay compared to the baseline controller configuration. This also confirms the results gained during the robust stability assessment in Section 6.1.1, where Table 6.4 and Table 6.6 reveal that the time delay margins reduce for the adaptive controllers considering the sensor cuts, especially with regard to angle of attack α. Considering the simulation results, the most sensitive configurations are the L1 Adaptive Augmentations, whereas the $\Delta\dot{q}$ Compensation Law exhibits a considerably lower sensitivity with regard to additional

time delays. On the other hand, a decrease with regard to the mean values of $M_{\mathcal{L}_2}$ and $M_{\mathcal{L}_\infty}$ indicates that all adaptive controllers are still able to increase the average performance considering this uncertainty case.

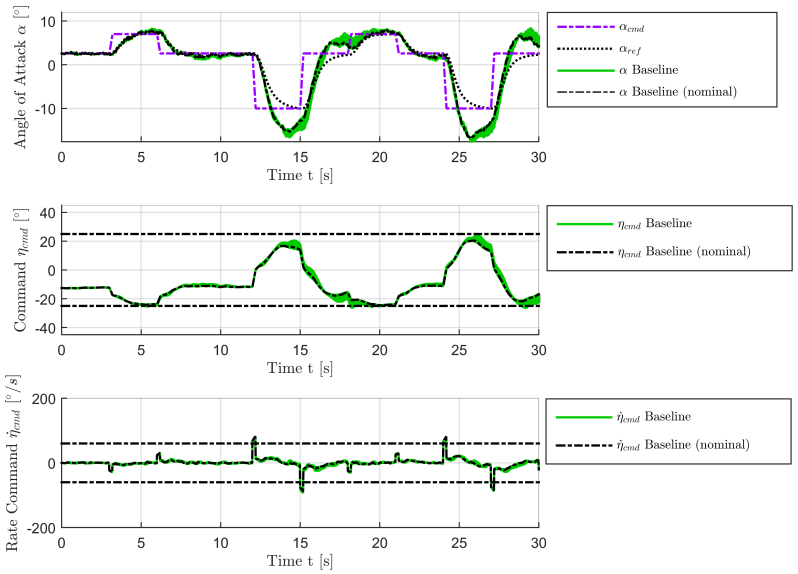

Figure 6.49. – Angle of attack α, elevator command η_{cmd} and elevator command rate $\dot{\eta}_{cmd}$ for example maneuver performed by enhanced, nonlinear aircraft model with baseline controller starting at $V_0 = 154.94\frac{m}{s}$ and $h_0 = 5000m$ considering variation of additional time delays $T_{D,\alpha}$, $T_{D,q}$ and $T_{D,\eta}$

Table 6.43. – Performance metrics $M_{\mathcal{L}_2}$, $M_{\mathcal{L}_\infty}$ and $M_{\mathcal{L}_{2,act}}$ (maximum, minimum, mean value and standard deviation) generated from example maneuver performed by enhanced, nonlinear aircraft model with baseline controller starting at $V_0 = 154.94\frac{m}{s}$ and $h_0 = 5000m$ considering variation of additional time delays $T_{D,\alpha}$, $T_{D,q}$ and $T_{D,\eta}$

	$M_{\mathcal{L}_2}$ $[-]$	$M_{\mathcal{L}_\infty}$ $[-]$	$M_{\mathcal{L}_{2,act}}$ $[-]$
max	9.20	0.153	15.13
min	7.77	0.142	14.34
$\varnothing$	8.51	0.148	14.75
σ	0.414	0.0032	0.211

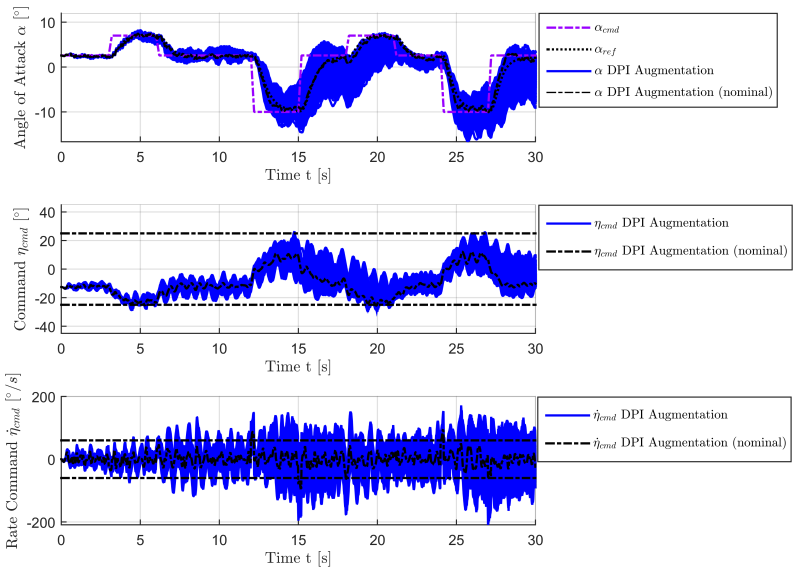

Figure 6.50. – Angle of attack α, elevator command η_{cmd} and elevator command rate $\dot{\eta}_{cmd}$ for example maneuver performed by enhanced, nonlinear aircraft model with DPI Augmentation starting at $V_0 = 154.94\frac{m}{s}$ and $h_0 = 5000m$ considering variation of additional time delays $T_{D,\alpha}$, $T_{D,q}$ and $T_{D,\eta}$

Table 6.44. – Performance metrics $M_{\mathcal{L}_2}$, $M_{\mathcal{L}_\infty}$ and $M_{\mathcal{L}_{2,act}}$ (maximum, minimum, mean value and standard deviation) generated from example maneuver performed by enhanced, nonlinear aircraft model with DPI Augmentation and comparison to baseline controller starting at $V_0 = 154.94\frac{m}{s}$ and $h_0 = 5000m$ considering variation of additional time delays $T_{D,\alpha}$, $T_{D,q}$ and $T_{D,\eta}$

	$M_{\mathcal{L}_2}$ [−]	$M_{\mathcal{L}_\infty}$ [−]	$M_{\mathcal{L}_{2,act}}$ [−]	$M_{\mathcal{L}_{2,rel}}$ [%]	$M_{\mathcal{L}_{\infty,rel}}$ [%]	$M_{\mathcal{L}_{2,act,rel}}$ [%]
max	11.77	0.200	58.47	127.9%	131.2%	386.4%
min	2.09	0.047	16.86	26.9%	32.9%	117.5%
∅	4.25	0.087	28.80	49.9%	58.7%	195.3%
σ	1.982	0.0333	9.602	479.0%	1027.3%	4548.4%

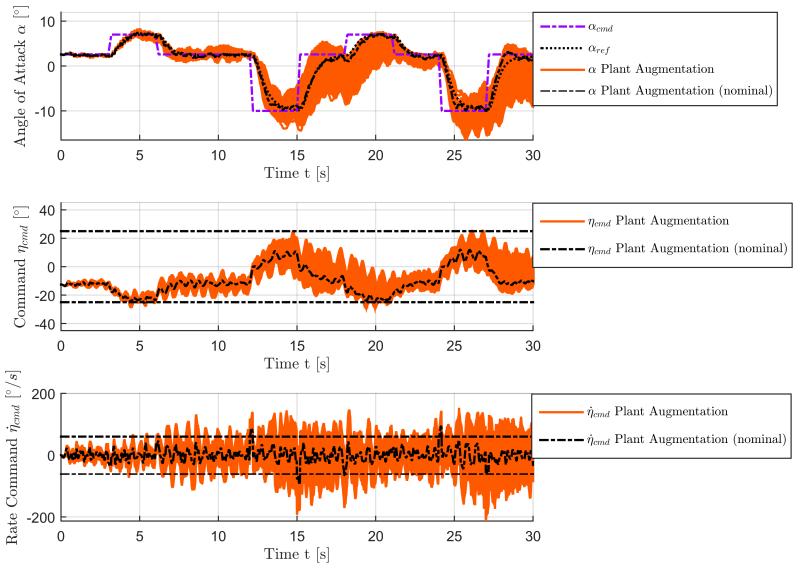

Figure 6.51. – Angle of attack α, elevator command η_{cmd} and elevator command rate $\dot{\eta}_{cmd}$ for example maneuver performed by enhanced, nonlinear aircraft model with Plant Augmentation starting at $V_0 = 154.94\frac{m}{s}$ and $h_0 = 5000m$ considering variation of additional time delays $T_{D,\alpha}$, $T_{D,q}$ and $T_{D,\eta}$

Table 6.45. – Performance metrics $M_{\mathcal{L}_2}$, $M_{\mathcal{L}_\infty}$ and $M_{\mathcal{L}_{2,act}}$ (maximum, minimum, mean value and standard deviation) generated from example maneuver performed by enhanced, nonlinear aircraft model with Plant Augmentation and comparison to baseline controller starting at $V_0 = 154.94\frac{m}{s}$ and $h_0 = 5000m$ considering variation of additional time delays $T_{D,\alpha}$, $T_{D,q}$ and $T_{D,\eta}$

	$M_{\mathcal{L}_2}$ [−]	$M_{\mathcal{L}_\infty}$ [−]	$M_{\mathcal{L}_{2,act}}$ [−]	$M_{\mathcal{L}_{2,rel}}$ [%]	$M_{\mathcal{L}_{\infty,rel}}$ [%]	$M_{\mathcal{L}_{2,act,rel}}$ [%]
max	13.33	0.213	57.24	145.0%	139.3%	378.3%
min	2.08	0.047	16.93	26.8%	33.4%	118.0%
∅	4.16	0.085	28.01	48.9%	57.2%	190.0%
σ	1.955	0.0316	9.078	472.5%	976.5%	4300.3%

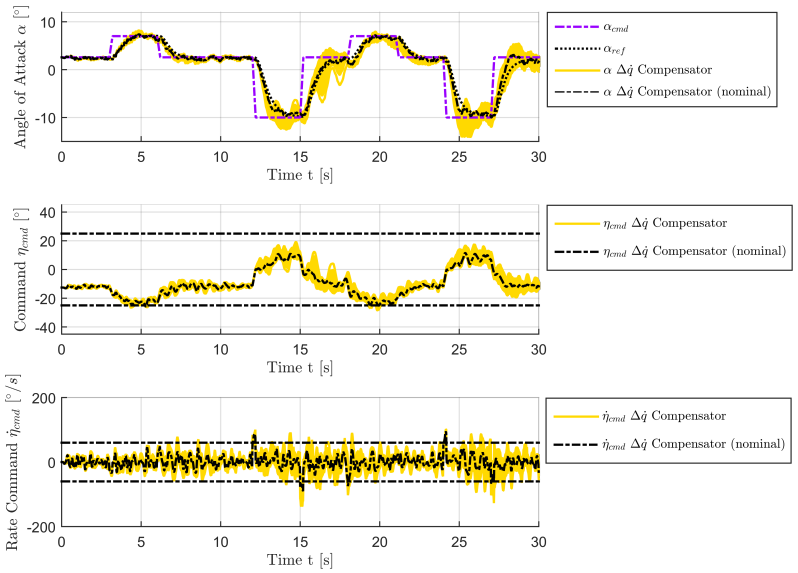

Figure 6.52. – Angle of attack α, elevator command η_{cmd} and elevator command rate $\dot{\eta}_{cmd}$ for example maneuver performed by enhanced, nonlinear aircraft model with $\Delta\dot{q}$ Compensation Law starting at $V_0 = 154.94\frac{m}{s}$ and $h_0 = 5000m$ considering variation of additional time delays $T_{D,\alpha}$, $T_{D,q}$ and $T_{D,\eta}$

Table 6.46. – Performance metrics $M_{\mathcal{L}_2}$, $M_{\mathcal{L}_\infty}$ and $M_{\mathcal{L}_{2,act}}$ (maximum, minimum, mean value and standard deviation) generated from example maneuver performed by enhanced, nonlinear aircraft model with $\Delta\dot{q}$ Compensation Law and comparison to baseline controller starting at $V_0 = 154.94\frac{m}{s}$ and $h_0 = 5000m$ considering variation of additional time delays $T_{D,\alpha}$, $T_{D,q}$ and $T_{D,\eta}$

	$M_{\mathcal{L}_2}$ $[-]$	$M_{\mathcal{L}_\infty}$ $[-]$	$M_{\mathcal{L}_{2,act}}$ $[-]$	$M_{\mathcal{L}_{2,rel}}$ $[\%]$	$M_{\mathcal{L}_{\infty,rel}}$ $[\%]$	$M_{\mathcal{L}_{2,act,rel}}$ $[\%]$
max	5.29	0.123	31.77	57.5%	80.7%	210.0%
min	1.97	0.043	18.77	25.3%	30.0%	130.8%
$\varnothing$	3.25	0.073	20.20	38.2%	49.4%	137.0%
σ	0.696	0.0117	1.572	168.3%	361.3%	744.6%

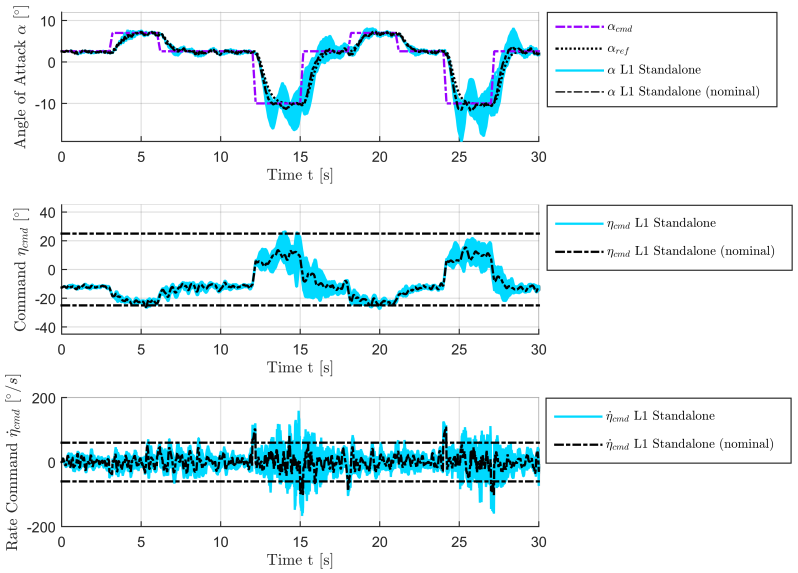

Figure 6.53. – Angle of attack α, elevator command η_{cmd} and elevator command rate $\dot{\eta}_{cmd}$ for example maneuver performed by enhanced, nonlinear aircraft model with L1 adaptive controller with Eigenstructure Assignment starting at $V_0 = 154.94\frac{m}{s}$ and $h_0 = 5000m$ considering variation of additional time delays $T_{D,\alpha}$, $T_{D,q}$ and $T_{D,\eta}$

Table 6.47. – Performance metrics $M_{\mathcal{L}_2}$, $M_{\mathcal{L}_\infty}$ and $M_{\mathcal{L}_{2,act}}$ (maximum, minimum, mean value and standard deviation) generated from example maneuver performed by enhanced, nonlinear aircraft model with L1 adaptive controller with Eigenstructure Assignment and comparison to baseline controller starting at $V_0 = 154.94\frac{m}{s}$ and $h_0 = 5000m$ considering variation of additional time delays $T_{D,\alpha}$, $T_{D,q}$ and $T_{D,\eta}$

	$M_{\mathcal{L}_2}$ $[-]$	$M_{\mathcal{L}_\infty}$ $[-]$	$M_{\mathcal{L}_{2,act}}$ $[-]$	$M_{\mathcal{L}_{2,rel}}$ $[\%]$	$M_{\mathcal{L}_{\infty,rel}}$ $[\%]$	$M_{\mathcal{L}_{2,act,rel}}$ $[\%]$
max	7.81	0.187	29.41	84.9%	122.1%	194.4%
min	1.83	0.041	19.15	23.6%	28.9%	133.5%
$\varnothing$	3.63	0.100	22.64	42.6%	67.7%	153.6%
σ	1.132	0.0311	1.956	273.5%	958.3%	926.7%

6.2.7. Uncertainty w.r.t. sensor delay in α measurement

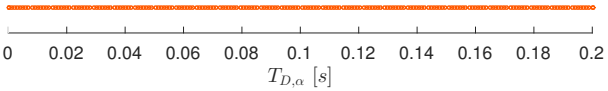

Figure 6.54. – Variation of additional time delay $T_{D,\alpha}$ applied to sensor measurements of angle of attack α

In the next step, additional time delay is only added to the angle of attack α measurement. This time, 200 evenly distributed parameter variations within the limits $[0s; 0.2s]$ are generated for the delay $T_{D,\alpha}$, which is also shown in Fig. 6.54.
The simulation results considering delay in the angle of attack α measurement are compiled in Fig. 6.55 and Table 6.48 for the baseline controller, in Fig. 6.56 and Table 6.49 for the DPI Augmentation, in Fig. 6.57 and Table 6.50 for the Plant Augmentation, in Fig. 6.58 and Table 6.51 for the $\Delta\dot{q}$ Compensation Law and in Fig. 6.59 and Table 6.52 for the standalone L1 adaptive controller with Eigenstructure Assignment. Although the scattering with regard to the angle of attack response is slightly reduced for the L1 adaptive controllers, which includes augmentations and standalone controller, the results are very similar to the ones gained in the last section. One can conclude from this that in this case, the L1 adaptive controllers exhibit their largest sensitivity with respect to time delays in the angle of attack α measurement, which is also confirmed by the following sections. The same comparison shows for the $\Delta\dot{q}$ Compensation Law that delay with regard to another sensor measurement is the main driver of scattering within the simulation results in Fig. 6.52 shown in the last section.

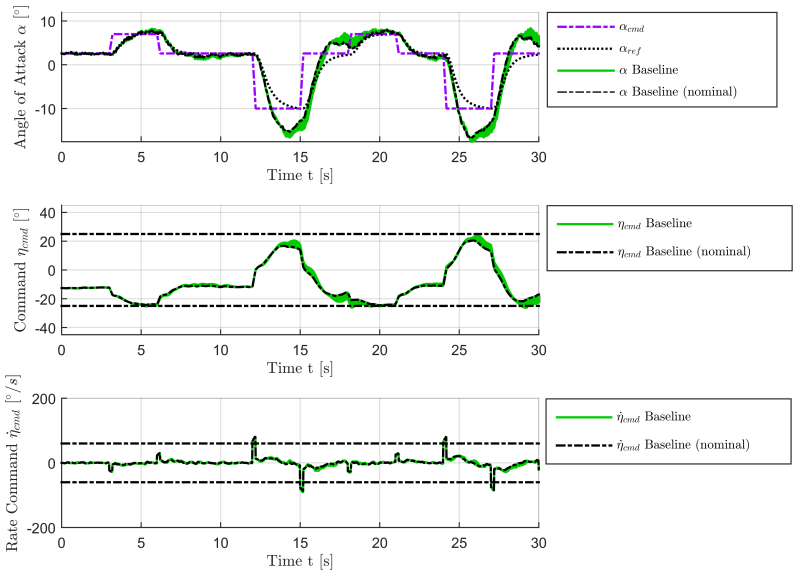

Figure 6.55. – Angle of attack α, elevator command η_{cmd} and elevator command rate $\dot{\eta}_{cmd}$ for example maneuver performed by enhanced, nonlinear aircraft model with baseline controller starting at $V_0 = 154.94\frac{m}{s}$ and $h_0 = 5000m$ considering variation of additional time delay $T_{D,\alpha}$

Table 6.48. – Performance metrics $M_{\mathcal{L}_2}$, $M_{\mathcal{L}_\infty}$ and $M_{\mathcal{L}_{2,act}}$ (maximum, minimum, mean value and standard deviation) generated from example maneuver performed by enhanced, nonlinear aircraft model with baseline controller starting at $V_0 = 154.94\frac{m}{s}$ and $h_0 = 5000m$ considering variation of additional time delay $T_{D,\alpha}$

	$M_{\mathcal{L}_2}$ $[-]$	$M_{\mathcal{L}_\infty}$ $[-]$	$M_{\mathcal{L}_{2,act}}$ $[-]$
max	9.20	0.153	15.13
min	7.79	0.142	14.45
$\varnothing$	8.52	0.148	14.78
σ	0.424	0.0031	0.204

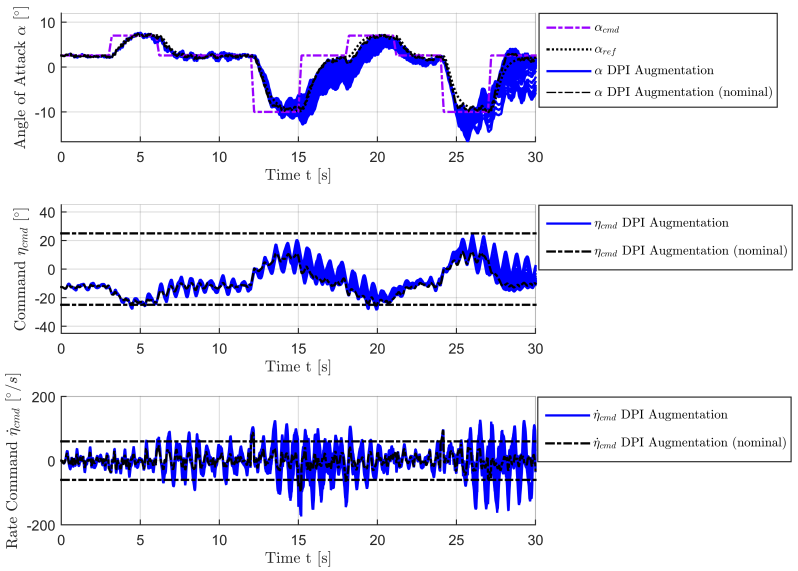

Figure 6.56. – Angle of attack α, elevator command η_{cmd} and elevator command rate $\dot{\eta}_{cmd}$ for example maneuver performed by enhanced, nonlinear aircraft model with DPI Augmentation starting at $V_0 = 154.94\frac{m}{s}$ and $h_0 = 5000m$ considering variation of additional time delay $T_{D,\alpha}$

Table 6.49. – Performance metrics $M_{\mathcal{L}_2}$, $M_{\mathcal{L}_\infty}$ and $M_{\mathcal{L}_{2,act}}$ (maximum, minimum, mean value and standard deviation) generated from example maneuver performed by enhanced, nonlinear aircraft model with DPI Augmentation and comparison to baseline controller starting at $V_0 = 154.94\frac{m}{s}$ and $h_0 = 5000m$ considering variation of additional time delay $T_{D,\alpha}$

	$M_{\mathcal{L}_2}$ $[-]$	$M_{\mathcal{L}_\infty}$ $[-]$	$M_{\mathcal{L}_{2,act}}$ $[-]$	$M_{\mathcal{L}_{2,rel}}$ $[\%]$	$M_{\mathcal{L}_{\infty,rel}}$ $[\%]$	$M_{\mathcal{L}_{2,act,rel}}$ $[\%]$
max	9.28	0.178	48.95	101.0%	116.9%	323.5%
min	2.29	0.047	19.48	29.4%	32.8%	134.8%
$\varnothing$	4.54	0.085	31.42	53.3%	57.7%	212.5%
σ	1.906	0.0339	7.205	448.9%	1094.4%	3525.6%

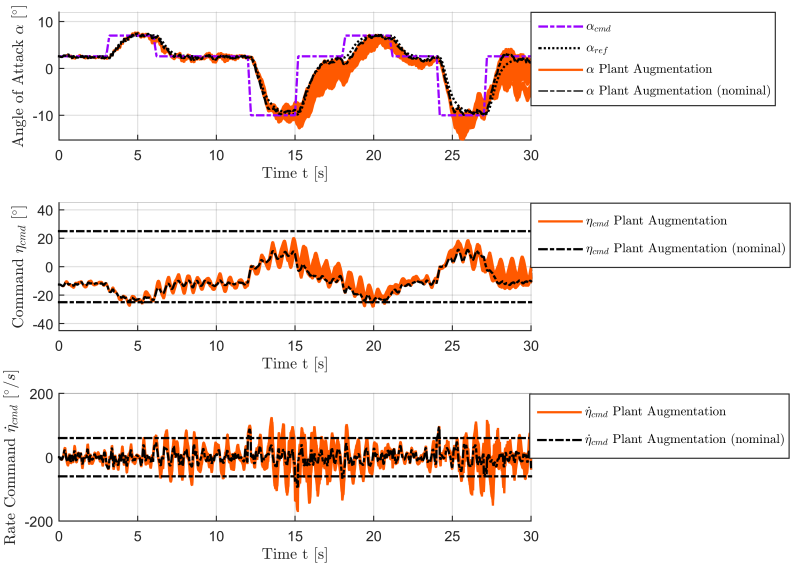

Figure 6.57. – Angle of attack α, elevator command η_{cmd} and elevator command rate $\dot{\eta}_{cmd}$ for example maneuver performed by enhanced, nonlinear aircraft model with Plant Augmentation starting at $V_0 = 154.94\frac{m}{s}$ and $h_0 = 5000m$ considering variation of additional time delay $T_{D,\alpha}$

Table 6.50. – Performance metrics $M_{\mathcal{L}_2}$, $M_{\mathcal{L}_\infty}$ and $M_{\mathcal{L}_{2,act}}$ (maximum, minimum, mean value and standard deviation) generated from example maneuver performed by enhanced, nonlinear aircraft model with Plant Augmentation and comparison to baseline controller starting at $V_0 = 154.94\frac{m}{s}$ and $h_0 = 5000m$ considering variation of additional time delay $T_{D,\alpha}$

	$M_{\mathcal{L}_2}$ [−]	$M_{\mathcal{L}_\infty}$ [−]	$M_{\mathcal{L}_{2,act}}$ [−]	$M_{\mathcal{L}_{2,rel}}$ [%]	$M_{\mathcal{L}_{\infty,rel}}$ [%]	$M_{\mathcal{L}_{2,act,rel}}$ [%]
max	8.12	0.160	42.49	88.3%	104.7%	280.8%
min	2.31	0.047	19.33	29.6%	33.3%	133.7%
∅	4.41	0.083	30.36	51.8%	55.7%	205.4%
σ	1.770	0.0306	6.776	417.0%	988.9%	3315.6%

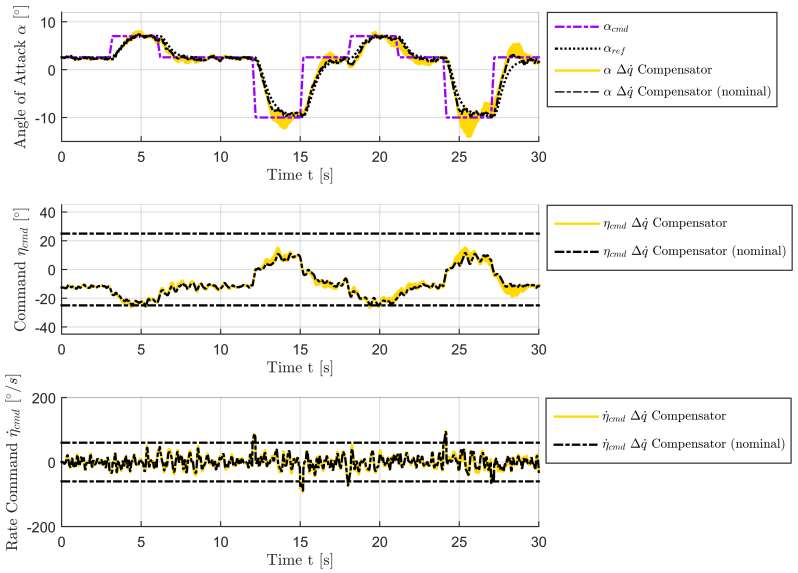

Figure 6.58. – Angle of attack α, elevator command η_{cmd} and elevator command rate $\dot{\eta}_{cmd}$ for example maneuver performed by enhanced, nonlinear aircraft model with $\Delta\dot{q}$ Compensation Law starting at $V_0 = 154.94\frac{m}{s}$ and $h_0 = 5000m$ considering variation of additional time delay $T_{D,\alpha}$

Table 6.51. – Performance metrics $M_{\mathcal{L}_2}$, $M_{\mathcal{L}_\infty}$ and $M_{\mathcal{L}_{2,act}}$ (maximum, minimum, mean value and standard deviation) generated from example maneuver performed by enhanced, nonlinear aircraft model with $\Delta\dot{q}$ Compensation Law and comparison to baseline controller starting at $V_0 = 154.94\frac{m}{s}$ and $h_0 = 5000m$ considering variation of additional time delay $T_{D,\alpha}$

	$M_{\mathcal{L}_2}$ $[-]$	$M_{\mathcal{L}_\infty}$ $[-]$	$M_{\mathcal{L}_{2,act}}$ $[-]$	$M_{\mathcal{L}_{2,rel}}$ $[\%]$	$M_{\mathcal{L}_{\infty,rel}}$ $[\%]$	$M_{\mathcal{L}_{2,act,rel}}$ $[\%]$
max	5.29	0.098	20.37	57.5%	64.5%	134.6%
min	2.40	0.050	19.03	30.8%	35.5%	131.7%
$\varnothing$	3.61	0.071	19.71	42.4%	47.8%	133.3%
σ	0.842	0.0114	0.430	198.4%	367.8%	210.3%

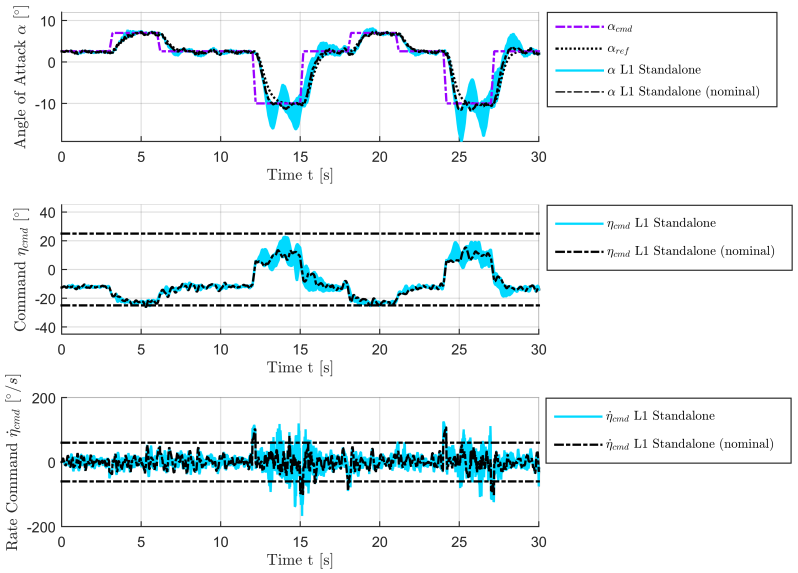

Figure 6.59. – Angle of attack α, elevator command η_{cmd} and elevator command rate $\dot{\eta}_{cmd}$ for example maneuver performed by enhanced, nonlinear aircraft model with L1 adaptive controller with Eigenstructure Assignment starting at $V_0 = 154.94\frac{m}{s}$ and $h_0 = 5000m$ considering variation of additional time delay $T_{D,\alpha}$

Table 6.52. – Performance metrics $M_{\mathcal{L}_2}$, $M_{\mathcal{L}_\infty}$ and $M_{\mathcal{L}_{2,act}}$ (maximum, minimum, mean value and standard deviation) generated from example maneuver performed by enhanced, nonlinear aircraft model with L1 adaptive controller with Eigenstructure Assignment and comparison to baseline controller starting at $V_0 = 154.94\frac{m}{s}$ and $h_0 = 5000m$ considering variation of additional time delay $T_{D,\alpha}$

	$M_{\mathcal{L}_2}$ [−]	$M_{\mathcal{L}_\infty}$ [−]	$M_{\mathcal{L}_{2,act}}$ [−]	$M_{\mathcal{L}_{2,rel}}$ [%]	$M_{\mathcal{L}_{\infty,rel}}$ [%]	$M_{\mathcal{L}_{2,act,rel}}$ [%]
max	7.48	0.187	27.39	81.4%	122.3%	181.0%
min	2.61	0.071	19.99	33.5%	50.2%	138.3%
∅	4.58	0.128	22.71	53.8%	86.4%	153.6%
σ	1.405	0.0336	2.210	331.1%	1086.3%	1081.5%

6.2.8. Uncertainty w.r.t. sensor delay in q measurement

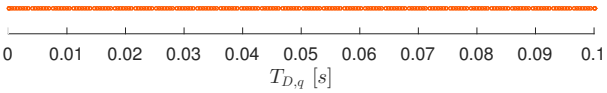

Figure 6.60. – Variation of additional time delay $T_{D,q}$ applied to sensor measurements of pitch rate q

After the investigation of time delay with regard to the angle of attack α measurement, this section focuses on performance assessments with respect to delays added to the pitch rate q measurement. Again, 200 evenly distributed variations are generated for $T_{D,q}$, but this time the limits $[0s; 0.1s]$ are chosen, which are shown in Fig. 6.60.
The simulation results considering delay in the pitch rate q measurement are summarized in Fig. 6.61 and Table 6.53 for the baseline controller, in Fig. 6.62 and Table 6.54 for the DPI Augmentation, in Fig. 6.63 and Table 6.55 for the Plant Augmentation, in Fig. 6.64 and Table 6.56 for the $\Delta\dot{q}$ Compensation Law and in Fig. 6.65 and Table 6.57 for the standalone L1 adaptive controller with Eigenstructure Assignment. At first, it can be seen that delay of the pitch rate measurement barely affects the performance of the baseline controller. This can be seen by means of the system responses in Fig. 6.61 and the standard deviations in Table 6.53. On the other hand, notable oscillations can be observed for the adaptive augmentations. In particular, it can be identified that the $\Delta\dot{q}$ Compensation Law is most sensitive with regard to delays in the pitch rate q measurement channel considering the combined delay assessment in Fig. 6.53. It is also worth noting that the additional delay barely has an effect on the performance of the standalone L1 adaptive controller. This can be explained by means of the fact that this controller inherits infinite phase margin and time delay margin with regard to the pitch rate q sensor cut (c.f. Table A.89 in Appendix A.6.6). Note that this statement also holds for the baseline controller with the exception of the envelope point corresponding to the lowest velocity (c.f. Table A.60 in Appendix A.6.2).

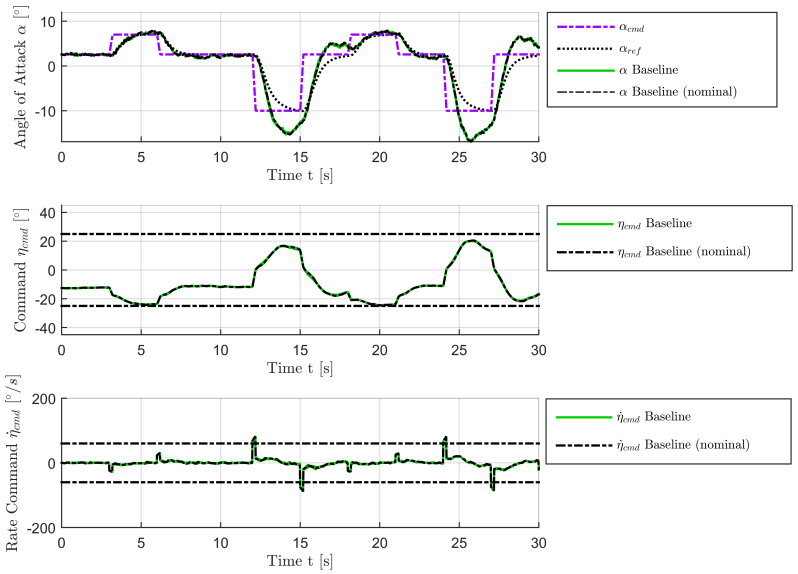

Figure 6.61. – Angle of attack α, elevator command η_{cmd} and elevator command rate $\dot{\eta}_{cmd}$ for example maneuver performed by enhanced, nonlinear aircraft model with baseline controller starting at $V_0 = 154.94\frac{m}{s}$ and $h_0 = 5000m$ considering variation of additional time delay $T_{D,q}$

Table 6.53. – Performance metrics $M_{\mathcal{L}_2}$, $M_{\mathcal{L}_\infty}$ and $M_{\mathcal{L}_{2,act}}$ (maximum, minimum, mean value and standard deviation) generated from example maneuver performed by enhanced, nonlinear aircraft model with baseline controller starting at $V_0 = 154.94\frac{m}{s}$ and $h_0 = 5000m$ considering variation of additional time delay $T_{D,q}$

	$M_{\mathcal{L}_2}$ $[-]$	$M_{\mathcal{L}_\infty}$ $[-]$	$M_{\mathcal{L}_{2,act}}$ $[-]$
max	7.79	0.143	14.45
min	7.77	0.142	14.34
$\varnothing$	7.78	0.142	14.40
σ	0.004	0.0003	0.033

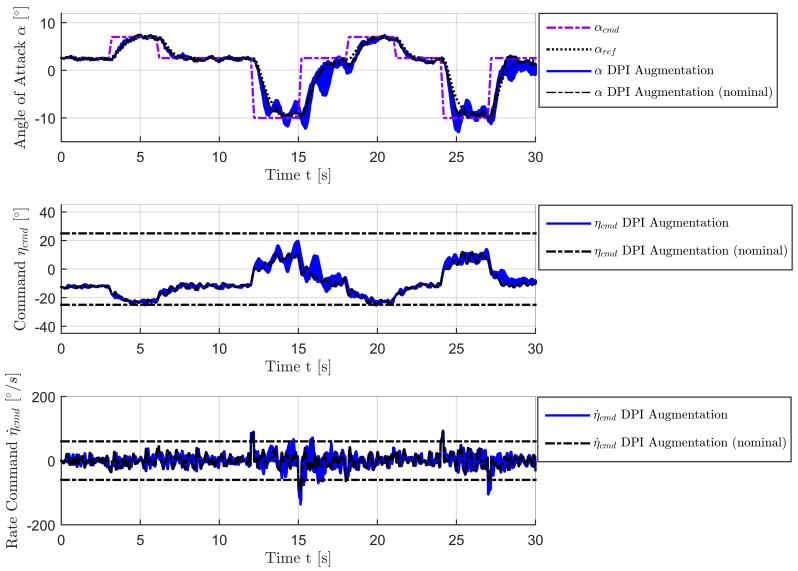

Figure 6.62. – Angle of attack α, elevator command η_{cmd} and elevator command rate $\dot{\eta}_{cmd}$ for example maneuver performed by enhanced, nonlinear aircraft model with DPI Augmentation starting at $V_0 = 154.94\frac{m}{s}$ and $h_0 = 5000m$ considering variation of additional time delay $T_{D,q}$

Table 6.54. – Performance metrics $M_{\mathcal{L}_2}$, $M_{\mathcal{L}_\infty}$ and $M_{\mathcal{L}_{2,act}}$ (maximum, minimum, mean value and standard deviation) generated from example maneuver performed by enhanced, nonlinear aircraft model with DPI Augmentation and comparison to baseline controller starting at $V_0 = 154.94\frac{m}{s}$ and $h_0 = 5000m$ considering variation of additional time delay $T_{D,q}$

	$M_{\mathcal{L}_2}$ $[-]$	$M_{\mathcal{L}_\infty}$ $[-]$	$M_{\mathcal{L}_{2,act}}$ $[-]$	$M_{\mathcal{L}_{2,rel}}$ $[\%]$	$M_{\mathcal{L}_{\infty,rel}}$ $[\%]$	$M_{\mathcal{L}_{2,act,rel}}$ $[\%]$
max	5.20	0.120	23.84	66.8%	84.2%	164.9%
min	2.18	0.046	16.98	28.1%	32.7%	118.4%
$\varnothing$	2.91	0.074	18.38	37.5%	51.8%	127.6%
σ	0.867	0.0225	1.729	21225.8%	7982.9%	5202.9%

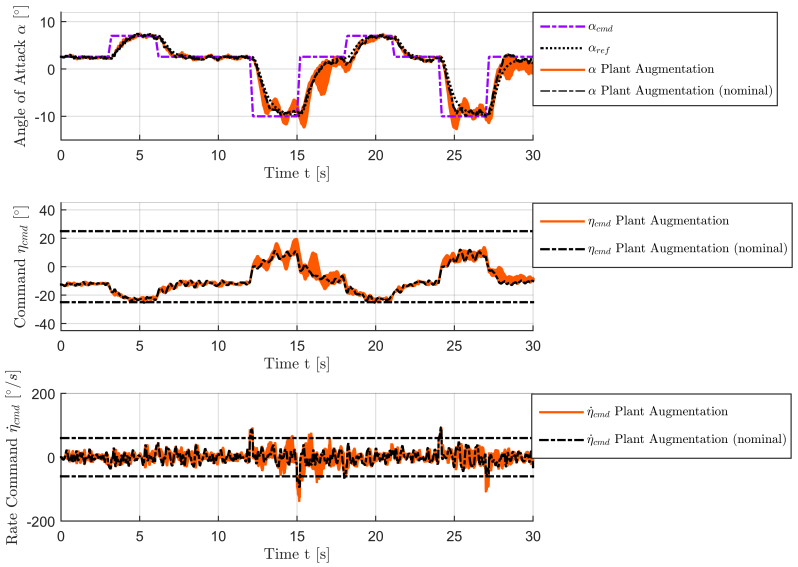

Figure 6.63. – Angle of attack α, elevator command η_{cmd} and elevator command rate $\dot{\eta}_{cmd}$ for example maneuver performed by enhanced, nonlinear aircraft model with Plant Augmentation starting at $V_0 = 154.94\frac{m}{s}$ and $h_0 = 5000m$ considering variation of additional time delay $T_{D,q}$

Table 6.55. – Performance metrics $M_{\mathcal{L}_2}$, $M_{\mathcal{L}_\infty}$ and $M_{\mathcal{L}_{2,act}}$ (maximum, minimum, mean value and standard deviation) generated from example maneuver performed by enhanced, nonlinear aircraft model with Plant Augmentation and comparison to baseline controller starting at $V_0 = 154.94\frac{m}{s}$ and $h_0 = 5000m$ considering variation of additional time delay $T_{D,q}$

	$M_{\mathcal{L}_2}$ $[-]$	$M_{\mathcal{L}_\infty}$ $[-]$	$M_{\mathcal{L}_{2,act}}$ $[-]$	$M_{\mathcal{L}_{2,rel}}$ $[\%]$	$M_{\mathcal{L}_{\infty,rel}}$ $[\%]$	$M_{\mathcal{L}_{2,act,rel}}$ $[\%]$
max	5.11	0.117	23.78	65.7%	82.1%	164.5%
min	2.20	0.046	17.04	28.3%	32.6%	118.8%
$\varnothing$	2.91	0.073	18.38	37.4%	51.3%	127.7%
σ	0.851	0.0216	1.690	20830.6%	7648.6%	5087.1%

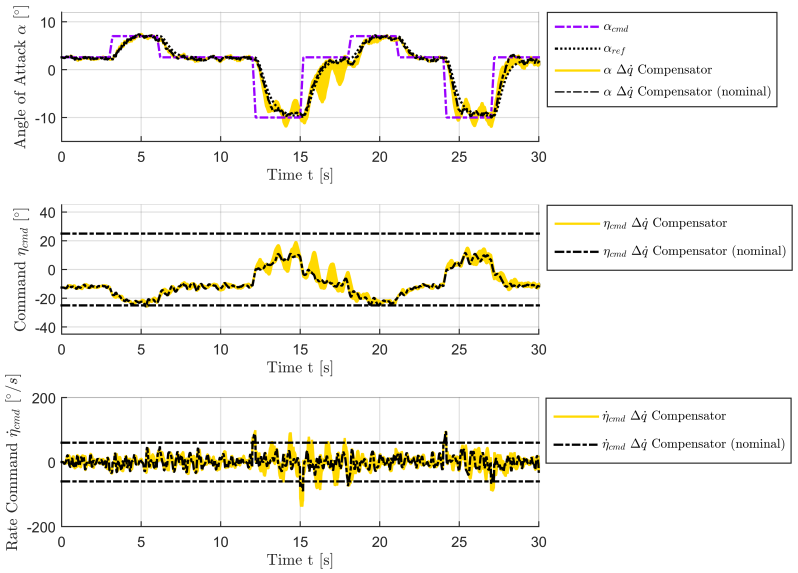

Figure 6.64. – Angle of attack α, elevator command η_{cmd} and elevator command rate $\dot{\eta}_{cmd}$ for example maneuver performed by enhanced, nonlinear aircraft model with $\Delta\dot{q}$ Compensation Law starting at $V_0 = 154.94\frac{m}{s}$ and $h_0 = 5000m$ considering variation of additional time delay $T_{D,q}$

Table 6.56. – Performance metrics $M_{\mathcal{L}_2}$, $M_{\mathcal{L}_\infty}$ and $M_{\mathcal{L}_{2,act}}$ (maximum, minimum, mean value and standard deviation) generated from example maneuver performed by enhanced, nonlinear aircraft model with $\Delta\dot{q}$ Compensation Law and comparison to baseline controller starting at $V_0 = 154.94\frac{m}{s}$ and $h_0 = 5000m$ considering variation of additional time delay $T_{D,q}$

	$M_{\mathcal{L}_2}$ $[-]$	$M_{\mathcal{L}_\infty}$ $[-]$	$M_{\mathcal{L}_{2,act}}$ $[-]$	$M_{\mathcal{L}_{2,rel}}$ $[\%]$	$M_{\mathcal{L}_{\infty,rel}}$ $[\%]$	$M_{\mathcal{L}_{2,act,rel}}$ $[\%]$
max	5.10	0.119	26.20	65.5%	83.3%	181.3%
min	2.31	0.048	18.86	29.7%	34.1%	131.5%
$\varnothing$	2.85	0.067	20.04	36.6%	46.8%	139.2%
σ	0.712	0.0156	1.719	17428.0%	5517.7%	5174.0%

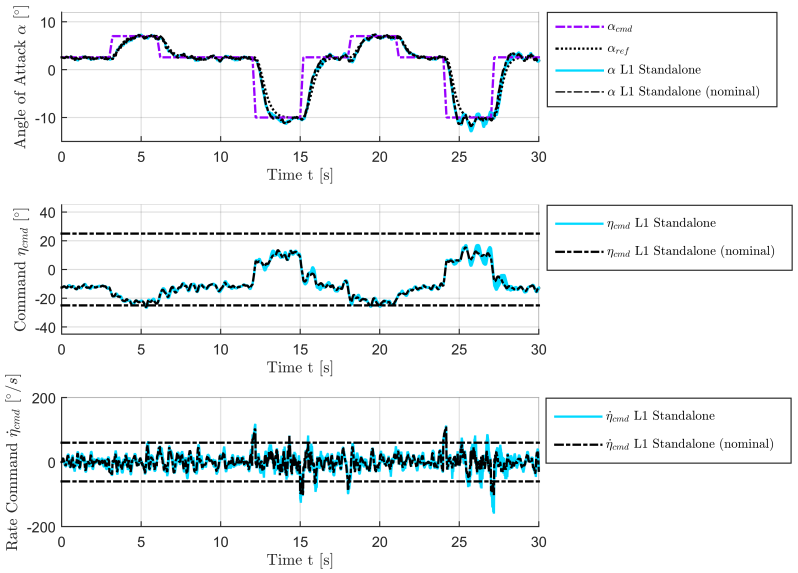

Figure 6.65. – Angle of attack α, elevator command η_{cmd} and elevator command rate $\dot{\eta}_{cmd}$ for example maneuver performed by enhanced, nonlinear aircraft model with L1 adaptive controller with Eigenstructure Assignment starting at $V_0 = 154.94\frac{m}{s}$ and $h_0 = 5000m$ considering variation of additional time delay $T_{D,q}$

Table 6.57. – Performance metrics $M_{\mathcal{L}_2}$, $M_{\mathcal{L}_\infty}$ and $M_{\mathcal{L}_{2,act}}$ (maximum, minimum, mean value and standard deviation) generated from example maneuver performed by enhanced, nonlinear aircraft model with L1 adaptive controller with Eigenstructure Assignment and comparison to baseline controller starting at $V_0 = 154.94\frac{m}{s}$ and $h_0 = 5000m$ considering variation of additional time delay $T_{D,q}$

	$M_{\mathcal{L}_2}$ $[-]$	$M_{\mathcal{L}_\infty}$ $[-]$	$M_{\mathcal{L}_{2,act}}$ $[-]$	$M_{\mathcal{L}_{2,rel}}$ $[\%]$	$M_{\mathcal{L}_{\infty,rel}}$ $[\%]$	$M_{\mathcal{L}_{2,act,rel}}$ $[\%]$
max	2.61	0.071	27.24	33.5%	50.1%	188.5%
min	2.52	0.068	22.18	32.4%	48.2%	154.7%
$\varnothing$	2.56	0.069	25.15	32.9%	48.7%	174.7%
σ	0.032	0.0010	1.537	775.9%	347.1%	4625.9%

6.2.9. Uncertainty w.r.t. sensor delay in η measurement

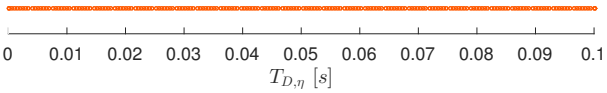

Figure 6.66. – Variation of additional time delay $T_{D,\eta}$ applied to sensor measurements of elevator deflection η

The last performance assessment with regard to sensor delay is carried out for the elevator deflection η measurement. For this purpose, the additional time delay $T_{D,\eta}$ is varied between $[0s; 0.1s]$ resulting in the even distribution of 200 parameter variations according to Fig. 6.66.
The accompanying simulation results are to be found in Fig. 6.67 and Table 6.58 for the baseline controller, in Fig. 6.68 and Table 6.59 for the DPI Augmentation, in Fig. 6.69 and Table 6.60 for the Plant Augmentation, in Fig. 6.70 and Table 6.61 for the $\Delta\dot{q}$ Compensation Law and in Fig. 6.71 and Table 6.62 for the standalone L1 adaptive controller with Eigenstructure Assignment. As it was expected, the variation of time delay with respect to the elevator deflection has no effect on the performance of the baseline controller, because it does not utilize actuator measurement. Furthermore, it can be observed that this variation has a stronger effect on the L1 Adaptive Augmentations in comparison to the $\Delta\dot{q}$ Compensation Law. Although, the results state good robustness against time delays in the elevator deflection measurement, which can also be observed for the standalone L1 adaptive controller.

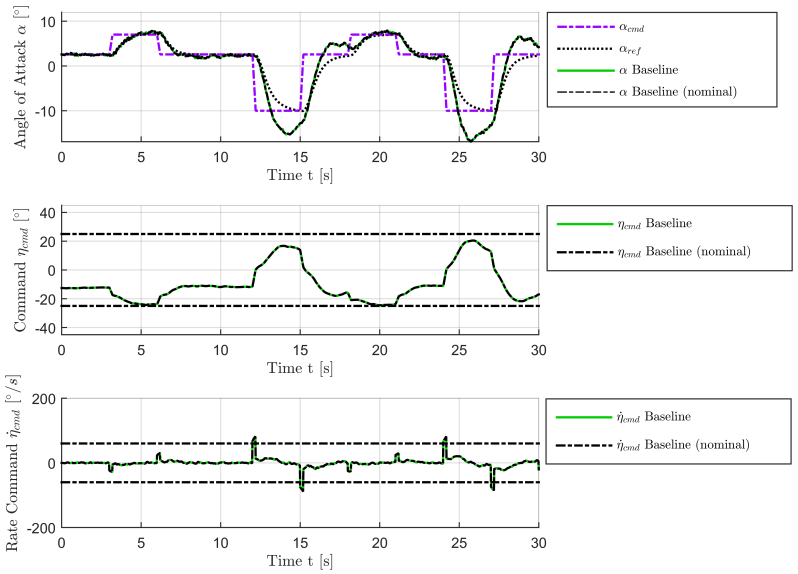

Figure 6.67. – Angle of attack α, elevator command η_{cmd} and elevator command rate $\dot{\eta}_{cmd}$ for example maneuver performed by enhanced, nonlinear aircraft model with baseline controller starting at $V_0 = 154.94\frac{m}{s}$ and $h_0 = 5000m$ considering variation of additional time delay $T_{D,\eta}$

Table 6.58. – Performance metrics $M_{\mathcal{L}_2}$, $M_{\mathcal{L}_\infty}$ and $M_{\mathcal{L}_{2,act}}$ (maximum, minimum, mean value and standard deviation) generated from example maneuver performed by enhanced, nonlinear aircraft model with baseline controller starting at $V_0 = 154.94\frac{m}{s}$ and $h_0 = 5000m$ considering variation of additional time delay $T_{D,\eta}$

	$M_{\mathcal{L}_2}$ $[-]$	$M_{\mathcal{L}_\infty}$ $[-]$	$M_{\mathcal{L}_{2,act}}$ $[-]$
max	7.79	0.142	14.45
min	7.79	0.142	14.45
$\varnothing$	7.79	0.142	14.45
σ	0.000	0.0000	0.000

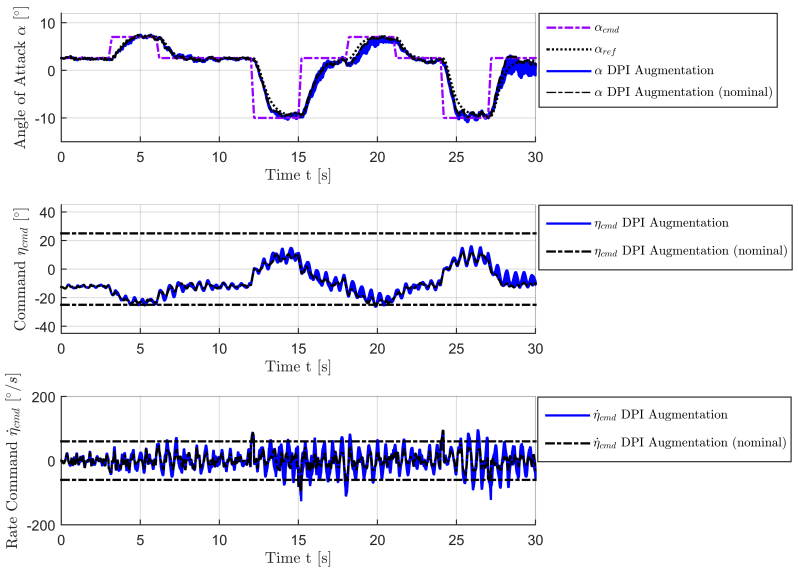

Figure 6.68. – Angle of attack α, elevator command η_{cmd} and elevator command rate $\dot{\eta}_{cmd}$ for example maneuver performed by enhanced, nonlinear aircraft model with DPI Augmentation starting at $V_0 = 154.94\frac{m}{s}$ and $h_0 = 5000m$ considering variation of additional time delay $T_{D,\eta}$

Table 6.59. – Performance metrics $M_{\mathcal{L}_2}$, $M_{\mathcal{L}_\infty}$ and $M_{\mathcal{L}_{2,act}}$ (maximum, minimum, mean value and standard deviation) generated from example maneuver performed by enhanced, nonlinear aircraft model with DPI Augmentation and comparison to baseline controller starting at $V_0 = 154.94\frac{m}{s}$ and $h_0 = 5000m$ considering variation of additional time delay $T_{D,\eta}$

	$M_{\mathcal{L}_2}$ $[-]$	$M_{\mathcal{L}_\infty}$ $[-]$	$M_{\mathcal{L}_{2,act}}$ $[-]$	$M_{\mathcal{L}_{2,rel}}$ [%]	$M_{\mathcal{L}_{\infty,rel}}$ [%]	$M_{\mathcal{L}_{2,act,rel}}$ [%]
max	3.34	0.060	34.46	42.9%	42.3%	238.4%
min	2.01	0.046	19.48	25.8%	32.2%	134.8%
∅	2.25	0.050	24.10	28.9%	34.8%	166.8%
σ	0.307	0.0038	4.203	-	-	-

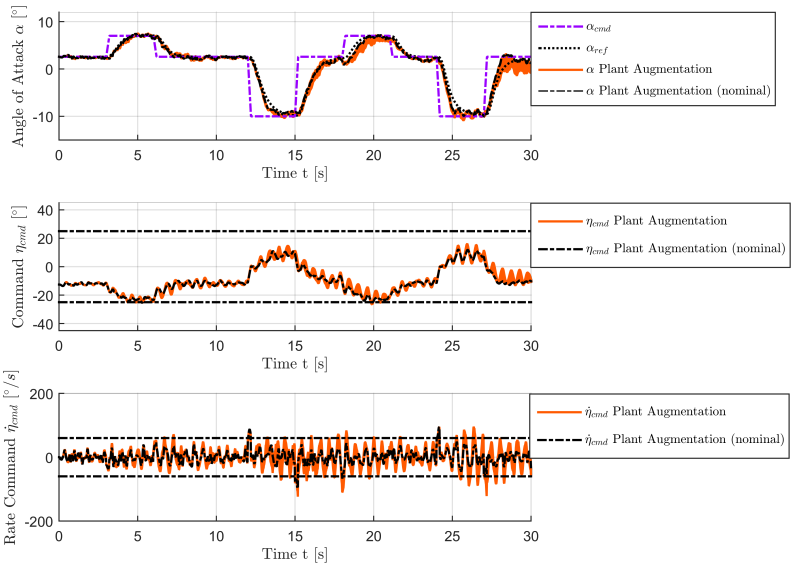

Figure 6.69. – Angle of attack α, elevator command η_{cmd} and elevator command rate $\dot{\eta}_{cmd}$ for example maneuver performed by enhanced, nonlinear aircraft model with Plant Augmentation starting at $V_0 = 154.94\frac{m}{s}$ and $h_0 = 5000m$ considering variation of additional time delay $T_{D,\eta}$

Table 6.60. – Performance metrics $M_{\mathcal{L}_2}$, $M_{\mathcal{L}_\infty}$ and $M_{\mathcal{L}_{2,act}}$ (maximum, minimum, mean value and standard deviation) generated from example maneuver performed by enhanced, nonlinear aircraft model with Plant Augmentation and comparison to baseline controller starting at $V_0 = 154.94\frac{m}{s}$ and $h_0 = 5000m$ considering variation of additional time delay $T_{D,\eta}$

	$M_{\mathcal{L}_2}$ $[-]$	$M_{\mathcal{L}_\infty}$ $[-]$	$M_{\mathcal{L}_{2,act}}$ $[-]$	$M_{\mathcal{L}_{2,rel}}$ $[\%]$	$M_{\mathcal{L}_{\infty,rel}}$ $[\%]$	$M_{\mathcal{L}_{2,act,rel}}$ $[\%]$
max	3.18	0.059	33.82	40.8%	41.2%	234.0%
min	2.01	0.046	19.33	25.8%	32.2%	133.7%
$\varnothing$	2.23	0.049	23.74	28.6%	34.5%	164.3%
σ	0.259	0.0035	4.018	-	-	-

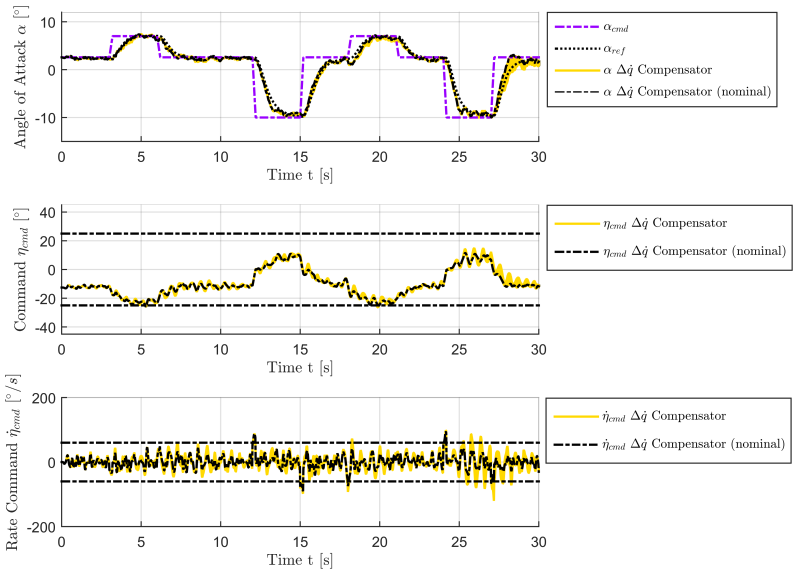

Figure 6.70. – Angle of attack α, elevator command η_{cmd} and elevator command rate $\dot{\eta}_{cmd}$ for example maneuver performed by enhanced, nonlinear aircraft model with $\Delta\dot{q}$ Compensation Law starting at $V_0 = 154.94\frac{m}{s}$ and $h_0 = 5000m$ considering variation of additional time delay $T_{D,\eta}$

Table 6.61. – Performance metrics $M_{\mathcal{L}_2}$, $M_{\mathcal{L}_\infty}$ and $M_{\mathcal{L}_{2,act}}$ (maximum, minimum, mean value and standard deviation) generated from example maneuver performed by enhanced, nonlinear aircraft model with $\Delta\dot{q}$ Compensation Law and comparison to baseline controller starting at $V_0 = 154.94\frac{m}{s}$ and $h_0 = 5000m$ considering variation of additional time delay $T_{D,\eta}$

	$M_{\mathcal{L}_2}$ $[-]$	$M_{\mathcal{L}_\infty}$ $[-]$	$M_{\mathcal{L}_{2,act}}$ $[-]$	$M_{\mathcal{L}_{2,rel}}$ $[\%]$	$M_{\mathcal{L}_{\infty,rel}}$ $[\%]$	$M_{\mathcal{L}_{2,act,rel}}$ $[\%]$
max	2.40	0.050	27.70	30.8%	35.5%	191.7%
min	1.88	0.042	19.03	24.2%	29.2%	131.7%
$\varnothing$	2.12	0.045	21.76	27.3%	31.6%	150.6%
σ	0.172	0.0032	2.522	-	-	-

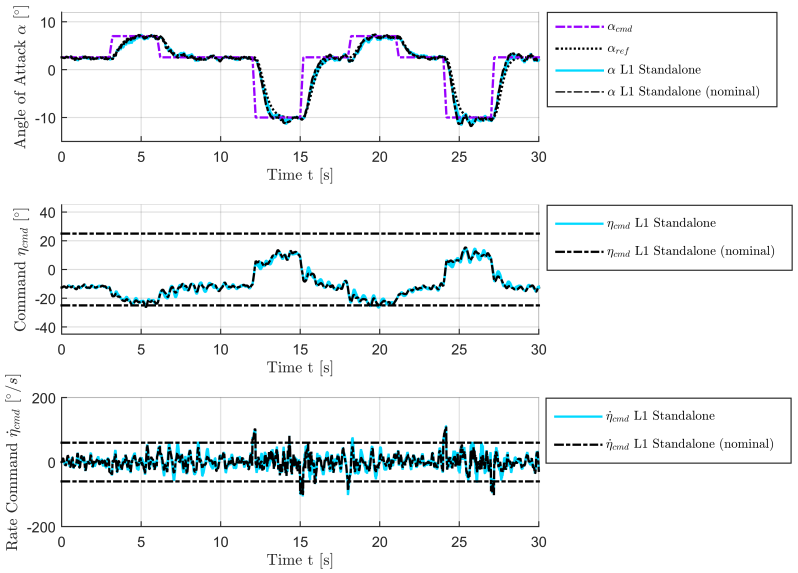

Figure 6.71. – Angle of attack α, elevator command η_{cmd} and elevator command rate $\dot{\eta}_{cmd}$ for example maneuver performed by enhanced, nonlinear aircraft model with L1 adaptive controller with Eigenstructure Assignment starting at $V_0 = 154.94\frac{m}{s}$ and $h_0 = 5000m$ considering variation of additional time delay $T_{D,\eta}$

Table 6.62. – Performance metrics $M_{\mathcal{L}_2}$, $M_{\mathcal{L}_\infty}$ and $M_{\mathcal{L}_{2,act}}$ (maximum, minimum, mean value and standard deviation) generated from example maneuver performed by enhanced, nonlinear aircraft model with L1 adaptive controller with Eigenstructure Assignment and comparison to baseline controller starting at $V_0 = 154.94\frac{m}{s}$ and $h_0 = 5000m$ considering variation of additional time delay $T_{D,\eta}$

	$M_{\mathcal{L}_2}$ $[-]$	$M_{\mathcal{L}_\infty}$ $[-]$	$M_{\mathcal{L}_{2,act}}$ $[-]$	$M_{\mathcal{L}_{2,rel}}$ $[\%]$	$M_{\mathcal{L}_{\infty,rel}}$ $[\%]$	$M_{\mathcal{L}_{2,act,rel}}$ $[\%]$
max	2.61	0.071	25.01	33.5%	50.2%	173.0%
min	1.83	0.041	22.18	23.5%	28.8%	153.5%
$\varnothing$	2.15	0.055	23.02	27.6%	38.5%	159.3%
σ	0.235	0.0092	0.820	-	-	-

6.2.10. Uncertainty w.r.t. sensor noise

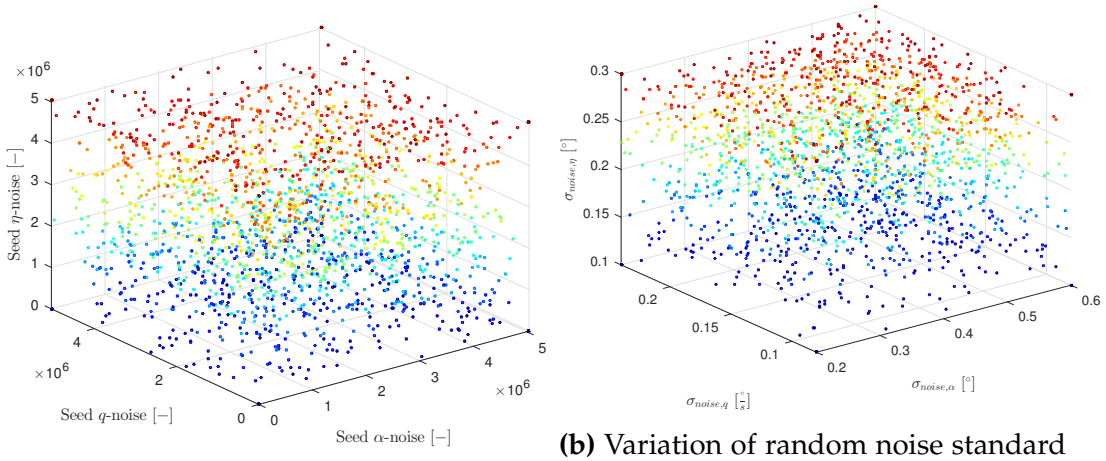

(a) Variation of random noise seeds applied in sensor measurements of angle-of-attack α, pitch rate q and elevator deflection η

(b) Variation of random noise standard deviations $\sigma_{noise,\alpha}$, $\sigma_{noise,q}$ and $\sigma_{noise,\eta}$ applied in sensor measurements of angle of attack α, pitch rate q and elevator deflection η

Figure 6.72. – Variation of random noise seeds and standard deviations applied in sensor measurements of angle of attack α, pitch rate q and elevator deflection η

The next sensor effect implemented in the sensor model according Section 2.6 to be considered for the performance assessments is measurement noise. Firstly, the impact of measurement noise simultaneously stemming from all relevant sensors on the controller performance is investigated, which are angle of attack α, pitch rate q and elevator deflection η. After that, the experiments are repeated considering measurement noise only for one sensor channel at a time.

In order to vary the amount of measurement noise, two sensor model parameters are considered per measurement in terms of the variation. These are the standard deviation of the Gaussian noise σ_{noise} and the seed used for the generation of the random numbers. Therefore, the standard deviations are randomly varied within the limits $[0.2°; 0.6°]$ for $\sigma_{noise,\alpha}$, $\left[0.08\frac{°}{s}; 0.24\frac{°}{s}\right]$ for $\sigma_{noise,q}$ and $[0.1°; 0.3°]$ for $\sigma_{noise,\eta}$. Here, the corner cases are included. The seeds are also randomly chosen considering the limits $[0; 5042063]$ for all sensor measurements. The resulting 2000 variations are also collected in Fig. 6.72.

For the purpose of investigating the isolated effect of measurement noise, turbulence as well as actuator backlash are deactivated for the following assessments. Furthermore, bias and scale factor errors are deactivated within the sensor models. At last, the commanded angle of attack α_{cmd} remains at α_0, which keeps the aircraft in a trimmed state.

Performance

The results of the simulations for the different controllers can be found in Fig. 6.73 and Table 6.63 for the baseline controller, in Fig. 6.74 and Table 6.64 for the DPI Augmentation, in Fig. 6.75 and Table 6.65 for the Plant Augmentation, in Fig. 6.76 and Table 6.66 for the $\Delta\dot{q}$ Compensation Law and in Fig. 6.77 and Table 6.67 for the standalone L1 Adaptive Controller with Eigenstructure Assignment. As it was already observed in the course of Chapter 5 and in Section 6.2.1 in terms of turbulence, also measurement noise is amplified to a higher degree through the adaptive controllers in comparison to the baseline controller. In particular, comparing $M_{\mathcal{L}_{2,act}}$ with regard to L1 Adaptive Augmentations and DPI baseline controller results in a factor of ≈ 12, by which the commanded actuator activity is increased. This increase can also be identified in the maximum values of the commanded elevator deflection $\dot{\eta}_{cmd}$. For the standalone L1 adaptive controller the same statement can be made, where the factor in activity increase is even around 25. The reason for this is the high gain parameter update law, which is part of the L1 adaptive controller, as it was already discussed in Section 5.2.2.3 and Section 5.2.4.2. It is also worth mentioning that application of the $\Delta\dot{q}$ Compensation Law results in an increase of commanded actuator activity by only factor 2. This is due to the fact that no high gain feedback of the measurements is included within the $\Delta\dot{q}$ Compensation Law.

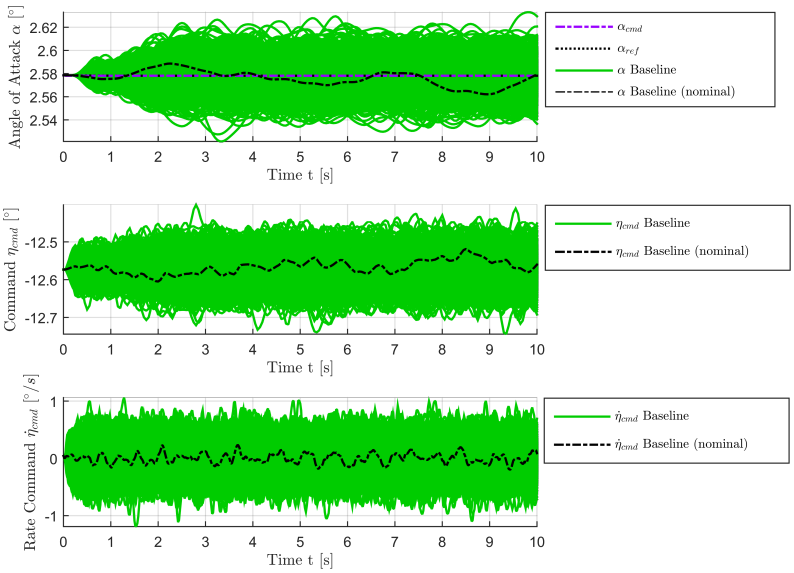

Figure 6.73. – Angle of attack α, elevator command η_{cmd} and elevator command rate $\dot{\eta}_{cmd}$ for zero maneuver performed by enhanced, nonlinear aircraft model with baseline controller starting at $V_0 = 154.94\frac{m}{s}$ and $h_0 = 5000m$ considering variation of noise seeds and noise standard deviations of angle-of-attack α, pitch rate q and elevator deflection η sensors

Table 6.63. – Performance metrics $M_{\mathcal{L}_2}$, $M_{\mathcal{L}_\infty}$ and $M_{\mathcal{L}_{2,act}}$ (maximum, minimum, mean value and standard deviation) generated from zero maneuver performed by enhanced, nonlinear aircraft model with baseline controller starting at $V_0 = 154.94\frac{m}{s}$ and $h_0 = 5000m$ considering variation of noise seeds and noise standard deviations of angle-of-attack α, pitch rate q and elevator deflection η sensors

	$M_{\mathcal{L}_2}$ $[-]$	$M_{\mathcal{L}_\infty}$ $[-]$	$M_{\mathcal{L}_{2,act}}$ $[-]$
max	0.037	0.0010	0.178
min	0.004	0.0001	0.035
$\varnothing$	0.016	0.0004	0.101
σ	0.0060	0.00014	0.0288

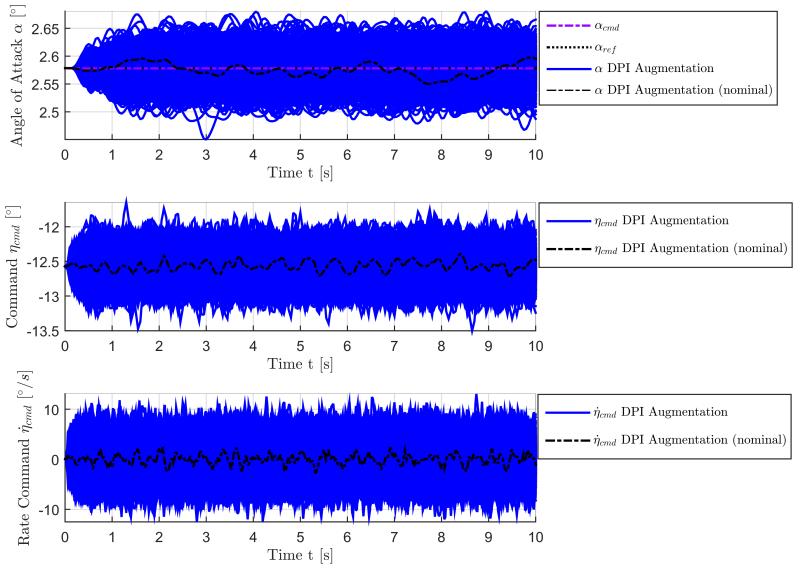

Figure 6.74. – Angle of attack α, elevator command η_{cmd} and elevator command rate $\dot{\eta}_{cmd}$ for zero maneuver performed by enhanced, nonlinear aircraft model with DPI Augmentation starting at $V_0 = 154.94\frac{m}{s}$ and $h_0 = 5000m$ considering variation of noise seeds and noise standard deviations of angle-of-attack α, pitch rate q and elevator deflection η sensors

Table 6.64. – Performance metrics $M_{\mathcal{L}_2}$, $M_{\mathcal{L}_\infty}$ and $M_{\mathcal{L}_{2,act}}$ (maximum, minimum, mean value and standard deviation) generated from zero maneuver performed by enhanced, nonlinear aircraft model with DPI Augmentation and comparison to baseline controller starting at $V_0 = 154.94\frac{m}{s}$ and $h_0 = 5000m$ considering variation of noise seeds and noise standard deviations of angle-of-attack α, pitch rate q and elevator deflection η sensors

	$M_{\mathcal{L}_2}$ $[-]$	$M_{\mathcal{L}_\infty}$ $[-]$	$M_{\mathcal{L}_{2,act}}$ $[-]$	$M_{\mathcal{L}_{2,rel}}$ $[\%]$	$M_{\mathcal{L}_{\infty,rel}}$ $[\%]$	$M_{\mathcal{L}_{2,act,rel}}$ $[\%]$
max	0.068	0.0022	1.944	183.6%	225.7%	1090.7%
min	0.012	0.0003	0.419	296.1%	318.7%	1186.2%
∅	0.035	0.0009	1.206	213.2%	234.9%	1196.1%
σ	0.0106	0.00029	0.3374	175.2%	201.8%	1172.7%

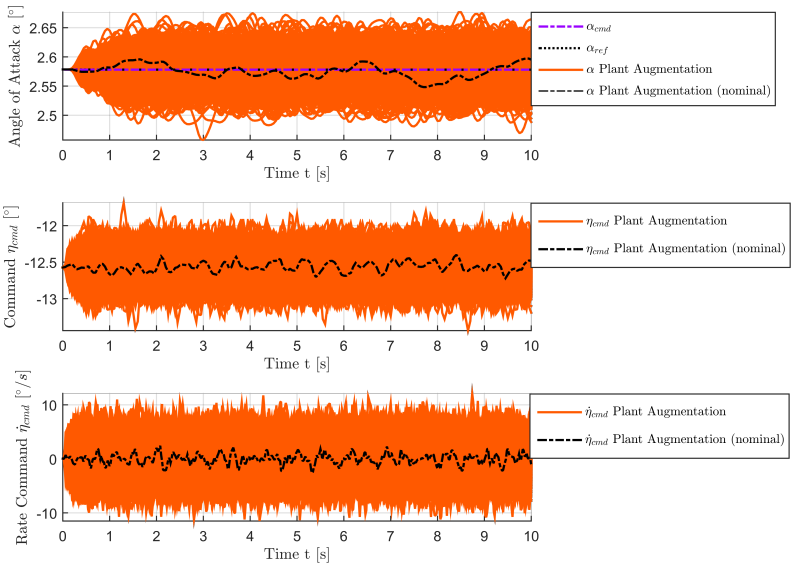

Figure 6.75. – Angle of attack α, elevator command η_{cmd} and elevator command rate $\dot{\eta}_{cmd}$ for zero maneuver performed by enhanced, nonlinear aircraft model with Plant Augmentation starting at $V_0 = 154.94\frac{m}{s}$ and $h_0 = 5000m$ considering variation of noise seeds and noise standard deviations of angle-of-attack α, pitch rate q and elevator deflection η sensors

Table 6.65. – Performance metrics $M_{\mathcal{L}_2}$, $M_{\mathcal{L}_\infty}$ and $M_{\mathcal{L}_{2,act}}$ (maximum, minimum, mean value and standard deviation) generated from zero maneuver performed by enhanced, nonlinear aircraft model with Plant Augmentation and comparison to baseline controller starting at $V_0 = 154.94\frac{m}{s}$ and $h_0 = 5000m$ considering variation of noise seeds and noise standard deviations of angle-of-attack α, pitch rate q and elevator deflection η sensors

	$M_{\mathcal{L}_2}$ [−]	$M_{\mathcal{L}_\infty}$ [−]	$M_{\mathcal{L}_{2,act}}$ [−]	$M_{\mathcal{L}_{2,rel}}$ [%]	$M_{\mathcal{L}_{\infty,rel}}$ [%]	$M_{\mathcal{L}_{2,act,rel}}$ [%]
max	0.067	0.0021	1.811	180.6%	213.0%	1016.0%
min	0.011	0.0003	0.388	276.8%	322.6%	1099.1%
∅	0.034	0.0009	1.126	208.9%	229.2%	1117.0%
σ	0.0104	0.00028	0.3147	172.4%	197.2%	1093.6%

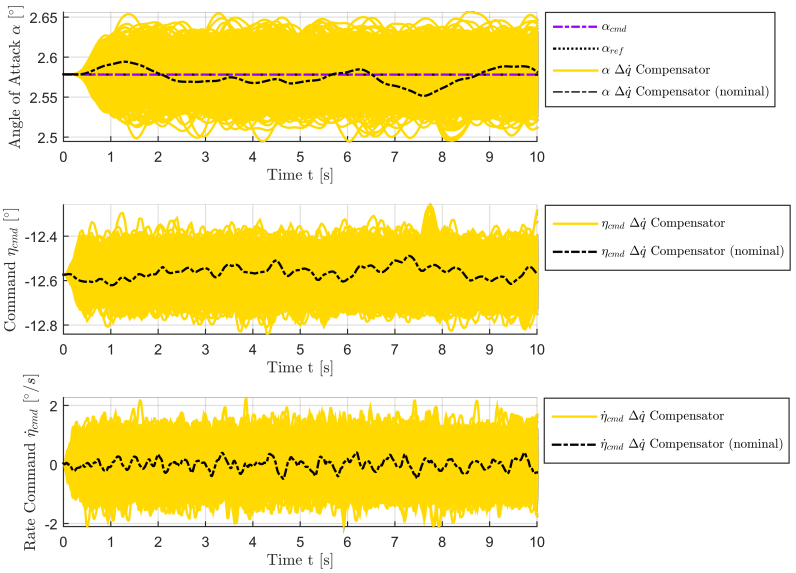

Figure 6.76. – Angle of attack α, elevator command η_{cmd} and elevator command rate $\dot{\eta}_{cmd}$ for zero maneuver performed by enhanced, nonlinear aircraft model with $\Delta\dot{q}$ Compensation Law starting at $V_0 = 154.94\frac{m}{s}$ and $h_0 = 5000m$ considering variation of noise seeds and noise standard deviations of angle-of-attack α, pitch rate q and elevator deflection η sensors

Table 6.66. – Performance metrics $M_{\mathcal{L}_2}$, $M_{\mathcal{L}_\infty}$ and $M_{\mathcal{L}_{2,act}}$ (maximum, minimum, mean value and standard deviation) generated from zero maneuver performed by enhanced, nonlinear aircraft model with $\Delta\dot{q}$ Compensation Law and comparison to baseline controller starting at $V_0 = 154.94\frac{m}{s}$ and $h_0 = 5000m$ considering variation of noise seeds and noise standard deviations of angle-of-attack α, pitch rate q and elevator deflection η sensors

	$M_{\mathcal{L}_2}$ $[-]$	$M_{\mathcal{L}_\infty}$ $[-]$	$M_{\mathcal{L}_{2,act}}$ $[-]$	$M_{\mathcal{L}_{2,rel}}$ $[\%]$	$M_{\mathcal{L}_{\infty,rel}}$ $[\%]$	$M_{\mathcal{L}_{2,act,rel}}$ $[\%]$
max	0.058	0.0015	0.355	157.9%	147.2%	199.2%
min	0.008	0.0002	0.081	188.6%	191.2%	228.3%
$\varnothing$	0.028	0.0007	0.214	170.9%	173.0%	212.2%
σ	0.0091	0.00022	0.0451	151.2%	155.7%	156.7%

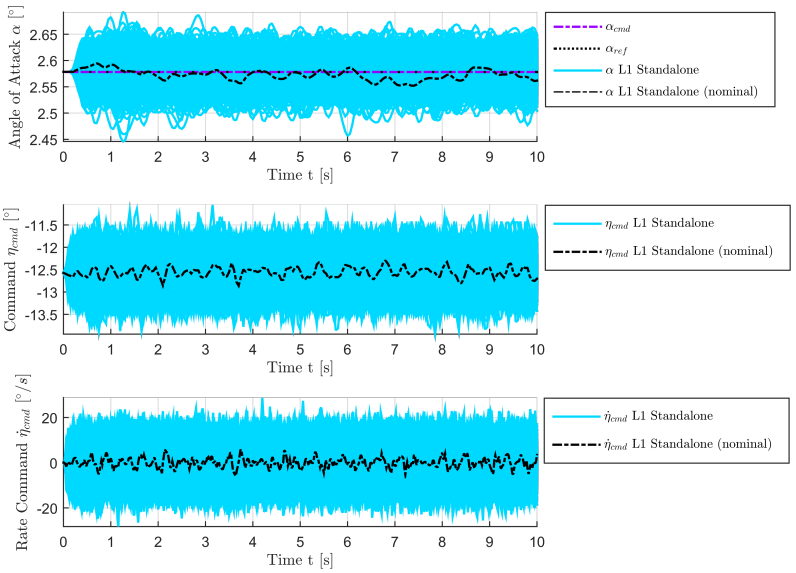

Figure 6.77. – Angle of attack α, elevator command η_{cmd} and elevator command rate $\dot{\eta}_{cmd}$ for zero maneuver performed by enhanced, nonlinear aircraft model with L1 adaptive controller with Eigenstructure Assignment starting at $V_0 = 154.94\frac{m}{s}$ and $h_0 = 5000m$ considering variation of noise seeds and noise standard deviations of angle-of-attack α, pitch rate q and elevator deflection η sensors

Table 6.67. – Performance metrics $M_{\mathcal{L}_2}$, $M_{\mathcal{L}_\infty}$ and $M_{\mathcal{L}_{2,act}}$ (maximum, minimum, mean value and standard deviation) generated from zero maneuver performed by enhanced, nonlinear aircraft model with L1 adaptive controller with Eigenstructure Assignment and comparison to baseline controller starting at $V_0 = 154.94\frac{m}{s}$ and $h_0 = 5000m$ considering variation of noise seeds and noise standard deviations of angle-of-attack α, pitch rate q and elevator deflection η sensors

	$M_{\mathcal{L}_2}$ $[-]$	$M_{\mathcal{L}_\infty}$ $[-]$	$M_{\mathcal{L}_{2,act}}$ $[-]$	$M_{\mathcal{L}_{2,rel}}$ $[\%]$	$M_{\mathcal{L}_{\infty,rel}}$ $[\%]$	$M_{\mathcal{L}_{2,act,rel}}$ $[\%]$
max	0.065	0.0023	4.112	174.4%	233.8%	2306.9%
min	0.013	0.0003	1.057	312.3%	361.1%	2994.1%
$\varnothing$	0.034	0.0009	2.541	207.6%	239.7%	2520.2%
σ	0.0100	0.00030	0.7134	165.9%	207.1%	2478.9%

6.2.11. Uncertainty w.r.t. sensor noise in α measurement

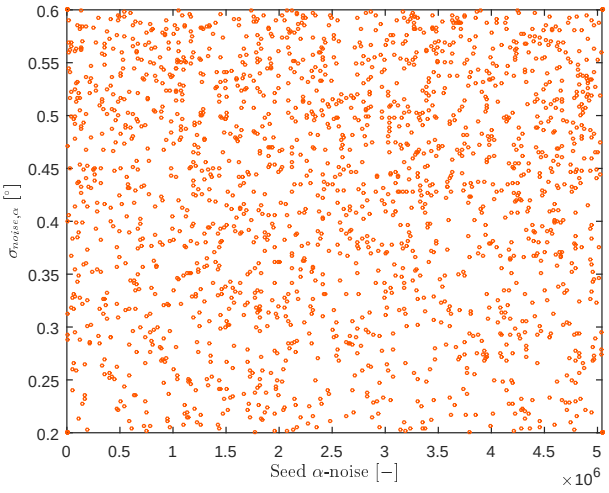

Figure 6.78. – Variation of random noise seed and standard deviation $\sigma_{noise,\alpha}$ applied in sensor measurement of angle of attack α

In this section, the effect of measurement noise in the angle of attack α sensor on the controller performances is investigated. Thus, the standard deviations $\sigma_{noise,\alpha}$ is randomly varied within $[0.2°; 0.6°]$. The corresponding seed is a random number between $[0; 5042063]$. Fig. 6.78 shows the resulting 2000 variations.
The results of the simulations, where the enhanced aircraft model is configured according to Section 6.2.11, are presented in Fig. 6.79 and Table 6.68 for the baseline controller, in Fig. 6.80 and Table 6.69 for the DPI Augmentation, in Fig. 6.81 and Table 6.70 for the Plant Augmentation, in Fig. 6.82 and Table 6.71 for the $\Delta\dot{q}$ Compensation Law and in Fig. 6.83 and Table 6.72 for the standalone L1 adaptive controller with Eigenstructure Assignment. One can see that the results are very similar to the ones shown in Section 6.2.10. Thus, it can be concluded that measurement noise with regard to the angle of attack α measurement constitutes the major influence on the controller performance of the control laws.

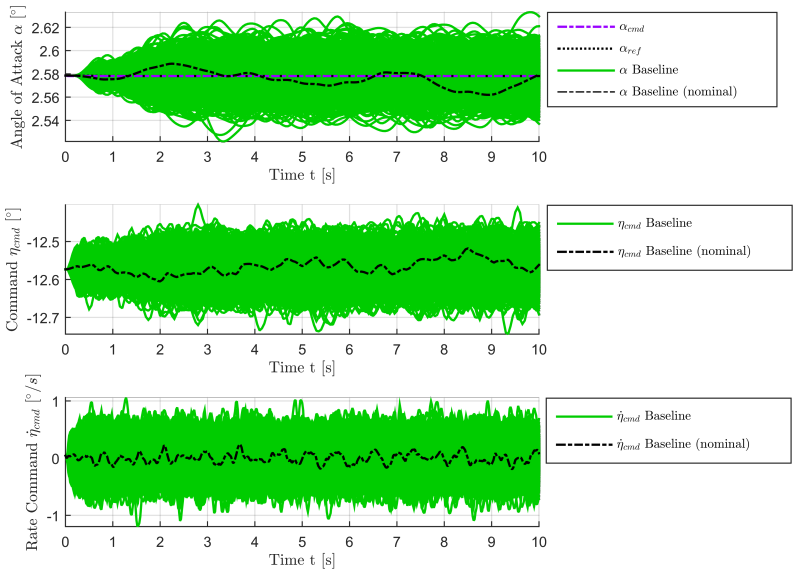

Figure 6.79. – Angle of attack α, elevator command η_{cmd} and elevator command rate $\dot{\eta}_{cmd}$ for zero maneuver performed by enhanced, nonlinear aircraft model with baseline controller starting at $V_0 = 154.94\frac{m}{s}$ and $h_0 = 5000m$ considering variation of noise seed and noise standard deviation of angle-of-attack α sensor

Table 6.68. – Performance metrics $M_{\mathcal{L}_2}$, $M_{\mathcal{L}_\infty}$ and $M_{\mathcal{L}_{2,act}}$ (maximum, minimum, mean value and standard deviation) generated from zero maneuver performed by enhanced, nonlinear aircraft model with baseline controller starting at $V_0 = 154.94\frac{m}{s}$ and $h_0 = 5000m$ considering variation of noise seed and noise standard deviation of angle-of-attack α sensor

	$M_{\mathcal{L}_2}$ $[-]$	$M_{\mathcal{L}_\infty}$ $[-]$	$M_{\mathcal{L}_{2,act}}$ $[-]$
max	0.037	0.0010	0.178
min	0.004	0.0001	0.041
$\varnothing$	0.016	0.0004	0.101
σ	0.0060	0.00014	0.0288

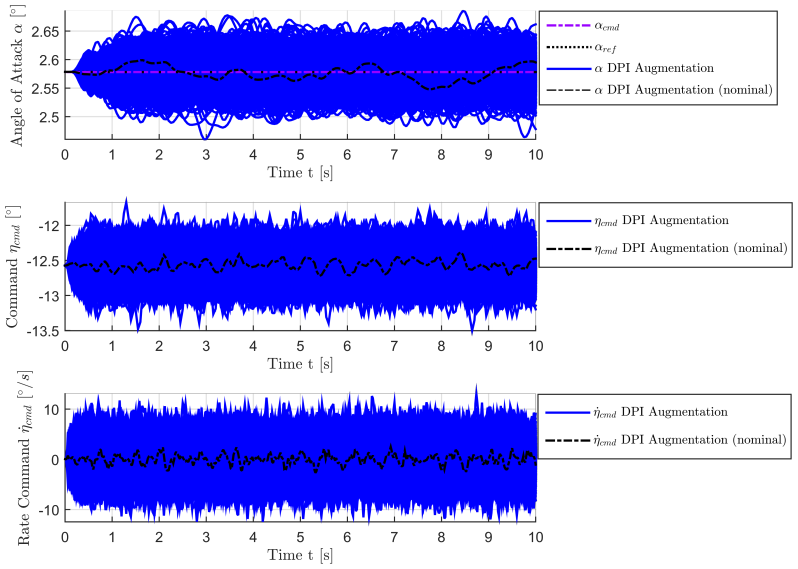

Figure 6.80. – Angle of attack α, elevator command η_{cmd} and elevator command rate $\dot{\eta}_{cmd}$ for zero maneuver performed by enhanced, nonlinear aircraft model with DPI Augmentation starting at $V_0 = 154.94\frac{m}{s}$ and $h_0 = 5000m$ considering variation of noise seed and noise standard deviation of angle-of-attack α sensor

Table 6.69. – Performance metrics $M_{\mathcal{L}_2}$, $M_{\mathcal{L}_\infty}$ and $M_{\mathcal{L}_{2,act}}$ (maximum, minimum, mean value and standard deviation) generated from zero maneuver performed by enhanced, nonlinear aircraft model with DPI Augmentation and comparison to baseline controller starting at $V_0 = 154.94\frac{m}{s}$ and $h_0 = 5000m$ considering variation of noise seed and noise standard deviation of angle-of-attack α sensor

	$M_{\mathcal{L}_2}$ $[-]$	$M_{\mathcal{L}_\infty}$ $[-]$	$M_{\mathcal{L}_{2,act}}$ $[-]$	$M_{\mathcal{L}_{2,rel}}$ $[\%]$	$M_{\mathcal{L}_{\infty,rel}}$ $[\%]$	$M_{\mathcal{L}_{2,act,rel}}$ $[\%]$
max	0.068	0.0021	1.916	183.7%	210.8%	1076.3%
min	0.011	0.0003	0.485	269.5%	318.5%	1195.6%
$\varnothing$	0.034	0.0009	1.197	205.7%	227.4%	1187.9%
σ	0.0108	0.00030	0.3391	178.7%	205.0%	1176.4%

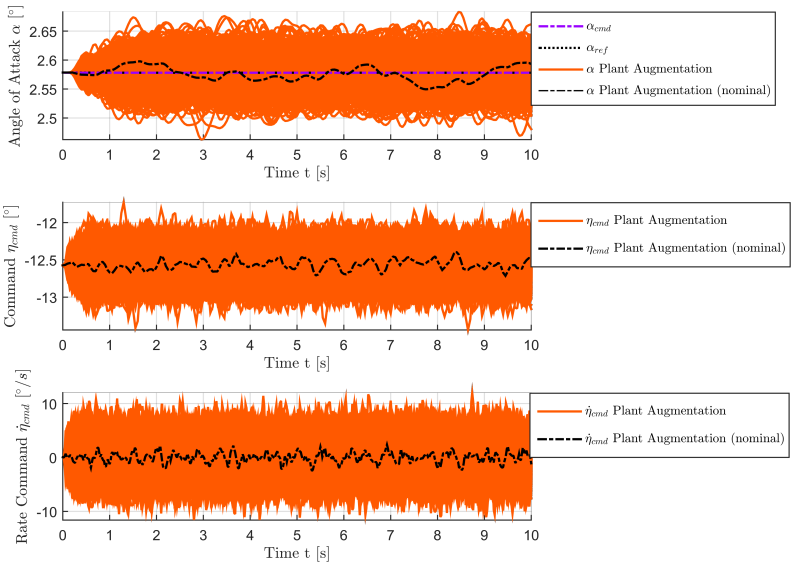

Figure 6.81. – Angle of attack α, elevator command η_{cmd} and elevator command rate $\dot{\eta}_{cmd}$ for zero maneuver performed by enhanced, nonlinear aircraft model with Plant Augmentation starting at $V_0 = 154.94\frac{m}{s}$ and $h_0 = 5000m$ considering variation of noise seed and noise standard deviation of angle-of-attack α sensor

Table 6.70. – Performance metrics $M_{\mathcal{L}_2}$, $M_{\mathcal{L}_\infty}$ and $M_{\mathcal{L}_{2,act}}$ (maximum, minimum, mean value and standard deviation) generated from zero maneuver performed by enhanced, nonlinear aircraft model with Plant Augmentation and comparison to baseline controller starting at $V_0 = 154.94\frac{m}{s}$ and $h_0 = 5000m$ considering variation of noise seed and noise standard deviation of angle-of-attack α sensor

	$M_{\mathcal{L}_2}$ $[-]$	$M_{\mathcal{L}_\infty}$ $[-]$	$M_{\mathcal{L}_{2,act}}$ $[-]$	$M_{\mathcal{L}_{2,rel}}$ $[\%]$	$M_{\mathcal{L}_{\infty,rel}}$ $[\%]$	$M_{\mathcal{L}_{2,act,rel}}$ $[\%]$
max	0.067	0.0020	1.788	180.7%	206.0%	1004.0%
min	0.011	0.0003	0.453	265.3%	304.0%	1114.4%
$\varnothing$	0.033	0.0009	1.115	201.4%	221.7%	1107.0%
σ	0.0106	0.00029	0.3160	176.0%	200.5%	1096.3%

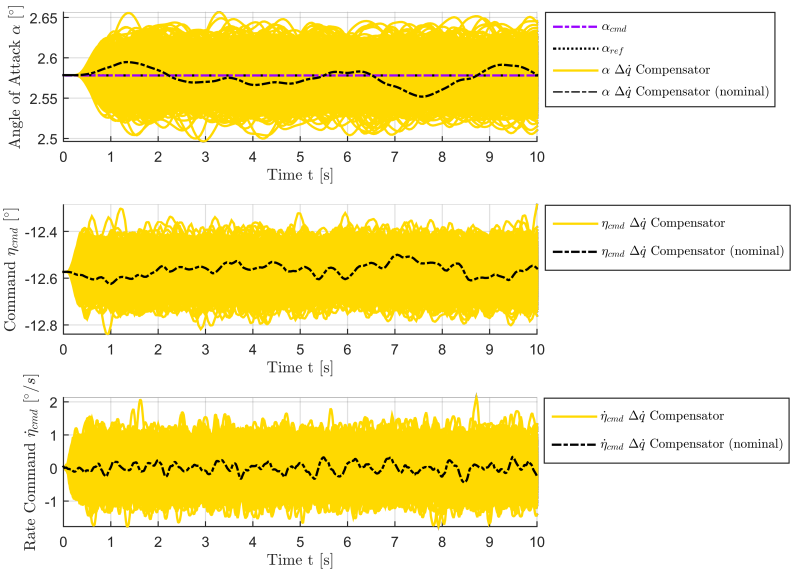

Figure 6.82. – Angle of attack α, elevator command η_{cmd} and elevator command rate $\dot{\eta}_{cmd}$ for zero maneuver performed by enhanced, nonlinear aircraft model with $\Delta\dot{q}$ Compensation Law starting at $V_0 = 154.94\frac{m}{s}$ and $h_0 = 5000m$ considering variation of noise seed and noise standard deviation of angle-of-attack α sensor

Table 6.71. – Performance metrics $M_{\mathcal{L}_2}$, $M_{\mathcal{L}_\infty}$ and $M_{\mathcal{L}_{2,act}}$ (maximum, minimum, mean value and standard deviation) generated from zero maneuver performed by enhanced, nonlinear aircraft model with $\Delta\dot{q}$ Compensation Law and comparison to baseline controller starting at $V_0 = 154.94\frac{m}{s}$ and $h_0 = 5000m$ considering variation of noise seed and noise standard deviation of angle-of-attack α sensor

	$M_{\mathcal{L}_2}$ $[-]$	$M_{\mathcal{L}_\infty}$ $[-]$	$M_{\mathcal{L}_{2,act}}$ $[-]$	$M_{\mathcal{L}_{2,rel}}$ $[\%]$	$M_{\mathcal{L}_{\infty,rel}}$ $[\%]$	$M_{\mathcal{L}_{2,act,rel}}$ $[\%]$
max	0.056	0.0014	0.312	150.3%	145.3%	175.4%
min	0.007	0.0002	0.067	184.3%	192.8%	165.7%
$\varnothing$	0.027	0.0006	0.173	162.4%	163.8%	171.7%
σ	0.0093	0.00023	0.0496	153.0%	157.8%	172.2%

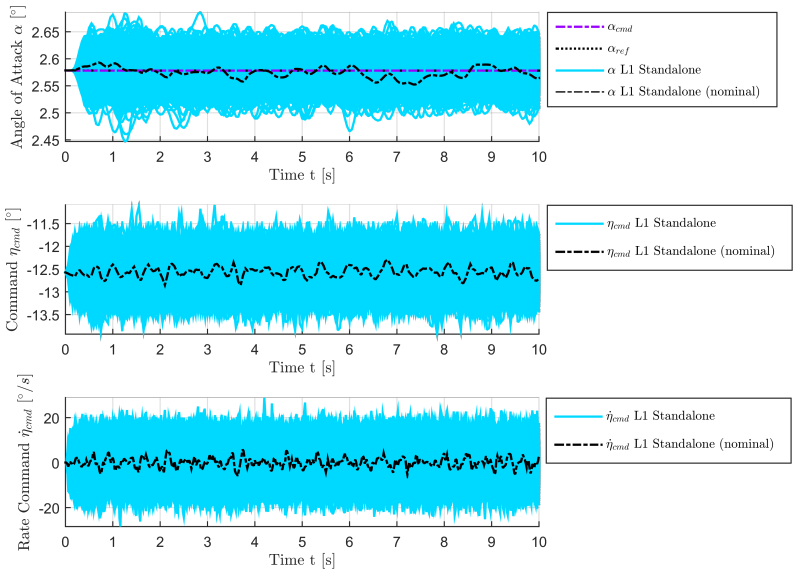

Figure 6.83. – Angle of attack α, elevator command η_{cmd} and elevator command rate $\dot{\eta}_{cmd}$ for zero maneuver performed by enhanced, nonlinear aircraft model with L1 adaptive controller with Eigenstructure Assignment starting at $V_0 = 154.94\frac{m}{s}$ and $h_0 = 5000m$ considering variation of noise seed and noise standard deviation of angle-of-attack α sensor

Table 6.72. – Performance metrics $M_{\mathcal{L}_2}$, $M_{\mathcal{L}_\infty}$ and $M_{\mathcal{L}_{2,act}}$ (maximum, minimum, mean value and standard deviation) generated from zero maneuver performed by enhanced, nonlinear aircraft model with L1 adaptive controller with Eigenstructure Assignment and comparison to baseline controller starting at $V_0 = 154.94\frac{m}{s}$ and $h_0 = 5000m$ considering variation of noise seed and noise standard deviation of angle-of-attack α sensor

	$M_{\mathcal{L}_2}$ $[-]$	$M_{\mathcal{L}_\infty}$ $[-]$	$M_{\mathcal{L}_{2,act}}$ $[-]$	$M_{\mathcal{L}_{2,rel}}$ $[\%]$	$M_{\mathcal{L}_{\infty,rel}}$ $[\%]$	$M_{\mathcal{L}_{2,act,rel}}$ $[\%]$
max	0.063	0.0023	4.098	170.0%	234.2%	2301.9%
min	0.011	0.0003	1.076	281.1%	328.6%	2649.9%
∅	0.033	0.0009	2.532	201.2%	233.8%	2513.0%
σ	0.0101	0.00030	0.7111	166.6%	206.9%	2467.0%

6.2.12. Uncertainty w.r.t. sensor noise in q measurement

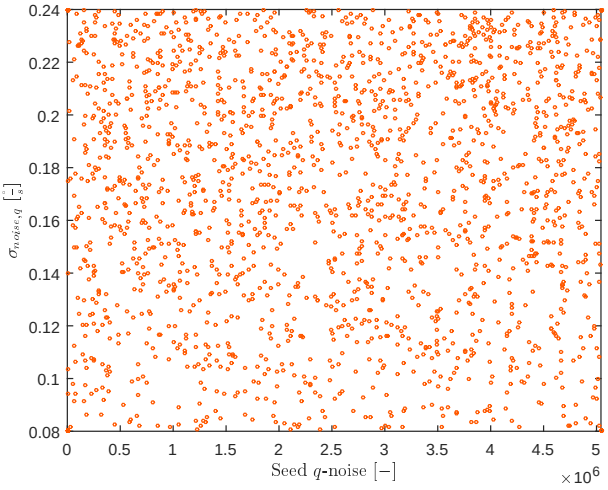

Figure 6.84. – Variation of random noise seed and standard deviation $\sigma_{noise,q}$ applied in sensor measurement of pitch rate q

In the next step, only measurement noise with regard to the pitch rate q measurement is applied on the enhanced aircraft model. The standard deviation of the measurement noise $\sigma_{noise,q}$ is randomly varied considering the limits $\left[0.08\frac{°}{s}; 0.24\frac{°}{s}\right]$. Again, the seed is a random number between $[0; 5042063]$. 2000 parameter variations are created and depicted in Fig. 6.84.
In order to draw comparisons, the results of the simulations are compiled in Fig. 6.85 and Table 6.73 for the baseline controller, in Fig. 6.86 and Table 6.74 for the DPI Augmentation, in Fig. 6.87 and Table 6.75 for the Plant Augmentation, in Fig. 6.88 and Table 6.76 for the $\Delta\dot{q}$ Compensation Law and in Fig. 6.89 and Table 6.77 for the standalone L1 adaptive controller with Eigenstructure Assignment. As expected, the amount of amplification is lower compared to the case shown in Section 6.2.11, where measurement noise with regard to angle of attack α was investigated. Nevertheless, also for the case of pitch rate measurement noise it can be observed that the adaptive controllers significantly increase commanded actuator activity compared to the baseline controller configuration. Furthermore, the increases detected for L1 Adaptive Augmentations and for the $\Delta\dot{q}$ Compensation Law are in the same range, in contrast to the assessments made in Section 6.2.10 and Section 6.2.11. This is due to the derivation of the pitch rate q, which is used within the $\Delta\dot{q}$ Compensation Law in order to calculate the pitch rate acceleration $\dot{q}$ and which amplifies noise within the pitch rate q channel. Thus, the amplification generated through the derivation is similar to the one stemming from the high gain update laws of the L1 Adaptive Augmentations.

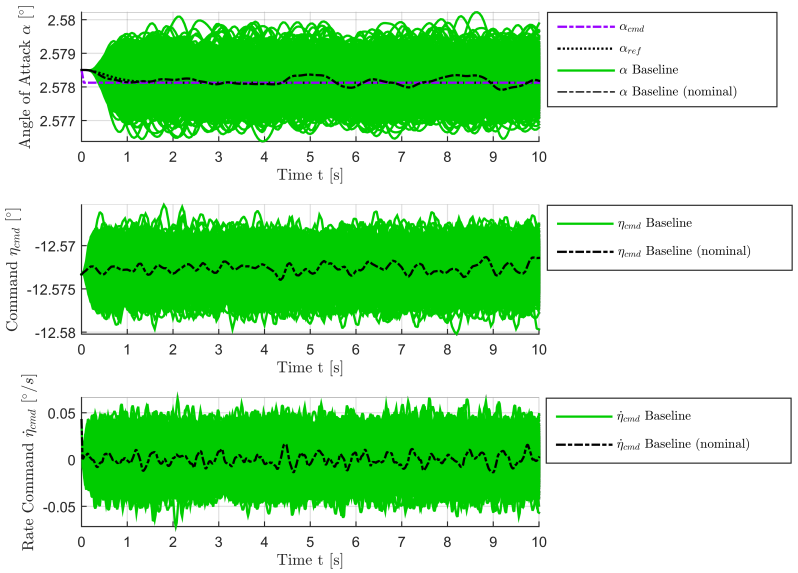

Figure 6.85. – Angle of attack α, elevator command η_{cmd} and elevator command rate $\dot{\eta}_{cmd}$ for zero maneuver performed by enhanced, nonlinear aircraft model with baseline controller starting at $V_0 = 154.94\frac{m}{s}$ and $h_0 = 5000m$ considering variation of noise seed and noise standard deviation of pitch rate q sensor

Table 6.73. – Performance metrics $M_{\mathcal{L}_2}$, $M_{\mathcal{L}_\infty}$ and $M_{\mathcal{L}_{2,act}}$ (maximum, minimum, mean value and standard deviation) generated from zero maneuver performed by enhanced, nonlinear aircraft model with baseline controller starting at $V_0 = 154.94\frac{m}{s}$ and $h_0 = 5000m$ considering variation of noise seed and noise standard deviation of pitch rate q sensor

	$M_{\mathcal{L}_2}$ $[-]$	$M_{\mathcal{L}_\infty}$ $[-]$	$M_{\mathcal{L}_{2,act}}$ $[-]$
max	0.001	0.0000	0.011
min	0.000	0.0000	0.003
$\varnothing$	0.001	0.0000	0.007
σ	0.0002	0.00001	0.0018

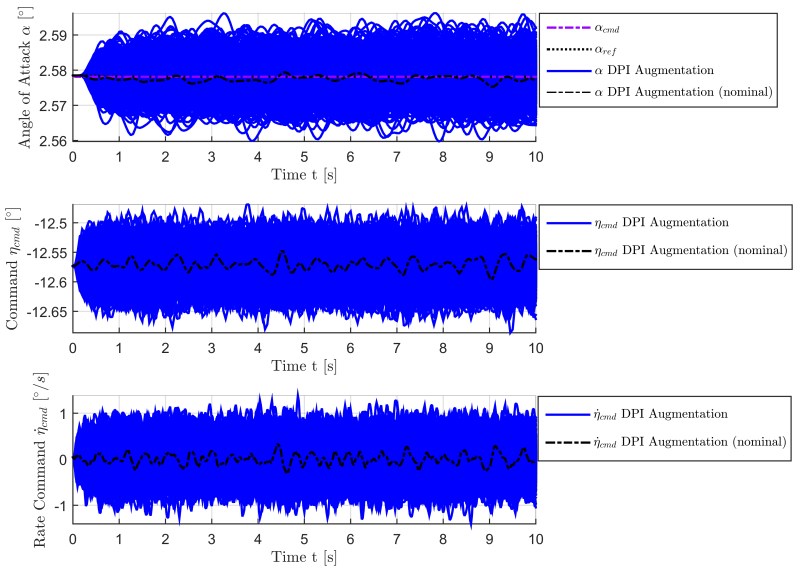

Figure 6.86. – Angle of attack α, elevator command η_{cmd} and elevator command rate $\dot{\eta}_{cmd}$ for zero maneuver performed by enhanced, nonlinear aircraft model with DPI Augmentation starting at $V_0 = 154.94\frac{m}{s}$ and $h_0 = 5000m$ considering variation of noise seed and noise standard deviation of pitch rate q sensor

Table 6.74. – Performance metrics $M_{\mathcal{L}_2}$, $M_{\mathcal{L}_\infty}$ and $M_{\mathcal{L}_{2,act}}$ (maximum, minimum, mean value and standard deviation) generated from zero maneuver performed by enhanced, nonlinear aircraft model with DPI Augmentation and comparison to baseline controller starting at $V_0 = 154.94\frac{m}{s}$ and $h_0 = 5000m$ considering variation of noise seed and noise standard deviation of pitch rate q sensor

	$M_{\mathcal{L}_2}$ [−]	$M_{\mathcal{L}_\infty}$ [−]	$M_{\mathcal{L}_{2,act}}$ [−]	$M_{\mathcal{L}_{2,rel}}$ [%]	$M_{\mathcal{L}_{\infty,rel}}$ [%]	$M_{\mathcal{L}_{2,act,rel}}$ [%]
max	0.012	0.0003	0.227	963.6%	879.4%	2059.2%
min	0.002	0.0000	0.050	822.9%	840.3%	1883.0%
∅	0.006	0.0001	0.131	893.5%	910.4%	1998.1%
σ	0.0021	0.00006	0.0373	1063.1%	1055.8%	2049.7%

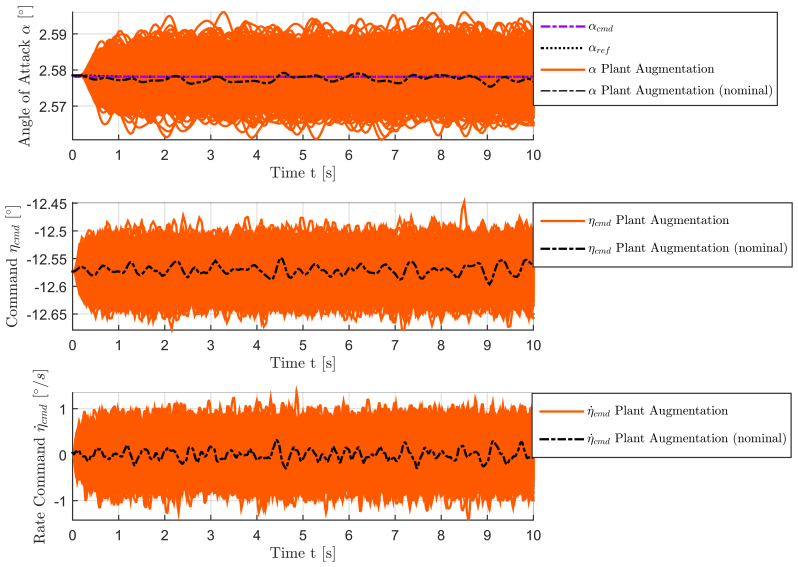

Figure 6.87. – Angle of attack α, elevator command η_{cmd} and elevator command rate $\dot{\eta}_{cmd}$ for zero maneuver performed by enhanced, nonlinear aircraft model with Plant Augmentation starting at $V_0 = 154.94\frac{m}{s}$ and $h_0 = 5000m$ considering variation of noise seed and noise standard deviation of pitch rate q sensor

Table 6.75. – Performance metrics $M_{\mathcal{L}_2}$, $M_{\mathcal{L}_\infty}$ and $M_{\mathcal{L}_{2,act}}$ (maximum, minimum, mean value and standard deviation) generated from zero maneuver performed by enhanced, nonlinear aircraft model with Plant Augmentation and comparison to baseline controller starting at $V_0 = 154.94\frac{m}{s}$ and $h_0 = 5000m$ considering variation of noise seed and noise standard deviation of pitch rate q sensor

	$M_{\mathcal{L}_2}$ $[-]$	$M_{\mathcal{L}_\infty}$ $[-]$	$M_{\mathcal{L}_{2,act}}$ $[-]$	$M_{\mathcal{L}_{2,rel}}$ $[\%]$	$M_{\mathcal{L}_{\infty,rel}}$ $[\%]$	$M_{\mathcal{L}_{2,act,rel}}$ $[\%]$
max	0.012	0.0003	0.214	970.8%	854.5%	1945.7%
min	0.002	0.0000	0.051	862.4%	892.6%	1902.7%
$\varnothing$	0.006	0.0001	0.128	875.1%	887.5%	1952.9%
σ	0.0021	0.00005	0.0365	1035.5%	1018.8%	2008.3%

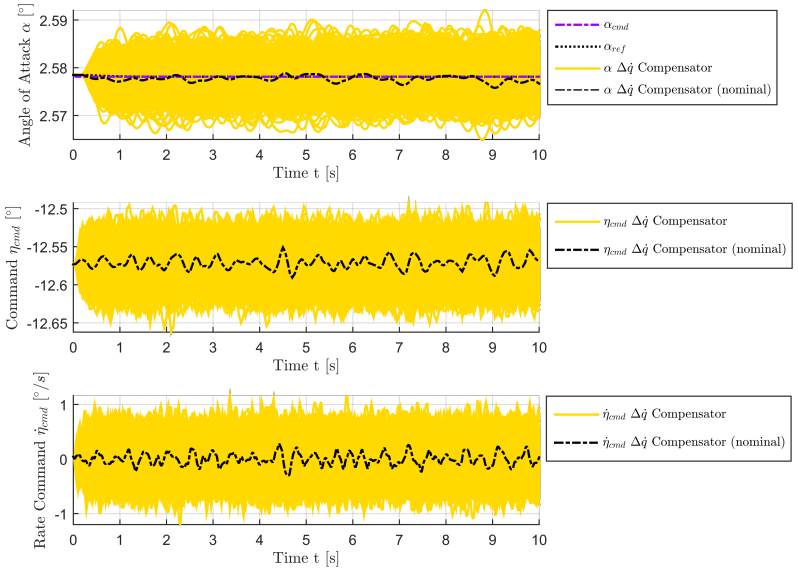

Figure 6.88. – Angle of attack α, elevator command η_{cmd} and elevator command rate $\dot{\eta}_{cmd}$ for zero maneuver performed by enhanced, nonlinear aircraft model with $\Delta\dot{q}$ Compensation Law starting at $V_0 = 154.94\frac{m}{s}$ and $h_0 = 5000m$ considering variation of noise seed and noise standard deviation of pitch rate q sensor

Table 6.76. – Performance metrics $M_{\mathcal{L}_2}$, $M_{\mathcal{L}_\infty}$ and $M_{\mathcal{L}_{2,act}}$ (maximum, minimum, mean value and standard deviation) generated from zero maneuver performed by enhanced, nonlinear aircraft model with $\Delta\dot{q}$ Compensation Law and comparison to baseline controller starting at $V_0 = 154.94\frac{m}{s}$ and $h_0 = 5000m$ considering variation of noise seed and noise standard deviation of pitch rate q sensor

	$M_{\mathcal{L}_2}$ $[-]$	$M_{\mathcal{L}_\infty}$ $[-]$	$M_{\mathcal{L}_{2,act}}$ $[-]$	$M_{\mathcal{L}_{2,rel}}$ $[\%]$	$M_{\mathcal{L}_{\infty,rel}}$ $[\%]$	$M_{\mathcal{L}_{2,act,rel}}$ $[\%]$
max	0.009	0.0002	0.186	725.6%	665.0%	1693.8%
min	0.001	0.0000	0.044	562.9%	603.1%	1648.8%
$\varnothing$	0.004	0.0001	0.111	630.6%	636.1%	1689.0%
σ	0.0013	0.00004	0.0308	668.3%	664.5%	1693.6%

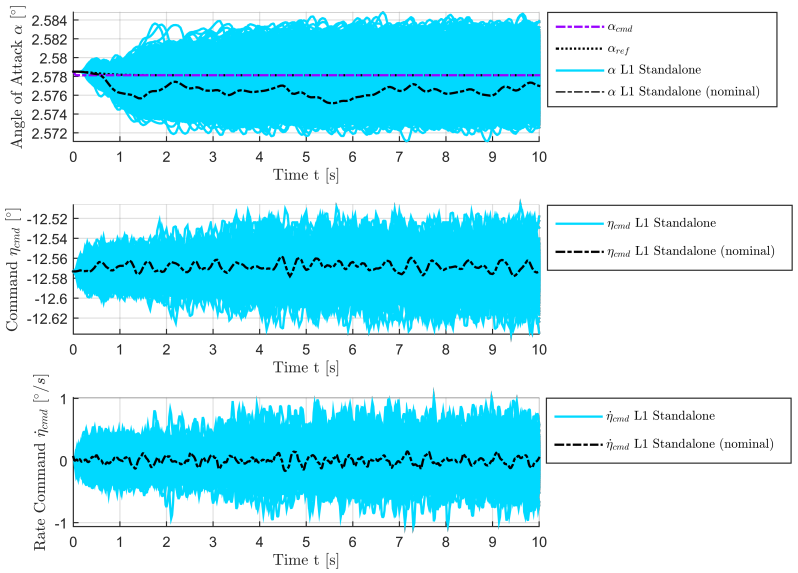

Figure 6.89. – Angle of attack α, elevator command η_{cmd} and elevator command rate $\dot{\eta}_{cmd}$ for zero maneuver performed by enhanced, nonlinear aircraft model with L1 adaptive controller with Eigenstructure Assignment starting at $V_0 = 154.94\frac{m}{s}$ and $h_0 = 5000m$ considering variation of noise seed and noise standard deviation of pitch rate q sensor

Table 6.77. – Performance metrics $M_{\mathcal{L}_2}$, $M_{\mathcal{L}_\infty}$ and $M_{\mathcal{L}_{2,act}}$ (maximum, minimum, mean value and standard deviation) generated from zero maneuver performed by enhanced, nonlinear aircraft model with L1 adaptive controller with Eigenstructure Assignment and comparison to baseline controller starting at $V_0 = 154.94\frac{m}{s}$ and $h_0 = 5000m$ considering variation of noise seed and noise standard deviation of pitch rate q sensor

	$M_{\mathcal{L}_2}$ $[-]$	$M_{\mathcal{L}_\infty}$ $[-]$	$M_{\mathcal{L}_{2,act}}$ $[-]$	$M_{\mathcal{L}_{2,rel}}$ $[\%]$	$M_{\mathcal{L}_{\infty,rel}}$ $[\%]$	$M_{\mathcal{L}_{2,act,rel}}$ $[\%]$
max	0.006	0.0001	0.112	487.5%	335.9%	1014.3%
min	0.001	0.0000	0.023	546.3%	602.7%	876.1%
∅	0.003	0.0001	0.065	485.6%	424.3%	998.1%
σ	0.0010	0.00002	0.0191	483.4%	375.0%	1053.0%

6.2.13. Uncertainty w.r.t. sensor noise in η measurement

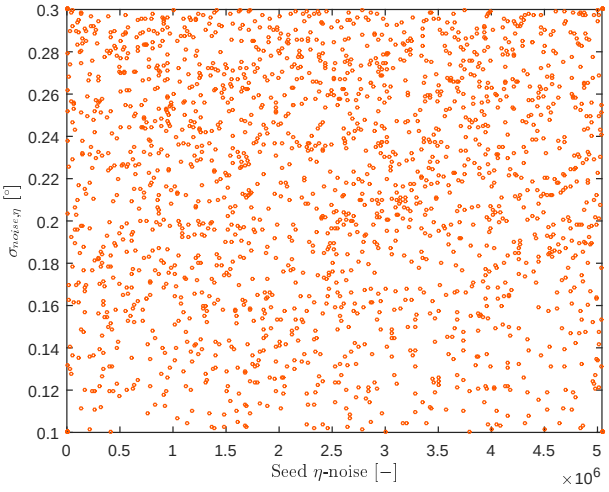

Figure 6.90. – Variation of random noise seed and standard deviation $\sigma_{noise,\eta}$ applied in sensor measurement of pitch rate η

The last assessment with regard to measurement noise considers the elevator deflection η sensor. Here, the standard deviation $\sigma_{noise,\eta}$ is randomly varied between $[0.1°; 0.3°]$ and the seed is randomly generated considering the limits $[0; 5042063]$. The resulting 2000 variations are illustrated in Fig. 6.90.
As the elevator deflection measurement is not utilized for the design of the DPI baseline controller, its simulation results are not depicted here. The results for the adaptive controllers are to be found in Fig. 6.91 and Table 6.78 for the DPI Augmentation, in Fig. 6.92 and Table 6.79 for the Plant Augmentation, in Fig. 6.93 and Table 6.80 for the $\Delta\dot{q}$ Compensation Law and in Fig. 6.94 and Table 6.81 for the standalone L1 adaptive controller with Eigenstructure Assignment. It can be concluded from the results, that the amount of noise amplification is very similar comparing the adaptive controllers, although a slightly higher amplification can be observed considering the standalone L1 adaptive controller.

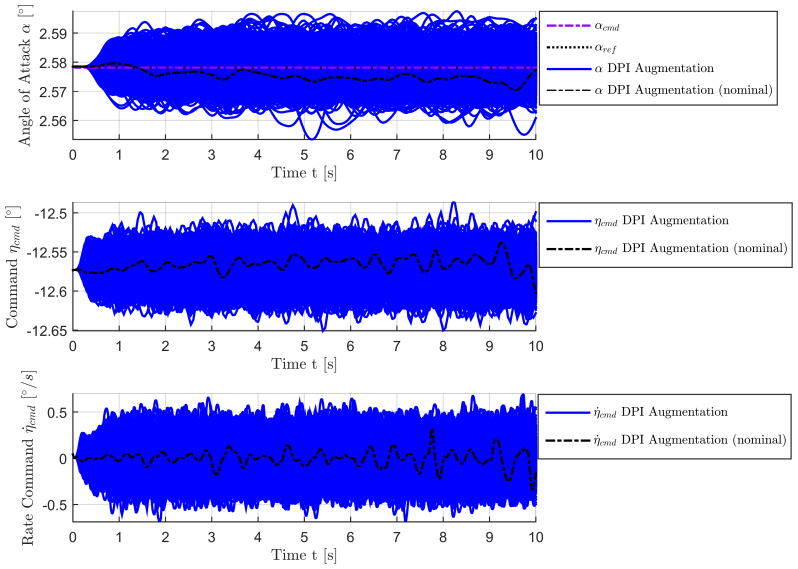

Figure 6.91. – Angle of attack α, elevator command η_{cmd} and elevator command rate $\dot{\eta}_{cmd}$ for zero maneuver performed by enhanced, nonlinear aircraft model with DPI Augmentation starting at $V_0 = 154.94\frac{m}{s}$ and $h_0 = 5000m$ considering variation of noise seed and noise standard deviation of elevator deflection η sensor

Table 6.78. – Performance metrics $M_{\mathcal{L}_2}$, $M_{\mathcal{L}_\infty}$ and $M_{\mathcal{L}_{2,act}}$ (maximum, minimum, mean value and standard deviation) generated from zero maneuver performed by enhanced, nonlinear aircraft model with DPI Augmentation and comparison to baseline controller starting at $V_0 = 154.94\frac{m}{s}$ and $h_0 = 5000m$ considering variation of noise seed and noise standard deviation of elevator deflection η sensor

	$M_{\mathcal{L}_2}$ $[-]$	$M_{\mathcal{L}_\infty}$ $[-]$	$M_{\mathcal{L}_{2,act}}$ $[-]$	$M_{\mathcal{L}_{2,rel}}$ $[\%]$	$M_{\mathcal{L}_{\infty,rel}}$ $[\%]$	$M_{\mathcal{L}_{2,act,rel}}$ $[\%]$
max	0.015	0.0004	0.115	-	-	-
min	0.002	0.0000	0.024	-	-	-
$\varnothing$	0.007	0.0002	0.068	-	-	-
σ	0.0025	0.00006	0.0176	-	-	-

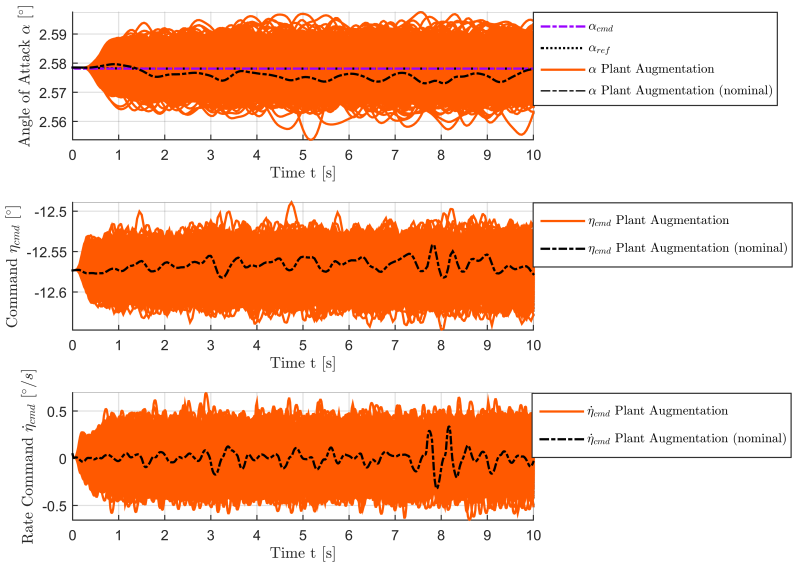

Figure 6.92. – Angle of attack α, elevator command η_{cmd} and elevator command rate $\dot{\eta}_{cmd}$ for zero maneuver performed by enhanced, nonlinear aircraft model with Plant Augmentation starting at $V_0 = 154.94\frac{m}{s}$ and $h_0 = 5000m$ considering variation of noise seed and noise standard deviation of elevator deflection η sensor

Table 6.79. – Performance metrics $M_{\mathcal{L}_2}$, $M_{\mathcal{L}_\infty}$ and $M_{\mathcal{L}_{2,act}}$ (maximum, minimum, mean value and standard deviation) generated from zero maneuver performed by enhanced, nonlinear aircraft model with Plant Augmentation and comparison to baseline controller starting at $V_0 = 154.94\frac{m}{s}$ and $h_0 = 5000m$ considering variation of noise seed and noise standard deviation of elevator deflection η sensor

	$M_{\mathcal{L}_2}$ $[-]$	$M_{\mathcal{L}_\infty}$ $[-]$	$M_{\mathcal{L}_{2,act}}$ $[-]$	$M_{\mathcal{L}_{2,rel}}$ $[\%]$	$M_{\mathcal{L}_{\infty,rel}}$ $[\%]$	$M_{\mathcal{L}_{2,act,rel}}$ $[\%]$
max	0.014	0.0004	0.116	-	-	-
min	0.002	0.0000	0.023	-	-	-
$\varnothing$	0.007	0.0002	0.066	-	-	-
σ	0.0024	0.00006	0.0167	-	-	-

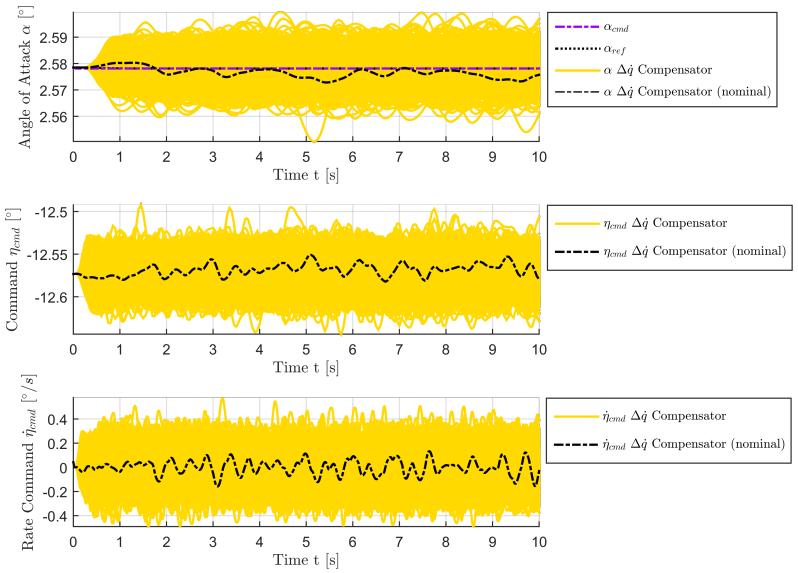

Figure 6.93. – Angle of attack α, elevator command η_{cmd} and elevator command rate $\dot{\eta}_{cmd}$ for zero maneuver performed by enhanced, nonlinear aircraft model with $\Delta\dot{q}$ Compensation Law starting at $V_0 = 154.94\frac{m}{s}$ and $h_0 = 5000m$ considering variation of noise seed and noise standard deviation of elevator deflection η sensor

Table 6.80. – Performance metrics $M_{\mathcal{L}_2}$, $M_{\mathcal{L}_\infty}$ and $M_{\mathcal{L}_{2,act}}$ (maximum, minimum, mean value and standard deviation) generated from zero maneuver performed by enhanced, nonlinear aircraft model with $\Delta\dot{q}$ Compensation Law and comparison to baseline controller starting at $V_0 = 154.94\frac{m}{s}$ and $h_0 = 5000m$ considering variation of noise seed and noise standard deviation of elevator deflection η sensor

	$M_{\mathcal{L}_2}$ $[-]$	$M_{\mathcal{L}_\infty}$ $[-]$	$M_{\mathcal{L}_{2,act}}$ $[-]$	$M_{\mathcal{L}_{2,rel}}$ $[\%]$	$M_{\mathcal{L}_{\infty,rel}}$ $[\%]$	$M_{\mathcal{L}_{2,act,rel}}$ $[\%]$
max	0.015	0.0005	0.089	-	-	-
min	0.002	0.0000	0.024	-	-	-
$\varnothing$	0.007	0.0002	0.054	-	-	-
σ	0.0022	0.00006	0.0122	-	-	-

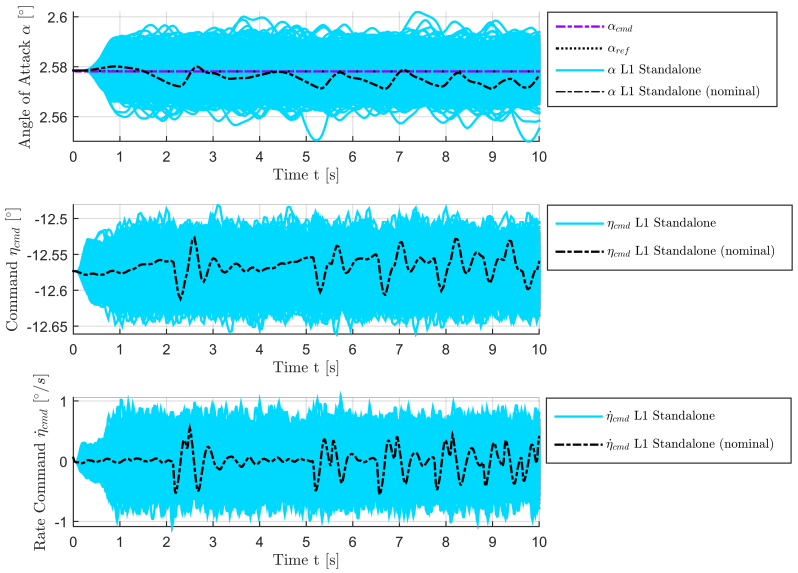

Figure 6.94. – Angle of attack α, elevator command η_{cmd} and elevator command rate $\dot{\eta}_{cmd}$ for zero maneuver performed by enhanced, nonlinear aircraft model with L1 adaptive controller with Eigenstructure Assignment starting at $V_0 = 154.94\frac{m}{s}$ and $h_0 = 5000m$ considering variation of noise seed and noise standard deviation of elevator deflection η sensor

Table 6.81. – Performance metrics $M_{\mathcal{L}_2}$, $M_{\mathcal{L}_\infty}$ and $M_{\mathcal{L}_{2,act}}$ (maximum, minimum, mean value and standard deviation) generated from zero maneuver performed by enhanced, nonlinear aircraft model with L1 adaptive controller with Eigenstructure Assignment and comparison to baseline controller starting at $V_0 = 154.94\frac{m}{s}$ and $h_0 = 5000m$ considering variation of noise seed and noise standard deviation of elevator deflection η sensor

	$M_{\mathcal{L}_2}$ $[-]$	$M_{\mathcal{L}_\infty}$ $[-]$	$M_{\mathcal{L}_{2,act}}$ $[-]$	$M_{\mathcal{L}_{2,rel}}$ $[\%]$	$M_{\mathcal{L}_{\infty,rel}}$ $[\%]$	$M_{\mathcal{L}_{2,act,rel}}$ $[\%]$
max	0.017	0.0005	0.156	-	-	-
min	0.003	0.0001	0.021	-	-	-
$\varnothing$	0.008	0.0002	0.107	-	-	-
σ	0.0021	0.00005	0.0191	-	-	-

6.2.14. Uncertainty w.r.t. structural mode

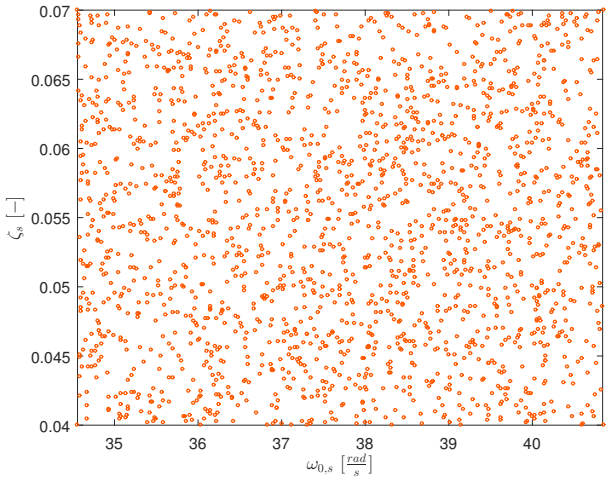

Figure 6.95. – Variation of natural frequency $\omega_{0,s}$ and relative damping ζ_s of structural mode

This section assesses variations of the parameters of the simple structural mode model according to Section 2.7 and their impact on the performance of the controller designs introduced in Chapter 4. For this purpose, both natural frequency $\omega_{0,s}$ and relative damping ζ_s included in Eq. (2.65) and Eq. (2.64) are randomly varied. Here, the limits $[5.5Hz; 6.5Hz]$ and $[0.04; 0.07]$ apply for $\omega_{0,s}$ and ζ_s, respectively. A total amount of 2000 variations is created and depicted in Fig. 6.95, which include the corner cases. Considering the described variations of the structural mode, the different controllers are combined with the enhanced aircraft model, in order to simulate the exemplary maneuver. The results are summarized in Fig. 6.96 and Table 6.82 for the baseline controller, in Fig. 6.97 and Table 6.83 for the DPI Augmentation, in Fig. 6.98 and Table 6.84 for the Plant Augmentation, in Fig. 6.99 and Table 6.85 for the $\Delta\dot{q}$ Compensation Law and in Fig. 6.100 and Table 6.86 for the standalone L1 adaptive controller with Eigenstructure Assignment. Firstly, it can be observed that the variation of the structural mode model does barely affect the performance of the baseline controller configuration. This can also be seen by means of the standard deviations of the three performance metrics $M_{\mathcal{L}_2}$, $M_{\mathcal{L}_\infty}$ and $M_{\mathcal{L}_{2,act}}$. Although the standard deviations are higher for the adaptive controllers, the effect of the parameter variation on the controller performance is still very small. The increase of commanded actuator activity in terms of $M_{\mathcal{L}_{2,act}}$ caused by the adaptive controllers stems again from the amplification of turbulence content within the measurements.

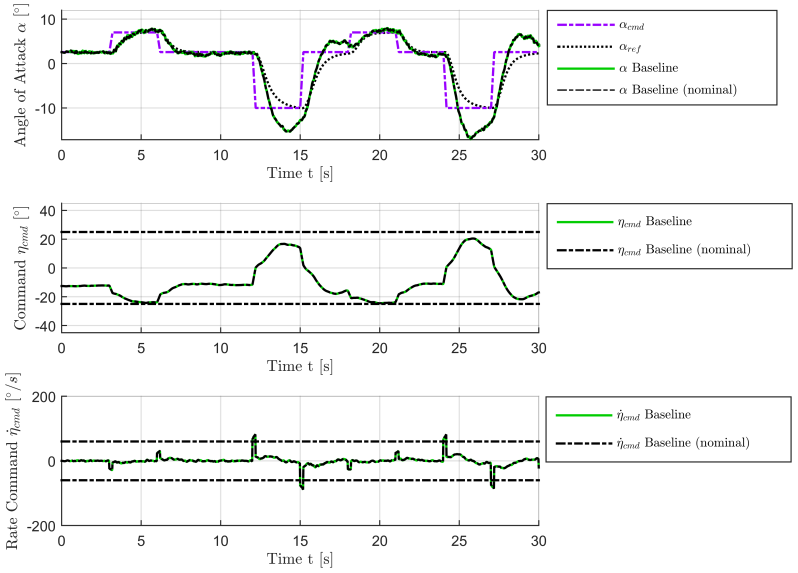

Figure 6.96. – Angle of attack α, elevator command η_{cmd} and elevator command rate $\dot{\eta}_{cmd}$ for example maneuver performed by enhanced, nonlinear aircraft model with baseline controller starting at $V_0 = 154.94\frac{m}{s}$ and $h_0 = 5000m$ considering variation of natural frequency $\omega_{0,s}$ and relative damping ζ_s of structural mode

Table 6.82. – Performance metrics $M_{\mathcal{L}_2}$, $M_{\mathcal{L}_\infty}$ and $M_{\mathcal{L}_{2,act}}$ (maximum, minimum, mean value and standard deviation) generated from example maneuver performed by enhanced, nonlinear aircraft model with baseline controller starting at $V_0 = 154.94\frac{m}{s}$ and $h_0 = 5000m$ considering variation of natural frequency $\omega_{0,s}$ and relative damping ζ_s of structural mode

	$M_{\mathcal{L}_2}$ $[-]$	$M_{\mathcal{L}_\infty}$ $[-]$	$M_{\mathcal{L}_{2,act}}$ $[-]$
max	7.79	0.146	14.47
min	7.78	0.142	14.44
$\varnothing$	7.79	0.143	14.45
σ	0.001	0.0009	0.006

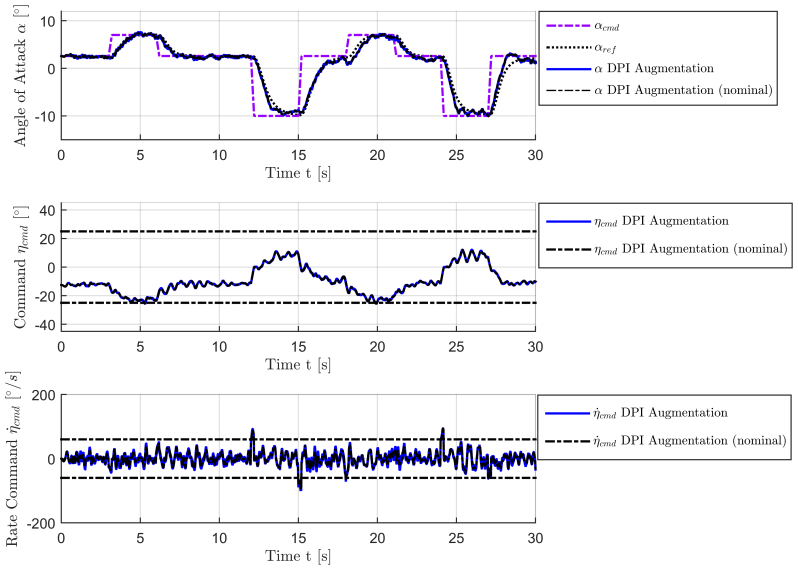

Figure 6.97. – Angle of attack α, elevator command η_{cmd} and elevator command rate $\dot{\eta}_{cmd}$ for example maneuver performed by enhanced, nonlinear aircraft model with DPI Augmentation starting at $V_0 = 154.94\frac{m}{s}$ and $h_0 = 5000m$ considering variation of natural frequency $\omega_{0,s}$ and relative damping ζ_s of structural mode

Table 6.83. – Performance metrics $M_{\mathcal{L}_2}$, $M_{\mathcal{L}_\infty}$ and $M_{\mathcal{L}_{2,act}}$ (maximum, minimum, mean value and standard deviation) generated from example maneuver performed by enhanced, nonlinear aircraft model with DPI Augmentation and comparison to baseline controller starting at $V_0 = 154.94\frac{m}{s}$ and $h_0 = 5000m$ considering variation of natural frequency $\omega_{0,s}$ and relative damping ζ_s of structural mode

	$M_{\mathcal{L}_2}$ $[-]$	$M_{\mathcal{L}_\infty}$ $[-]$	$M_{\mathcal{L}_{2,act}}$ $[-]$	$M_{\mathcal{L}_{2,rel}}$ $[\%]$	$M_{\mathcal{L}_{\infty,rel}}$ $[\%]$	$M_{\mathcal{L}_{2,act,rel}}$ $[\%]$
max	2.35	0.048	20.82	30.1%	32.6%	143.9%
min	2.27	0.046	18.86	29.1%	32.1%	130.6%
$\varnothing$	2.29	0.047	19.52	29.4%	32.6%	135.1%
σ	0.016	0.0004	0.405	1079.8%	40.4%	6486.2%

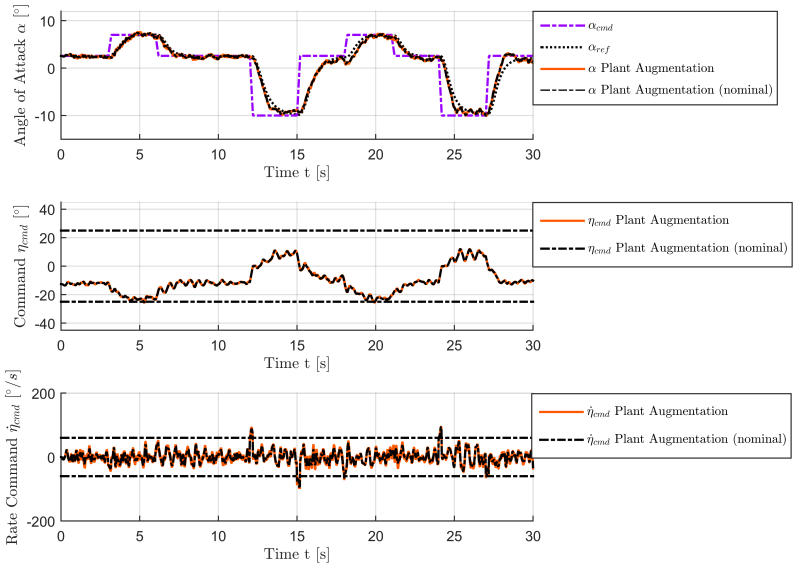

Figure 6.98. – Angle of attack α, elevator command η_{cmd} and elevator command rate $\dot{\eta}_{cmd}$ for example maneuver performed by enhanced, nonlinear aircraft model with Plant Augmentation starting at $V_0 = 154.94\frac{m}{s}$ and $h_0 = 5000m$ considering variation of natural frequency $\omega_{0,s}$ and relative damping ζ_s of structural mode

Table 6.84. – Performance metrics $M_{\mathcal{L}_2}$, $M_{\mathcal{L}_\infty}$ and $M_{\mathcal{L}_{2,act}}$ (maximum, minimum, mean value and standard deviation) generated from example maneuver performed by enhanced, nonlinear aircraft model with Plant Augmentation and comparison to baseline controller starting at $V_0 = 154.94\frac{m}{s}$ and $h_0 = 5000m$ considering variation of natural frequency $\omega_{0,s}$ and relative damping ζ_s of structural mode

	$M_{\mathcal{L}_2}$ $[-]$	$M_{\mathcal{L}_\infty}$ $[-]$	$M_{\mathcal{L}_{2,act}}$ $[-]$	$M_{\mathcal{L}_{2,rel}}$ $[\%]$	$M_{\mathcal{L}_{\infty,rel}}$ $[\%]$	$M_{\mathcal{L}_{2,act,rel}}$ $[\%]$
max	2.35	0.048	20.64	30.2%	33.2%	142.7%
min	2.28	0.046	18.71	29.3%	32.4%	129.5%
$\varnothing$	2.31	0.047	19.36	29.6%	33.0%	134.0%
σ	0.014	0.0004	0.399	975.2%	46.4%	6403.1%

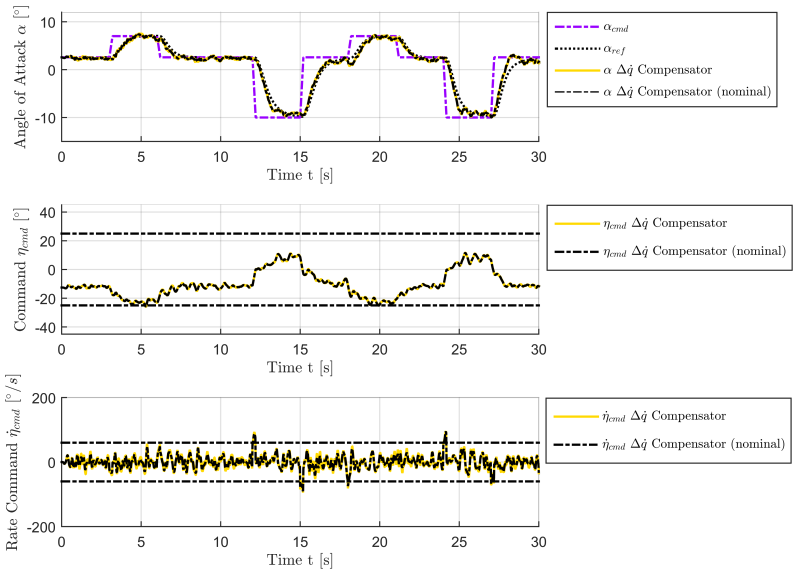

Figure 6.99. – Angle of attack α, elevator command η_{cmd} and elevator command rate $\dot{\eta}_{cmd}$ for example maneuver performed by enhanced, nonlinear aircraft model with $\Delta\dot{q}$ Compensation Law starting at $V_0 = 154.94\frac{m}{s}$ and $h_0 = 5000m$ considering variation of natural frequency $\omega_{0,s}$ and relative damping ζ_s of structural mode

Table 6.85. – Performance metrics $M_{\mathcal{L}_2}$, $M_{\mathcal{L}_\infty}$ and $M_{\mathcal{L}_{2,act}}$ (maximum, minimum, mean value and standard deviation) generated from example maneuver performed by enhanced, nonlinear aircraft model with $\Delta\dot{q}$ Compensation Law and comparison to baseline controller starting at $V_0 = 154.94\frac{m}{s}$ and $h_0 = 5000m$ considering variation of natural frequency $\omega_{0,s}$ and relative damping ζ_s of structural mode

	$M_{\mathcal{L}_2}$ $[-]$	$M_{\mathcal{L}_\infty}$ $[-]$	$M_{\mathcal{L}_{2,act}}$ $[-]$	$M_{\mathcal{L}_{2,rel}}$ $[\%]$	$M_{\mathcal{L}_{\infty,rel}}$ $[\%]$	$M_{\mathcal{L}_{2,act,rel}}$ $[\%]$
max	2.42	0.052	20.49	31.0%	35.9%	141.6%
min	2.36	0.048	18.43	30.4%	33.7%	127.6%
$\varnothing$	2.39	0.049	19.11	30.7%	34.6%	132.2%
σ	0.012	0.0011	0.433	781.4%	118.4%	6948.4%

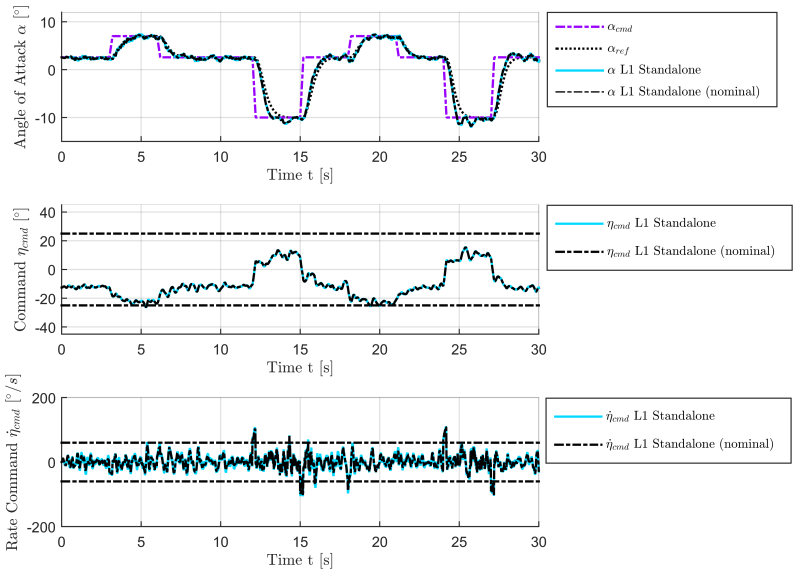

Figure 6.100. – Angle of attack α, elevator command η_{cmd} and elevator command rate $\dot{\eta}_{cmd}$ for example maneuver performed by enhanced, nonlinear aircraft model with L1 adaptive controller with Eigenstructure Assignment starting at $V_0 = 154.94\frac{m}{s}$ and $h_0 = 5000m$ considering variation of natural frequency $\omega_{0,s}$ and relative damping ζ_s of structural mode

Table 6.86. – Performance metrics $M_{\mathcal{L}_2}$, $M_{\mathcal{L}_\infty}$ and $M_{\mathcal{L}_{2,act}}$ (maximum, minimum, mean value and standard deviation) generated from example maneuver performed by enhanced, nonlinear aircraft model with L1 adaptive controller with Eigenstructure Assignment and comparison to baseline controller starting at $V_0 = 154.94\frac{m}{s}$ and $h_0 = 5000m$ considering variation of natural frequency $\omega_{0,s}$ and relative damping ζ_s of structural mode

	$M_{\mathcal{L}_2}$ [−]	$M_{\mathcal{L}_\infty}$ [−]	$M_{\mathcal{L}_{2,act}}$ [−]	$M_{\mathcal{L}_{2,rel}}$ [%]	$M_{\mathcal{L}_{\infty,rel}}$ [%]	$M_{\mathcal{L}_{2,act,rel}}$ [%]
max	2.62	0.074	23.49	33.7%	50.6%	162.3%
min	2.60	0.071	21.66	33.4%	50.0%	150.0%
∅	2.61	0.072	22.29	33.5%	50.7%	154.2%
σ	0.005	0.0007	0.425	333.0%	72.0%	6813.1%

6.2.15. Uncertainty w.r.t. actuator dynamics

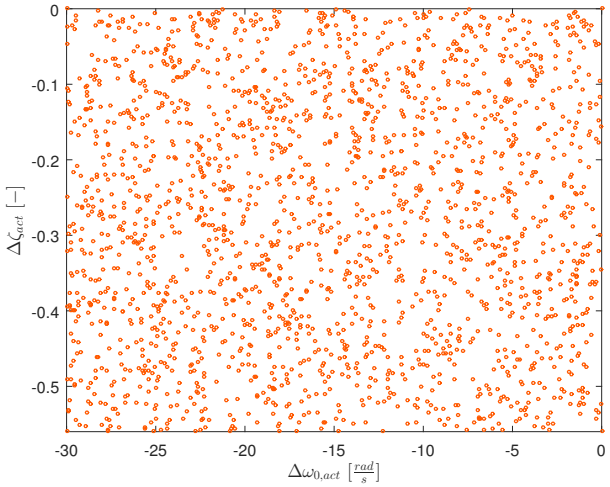

Figure 6.101. – Variation of additive uncertainties w.r.t. elevator natural frequency $\Delta\omega_{0,act}$ and relative damping $\Delta\zeta_{act}$

After the assessment of uncertainties applied to the simple structural mode model, parameter variations are now investigated with regard to the actuator model, which was introduced in Section 2.5. The second order dynamics of the actuator are defined in Eq. (2.53) and exhibit a natural frequency of $\omega_{0,act} = 40\frac{rad}{s}$ and a relative damping of $\zeta_{act} = 0.71$. For this assessment, additive uncertainties $\Delta\omega_{0,act}$ and $\Delta\zeta_{act}$ are applied to these model parameters according to

$$\omega_{0,act,perturb} = \omega_{0,act} + \Delta\omega_{0,act} \tag{6.2}$$

and

$$\zeta_{act,perturb} = \zeta_{act} + \Delta\zeta_{act}. \tag{6.3}$$

The uncertainties are randomly varied between $\left[-30\frac{rad}{s}; 0\frac{rad}{s}\right]$ in case of $\Delta\omega_{0,act}$ and $[-0.56; 0]$ in case of $\Delta\zeta_{act}$, respectively. This results in minimum values of $\omega_{0,act,perturb,min} = 10\frac{rad}{s}$ and $\zeta_{act,perturb,min} = 0.15$. In total 2000 variations are generated, which are shown in Fig. 6.101.
The results of the simulations for the different controllers are compiled in Fig. 6.102 and Table 6.87 for the baseline controller, in Fig. 6.103 and Table 6.88 for the DPI Augmentation, in Fig. 6.104 and Table 6.89 for the Plant Augmentation, in Fig. 6.105 and Table 6.90 for the $\Delta\dot{q}$ Compensation Law and in Fig. 6.106 and Table 6.91 for the standalone L1 adaptive controller with Eigenstructure Assignment. All of the controllers still exhibit stable performances, despite the considered degradation of the actuator model. Although, oscillations can be detected for the adaptive controllers,

which are not apparent considering the baseline controller. The largest scattering with regard to the angle of attack α system response appears for the L1 Adaptive Augmentations, especially during the $\alpha_{min} = -10^{\circ}$ sections. This is also confirmed by the standard deviations of $M_{\mathcal{L}_2}$ for both DPI and Plant Augmentation. In comparison to the L1 Adaptive Augmentations, the the standard deviation of $M_{\mathcal{L}_2}$ belonging to the $\Delta\dot{q}$ Compensation Law simulations is reduced by approximately 50%. At last it can be stated that, apart from the baseline controller, the actuator model parameter variation has the smallest influence on the standalone L1 adaptive controller.

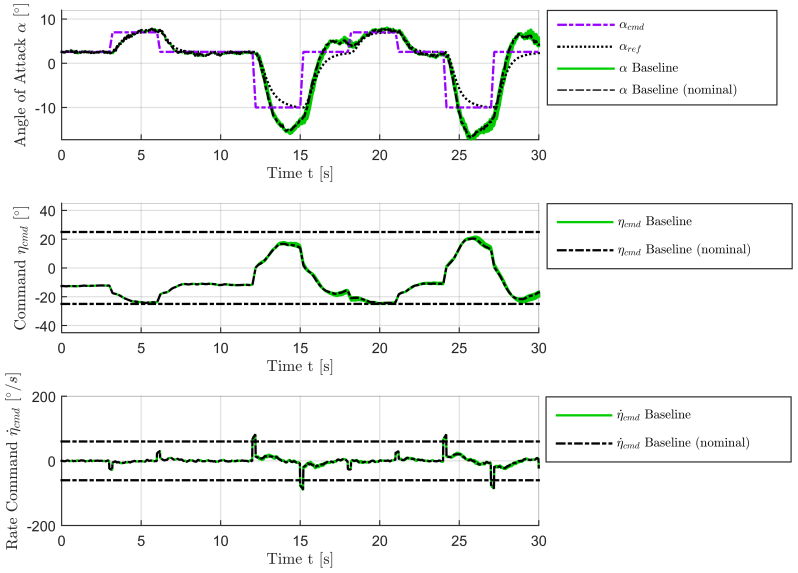

Figure 6.102. – Angle of attack α, elevator command η_{cmd} and elevator command rate $\dot{\eta}_{cmd}$ for example maneuver performed by enhanced, nonlinear aircraft model with baseline controller starting at $V_0 = 154.94\frac{m}{s}$ and $h_0 = 5000m$ considering variation of additive uncertainties w.r.t. elevator natural frequency $\Delta\omega_{0,act}$ and relative damping $\Delta\zeta_{act}$

Table 6.87. – Performance metrics $M_{\mathcal{L}_2}$, $M_{\mathcal{L}_\infty}$ and $M_{\mathcal{L}_{2,act}}$ (maximum, minimum, mean value and standard deviation) generated from example maneuver performed by enhanced, nonlinear aircraft model with baseline controller starting at $V_0 = 154.94\frac{m}{s}$ and $h_0 = 5000m$ considering variation of additive uncertainties w.r.t. elevator natural frequency $\Delta\omega_{0,act}$ and relative damping $\Delta\zeta_{act}$

	$M_{\mathcal{L}_2}$ $[-]$	$M_{\mathcal{L}_\infty}$ $[-]$	$M_{\mathcal{L}_{2,act}}$ $[-]$
max	8.12	0.151	14.69
min	7.78	0.141	14.41
$\varnothing$	7.84	0.144	14.49
σ	0.059	0.0013	0.056

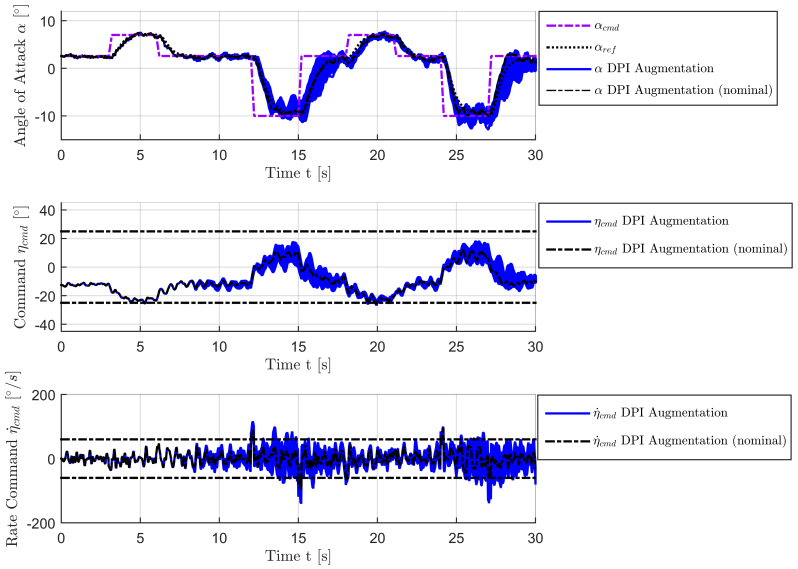

Figure 6.103. – Angle of attack α, elevator command η_{cmd} and elevator command rate $\dot{\eta}_{cmd}$ for example maneuver performed by enhanced, nonlinear aircraft model with DPI Augmentation starting at $V_0 = 154.94\frac{m}{s}$ and $h_0 = 5000m$ considering variation of additive uncertainties w.r.t. elevator natural frequency $\Delta\omega_{0,act}$ and relative damping $\Delta\zeta_{act}$

Table 6.88. – Performance metrics $M_{\mathcal{L}_2}$, $M_{\mathcal{L}_\infty}$ and $M_{\mathcal{L}_{2,act}}$ (maximum, minimum, mean value and standard deviation) generated from example maneuver performed by enhanced, nonlinear aircraft model with DPI Augmentation and comparison to baseline controller starting at $V_0 = 154.94\frac{m}{s}$ and $h_0 = 5000m$ considering variation of additive uncertainties w.r.t. elevator natural frequency $\Delta\omega_{0,act}$ and relative damping $\Delta\zeta_{act}$

	$M_{\mathcal{L}_2}$ $[-]$	$M_{\mathcal{L}_\infty}$ $[-]$	$M_{\mathcal{L}_{2,act}}$ $[-]$	$M_{\mathcal{L}_{2,rel}}$ $[\%]$	$M_{\mathcal{L}_{\infty,rel}}$ $[\%]$	$M_{\mathcal{L}_{2,act,rel}}$ $[\%]$
max	4.10	0.106	29.24	50.5%	70.1%	199.0%
min	1.75	0.036	19.34	22.5%	25.2%	134.3%
$\varnothing$	2.32	0.049	20.56	29.6%	34.3%	141.9%
σ	0.337	0.0096	1.606	575.9%	743.4%	2846.9%

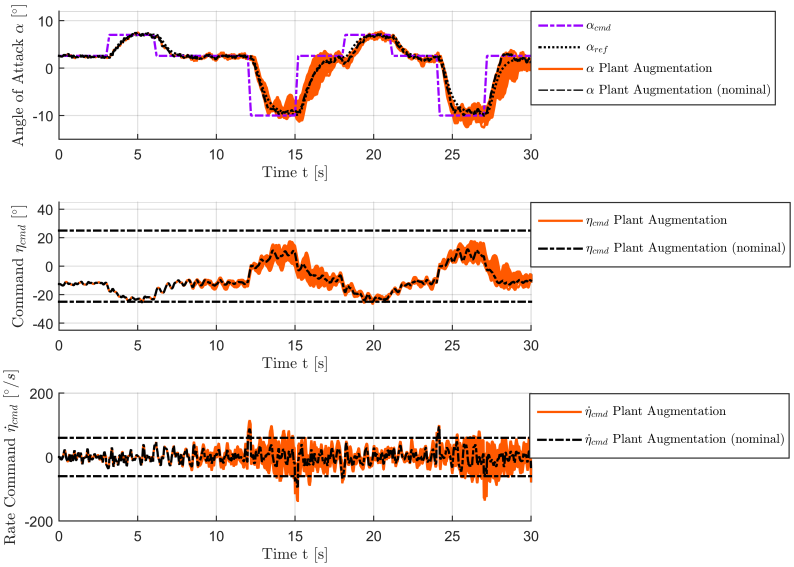

Figure 6.104. – Angle of attack α, elevator command η_{cmd} and elevator command rate $\dot{\eta}_{cmd}$ for example maneuver performed by enhanced, nonlinear aircraft model with Plant Augmentation starting at $V_0 = 154.94\frac{m}{s}$ and $h_0 = 5000m$ considering variation of additive uncertainties w.r.t. elevator natural frequency $\Delta\omega_{0,act}$ and relative damping $\Delta\zeta_{act}$

Table 6.89. – Performance metrics $M_{\mathcal{L}_2}$, $M_{\mathcal{L}_\infty}$ and $M_{\mathcal{L}_{2,act}}$ (maximum, minimum, mean value and standard deviation) generated from example maneuver performed by enhanced, nonlinear aircraft model with Plant Augmentation and comparison to baseline controller starting at $V_0 = 154.94\frac{m}{s}$ and $h_0 = 5000m$ considering variation of additive uncertainties w.r.t. elevator natural frequency $\Delta\omega_{0,act}$ and relative damping $\Delta\zeta_{act}$

	$M_{\mathcal{L}_2}$ $[-]$	$M_{\mathcal{L}_\infty}$ $[-]$	$M_{\mathcal{L}_{2,act}}$ $[-]$	$M_{\mathcal{L}_{2,rel}}$ $[\%]$	$M_{\mathcal{L}_{\infty,rel}}$ $[\%]$	$M_{\mathcal{L}_{2,act,rel}}$ $[\%]$
max	4.13	0.105	28.78	50.9%	69.5%	195.9%
min	1.74	0.036	19.24	22.4%	25.5%	133.6%
$\varnothing$	2.33	0.049	20.31	29.7%	34.2%	140.2%
σ	0.317	0.0090	1.507	541.8%	699.7%	2671.8%

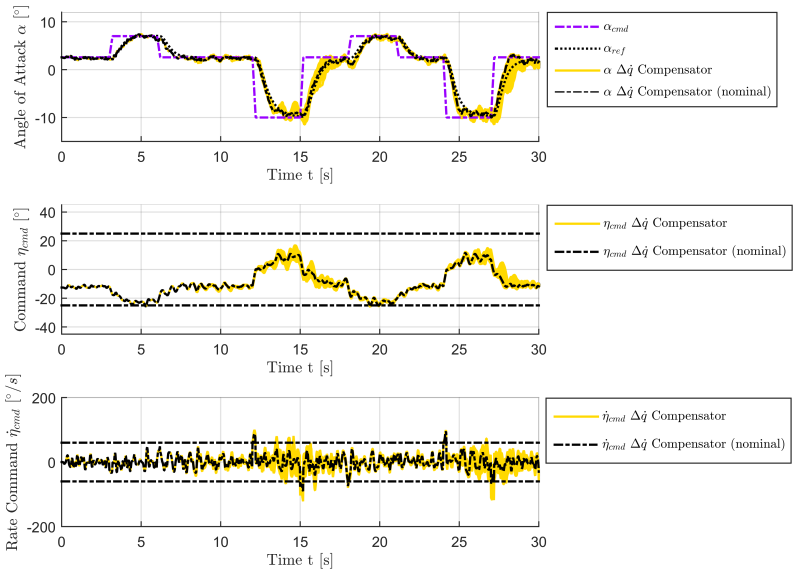

Figure 6.105. – Angle of attack α, elevator command η_{cmd} and elevator command rate $\dot{\eta}_{cmd}$ for example maneuver performed by enhanced, nonlinear aircraft model with $\Delta\dot{q}$ Compensation Law starting at $V_0 = 154.94\frac{m}{s}$ and $h_0 = 5000m$ considering variation of additive uncertainties w.r.t. elevator natural frequency $\Delta\omega_{0,act}$ and relative damping $\Delta\zeta_{act}$

Table 6.90. – Performance metrics $M_{\mathcal{L}_2}$, $M_{\mathcal{L}_\infty}$ and $M_{\mathcal{L}_{2,act}}$ (maximum, minimum, mean value and standard deviation) generated from example maneuver performed by enhanced, nonlinear aircraft model with $\Delta\dot{q}$ Compensation Law and comparison to baseline controller starting at $V_0 = 154.94\frac{m}{s}$ and $h_0 = 5000m$ considering variation of additive uncertainties w.r.t. elevator natural frequency $\Delta\omega_{0,act}$ and relative damping $\Delta\zeta_{act}$

	$M_{\mathcal{L}_2}$ $[-]$	$M_{\mathcal{L}_\infty}$ $[-]$	$M_{\mathcal{L}_{2,act}}$ $[-]$	$M_{\mathcal{L}_{2,rel}}$ $[\%]$	$M_{\mathcal{L}_{\infty,rel}}$ $[\%]$	$M_{\mathcal{L}_{2,act,rel}}$ $[\%]$
max	3.28	0.078	24.13	40.4%	52.0%	164.2%
min	1.88	0.044	19.03	24.2%	31.3%	132.1%
$\varnothing$	2.39	0.051	19.42	30.4%	35.6%	134.1%
σ	0.164	0.0033	0.585	280.0%	255.1%	1037.0%

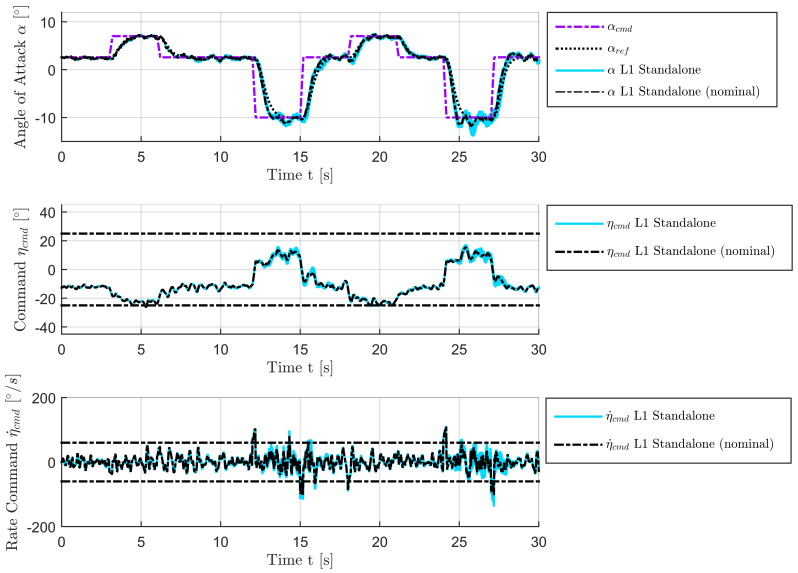

Figure 6.106. – Angle of attack α, elevator command η_{cmd} and elevator command rate $\dot{\eta}_{cmd}$ for example maneuver performed by enhanced, nonlinear aircraft model with L1 adaptive controller with Eigenstructure Assignment starting at $V_0 = 154.94\frac{m}{s}$ and $h_0 = 5000m$ considering variation of additive uncertainties w.r.t. elevator natural frequency $\Delta\omega_{0,act}$ and relative damping $\Delta\zeta_{act}$

Table 6.91. – Performance metrics $M_{\mathcal{L}_2}$, $M_{\mathcal{L}_\infty}$ and $M_{\mathcal{L}_{2,act}}$ (maximum, minimum, mean value and standard deviation) generated from example maneuver performed by enhanced, nonlinear aircraft model with L1 adaptive controller with Eigenstructure Assignment and comparison to baseline controller starting at $V_0 = 154.94\frac{m}{s}$ and $h_0 = 5000m$ considering variation of additive uncertainties w.r.t. elevator natural frequency $\Delta\omega_{0,act}$ and relative damping $\Delta\zeta_{act}$

	$M_{\mathcal{L}_2}$ [−]	$M_{\mathcal{L}_\infty}$ [−]	$M_{\mathcal{L}_{2,act}}$ [−]	$M_{\mathcal{L}_{2,rel}}$ [%]	$M_{\mathcal{L}_{\infty,rel}}$ [%]	$M_{\mathcal{L}_{2,act,rel}}$ [%]
max	2.91	0.086	23.72	35.8%	57.0%	161.4%
min	2.19	0.064	22.05	28.2%	45.1%	153.1%
∅	2.56	0.071	22.40	32.6%	49.7%	154.6%
σ	0.115	0.0020	0.276	195.6%	157.6%	488.8%

6.2.16. Uncertainty w.r.t. gust

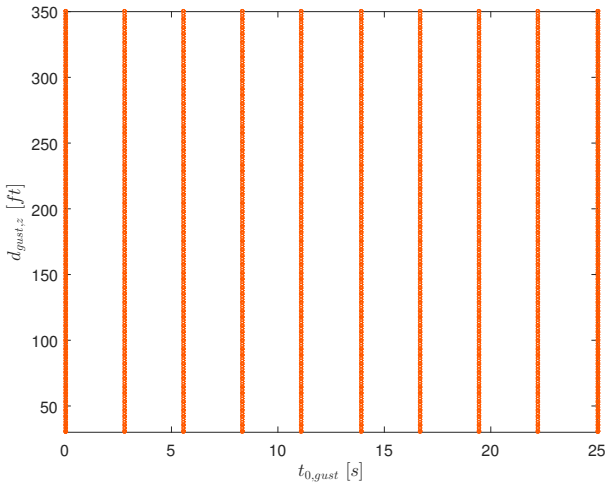

Figure 6.107. – Variation of gust length $d_{gust,z}$ and starting time $t_{0,gust}$

The last assessments of this chapter cover comparisons of the proposed controller design with regard to their performance considering atmospheric disturbances. In particular, this chapter takes the effect of longitudinal gust on the controller performances into account. The gust model, which is utilized here, was introduced in Section 2.4. For these investigations, the peak amplitude of the gust is set to $v_{gust} = 60\frac{ft}{s} \approx 18.29\frac{m}{s}$ in accordance to [111, p. 29]. The gust length d_{gust} is varied within the interval $[30ft; 350ft]$, which corresponds to $[9.14m; 106.68m]$, generating 200 evenly distributed parameter values. Furthermore, 10 also evenly distributed values for the starting time $t_{0,gust}$ are chosen considering the limits $[0s; 25s]$. Thus, in total 2000 combined variations are created, which are also depicted in Fig. 6.107.
The results of the corresponding simulations can be found in Fig. 6.108 and Table 6.92 for the baseline controller, in Fig. 6.109 and Table 6.93 for the DPI Augmentation, in Fig. 6.110 and Table 6.94 for the Plant Augmentation, in Fig. 6.111 and Table 6.95 for the $\Delta\dot{q}$ Compensation Law and in Fig. 6.112 and Table 6.96 for the standalone L1 adaptive controller with Eigenstructure Assignment. One can see that all controller designs manage to generate a stable system response considering the gust variations. As it was observed before during the investigation of different disturbances, an application of the L1 adaptive controllers leads to stronger commanded actuator activity compared to the baseline controller, which is confirmed by means of the metric $M_{\mathcal{L}_{2,act}}$. This stems again from the high gain parameter update law, which amplifies disturbances and is an essential part of the L1 Adaptive Control approach. Furthermore, their system responses exhibit larger scattering, which can also be seen considering the standard deviation of $M_{\mathcal{L}_2}$. It should be noted that this is not the case for the $\Delta\dot{q}$ Compensation Law, although commanded actuator activity slightly increases also in this case.

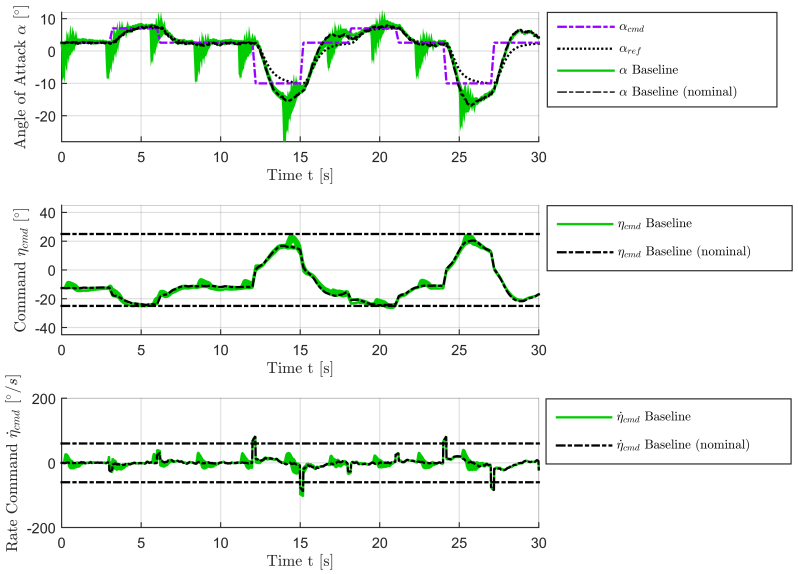

Figure 6.108. – Angle of attack α, elevator command η_{cmd} and elevator command rate $\dot{\eta}_{cmd}$ for example maneuver performed by enhanced, nonlinear aircraft model with baseline controller starting at $V_0 = 154.94\frac{m}{s}$ and $h_0 = 5000m$ considering variation of gust length $d_{gust,z}$ and starting time $t_{0,gust}$

Table 6.92. – Performance metrics $M_{\mathcal{L}_2}$, $M_{\mathcal{L}_\infty}$ and $M_{\mathcal{L}_{2,act}}$ (maximum, minimum, mean value and standard deviation) generated from example maneuver performed by enhanced, nonlinear aircraft model with baseline controller starting at $V_0 = 154.94\frac{m}{s}$ and $h_0 = 5000m$ considering variation of gust length $d_{gust,z}$ and starting time $t_{0,gust}$

	$M_{\mathcal{L}_2}$ $[-]$	$M_{\mathcal{L}_\infty}$ $[-]$	$M_{\mathcal{L}_{2,act}}$ $[-]$
max	8.27	0.335	15.24
min	7.35	0.134	14.08
$\varnothing$	7.67	0.159	14.51
σ	0.193	0.0365	0.205

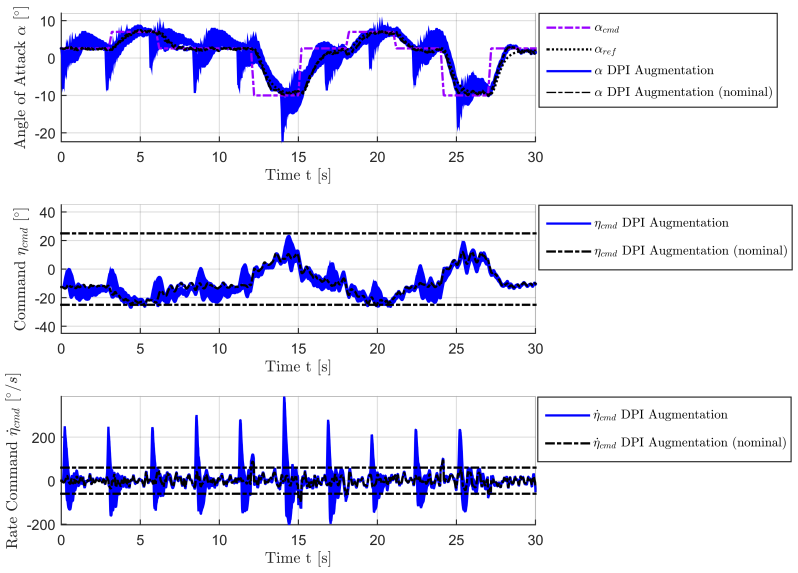

Figure 6.109. – Angle of attack α, elevator command η_{cmd} and elevator command rate $\dot{\eta}_{cmd}$ for example maneuver performed by enhanced, nonlinear aircraft model with DPI Augmentation starting at $V_0 = 154.94\frac{m}{s}$ and $h_0 = 5000m$ considering variation of gust length $d_{gust,z}$ and starting time $t_{0,gust}$

Table 6.93. – Performance metrics $M_{\mathcal{L}_2}$, $M_{\mathcal{L}_\infty}$ and $M_{\mathcal{L}_{2,act}}$ (maximum, minimum, mean value and standard deviation) generated from example maneuver performed by enhanced, nonlinear aircraft model with DPI Augmentation and comparison to baseline controller starting at $V_0 = 154.94\frac{m}{s}$ and $h_0 = 5000m$ considering variation of gust length $d_{gust,z}$ and starting time $t_{0,gust}$

	$M_{\mathcal{L}_2}$ [−]	$M_{\mathcal{L}_\infty}$ [−]	$M_{\mathcal{L}_{2,act}}$ [−]	$M_{\mathcal{L}_{2,rel}}$ [%]	$M_{\mathcal{L}_{\infty,rel}}$ [%]	$M_{\mathcal{L}_{2,act,rel}}$ [%]
max	4.54	0.236	31.31	55.0%	70.5%	205.4%
min	2.29	0.047	19.48	31.1%	34.9%	138.4%
∅	3.09	0.105	22.87	40.2%	66.1%	157.7%
σ	0.356	0.0373	2.082	184.3%	102.2%	1017.2%

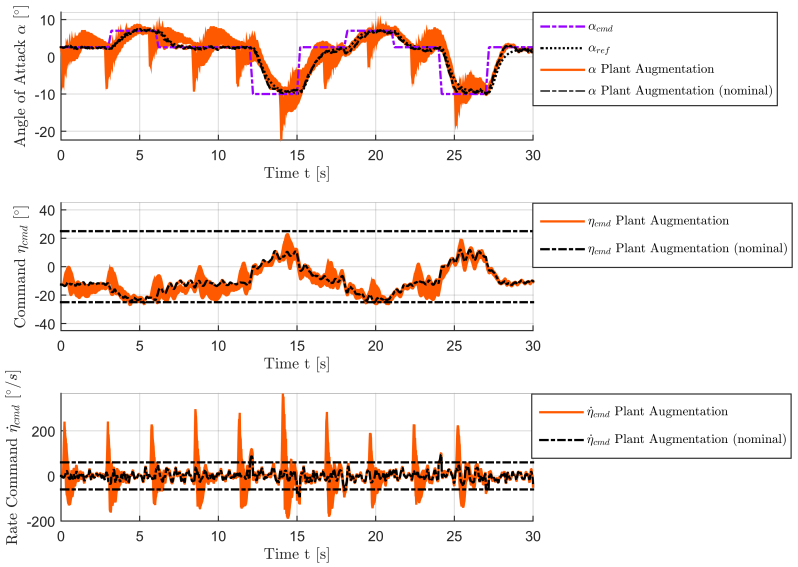

Figure 6.110. – Angle of attack α, elevator command η_{cmd} and elevator command rate $\dot{\eta}_{cmd}$ for example maneuver performed by enhanced, nonlinear aircraft model with Plant Augmentation starting at $V_0 = 154.94\frac{m}{s}$ and $h_0 = 5000m$ considering variation of gust length $d_{gust,z}$ and starting time $t_{0,gust}$

Table 6.94. – Performance metrics $M_{\mathcal{L}_2}$, $M_{\mathcal{L}_\infty}$ and $M_{\mathcal{L}_{2,act}}$ (maximum, minimum, mean value and standard deviation) generated from example maneuver performed by enhanced, nonlinear aircraft model with Plant Augmentation and comparison to baseline controller starting at $V_0 = 154.94\frac{m}{s}$ and $h_0 = 5000m$ considering variation of gust length $d_{gust,z}$ and starting time $t_{0,gust}$

	$M_{\mathcal{L}_2}$ [−]	$M_{\mathcal{L}_\infty}$ [−]	$M_{\mathcal{L}_{2,act}}$ [−]	$M_{\mathcal{L}_{2,rel}}$ [%]	$M_{\mathcal{L}_{\infty,rel}}$ [%]	$M_{\mathcal{L}_{2,act,rel}}$ [%]
max	4.62	0.235	30.13	55.9%	70.4%	197.7%
min	2.31	0.047	19.33	31.4%	35.4%	137.3%
∅	3.07	0.105	22.47	40.0%	65.9%	154.9%
σ	0.347	0.0374	1.911	180.0%	102.6%	933.6%

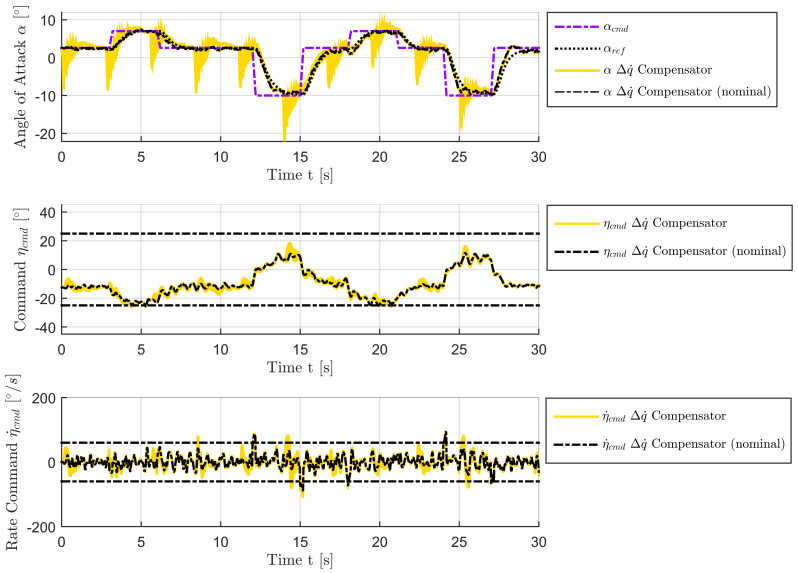

Figure 6.111. – Angle of attack α, elevator command η_{cmd} and elevator command rate $\dot{\eta}_{cmd}$ for example maneuver performed by enhanced, nonlinear aircraft model with $\Delta\dot{q}$ Compensation Law starting at $V_0 = 154.94\frac{m}{s}$ and $h_0 = 5000m$ considering variation of gust length $d_{gust,z}$ and starting time $t_{0,gust}$

Table 6.95. – Performance metrics $M_{\mathcal{L}_2}$, $M_{\mathcal{L}_\infty}$ and $M_{\mathcal{L}_{2,act}}$ (maximum, minimum, mean value and standard deviation) generated from example maneuver performed by enhanced, nonlinear aircraft model with $\Delta\dot{q}$ Compensation Law and comparison to baseline controller starting at $V_0 = 154.94\frac{m}{s}$ and $h_0 = 5000m$ considering variation of gust length $d_{gust,z}$ and starting time $t_{0,gust}$

	$M_{\mathcal{L}_2}$ $[-]$	$M_{\mathcal{L}_\infty}$ $[-]$	$M_{\mathcal{L}_{2,act}}$ $[-]$	$M_{\mathcal{L}_{2,rel}}$ $[\%]$	$M_{\mathcal{L}_{\infty,rel}}$ $[\%]$	$M_{\mathcal{L}_{2,act,rel}}$ $[\%]$
max	3.51	0.231	21.04	42.4%	69.1%	138.0%
min	2.40	0.050	19.03	32.6%	37.7%	135.2%
$\varnothing$	2.85	0.102	19.93	37.2%	64.3%	137.4%
σ	0.191	0.0389	0.427	98.8%	106.6%	208.8%

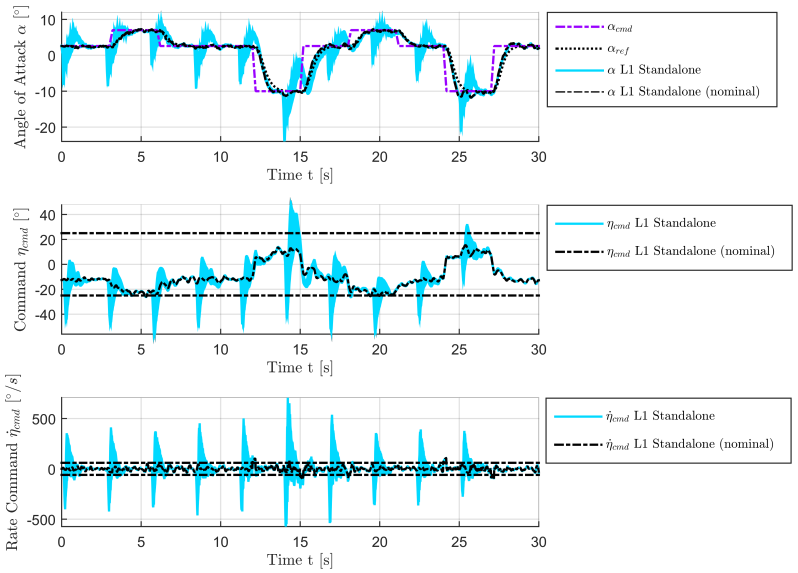

Figure 6.112. – Angle of attack α, elevator command η_{cmd} and elevator command rate $\dot{\eta}_{cmd}$ for example maneuver performed by enhanced, nonlinear aircraft model with L1 adaptive controller with Eigenstructure Assignment starting at $V_0 = 154.94\frac{m}{s}$ and $h_0 = 5000m$ considering variation of gust length $d_{gust,z}$ and starting time $t_{0,gust}$

Table 6.96. – Performance metrics $M_{\mathcal{L}_2}$, $M_{\mathcal{L}_\infty}$ and $M_{\mathcal{L}_{2,act}}$ (maximum, minimum, mean value and standard deviation) generated from example maneuver performed by enhanced, nonlinear aircraft model with L1 adaptive controller with Eigenstructure Assignment and comparison to baseline controller starting at $V_0 = 154.94\frac{m}{s}$ and $h_0 = 5000m$ considering variation of gust length $d_{gust,z}$ and starting time $t_{0,gust}$

	$M_{\mathcal{L}_2}$ $[-]$	$M_{\mathcal{L}_\infty}$ $[-]$	$M_{\mathcal{L}_{2,act}}$ $[-]$	$M_{\mathcal{L}_{2,rel}}$ $[\%]$	$M_{\mathcal{L}_{\infty,rel}}$ $[\%]$	$M_{\mathcal{L}_{2,act,rel}}$ $[\%]$
max	4.69	0.248	51.05	56.7%	74.1%	335.0%
min	2.61	0.067	22.18	35.5%	50.0%	157.6%
$\varnothing$	3.15	0.105	28.39	41.1%	66.3%	195.7%
σ	0.405	0.0410	5.070	209.9%	112.3%	2477.4%

6.2.17. Uncertainty w.r.t. turbulence with q_w

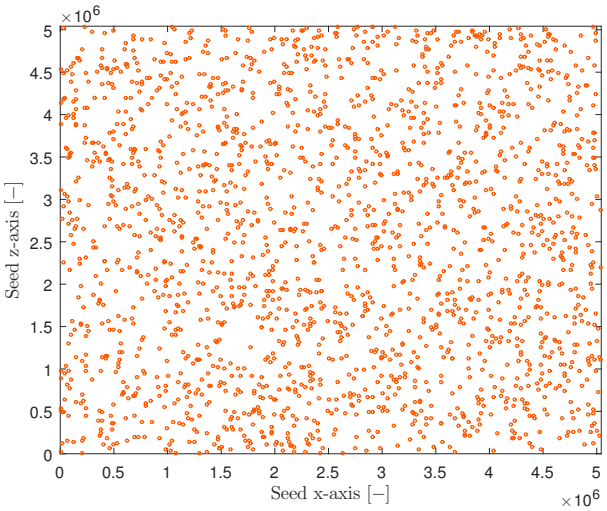

Figure 6.113. – Variation of noise seeds for dryden turbulence model

At last, the controller performances are further investigated considering turbulence according to the dryden turbulence model, which was introduced in Section 2.3. In particular, the effect of severe turbulence (probability of exceedance 10^{-5}) is examined. Here, variations on the seeds are introduced, which are utilized to generate the normally distributed white noise $N(0,1)$ within the dryden turbulence model. $N(0,1)$ is the input to the shaping filters in Eq. (2.51), which are used to calculate the wind velocities $\left(u_W^G\right)_0^0$ and $\left(w_W^G\right)_0^0$ according to the dryden spectra in Eq. (2.50). Note that the pitch rate resulting from turbulence q_W is calculated using $\left(w_W^G\right)_0^0$. Thus, they are based on the same normally distributed white noise $N(0,1)$ input and therefore also based on the same seed.
In order to vary the seeds corresponding to $\left(u_W^G\right)_0^0$ (x-axis) and $\left(w_W^G\right)_0^0$ (z-axis), they are randomly chosen considering the limits $[0; 5042063]$. This way, 2000 parameter variations are generated, which are shown in Fig. 6.113.
Two different assessments are shown in the following. This section features simulations, where the complete dryden turbulence model according to Section 2.3 is utilized. After that, the same assessment is shown for the case, where the pitch rate generated by turbulence is constantly set to $q_W = 0$.
Simulation results considering variations of the seeds, which are used to generate a representation of severe turbulence (probability of exceedance 10^{-5}), are summarized in Fig. 6.114 and Table 6.97 for the baseline controller, in Fig. 6.115 and Table 6.98 for the DPI Augmentation, in Fig. 6.116 and Table 6.99 for the Plant Augmentation, in Fig. 6.117 and Table 6.100 for the $\Delta\dot{q}$ Compensation Law and in Fig. 6.118 and Table 6.101 for the standalone L1 adaptive controller with Eigenstructure Assignment,

where the calculation of q_W according to Eq. (2.51) is active. First of all, it can be stated that all controllers remain stable considering variations of severe turbulence. As it was already observed before, application of the adaptive controllers leads to increased commanded actuator activity, which can be read from the mean values of $M_{\mathcal{L}_{2,act}}$. Compared to the L1 Adaptive Augmentations, the activity is slightly higher for the $\Delta\dot{q}$ Compensation Law, whereas the standalone L1 adaptive controller shows the highest commanded actuator activity. Furthermore, the standard deviation of $M_{\mathcal{L}_2}$ indicates that the adaptive augmentations, which includes both L1 Adaptive Augmentations and $\Delta\dot{q}$ Compensation Law, exhibit larger scattering with regard to the system response in angle of attack α. It should be noted that the scattering using the standalone L1 adaptive controller is even decreased compared to the baseline controller, where also the overall performance in terms of the mean value of $M_{\mathcal{L}_2}$ surpasses the value of the baseline controller. This is also confirmed by the metric evaluating the largest deviation from the reference behavior $M_{\mathcal{L}_\infty}$, which decreases in case of application of the standalone L1 adaptive controller.

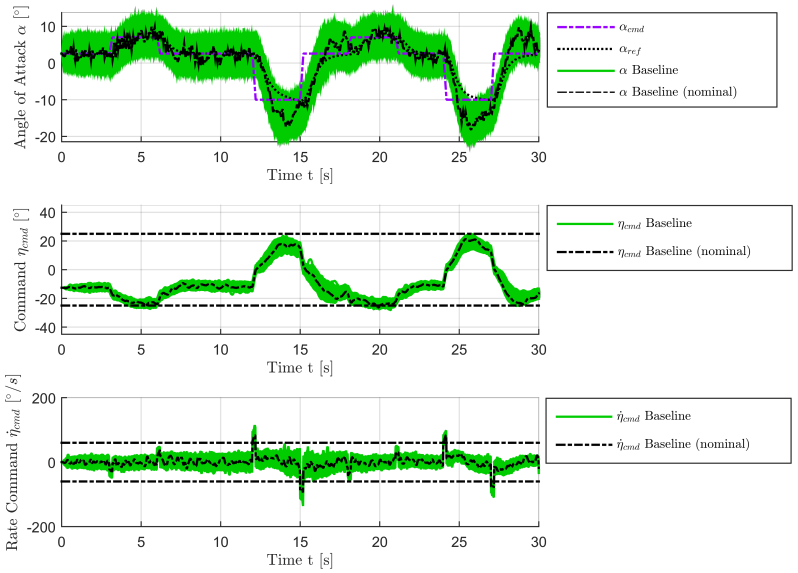

Figure 6.114. – Angle of attack α, elevator command η_{cmd} and elevator command rate $\dot{\eta}_{cmd}$ for example maneuver performed by enhanced, nonlinear aircraft model with baseline controller starting at $V_0 = 154.94\frac{m}{s}$ and $h_0 = 5000m$ considering variation of noise seeds for dryden turbulence model

Table 6.97. – Performance metrics $M_{\mathcal{L}_2}$, $M_{\mathcal{L}_\infty}$ and $M_{\mathcal{L}_{2,act}}$ (maximum, minimum, mean value and standard deviation) generated from example maneuver performed by enhanced, nonlinear aircraft model with baseline controller starting at $V_0 = 154.94\frac{m}{s}$ and $h_0 = 5000m$ considering variation of noise seeds for dryden turbulence model

	$M_{\mathcal{L}_2}$ $[-]$	$M_{\mathcal{L}_\infty}$ $[-]$	$M_{\mathcal{L}_{2,act}}$ $[-]$
max	10.14	0.232	17.40
min	7.11	0.130	14.08
$\varnothing$	8.70	0.175	15.62
σ	0.426	0.0143	0.388

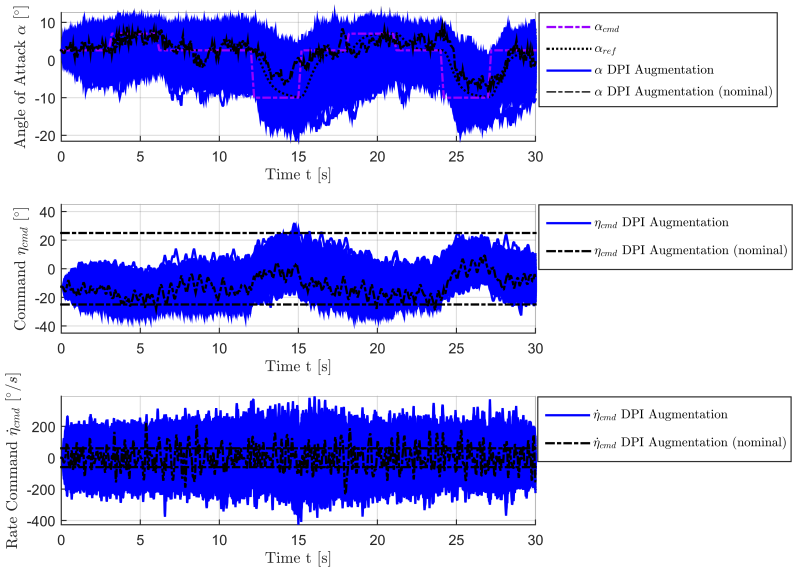

Figure 6.115. – Angle of attack α, elevator command η_{cmd} and elevator command rate $\dot{\eta}_{cmd}$ for example maneuver performed by enhanced, nonlinear aircraft model with DPI Augmentation starting at $V_0 = 154.94\frac{m}{s}$ and $h_0 = 5000m$ considering variation of noise seeds for dryden turbulence model

Table 6.98. – Performance metrics $M_{\mathcal{L}_2}$, $M_{\mathcal{L}_\infty}$ and $M_{\mathcal{L}_{2,act}}$ (maximum, minimum, mean value and standard deviation) generated from example maneuver performed by enhanced, nonlinear aircraft model with DPI Augmentation and comparison to baseline controller starting at $V_0 = 154.94\frac{m}{s}$ and $h_0 = 5000m$ considering variation of noise seeds for dryden turbulence model

	$M_{\mathcal{L}_2}$ $[-]$	$M_{\mathcal{L}_\infty}$ $[-]$	$M_{\mathcal{L}_{2,act}}$ $[-]$	$M_{\mathcal{L}_{2,rel}}$ $[\%]$	$M_{\mathcal{L}_{\infty,rel}}$ $[\%]$	$M_{\mathcal{L}_{2,act,rel}}$ $[\%]$
max	18.18	0.342	98.59	179.2%	147.2%	566.6%
min	4.58	0.078	41.45	64.4%	59.6%	294.4%
$\varnothing$	8.65	0.161	59.55	99.4%	92.2%	381.3%
σ	1.613	0.0346	7.570	378.9%	241.3%	1949.8%

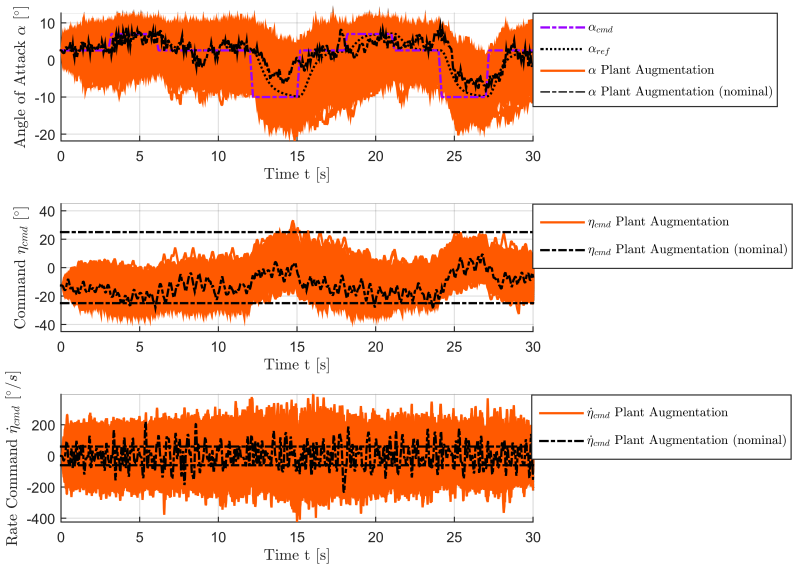

Figure 6.116. – Angle of attack α, elevator command η_{cmd} and elevator command rate $\dot{\eta}_{cmd}$ for example maneuver performed by enhanced, nonlinear aircraft model with Plant Augmentation starting at $V_0 = 154.94\frac{m}{s}$ and $h_0 = 5000m$ considering variation of noise seeds for dryden turbulence model

Table 6.99. – Performance metrics $M_{\mathcal{L}_2}$, $M_{\mathcal{L}_\infty}$ and $M_{\mathcal{L}_{2,act}}$ (maximum, minimum, mean value and standard deviation) generated from example maneuver performed by enhanced, nonlinear aircraft model with Plant Augmentation and comparison to baseline controller starting at $V_0 = 154.94\frac{m}{s}$ and $h_0 = 5000m$ considering variation of noise seeds for dryden turbulence model

	$M_{\mathcal{L}_2}$ $[-]$	$M_{\mathcal{L}_\infty}$ $[-]$	$M_{\mathcal{L}_{2,act}}$ $[-]$	$M_{\mathcal{L}_{2,rel}}$ $[\%]$	$M_{\mathcal{L}_{\infty,rel}}$ $[\%]$	$M_{\mathcal{L}_{2,act,rel}}$ $[\%]$
max	18.08	0.335	98.24	178.3%	144.5%	564.6%
min	4.59	0.081	41.65	64.6%	62.2%	295.9%
$\varnothing$	8.68	0.162	59.49	99.8%	92.4%	380.9%
σ	1.616	0.0346	7.549	379.7%	241.1%	1944.4%

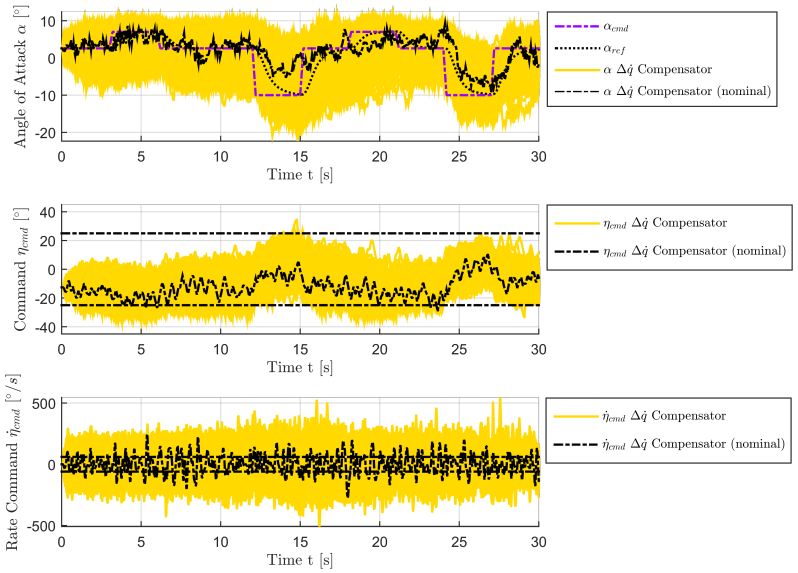

Figure 6.117. – Angle of attack α, elevator command η_{cmd} and elevator command rate $\dot{\eta}_{cmd}$ for example maneuver performed by enhanced, nonlinear aircraft model with $\Delta\dot{q}$ Compensation Law starting at $V_0 = 154.94\frac{m}{s}$ and $h_0 = 5000m$ considering variation of noise seeds for dryden turbulence model

Table 6.100. – Performance metrics $M_{\mathcal{L}_2}$, $M_{\mathcal{L}_\infty}$ and $M_{\mathcal{L}_{2,act}}$ (maximum, minimum, mean value and standard deviation) generated from example maneuver performed by enhanced, nonlinear aircraft model with $\Delta\dot{q}$ Compensation Law and comparison to baseline controller starting at $V_0 = 154.94\frac{m}{s}$ and $h_0 = 5000m$ considering variation of noise seeds for dryden turbulence model

	$M_{\mathcal{L}_2}$ $[-]$	$M_{\mathcal{L}_\infty}$ $[-]$	$M_{\mathcal{L}_{2,act}}$ $[-]$	$M_{\mathcal{L}_{2,rel}}$ $[\%]$	$M_{\mathcal{L}_{\infty,rel}}$ $[\%]$	$M_{\mathcal{L}_{2,act,rel}}$ $[\%]$
max	18.29	0.342	120.01	180.3%	147.4%	689.7%
min	5.25	0.088	40.78	73.8%	67.7%	289.7%
$\varnothing$	9.00	0.169	62.89	103.4%	96.4%	402.6%
σ	1.717	0.0364	9.543	403.4%	253.8%	2458.0%

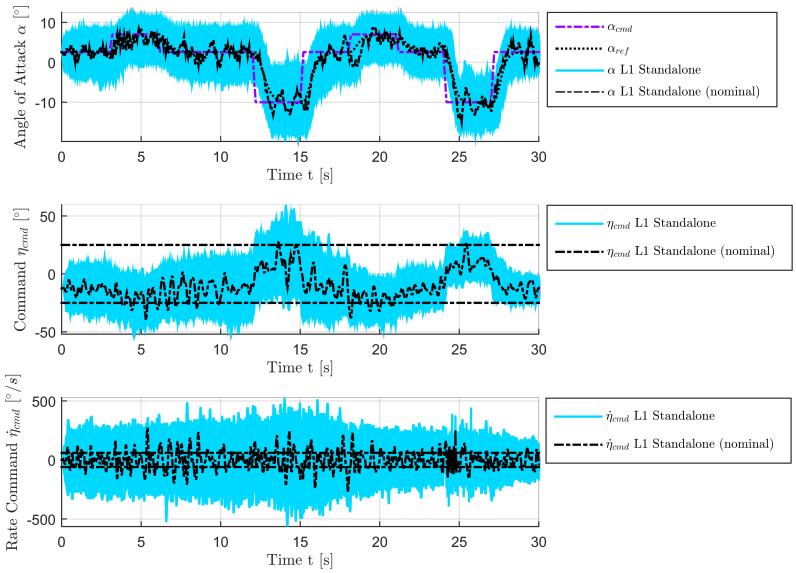

Figure 6.118. – Angle of attack α, elevator command η_{cmd} and elevator command rate $\dot{\eta}_{cmd}$ for example maneuver performed by enhanced, nonlinear aircraft model with L1 adaptive controller with Eigenstructure Assignment starting at $V_0 = 154.94\frac{m}{s}$ and $h_0 = 5000m$ considering variation of noise seeds for dryden turbulence model

Table 6.101. – Performance metrics $M_{\mathcal{L}_2}$, $M_{\mathcal{L}_\infty}$ and $M_{\mathcal{L}_{2,act}}$ (maximum, minimum, mean value and standard deviation) generated from example maneuver performed by enhanced, nonlinear aircraft model with L1 adaptive controller with Eigenstructure Assignment and comparison to baseline controller starting at $V_0 = 154.94\frac{m}{s}$ and $h_0 = 5000m$ considering variation of noise seeds for dryden turbulence model

	$M_{\mathcal{L}_2}$ $[-]$	$M_{\mathcal{L}_\infty}$ $[-]$	$M_{\mathcal{L}_{2,act}}$ $[-]$	$M_{\mathcal{L}_{2,rel}}$ $[\%]$	$M_{\mathcal{L}_{\infty,rel}}$ $[\%]$	$M_{\mathcal{L}_{2,act,rel}}$ $[\%]$
max	7.49	0.212	92.69	73.9%	91.3%	532.7%
min	4.32	0.072	61.23	60.7%	55.1%	435.0%
$\varnothing$	5.50	0.114	75.39	63.3%	65.3%	482.7%
σ	0.406	0.0174	4.888	95.3%	121.6%	1259.1%

6.2.18. Uncertainty w.r.t. turbulence without q_w

In this section, the assessments shown in Section 6.2.17 are repeated neglecting the pitch rate generated by turbulence q_W according to the dryden turbulence model Eq. (2.51), which is introduced in Section 2.3. Thus, this value is constantly set to $q_W = 0$ during simulations. For this purpose, also the same variations on the seeds, which are shown in Fig. 6.113, are utilized.
The corresponding results can be found in Fig. 6.119 and Table 6.102 for the baseline controller, in Fig. 6.120 and Table 6.103 for the DPI Augmentation, in Fig. 6.121 and Table 6.104 for the Plant Augmentation, in Fig. 6.122 and Table 6.105 for the $\Delta\dot{q}$ Compensation Law and in Fig. 6.123 and Table 6.106 for the standalone L1 adaptive controller with Eigenstructure Assignment. Firstly, it can be observed that the performance of the baseline controller barely changes in comparison to the results shown in Section 6.2.17. Although, one can clearly see in the same comparison that the commanded actuator activity significantly decreases for the L1 Adaptive Augmentations, which is indicated by the metric $M_{\mathcal{L}_{2,act}}$. In consequence, also the scattering with regard to the system response reduces, which can be seen in the standard deviation of $M_{\mathcal{L}_2}$. Its mean value and the one of $M_{\mathcal{L}_\infty}$ even indicate a performance increase. The same statements can be made for the $\Delta\dot{q}$ Compensation Law, where the metric $M_{\mathcal{L}_{2,act}}$ is even at almost the same level as for the baseline controller. At last, it can be seen that the results for the standalone L1 adaptive controller are very similar to the ones gained with pitch rate generated by turbulence q_W shown in Section 6.2.17.

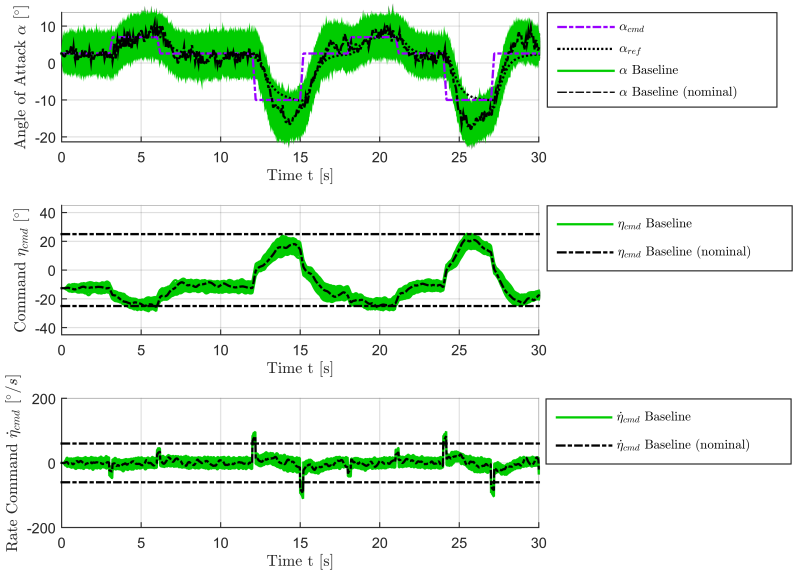

Figure 6.119. – Angle of attack α, elevator command η_{cmd} and elevator command rate $\dot{\eta}_{cmd}$ for example maneuver performed by enhanced, nonlinear aircraft model with baseline controller starting at $V_0 = 154.94\frac{m}{s}$ and $h_0 = 5000m$ considering variation of noise seeds for dryden turbulence model without q_w

Table 6.102. – Performance metrics $M_{\mathcal{L}_2}$, $M_{\mathcal{L}_\infty}$ and $M_{\mathcal{L}_{2,act}}$ (maximum, minimum, mean value and standard deviation) generated from example maneuver performed by enhanced, nonlinear aircraft model with baseline controller starting at $V_0 = 154.94\frac{m}{s}$ and $h_0 = 5000m$ considering variation of noise seeds for dryden turbulence model without q_w

	$M_{\mathcal{L}_2}$ $[-]$	$M_{\mathcal{L}_\infty}$ $[-]$	$M_{\mathcal{L}_{2,act}}$ $[-]$
max	9.76	0.231	16.08
min	6.87	0.118	13.86
$\varnothing$	8.56	0.170	14.98
σ	0.407	0.0147	0.300

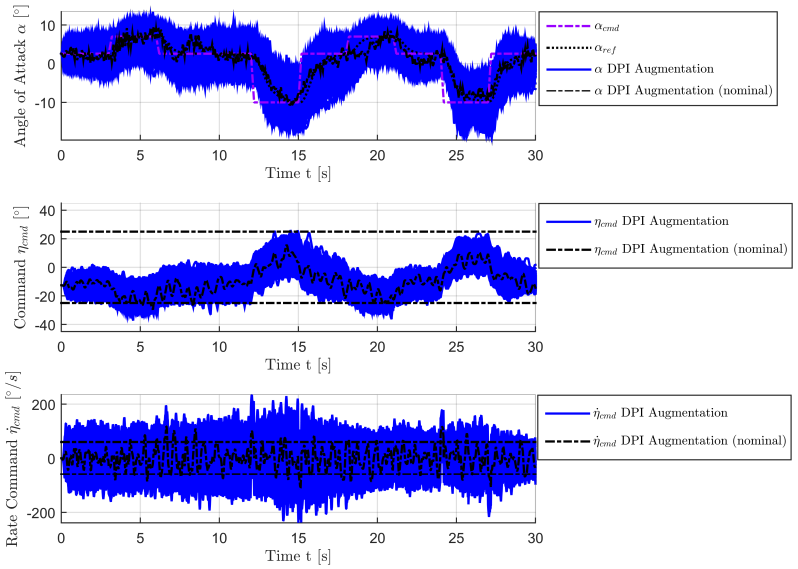

Figure 6.120. – Angle of attack α, elevator command η_{cmd} and elevator command rate $\dot{\eta}_{cmd}$ for example maneuver performed by enhanced, nonlinear aircraft model with DPI Augmentation starting at $V_0 = 154.94\frac{m}{s}$ and $h_0 = 5000m$ considering variation of noise seeds for dryden turbulence model without q_w

Table 6.103. – Performance metrics $M_{\mathcal{L}_2}$, $M_{\mathcal{L}_\infty}$ and $M_{\mathcal{L}_{2,act}}$ (maximum, minimum, mean value and standard deviation) generated from example maneuver performed by enhanced, nonlinear aircraft model with DPI Augmentation and comparison to baseline controller starting at $V_0 = 154.94\frac{m}{s}$ and $h_0 = 5000m$ considering variation of noise seeds for dryden turbulence model without q_w

	$M_{\mathcal{L}_2}$ $[-]$	$M_{\mathcal{L}_\infty}$ $[-]$	$M_{\mathcal{L}_{2,act}}$ $[-]$	$M_{\mathcal{L}_{2,rel}}$ $[\%]$	$M_{\mathcal{L}_{\infty,rel}}$ $[\%]$	$M_{\mathcal{L}_{2,act,rel}}$ $[\%]$
max	10.79	0.233	43.89	110.5%	100.9%	272.9%
min	4.30	0.075	25.95	62.6%	64.1%	187.2%
$\varnothing$	5.96	0.116	34.96	69.7%	68.4%	233.4%
σ	0.718	0.0207	2.535	176.3%	140.9%	845.7%

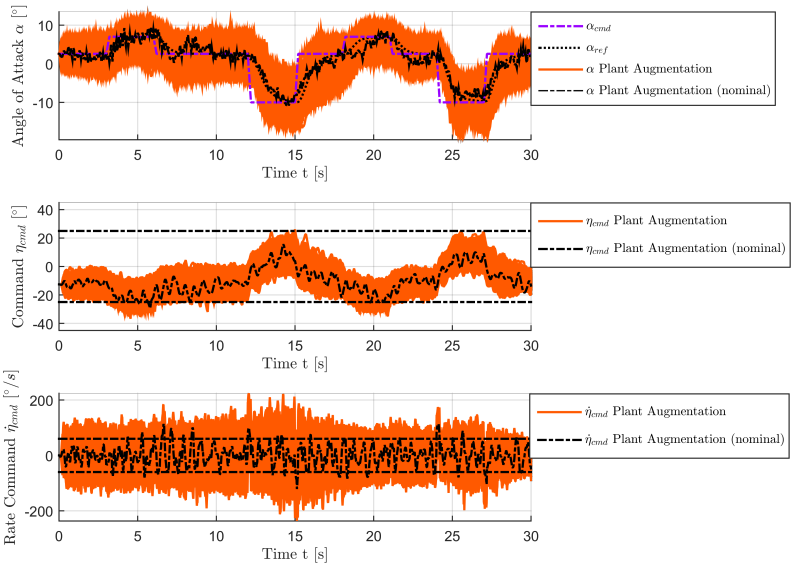

Figure 6.121. – Angle of attack α, elevator command η_{cmd} and elevator command rate $\dot{\eta}_{cmd}$ for example maneuver performed by enhanced, nonlinear aircraft model with Plant Augmentation starting at $V_0 = 154.94\frac{m}{s}$ and $h_0 = 5000m$ considering variation of noise seeds for dryden turbulence model without q_w

Table 6.104. – Performance metrics $M_{\mathcal{L}_2}$, $M_{\mathcal{L}_\infty}$ and $M_{\mathcal{L}_{2,act}}$ (maximum, minimum, mean value and standard deviation) generated from example maneuver performed by enhanced, nonlinear aircraft model with Plant Augmentation and comparison to baseline controller starting at $V_0 = 154.94\frac{m}{s}$ and $h_0 = 5000m$ considering variation of noise seeds for dryden turbulence model without q_w

	$M_{\mathcal{L}_2}$ $[-]$	$M_{\mathcal{L}_\infty}$ $[-]$	$M_{\mathcal{L}_{2,act}}$ $[-]$	$M_{\mathcal{L}_{2,rel}}$ $[\%]$	$M_{\mathcal{L}_{\infty,rel}}$ $[\%]$	$M_{\mathcal{L}_{2,act,rel}}$ $[\%]$
max	10.08	0.217	41.05	103.2%	93.9%	255.2%
min	4.23	0.073	25.55	61.5%	62.1%	184.3%
$\varnothing$	5.78	0.113	33.39	67.6%	66.5%	223.0%
σ	0.662	0.0194	2.250	162.7%	132.2%	750.6%

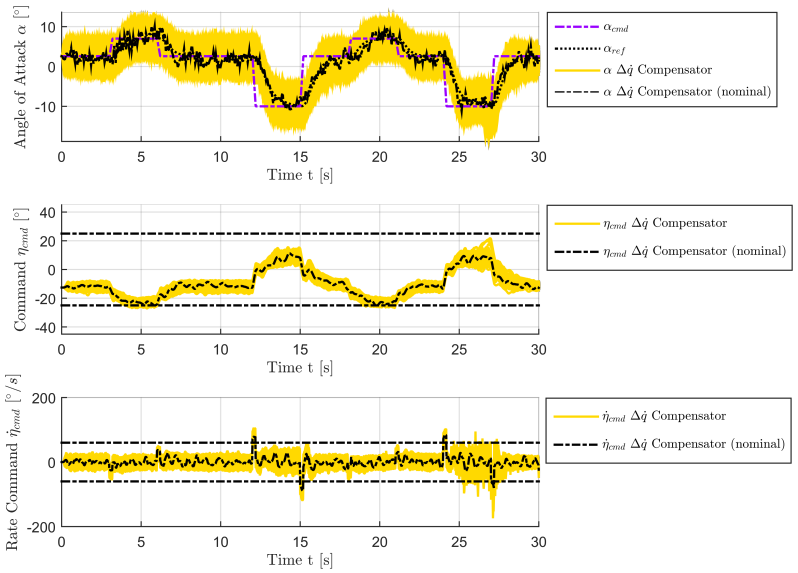

Figure 6.122. – Angle of attack α, elevator command η_{cmd} and elevator command rate $\dot{\eta}_{cmd}$ for example maneuver performed by enhanced, nonlinear aircraft model with $\Delta\dot{q}$ Compensation Law starting at $V_0 = 154.94\frac{m}{s}$ and $h_0 = 5000m$ considering variation of noise seeds for dryden turbulence model without q_w

Table 6.105. – Performance metrics $M_{\mathcal{L}_2}$, $M_{\mathcal{L}_\infty}$ and $M_{\mathcal{L}_{2,act}}$ (maximum, minimum, mean value and standard deviation) generated from example maneuver performed by enhanced, nonlinear aircraft model with $\Delta\dot{q}$ Compensation Law and comparison to baseline controller starting at $V_0 = 154.94\frac{m}{s}$ and $h_0 = 5000m$ considering variation of noise seeds for dryden turbulence model without q_w

	$M_{\mathcal{L}_2}$ $[-]$	$M_{\mathcal{L}_\infty}$ $[-]$	$M_{\mathcal{L}_{2,act}}$ $[-]$	$M_{\mathcal{L}_{2,rel}}$ $[\%]$	$M_{\mathcal{L}_{\infty,rel}}$ $[\%]$	$M_{\mathcal{L}_{2,act,rel}}$ $[\%]$
max	5.38	0.150	17.44	55.1%	65.0%	108.4%
min	3.60	0.063	13.34	52.4%	53.7%	96.2%
$\varnothing$	4.41	0.089	15.28	51.5%	52.5%	102.0%
σ	0.269	0.0118	0.596	66.0%	80.0%	198.8%

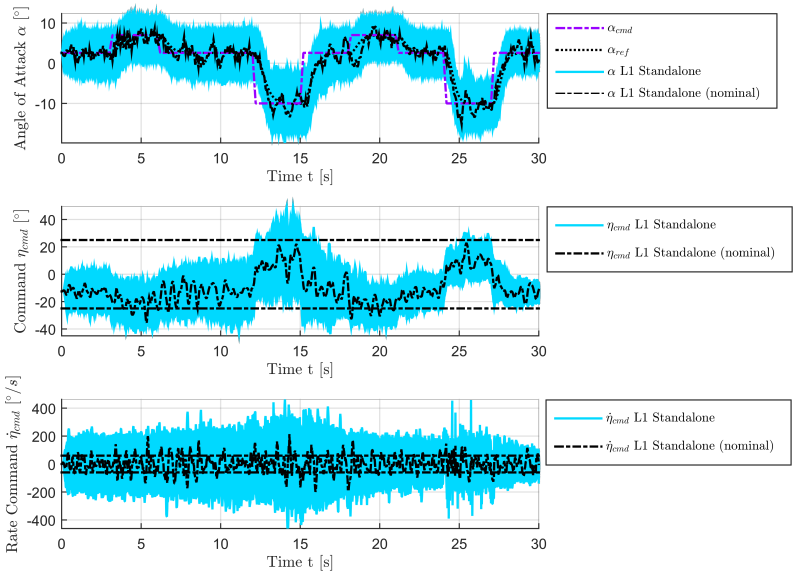

Figure 6.123. – Angle of attack α, elevator command η_{cmd} and elevator command rate $\dot{\eta}_{cmd}$ for example maneuver performed by enhanced, nonlinear aircraft model with L1 adaptive controller with Eigenstructure Assignment starting at $V_0 = 154.94\frac{m}{s}$ and $h_0 = 5000m$ considering variation of noise seeds for dryden turbulence model without q_w

Table 6.106. – Performance metrics $M_{\mathcal{L}_2}$, $M_{\mathcal{L}_\infty}$ and $M_{\mathcal{L}_{2,act}}$ (maximum, minimum, mean value and standard deviation) generated from example maneuver performed by enhanced, nonlinear aircraft model with L1 adaptive controller with Eigenstructure Assignment and comparison to baseline controller starting at $V_0 = 154.94\frac{m}{s}$ and $h_0 = 5000m$ considering variation of noise seeds for dryden turbulence model without q_w

	$M_{\mathcal{L}_2}$ $[-]$	$M_{\mathcal{L}_\infty}$ $[-]$	$M_{\mathcal{L}_{2,act}}$ $[-]$	$M_{\mathcal{L}_{2,rel}}$ $[\%]$	$M_{\mathcal{L}_{\infty,rel}}$ $[\%]$	$M_{\mathcal{L}_{2,act,rel}}$ $[\%]$
max	6.53	0.178	73.27	66.9%	76.9%	455.6%
min	4.13	0.070	47.84	60.1%	59.4%	345.0%
$\varnothing$	5.20	0.109	58.68	60.8%	64.1%	391.8%
σ	0.346	0.0162	3.888	85.0%	109.9%	1297.3%

6.3. Summary

In order to conclude this chapter on controller comparisons, the most important findings and observations are summarized again in the following section.
First of all it can be stated that the robust stability properties with regard to the bottleneck cut of L1 Adaptive Augmentations and $\Delta\dot{q}$ Compensation Law are very similar compared to the baseline controller configuration. Furthermore, no significant differences between the Closed-Loop and Plant Augmentation architectures can be detected here. One can also see that the standalone L1 adaptive controller inherits infinite phase margin with regard to the bottleneck cut. The consideration of uncertainties with respect to aerodynamic coefficients in the aircraft model shows that robust stability can be increased by means of the adaptive augmentations. Although, for the standalone adaptive controller three critical uncertainty cases are found, which are not compliant to the required robustness margins, i.e. the nichols diamond is crossed by the frequency responses.
In terms of performance it can be observed that the adaptive controllers manage to decrease the error between actual system response and desired reference dynamics even considering nominal system dynamics, while generating smooth, oscillation-free control commands. In this case they compensate for nonlinearities included in the aircraft dynamics. Although, one has to note that for the standalone L1 adaptive controller a residual steady-state error remains, which is due to the missing integral portion in the control law. A possible solution to this issue is provided in Chapter 8.
The performance increase can be observed to an even higher degree, when uncertainties with regard to aerodynamic coefficients and rapid CG-shifts are considered. On the other hand, it shows that adaptive controllers are more sensitive with regard to additional delay in the sensor measurements. For the L1 adaptive controllers the most critical channel is the angle of attack α measurement, whereas for the $\Delta\dot{q}$ Compensation Law the pitch rate q measurement can be identified. Although, the variation of the parameters of the simple structural mode model shows low impact on the controller performances, the adaptive controllers are more sensitive with regard to degradation of the actuator model in terms of decreased natural frequency and relative damping. It is also important to mention that the adaptive controllers amplify measurement noise to a higher degree in comparison to the baseline controller configuration. This statement holds also, when the effect of turbulence and gust on the controller performances are investigated. However, the system responses are still stable in these cases. Last but not least, also in terms of performance, no significant difference between the two proposed L1 adaptive augmentation architectures can be observed.

7. Conclusion

The main focus of this PhD thesis is the investigation of adaptive control strategies with regard to implementation in aircraft FCS. For this purpose, a DPI baseline controller is designed at first, which shapes the short-period dynamics of a nonlinear, longitudinal F-16 aircraft model and ensures tracking of angle of attack command α_{cmd}. This controller serves as a reference for the comparisons against adaptive controllers.

After that, adaptive augmentations are constructed for the proposed baseline controller, which utilize L1 Adaptive Control with piecewise constant update laws. Here, the specific structure of the DPI baseline controller has to be taken into account, besides actuator dynamics, delays and filter transfer functions. In terms of the augmentation architecture, two different approaches are proposed in this thesis. The Closed-Loop Augmentation enhances the combination of aircraft and baseline controller, whereas the Plant Augmentation is designed considering only the open-loop aircraft. In case of Plant Augmentation, the baseline controller is applied to a combination of aircraft and adaptive controller, which has the goal to establish reference dynamics with regard to the open-loop aircraft. It can be shown by means of simulation results that both architectures are very similar in terms of both robust stability and performance, despite the differences considering the controller structures. Thus, the design of an adaptive augmentation can be significantly simplified by means of the Plant Augmentation approach, because in this case it is not necessary to consider the baseline controller within the state predictor.

Furthermore, a hedging enhancement, which utilizes actuator deflection measurement, is proposed for the state predictors of both augmentation approaches. Through the application of hedging, it is possible for the baseline controller with adaptive augmentation to achieve the same robust stability margins with regard to the bottleneck cut compared to the reference baseline controller configuration. Thus, the L1 adaptive augmentations do not exhibit any disadvantage compared to conventional control laws in this matter. This is an advancement in terms of potential certification of such adaptive augmentations according to [111]. Moreover, it can be shown that the architecture of the state predictor can be further simplified by means of hedging, in case Plant Augmentation or the standalone L1 adaptive controller are used. This is because it is not necessary to model the plant input dynamics within the state predictor, since actuator measurement is utilized.

In order to present an alternative approach for the adaptive augmentation, another reference model-based adaptive control law according to Delannoy et. al. [23] is also

applied to the DPI baseline controller, which is denoted as $\Delta\dot{q}$ Compensation Law in the context of this thesis. This control law calculates a deviation between the pitch rate acceleration, which acts on the aircraft, and the corresponding output of a linear reference model. By means of this deviation a compensating actuator command can be estimated. It shows that its robust stabilty properties and potential to increase the aircraft performance is very comparable to the adaptive augmentations using L1 Adaptive Control.

In the next step, a standalone L1 adaptive controller is introduced. This controller uses a modification of the state predictor, which is contributed by this thesis. By means of this modification, which is the addition of linear feedback of the estimated states to both matched and unmatched inputs of the predictor, it is possible to precisely place the system poles. This is achieved through the additional application of Eigenstructure Assignment. It can be shown by means of the exemplary longitudinal F-16 aircraft model, that the short-period poles are precisely set according to the desired values by means of the proposed technique, despite the additional presence of actuator dynamics, filter dynamics and delay. Exact shaping of the plant dynamics considering these additional dynamics is not possible using the textbook L1 Adaptive Control approach according to [59]. On the other hand, it is also demonstrated that a residual steady-state error remains, if the standalone adaptive controller is used for tracking of commanded angle of attack α_{cmd}. The reason for this is the missing integral portion of the control law, which is not present in a standalone L1 adaptive controller. Chapter 8 points out a modification of the piecewise constant update law, which could serve as a possible solution for this issue.

After the controller designs have been presented, they are thoroughly examined in terms of performance and robust stability. Robust stability of the proposed control laws can be investigated by means of conventional, linear methods in the frequency-domain, because the application of L1 adaptive control with piecewise constant update laws results in a linear control law. This is especially beneficial in terms of controller certification according to [111]. Furthermore, the $\Delta\dot{q}$ Compensation Law is also linear by design. Thus, it is possible to calculate the well-known robust stability properties gain and phase margin considering the adaptive controllers. In addition to the calculation of margins, the open-loop frequency responses can also be depicted in terms of nichols plots, which facilitate the illustration of required robustness margins by means of nichols diamonds. The resulting nichols plots with respect to the bottleneck cut show that the L1 adaptive augmentations, where the proposed hedging technique is applied, and the $\Delta\dot{q}$ Compensation Law are very comparable to the baseline controller configuration considering robust stability. Moreover, it can be shown that the adaptive augmentations increase robust stability, in case uncertainty with regard to aerodynamic coefficients is considered. Although, it can also be stated that the sensitivity against phase or gain disturbances with respect to the sensor measurements increases, when the adaptive augmentations are applied.

In addition to the frequency-domain robust stability assessments, also a time-domain based assessment is introduced and exemplarily applied to the DPI Augmentation. By means of this method, it is possible to determine a simulation based estimation of gain margin and time delay margin. Furthermore, this thesis provides a method to estimate the phase margin using these simulation based results. Another contribution in this context is the visual representation of the identified results, where also minimum robustness margins similar to a nichols diamond can be directly taken into account. In a nutshell, this visualization approach could also serve as a foundation, in order to assess robust stability properties of nonlinear control laws.
Besides presenting simulation results using a basic version of the aircraft model, the performance assessments are also carried out with an enhanced variant of the F-16 aircraft model. This is one of the main contributions of this thesis. The enhanced aircraft model comprises more realistic sensor models, which contain jitter, measurement noise, discrete-time sampling, quantization, anti-aliasing, scale factor errors and bias. On the other hand, the 2nd order actuator model, which includes rate and absolute deflection saturations, is enhanced by means of the backlash effect. Furthermore, atmospheric disturbances in terms of turbulence and gust are taken into account. A simple model of a structural mode is introduced, in order to include an additional dynamic disturbance on the aircraft outputs. In order to increase the relevance of the simulation assessments in terms of real world applications even further, discrete-time representations of the control laws are applied to the enhanced aircraft model, considering limited sample rate.
Despite the introduction of reality effects, the adaptive controllers are still capable of increasing the system performance considering uncertainties with regard to aerodynamic coefficients within the aircraft model, but also considering rapid CG-shifts, which destabilize the open-loop aircraft. Although, this can only be achieved at the cost of increased disturbance amplification. In particular, this can be observed for the assessments on variations of measurement noise and, to an even higher degree, also of turbulence. The critical measurements are angle of attack α considering the L1 adaptive controllers and pitch rate q considering the $\Delta\dot{q}$ Compensation Law. Thus, in case of a potential application of the proposed controller designs, the quality of the sensor measurements and the accompanying filtering has to be increased, in order to attenuate this effect.
But apart from increased disturbance amplification, it can be concluded that the proposed adaptive augmentations offer a remarkable improvement in terms of performance considering plant uncertainties, when the simulation results are compared to the baseline controller configuration. At the same time, the robust stability properties phase and gain margin are not harmed considering the bottleneck cut. In a nutshell, the application of adaptive control in FCS could be a major contribution to increasing safety, reducing controller design effort and exploiting the full potential of an aircraft within its physical limits.

8. Outlook

It was stated in the conclusion that the quality of the sensor measurements has to be increased, in order to cope with the drawbacks of the proposed adaptive controller designs. In particular, high frequency content stemming from measurement noise and turbulence has to be further reduced. Thus, it would be very promising to apply more sophisticated sensor filtering algorithms, which exceed the simple low-pass filtering of the sensor signals, as it is applied in this thesis. One possibility would be the application of a Kalman Filter [63, 141], in order to attenuate the impact of high-frequency disturbance. Another interesting approach was presented in [26, pp. 26-30] and [27], where complementary filtering [48] is used to pre-process angle of attack α measurement for a L1 adaptive controller.

Furthermore, as it was already discussed, the adaptive controller designs presented in this thesis result in a linear control law. Thus, robustness with regard to the sensor cuts could also be further investigated by means of μ-analysis [29, 142, 108]. This way, also the impact of combined uncertainties included in more than one sensor channel could be assessed, in contrast to the robust stability assessments shown in this thesis.

In terms of the residual steady-state error of the proposed standalone L1 adaptive controller, a modification of piecewise constant update law within the L1 adaptive controller could give remedy. This modification is proposed in [73] and introduces a discrete-time integration of the estimation error, which is added to the parameter update law. Therefore, this modification could remove the residual steady-state error due to the added integral portion within the control law.

One goal of this thesis was to highlight the potential of certification of the proposed adaptive controller designs. In order to increase this potential, it would be beneficial to show thorough comparisons to control laws, which are already certificated, and to stress similarities between them. Moreover, adaptive augmentations could also be applied to baseline controllers, which are designed according to methods of robust control theory e.g. H_∞ or LPV [7, 116, 114]. The additional application of hedging, as it is proposed in this thesis, could combine the advantages of robust control and adaptive control.

Exceeding the assessments utilizing the simple structural mode model in this thesis, it would also be very interesting to investigate the application of the proposed controller designs to a flexible aircraft model, in order to further analyze the impact of multiple structural modes and to consider the coupling of rigid-body and flexible states. In

particular, the impact of structural modes, whose frequencies are near to the range of the rigid-body dynamics, should be addressed.
In terms of UAV applications, it could also be interesting to consider nonlinear dynamics within the state predictor of the proposed L1 adaptive controllers. This way, it could be possible to increase the potential in terms of agility, instead of forcing the UAV to behave according to linear reference dynamics. The possibility to consider nonlinear reference dynamics is investigated in [132, 77].
In this sense, also more sophisticated, nonlinear actuator models could be taken into account for the assessments. Here, the advantages of hedging could be even more evident, since it can be avoided to add an actuator model to the state predictor, in case the Plant Augmentation approach or the standalone L1 adaptive controller are considered.

Bibliography

[1] M. J. Abzug and E. E. Larrabee. *Airplane Stability and Control - A History of the Technologies That Made Aviation Possible*. Second Edition. Cambridge Aerospace Series 14. The Edinburgh Building, Cambridge CB2 2RU, UK: Cambridge University Press, 2005.

[2] K. Ackerman, E. Xargay, R. Choe, N. Hovakimyan, M. C. Cotting, R. B. Jeffrey, M. P. Blackstun, T. P. Fulkerson, T. R. Lau, and S. S. Stephens. "L1 Stability Augmentation System for Calspan's Variable-Stability Learjet". In: *AIAA SciTech*. American Institute of Aeronautics and Astronautics, Jan. 2016.

[3] *Application of Multivariable Control Theory to Aircraft Control Laws*. Tech. rep. WL-TR-96-3099. Honeywell Technology Center, Lockheed Martin Skunk Works, Lockheed Martin Tactical Aircraft Systems, May 1996.

[4] K. J. Aström and B. Wittenmark. *Computer-Controlled Systems - Theory and Design*. 3rd edition. Prentice Hall, 1997.

[5] D. H. Baldelli, P. C. Chen, and J. Panza. "Unified Aeroelastic and Flight Dynamic Formulation via Rational Function Approximations". In: *Journal of Aircraft* 43.3 (May 2006), pp. 763–772.

[6] S. Banerjee. "L1 Adaptive Control Augmentation for a Hypersonic Glider". PhD thesis. Australia: The University of Queensland, 2015.

[7] D. G. Bates, R Kureemun, and I Postlethwaite. "Quantifying the robustness of flight control systems using Nichols exclusion regions and the structured singular value". In: *Proceedings of the Institution of Mechanical Engineers, Part I: Journal of Systems and Control Engineering* 215.6 (2001), pp. 625–638. eprint: `http://pii.sagepub.com/content/215/6/625.full.pdf+html`.

[8] D. Bates and I. Postlethwaite. *Robust Multivariable Control of Aerospace Systems*. Delft, Netherlands: DUP Science, 2002.

[9] T. Berger, M. Tischler, S. G. Hagerott, D. Gangsaas, and N. Saeed. "Longitudinal Control Law Design and Handling Qualities Optimization for a Business Jet Flight Control System". In: *Guidance, Navigation, and Control and Co-located Conferences*. American Institute of Aeronautics and Astronautics, Aug. 2012.

[10] M. Bichlmeier. "An L1 Adaptive Output Feedback Controller using Modified Piecewise Constant Adaptation Law". In: *AIAA SciTech*. American Institute of Aeronautics and Astronautics, Jan. 2016.

[11] M. Bichlmeier, F. Holzapfel, E. Xargay, and N. Hovakimyan. "L1 Adaptive Augmentation of a Helicopter Baseline Controller". In: *Guidance, Navigation, and Control and Co-located Conferences*. American Institute of Aeronautics and Astronautics, Aug. 2013.

[12] T. Bierling. "Comparative Analysis of Adaptive Control Techniques for Improved Robust Performance". PhD thesis. TU München, 2014.

[13] T. Bierling, L. Höcht, F. Holzapfel, R. Maier, and A. Wildschek. "Comparative Analysis of MRAC Architectures in a Unified Framework". In: *Guidance, Navigation, and Control and Co-located Conferences*. American Institute of Aeronautics and Astronautics, Aug. 2010.

[14] H. W. Bode. *Network Analysis & Feedback Amplifier Design*. 10th. Boston, MA, USA: D. Van Nostrand Company, Inc., Jan. 1955.

[15] H. W. Bode. "Relations between attenuation and phase in feedback amplifier design". In: *Bell System Technical Journal, The* 19.3 (July 1940), pp. 421–454.

[16] R. Brockhaus, W. Alles, and R. Luckner. *Flugregelung*. 3. Berlin, Germany: Springer-Verlag, 2011.

[17] C. Cao and N. Hovakimyan. "L1 Adaptive Output-Feedback Controller for Non-Strictly-Positive-Real Reference Systems: Missile Longitudinal Autopilot Design". In: *Journal of Guidance, Control, and Dynamics* 32.3 (May 2009), pp. 717–726.

[18] C. Cao and N. Hovakimyan. "L1 Adaptive Output Feedback Controller for Non Strictly Positive Real Reference Systems with Applications to Aerospace Examples". In: *Guidance, Navigation, and Control and Co-located Conferences*. American Institute of Aeronautics and Astronautics, Aug. 2008.

[19] E. Capello, G. Guglieri, and F. Quagliotti. "A Comprehensive Robust Adaptive Controller for Gust Load Alleviation". In: *The Scientific World Journal* vol. 2014.Article ID 609027 (2014), 12 pages.

[20] J. Che, I. Gregory, and C. Cao. "Integrated Flight/Structural Mode Control for Very Flexible Aircraft Using L1 Adaptive Output Feedback Controller". In: *Guidance, Navigation, and Control and Co-located Conferences*. American Institute of Aeronautics and Astronautics, Aug. 2012.

[21] R. Choe, E. Kharisov, N. Hovakimyan, and C. Meckstroth. "Perching Maneuver for an MAV Augmented with an L1 Adaptive Controller". In: *Guidance, Navigation, and Control and Co-located Conferences*. American Institute of Aeronautics and Astronautics, Aug. 2011.

[22] M. C. Cotting, R. B. Jeffrey, M. P. Blackstun, T. P. Fulkerson, T. R. Lau, S. S. Stephens, K. Ackerman, E. Xargay, R. Choe, and N. Hovakimyan. "'Can I Get L1 On?!' Providing Consistent Handling Qualities on Calspan's Variable-Stability Learjet". In: *AIAA SciTech*. American Institute of Aeronautics and Astronautics, Jan. 2016.

[23] S. Delannoy and S. Oudin. "Longitudinal control law for modern long range civil aircraft". In: *CEAS EuroGNC Conference*. Apr. 2013.

[24] *Deutsche Luftfahrtnorm LN 9300: Bezeichnungen in der Flugmechanik*. Cologne, Germany: Beuth, Dec. 1970.

[25] J. Dodenhöft. *Design and Comparison of Certifiable Model Following Control Architectures for a F-16 Aircraft Model*. Semester Thesis, Technische Universität München. supervised by Fabian Hellmundt, Miguel Leitao and Florian Holzapfel. 2015.

[26] J. Dodenhöft. *Design and Piloted Evaluation of an L1 Adaptive Controller for NASA's Transport Class Model*. Master Thesis, Technische Universität München. 2016.

[27] J. Dodenhöft, R. Choe, K. Ackerman, F. Holzapfel, and N. Hovakimyan. "Design and Evaluation of an L1 Adaptive Controller for NASA's Transport Class Model". In: *AIAA SciTech Forum*. American Institute of Aeronautics and Astronautics, Jan. 2017, pp. –.

[28] W. Dong, J. A. Farell, M. Polycarpou, and M. Sharma. "Command Filtered Adaptive Backstepping". In: *American Control Conference*. Baltimore, MD, USA, June 2010, pp. 105–110.

[29] J. Doyle. "Analysis of feedback systems with structured uncertainties". In: *IEE Proceedings D - Control Theory and Applications* 129.6 (Nov. 1982), pp. 242–250.

[30] A. V. Efremov, V. V. Rodchenko, and S. Boris. *Investigation of Pilot Induced Oscillation Tendency and Prediction Criteria Development*. Tech. rep. WL-TR-96-3109. Wright Patterson AFB, OH: Wright Laboratory, May 1996.

[31] D. Erdos, T. Shima, E. Kharisov, and N. Hovakimyan. "L1 Adaptive Control Integrated Missile Autopilot and Guidance". In: *Guidance, Navigation, and Control and Co-located Conferences*. American Institute of Aeronautics and Astronautics, Aug. 2012.

[32] B. Etkin. *Dynamics of Atmospheric Flight*. Mineola, New York: Dover Publications Inc., 2005.

[33] M. S. Fadali and A. Visioli. *Digital Control Engineering - Analysis and Design*. Burlington, MA: Academic Press, 2009.

[34] L. F. Faleiro. "The application of eigenstructure assignment to the design of flight control systems". PhD thesis. Loughborough University, UK, 1998.

[35] W. Falkena. "Investigation of Practical Flight Control Systems for Small Aircraft". PhD thesis. Netherlands: TU Delft, 2012.

[36] J. A. Farell, M. Polycarpou, M. Sharma, and W. Dong. "Command Filtered Backstepping". In: *American Control Conference*. Seattle, Washington, USA, June 2008, pp. 1923–1928.

[37] J. Farineau. "Lateral Electric Flight Control Laws of a Civil Aircraft Based Upon Eigen Structure Assignment Technique". In: *AIAA Guidance, Navigation and Control Conference*. American Institute of Aeronautics and Astronautics, 1989.

[38] M. Geiser, E. Xargay, N. Hovakimyan, T. Bierling, and F. Holzapfel. "L1 Adaptive Augmented Dynamic Inversion Controller for a High Agility UAV". In: *Guidance, Navigation, and Control and Co-located Conferences*. American Institute of Aeronautics and Astronautics, Aug. 2011.

[39] G. Golub and C. van Loan. *Matrix Computations*. 3rd ed. The Johns Hopkins University Press, 1996.

[40] I. Gregory, E. Xargay, C. Cao, and N. Hovakimyan. "Flight Test of an L1 Adaptive Controller on the NASA AirSTAR Flight Test Vehicle". In: *Guidance, Navigation, and Control and Co-located Conferences*. American Institute of Aeronautics and Astronautics, Aug. 2010.

[41] I. Gregory, E. Xargay, C. Cao, and N. Hovakimyan. "Flight Test of L1 Adaptive Control Law: Offset Landings and Large Flight Envelope Modeling Work". In: *Guidance, Navigation, and Control and Co-located Conferences*. American Institute of Aeronautics and Astronautics, Aug. 2011.

[42] I. Gregory, C. Cao, E. Xargay, N. Hovakimyan, and X. Zou. "L1 Adaptive Control Design for NASA AirSTAR Flight Test Vehicle". In: *Guidance, Navigation, and Control and Co-located Conferences*. American Institute of Aeronautics and Astronautics, Aug. 2009.

[43] B. Griffin, J. Burken, and E. Xargay. "L1 Adaptive Control Augmentation System with Application to the X-29 Lateral/Directional Dynamics: A Multi-Input Multi-Output Approach". In: *Guidance, Navigation, and Control and Co-located Conferences*. American Institute of Aeronautics and Astronautics, Aug. 2010.

[44] M. Hanel. *Robust Integrated Flight and Aeroelastic Control System Design for a Large Transport Aircraft*. Vol. Reihe 8. Fortschritt-Berichte VDI Nr. 866. Düsseldorf: VDI Verlag, 2001.

[45] L. Höcht. "Advances in Stability Analysis for Model Reference Adaptive Control Systems and Application to Unmanned Aerial Systems". PhD thesis. TU München, 2014.

[46] C. D. Heise, S. P. Schatz, and F. Holzapfel. "Modified Extended State Observer Control of Linear Systems". In: *AIAA SciTech*. American Institute of Aeronautics and Astronautics, Jan. 2016.

[47] M. Heller. *Untersuchung zur Steuerung und Robusten Regelung der Seitenbewegung von Hyperschall-Flugzeugen*. München: Herbert Utz Verlag, 1999.

[48] M. Heller, S. Myschik, F. Holzapfel, and G. Sachs. "Angles of Attack and Sideslip Determination Using Navigation Data for Small Aircraft". In: *Guidance, Navigation, and Control and Co-located Conferences*. American Institute of Aeronautics and Astronautics, Aug. 2003, pp. –.

[49] F. Hellmundt. *Auslegung und Implementierung eines Reglers für einen generischen Boden-Luft-Luftflugkörper mittels Command Filtered Adaptive Backstepping (Design and Implementation of a Command Filtered Adaptive Backstepping Controller for a Surface-to-air Missile)*. Semester Thesis, Technische Universität München, Germany. Nov. 2012.

[50] F. Hellmundt. *Entwurf von Regelgesetzen mit Gain Scheduling für die Robustheitsanalyse von Konfigurationsmodifikationen eines Flugzeugs unter Berücksichtigung der erreichbaren Handling Qualities (Design of Flight Control Laws with Gain Scheduling for Robustness Assessment of Configuration Modifications of an Aircraft with respect to the achieveable Handling Qualities)*. Diploma Thesis, Technische Universität München, Germany. May 2013.

[51] F. Hellmundt, J. Dodenhöft, and F. Holzapfel. "L1 Adaptive Control with Eigenstructure Assignment for Pole Placement considering Actuator Dynamics and Delays". In: *AIAA Scitech*. American Institute of Aeronautics and Astronautics, Jan. 2016.

[52] F. Hellmundt, A. Wildschek, R. Maier, R. Osterhuber, and F. Holzapfel. "Comparison of L1 Adaptive Augmentation Strategies for a Differential PI Baseline Controller on a Longitudinal F16 Aircraft Model". In: *Advances in Aerospace Guidance, Navigation and Control*. Ed. by J. Bordeneuve-Guibé, A. Drouin, and C. Roos. Springer International Publishing, 2015, pp. 99–118.

[53] F. Hellmundt, R. Maier, M. Leitao, C. Heise, and F. Holzapfel. "Performance Assessment of L1 Adaptive Augmentation Strategies for an Enhanced Longitudinal F16 Aircraft Model". In: *Proceedings of the 3rd CEAS EuroGNC, Specialist Conference on Guidance, Navigation & Control*. Toulouse, France, Apr. 2015.

[54] F. Holzapfel, M. Heller, M. Weingartner, G. Sachs, and O. da Costa. "Development of control laws for the simulation of a new transport aircraft". In: *Proceedings of the Institution of Mechanical Engineers, Part G: Journal of Aerospace Engineering* Vol. 223 (2009), pp. 141–156.

[55] F. Holzapfel. *Flight Controls I, Lecture Notes*. Munich, Germany: Technical University of Munich, Institute of Flight System Dynamics, 2010.

[56] F. Holzapfel. *Flugsystemdynamik I (Flight System Dynamics I), Lecture Notes*. Munich, Germany: Technical University of Munich, Institute of Flight System Dynamics, 2009.

[57] F. Holzapfel and M. Weingartner. *Flugsystemdynamik II (Flight System Dynamics II), Lecture Notes*. Technical University of Munich, Institute of Flight System Dynamics, 2011.

[58] N. Hovakimyan, C. Cao, E. Kharisov, E. Xargay, and I. Gregory. "Adaptive Control for Safety-Critical Systems". In: *Control Systems, IEEE* 31.5 (2011), pp. 54–104.

[59] N. Hovakimyan and C. Chengyu. *L1 Adaptive Control Theory - Guaranteed Robustness with Fast Adaptation*. Ed. by R. C. Smith. Society for Industrial and Applied Mathematics, 2010.

[60] O. Härkegård. "Modifying L1 Adaptive Control for Augmented Angle of Attack Control". In: *Guidance, Navigation, and Control and Co-located Conferences*. American Institute of Aeronautics and Astronautics, Aug. 2009.

[61] *ISO 2533:1975 - Standard Atmosphere*. Geneva, Switzerland: International Organization for Standardization, May 1975.

[62] E. N. Johnson. "Limited Authority Adaptive Flight Control". PhD thesis. Georgia Institute of Technology, 2000.

[63] R. E. Kalman. "A New Approach to Linear Filtering and Prediction Problems". In: *Transactions of the ASME–Journal of Basic Engineering* 82.Series D (1960), pp. 35–45.

[64] E. Kharisov and N. Hovakimyan. "L1 adaptive output feedback controller for minimum phase systems". In: *American Control Conference (ACC), 2011*. 2011, pp. 1182–1187.

[65] E. Kharisov. "L1 Adaptive Output-Feedback Control Architectures". PhD thesis. University of Illinois at Urbana-Champaign, 2013.

[66] K. Kim, E. Kharisov, and N. Hovakimyan. "Filter Design for L1 Adaptive Output-Feedback Controller". In: *Decision and Control and European Control Conference (CDC-ECC), 2011 50th IEEE Conference on*. Dec. 2011, pp. 5653–5658.

[67] M. Krstic, I. Kanellakopoulos, and P. V. Kokotovic. *Nonlinear and Adaptive Control Design*. New York, NY: John Wiley & Sons, 1995.

[68] R. Lange. "Nonlinear adaptive control of an endo-atmospheric dual-actuator interceptor". PhD thesis. Munich, Germany: TU München, Sept. 2012.

[69] A. Lawrence. *Modern Inertial Technology - Navigation, Guidance, and Control*. 2nd. New York, NY: Springer-Verlag, 1998.

[70] H. P. Lee, H. M. Youssef, and R. P. Hanel. "Application of Eigenstructure Assignment to the Design of STOVL Flight Control System". In: *Guidance, Navigation and Control Conference*. American Institute of Aeronautics and Astronautics, 1988.

[71] T. Leman, E. Xargay, G. Dullerud, N. Hovakimyan, and T. Wendel. "L1 Adaptive Control Augmentation System for the X-48B Aircraft". In: *Guidance, Navigation, and Control and Co-located Conferences*. American Institute of Aeronautics and Astronautics, Aug. 2009.

[72] D. Li, N. Hovakimyan, and C. Cao. "L1 Adaptive Controller in the Presence of Input Saturation". In: *Guidance, Navigation, and Control and Co-located Conferences*. American Institute of Aeronautics and Astronautics, Aug. 2009.

[73] Z. Li and N. Hovakimyan. "L1 adaptive controller for MIMO systems with unmatched uncertainties using modified piecewise constant adaptation law". In: *Decision and Control (CDC), 2012 IEEE 51st Annual Conference on*. Dec. 2012, pp. 7303–7308.

[74] W. G. Luber. "Flutter Prediction on a Combat Aircraft Involving Backlash on Control Surfaces". In: *IMAC XVI - 16th International Modal Analysis Conference*. Society for Experimental Mechanics, Inc, 1998, pp. 291–299.

[75] J. Lunze. *Regelungstechnik 1 - Systemtheoretische Grundlagen, Analyse und Entwurf einschleifiger Regelungen*. 9. Auflage. Berlin: Springer Vieweg, 2013.

[76] J. Lunze. *Regelungstechnik 2 - Mehrgrößensysteme, Digitale Regelung*. 7. Auflage. Berlin: Springer Vieweg, 2013.

[77] S. Mallikarjunan, B. Nesbitt, E. Kharisov, E. Xargay, N. Hovakimyan, and C. Cao. "L1 Adaptive Controller for Attitude Control of Multirotors". In: *Guidance, Navigation, and Control and Co-located Conferences*. American Institute of Aeronautics and Astronautics, Aug. 2012.

[78] Mathworks. *MATLAB 2015a Documentation*. `www.mathworks.com/help/aeroblks/drydenwindturbulencemodelcontinuous.html`. Accessed on 14th April 2016.

[79] Mathworks. *MATLAB 2015a Documentation*. `www.mathworks.com/help/aeroblks/discretewindgustmodel.html`. Accessed on 22nd May 2016.

[80] *MATLAB version 8.5.0.197613 (R2015a)*. The Mathworks, Inc. Natick, Massachusetts, 2015.

[81] *MIL-F-8785C*. Department of Defence, USA, 1980.

[82] *MIL-HDBK-1797A*. Department of Defence, USA, 1997.

[83] I. Moir, A. G. Seabridge, and M. Jukes. *Civil Avionics Systems*. 2nd. Aerospace Series. Chichester, West Sussex, UK: John Wiley & Sons, Ltd, 2013.

[84] B. Moore. "On the flexibility offered by state feedback in multivariable systems beyond closed loop eigenvalue assignment". In: *Automatic Control, IEEE Transactions on* 21.5 (Oct. 1976), pp. 689–692.

[85] D. J. Moorhouse and R. J. Woodcock. *Background Information and User Guide for MIL-F-8785C, Military Specification - Flying Qualities of piloted Airplanes*. Tech. rep. Airforce Wright Aeronautical Laboratories, July 1982.

[86] N. Moritz and R. Osterhuber. "Three-Stage Gradient-Based Optimization Scheme in Design of Feedback Gains Within Eurofighter Primary Control Laws". In: *Guidance, Navigation, and Control and Co-located Conferences*. American Institute of Aeronautics and Astronautics, Aug. 2006.

[87] A. Myleus, D. Simon, and P. Rosander. "Design and Test of Discrete Time Adaptive Backup Flight Control Laws". In: *Proceedings of the 19th IFAC World Congress*. Vol. 19. 2014, pp. 2213–2218.

[88] K. Narendra and P. Kudva. "Stable Adaptive Schemes for System Identification and Control - Part II". In: *Systems, Man and Cybernetics, IEEE Transactions on* SMC-4.6 (Nov. 1974), pp. 552–560.

[89] K. Narendra and P. Kudva. "Stable Adaptive Schemes for System Identification and Control-Part I". In: *Systems, Man and Cybernetics, IEEE Transactions on* SMC-4.6 (Nov. 1974), pp. 542–551.

[90] K. S. Narendra and A. M. Annaswamy. *Stable Adaptive Systems*. Mineola, New York: Dover Publications Inc., 2005.

[91] L. T. Nguyen, M. E. Ogburn, W. P. Gilbert, K. S. Kibler, P. W. Brown, and P. L. Deal. *Simulator Study of Stall/Post-Stall Characteristics of a Fighter Airplane With Relaxed Longitudinal Static Stability*. Tech. rep. Hampton, Virginia: NASA Langley Research Center, 1979.

[92] N. B. Nichols, W. P. Manger, and E. H. Krohn. "General Design Principles for Servomechanisms". In: *Theory of Servomechanisms*. Ed. by H. M. James, N. B. Nichols, and R. S. Phillips. Dover Publications Inc., Nov. 1965, pp. 134–230.

[93] H. Nyquist. "Regeneration theory". In: *Bell System Technical Journal* 11 (Jan. 1932), pp. 126–147.

[94] H.-C. Oelker, R. Osterhuber, and M. Hanel. "Experiences with Eurofighter Handling Qualities Testing". In: *Guidance, Navigation, and Control and Co-located Conferences*. American Institute of Aeronautics and Astronautics, Aug. 2009.

[95] E. van Oort. "Adaptive Backstepping and Safety Analysis for Modern Fighter Aircraft". PhD thesis. TU Delft, 2011.

[96] P. Osburn, H. P. Whitaker, and A. Kezer. "New developements in the design of model reference adaptive control". In: *Proceedings of the IAS 29th Annual Meeting*. New York, 1961.

[97] R. Osterhuber, M. Hanel, and R. Hammon. "Realization of the Eurofighter 2000 Primary Lateral/Directional Flight Control Laws with Differential PI-Algorithm". In: *Guidance, Navigation, and Control and Co-located Conferences*. American Institute of Aeronautics and Astronautics, Aug. 2004.

[98] S. Oudin, G. Puyou, and S. Delannoy. "Method and device for estimating an unwanted pitch moment of an aircraft and application to the pitch control of the aircraft". English. Pat. US 2014/0236399 A1 (Toulouse, France). 2014.

[99] V. Patel, C. Cao, N. Hovakimyan, K. Wise, and E. Lavretsky. "L1 Adaptive Controller for Tailless Unstable Aircraft". In: *American Control Conference, 2007. ACC '07*. 2007, pp. 5272–5277.

[100] F. Peter, F. Hellmundt, F. Holzapfel, and F. Chew. "Anti-Windup Command Filtered Adaptive Backstepping Autopilot Design for a Tail-Controlled Air-Defense Missile". In: *Guidance, Navigation, and Control and Co-located Conferences*. American Institute of Aeronautics and Astronautics, Aug. 2013.

[101] F. Peter, F. Holzapfel, E. Xargay, and N. Hovakimyan. "L1 Adaptive Augmentation of a Missile Autopilot". In: *Guidance, Navigation, and Control and Co-located Conferences*. American Institute of Aeronautics and Astronautics, Aug. 2012.

[102] E. Peterson, J. Kreer, and L. Ware. "Regeneration Theory and Experiment". In: *Radio Engineers, Proceedings of the Institute of* 22.10 (Oct. 1934), pp. 1191–1210.

[103] A. Pettersson, K. Astrom, A. Robertsson, and R. Johansson. "Analysis of linear L1 adaptive control architectures for aerospace applications". In: *Decision and Control (CDC), 2012 IEEE 51st Annual Conference on*. Dec. 2012, pp. 1136–1141.

[104] A. Pettersson, K. Aström, A. Robertsson, and R. Johansson. "Augmenting L1 adaptive control of piecewise constant type to a fighter aircraft. Performance and robustness evaluation for rapid maneuvering." In: *Guidance, Navigation, and Control and Co-located Conferences*. American Institute of Aeronautics and Astronautics, Aug. 2012.

[105] Z. Prime, C. Doolan, and B. Cazzolato. "Longitudinal L1 Adaptive Control of a Hypersonic Reentry Experiment". In: *15th Australian International Aerospace Congress*. 2013.

[106] J. G. Proakis and D. Manolakis. *Digital Signal Processing - Principles, Algorithms, and Applications*. 4th. Harlow, England: Pearson Education Limited, 2007.

[107] L. Rade and B. Westergren. *Springers mathematische Formeln*. Ed. by P. Vachenauer. 3rd ed. Springer-Verlag, 2000.

[108] C. Roos, F. Lescher, J. M. Biannic, C. Döll, and G. Ferreres. "A set of μ-analysis based tools to evaluate the robustness properties of high-dimensional uncertain systems". In: *2011 IEEE International Symposium on Computer-Aided Control System Design (CACSD)*. Sept. 2011, pp. 644–649.

[109] W. J. Rugh and J. S. Shamma. "Research on gain scheduling". In: *Automatica* 36 (2000), pp. 1401–1425.

[110] G. Sachs, M. Heller, and L. Wahlberg. "Robust control of a hypersonic experimental vehicle with ramjet engines". In: *Guidance, Navigation, and Control and Co-located Conferences*. American Institute of Aeronautics and Astronautics, July 1996.

[111] *SAE AS94900 - Aerospace - Flight Control Systems - Design, Installation and Test of Piloted Military Aircraft, General Specification For*. SAE International, 2007.

[112] P. Seiler, A. Dorobantu, and G. Balas. "Robustness Analysis of an L1 Adaptive Controller". In: *Guidance, Navigation, and Control and Co-located Conferences*. American Institute of Aeronautics and Astronautics, Aug. 2010.

[113] K. Seywald. "Impact of Aeroelasticity on Flight Dynamics and Handling Qualities of Novel Aircraft Configurations". PhD thesis. Munich: TU Munich, 2016.

[114] J. S. Shamma. *Control of Linear Parameter Varying Systems with Applications*. Ed. by J. Mohammadpour and C. W. Scherer. New York, NY: Springer-Verlag, 2012.

[115] L. Singh, P. Miotto, and L. S. Breger. "L1 Adaptive Control Design for Improved Handling of the F/A-18 class of Aircraft". In: *Guidance, Navigation, and Control and Co-located Conferences*. American Institute of Aeronautics and Astronautics, Aug. 2013.

[116] S. Skogestad and I. Postlethwaite. *Multivariable Feedback Control - Analysis and Design*. Chichester, England: John Wiley & Sons, 1996.

[117] J.-J. E. Slotine and W. Li. *Applied Nonlinear Control*. Englewood CJiffs, New Jersey, USA: Prentice Hall, 1991.

[118] L. Sonneveldt. "Adaptive Backstepping Flight Control for Modern Fighter Aircraft". PhD thesis. Delft: TU Delft, July 2010.

[119] T. Souanef and W. Fichter. "Advances in Aerospace Guidance, Navigation and Control: Selected Papers of the Third CEAS Specialist Conference on Guidance, Navigation and Control held in Toulouse". In: ed. by J. Bordeneuve-Guibé, A. Drouin, and C. Roos. Cham: Springer International Publishing, 2015. Chap. Fault Tolerant L1 Adaptive Control Based on Degraded Models, pp. 135–149.

[120] V. Stepanyan, K. Krishnakumar, N. Nguyen, and L. V. Eykeren. "Stability and Performance Metrics for Adaptive Flight Control". In: *Guidance, Navigation, and Control and Co-located Conferences*. American Institute of Aeronautics and Astronautics, Aug. 2009.

[121] B. Stevens and F. Lewis. *Aircraft Control and Simulation*. John Wiley & Sons, 2003.

[122] B. L. Stevens, F. L. Lewis, and E. N. Johnson. *Aircraft Control and Simulation*. Hoboken, New Jersey: John Wiley & Sons, 2016.

[123] O. Stroosma, H. Damveld, J. A Mulder, R. Choe, E. Xargay, and N. Hovakimyan. "A Handling Qualities Assessment of a Business Jet Augmented with an L1 Adaptive Controller". In: *Guidance, Navigation, and Control and Co-located Conferences*. American Institute of Aeronautics and Astronautics, Aug. 2011.

[124] D. Sun, R. Choe, E. Xargay, and N. Hovakimyan. "An L1 Adaptive Backup Flight Control Law for Transport Aircraft with Vertical-Tail Damage". In: *AIAA SciTech*. American Institute of Aeronautics and Astronautics, Jan. 2016.

[125] N. Tekles, J. Chongvisal, E. Xargay, R. Choe, D. A. Talleur, N. Hovakimyan, and C. M. Belcastro. "Design of a Flight Envelope Protection System for NASA's Transport Class Model". In: *Journal of Guidance, Control, and Dynamics* (Aug. 2016), pp. 1–15.

[126] A. Tewari. *Aeroservoelasticity - Modeling and Control*. Control Engineering. New York, USA: Springer-Verlag, 2015.

[127] A. Tewari. *Modern Control Design with MATLAB and Simulink*. Chichester, UK: John Wiley & Sons, 2002.

[128] J. Wang. "Novel Control Approaches to Quadrotors Inspired by Dynamic Inversion and Backstepping". PhD thesis. TU München, 2015.

[129] J. Wang, F. Holzapfel, E. Xargay, and N. Hovakimyan. "Non-cascaded Dynamic Inversion Design for Quadrotor Position Control with L1 Augmentation". In: *CEAS EuroGNC Conference*. 2013.

[130] J. Wang, C. Cao, N. Hovakimyan, R. Hindman, and D. B. Ridgely. "L1 Adaptive Controller for a Missile longitudinal Autopilot Design". In: *Guidance, Navigation, and Control and Co-located Conferences*. American Institute of Aeronautics and Astronautics, Aug. 2008.

[131] M. Wang, F. Holzapfel, S. Zhang, and F. Zhang. "Backup Controller for Large Transport Aircraft with Insufficient Natural Stability". In: *Journal of Guidance, Control, and Dynamics* (Dec. 2016), pp. 1–14.

[132] X. Wang and N. Hovakimyan. "L1 adaptive controller for nonlinear reference systems". In: *American Control Conference (ACC), 2011*. 2011.

[133] X. Wang and N. Hovakimyan. "L1 adaptive controller for nonlinear time-varying reference systems". In: *Systems & Control Letters* 61.4 (2012), pp. 455 –463.

[134] Wikimedia. *File:GENERAL DYNAMICS F-16 FIGHTING FALCON.svg - Wikimedia Commons*. `https://upload.wikimedia.org/wikipedia/commons/9/91/GENERAL_DYNAMICS_F-16_FIGHTING_FALCON.svg`. Downloaded: 13.04.2016. July 2011.

[135] Wikimedia. *File:Norwegian F16A over Balkans.jpg - Wikimedia Commons*. `http://commons.wikimedia.org/wiki/File:Norwegian_F16A_over_Balkans.jpg`. Downloaded: 29.10.2014. May 1999.

[136] K. Wise, E. Lavretsky, N. Hovakimyan, C. Cao, and J. Wang. "Verifiable Adaptive Control: UCAV and Aerial Refueling". In: *Guidance, Navigation, and Control and Co-located Conferences*. American Institute of Aeronautics and Astronautics, Aug. 2008.

[137] K. A. Wise, J. L. Sedwick, and Y. Ikeda. *Nonlinear Control Of Fighter Aircraft*. Tech. rep. St. Louis, Missouri: The Boeing Company, June 1999.

[138] E. Xargay, N. Hovakimyan, and C. Cao. "L1 adaptive controller for multi-input multi-output systems in the presence of nonlinear unmatched uncertainties". In: *American Control Conference (ACC), 2010*. 2010, pp. 874–879.

[139] E. Xargay, V. Dobrokhodov, N. Hovakimyan, I. Kaminer, I. Kitsios, C. Cao, I. M. Gregory, and L. Valavani. "Experimental Validation of L1 Adaptive Control: The Rohrs Counterexample in Flight". In: *Journal of Guidance, Control, and Dynamics* 34.5 (Sept. 2011), pp. 1311–1328.

[140] E. Xargay, N. Hovakimyan, V. Dobrokhodov, R. Statnikov, I. Kaminer, C. Cao, and I. Gregory. "L1 Adaptive Flight Control System: Systematic Design and Verification and Validation of Control Metrics". In: *Guidance, Navigation, and Control and Co-located Conferences*. American Institute of Aeronautics and Astronautics, Aug. 2010.

[141] P. Zarchan and H. Musoff. *Fundamentals of Kalman Filtering*. Ed. by F. K. Lu. 3rd edition. Progress in Astronautics and Aeronautics. American Institute of Aeronautics and Astronautics, 2009.

[142] K. Zhou, J. C. Doyle, and K. Glover. *Robust and Optimal Control*. Prentice Hall, 1996.

[143] P. H. Zipfel. *Modeling and Simulation of Aerospace Vehicle Dynamics*. Ed. by J. S. Przemieniecki. Reston, Virginia: American Institute of Aeronautics and Astronautics, Inc., 2000.

List of Figures

List of Tables

A. Appendix

A.1. Aerodynamic coefficients of the F-16 model

In the following section, the values of the dimensionless aerodynamic coefficients of the F-16 model $C_{X,0}$, $C_{X,LEF}$, $C_{X,q}$, $C_{X,q,LEF}$, $C_{Z,0}$, $C_{Z,LEF}$, $C_{Z,q}$, $C_{Z,q,LEF}$, $C_{m,0}$, $C_{m,LEF}$, $C_{m,q}$, $C_{m,q,LEF}$ and $C_{m,\Delta}$ are shown by means of diagrams as functions of angle of attack α and elevator deflection η.

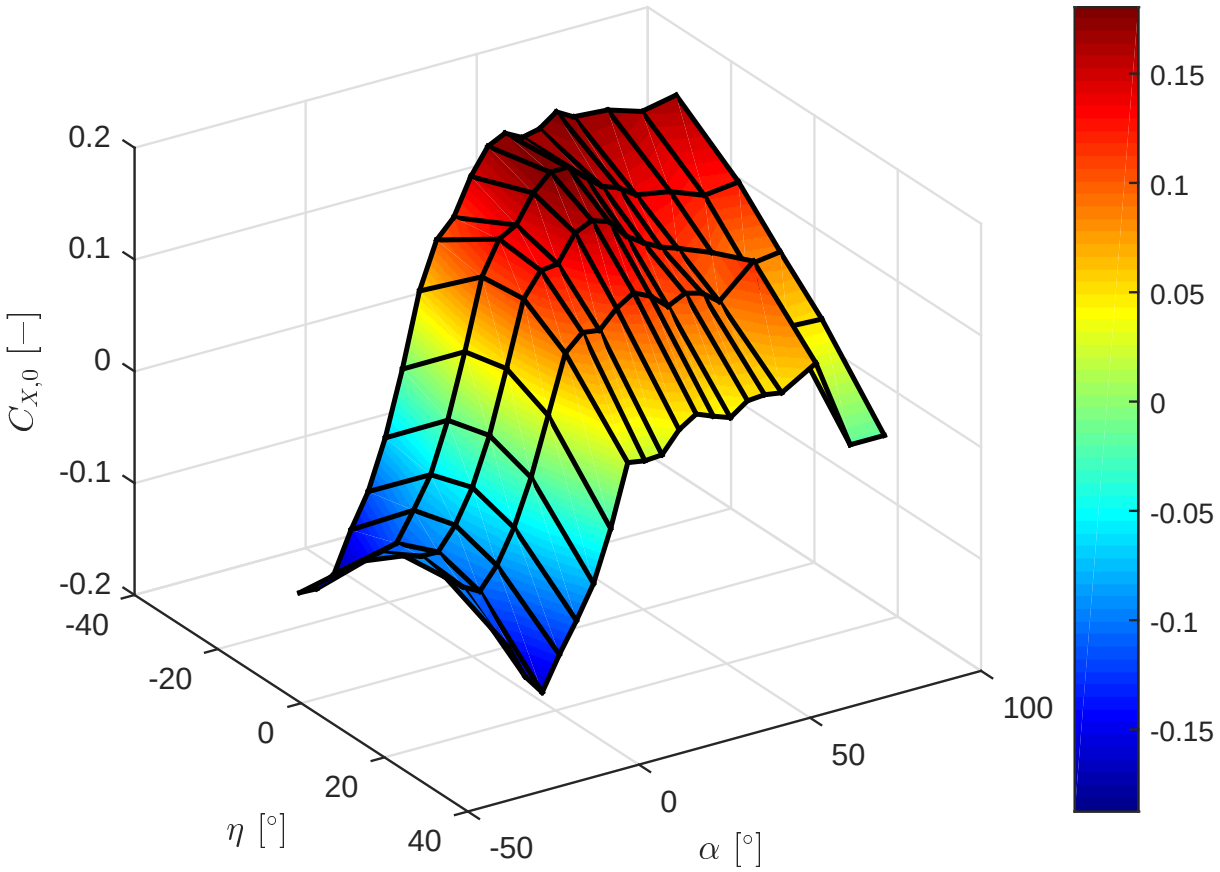

Figure A.1. – Aerodynamic coefficient $C_{X,0}$

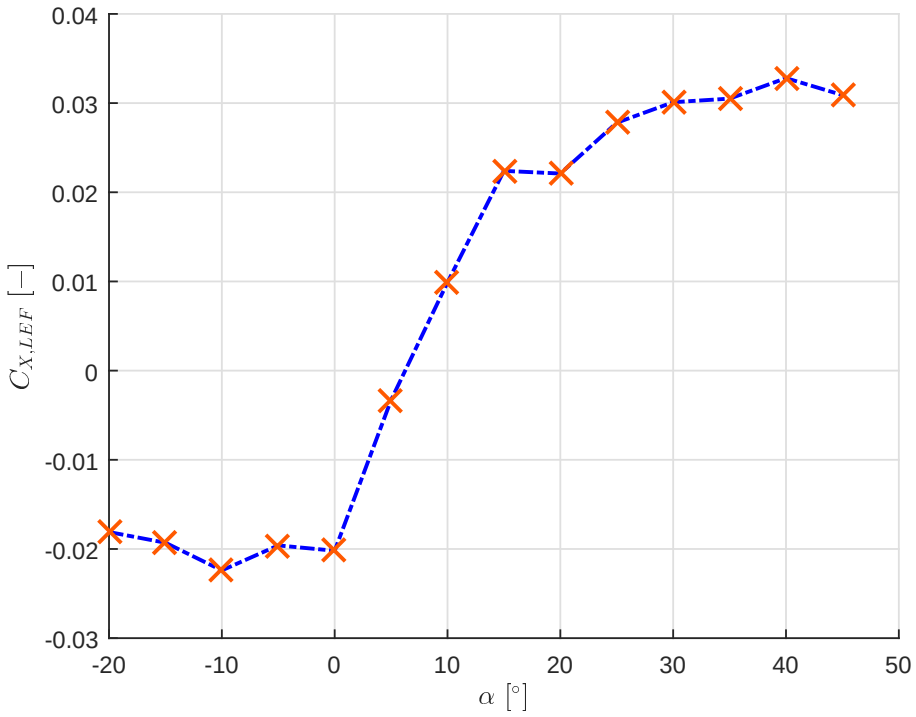

Figure A.2. – Aerodynamic coefficient $C_{X,LEF}$

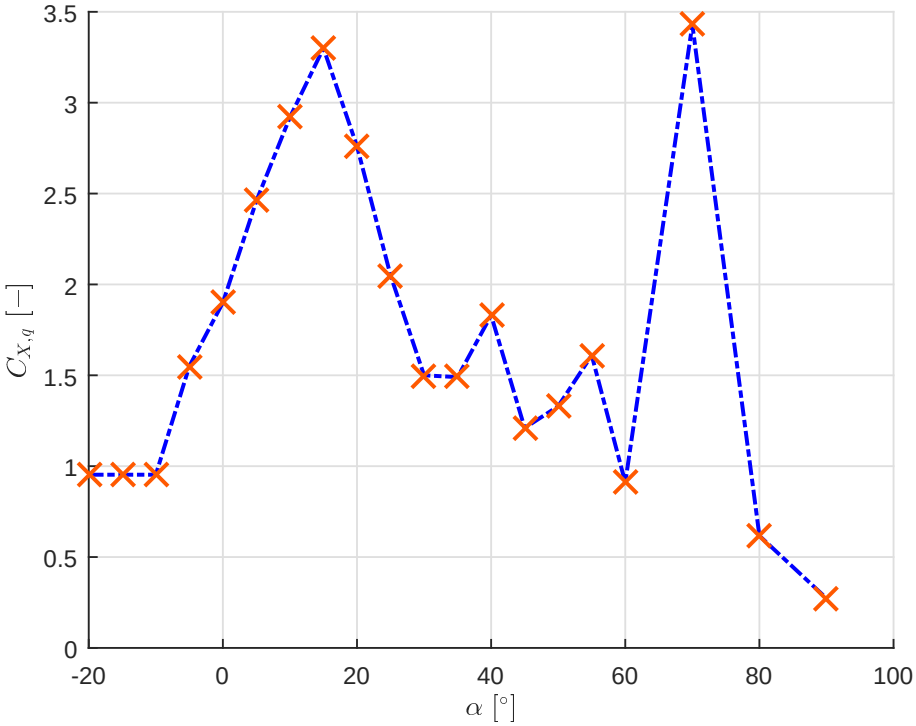

Figure A.3. – Aerodynamic coefficient $C_{X,q}$

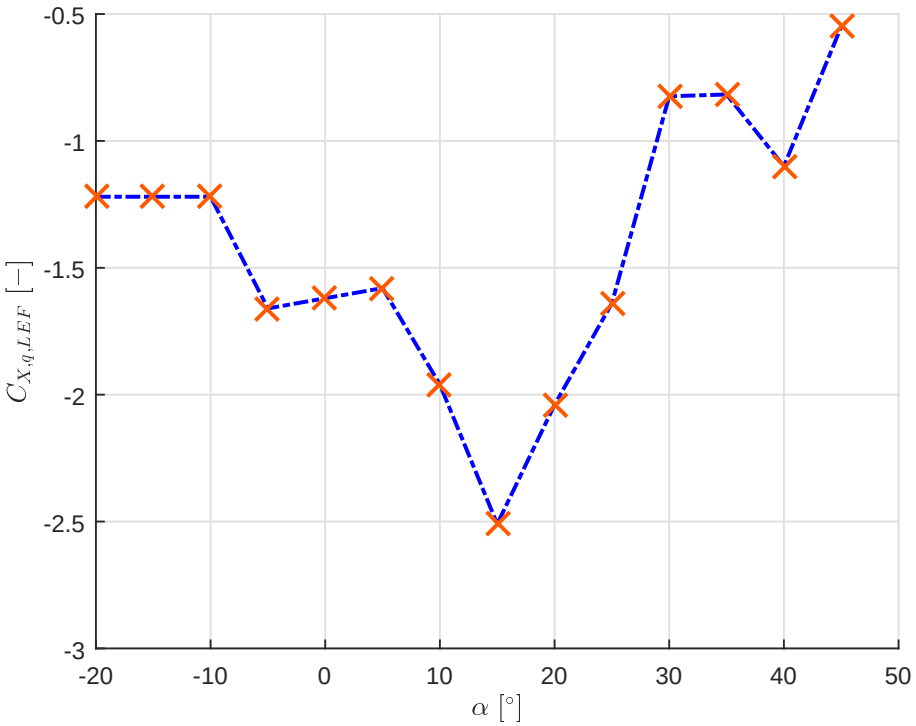

Figure A.4. – Aerodynamic coefficient $C_{X,q,LEF}$

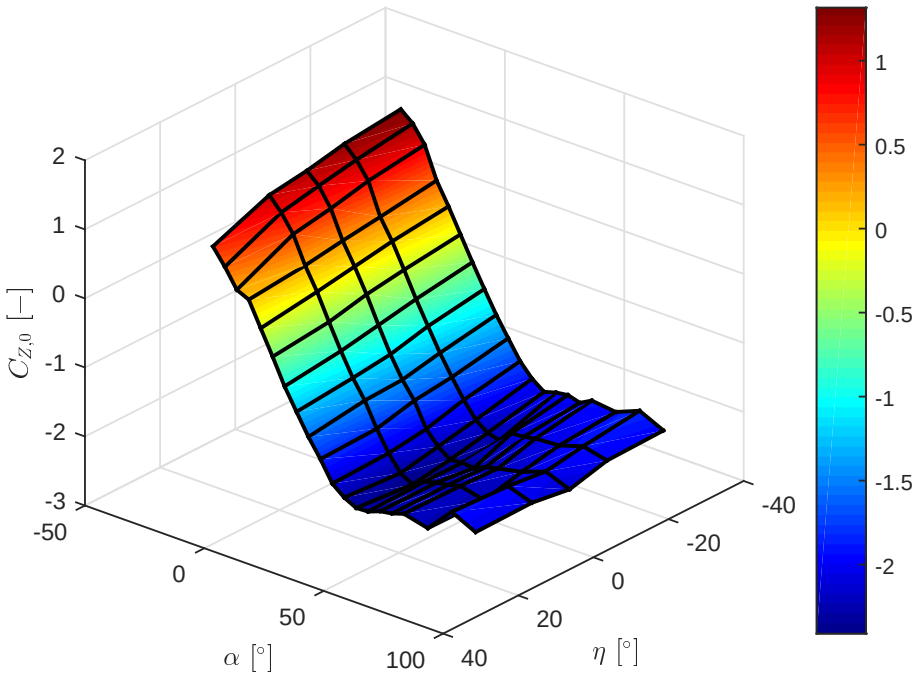

Figure A.5. – Aerodynamic coefficient $C_{Z,0}$

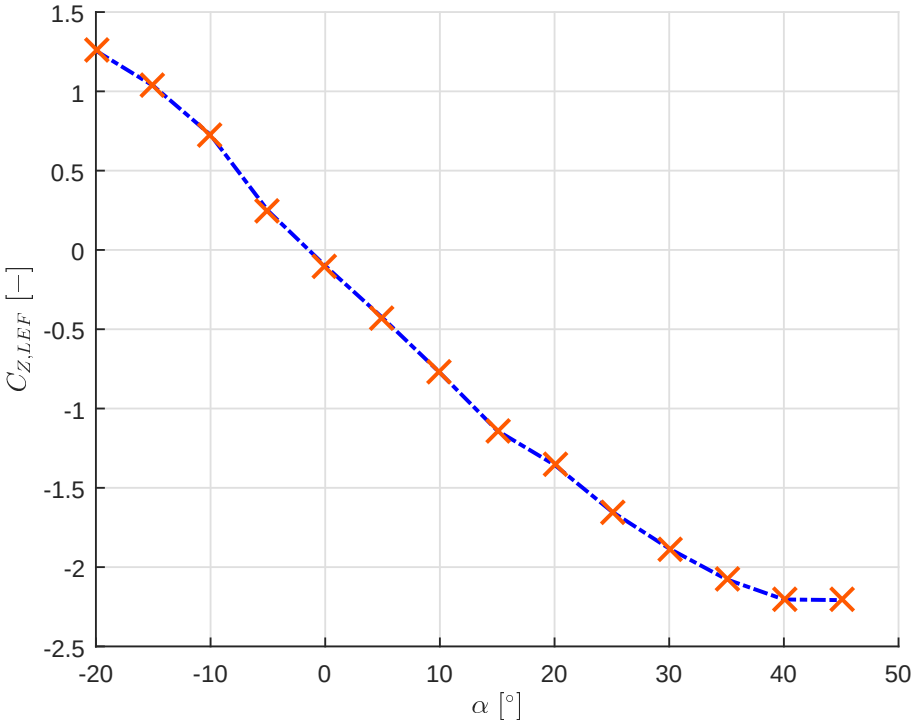

Figure A.6. – Aerodynamic coefficient $C_{Z,LEF}$

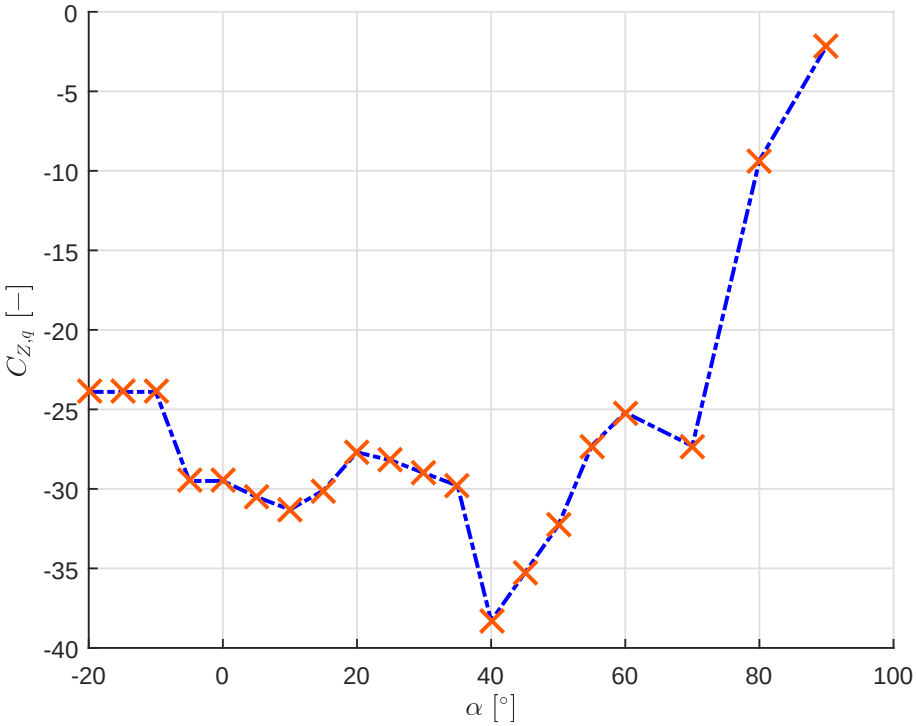

Figure A.7. – Aerodynamic coefficient $C_{Z,q}$

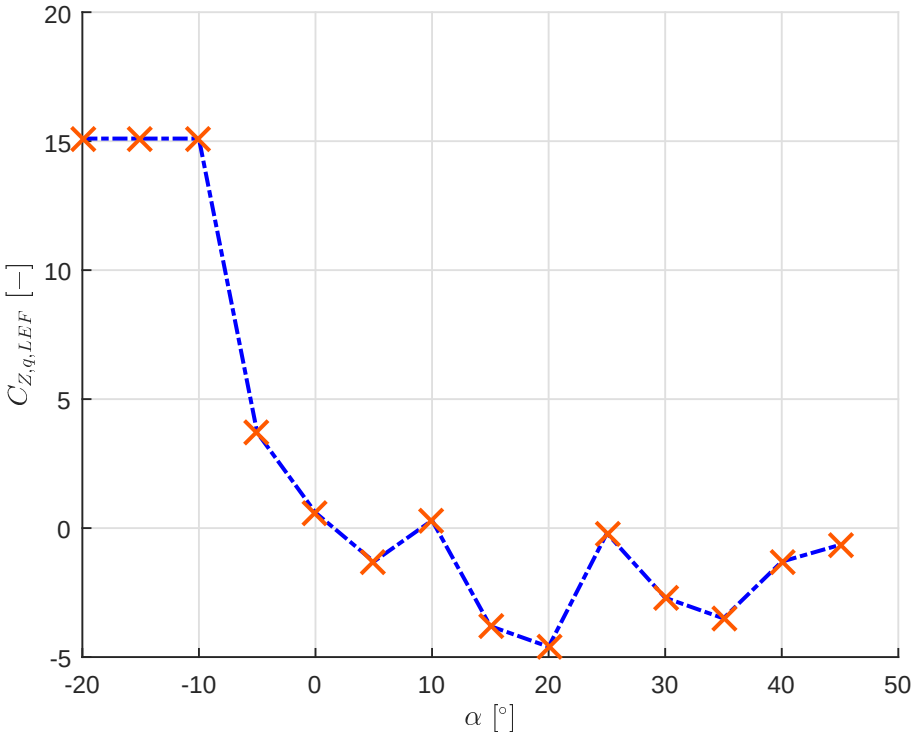

Figure A.8. – Aerodynamic coefficient $C_{Z,q,LEF}$

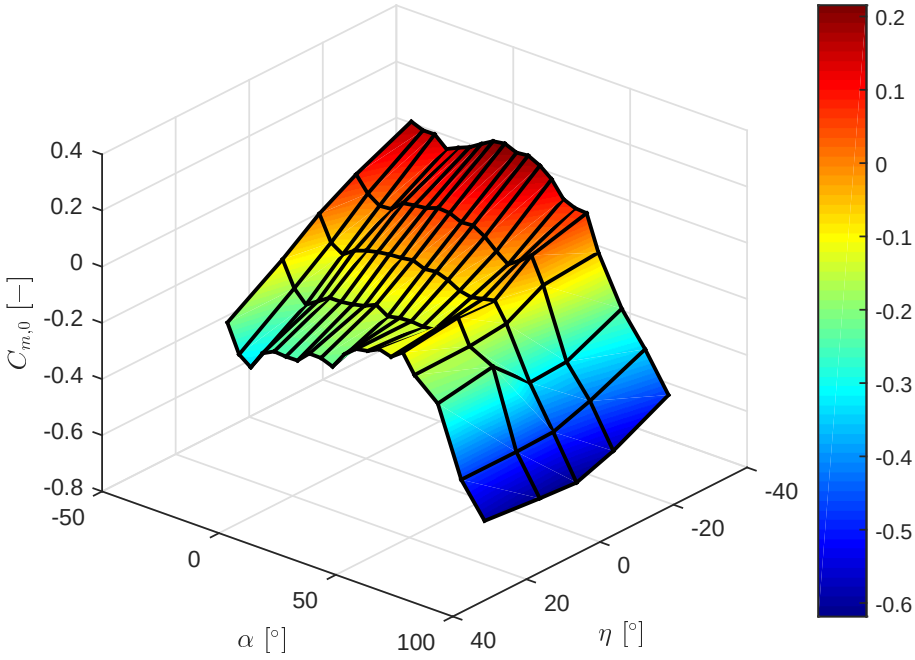

Figure A.9. – Aerodynamic coefficient $C_{m,0}$

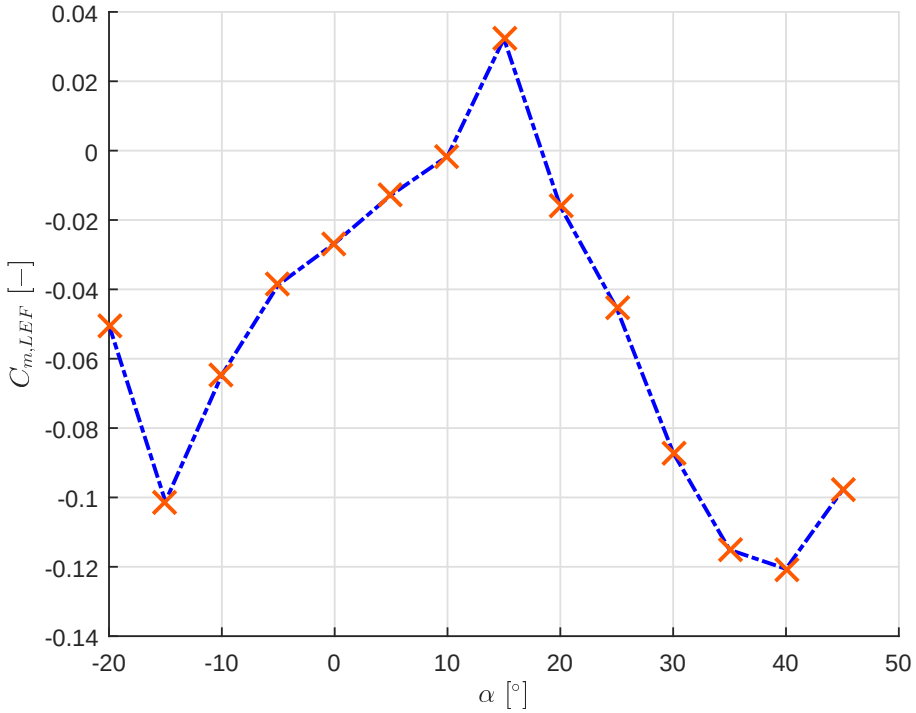

Figure A.10. – Aerodynamic coefficient $C_{m,LEF}$

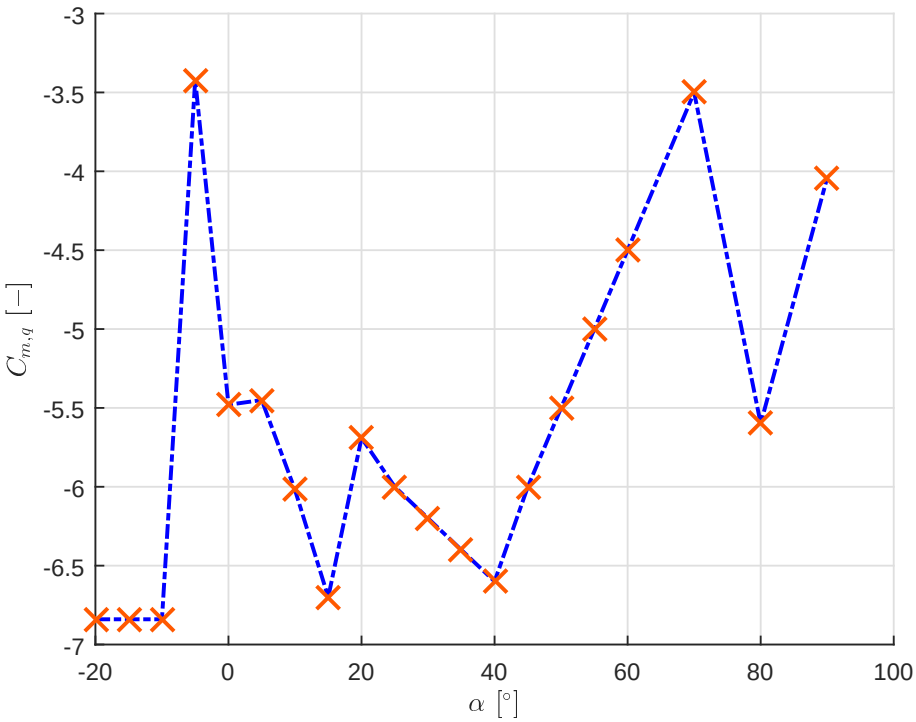

Figure A.11. – Aerodynamic coefficient $C_{m,q}$

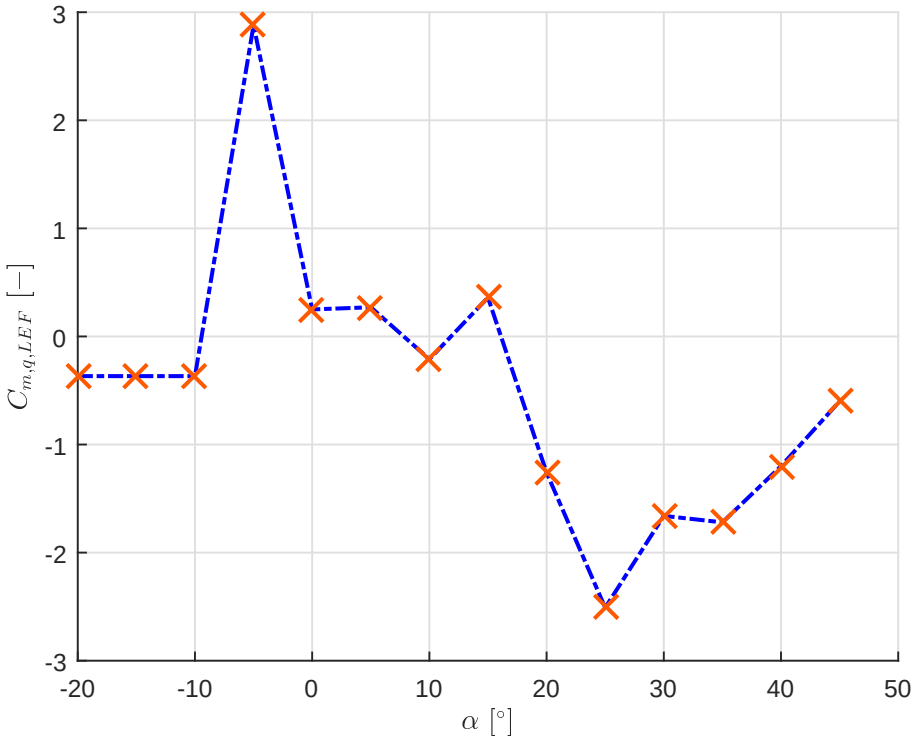

Figure A.12. – Aerodynamic coefficient $C_{m,q,LEF}$

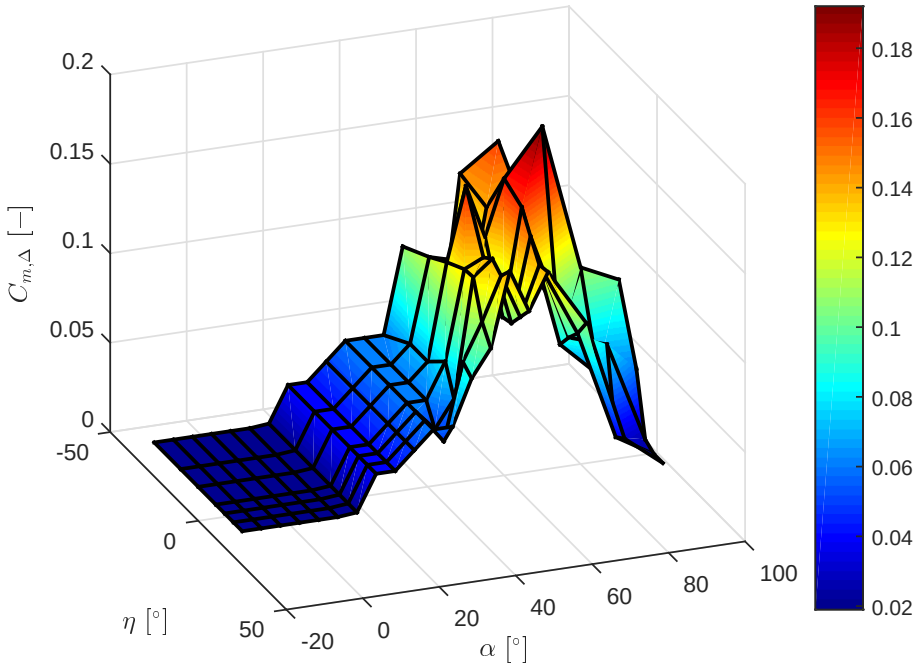

Figure A.13. – Aerodynamic coefficient $C_{m,\Delta}$

A.2. Propulsion data of the F-16 model

Next to the aerodynamic coefficients, figures showing the values of the thrust force $\left(X_P^G\right)_B$ used for the F-16 model as functions of thrust lever position δ_T and altitude h for different mach numbers Ma are now introduced.

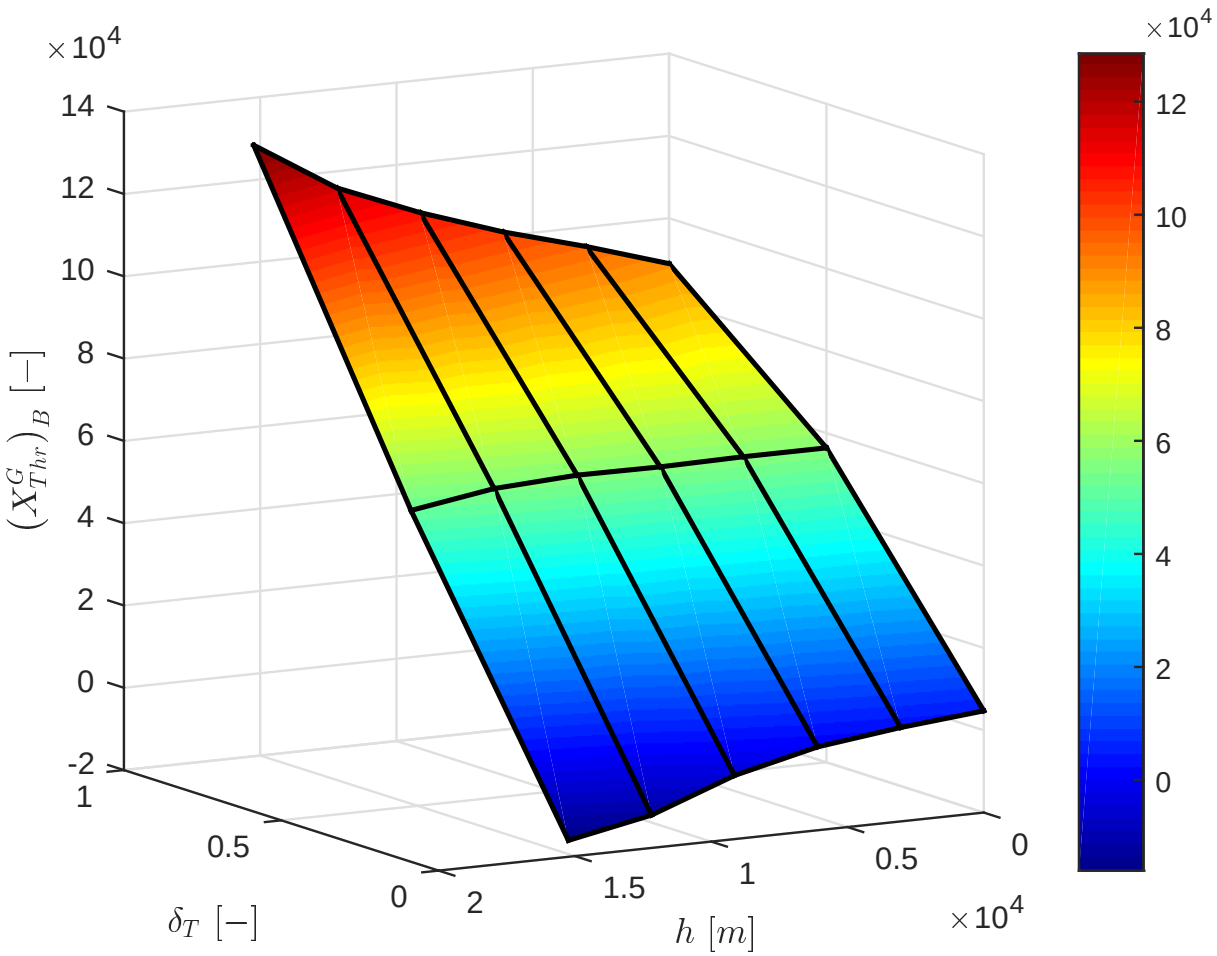

Figure A.14. – Thrust force $\left(X_{Thr}^G\right)_B$ for $Ma = 0$

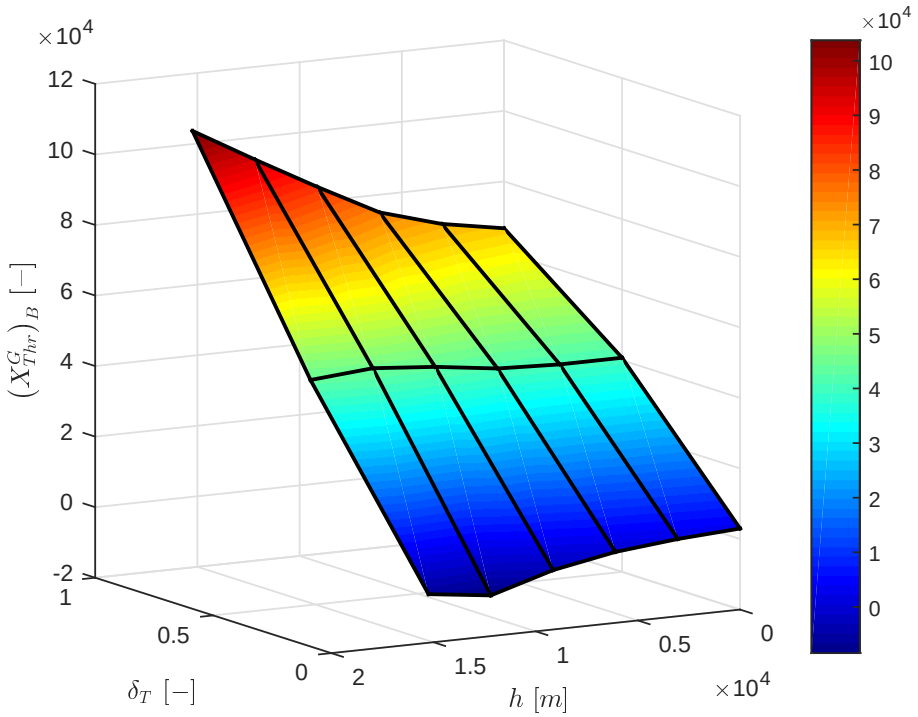

Figure A.15. – Thrust force $\left(X^G_{Thr}\right)_B$ for $Ma = 0.2$

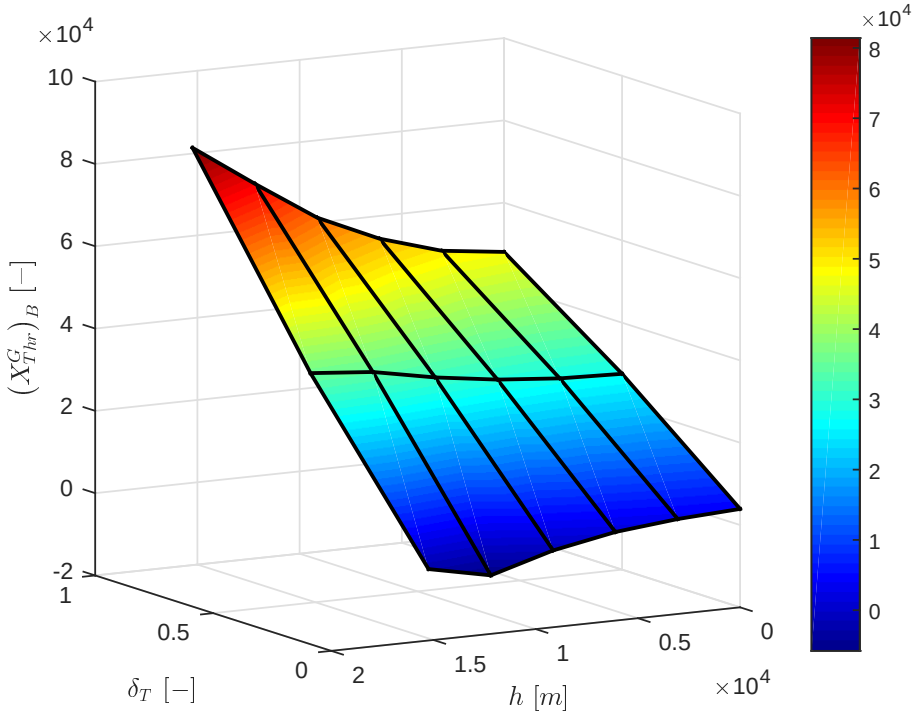

Figure A.16. – Thrust force $\left(X^G_{Thr}\right)_B$ for $Ma = 0.4$

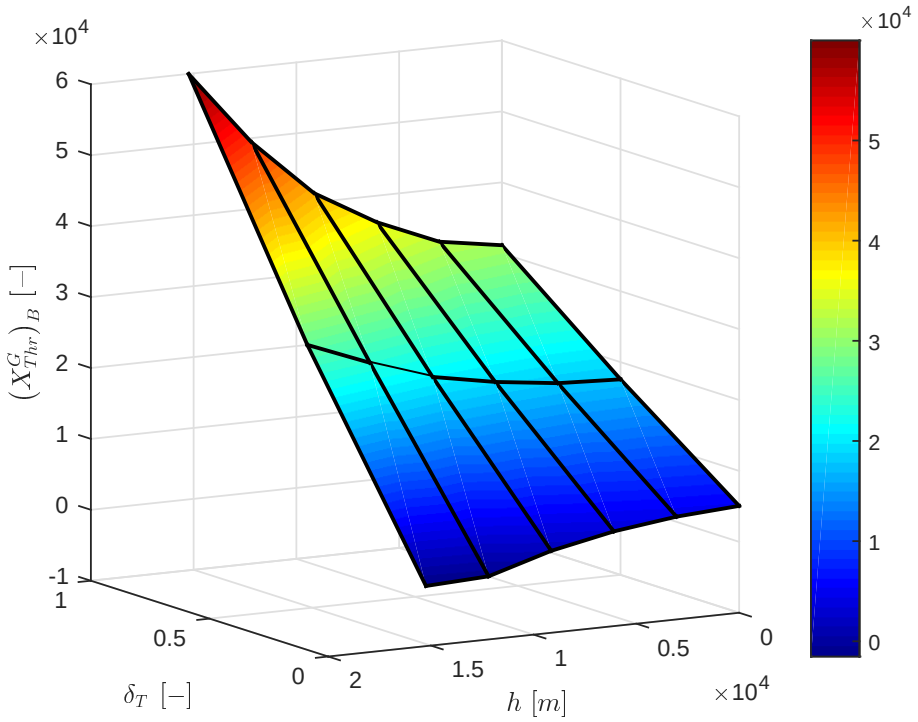

Figure A.17. – Thrust force $\left(X^G_{Thr}\right)_B$ for $Ma = 0.6$

A.3. Linearized models of the longitudinal F-16 dynamics

This section contains linear models of the longitudinal F-16 dynamics according to Eq. (2.43) in Section 2.1.4 at an altitude of $h = 5000m$ and different velocities according to Table 2.2, where the trim results of Fig. 2.4 and Fig. 2.5 shown in Section 2.1.3 are used. The results are gained using a CG position of $0.30\bar{c}$, which corresponds to a shift of 5% forward in comparison to the reference CG, which lies at $0.35\bar{c}$ (c.f. Section 2.1.1).

Envelope point $V = 102.88\frac{m}{s}$ **and** $h = 5000m$

$$\begin{pmatrix} \dot{V} \\ \dot{\gamma} \\ \dot{\alpha} \\ \dot{q} \end{pmatrix} = \begin{pmatrix} -0.03663 & -9.80665 & -10.74051 & -0.51136 \\ 0.00181 & 0.00000 & 0.90583 & 0.05991 \\ -0.00181 & 0.00000 & -0.90583 & 0.94009 \\ 0.00000 & 0.00000 & -4.91317 & -0.90604 \end{pmatrix} \begin{pmatrix} V \\ \gamma \\ \alpha \\ q \end{pmatrix} + \begin{pmatrix} 1.79116 & 6.88363 \\ 0.04734 & 0.00748 \\ -0.04734 & -0.00748 \\ -2.49051 & 0.00000 \end{pmatrix} \begin{pmatrix} \eta \\ \delta_T \end{pmatrix} \tag{A.1a}$$

$$\textbf{Phugoid}: \omega_{0,ph} = 0.13\frac{rad}{s}, \zeta_{ph} = 0.13 \tag{A.1b}$$

$$\textbf{Short-period}: \omega_{0,sp} = 2.33\frac{rad}{s}, \zeta_{sp} = 0.39 \tag{A.1c}$$

Envelope point $V = 110.32\frac{m}{s}$ **and** $h = 5000m$

$$\begin{pmatrix} \dot{V} \\ \dot{\gamma} \\ \dot{\alpha} \\ \dot{q} \end{pmatrix} = \begin{pmatrix} -0.03508 & -9.80665 & -9.31150 & -0.45459 \\ 0.00158 & 0.00000 & 0.97492 & 0.06024 \\ -0.00158 & 0.00000 & -0.97492 & 0.93976 \\ 0.00000 & 0.00000 & -5.84084 & -0.95756 \end{pmatrix} \begin{pmatrix} V \\ \gamma \\ \alpha \\ q \end{pmatrix} + \begin{pmatrix} 2.16386 & 6.55736 \\ 0.04873 & 0.00574 \\ -0.04873 & -0.00574 \\ -2.76964 & 0.00000 \end{pmatrix} \begin{pmatrix} \eta \\ \delta_T \end{pmatrix} \tag{A.2a}$$

$$\textbf{Phugoid}: \omega_{0,ph} = 0.12\frac{rad}{s}, \zeta_{ph} = 0.13 \tag{A.2b}$$

$$\textbf{Short-period}: \omega_{0,sp} = 2.53\frac{rad}{s}, \zeta_{sp} = 0.38 \tag{A.2c}$$

Envelope point $V = 117.75\frac{m}{s}$ **and** $h = 5000m$

$$\begin{pmatrix} \dot{V} \\ \dot{\gamma} \\ \dot{\alpha} \\ \dot{q} \end{pmatrix} = \begin{pmatrix} -0.03445 & -9.80665 & -9.05369 & -0.40355 \\ 0.00139 & 0.00000 & 1.00951 & 0.06022 \\ -0.00139 & 0.00000 & -1.00951 & 0.93978 \\ 0.00000 & 0.00000 & -6.71914 & -1.01149 \end{pmatrix} \begin{pmatrix} V \\ \gamma \\ \alpha \\ q \end{pmatrix} + \begin{pmatrix} 2.55369 & 6.22729 \\ 0.05049 & 0.00445 \\ -0.05049 & -0.00445 \\ -3.08052 & 0.00000 \end{pmatrix} \begin{pmatrix} \eta \\ \delta_T \end{pmatrix} \tag{A.3a}$$

$$\textbf{Phugoid}: \omega_{0,ph} = 0.11\frac{rad}{s}, \zeta_{ph} = 0.14 \tag{A.3b}$$

$$\textbf{Short-period}: \omega_{0,sp} = 2.71\frac{rad}{s}, \zeta_{sp} = 0.37 \tag{A.3c}$$

Envelope point $V = 125.19\frac{m}{s}$ **and** $h = 5000m$

$$\begin{pmatrix} \dot{V} \\ \dot{\gamma} \\ \dot{\alpha} \\ \dot{q} \end{pmatrix} = \begin{pmatrix} -0.03435 & -9.80665 & -7.53404 & -0.36047 \\ 0.00123 & 0.00000 & 1.07413 & 0.05958 \\ -0.00123 & 0.00000 & -1.07413 & 0.94042 \\ 0.00000 & 0.00000 & -7.67848 & -1.06986 \end{pmatrix} \begin{pmatrix} V \\ \gamma \\ \alpha \\ q \end{pmatrix} + \begin{pmatrix} 2.95662 & 5.89475 \\ 0.05298 & 0.00346 \\ -0.05298 & -0.00346 \\ -3.44393 & 0.00000 \end{pmatrix} \begin{pmatrix} \eta \\ \delta_T \end{pmatrix} \tag{A.4a}$$

$$\textbf{Phugoid}: \omega_{0,ph} = 0.11\frac{rad}{s}, \zeta_{ph} = 0.15 \tag{A.4b}$$

$$\textbf{Short-period}: \omega_{0,sp} = 2.89\frac{rad}{s}, \zeta_{sp} = 0.37 \tag{A.4c}$$

Envelope point $V = 132.63\frac{m}{s}$ **and** $h = 5000m$

$$\begin{pmatrix} \dot{V} \\ \dot{\gamma} \\ \dot{\alpha} \\ \dot{q} \end{pmatrix} = \begin{pmatrix} -0.03293 & -9.80665 & -5.91560 & -0.32238 \\ 0.00110 & 0.00000 & 1.13862 & 0.05904 \\ -0.00110 & 0.00000 & -1.13862 & 0.94096 \\ 0.00000 & 0.00000 & -8.69839 & -1.12853 \end{pmatrix} \begin{pmatrix} V \\ \gamma \\ \alpha \\ q \end{pmatrix} + \begin{pmatrix} 3.38309 & 5.58479 \\ 0.05550 & 0.00272 \\ -0.05550 & -0.00272 \\ -3.82949 & 0.00000 \end{pmatrix} \begin{pmatrix} \eta \\ \delta_T \end{pmatrix} \tag{A.5a}$$

$$\textbf{Phugoid}: \omega_{0,ph} = 0.10\frac{rad}{s}, \zeta_{ph} = 0.16 \tag{A.5b}$$

$$\textbf{Short-period}: \omega_{0,sp} = 3.08\frac{rad}{s}, \zeta_{sp} = 0.37 \tag{A.5c}$$

Envelope point $V = 140.07\frac{m}{s}$ **and** $h = 5000m$

$$\begin{pmatrix} \dot{V} \\ \dot{\gamma} \\ \dot{\alpha} \\ \dot{q} \end{pmatrix} = \begin{pmatrix} -0.03395 & -9.80665 & -4.19950 & -0.28832 \\ 0.00099 & 0.00000 & 1.20302 & 0.05857 \\ -0.00099 & 0.00000 & -1.20302 & 0.94143 \\ 0.00000 & 0.00000 & -9.77862 & -1.18743 \end{pmatrix} \begin{pmatrix} V \\ \gamma \\ \alpha \\ q \end{pmatrix} + \begin{pmatrix} 3.83323 & 5.29026 \\ 0.05805 & 0.00215 \\ -0.05805 & -0.00215 \\ -4.23722 & 0.00000 \end{pmatrix} \begin{pmatrix} \eta \\ \delta_T \end{pmatrix} \tag{A.6a}$$

$$\textbf{Phugoid}: \omega_{0,ph} = 0.09\frac{rad}{s}, \zeta_{ph} = 0.17 \tag{A.6b}$$

$$\textbf{Short-period}: \omega_{0,sp} = 3.26\frac{rad}{s}, \zeta_{sp} = 0.37 \tag{A.6c}$$

Envelope point $V = 147.50\frac{m}{s}$ **and** $h = 5000m$

$$\begin{pmatrix} \dot{V} \\ \dot{\gamma} \\ \dot{\alpha} \\ \dot{q} \end{pmatrix} = \begin{pmatrix} -0.03550 & -9.80665 & -2.38656 & -0.25757 \\ 0.00089 & 0.00000 & 1.26735 & 0.05818 \\ -0.00089 & 0.00000 & -1.26735 & 0.94182 \\ 0.00000 & 0.00000 & -10.91898 & -1.24655 \end{pmatrix} \begin{pmatrix} V \\ \gamma \\ \alpha \\ q \end{pmatrix} + \begin{pmatrix} 4.30718 & 4.99491 \\ 0.06063 & 0.00171 \\ -0.06063 & -0.00171 \\ -4.66714 & 0.00000 \end{pmatrix} \begin{pmatrix} \eta \\ \delta_T \end{pmatrix} \tag{A.7a}$$

$$\textbf{Phugoid}: \omega_{0,ph} = 0.09\frac{rad}{s},\ \zeta_{ph} = 0.19 \tag{A.7b}$$

$$\textbf{Short-period}: \omega_{0,sp} = 3.44\frac{rad}{s},\ \zeta_{sp} = 0.37 \tag{A.7c}$$

Envelope point $V = 154.94\frac{m}{s}$ **and** $h = 5000m$

$$\begin{pmatrix} \dot{V} \\ \dot{\gamma} \\ \dot{\alpha} \\ \dot{q} \end{pmatrix} = \begin{pmatrix} -0.03757 & -9.80665 & -0.47734 & -0.22957 \\ 0.00081 & 0.00000 & 1.33162 & 0.05783 \\ -0.00081 & 0.00000 & -1.33162 & 0.94217 \\ -0.00000 & 0.00000 & -12.11932 & -1.30584 \end{pmatrix} \begin{pmatrix} V \\ \gamma \\ \alpha \\ q \end{pmatrix} + \begin{pmatrix} 4.80502 & 4.69897 \\ 0.06323 & 0.00137 \\ -0.06323 & -0.00137 \\ -5.11926 & 0.00000 \end{pmatrix} \begin{pmatrix} \eta \\ \delta_T \end{pmatrix} \tag{A.8a}$$

$$\textbf{Phugoid}: \omega_{0,ph} = 0.09\frac{rad}{s},\ \zeta_{ph} = 0.22 \tag{A.8b}$$

$$\textbf{Short-period}: \omega_{0,sp} = 3.63\frac{rad}{s},\ \zeta_{sp} = 0.36 \tag{A.8c}$$

Envelope point $V = 162.38\frac{m}{s}$ **and** $h = 5000m$

$$\begin{pmatrix} \dot{V} \\ \dot{\gamma} \\ \dot{\alpha} \\ \dot{q} \end{pmatrix} = \begin{pmatrix} -0.04016 & -9.80665 & 1.52773 & -0.20386 \\ 0.00073 & 0.00000 & 1.39584 & 0.05753 \\ -0.00073 & 0.00000 & -1.39584 & 0.94247 \\ -0.00000 & 0.00000 & -13.37953 & -1.36529 \end{pmatrix} \begin{pmatrix} V \\ \gamma \\ \alpha \\ q \end{pmatrix} + \begin{pmatrix} 5.32682 & 4.40262 \\ 0.06584 & 0.00109 \\ -0.06584 & -0.00109 \\ -5.59358 & 0.00000 \end{pmatrix} \begin{pmatrix} \eta \\ \delta_T \end{pmatrix} \tag{A.9a}$$

$$\textbf{Phugoid}: \omega_{0,ph} = 0.08\frac{rad}{s}, \zeta_{ph} = 0.24 \tag{A.9b}$$

$$\textbf{Short-period}: \omega_{0,sp} = 3.81\frac{rad}{s}, \zeta_{sp} = 0.36 \tag{A.9c}$$

Envelope point $V = 169.81\frac{m}{s}$ **and** $h = 5000m$

$$\begin{pmatrix} \dot{V} \\ \dot{\gamma} \\ \dot{\alpha} \\ \dot{q} \end{pmatrix} = \begin{pmatrix} -0.04331 & -9.80665 & 3.62835 & -0.18009 \\ 0.00067 & 0.00000 & 1.46003 & 0.05727 \\ -0.00067 & 0.00000 & -1.46003 & 0.94273 \\ -0.00000 & 0.00000 & -14.69950 & -1.42487 \end{pmatrix} \begin{pmatrix} V \\ \gamma \\ \alpha \\ q \end{pmatrix} + \begin{pmatrix} 5.87265 & 4.10596 \\ 0.06848 & 0.00087 \\ -0.06848 & -0.00087 \\ -6.09012 & 0.00000 \end{pmatrix} \begin{pmatrix} \eta \\ \delta_T \end{pmatrix} \tag{A.10a}$$

$$\textbf{Phugoid}: \omega_{0,ph} = 0.08\frac{rad}{s}, \zeta_{ph} = 0.28 \tag{A.10b}$$

$$\textbf{Short-period}: \omega_{0,sp} = 3.99\frac{rad}{s}, \zeta_{sp} = 0.36 \tag{A.10c}$$

Envelope point $V = 177.25\frac{m}{s}$ **and** $h = 5000m$

$$\begin{pmatrix} \dot{V} \\ \dot{\gamma} \\ \dot{\alpha} \\ \dot{q} \end{pmatrix} = \begin{pmatrix} -0.04631 & -9.80665 & 5.82426 & -0.15799 \\ 0.00062 & 0.00000 & 1.52420 & 0.05704 \\ -0.00062 & 0.00000 & -1.52420 & 0.94296 \\ -0.00000 & 0.00000 & -16.07916 & -1.48458 \end{pmatrix} \begin{pmatrix} V \\ \gamma \\ \alpha \\ q \end{pmatrix} + \begin{pmatrix} 6.44255 & 3.88237 \\ 0.07112 & 0.00071 \\ -0.07112 & -0.00071 \\ -6.60886 & 0.00000 \end{pmatrix} \begin{pmatrix} \eta \\ \delta_T \end{pmatrix} \tag{A.11a}$$

$$\textbf{Phugoid}: \omega_{0,ph} = 0.07\frac{rad}{s}, \zeta_{ph} = 0.31 \tag{A.11b}$$

$$\textbf{Short-period}: \omega_{0,sp} = 4.17\frac{rad}{s}, \zeta_{sp} = 0.36 \tag{A.11c}$$

Envelope point $V = 184.69\frac{m}{s}$ **and** $h = 5000m$

$$\begin{pmatrix} \dot{V} \\ \dot{\gamma} \\ \dot{\alpha} \\ \dot{q} \end{pmatrix} = \begin{pmatrix} -0.04934 & -9.80665 & 8.11531 & -0.13730 \\ 0.00057 & 0.00000 & 1.58834 & 0.05684 \\ -0.00057 & 0.00000 & -1.58834 & 0.94316 \\ -0.00000 & 0.00000 & -17.51844 & -1.54439 \end{pmatrix} \begin{pmatrix} V \\ \gamma \\ \alpha \\ q \end{pmatrix} + \begin{pmatrix} 7.03657 & 3.69157 \\ 0.07378 & 0.00058 \\ -0.07378 & -0.00058 \\ -7.14983 & 0.00000 \end{pmatrix} \begin{pmatrix} \eta \\ \delta_T \end{pmatrix} \tag{A.12a}$$

$$\textbf{Phugoid}: \omega_{0,ph} = 0.07\frac{rad}{s}, \zeta_{ph} = 0.34 \tag{A.12b}$$

$$\textbf{Short-period}: \omega_{0,sp} = 4.36\frac{rad}{s}, \zeta_{sp} = 0.36 \tag{A.12c}$$

Envelope point $V = 192.13\frac{m}{s}$ **and** $h = 5000m$

$$\begin{pmatrix} \dot{V} \\ \dot{\gamma} \\ \dot{\alpha} \\ \dot{q} \end{pmatrix} = \begin{pmatrix} -0.05279 & -9.80665 & 10.49993 & -0.11787 \\ 0.00052 & 0.00000 & 1.65242 & 0.05666 \\ -0.00052 & 0.00000 & -1.65242 & 0.94334 \\ -0.00000 & 0.00000 & -19.01422 & -1.60429 \end{pmatrix} \begin{pmatrix} V \\ \gamma \\ \alpha \\ q \end{pmatrix} + \begin{pmatrix} 2.30119 & 3.50067 \\ 0.10513 & 0.00048 \\ -0.10513 & -0.00048 \\ -11.55320 & 0.00000 \end{pmatrix} \begin{pmatrix} \eta \\ \delta_T \end{pmatrix} \tag{A.13a}$$

$$\textbf{Phugoid}: \omega_{0,ph} = 0.07\frac{rad}{s}, \zeta_{ph} = 0.38 \tag{A.13b}$$

$$\textbf{Short-period}: \omega_{0,sp} = 4.54\frac{rad}{s}, \zeta_{sp} = 0.36 \tag{A.13c}$$

Envelope point $V = 199.56\frac{m}{s}$ **and** $h = 5000m$

$$\begin{pmatrix} \dot{V} \\ \dot{\gamma} \\ \dot{\alpha} \\ \dot{q} \end{pmatrix} = \begin{pmatrix} -0.05050 & -9.80665 & 12.94389 & -0.09970 \\ 0.00049 & 0.00000 & 1.71556 & 0.05650 \\ -0.00049 & 0.00000 & -1.71556 & 0.94350 \\ -0.00000 & 0.00000 & -20.49217 & -1.66429 \end{pmatrix} \begin{pmatrix} V \\ \gamma \\ \alpha \\ q \end{pmatrix} + \begin{pmatrix} 2.55230 & 3.34338 \\ 0.10950 & 0.00040 \\ -0.10950 & -0.00040 \\ -12.47871 & 0.00000 \end{pmatrix} \begin{pmatrix} \eta \\ \delta_T \end{pmatrix} \tag{A.14a}$$

$$\textbf{Phugoid}: \omega_{0,ph} = 0.07\frac{rad}{s}, \zeta_{ph} = 0.38 \tag{A.14b}$$

$$\textbf{Short-period}: \omega_{0,sp} = 4.71\frac{rad}{s}, \zeta_{sp} = 0.36 \tag{A.14c}$$

Envelope point $V = 207.00\frac{m}{s}$ **and** $h = 5000m$

$$\begin{pmatrix} \dot{V} \\ \dot{\gamma} \\ \dot{\alpha} \\ \dot{q} \end{pmatrix} = \begin{pmatrix} -0.05454 & -9.80665 & 15.48058 & -0.08246 \\ 0.00045 & 0.00000 & 1.77872 & 0.05636 \\ -0.00045 & 0.00000 & -1.77872 & 0.94364 \\ -0.00000 & 0.00000 & -22.02628 & -1.72437 \end{pmatrix} \begin{pmatrix} V \\ \gamma \\ \alpha \\ q \end{pmatrix} + \begin{pmatrix} 2.81328 & 3.18691 \\ 0.11386 & 0.00033 \\ -0.11386 & -0.00033 \\ -13.43937 & 0.00000 \end{pmatrix} \begin{pmatrix} \eta \\ \delta_T \end{pmatrix} \tag{A.15a}$$

$$\textbf{Phugoid}: \omega_{0,ph} = 0.06\frac{rad}{s}, \zeta_{ph} = 0.43 \tag{A.15b}$$

$$\textbf{Short-period}: \omega_{0,sp} = 4.88\frac{rad}{s}, \zeta_{sp} = 0.36 \tag{A.15c}$$

A.4. Poles of linearized closed-loop models

A.4.1. Baseline Controller

Table A.1. – Baseline Controller (simple aircraft model, discrete-time integrators): Poles of linearized closed-loop model for transfer function $\alpha_{cmd} \rightarrow \alpha$ at envelope point $V = 154.94\frac{m}{s}$ and $h = 5000m$

	Poles $[-]$	$\omega_0 \left[\frac{rad}{s}\right]$	$\zeta\ [-]$
1	-0.001	1.46e-03	1.000
2	-0.016+0.095i	0.10	0.166
3	-0.016-0.095i	0.10	0.166
4	-1.001	1.00	1.000
5	-3.645+1.198i	3.84	0.950
6	-3.645-1.198i	3.84	0.950
7	-25.578	25.58	1.000
8	-46.547	46.55	1.000
9	-44.059+37.108i	57.60	0.765
10	-44.059-37.108i	57.60	0.765
11	-209.440	209.44	1.000
12	-209.440	209.44	1.000
13	-209.440	209.44	1.000
14	-209.440	209.44	1.000

Table A.2. – Baseline Controller (simple aircraft model, continuous integrators): Poles of linearized closed-loop model for transfer function $\alpha_{cmd} \rightarrow \alpha$ at envelope point $V = 154.94\frac{m}{s}$ and $h = 5000m$

	Poles $[-]$	$\omega_0 \left[\frac{rad}{s}\right]$	$\zeta\ [-]$
1	-0.001	1.46e-03	1.000
2	-0.016+0.095i	0.10	0.166
3	-0.016-0.095i	0.10	0.166
4	-1.001	1.00	1.000
5	-3.645+1.198i	3.84	0.950
6	-3.645-1.198i	3.84	0.950
7	-25.578	25.58	1.000
8	-46.547	46.55	1.000
9	-44.059+37.108i	57.60	0.765
10	-44.059-37.108i	57.60	0.765
11	-209.440	209.44	1.000
12	-209.440	209.44	1.000
13	-209.440	209.44	1.000
14	-209.440	209.44	1.000

Table A.3. – Baseline Controller (enhanced aircraft model, discrete-time integrators): Poles of linearized closed-loop model for transfer function $\alpha_{cmd} \rightarrow \alpha$ at envelope point $V = 154.94\frac{m}{s}$ and $h = 5000m$

	Poles $[-]$	$\omega_0 \left[\frac{rad}{s}\right]$	$\zeta\ [-]$		Poles $[-]$	$\omega_0 \left[\frac{rad}{s}\right]$	$\zeta\ [-]$
1	-0.001	1.46e-03	1.000	**14**	-7.685-36.780i	37.57	0.205
2	-0.017+0.095i	0.10	0.172	**15**	-7.540+36.937i	37.70	0.200
3	-0.017-0.095i	0.10	0.172	**16**	-7.540-36.937i	37.70	0.200
4	-0.938	0.94	1.000	**17**	-7.402+37.075i	37.81	0.196
5	-2.584+1.687i	3.09	0.837	**18**	-7.402-37.075i	37.81	0.196
6	-2.584-1.687i	3.09	0.837	**19**	-28.329+28.012i	39.84	0.711
7	-13.043	13.04	1.000	**20**	-28.329-28.012i	39.84	0.711
8	-11.618+6.633i	13.38	0.868	**21**	-209.440	209.44	1.000
9	-11.618-6.633i	13.38	0.868	**22**	-209.440	209.44	1.000
10	-9.899+9.899i	14.00	0.707	**23**	-209.440	209.44	1.000
11	-9.899-9.899i	14.00	0.707	**24**	-209.440	209.44	1.000
12	-19.820	19.82	1.000	**25**	-200.000+115.470i	230.94	0.866
13	-7.685+36.780i	37.57	0.205	**26**	-200.000-115.470i	230.94	0.866

Table A.4. – Baseline Controller (enhanced aircraft model, continuous integrators): Poles of linearized closed-loop model for transfer function $\alpha_{cmd} \rightarrow \alpha$ at envelope point $V = 154.94\frac{m}{s}$ and $h = 5000m$

	Poles $[-]$	$\omega_0 \left[\frac{rad}{s}\right]$	$\zeta\ [-]$		Poles $[-]$	$\omega_0 \left[\frac{rad}{s}\right]$	$\zeta\ [-]$
1	-0.001	1.46e-03	1.000	**14**	-7.659-36.805i	37.59	0.204
2	-0.017+0.095i	0.10	0.172	**15**	-7.540+36.937i	37.70	0.200
3	-0.017-0.095i	0.10	0.172	**16**	-7.540-36.937i	37.70	0.200
4	-1.001	1.00	1.000	**17**	-7.426+37.056i	37.79	0.196
5	-3.645+1.198i	3.84	0.950	**18**	-7.426-37.056i	37.79	0.196
6	-3.645-1.198i	3.84	0.950	**19**	-28.364+28.076i	39.91	0.711
7	-4.593	4.59	1.000	**20**	-28.364-28.076i	39.91	0.711
8	-9.899+9.899i	14.00	0.707	**21**	-209.440	209.44	1.000
9	-9.899-9.899i	14.00	0.707	**22**	-209.440	209.44	1.000
10	-14.153	14.15	1.000	**23**	-209.440	209.44	1.000
11	-11.885+8.828i	14.81	0.803	**24**	-209.440	209.44	1.000
12	-11.885-8.828i	14.81	0.803	**25**	-200.000+115.470i	230.94	0.866
13	-7.659+36.805i	37.59	0.204	**26**	-200.000-115.470i	230.94	0.866

A.4.2. DPI Augmentation

Table A.5. – DPI Augmentation (simple aircraft model, discrete-time integrators): Poles of linearized closed-loop model for transfer function $\alpha_{cmd} \rightarrow \alpha$ at envelope point $V = 154.94\frac{m}{s}$ and $h = 5000m$

	Poles $[-]$	ω_0 $\left[\frac{rad}{s}\right]$	ζ $[-]$		Poles $[-]$	ω_0 $\left[\frac{rad}{s}\right]$	ζ $[-]$
1	-3.53e-14	3.53e-14	1.000	**21**	-54.545+31.492i	62.98	0.866
2	-1.96e-13	1.96e-13	1.000	**22**	-54.545-31.492i	62.98	0.866
3	1.20e-12	1.20e-12	-1.000	**23**	-59.878+44.881i	74.83	0.800
4	-0.001	1.46e-03	1.000	**24**	-59.878-44.881i	74.83	0.800
5	-0.013+0.095i	0.10	0.140	**25**	-75.426	75.43	1.000
6	-0.013-0.095i	0.10	0.140	**26**	-192.564	192.56	1.000
7	-1.006	1.01	1.000	**27**	-199.875	199.87	1.000
8	-3.494	3.49	1.000	**28**	-209.440	209.44	1.000
9	-6.163+1.818i	6.43	0.959	**29**	-209.440	209.44	1.000
10	-6.163-1.818i	6.43	0.959	**30**	-209.440	209.44	1.000
11	-6.860	6.86	1.000	**31**	-209.440	209.44	1.000
12	-7.000	7.00	1.000	**32**	-209.440	209.44	1.000
13	-20.597+27.456i	34.32	0.600	**33**	-209.440	209.44	1.000
14	-20.597-27.456i	34.32	0.600	**34**	-209.440	209.44	1.000
15	-28.400+28.168i	40.00	0.710	**35**	-209.440	209.44	1.000
16	-28.400-28.168i	40.00	0.710	**36**	-209.440	209.44	1.000
17	-35.681+28.312i	45.55	0.783	**37**	-209.440	209.44	1.000
18	-35.681-28.312i	45.55	0.783	**38**	-209.440	209.44	1.000
19	-50.592+21.328i	54.90	0.921	**39**	-214.181	214.18	1.000
20	-50.592-21.328i	54.90	0.921				

Table A.6. – DPI Augmentation (simple aircraft model, discrete-time integrators): Poles of linearized closed-loop model for transfer function $\alpha_{cmd} \rightarrow \alpha$ at envelope point $V = 154.94\frac{m}{s}$ and $h = 5000m$ considering additional gain of $19.32dB$ upstream the actuator. The gain disturbance is chosen slightly higher than the determined gain margin of the closed-loop at this envelope point ($19.27dB$) and thus the closed-loop is unstable (c.f. poles 11 and 12)

	Poles $[-]$	$\omega_0 \left[\frac{rad}{s}\right]$	$\zeta\ [-]$		Poles $[-]$	$\omega_0 \left[\frac{rad}{s}\right]$	$\zeta\ [-]$
1	4.91e-14	4.91e-14	-1.000	**21**	-54.545-31.492i	62.98	0.866
2	-3.25e-13	3.25e-13	1.000	**22**	-74.387+13.805i	75.66	0.983
3	4.05e-13	4.05e-13	-1.000	**23**	-74.387-13.805i	75.66	0.983
4	-0.001	1.46e-03	1.000	**24**	-67.106+65.216i	93.58	0.717
5	-0.014+0.095i	0.10	0.147	**25**	-67.106-65.216i	93.58	0.717
6	-0.014-0.095i	0.10	0.147	**26**	-165.700	165.70	1.000
7	-0.419+1.627i	1.68	0.249	**27**	-200.171	200.17	1.000
8	-0.419-1.627i	1.68	0.249	**28**	-209.440	209.44	1.000
9	-6.995	7.00	1.000	**29**	-209.440	209.44	1.000
10	-7.000	7.00	1.000	**30**	-209.440	209.44	1.000
11	0.009+21.187i	21.19	-0.000	**31**	-209.440	209.44	1.000
12	0.009-21.187i	21.19	-0.000	**32**	-209.440	209.44	1.000
13	-17.128+22.306i	28.12	0.609	**33**	-209.440	209.44	1.000
14	-17.128-22.306i	28.12	0.609	**34**	-209.440	209.44	1.000
15	-30.087	30.09	1.000	**35**	-209.440	209.44	1.000
16	-28.400+28.168i	40.00	0.710	**36**	-209.440	209.44	1.000
17	-28.400-28.168i	40.00	0.710	**37**	-209.440	209.44	1.000
18	-39.335+35.139i	52.74	0.746	**38**	-209.440	209.44	1.000
19	-39.335-35.139i	52.74	0.746	**39**	-239.540	239.54	1.000
20	-54.545+31.492i	62.98	0.866				

Table A.7. – DPI Augmentation (simple aircraft model, discrete-time integrators): Poles of linearized closed-loop model for transfer function $\alpha_{cmd} \rightarrow \alpha$ at envelope point $V = 154.94\frac{m}{s}$ and $h = 5000m$ considering additional time delay of $2.475s$ upstream the actuator, which corresponds to a phase disturbance of 87.92° at $\omega_{gc} = 0.62\frac{rad}{s}$. The phase disturbance is chosen slightly higher than the determined phase margin of the closed-loop at this envelope point (87.23°) and thus the closed-loop is unstable (c.f. poles 7 and 8)

	Poles $[-]$	ω_0 $\left[\frac{rad}{s}\right]$	ζ $[-]$
1	3.40e-13	3.40e-13	-1.000
2	-3.42e-13+2.34e-13i	4.14e-13	0.825
3	-3.42e-13-2.34e-13i	4.14e-13	0.825
4	-0.001	1.46e-03	1.000
5	-0.013+0.095i	0.10	0.139
6	-0.013-0.095i	0.10	0.139
7	0.001+0.620i	0.62	-0.001
8	0.001-0.620i	0.62	-0.001
9	-0.701+2.387i	2.49	0.282
10	-0.701-2.387i	2.49	0.282
11	-6.991	6.99	1.000
12	-7.000	7.00	1.000
13	-8.924+6.170i	10.85	0.823
14	-8.924-6.170i	10.85	0.823
15	-20.350+27.669i	34.35	0.592
16	-20.350-27.669i	34.35	0.592
17	-28.400+28.168i	40.00	0.710
18	-28.400-28.168i	40.00	0.710
19	-36.337+28.239i	46.02	0.790
20	-36.337-28.239i	46.02	0.790
21	-49.961+20.418i	53.97	0.926
22	-49.961-20.418i	53.97	0.926
23	-54.545+31.492i	62.98	0.866
24	-54.545-31.492i	62.98	0.866
25	-60.134+45.048i	75.14	0.800
26	-60.134-45.048i	75.14	0.800
27	-75.253	75.25	1.000
28	-192.365	192.36	1.000
29	-199.887	199.89	1.000
30	-209.440	209.44	1.000
31	-209.440	209.44	1.000
32	-209.440	209.44	1.000
33	-209.440	209.44	1.000
34	-209.440	209.44	1.000
35	-209.440	209.44	1.000
36	-209.440	209.44	1.000
37	-209.440	209.44	1.000
38	-209.440+0.000i	209.44	1.000
39	-209.440-0.000i	209.44	1.000
40	-209.440	209.44	1.000
41	-214.342	214.34	1.000

Table A.8. – DPI Augmentation (simple aircraft model, continuous integrators): Poles of linearized closed-loop model for transfer function $\alpha_{cmd} \rightarrow \alpha$ at envelope point $V = 154.94\frac{m}{s}$ and $h = 5000m$

	Poles $[-]$	$\omega_0 \left[\frac{rad}{s}\right]$	$\zeta\ [-]$
1	2.41e-14	2.41e-14	-1.000
2	-2.49e-14	2.49e-14	1.000
3	7.70e-13	7.70e-13	-1.000
4	-0.001	1.46e-03	1.000
5	-0.013+0.095i	0.10	0.140
6	-0.013-0.095i	0.10	0.140
7	-1.002	1.00	1.000
8	-3.641+1.216i	3.84	0.948
9	-3.641-1.216i	3.84	0.948
10	-6.999	7.00	1.000
11	-7.000	7.00	1.000
12	-15.000	15.00	1.000
13	-25.695	25.70	1.000
14	-24.453+27.203i	36.58	0.669
15	-24.453-27.203i	36.58	0.669
16	-28.400+28.168i	40.00	0.710
17	-28.400-28.168i	40.00	0.710
18	-46.303	46.30	1.000
19	-44.083+37.111i	57.62	0.765
20	-44.083-37.111i	57.62	0.765
21	-54.545+31.492i	62.98	0.866
22	-54.545-31.492i	62.98	0.866
23	-55.955+38.960i	68.18	0.821
24	-55.955-38.960i	68.18	0.821
25	-77.706	77.71	1.000
26	-100.233+1.433i	100.24	1.000
27	-100.233-1.433i	100.24	1.000
28	-105.935	105.94	1.000
29	-209.440+0.000i	209.44	1.000
30	-209.440-0.000i	209.44	1.000
31	-209.440	209.44	1.000
32	-209.440	209.44	1.000
33	-209.440	209.44	1.000
34	-209.440	209.44	1.000
35	-209.440	209.44	1.000
36	-209.440	209.44	1.000
37	-209.440	209.44	1.000
38	-209.440	209.44	1.000
39	-209.440	209.44	1.000

Table A.9. – DPI Augmentation (enhanced aircraft model, discrete-time integrators): Poles of linearized closed-loop model for transfer function $\alpha_{cmd} \rightarrow \alpha$ at envelope point $V = 154.94\frac{m}{s}$ and $h = 5000m$

	Poles $[-]$	ω_0 $\left[\frac{rad}{s}\right]$	ζ $[-]$		Poles $[-]$	ω_0 $\left[\frac{rad}{s}\right]$	ζ $[-]$
1	-7.62e-14	7.62e-14	1.000	**37**	-7.540-36.937i	37.70	0.200
2	1.79e-13	1.79e-13	-1.000	**38**	-7.540+36.937i	37.70	0.200
3	-9.44e-13	9.44e-13	1.000	**39**	-7.540-36.937i	37.70	0.200
4	-0.001	1.46e-03	1.000	**40**	-7.499+36.954i	37.71	0.199
5	-0.014+0.095i	0.10	0.146	**41**	-7.499-36.954i	37.71	0.199
6	-0.014-0.095i	0.10	0.146	**42**	-7.458+37.480i	38.22	0.195
7	-0.966	0.97	1.000	**43**	-7.458-37.480i	38.22	0.195
8	-3.118	3.12	1.000	**44**	-28.404+28.160i	40.00	0.710
9	-3.073+2.340i	3.86	0.796	**45**	-28.404-28.160i	40.00	0.710
10	-3.073-2.340i	3.86	0.796	**46**	-28.400+28.168i	40.00	0.710
11	-6.988	6.99	1.000	**47**	-28.400-28.168i	40.00	0.710
12	-7.000	7.00	1.000	**48**	-27.627+29.832i	40.66	0.679
13	-9.899+9.899i	14.00	0.707	**49**	-27.627-29.832i	40.66	0.679
14	-9.899-9.899i	14.00	0.707	**50**	-77.394	77.39	1.000
15	-9.899+9.899i	14.00	0.707	**51**	-200.196	200.20	1.000
16	-9.899-9.899i	14.00	0.707	**52**	-200.305+7.090i	200.43	0.999
17	-9.899+9.899i	14.00	0.707	**53**	-200.305-7.090i	200.43	0.999
18	-9.899-9.899i	14.00	0.707	**54**	-204.348	204.35	1.000
19	-14.036	14.04	1.000	**55**	-209.440+0.000i	209.44	1.000
20	-10.025+9.933i	14.11	0.710	**56**	-209.440-0.000i	209.44	1.000
21	-10.025-9.933i	14.11	0.710	**57**	-209.440+0.000i	209.44	1.000
22	-14.129	14.13	1.000	**58**	-209.440-0.000i	209.44	1.000
23	-8.421+11.789i	14.49	0.581	**59**	-209.440	209.44	1.000
24	-8.421-11.789i	14.49	0.581	**60**	-209.440	209.44	1.000
25	-19.820	19.82	1.000	**61**	-209.440	209.44	1.000
26	-19.820	19.82	1.000	**62**	-209.440	209.44	1.000
27	-32.149	32.15	1.000	**63**	-209.440	209.44	1.000
28	-7.457+36.337i	37.09	0.201	**64**	-209.440	209.44	1.000
29	-7.457-36.337i	37.09	0.201	**65**	-209.440	209.44	1.000
30	-7.582+36.920i	37.69	0.201	**66**	-200.000+115.470i	230.94	0.866
31	-7.582-36.920i	37.69	0.201	**67**	-200.000-115.470i	230.94	0.866
32	-7.540+36.937i	37.70	0.200	**68**	-200.000+115.470i	230.94	0.866
33	-7.540-36.937i	37.70	0.200	**69**	-200.000-115.470i	230.94	0.866
34	-7.540+36.937i	37.70	0.200	**70**	-200.007+115.461i	230.94	0.866
35	-7.540-36.937i	37.70	0.200	**71**	-200.007-115.461i	230.94	0.866
36	-7.540+36.937i	37.70	0.200				

Table A.10. – DPI Augmentation (enhanced aircraft model, continuous integrators): Poles of linearized closed-loop model for transfer function $\alpha_{cmd} \rightarrow \alpha$ at envelope point $V = 154.94\frac{m}{s}$ and $h = 5000m$

	Poles $[-]$	$\omega_0 \left[\frac{rad}{s}\right]$	$\zeta\ [-]$		Poles $[-]$	$\omega_0 \left[\frac{rad}{s}\right]$	$\zeta\ [-]$
1	3.36e-14	3.36e-14	-1.000	**36**	-7.540+36.937i	37.70	0.200
2	-4.50e-14+1.84e-13i	1.90e-13	0.237	**37**	-7.540-36.937i	37.70	0.200
3	-4.50e-14-1.84e-13i	1.90e-13	0.237	**38**	-7.540+36.937i	37.70	0.200
4	-0.001	1.46e-03	1.000	**39**	-7.540-36.937i	37.70	0.200
5	-0.014+0.095i	0.10	0.146	**40**	-7.523+37.036i	37.79	0.199
6	-0.014-0.095i	0.10	0.146	**41**	-7.523-37.036i	37.79	0.199
7	-1.002	1.00	1.000	**42**	-7.426+37.056i	37.79	0.196
8	-3.587+1.226i	3.79	0.946	**43**	-7.426-37.056i	37.79	0.196
9	-3.587-1.226i	3.79	0.946	**44**	-28.364+28.077i	39.91	0.711
10	-4.724	4.72	1.000	**45**	-28.364-28.077i	39.91	0.711
11	-7.000	7.00	1.000	**46**	-28.367+28.195i	40.00	0.709
12	-7.002	7.00	1.000	**47**	-28.367-28.195i	40.00	0.709
13	-9.740+9.849i	13.85	0.703	**48**	-28.400+28.168i	40.00	0.710
14	-9.740-9.849i	13.85	0.703	**49**	-28.400-28.168i	40.00	0.710
15	-9.899+9.899i	14.00	0.707	**50**	-77.589	77.59	1.000
16	-9.899-9.899i	14.00	0.707	**51**	-100.043	100.04	1.000
17	-9.899+9.899i	14.00	0.707	**52**	-100.653+1.701i	100.67	1.000
18	-9.899-9.899i	14.00	0.707	**53**	-100.653-1.701i	100.67	1.000
19	-9.899+9.899i	14.00	0.707	**54**	-209.440	209.44	1.000
20	-9.899-9.899i	14.00	0.707	**55**	-209.440	209.44	1.000
21	-14.153	14.15	1.000	**56**	-209.440	209.44	1.000
22	-14.153	14.15	1.000	**57**	-209.440	209.44	1.000
23	-14.153	14.15	1.000	**58**	-209.440	209.44	1.000
24	-14.636	14.64	1.000	**59**	-209.440	209.44	1.000
25	-11.877+8.826i	14.80	0.803	**60**	-209.440	209.44	1.000
26	-11.877-8.826i	14.80	0.803	**61**	-209.440	209.44	1.000
27	-14.919	14.92	1.000	**62**	-209.440	209.44	1.000
28	-7.658+36.805i	37.59	0.204	**63**	-209.440	209.44	1.000
29	-7.658-36.805i	37.59	0.204	**64**	-209.440	209.44	1.000
30	-7.552+36.836i	37.60	0.201	**65**	-200.000+115.470i	230.94	0.866
31	-7.552-36.836i	37.60	0.201	**66**	-200.000-115.470i	230.94	0.866
32	-7.540+36.937i	37.70	0.200	**67**	-200.000+115.470i	230.94	0.866
33	-7.540-36.937i	37.70	0.200	**68**	-200.000-115.470i	230.94	0.866
34	-7.540+36.937i	37.70	0.200	**69**	-200.000+115.470i	230.94	0.866
35	-7.540-36.937i	37.70	0.200	**70**	-200.000-115.470i	230.94	0.866

A.4.3. Plant Augmentation

Table A.11. – Plant Augmentation (simple aircraft model, discrete-time integrators): Poles of linearized closed-loop model for transfer function $\alpha_{cmd} \rightarrow \alpha$ at envelope point $V = 154.94\frac{m}{s}$ and $h = 5000m$

	Poles $[-]$	$\omega_0 \left[\frac{rad}{s}\right]$	ζ $[-]$		Poles $[-]$	$\omega_0 \left[\frac{rad}{s}\right]$	ζ $[-]$
1	-0.001	1.46e-03	1.000	**12**	-58.336-40.672i	71.11	0.820
2	-0.015+0.095i	0.10	0.151	**13**	-79.013	79.01	1.000
3	-0.015-0.095i	0.10	0.151	**14**	-196.506	196.51	1.000
4	-1.004	1.00	1.000	**15**	-209.423	209.42	1.000
5	-3.815	3.82	1.000	**16**	-209.440	209.44	1.000
6	-5.948+1.130i	6.05	0.982	**17**	-209.440	209.44	1.000
7	-5.948-1.130i	6.05	0.982	**18**	-209.440	209.44	1.000
8	-6.896	6.90	1.000	**19**	-209.440	209.44	1.000
9	-23.954+25.520i	35.00	0.684	**20**	-209.440	209.44	1.000
10	-23.954-25.520i	35.00	0.684	**21**	-209.440	209.44	1.000
11	-58.336+40.672i	71.11	0.820				

Table A.12. – Plant Augmentation (simple aircraft model, continuous integrators): Poles of linearized closed-loop model for transfer function $\alpha_{cmd} \rightarrow \alpha$ at envelope point $V = 154.94\frac{m}{s}$ and $h = 5000m$

	Poles $[-]$	$\omega_0 \left[\frac{rad}{s}\right]$	ζ $[-]$		Poles $[-]$	$\omega_0 \left[\frac{rad}{s}\right]$	ζ $[-]$
1	-0.001	1.46e-03	1.000	**12**	-44.073-37.109i	57.62	0.765
2	-0.016+0.095i	0.10	0.165	**13**	-77.657	77.66	1.000
3	-0.016-0.095i	0.10	0.165	**14**	-100.644+1.697i	100.66	1.000
4	-1.001	1.00	1.000	**15**	-100.644-1.697i	100.66	1.000
5	-3.653+1.192i	3.84	0.951	**16**	-209.440	209.44	1.000
6	-3.653-1.192i	3.84	0.951	**17**	-209.440	209.44	1.000
7	-6.968	6.97	1.000	**18**	-209.440	209.44	1.000
8	-15.001	15.00	1.000	**19**	-209.440	209.44	1.000
9	-25.661	25.66	1.000	**20**	-209.440	209.44	1.000
10	-46.395	46.40	1.000	**21**	-209.440	209.44	1.000
11	-44.073+37.109i	57.62	0.765				

Table A.13. – Plant Augmentation (enhanced aircraft model, discrete-time integrators): Poles of linearized closed-loop model for transfer function $\alpha_{cmd} \rightarrow \alpha$ at envelope point $V = 154.94\frac{m}{s}$ and $h = 5000m$

	Poles $[-]$	ω_0 $\left[\frac{rad}{s}\right]$	ζ $[-]$		Poles $[-]$	ω_0 $\left[\frac{rad}{s}\right]$	ζ $[-]$
1	-0.001	1.46e-03	1.000	**21**	-7.540-36.937i	37.70	0.200
2	-0.014+0.095i	0.10	0.146	**22**	-7.540+36.937i	37.70	0.200
3	-0.014-0.095i	0.10	0.146	**23**	-7.540-36.937i	37.70	0.200
4	-0.966	0.97	1.000	**24**	-7.462+37.475i	38.21	0.195
5	-3.108	3.11	1.000	**25**	-7.462-37.475i	38.21	0.195
6	-3.057+2.337i	3.85	0.794	**26**	-27.654+29.809i	40.66	0.680
7	-3.057-2.337i	3.85	0.794	**27**	-27.654-29.809i	40.66	0.680
8	-6.992	6.99	1.000	**28**	-77.408	77.41	1.000
9	-9.899+9.899i	14.00	0.707	**29**	-200.425+6.993i	200.55	0.999
10	-9.899-9.899i	14.00	0.707	**30**	-200.425-6.993i	200.55	0.999
11	-9.899+9.899i	14.00	0.707	**31**	-204.100	204.10	1.000
12	-9.899-9.899i	14.00	0.707	**32**	-209.440	209.44	1.000
13	-8.527+11.851i	14.60	0.584	**33**	-209.440	209.44	1.000
14	-8.527-11.851i	14.60	0.584	**34**	-209.440	209.44	1.000
15	-19.820	19.82	1.000	**35**	-209.440	209.44	1.000
16	-19.820	19.82	1.000	**36**	-209.440	209.44	1.000
17	-32.070	32.07	1.000	**37**	-209.440	209.44	1.000
18	-7.457+36.346i	37.10	0.201	**38**	-200.008+115.461i	230.94	0.866
19	-7.457-36.346i	37.10	0.201	**39**	-200.008-115.461i	230.94	0.866
20	-7.540+36.937i	37.70	0.200				

Table A.14. – Plant Augmentation (enhanced aircraft model, continuous integrators): Poles of linearized closed-loop model for transfer function $\alpha_{cmd} \rightarrow \alpha$ at envelope point $V = 154.94\frac{m}{s}$ and $h = 5000m$

	Poles $[-]$	$\omega_0 \left[\frac{rad}{s}\right]$	$\zeta\ [-]$		Poles $[-]$	$\omega_0 \left[\frac{rad}{s}\right]$	$\zeta\ [-]$
1	-0.001	1.46e-03	1.000	**20**	-7.540+36.937i	37.70	0.200
2	-0.016+0.095i	0.10	0.171	**21**	-7.540-36.937i	37.70	0.200
3	-0.016-0.095i	0.10	0.171	**22**	-7.540+36.937i	37.70	0.200
4	-1.000	1.00	1.000	**23**	-7.540-36.937i	37.70	0.200
5	-3.710+1.227i	3.91	0.949	**24**	-7.426+37.056i	37.79	0.196
6	-3.710-1.227i	3.91	0.949	**25**	-7.426-37.056i	37.79	0.196
7	-4.346	4.35	1.000	**26**	-28.364+28.077i	39.91	0.711
8	-7.140	7.14	1.000	**27**	-28.364-28.077i	39.91	0.711
9	-9.899+9.899i	14.00	0.707	**28**	-77.589	77.59	1.000
10	-9.899-9.899i	14.00	0.707	**29**	-100.651+1.697i	100.67	1.000
11	-9.899+9.899i	14.00	0.707	**30**	-100.651-1.697i	100.67	1.000
12	-9.899-9.899i	14.00	0.707	**31**	-209.440	209.44	1.000
13	-14.153	14.15	1.000	**32**	-209.440	209.44	1.000
14	-14.153	14.15	1.000	**33**	-209.440	209.44	1.000
15	-11.875+8.827i	14.80	0.803	**34**	-209.440	209.44	1.000
16	-11.875-8.827i	14.80	0.803	**35**	-209.440	209.44	1.000
17	-14.999	15.00	1.000	**36**	-209.440	209.44	1.000
18	-7.659+36.805i	37.59	0.204	**37**	-200.000+115.470i	230.94	0.866
19	-7.659-36.805i	37.59	0.204	**38**	-200.000-115.470i	230.94	0.866

A.4.4. $\Delta\dot{q}$ Compensation Law

Table A.15. – $\Delta\dot{q}$ Compensation (simple aircraft model, discrete-time integrators): Poles of linearized closed-loop model for transfer function $\alpha_{cmd} \rightarrow \alpha$ at envelope point $V = 154.94\frac{m}{s}$ and $h = 5000m$

	Poles $[-]$	ω_0 $\left[\frac{rad}{s}\right]$	ζ $[-]$
1	-0.001	1.46e-03	1.000
2	-0.016+0.095i	0.10	0.166
3	-0.016-0.095i	0.10	0.166
4	-1.001	1.00	1.000
5	-3.396+1.276i	3.63	0.936
6	-3.396-1.276i	3.63	0.936
7	-12.249+10.797i	16.33	0.750
8	-12.249-10.797i	16.33	0.750
9	-36.708+45.960i	58.82	0.624
10	-36.708-45.960i	58.82	0.624
11	-82.451	82.45	1.000
12	-206.813	206.81	1.000
13	-209.440	209.44	1.000
14	-209.440	209.44	1.000
15	-209.440	209.44	1.000
16	-209.440	209.44	1.000
17	-209.440	209.44	1.000

Table A.16. – $\Delta\dot{q}$ Compensation (simple aircraft model, continuous integrators): Poles of linearized closed-loop model for transfer function $\alpha_{cmd} \rightarrow \alpha$ at envelope point $V = 154.94\frac{m}{s}$ and $h = 5000m$

	Poles $[-]$	ω_0 $\left[\frac{rad}{s}\right]$	ζ $[-]$
1	-0.001	1.46e-03	1.000
2	-0.016+0.095i	0.10	0.166
3	-0.016-0.095i	0.10	0.166
4	-1.001	1.00	1.000
5	-3.396+1.276i	3.63	0.936
6	-3.396-1.276i	3.63	0.936
7	-12.249+10.797i	16.33	0.750
8	-12.249-10.797i	16.33	0.750
9	-36.708+45.960i	58.82	0.624
10	-36.708-45.960i	58.82	0.624
11	-82.451	82.45	1.000
12	-206.813	206.81	1.000
13	-209.440	209.44	1.000
14	-209.440	209.44	1.000
15	-209.440	209.44	1.000
16	-209.440	209.44	1.000
17	-209.440	209.44	1.000

Table A.17. – $\Delta\dot{q}$ Compensation (enhanced aircraft model, discrete-time integrators): Poles of linearized closed-loop model for transfer function $\alpha_{cmd} \rightarrow \alpha$ at envelope point $V = 154.94\frac{m}{s}$ and $h = 5000m$

	Poles $[-]$	ω_0 $\left[\frac{rad}{s}\right]$	ζ $[-]$
1	-0.001	1.46e-03	1.000
2	-0.017+0.095i	0.10	0.172
3	-0.017-0.095i	0.10	0.172
4	-0.961	0.96	1.000
5	-2.771+1.479i	3.14	0.882
6	-2.771-1.479i	3.14	0.882
7	-12.060	12.06	1.000
8	-11.721+6.337i	13.32	0.880
9	-11.721-6.337i	13.32	0.880
10	-9.899+9.899i	14.00	0.707
11	-9.899-9.899i	14.00	0.707
12	-9.899+9.899i	14.00	0.707
13	-9.899-9.899i	14.00	0.707
14	-17.468	17.47	1.000
15	-19.820	19.82	1.000
16	-19.820	19.82	1.000
17	-7.681+36.752i	37.55	0.205
18	-7.681-36.752i	37.55	0.205
19	-7.540+36.937i	37.70	0.200
20	-7.540-36.937i	37.70	0.200
21	-7.540+36.937i	37.70	0.200
22	-7.540-36.937i	37.70	0.200
23	-7.403+37.098i	37.83	0.196
24	-7.403-37.098i	37.83	0.196
25	-28.289+28.036i	39.83	0.710
26	-28.289-28.036i	39.83	0.710
27	-199.983	199.98	1.000
28	-209.440	209.44	1.000
29	-209.440	209.44	1.000
30	-209.440	209.44	1.000
31	-209.440	209.44	1.000
32	-209.440	209.44	1.000
33	-209.453	209.45	1.000
34	-200.000+115.470i	230.94	0.866
35	-200.000-115.470i	230.94	0.866

Table A.18. – $\Delta\dot{q}$ Compensation (enhanced aircraft model, continuous integrators): Poles of linearized closed-loop model for transfer function $\alpha_{cmd} \rightarrow \alpha$ at envelope point $V = 154.94\frac{m}{s}$ and $h = 5000m$

	Poles $[-]$	$\omega_0 \left[\frac{rad}{s}\right]$	ζ $[-]$		Poles $[-]$	$\omega_0 \left[\frac{rad}{s}\right]$	ζ $[-]$
1	-0.001	1.46e-03	1.000	**18**	-7.958-36.820i	37.67	0.211
2	-0.017+0.095i	0.10	0.172	**19**	-7.540+36.937i	37.70	0.200
3	-0.017-0.095i	0.10	0.172	**20**	-7.540-36.937i	37.70	0.200
4	-1.001	1.00	1.000	**21**	-7.540+36.937i	37.70	0.200
5	-2.924+1.108i	3.13	0.935	**22**	-7.540-36.937i	37.70	0.200
6	-2.924-1.108i	3.13	0.935	**23**	-7.201+37.038i	37.73	0.191
7	-6.420+4.814i	8.02	0.800	**24**	-7.201-37.038i	37.73	0.191
8	-6.420-4.814i	8.02	0.800	**25**	-28.595+27.368i	39.58	0.722
9	-9.899+9.899i	14.00	0.707	**26**	-28.595-27.368i	39.58	0.722
10	-9.899-9.899i	14.00	0.707	**27**	-209.440	209.44	1.000
11	-9.899+9.899i	14.00	0.707	**28**	-209.440	209.44	1.000
12	-9.899-9.899i	14.00	0.707	**29**	-209.440	209.44	1.000
13	-14.153	14.15	1.000	**30**	-209.440	209.44	1.000
14	-14.153	14.15	1.000	**31**	-209.440	209.44	1.000
15	-16.674+11.331i	20.16	0.827	**32**	-209.444	209.44	1.000
16	-16.674-11.331i	20.16	0.827	**33**	-200.001+115.471i	230.94	0.866
17	-7.958+36.820i	37.67	0.211	**34**	-200.001-115.471i	230.94	0.866

A.4.5. L1 adaptive controller with Eigenstructure Assignment

Table A.19. – L1 Standalone (simple aircraft model, discrete-time integrators): Poles of linearized closed-loop model for transfer function $\alpha_{cmd} \rightarrow \alpha$ at envelope point $V = 154.94\frac{m}{s}$ and $h = 5000m$

	Poles $[-]$	$\omega_0 \left[\frac{rad}{s}\right]$	$\zeta\ [-]$
1	-0.001	1.46e-03	1.000
2	-0.018+0.087i	0.09	0.205
3	-0.018-0.087i	0.09	0.205
4	-3.415	3.42	1.000
5	-3.880+2.271i	4.50	0.863
6	-3.880-2.271i	4.50	0.863
7	-8.814	8.81	1.000
8	-19.055+30.869i	36.28	0.525
9	-19.055-30.869i	36.28	0.525
10	-74.666	74.67	1.000
11	-64.527+48.318i	80.61	0.800
12	-64.527-48.318i	80.61	0.800
13	-206.732+16.085i	207.36	0.997
14	-206.732-16.085i	207.36	0.997

Table A.20. – L1 Standalone (simple aircraft model, continuous integrators): Poles of linearized closed-loop model for transfer function $\alpha_{cmd} \rightarrow \alpha$ at envelope point $V = 154.94\frac{m}{s}$ and $h = 5000m$

	Poles $[-]$	$\omega_0 \left[\frac{rad}{s}\right]$	$\zeta\ [-]$
1	-0.001	1.46e-03	1.000
2	-0.018+0.087i	0.09	0.205
3	-0.018-0.087i	0.09	0.205
4	-3.615+1.204i	3.81	0.949
5	-3.615-1.204i	3.81	0.949
6	-7.055+0.654i	7.08	0.996
7	-7.055-0.654i	7.08	0.996
8	-28.407+30.199i	41.46	0.685
9	-28.407-30.199i	41.46	0.685
10	-56.541+31.745i	64.84	0.872
11	-56.541-31.745i	64.84	0.872
12	-74.761	74.76	1.000
13	-101.960+4.694i	102.07	0.999
14	-101.960-4.694i	102.07	0.999

Table A.21. – L1 Standalone (enhanced aircraft model, discrete-time integrators): Poles of linearized closed-loop model for transfer function $\alpha_{cmd} \rightarrow \alpha$ at envelope point $V = 154.94\frac{m}{s}$ and $h = 5000m$

	Poles $[-]$	ω_0 $\left[\frac{rad}{s}\right]$	ζ $[-]$		Poles $[-]$	ω_0 $\left[\frac{rad}{s}\right]$	ζ $[-]$
1	-0.001	1.46e-03	1.000	**17**	-7.371+36.235i	36.98	0.199
2	-0.018+0.096i	0.10	0.187	**18**	-7.371-36.235i	36.98	0.199
3	-0.018-0.096i	0.10	0.187	**19**	-7.540+36.937i	37.70	0.200
4	-3.306	3.31	1.000	**20**	-7.540-36.937i	37.70	0.200
5	-3.083+2.233i	3.81	0.810	**21**	-7.540+36.937i	37.70	0.200
6	-3.083-2.233i	3.81	0.810	**22**	-7.540-36.937i	37.70	0.200
7	-8.447	8.45	1.000	**23**	-7.464+37.591i	38.32	0.195
8	-9.899+9.899i	14.00	0.707	**24**	-7.464-37.591i	38.32	0.195
9	-9.899-9.899i	14.00	0.707	**25**	-27.800+30.487i	41.26	0.674
10	-9.899+9.899i	14.00	0.707	**26**	-27.800-30.487i	41.26	0.674
11	-9.899-9.899i	14.00	0.707	**27**	-78.165	78.17	1.000
12	-7.536+12.299i	14.42	0.522	**28**	-192.691	192.69	1.000
13	-7.536-12.299i	14.42	0.522	**29**	-205.842+7.635i	205.98	0.999
14	-19.820	19.82	1.000	**30**	-205.842-7.635i	205.98	0.999
15	-19.820	19.82	1.000	**31**	-200.017+115.471i	230.96	0.866
16	-32.651	32.65	1.000	**32**	-200.017-115.471i	230.96	0.866

Table A.22. – L1 Standalone (enhanced aircraft model, continuous integrators): Poles of linearized closed-loop model for transfer function $\alpha_{cmd} \rightarrow \alpha$ at envelope point $V = 154.94\frac{m}{s}$ and $h = 5000m$

	Poles $[-]$	ω_0 $\left[\frac{rad}{s}\right]$	ζ $[-]$
1	-0.001	1.46e-03	1.000
2	-0.018+0.096i	0.10	0.187
3	-0.018-0.096i	0.10	0.187
4	-3.596+1.184i	3.79	0.950
5	-3.596-1.184i	3.79	0.950
6	-6.566+0.798i	6.61	0.993
7	-6.566-0.798i	6.61	0.993
8	-9.899+9.899i	14.00	0.707
9	-9.899-9.899i	14.00	0.707
10	-9.899+9.899i	14.00	0.707
11	-9.899-9.899i	14.00	0.707
12	-10.795+9.117i	14.13	0.764
13	-10.795-9.117i	14.13	0.764
14	-14.153	14.15	1.000
15	-14.153	14.15	1.000
16	-16.696	16.70	1.000
17	-7.570+36.868i	37.64	0.201
18	-7.570-36.868i	37.64	0.201
19	-7.540+36.937i	37.70	0.200
20	-7.540-36.937i	37.70	0.200
21	-7.540+36.937i	37.70	0.200
22	-7.540-36.937i	37.70	0.200
23	-7.509+37.004i	37.76	0.199
24	-7.509-37.004i	37.76	0.199
25	-28.390+28.150i	39.98	0.710
26	-28.390-28.150i	39.98	0.710
27	-77.587	77.59	1.000
28	-100.597+1.206i	100.60	1.000
29	-100.597-1.206i	100.60	1.000
30	-200.000+115.470i	230.94	0.866
31	-200.000-115.470i	230.94	0.866

A.5. Robust stability of control laws (basic aircraft model)

A.5.1. Comparison between DPI and Plant Augmentation

Page intentionally left blank

Table A.23. – Robust stability properties gain margin (GM), phase margin Φ_m, time delay margins (TDM) and corresponding gain-crossover frequencies $\omega_{gc,\Phi}$ and $\omega_{gc,TDM}$ for robust stability comparison of DPI and Plant Augmentation with and without hedging at $V = 154.94\frac{m}{s}$ generated for α loop cut (basic aircraft model)

Controller	**GM** $[dB]$	$\Phi_m\,[^\circ]$	$\omega_{gc,\Phi}\left[\frac{rad}{s}\right]$	**TDM** $[s]$	$\omega_{gc,TDM}\left[\frac{rad}{s}\right]$
Baseline	12.69	70.24	0.55	2.239	0.55
	$-\infty$	-289.76	0.55	-9.235	0.55
DPI Augmentation	5.25	57.43	0.92	1.091	0.92
	-13.29	-302.57	0.92	-5.749	0.92
DPI Augmentation (no hedg.)	5.25	57.43	0.92	1.091	0.92
	-13.29	-302.57	0.92	-5.749	0.92
Plant Augmentation	6.99	59.52	1.16	0.898	1.16
	-14.58	-300.48	1.16	-4.533	1.16
Plant Augmentation (no hedg.)	6.99	59.52	1.16	0.898	1.16
	-14.58	-300.48	1.16	-4.533	1.16

Table A.24. – Robust stability properties gain margin (GM), phase margin Φ_m, time delay margins (TDM) and corresponding gain-crossover frequencies $\omega_{gc,\Phi}$ and $\omega_{gc,TDM}$ for robust stability comparison of DPI and Plant Augmentation with and without hedging at $V = 154.94\frac{m}{s}$ generated for q loop cut (basic aircraft model)

Controller	**GM** $[dB]$	$\Phi_m\,[^\circ]$	$\omega_{gc,\Phi}\left[\frac{rad}{s}\right]$	**TDM** $[s]$	$\omega_{gc,TDM}\left[\frac{rad}{s}\right]$
Baseline	15.54	101.74	4.39	0.404	4.39
	$-\infty$	-137.46	1.92	-1.026	4.39
DPI Augmentation	6.13	29.35	8.20	0.062	8.20
	-5.62	-65.95	0.93	-0.704	8.20
DPI Augmentation (no hedg.)	6.13	29.35	8.20	0.062	8.20
	-5.62	-65.95	0.93	-0.704	8.20
Plant Augmentation	6.62	34.07	8.41	0.071	8.41
	-7.30	-71.97	1.14	-0.676	8.41
Plant Augmentation (no hedg.)	6.62	34.07	8.41	0.071	8.41
	-7.30	-71.97	1.14	-0.676	8.41

A.5.2. Baseline Controller

Page intentionally left blank

Table A.25. – Robust stability properties gain margin (GM), phase margin Φ_m, time delay margins (TDM) and corresponding gain-crossover frequencies $\omega_{gc,\Phi}$ and $\omega_{gc,TDM}$ for robust stability assessment of baseline controller at envelope points according to Table 2.2 generated for α loop cut (basic aircraft model)

Velocity $V\ \left[\frac{m}{s}\right]$	**GM** $[dB]$	$\Phi_m\ [^\circ]$	$\omega_{gc,\Phi}\ \left[\frac{rad}{s}\right]$	**TDM** $[s]$	$\omega_{gc,TDM}\ \left[\frac{rad}{s}\right]$
102.88	22.51	73.46	0.59	2.181	0.59
	$-\infty$	-286.54	0.59	-8.507	0.59
110.32	19.95	73.01	0.58	2.209	0.58
	$-\infty$	-286.99	0.58	-8.681	0.58
117.75	17.86	72.41	0.57	2.230	0.57
	$-\infty$	-287.59	0.57	-8.857	0.57
125.19	16.35	72.02	0.56	2.237	0.56
	$-\infty$	-287.98	0.56	-8.947	0.56
132.63	15.15	71.58	0.56	2.240	0.56
	$-\infty$	-288.42	0.56	-9.025	0.56
140.07	14.18	71.13	0.55	2.241	0.55
	$-\infty$	-288.87	0.55	-9.099	0.55
147.50	13.37	70.68	0.55	2.240	0.55
	$-\infty$	-289.32	0.55	-9.169	0.55
154.94	12.69	70.24	0.55	2.239	0.55
	$-\infty$	-289.76	0.55	-9.235	0.55
162.38	12.10	69.80	0.54	2.236	0.54
	$-\infty$	-290.20	0.54	-9.298	0.54
169.81	11.60	69.38	0.54	2.234	0.54
	$-\infty$	-290.62	0.54	-9.357	0.54
177.25	11.16	68.97	0.54	2.231	0.54
	$-\infty$	-291.03	0.54	-9.414	0.54
184.69	10.78	68.57	0.54	2.228	0.54
	$-\infty$	-291.43	0.54	-9.468	0.54
192.13	10.41	68.35	0.53	2.240	0.53
	$-\infty$	-291.65	0.53	-9.557	0.53
199.56	10.15	68.05	0.53	2.235	0.53
	$-\infty$	-291.95	0.53	-9.587	0.53
207.00	9.91	67.74	0.53	2.229	0.53
	$-\infty$	-292.26	0.53	-9.617	0.53

Table A.26. – Robust stability properties gain margin (GM), phase margin Φ_m, time delay margins (TDM) and corresponding gain-crossover frequencies $\omega_{gc,\Phi}$ and $\omega_{gc,TDM}$ for robust stability assessment of baseline controller at envelope points according to Table 2.2 generated for q loop cut (basic aircraft model)

Velocity $V\ \left[\frac{m}{s}\right]$	**GM** $[dB]$	$\Phi_m\ [^\circ]$	$\omega_{gc,\Phi}\ \left[\frac{rad}{s}\right]$	**TDM** $[s]$	$\omega_{gc,TDM}\ \left[\frac{rad}{s}\right]$
102.88	11.84	90.09	3.86	0.407	3.86
	$-\infty$	-113.27	1.34	-1.220	3.86
110.32	12.97	91.03	3.97	0.400	3.97
	$-\infty$	-116.45	1.41	-1.181	3.97
117.75	14.30	92.37	4.06	0.397	4.06
	$-\infty$	-119.01	1.49	-1.151	4.06
125.19	15.64	93.77	4.15	0.395	4.15
	$-\infty$	-122.41	1.57	-1.120	4.15
132.63	15.78	95.37	4.23	0.394	4.23
	$-\infty$	-125.92	1.65	-1.093	4.23
140.07	15.68	97.21	4.29	0.395	4.29
	$-\infty$	-129.52	1.73	-1.068	4.29
147.50	15.60	99.45	4.36	0.398	4.36
	$-\infty$	-133.48	1.83	-1.044	4.36
154.94	15.54	101.74	4.39	0.404	4.39
	$-\infty$	-137.46	1.92	-1.026	4.39
162.38	15.50	104.62	4.42	0.413	4.42
	$-\infty$	-141.85	2.03	-1.007	4.42
169.81	15.48	107.71	4.44	0.424	4.44
	$-\infty$	-146.42	2.15	-0.993	4.44
177.25	15.47	111.37	4.43	0.439	4.43
	$-\infty$	-151.66	2.28	-0.979	4.43
184.69	15.48	115.75	4.40	0.459	4.40
	$-\infty$	-157.35	2.43	-0.968	4.40
192.13	15.51	121.16	4.33	0.488	4.33
	$-\infty$	-164.32	2.60	-0.962	4.33
199.56	15.54	127.48	4.24	0.524	4.24
	$-\infty$	-171.88	2.80	-0.956	4.24
207.00	15.58	136.34	4.08	0.583	4.08
	$-\infty$	-182.22	3.07	-0.956	4.08

A.5.3. DPI Augmentation

Page intentionally left blank

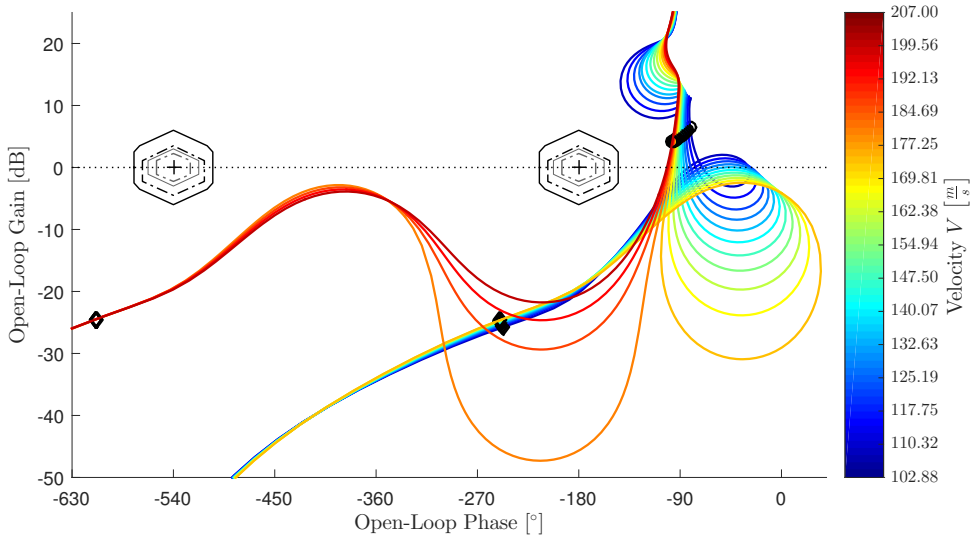

Figure A.18. – Nichols plot for robust stability assessment of DPI Augmentation at envelope points according to Table 2.2 generated for η_{cmd} (bottleneck) loop cut (basic aircraft model)

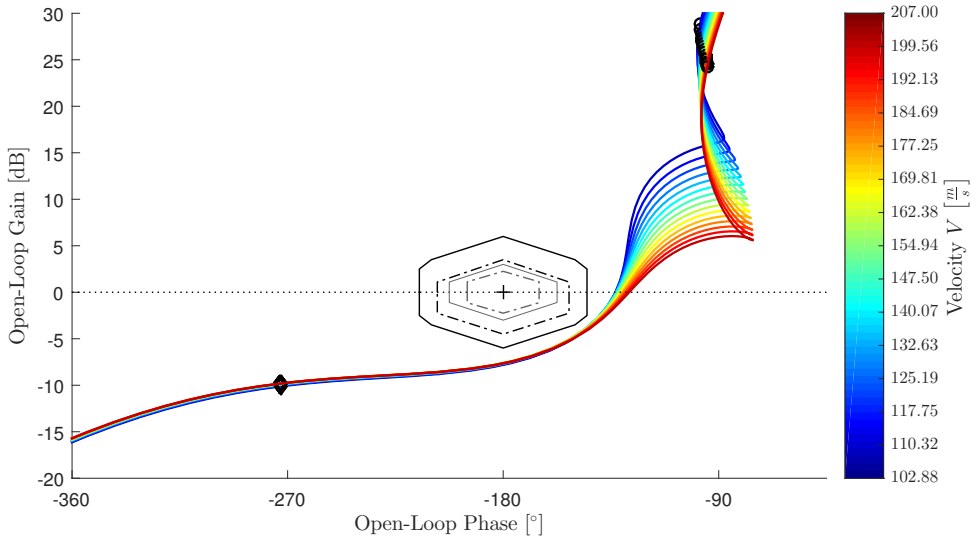

Figure A.19. – Nichols plot for robust stability assessment of DPI Augmentation without hedging at envelope points according to Table 2.2 generated for η_{cmd} (bottleneck) loop cut (basic aircraft model)

Table A.27. – Robust stability properties gain margin (GM), phase margin Φ_m, time delay margins (TDM) and corresponding gain-crossover frequencies $\omega_{gc,\Phi}$ and $\omega_{gc,TDM}$ for robust stability assessment of DPI Augmentation at envelope points according to Table 2.2 generated for η_{cmd} (bottleneck) loop cut (basic aircraft model)

Velocity $V\ \left[\frac{m}{s}\right]$	**GM** $[dB]$	$\Phi_m\ [^\circ]$	$\omega_{gc,\Phi}\ \left[\frac{rad}{s}\right]$	**TDM** $[s]$	$\omega_{gc,TDM}\ \left[\frac{rad}{s}\right]$
102.88	20.19	97.42	3.28	0.518	3.28
	$-\infty$	-209.36	1.81	-1.396	3.28
110.32	19.90	102.85	3.39	0.530	3.39
	$-\infty$	-207.68	2.11	-1.326	3.39
117.75	19.76	99.43	0.67	0.551	3.45
	$-\infty$	-207.25	2.39	-1.271	3.45
125.19	19.58	96.29	0.66	0.585	3.48
	$-\infty$	-210.53	2.70	-1.223	3.48
132.63	19.45	93.60	0.65	0.672	3.37
	$-\infty$	-220.09	3.14	-1.191	3.37
140.07	19.36	91.21	0.64	2.497	0.64
	$-\infty$	-268.79	0.64	-7.359	0.64
147.50	19.30	89.11	0.63	2.473	0.63
	$-\infty$	-270.89	0.63	-7.518	0.63
154.94	19.27	87.23	0.62	2.451	0.62
	$-\infty$	-272.77	0.62	-7.664	0.62
162.38	19.27	85.52	0.61	2.430	0.61
	$-\infty$	-274.48	0.61	-7.798	0.61
169.81	19.30	83.98	0.61	2.411	0.61
	$-\infty$	-276.02	0.61	-7.923	0.61
177.25	19.35	82.57	0.60	2.393	0.60
	$-\infty$	-277.43	0.60	-8.040	0.60
184.69	19.42	81.27	0.60	2.377	0.60
	$-\infty$	-278.73	0.60	-8.151	0.60
192.13	19.46	80.16	0.59	2.359	0.59
	$-\infty$	-279.84	0.59	-8.236	0.59
199.56	19.56	79.17	0.59	2.344	0.59
	$-\infty$	-280.83	0.59	-8.313	0.59
207.00	19.67	78.24	0.59	2.330	0.59
	$-\infty$	-281.76	0.59	-8.389	0.59

Table A.28. – Robust stability properties gain margin (GM), phase margin Φ_m, time delay margins (TDM) and corresponding gain-crossover frequencies $\omega_{gc,\Phi}$ and $\omega_{gc,TDM}$ for robust stability assessment of DPI Augmentation without hedging at envelope points according to Table 2.2 generated for η_{cmd} (bottleneck) loop cut (basic aircraft model)

Velocity $V\ \left[\frac{m}{s}\right]$	**GM** $[dB]$	$\Phi_m\ [^\circ]$	$\omega_{gc,\Phi}\ \left[\frac{rad}{s}\right]$	**TDM** $[s]$	$\omega_{gc,TDM}\ \left[\frac{rad}{s}\right]$
102.88	7.81	46.95	7.59	0.108	7.59
	$-\infty$	-313.05	7.59	-0.720	7.59
110.32	7.76	46.86	7.69	0.106	7.69
	$-\infty$	-313.14	7.69	-0.711	7.69
117.75	7.73	46.86	7.79	0.105	7.79
	$-\infty$	-313.14	7.79	-0.701	7.79
125.19	7.69	46.99	7.86	0.104	7.86
	$-\infty$	-313.01	7.86	-0.695	7.86
132.63	7.67	47.14	7.94	0.104	7.94
	$-\infty$	-312.86	7.94	-0.688	7.94
140.07	7.64	47.34	8.02	0.103	8.02
	$-\infty$	-312.66	8.02	-0.680	8.02
147.50	7.63	47.69	8.08	0.103	8.08
	$-\infty$	-312.31	8.08	-0.675	8.08
154.94	7.62	48.03	8.16	0.103	8.16
	$-\infty$	-311.97	8.16	-0.667	8.16
162.38	7.61	48.47	8.23	0.103	8.23
	$-\infty$	-311.53	8.23	-0.661	8.23
169.81	7.61	49.00	8.28	0.103	8.28
	$-\infty$	-311.00	8.28	-0.655	8.28
177.25	7.61	49.58	8.35	0.104	8.35
	$-\infty$	-310.42	8.35	-0.649	8.35
184.69	7.62	50.26	8.39	0.105	8.39
	$-\infty$	-309.74	8.39	-0.644	8.39
192.13	7.62	50.97	8.45	0.105	8.45
	$-\infty$	-309.03	8.45	-0.638	8.45
199.56	7.64	51.74	8.49	0.106	8.49
	$-\infty$	-308.26	8.49	-0.634	8.49
207.00	7.65	52.60	8.55	0.107	8.55
	$-\infty$	-307.40	8.55	-0.628	8.55

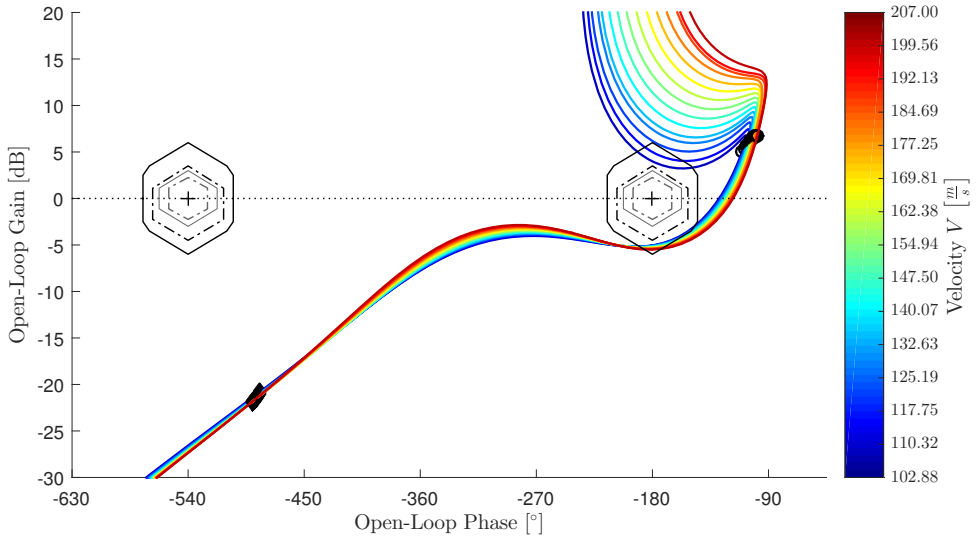

Figure A.20. – Nichols plot for robust stability assessment of DPI Augmentation at envelope points according to Table 2.2 generated for α loop cut (basic aircraft model)

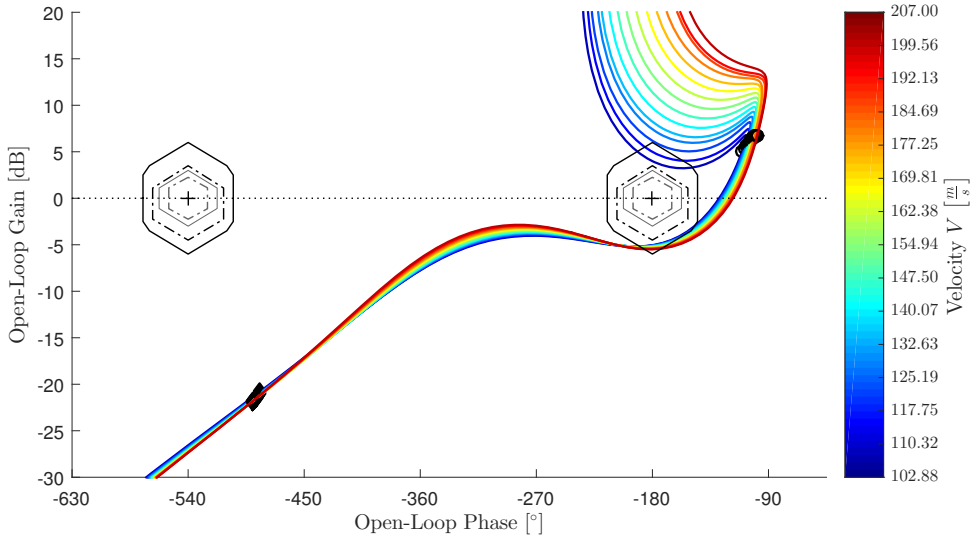

Figure A.21. – Nichols plot for robust stability assessment of DPI Augmentation without hedging at envelope points according to Table 2.2 generated for α loop cut (basic aircraft model)

Table A.29. – Robust stability properties gain margin (GM), phase margin Φ_m, time delay margins (TDM) and corresponding gain-crossover frequencies $\omega_{gc,\Phi}$ and $\omega_{gc,TDM}$ for robust stability assessment of DPI Augmentation at envelope points according to Table 2.2 generated for α loop cut (basic aircraft model)

Velocity $V\ \left[\frac{m}{s}\right]$	**GM** $[dB]$	$\Phi_m\ [^\circ]$	$\omega_{gc,\Phi}\ \left[\frac{rad}{s}\right]$	**TDM** $[s]$	$\omega_{gc,TDM}\ \left[\frac{rad}{s}\right]$
102.88	5.04	51.65	0.83	1.092	0.83
	-3.99	-308.35	0.83	-6.519	0.83
110.32	5.07	52.67	0.84	1.089	0.84
	-5.00	-307.33	0.84	-6.354	0.84
117.75	5.07	53.00	0.87	1.069	0.87
	-6.18	-307.00	0.87	-6.191	0.87
125.19	5.11	53.98	0.88	1.072	0.88
	-7.43	-306.02	0.88	-6.080	0.88
132.63	5.15	54.93	0.89	1.078	0.89
	-8.24	-305.07	0.89	-5.986	0.89
140.07	5.19	55.81	0.90	1.083	0.90
	-9.74	-304.19	0.90	-5.900	0.90
147.50	5.22	56.64	0.91	1.086	0.91
	-11.39	-303.36	0.91	-5.819	0.91
154.94	5.25	57.43	0.92	1.091	0.92
	-13.29	-302.57	0.92	-5.749	0.92
162.38	5.28	58.19	0.93	1.097	0.93
	-15.50	-301.81	0.93	-5.687	0.93
169.81	5.31	58.92	0.93	1.102	0.93
	-18.25	-301.08	0.93	-5.633	0.93
177.25	5.34	59.61	0.94	1.108	0.94
	-21.96	-300.39	0.94	-5.583	0.94
184.69	5.38	60.28	0.94	1.114	0.94
	$-\infty$	-299.72	0.94	-5.539	0.94
192.13	5.42	61.30	0.94	1.136	0.94
	$-\infty$	-298.70	0.94	-5.536	0.94
199.56	5.46	61.91	0.95	1.142	0.95
	$-\infty$	-298.09	0.95	-5.499	0.95
207.00	5.49	62.49	0.95	1.148	0.95
	$-\infty$	-297.51	0.95	-5.464	0.95

Table A.30. – Robust stability properties gain margin (GM), phase margin Φ_m, time delay margins (TDM) and corresponding gain-crossover frequencies $\omega_{gc,\Phi}$ and $\omega_{gc,TDM}$ for robust stability assessment of DPI Augmentation without hedging at envelope points according to Table 2.2 generated for α loop cut (basic aircraft model)

Velocity $V\ \left[\frac{m}{s}\right]$	**GM** $[dB]$	$\Phi_m\ [^\circ]$	$\omega_{gc,\Phi}\ \left[\frac{rad}{s}\right]$	**TDM** $[s]$	$\omega_{gc,TDM}\ \left[\frac{rad}{s}\right]$
102.88	5.04	51.65	0.83	1.092	0.83
	-3.99	-308.35	0.83	-6.519	0.83
110.32	5.07	52.67	0.84	1.089	0.84
	-5.00	-307.33	0.84	-6.354	0.84
117.75	5.07	53.00	0.87	1.069	0.87
	-6.18	-307.00	0.87	-6.191	0.87
125.19	5.11	53.98	0.88	1.072	0.88
	-7.43	-306.02	0.88	-6.080	0.88
132.63	5.15	54.93	0.89	1.078	0.89
	-8.24	-305.07	0.89	-5.986	0.89
140.07	5.19	55.81	0.90	1.083	0.90
	-9.74	-304.19	0.90	-5.900	0.90
147.50	5.22	56.64	0.91	1.086	0.91
	-11.39	-303.36	0.91	-5.819	0.91
154.94	5.25	57.43	0.92	1.091	0.92
	-13.29	-302.57	0.92	-5.749	0.92
162.38	5.28	58.19	0.93	1.097	0.93
	-15.50	-301.81	0.93	-5.687	0.93
169.81	5.31	58.92	0.93	1.102	0.93
	-18.25	-301.08	0.93	-5.633	0.93
177.25	5.34	59.61	0.94	1.108	0.94
	-21.96	-300.39	0.94	-5.583	0.94
184.69	5.38	60.28	0.94	1.114	0.94
	$-\infty$	-299.72	0.94	-5.539	0.94
192.13	5.42	61.30	0.94	1.136	0.94
	$-\infty$	-298.70	0.94	-5.536	0.94
199.56	5.46	61.91	0.95	1.142	0.95
	$-\infty$	-298.09	0.95	-5.499	0.95
207.00	5.49	62.49	0.95	1.148	0.95
	$-\infty$	-297.51	0.95	-5.464	0.95

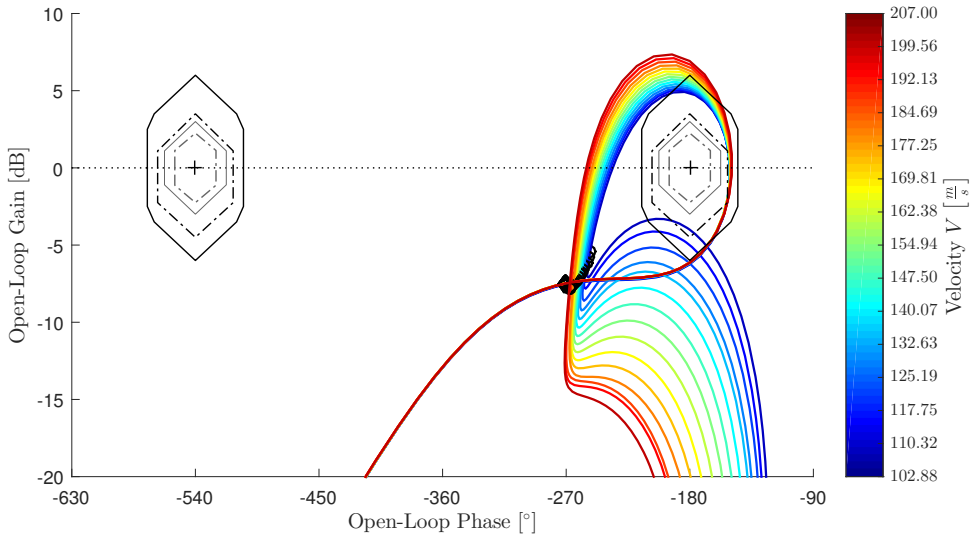

Figure A.22. – Nichols plot for robust stability assessment of DPI Augmentation at envelope points according to Table 2.2 generated for q loop cut (basic aircraft model)

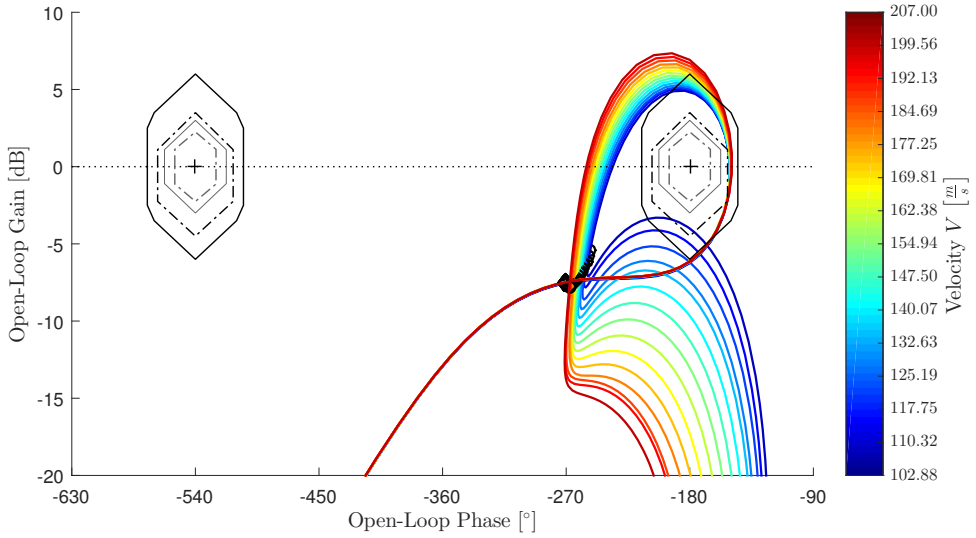

Figure A.23. – Nichols plot for robust stability assessment of DPI Augmentation without hedging at envelope points according to Table 2.2 generated for q loop cut (basic aircraft model)

Table A.31. – Robust stability properties gain margin (GM), phase margin Φ_m, time delay margins (TDM) and corresponding gain-crossover frequencies $\omega_{gc,\Phi}$ and $\omega_{gc,TDM}$ for robust stability assessment of DPI Augmentation at envelope points according to Table 2.2 generated for q loop cut (basic aircraft model)

Velocity $V\ \left[\frac{m}{s}\right]$	**GM** $[dB]$	$\Phi_m\ [^\circ]$	$\omega_{gc,\Phi}\ \left[\frac{rad}{s}\right]$	**TDM** $[s]$	$\omega_{gc,TDM}\ \left[\frac{rad}{s}\right]$
102.88	4.01	29.37	7.70	0.067	7.70
	-4.82	-56.04	0.83	-0.750	7.70
110.32	5.01	29.33	7.77	0.066	7.77
	-4.92	-57.67	0.85	-0.743	7.77
117.75	6.19	29.26	7.84	0.065	7.84
	-5.01	-58.53	0.87	-0.737	7.84
125.19	6.17	29.22	7.91	0.064	7.91
	-5.14	-60.11	0.88	-0.730	7.91
132.63	6.16	29.21	7.99	0.064	7.99
	-5.25	-61.66	0.90	-0.723	7.99
140.07	6.15	29.22	8.06	0.063	8.06
	-5.36	-63.11	0.91	-0.716	8.06
147.50	6.14	29.27	8.13	0.063	8.13
	-5.49	-64.54	0.92	-0.710	8.13
154.94	6.13	29.35	8.20	0.062	8.20
	-5.62	-65.95	0.93	-0.704	8.20
162.38	6.13	29.45	8.26	0.062	8.26
	-5.77	-67.33	0.94	-0.698	8.26
169.81	6.13	29.58	8.33	0.062	8.33
	-5.93	-68.68	0.95	-0.693	8.33
177.25	6.13	29.73	8.39	0.062	8.39
	-6.11	-70.01	0.95	-0.687	8.39
184.69	6.13	29.91	8.45	0.062	8.45
	-6.29	-71.30	0.96	-0.682	8.45
192.13	6.13	30.13	8.50	0.062	8.50
	-6.50	-72.98	0.96	-0.677	8.50
199.56	6.14	30.34	8.56	0.062	8.56
	-6.70	-74.18	0.97	-0.672	8.56
207.00	6.14	30.58	8.61	0.062	8.61
	-6.91	-75.35	0.97	-0.668	8.61

Table A.32. – Robust stability properties gain margin (GM), phase margin Φ_m, time delay margins (TDM) and corresponding gain-crossover frequencies $\omega_{gc,\Phi}$ and $\omega_{gc,TDM}$ for robust stability assessment of DPI Augmentation without hedging at envelope points according to Table 2.2 generated for q loop cut (basic aircraft model)

Velocity V $\left[\frac{m}{s}\right]$	**GM** $[dB]$	Φ_m $[^\circ]$	$\omega_{gc,\Phi}$ $\left[\frac{rad}{s}\right]$	**TDM** $[s]$	$\omega_{gc,TDM}$ $\left[\frac{rad}{s}\right]$
102.88	4.01	29.37	7.70	0.067	7.70
	-4.82	-56.04	0.83	-0.750	7.70
110.32	5.01	29.33	7.77	0.066	7.77
	-4.92	-57.67	0.85	-0.743	7.77
117.75	6.19	29.26	7.84	0.065	7.84
	-5.01	-58.53	0.87	-0.737	7.84
125.19	6.17	29.22	7.91	0.064	7.91
	-5.14	-60.11	0.88	-0.730	7.91
132.63	6.16	29.21	7.99	0.064	7.99
	-5.25	-61.66	0.90	-0.723	7.99
140.07	6.15	29.22	8.06	0.063	8.06
	-5.36	-63.11	0.91	-0.716	8.06
147.50	6.14	29.27	8.13	0.063	8.13
	-5.49	-64.54	0.92	-0.710	8.13
154.94	6.13	29.35	8.20	0.062	8.20
	-5.62	-65.95	0.93	-0.704	8.20
162.38	6.13	29.45	8.26	0.062	8.26
	-5.77	-67.33	0.94	-0.698	8.26
169.81	6.13	29.58	8.33	0.062	8.33
	-5.93	-68.68	0.95	-0.693	8.33
177.25	6.13	29.73	8.39	0.062	8.39
	-6.11	-70.01	0.95	-0.687	8.39
184.69	6.13	29.91	8.45	0.062	8.45
	-6.29	-71.30	0.96	-0.682	8.45
192.13	6.13	30.13	8.50	0.062	8.50
	-6.50	-72.98	0.96	-0.677	8.50
199.56	6.14	30.34	8.56	0.062	8.56
	-6.70	-74.18	0.97	-0.672	8.56
207.00	6.14	30.58	8.61	0.062	8.61
	-6.91	-75.35	0.97	-0.668	8.61

A.5.4. Plant Augmentation

Page intentionally left blank

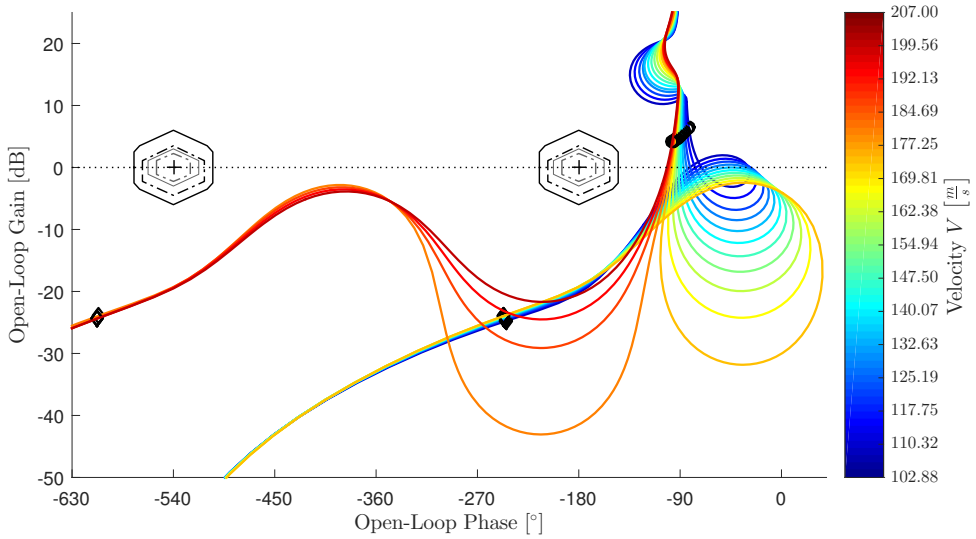

Figure A.24. – Nichols plot for robust stability assessment of Plant Augmentation at envelope points according to Table 2.2 generated for η_{cmd} (bottleneck) loop cut (basic aircraft model)

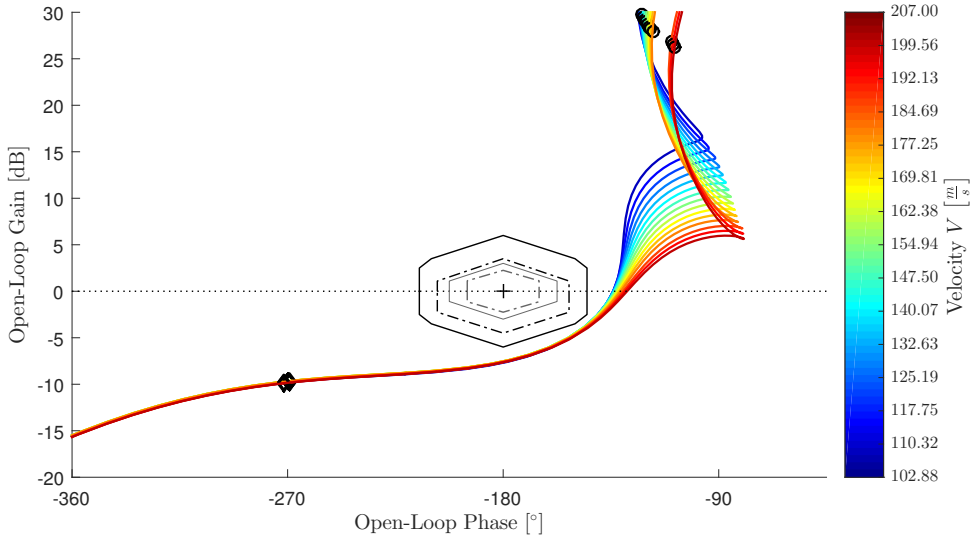

Figure A.25. – Nichols plot for robust stability assessment of Plant Augmentation without hedging at envelope points according to Table 2.2 generated for η_{cmd} (bottleneck) loop cut (basic aircraft model)

Table A.33. – Robust stability properties gain margin (GM), phase margin Φ_m, time delay margins (TDM) and corresponding gain-crossover frequencies $\omega_{gc,\Phi}$ and $\omega_{gc,TDM}$ for robust stability assessment of Plant Augmentation at envelope points according to Table 2.2 generated for η_{cmd} (bottleneck) loop cut (basic aircraft model)

Velocity $V\ \left[\frac{m}{s}\right]$	**GM** $[dB]$	$\Phi_m\ [^\circ]$	$\omega_{gc,\Phi}\ \left[\frac{rad}{s}\right]$	**TDM** $[s]$	$\omega_{gc,TDM}\ \left[\frac{rad}{s}\right]$
102.88	20.22	98.47	3.26	0.527	3.26
	$-\infty$	-209.62	1.82	-1.398	3.26
110.32	19.93	103.33	0.71	0.539	3.37
	$-\infty$	-207.84	2.13	-1.327	3.37
117.75	19.79	98.88	0.68	0.561	3.43
	$-\infty$	-207.44	2.40	-1.272	3.43
125.19	19.61	95.83	0.66	0.596	3.45
	$-\infty$	-210.96	2.72	-1.223	3.45
132.63	19.46	93.20	0.65	2.504	0.65
	$-\infty$	-266.80	0.65	-7.167	0.65
140.07	19.35	90.85	0.64	2.482	0.64
	$-\infty$	-269.15	0.64	-7.352	0.64
147.50	19.28	88.80	0.63	2.460	0.63
	$-\infty$	-271.20	0.63	-7.512	0.63
154.94	19.23	86.95	0.62	2.439	0.62
	$-\infty$	-273.05	0.62	-7.659	0.62
162.38	19.21	85.28	0.62	2.419	0.62
	$-\infty$	-274.72	0.62	-7.794	0.62
169.81	19.22	83.76	0.61	2.401	0.61
	$-\infty$	-276.24	0.61	-7.920	0.61
177.25	19.25	82.36	0.60	2.384	0.60
	$-\infty$	-277.64	0.60	-8.038	0.60
184.69	19.29	81.09	0.60	2.369	0.60
	$-\infty$	-278.91	0.60	-8.148	0.60
192.13	19.33	80.11	0.59	2.359	0.59
	$-\infty$	-279.89	0.59	-8.240	0.59
199.56	19.41	79.13	0.59	2.343	0.59
	$-\infty$	-280.87	0.59	-8.318	0.59
207.00	19.51	78.21	0.59	2.330	0.59
	$-\infty$	-281.79	0.59	-8.393	0.59

Table A.34. – Robust stability properties gain margin (GM), phase margin Φ_m, time delay margins (TDM) and corresponding gain-crossover frequencies $\omega_{gc,\Phi}$ and $\omega_{gc,TDM}$ for robust stability assessment of Plant Augmentation without hedging at envelope points according to Table 2.2 generated for η_{cmd} (bottleneck) loop cut (basic aircraft model)

Velocity $V\ \left[\frac{m}{s}\right]$	**GM** $[dB]$	$\Phi_m\ [^\circ]$	$\omega_{gc,\Phi}\ \left[\frac{rad}{s}\right]$	**TDM** $[s]$	$\omega_{gc,TDM}\ \left[\frac{rad}{s}\right]$
102.88	7.68	45.97	7.70	0.104	7.70
	$-\infty$	-314.03	7.70	-0.712	7.70
110.32	7.64	45.87	7.80	0.103	7.80
	$-\infty$	-314.13	7.80	-0.703	7.80
117.75	7.62	45.84	7.90	0.101	7.90
	$-\infty$	-314.16	7.90	-0.694	7.90
125.19	7.59	45.93	7.97	0.101	7.97
	$-\infty$	-314.07	7.97	-0.688	7.97
132.63	7.57	46.12	8.03	0.100	8.03
	$-\infty$	-313.88	8.03	-0.682	8.03
140.07	7.55	46.28	8.12	0.100	8.12
	$-\infty$	-313.72	8.12	-0.674	8.12
147.50	7.54	46.60	8.18	0.099	8.18
	$-\infty$	-313.40	8.18	-0.669	8.18
154.94	7.53	46.95	8.24	0.099	8.24
	$-\infty$	-313.05	8.24	-0.663	8.24
162.38	7.52	47.36	8.31	0.099	8.31
	$-\infty$	-312.64	8.31	-0.657	8.31
169.81	7.53	47.90	8.36	0.100	8.36
	$-\infty$	-312.10	8.36	-0.652	8.36
177.25	7.53	48.45	8.42	0.100	8.42
	$-\infty$	-311.55	8.42	-0.646	8.42
184.69	7.54	49.11	8.47	0.101	8.47
	$-\infty$	-310.89	8.47	-0.641	8.47
192.13	7.60	50.06	8.46	0.103	8.46
	$-\infty$	-309.94	8.46	-0.640	8.46
199.56	7.62	50.85	8.49	0.105	8.49
	$-\infty$	-309.15	8.49	-0.635	8.49
207.00	7.64	51.72	8.54	0.106	8.54
	$-\infty$	-308.28	8.54	-0.630	8.54

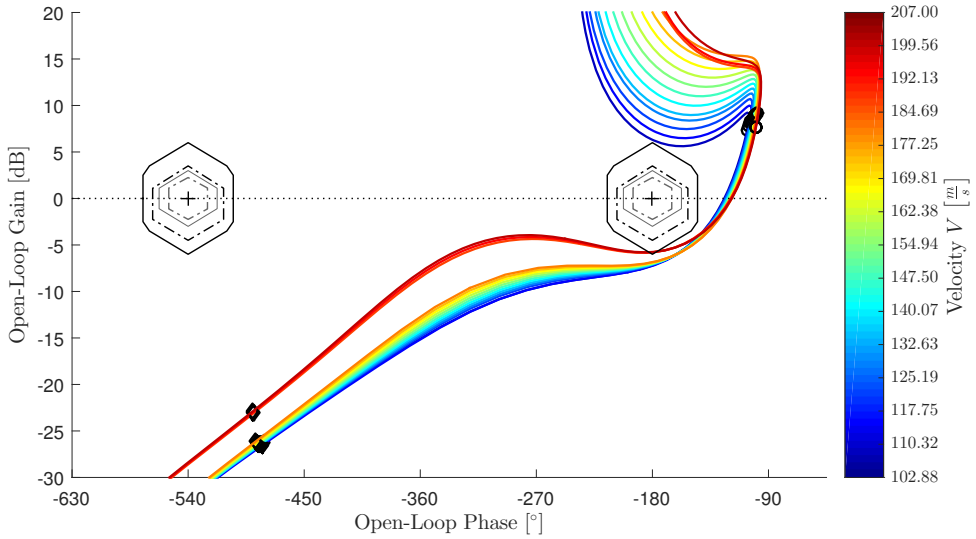

Figure A.26. – Nichols plot for robust stability assessment of Plant Augmentation at envelope points according to Table 2.2 generated for α loop cut (basic aircraft model)

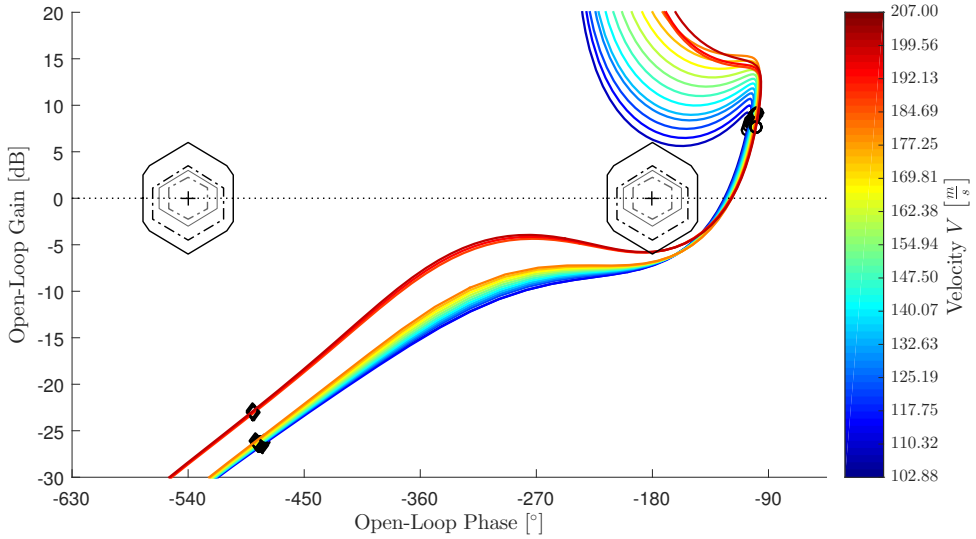

Figure A.27. – Nichols plot for robust stability assessment of Plant Augmentation without hedging at envelope points according to Table 2.2 generated for α loop cut (basic aircraft model)

Table A.35. – Robust stability properties gain margin (GM), phase margin Φ_m, time delay margins (TDM) and corresponding gain-crossover frequencies $\omega_{gc,\Phi}$ and $\omega_{gc,TDM}$ for robust stability assessment of Plant Augmentation at envelope points according to Table 2.2 generated for α loop cut (basic aircraft model)

Velocity $V\ \left[\frac{m}{s}\right]$	**GM** $[dB]$	$\Phi_m\ [^\circ]$	$\omega_{gc,\Phi}\ \left[\frac{rad}{s}\right]$	**TDM** $[s]$	$\omega_{gc,TDM}\ \left[\frac{rad}{s}\right]$
102.88	7.21	55.69	1.01	0.967	1.01
	-6.31	-304.31	1.01	-5.282	1.01
110.32	7.24	56.60	1.04	0.953	1.04
	-7.32	-303.40	1.04	-5.109	1.04
117.75	7.13	56.57	1.06	0.929	1.06
	-8.41	-303.43	1.06	-4.983	1.06
125.19	7.10	57.21	1.09	0.919	1.09
	-9.54	-302.79	1.09	-4.863	1.09
132.63	7.07	57.83	1.11	0.911	1.11
	-10.26	-302.17	1.11	-4.761	1.11
140.07	7.04	58.42	1.13	0.905	1.13
	-11.58	-301.58	1.13	-4.674	1.13
147.50	7.01	58.98	1.14	0.901	1.14
	-13.01	-301.02	1.14	-4.599	1.14
154.94	6.99	59.52	1.16	0.898	1.16
	-14.58	-300.48	1.16	-4.533	1.16
162.38	6.95	60.04	1.17	0.896	1.17
	-16.26	-299.96	1.17	-4.475	1.17
169.81	6.91	60.53	1.18	0.894	1.18
	-18.13	-299.47	1.18	-4.424	1.18
177.25	6.87	61.01	1.19	0.893	1.19
	-20.02	-298.99	1.19	-4.378	1.19
184.69	6.84	61.47	1.20	0.893	1.20
	-22.01	-298.53	1.20	-4.337	1.20
192.13	5.79	60.64	1.04	1.013	1.04
	-23.21	-299.36	1.04	-5.003	1.04
199.56	5.77	61.11	1.05	1.020	1.05
	-23.79	-298.89	1.05	-4.990	1.05
207.00	5.75	61.56	1.05	1.027	1.05
	-27.28	-298.44	1.05	-4.981	1.05

Table A.36. – Robust stability properties gain margin (GM), phase margin Φ_m, time delay margins (TDM) and corresponding gain-crossover frequencies $\omega_{gc,\Phi}$ and $\omega_{gc,TDM}$ for robust stability assessment of Plant Augmentation without hedging at envelope points according to Table 2.2 generated for α loop cut (basic aircraft model)

Velocity $V\ \left[\frac{m}{s}\right]$	**GM** $[dB]$	$\Phi_m\ [^\circ]$	$\omega_{gc,\Phi}\ \left[\frac{rad}{s}\right]$	**TDM** $[s]$	$\omega_{gc,TDM}\ \left[\frac{rad}{s}\right]$
102.88	7.21	55.69	1.01	0.967	1.01
	-6.31	-304.31	1.01	-5.282	1.01
110.32	7.24	56.60	1.04	0.953	1.04
	-7.32	-303.40	1.04	-5.109	1.04
117.75	7.13	56.57	1.06	0.929	1.06
	-8.41	-303.43	1.06	-4.983	1.06
125.19	7.10	57.21	1.09	0.919	1.09
	-9.54	-302.79	1.09	-4.863	1.09
132.63	7.07	57.83	1.11	0.911	1.11
	-10.26	-302.17	1.11	-4.761	1.11
140.07	7.04	58.42	1.13	0.905	1.13
	-11.58	-301.58	1.13	-4.674	1.13
147.50	7.01	58.98	1.14	0.901	1.14
	-13.01	-301.02	1.14	-4.599	1.14
154.94	6.99	59.52	1.16	0.898	1.16
	-14.58	-300.48	1.16	-4.533	1.16
162.38	6.95	60.04	1.17	0.896	1.17
	-16.26	-299.96	1.17	-4.475	1.17
169.81	6.91	60.53	1.18	0.894	1.18
	-18.13	-299.47	1.18	-4.424	1.18
177.25	6.87	61.01	1.19	0.893	1.19
	-20.02	-298.99	1.19	-4.378	1.19
184.69	6.84	61.47	1.20	0.893	1.20
	-22.01	-298.53	1.20	-4.337	1.20
192.13	5.79	60.64	1.04	1.013	1.04
	-23.21	-299.36	1.04	-5.003	1.04
199.56	5.77	61.11	1.05	1.020	1.05
	-23.79	-298.89	1.05	-4.990	1.05
207.00	5.75	61.56	1.05	1.027	1.05
	-27.28	-298.44	1.05	-4.981	1.05

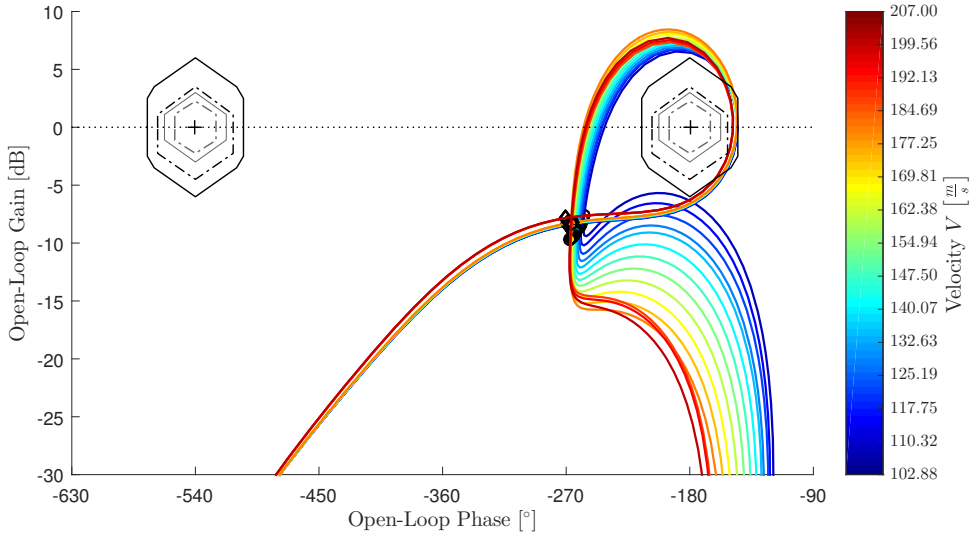

Figure A.28. – Nichols plot for robust stability assessment of Plant Augmentation at envelope points according to Table 2.2 generated for q loop cut (basic aircraft model)

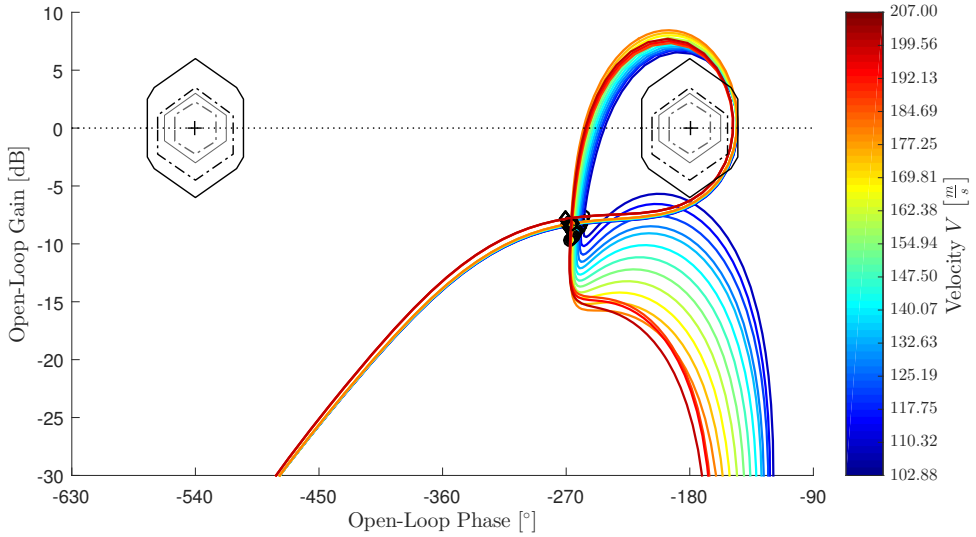

Figure A.29. – Nichols plot for robust stability assessment of Plant Augmentation without hedging at envelope points according to Table 2.2 generated for q loop cut (basic aircraft model)

Table A.37. – Robust stability properties gain margin (GM), phase margin Φ_m, time delay margins (TDM) and corresponding gain-crossover frequencies $\omega_{gc,\Phi}$ and $\omega_{gc,TDM}$ for robust stability assessment of Plant Augmentation at envelope points according to Table 2.2 generated for q loop cut (basic aircraft model)

Velocity $V\ \left[\frac{m}{s}\right]$	**GM** $[dB]$	$\Phi_m\ [^\circ]$	$\omega_{gc,\Phi}\ \left[\frac{rad}{s}\right]$	**TDM** $[s]$	$\omega_{gc,TDM}\ \left[\frac{rad}{s}\right]$
102.88	6.35	34.86	7.88	0.077	7.88
	-6.44	-62.11	0.99	-0.720	7.88
110.32	6.77	34.76	7.98	0.076	7.98
	-6.61	-63.97	1.02	-0.711	7.98
117.75	6.74	34.52	8.04	0.075	8.04
	-6.63	-64.76	1.04	-0.706	8.04
125.19	6.71	34.35	8.12	0.074	8.12
	-6.72	-66.23	1.07	-0.700	8.12
132.63	6.68	34.23	8.20	0.073	8.20
	-6.84	-67.70	1.09	-0.693	8.20
140.07	6.66	34.14	8.28	0.072	8.28
	-6.97	-69.14	1.11	-0.687	8.28
147.50	6.64	34.08	8.35	0.071	8.35
	-7.13	-70.57	1.12	-0.681	8.35
154.94	6.62	34.07	8.41	0.071	8.41
	-7.30	-71.97	1.14	-0.676	8.41
162.38	6.61	34.08	8.48	0.070	8.48
	-7.50	-73.35	1.15	-0.671	8.48
169.81	6.60	34.24	8.53	0.070	8.53
	-7.66	-74.76	1.16	-0.667	8.53
177.25	6.59	34.30	8.59	0.070	8.59
	-7.85	-76.06	1.17	-0.662	8.59
184.69	6.58	34.41	8.65	0.069	8.65
	-8.05	-77.36	1.18	-0.657	8.65
192.13	6.28	31.24	8.55	0.064	8.55
	-6.94	-74.06	1.03	-0.671	8.55
199.56	6.27	31.32	8.60	0.064	8.60
	-7.08	-75.05	1.03	-0.667	8.60
207.00	6.26	31.43	8.65	0.063	8.65
	-7.22	-76.01	1.03	-0.663	8.65

Table A.38. – Robust stability properties gain margin (GM), phase margin Φ_m, time delay margins (TDM) and corresponding gain-crossover frequencies $\omega_{gc,\Phi}$ and $\omega_{gc,TDM}$ for robust stability assessment of Plant Augmentation without hedging at envelope points according to Table 2.2 generated for q loop cut (basic aircraft model)

Velocity V $\left[\frac{m}{s}\right]$	**GM** $[dB]$	Φ_m $[^\circ]$	$\omega_{gc,\Phi}$ $\left[\frac{rad}{s}\right]$	**TDM** $[s]$	$\omega_{gc,TDM}$ $\left[\frac{rad}{s}\right]$
102.88	6.35	34.86	7.88	0.077	7.88
	-6.44	-62.11	0.99	-0.720	7.88
110.32	6.77	34.76	7.98	0.076	7.98
	-6.61	-63.97	1.02	-0.711	7.98
117.75	6.74	34.52	8.04	0.075	8.04
	-6.63	-64.76	1.04	-0.706	8.04
125.19	6.71	34.35	8.12	0.074	8.12
	-6.72	-66.23	1.07	-0.700	8.12
132.63	6.68	34.23	8.20	0.073	8.20
	-6.84	-67.70	1.09	-0.693	8.20
140.07	6.66	34.14	8.28	0.072	8.28
	-6.97	-69.14	1.11	-0.687	8.28
147.50	6.64	34.08	8.35	0.071	8.35
	-7.13	-70.57	1.12	-0.681	8.35
154.94	6.62	34.07	8.41	0.071	8.41
	-7.30	-71.97	1.14	-0.676	8.41
162.38	6.61	34.08	8.48	0.070	8.48
	-7.50	-73.35	1.15	-0.671	8.48
169.81	6.60	34.24	8.53	0.070	8.53
	-7.66	-74.76	1.16	-0.667	8.53
177.25	6.59	34.30	8.59	0.070	8.59
	-7.85	-76.06	1.17	-0.662	8.59
184.69	6.58	34.41	8.65	0.069	8.65
	-8.05	-77.36	1.18	-0.657	8.65
192.13	6.28	31.24	8.55	0.064	8.55
	-6.94	-74.06	1.03	-0.671	8.55
199.56	6.27	31.32	8.60	0.064	8.60
	-7.08	-75.05	1.03	-0.667	8.60
207.00	6.26	31.43	8.65	0.063	8.65
	-7.22	-76.01	1.03	-0.663	8.65

A.5.5. $\Delta\dot{q}$ Compensation Law

Page intentionally left blank

Table A.39. – Robust stability properties gain margin (GM), phase margin Φ_m, time delay margins (TDM) and corresponding gain-crossover frequencies $\omega_{gc,\Phi}$ and $\omega_{gc,TDM}$ for robust stability comparison of $\Delta\dot{q}$ Compensation Law with and without $\dot{q}$ measurement at $V = 154.94\frac{m}{s}$ generated for α loop cut (basic aircraft model)

Controller	**GM** $[dB]$	$\Phi_m\,[^\circ]$	$\omega_{gc,\Phi}\left[\frac{rad}{s}\right]$	**TDM** $[s]$	$\omega_{gc,TDM}\left[\frac{rad}{s}\right]$
Baseline	12.69	70.24	0.55	2.239	0.55
	$-\infty$	-289.76	0.55	-9.235	0.55
$\Delta\dot{q}$ Compensator	13.20	64.46	1.62	0.693	1.62
	-18.41	-295.54	1.62	-3.179	1.62
$\Delta\dot{q}$ Compensator (no $\dot{q}$-meas.)	13.38	64.56	1.62	0.696	1.62
	-18.41	-295.44	1.62	-3.183	1.62

Table A.40. – Robust stability properties gain margin (GM), phase margin Φ_m, time delay margins (TDM) and corresponding gain-crossover frequencies $\omega_{gc,\Phi}$ and $\omega_{gc,TDM}$ for robust stability comparison of $\Delta\dot{q}$ Compensation Law with and without $\dot{q}$ measurement at $V = 154.94\frac{m}{s}$ generated for q loop cut (basic aircraft model)

Controller	**GM** $[dB]$	$\Phi_m\,[^\circ]$	$\omega_{gc,\Phi}\left[\frac{rad}{s}\right]$	**TDM** $[s]$	$\omega_{gc,TDM}\left[\frac{rad}{s}\right]$
Baseline	15.54	101.74	4.39	0.404	4.39
	$-\infty$	-137.46	1.92	-1.026	4.39
$\Delta\dot{q}$ Compensator	13.25	69.48	5.01	0.242	5.01
	$-\infty$	-106.89	1.38	-1.011	5.01
$\Delta\dot{q}$ Compensator (no $\dot{q}$-meas.)	6.63	38.43	9.56	0.070	9.56
	-11.17	-82.27	1.63	-0.587	9.56

Table A.41. – Robust stability properties gain margin (GM), phase margin Φ_m, time delay margins (TDM) and corresponding gain-crossover frequencies $\omega_{gc,\Phi}$ and $\omega_{gc,TDM}$ for robust stability assessment of $\Delta\dot{q}$ Compensation Law with $\dot{q}$ measurement at $V = 154.94\frac{m}{s}$ generated for $\dot{q}$ loop cut (basic aircraft model)

Controller	**GM** $[dB]$	$\Phi_m\,[^\circ]$	$\omega_{gc,\Phi}\left[\frac{rad}{s}\right]$	**TDM** $[s]$	$\omega_{gc,TDM}\left[\frac{rad}{s}\right]$
$\Delta\dot{q}$ Compensator	8.27	53.05	10.67	0.087	10.67
	-20.47	-76.30	3.75	-0.356	3.75

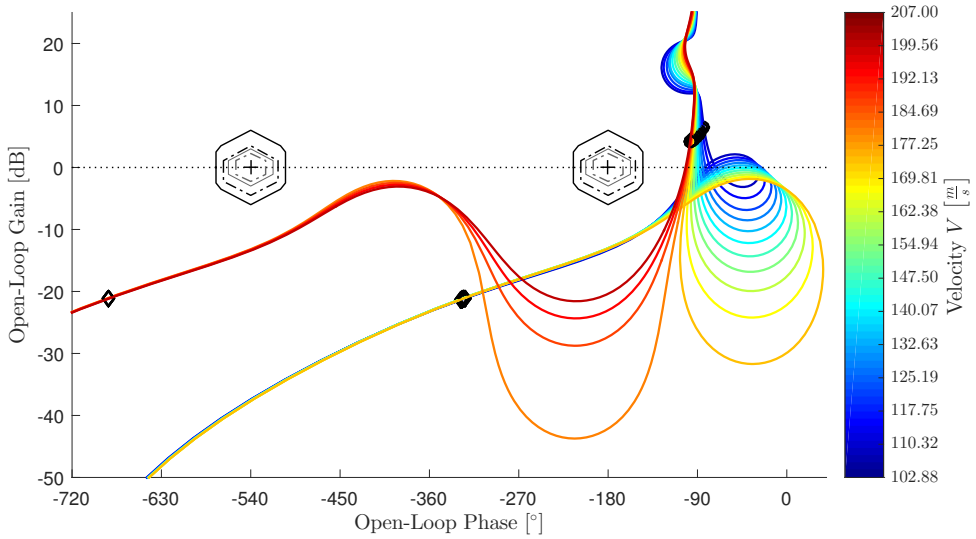

Figure A.30. – Nichols plot for robust stability assessment of $\Delta\dot{q}$ Compensation Law at envelope points according to Table 2.2 generated for η_{cmd} (bottleneck) loop cut (basic aircraft model)

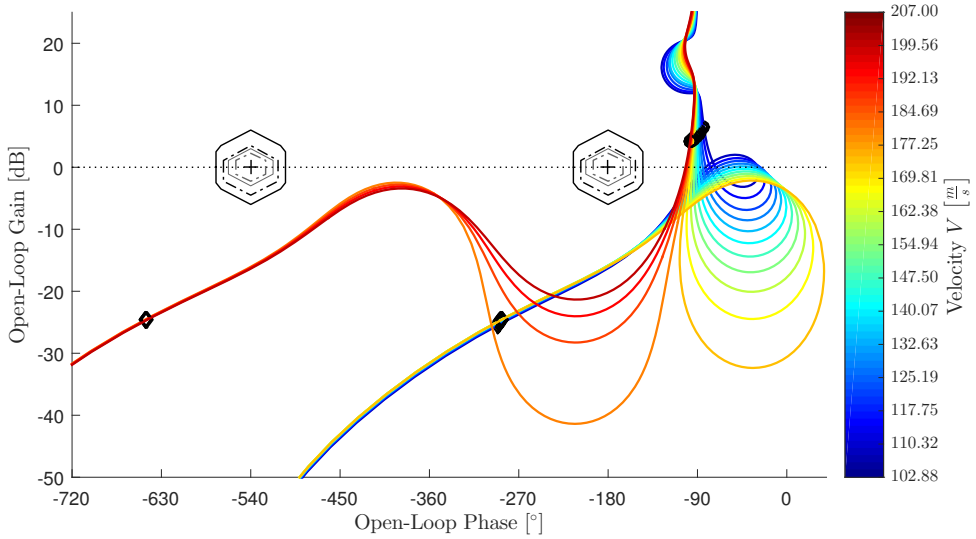

Figure A.31. – Nichols plot for robust stability assessment of $\Delta\dot{q}$ Compensation Law with $\dot{q}$ measurement at envelope points according to Table 2.2 generated for η_{cmd} (bottleneck) loop cut (basic aircraft model)

Table A.42. – Robust stability properties gain margin (GM), phase margin Φ_m, time delay margins (TDM) and corresponding gain-crossover frequencies $\omega_{gc,\Phi}$ and $\omega_{gc,TDM}$ for robust stability assessment of $\Delta\dot{q}$ Compensation Law with $\dot{q}$ measurement at envelope points according to Table 2.2 generated for η_{cmd} (bottleneck) loop cut (basic aircraft model)

Velocity $V\ \left[\frac{m}{s}\right]$	**GM** $[dB]$	$\Phi_m\ [^\circ]$	$\omega_{gc,\Phi}\ \left[\frac{rad}{s}\right]$	**TDM** $[s]$	$\omega_{gc,TDM}\ \left[\frac{rad}{s}\right]$
102.88	16.28	98.00	3.31	0.517	3.31
	$-\infty$	-209.56	1.83	-1.383	3.31
110.32	16.12	102.74	0.72	0.527	3.42
	$-\infty$	-207.41	2.12	-1.312	3.42
117.75	16.07	98.33	0.68	0.544	3.49
	$-\infty$	-206.57	2.39	-1.256	3.49
125.19	15.97	95.36	0.66	0.571	3.54
	$-\infty$	-209.07	2.69	-1.206	3.54
132.63	15.90	92.78	0.65	0.628	3.50
	$-\infty$	-215.31	3.06	-1.167	3.50
140.07	15.86	90.47	0.64	2.464	0.64
	$-\infty$	-269.53	0.64	-7.341	0.64
147.50	15.84	88.44	0.63	2.445	0.63
	$-\infty$	-271.56	0.63	-7.508	0.63
154.94	15.85	86.63	0.62	2.424	0.62
	$-\infty$	-273.37	0.62	-7.650	0.62
162.38	15.87	84.98	0.62	2.406	0.62
	$-\infty$	-275.02	0.62	-7.786	0.62
169.81	15.91	83.48	0.61	2.389	0.61
	$-\infty$	-276.52	0.61	-7.913	0.61
177.25	15.97	82.11	0.60	2.373	0.60
	$-\infty$	-277.89	0.60	-8.031	0.60
184.69	16.05	80.86	0.60	2.359	0.60
	$-\infty$	-279.14	0.60	-8.143	0.60
192.13	16.15	79.61	0.59	2.346	0.59
	$-\infty$	-280.39	0.59	-8.261	0.59
199.56	16.25	78.81	0.59	2.335	0.59
	$-\infty$	-281.19	0.59	-8.333	0.59
207.00	16.36	77.91	0.59	2.322	0.59
	$-\infty$	-282.09	0.59	-8.409	0.59

Table A.43. – Robust stability properties gain margin (GM), phase margin Φ_m, time delay margins (TDM) and corresponding gain-crossover frequencies $\omega_{gc,\Phi}$ and $\omega_{gc,TDM}$ for robust stability assessment of $\Delta\dot{q}$ Compensation Law at envelope points according to Table 2.2 generated for η_{cmd} (bottleneck) loop cut (basic aircraft model)

Velocity $V\ \left[\frac{m}{s}\right]$	**GM** $[dB]$	$\Phi_m\ [^\circ]$	$\omega_{gc,\Phi}\ \left[\frac{rad}{s}\right]$	**TDM** $[s]$	$\omega_{gc,TDM}\ \left[\frac{rad}{s}\right]$
102.88	13.32	96.65	3.37	0.501	3.37
	$-\infty$	-209.23	1.82	-1.365	3.37
110.32	13.20	101.26	3.49	0.507	3.49
	$-\infty$	-206.87	2.11	-1.295	3.49
117.75	13.16	98.35	0.68	0.519	3.57
	$-\infty$	-205.67	2.37	-1.240	3.57
125.19	13.09	95.38	0.66	0.539	3.64
	$-\infty$	-207.40	2.65	-1.189	3.64
132.63	13.05	92.79	0.65	0.573	3.65
	$-\infty$	-211.42	2.97	-1.146	3.65
140.07	13.02	90.48	0.64	2.465	0.64
	$-\infty$	-269.52	0.64	-7.341	0.64
147.50	13.00	88.45	0.63	2.445	0.63
	$-\infty$	-271.55	0.63	-7.507	0.63
154.94	13.01	86.64	0.62	2.425	0.62
	$-\infty$	-273.36	0.62	-7.650	0.62
162.38	13.03	84.99	0.62	2.407	0.62
	$-\infty$	-275.01	0.62	-7.786	0.62
169.81	13.07	83.49	0.61	2.389	0.61
	$-\infty$	-276.51	0.61	-7.913	0.61
177.25	13.12	82.12	0.60	2.373	0.60
	$-\infty$	-277.88	0.60	-8.031	0.60
184.69	13.18	80.86	0.60	2.359	0.60
	$-\infty$	-279.14	0.60	-8.143	0.60
192.13	13.25	79.62	0.59	2.346	0.59
	$-\infty$	-280.38	0.59	-8.262	0.59
199.56	13.32	78.82	0.59	2.336	0.59
	$-\infty$	-281.18	0.59	-8.333	0.59
207.00	13.41	77.91	0.59	2.323	0.59
	$-\infty$	-282.09	0.59	-8.409	0.59

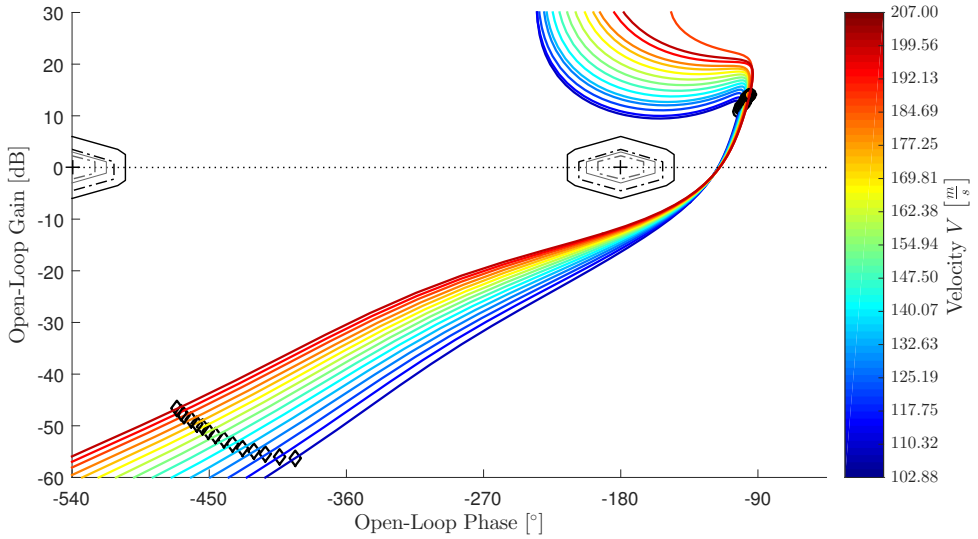

Figure A.32. – Nichols plot for robust stability assessment of $\Delta\dot{q}$ Compensation Law at envelope points according to Table 2.2 generated for α loop cut (basic aircraft model)

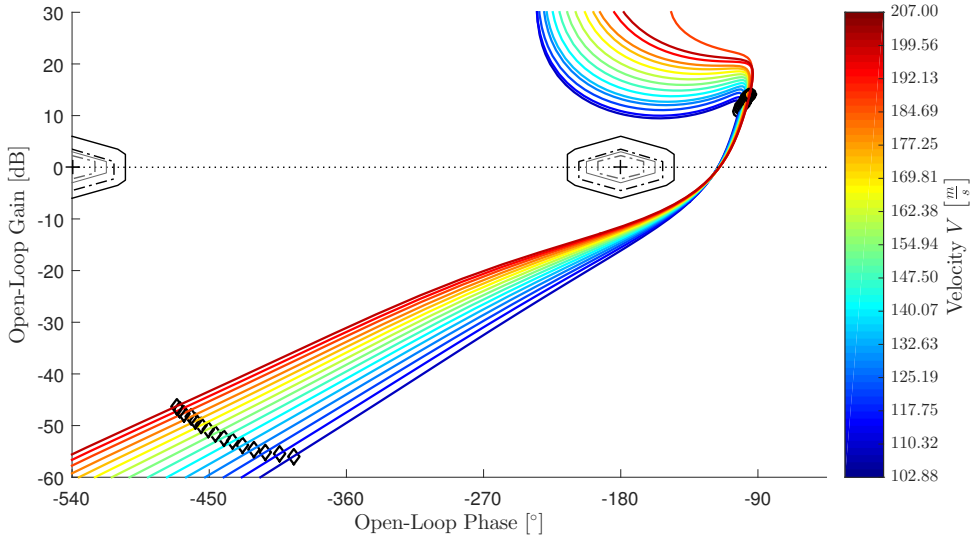

Figure A.33. – Nichols plot for robust stability assessment of $\Delta\dot{q}$ Compensation Law with $\dot{q}$ measurement at envelope points according to Table 2.2 generated for α loop cut (basic aircraft model)

Table A.44. – Robust stability properties gain margin (GM), phase margin Φ_m, time delay margins (TDM) and corresponding gain-crossover frequencies $\omega_{gc,\Phi}$ and $\omega_{gc,TDM}$ for robust stability assessment of $\Delta\dot{q}$ Compensation Law at envelope points according to Table 2.2 generated for α loop cut (basic aircraft model)

Velocity $V\ \left[\frac{m}{s}\right]$	**GM** $[dB]$	$\Phi_m\ [^\circ]$	$\omega_{gc,\Phi}\ \left[\frac{rad}{s}\right]$	**TDM** $[s]$	$\omega_{gc,TDM}\ \left[\frac{rad}{s}\right]$
102.88	16.36	63.69	1.32	0.841	1.32
	-10.34	-296.31	1.32	-3.911	1.32
110.32	15.77	63.99	1.37	0.815	1.37
	-10.89	-296.01	1.37	-3.770	1.37
117.75	15.27	63.78	1.41	0.788	1.41
	-12.07	-296.22	1.41	-3.661	1.41
125.19	14.83	63.99	1.46	0.766	1.46
	-13.23	-296.01	1.46	-3.543	1.46
132.63	14.42	64.17	1.50	0.745	1.50
	-13.99	-295.83	1.50	-3.436	1.50
140.07	14.05	64.32	1.54	0.727	1.54
	-15.35	-295.68	1.54	-3.343	1.54
147.50	13.70	64.45	1.58	0.711	1.58
	-16.82	-295.55	1.58	-3.259	1.58
154.94	13.38	64.56	1.62	0.696	1.62
	-18.41	-295.44	1.62	-3.183	1.62
162.38	13.09	64.65	1.66	0.682	1.66
	-20.09	-295.35	1.66	-3.115	1.66
169.81	12.81	64.66	1.69	0.666	1.69
	-21.95	-295.34	1.69	-3.043	1.69
177.25	12.55	64.65	1.73	0.652	1.73
	-23.76	-295.35	1.73	-2.978	1.73
184.69	12.30	64.62	1.77	0.638	1.77
	-25.27	-295.38	1.77	-2.918	1.77
192.13	12.06	64.82	1.79	0.631	1.79
	$-\infty$	-295.18	1.79	-2.874	1.79
199.56	11.85	64.82	1.83	0.620	1.83
	-28.29	-295.18	1.83	-2.822	1.83
207.00	11.65	64.79	1.86	0.609	1.86
	-30.84	-295.21	1.86	-2.774	1.86

Table A.45. – Robust stability properties gain margin (GM), phase margin Φ_m, time delay margins (TDM) and corresponding gain-crossover frequencies $\omega_{gc,\Phi}$ and $\omega_{gc,TDM}$ for robust stability assessment of $\Delta\dot{q}$ Compensation Law with $\dot{q}$ measurement at envelope points according to Table 2.2 generated for α loop cut (basic aircraft model)

Velocity $V\ \left[\frac{m}{s}\right]$	**GM** $[dB]$	$\Phi_m\ [^\circ]$	$\omega_{gc,\Phi}\ \left[\frac{rad}{s}\right]$	**TDM** $[s]$	$\omega_{gc,TDM}\ \left[\frac{rad}{s}\right]$
102.88	16.13	63.61	1.32	0.838	1.32
	-10.34	-296.39	1.32	-3.906	1.32
110.32	15.55	63.91	1.37	0.813	1.37
	-10.89	-296.09	1.37	-3.765	1.37
117.75	15.06	63.69	1.41	0.786	1.41
	-12.07	-296.31	1.41	-3.656	1.41
125.19	14.62	63.90	1.46	0.763	1.46
	-13.23	-296.10	1.46	-3.538	1.46
132.63	14.22	64.07	1.51	0.743	1.51
	-13.99	-295.93	1.51	-3.432	1.51
140.07	13.86	64.22	1.55	0.725	1.55
	-15.35	-295.78	1.55	-3.338	1.55
147.50	13.52	64.35	1.59	0.708	1.59
	-16.82	-295.65	1.59	-3.254	1.59
154.94	13.20	64.46	1.62	0.693	1.62
	-18.41	-295.54	1.62	-3.179	1.62
162.38	12.91	64.55	1.66	0.680	1.66
	-20.09	-295.45	1.66	-3.111	1.66
169.81	12.64	64.55	1.70	0.664	1.70
	-21.95	-295.45	1.70	-3.039	1.70
177.25	12.38	64.53	1.73	0.649	1.73
	-23.76	-295.47	1.73	-2.974	1.73
184.69	12.14	64.51	1.77	0.636	1.77
	-25.27	-295.49	1.77	-2.914	1.77
192.13	11.92	64.71	1.80	0.629	1.80
	$-\infty$	-295.29	1.80	-2.870	1.80
199.56	11.71	64.70	1.83	0.617	1.83
	-28.29	-295.30	1.83	-2.818	1.83
207.00	11.52	64.67	1.86	0.607	1.86
	-30.84	-295.33	1.86	-2.771	1.86

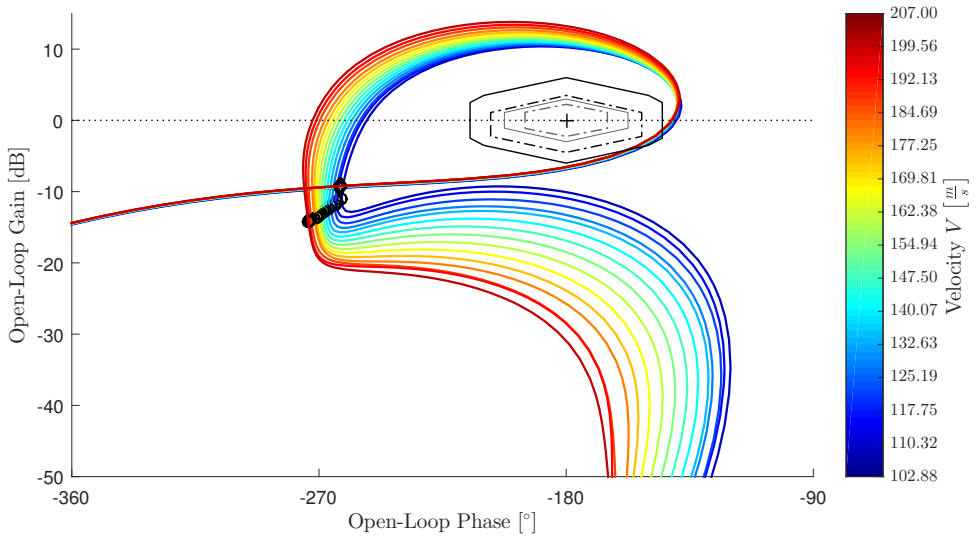

Figure A.34. – Nichols plot for robust stability assessment of $\Delta\dot{q}$ Compensation Law at envelope points according to Table 2.2 generated for q loop cut (basic aircraft model)

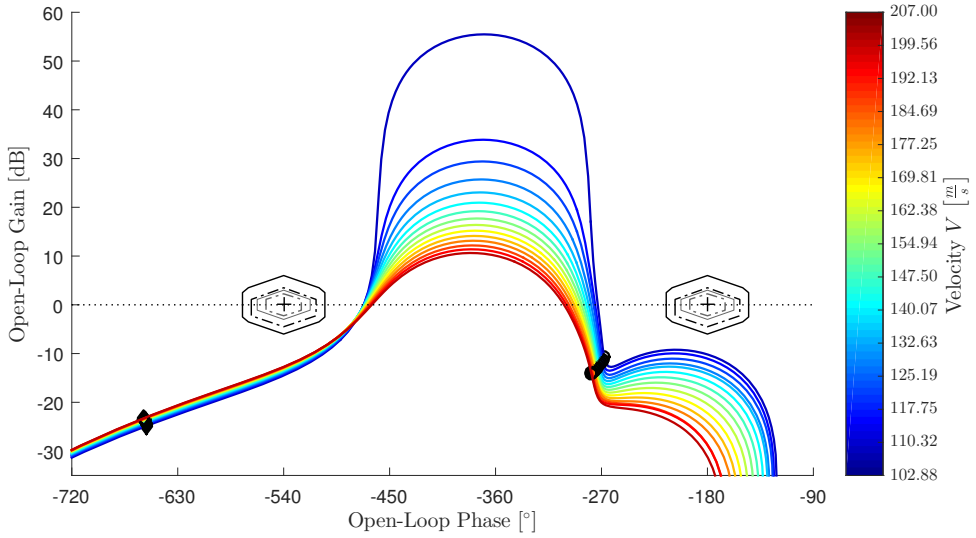

Figure A.35. – Nichols plot for robust stability assessment of $\Delta\dot{q}$ Compensation Law with $\dot{q}$ measurement at envelope points according to Table 2.2 generated for q loop cut (basic aircraft model)

Table A.46. – Robust stability properties gain margin (GM), phase margin Φ_m, time delay margins (TDM) and corresponding gain-crossover frequencies $\omega_{gc,\Phi}$ and $\omega_{gc,TDM}$ for robust stability assessment of $\Delta\dot{q}$ Compensation Law at envelope points according to Table 2.2 generated for q loop cut (basic aircraft model)

Velocity $V\ \left[\frac{m}{s}\right]$	**GM** $[dB]$	$\Phi_m\ [^\circ]$	$\omega_{gc,\Phi}\ \left[\frac{rad}{s}\right]$	**TDM** $[s]$	$\omega_{gc,TDM}\ \left[\frac{rad}{s}\right]$
102.88	6.88	40.07	8.94	0.078	8.94
	-10.25	-72.58	1.29	-0.625	8.94
110.32	6.83	39.62	9.04	0.076	9.04
	-10.34	-74.19	1.34	-0.618	9.04
117.75	6.80	39.36	9.13	0.075	9.13
	-10.41	-75.06	1.39	-0.613	9.13
125.19	6.76	39.05	9.22	0.074	9.22
	-10.52	-76.56	1.44	-0.607	9.22
132.63	6.72	38.81	9.31	0.073	9.31
	-10.65	-78.02	1.49	-0.602	9.31
140.07	6.69	38.64	9.39	0.072	9.39
	-10.80	-79.44	1.54	-0.597	9.39
147.50	6.66	38.55	9.47	0.071	9.47
	-10.98	-80.85	1.58	-0.592	9.47
154.94	6.63	38.43	9.56	0.070	9.56
	-11.17	-82.27	1.63	-0.587	9.56
162.38	6.61	38.26	9.66	0.069	9.66
	-11.39	-83.70	1.67	-0.582	9.66
169.81	6.59	38.14	9.75	0.068	9.75
	-11.64	-85.14	1.72	-0.576	9.75
177.25	6.58	38.07	9.85	0.067	9.85
	-11.90	-86.55	1.76	-0.571	9.85
184.69	6.56	38.08	9.93	0.067	9.93
	-12.19	-87.91	1.81	-0.566	9.93
192.13	6.55	38.30	9.97	0.067	9.97
	-12.53	-89.65	1.84	-0.563	9.97
199.56	6.54	38.47	10.02	0.067	10.02
	-12.86	-90.99	1.89	-0.560	10.02
207.00	6.54	38.50	10.11	0.066	10.11
	-13.22	-92.36	1.93	-0.555	10.11

Table A.47. – Robust stability properties gain margin (GM), phase margin Φ_m, time delay margins (TDM) and corresponding gain-crossover frequencies $\omega_{gc,\Phi}$ and $\omega_{gc,TDM}$ for robust stability assessment of $\Delta\dot{q}$ Compensation Law with $\dot{q}$ measurement at envelope points according to Table 2.2 generated for q loop cut (basic aircraft model)

Velocity $V\ \left[\frac{m}{s}\right]$	**GM** $[dB]$	$\Phi_m\ [^\circ]$	$\omega_{gc,\Phi}\ \left[\frac{rad}{s}\right]$	**TDM** $[s]$	$\omega_{gc,TDM}\ \left[\frac{rad}{s}\right]$
102.88	10.19	68.01	4.24	0.280	4.24
	$-\infty$	-93.16	1.09	-1.202	4.24
110.32	11.04	67.95	4.39	0.270	4.39
	$-\infty$	-95.41	1.14	-1.160	4.39
117.75	12.22	68.02	4.51	0.264	4.51
	$-\infty$	-96.77	1.18	-1.131	4.51
125.19	13.40	68.14	4.62	0.257	4.62
	$-\infty$	-98.79	1.22	-1.102	4.62
132.63	13.68	68.37	4.73	0.252	4.73
	$-\infty$	-100.83	1.26	-1.076	4.73
140.07	13.52	68.70	4.82	0.249	4.82
	$-\infty$	-102.86	1.30	-1.055	4.82
147.50	13.37	69.08	4.91	0.245	4.91
	$-\infty$	-104.88	1.34	-1.034	4.91
154.94	13.25	69.48	5.01	0.242	5.01
	$-\infty$	-106.89	1.38	-1.011	5.01
162.38	13.14	70.05	5.08	0.240	5.08
	$-\infty$	-108.90	1.42	-0.995	5.08
169.81	13.04	70.60	5.18	0.238	5.18
	$-\infty$	-110.98	1.46	-0.974	5.18
177.25	12.96	71.35	5.23	0.238	5.23
	$-\infty$	-113.04	1.50	-0.963	5.23
184.69	12.89	72.13	5.30	0.237	5.30
	$-\infty$	-115.23	1.54	-0.947	5.30
192.13	12.83	73.02	5.34	0.239	5.34
	$-\infty$	-117.66	1.58	-0.938	5.34
199.56	12.78	73.90	5.40	0.239	5.40
	$-\infty$	-119.75	1.62	-0.925	5.40
207.00	12.73	74.85	5.44	0.240	5.44
	$-\infty$	-121.86	1.66	-0.915	5.44

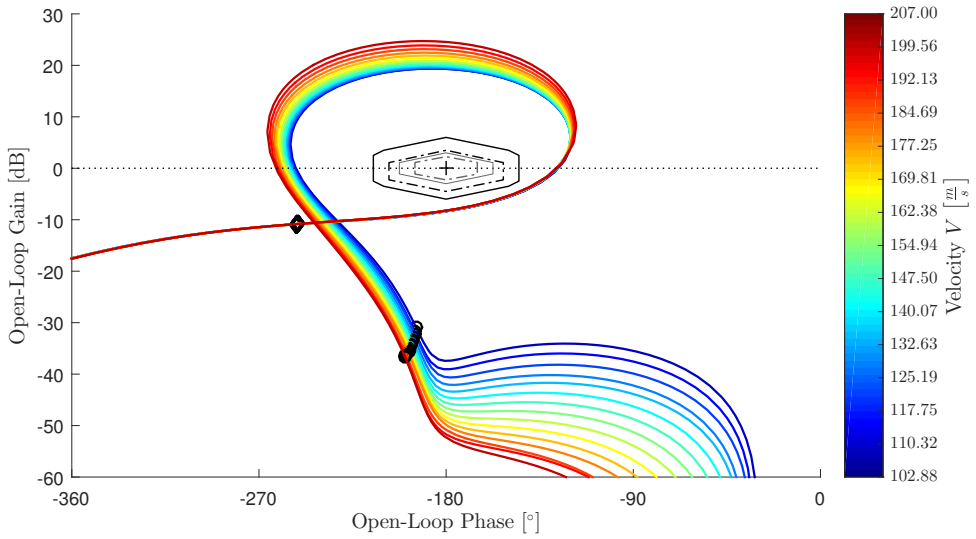

Figure A.36. – Nichols plot for robust stability assessment of $\Delta\dot{q}$ Compensation Law with $\dot{q}$ measurement at envelope points according to Table 2.2 generated for $\dot{q}$ loop cut (basic aircraft model)

Table A.48. – Robust stability properties gain margin (GM), phase margin Φ_m, time delay margins (TDM) and corresponding gain-crossover frequencies $\omega_{gc,\Phi}$ and $\omega_{gc,TDM}$ for robust stability assessment of $\Delta\dot{q}$ Compensation Law with $\dot{q}$ measurement at envelope points according to Table 2.2 generated for $\dot{q}$ loop cut (basic aircraft model)

Velocity V $\left[\frac{m}{s}\right]$	**GM** $[dB]$	Φ_m $[^\circ]$	$\omega_{gc,\Phi}$ $\left[\frac{rad}{s}\right]$	**TDM** $[s]$	$\omega_{gc,TDM}$ $\left[\frac{rad}{s}\right]$
102.88	8.37 -19.31	53.76 -72.22	10.03 3.05	0.094 -0.413	10.03 3.05
110.32	8.35 -19.33	53.52 -72.73	10.13 3.16	0.092 -0.401	10.13 3.16
117.75	8.33 -19.40	53.42 -73.01	10.22 3.25	0.091 -0.392	10.22 3.25
125.19	8.32 -19.52	53.30 -73.63	10.31 3.36	0.090 -0.383	10.31 3.36
132.63	8.30 -19.69	53.22 -74.34	10.40 3.46	0.089 -0.375	10.40 3.46
140.07	8.29 -19.90	53.19 -75.10	10.48 3.56	0.089 -0.368	10.48 3.56
147.50	8.28 -20.16	53.19 -75.70	10.56 3.65	0.088 -0.361	10.56 3.65
154.94	8.27 -20.47	53.05 -76.30	10.67 3.75	0.087 -0.356	10.67 3.75
162.38	8.26 -20.83	52.96 -76.98	10.77 3.83	0.086 -0.350	10.77 3.83
169.81	8.25 -21.25	52.90 -77.72	10.87 3.92	0.085 -0.346	10.87 3.92
177.25	8.24 -21.74	52.87 -78.52	10.97 4.01	0.084 -0.342	10.97 4.01
184.69	8.24 -22.31	52.88 -79.35	11.06 4.10	0.083 -0.338	11.06 4.10
192.13	8.23 -22.98	52.91 -80.31	11.14 4.17	0.083 -0.336	11.14 4.17
199.56	8.22 -23.70	52.97 -81.02	11.22 4.25	0.082 -0.333	11.22 4.25
207.00	8.22 -24.54	53.06 -81.70	11.30 4.32	0.082 -0.330	11.30 4.32

A.5.6. L1 adaptive controller with Eigenstructure Assignment

Page intentionally left blank

Table A.49. – Robust stability properties gain margin (GM), phase margin Φ_m, time delay margins (TDM) and corresponding gain-crossover frequencies $\omega_{gc,\Phi}$ and $\omega_{gc,TDM}$ for robust stability comparison of L1 adaptive controller with Eigenstructure Assignment with and without hedging at V = 154.94$\frac{m}{s}$ generated for α loop cut (basic aircraft model)

Controller	**GM** $[dB]$	Φ_m $[^\circ]$	$\omega_{gc,\Phi}$ $\left[\frac{rad}{s}\right]$	**TDM** $[s]$	$\omega_{gc,TDM}$ $\left[\frac{rad}{s}\right]$
Baseline	12.69	70.24	0.55	2.239	0.55
	$-\infty$	-289.76	0.55	-9.235	0.55
L1 Standalone	12.47	78.84	5.27	0.261	5.27
	$-\infty$	-281.16	5.27	-0.932	5.27
L1 Standalone (no hedg.)	12.77	78.57	5.27	0.260	5.27
	$-\infty$	-281.43	5.27	-0.933	5.27

Table A.50. – Robust stability properties gain margin (GM), phase margin Φ_m, time delay margins (TDM) and corresponding gain-crossover frequencies $\omega_{gc,\Phi}$ and $\omega_{gc,TDM}$ for robust stability comparison of L1 adaptive controller with Eigenstructure Assignment with and without hedging at V = 154.94$\frac{m}{s}$ generated for q loop cut (basic aircraft model)

Controller	**GM** $[dB]$	Φ_m $[^\circ]$	$\omega_{gc,\Phi}$ $\left[\frac{rad}{s}\right]$	**TDM** $[s]$	$\omega_{gc,TDM}$ $\left[\frac{rad}{s}\right]$
Baseline	15.54	101.74	4.39	0.404	4.39
	$-\infty$	-137.46	1.92	-1.026	4.39
L1 Standalone	12.56	∞	0.00	∞	0.00
	$-\infty$	$-\infty$	0.00	$-\infty$	0.00
L1 Standalone (no hedg.)	13.10	∞	0.00	∞	0.00
	$-\infty$	$-\infty$	0.00	$-\infty$	0.00

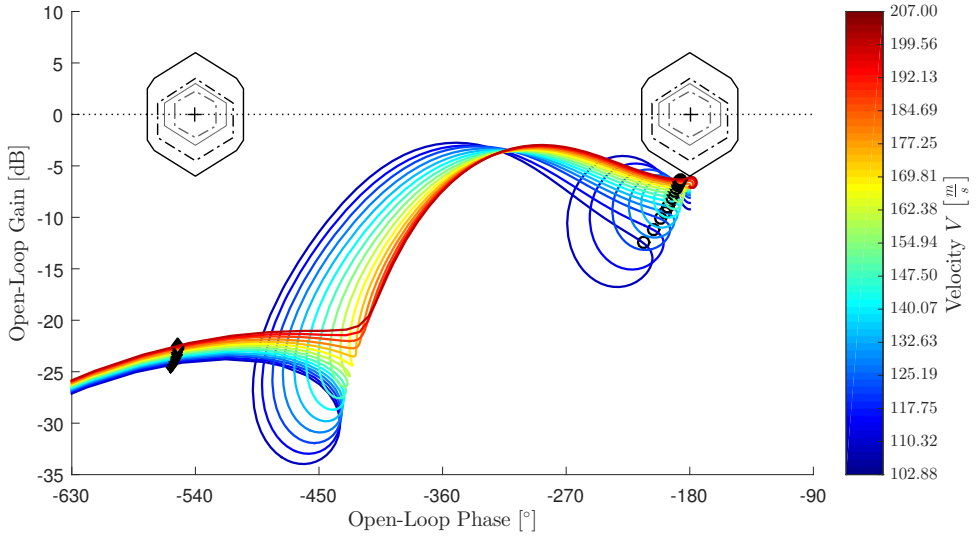

Figure A.37. – Nichols plot for robust stability assessment of L1 adaptive controller with Eigenstructure Assignment at envelope points according to Table 2.2 generated for η_{cmd} (bottleneck) loop cut (basic aircraft model)

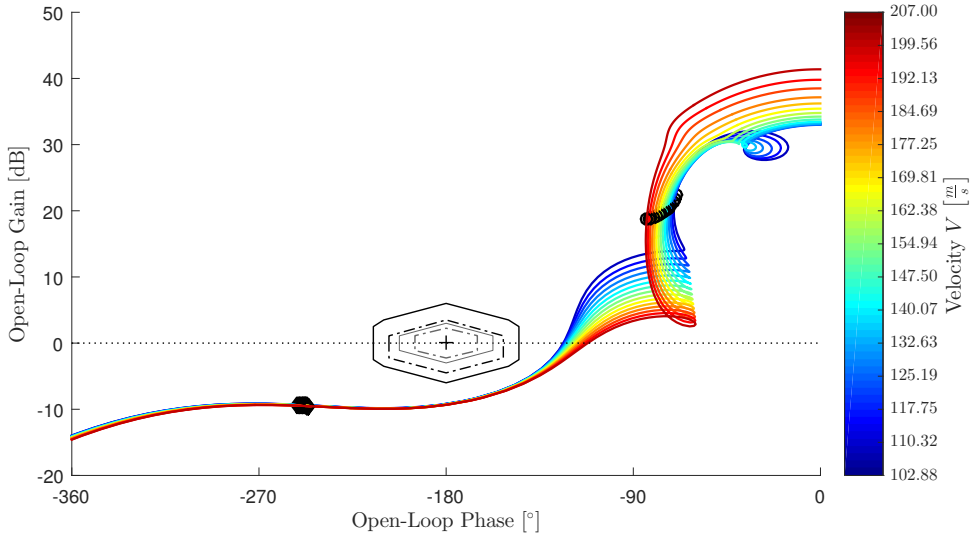

Figure A.38. – Nichols plot for robust stability assessment of L1 adaptive controller with Eigenstructure Assignment without hedging at envelope points according to Table 2.2 generated for η_{cmd} (bottleneck) loop cut (basic aircraft model)

Table A.51. – Robust stability properties gain margin (GM), phase margin Φ_m, time delay margins (TDM) and corresponding gain-crossover frequencies $\omega_{gc,\Phi}$ and $\omega_{gc,TDM}$ for robust stability assessment of L1 adaptive controller with Eigenstructure Assignment at envelope points according to Table 2.2 generated for η_{cmd} (bottleneck) loop cut (basic aircraft model)

Velocity $V\ \left[\frac{m}{s}\right]$	**GM** $[dB]$	$\Phi_m\ [^\circ]$	$\omega_{gc,\Phi}\ \left[\frac{rad}{s}\right]$	**TDM** $[s]$	$\omega_{gc,TDM}\ \left[\frac{rad}{s}\right]$
102.88	24.02	∞	0.00	∞	0.00
	$-\infty$	$-\infty$	0.00	$-\infty$	0.00
110.32	23.87	∞	0.00	∞	0.00
	$-\infty$	$-\infty$	0.00	$-\infty$	0.00
117.75	23.72	∞	0.00	∞	0.00
	$-\infty$	$-\infty$	0.00	$-\infty$	0.00
125.19	23.59	∞	0.00	∞	0.00
	$-\infty$	$-\infty$	0.00	$-\infty$	0.00
132.63	23.46	∞	0.00	∞	0.00
	$-\infty$	$-\infty$	0.00	$-\infty$	0.00
140.07	23.33	∞	0.00	∞	0.00
	$-\infty$	$-\infty$	0.00	$-\infty$	0.00
147.50	23.20	∞	0.00	∞	0.00
	$-\infty$	$-\infty$	0.00	$-\infty$	0.00
154.94	23.05	∞	0.00	∞	0.00
	$-\infty$	$-\infty$	0.00	$-\infty$	0.00
162.38	22.92	∞	0.00	∞	0.00
	$-\infty$	$-\infty$	0.00	$-\infty$	0.00
169.81	22.78	∞	0.00	∞	0.00
	$-\infty$	$-\infty$	0.00	$-\infty$	0.00
177.25	22.64	∞	0.00	∞	0.00
	$-\infty$	$-\infty$	0.00	$-\infty$	0.00
184.69	6.80	∞	0.00	∞	0.00
	$-\infty$	$-\infty$	0.00	$-\infty$	0.00
192.13	6.46	∞	0.00	∞	0.00
	$-\infty$	$-\infty$	0.00	$-\infty$	0.00
199.56	6.24	∞	0.00	∞	0.00
	$-\infty$	$-\infty$	0.00	$-\infty$	0.00
207.00	6.09	∞	0.00	∞	0.00
	$-\infty$	$-\infty$	0.00	$-\infty$	0.00

Table A.52. – Robust stability properties gain margin (GM), phase margin Φ_m, time delay margins (TDM) and corresponding gain-crossover frequencies $\omega_{gc,\Phi}$ and $\omega_{gc,TDM}$ for robust stability assessment of L1 adaptive controller with Eigenstructure Assignment without hedging at envelope points according to Table 2.2 generated for η_{cmd} (bottleneck) loop cut (basic aircraft model)

Velocity $V\ \left[\frac{m}{s}\right]$	**GM** $[dB]$	$\Phi_m\ [^\circ]$	$\omega_{gc,\Phi}\ \left[\frac{rad}{s}\right]$	**TDM** $[s]$	$\omega_{gc,TDM}\ \left[\frac{rad}{s}\right]$
102.88	9.17	56.25	6.91	0.142	6.91
	$-\infty$	-303.75	6.91	-0.767	6.91
110.32	9.19	56.58	6.97	0.142	6.97
	$-\infty$	-303.42	6.97	-0.760	6.97
117.75	9.20	56.98	7.04	0.141	7.04
	$-\infty$	-303.02	7.04	-0.751	7.04
125.19	9.22	57.43	7.11	0.141	7.11
	$-\infty$	-302.57	7.11	-0.742	7.11
132.63	9.23	58.02	7.17	0.141	7.17
	$-\infty$	-301.98	7.17	-0.735	7.17
140.07	9.25	58.64	7.24	0.141	7.24
	$-\infty$	-301.36	7.24	-0.726	7.24
147.50	9.26	59.39	7.30	0.142	7.30
	$-\infty$	-300.61	7.30	-0.719	7.30
154.94	9.27	60.19	7.37	0.142	7.37
	$-\infty$	-299.81	7.37	-0.710	7.37
162.38	9.28	61.09	7.43	0.143	7.43
	$-\infty$	-298.91	7.43	-0.702	7.43
169.81	9.29	62.06	7.50	0.144	7.50
	$-\infty$	-297.94	7.50	-0.693	7.50
177.25	9.30	63.12	7.56	0.146	7.56
	$-\infty$	-296.88	7.56	-0.686	7.56
184.69	9.31	64.28	7.63	0.147	7.63
	$-\infty$	-295.72	7.63	-0.676	7.63
192.13	9.33	65.54	7.69	0.149	7.69
	$-\infty$	-294.46	7.69	-0.668	7.69
199.56	9.33	66.77	7.74	0.151	7.74
	$-\infty$	-293.23	7.74	-0.661	7.74
207.00	9.33	68.10	7.78	0.153	7.78
	$-\infty$	-291.90	7.78	-0.655	7.78

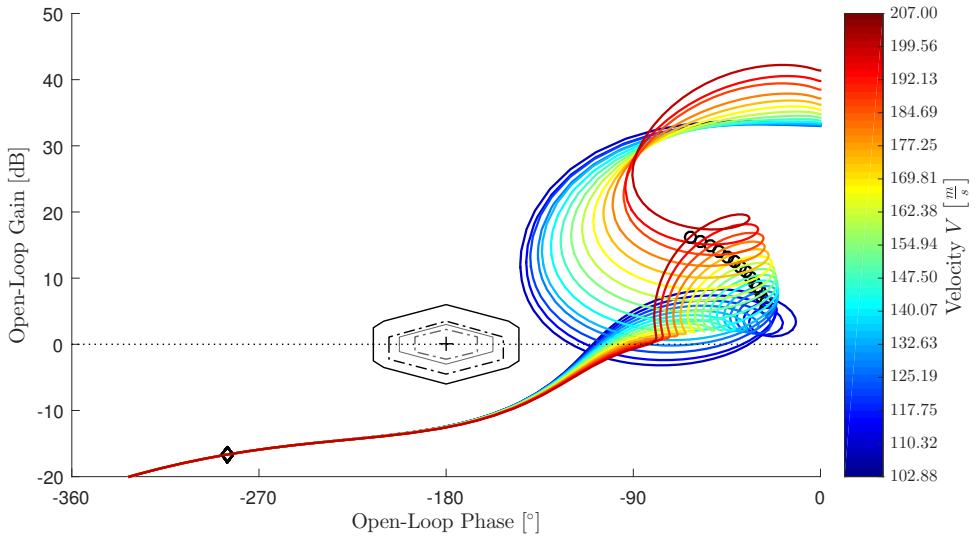

Figure A.39. – Nichols plot for robust stability assessment of L1 adaptive controller with Eigenstructure Assignment at envelope points according to Table 2.2 generated for α loop cut (basic aircraft model)

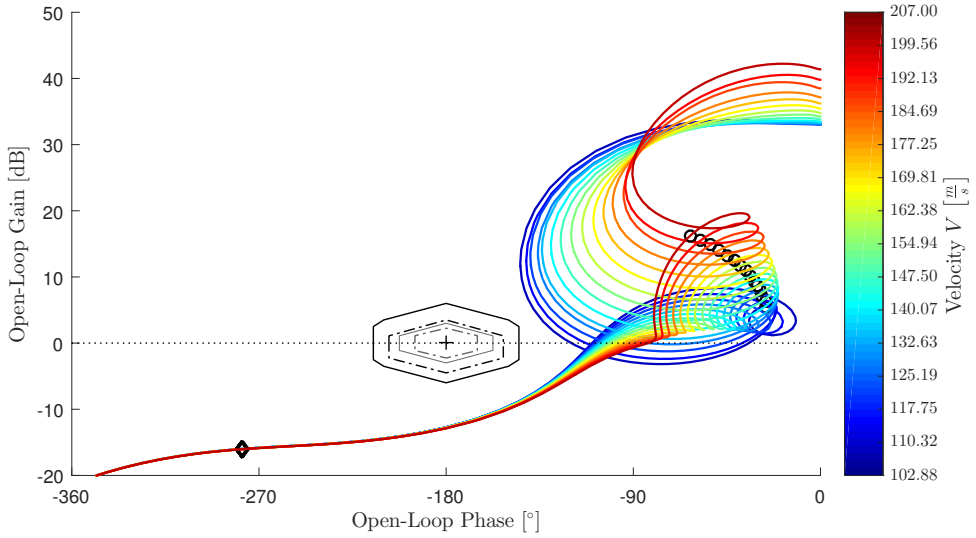

Figure A.40. – Nichols plot for robust stability assessment of L1 adaptive controller with Eigenstructure Assignment without hedging at envelope points according to Table 2.2 generated for α loop cut (basic aircraft model)

Table A.53. – Robust stability properties gain margin (GM), phase margin Φ_m, time delay margins (TDM) and corresponding gain-crossover frequencies $\omega_{gc,\Phi}$ and $\omega_{gc,TDM}$ for robust stability assessment of L1 adaptive controller with Eigenstructure Assignment at envelope points according to Table 2.2 generated for α loop cut (basic aircraft model)

Velocity $V\ \left[\frac{m}{s}\right]$	**GM** $[dB]$	$\Phi_m\ [^\circ]$	$\omega_{gc,\Phi}\ \left[\frac{rad}{s}\right]$	**TDM** $[s]$	$\omega_{gc,TDM}\ \left[\frac{rad}{s}\right]$
102.88	12.40	60.29	0.13	0.228	5.40
	$-\infty$	-214.51	0.17	-0.936	5.40
110.32	12.41	67.27	0.12	0.230	5.41
	$-\infty$	-217.72	0.15	-0.931	5.41
117.75	12.41	72.16	5.41	0.233	5.41
	$-\infty$	-226.46	0.14	-0.928	5.41
125.19	12.42	73.17	5.41	0.236	5.41
	$-\infty$	-241.14	0.12	-0.926	5.41
132.63	12.43	74.40	5.40	0.240	5.40
	$-\infty$	-285.60	5.40	-0.923	5.40
140.07	12.44	75.67	5.37	0.246	5.37
	$-\infty$	-284.33	5.37	-0.925	5.37
147.50	12.45	77.15	5.32	0.253	5.32
	$-\infty$	-282.85	5.32	-0.927	5.32
154.94	12.47	78.84	5.27	0.261	5.27
	$-\infty$	-281.16	5.27	-0.932	5.27
162.38	12.48	80.72	5.19	0.272	5.19
	$-\infty$	-279.28	5.19	-0.940	5.19
169.81	12.49	82.85	5.08	0.284	5.08
	$-\infty$	-277.15	5.08	-0.951	5.08
177.25	12.50	85.31	4.95	0.301	4.95
	$-\infty$	-274.69	4.95	-0.968	4.95
184.69	12.51	88.15	4.77	0.322	4.77
	$-\infty$	-271.85	4.77	-0.994	4.77
192.13	12.54	91.49	4.52	0.353	4.52
	$-\infty$	-268.51	4.52	-1.037	4.52
199.56	12.55	95.02	4.18	0.397	4.18
	$-\infty$	-264.98	4.18	-1.106	4.18
207.00	12.56	97.32	3.76	0.452	3.76
	$-\infty$	-262.68	3.76	-1.220	3.76

Table A.54. – Robust stability properties gain margin (GM), phase margin Φ_m, time delay margins (TDM) and corresponding gain-crossover frequencies $\omega_{gc,\Phi}$ and $\omega_{gc,TDM}$ for robust stability assessment of L1 adaptive controller with Eigenstructure Assignment without hedging at envelope points according to Table 2.2 generated for α loop cut (basic aircraft model)

Velocity $V\ \left[\frac{m}{s}\right]$	**GM** $[dB]$	$\Phi_m\ [^\circ]$	$\omega_{gc,\Phi}\ \left[\frac{rad}{s}\right]$	**TDM** $[s]$	$\omega_{gc,TDM}\ \left[\frac{rad}{s}\right]$
102.88	12.70	60.29	0.13	0.227	5.40
	$-\infty$	-214.51	0.17	-0.937	5.40
110.32	12.71	67.27	0.12	0.229	5.41
	$-\infty$	-217.73	0.15	-0.932	5.41
117.75	12.72	71.84	5.41	0.232	5.41
	$-\infty$	-226.47	0.14	-0.929	5.41
125.19	12.73	72.85	5.41	0.235	5.41
	$-\infty$	-241.15	0.12	-0.927	5.41
132.63	12.74	74.09	5.40	0.239	5.40
	$-\infty$	-285.91	5.40	-0.924	5.40
140.07	12.75	75.36	5.37	0.245	5.37
	$-\infty$	-284.64	5.37	-0.926	5.37
147.50	12.76	76.86	5.32	0.252	5.32
	$-\infty$	-283.14	5.32	-0.928	5.32
154.94	12.77	78.57	5.27	0.260	5.27
	$-\infty$	-281.43	5.27	-0.933	5.27
162.38	12.78	80.46	5.19	0.271	5.19
	$-\infty$	-279.54	5.19	-0.941	5.19
169.81	12.80	82.62	5.08	0.284	5.08
	$-\infty$	-277.38	5.08	-0.952	5.08
177.25	12.81	85.10	4.95	0.300	4.95
	$-\infty$	-274.90	4.95	-0.969	4.95
184.69	12.83	87.97	4.77	0.322	4.77
	$-\infty$	-272.03	4.77	-0.995	4.77
192.13	12.85	91.36	4.51	0.353	4.51
	$-\infty$	-268.64	4.51	-1.039	4.51
199.56	12.87	94.96	4.17	0.397	4.17
	$-\infty$	-265.04	4.17	-1.109	4.17
207.00	12.88	97.25	3.75	0.453	3.75
	$-\infty$	-262.75	3.75	-1.224	3.75

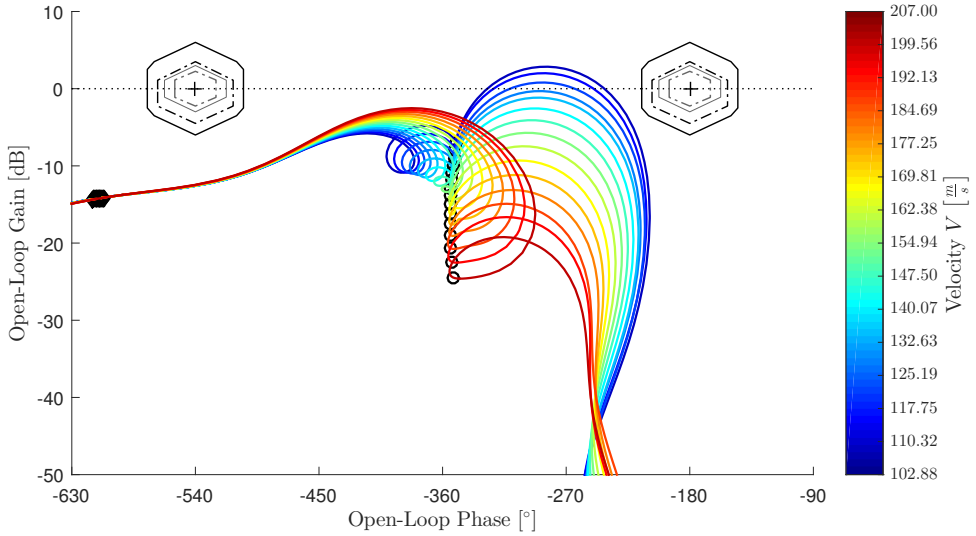

Figure A.41. – Nichols plot for robust stability assessment of L1 adaptive controller with Eigenstructure Assignment at envelope points according to Table 2.2 generated for q loop cut (basic aircraft model)

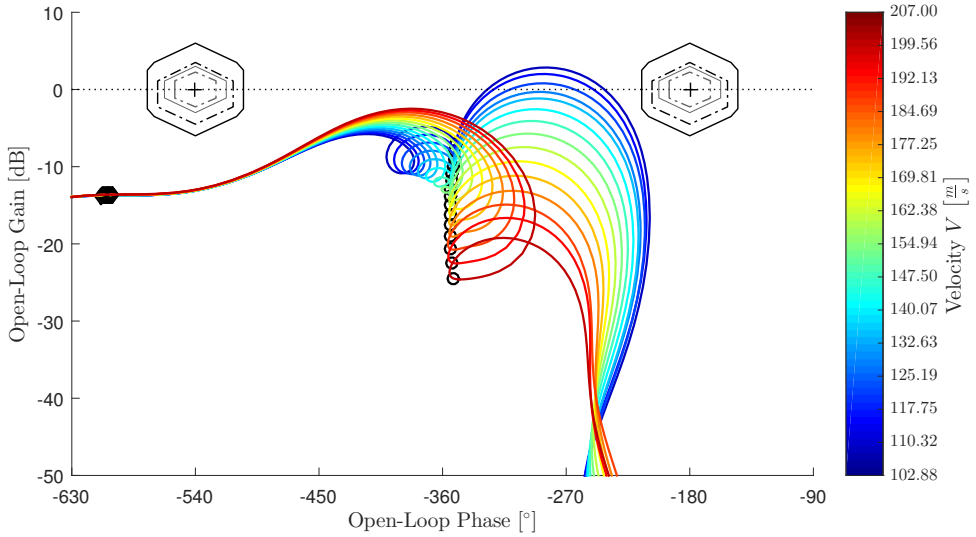

Figure A.42. – Nichols plot for robust stability assessment of L1 adaptive controller with Eigenstructure Assignment without hedging at envelope points according to Table 2.2 generated for q loop cut (basic aircraft model)

Table A.55. – Robust stability properties gain margin (GM), phase margin Φ_m, time delay margins (TDM) and corresponding gain-crossover frequencies $\omega_{gc,\Phi}$ and $\omega_{gc,TDM}$ for robust stability assessment of L1 adaptive controller with Eigenstructure Assignment at envelope points according to Table 2.2 generated for q loop cut (basic aircraft model)

Velocity $V\ \left[\frac{m}{s}\right]$	**GM** $[dB]$	$\Phi_m\ [^\circ]$	$\omega_{gc,\Phi}\ \left[\frac{rad}{s}\right]$	**TDM** $[s]$	$\omega_{gc,TDM}\ \left[\frac{rad}{s}\right]$
102.88	12.58	212.63	0.17	22.391	0.17
	$-\infty$	-62.24	0.13	-8.565	0.13
110.32	12.58	217.22	0.15	25.196	0.15
	$-\infty$	-70.13	0.12	-10.086	0.12
117.75	12.58	229.27	0.13	29.648	0.13
	$-\infty$	-83.90	0.12	-12.350	0.12
125.19	12.58	∞	0.00	∞	0.00
	$-\infty$	$-\infty$	0.00	$-\infty$	0.00
132.63	12.58	∞	0.00	∞	0.00
	$-\infty$	$-\infty$	0.00	$-\infty$	0.00
140.07	12.58	∞	0.00	∞	0.00
	$-\infty$	$-\infty$	0.00	$-\infty$	0.00
147.50	12.57	∞	0.00	∞	0.00
	$-\infty$	$-\infty$	0.00	$-\infty$	0.00
154.94	12.56	∞	0.00	∞	0.00
	$-\infty$	$-\infty$	0.00	$-\infty$	0.00
162.38	12.55	∞	0.00	∞	0.00
	$-\infty$	$-\infty$	0.00	$-\infty$	0.00
169.81	12.53	∞	0.00	∞	0.00
	$-\infty$	$-\infty$	0.00	$-\infty$	0.00
177.25	12.52	∞	0.00	∞	0.00
	$-\infty$	$-\infty$	0.00	$-\infty$	0.00
184.69	12.50	∞	0.00	∞	0.00
	$-\infty$	$-\infty$	0.00	$-\infty$	0.00
192.13	12.50	∞	0.00	∞	0.00
	$-\infty$	$-\infty$	0.00	$-\infty$	0.00
199.56	12.47	∞	0.00	∞	0.00
	$-\infty$	$-\infty$	0.00	$-\infty$	0.00
207.00	12.45	∞	0.00	∞	0.00
	$-\infty$	$-\infty$	0.00	$-\infty$	0.00

Table A.56. – Robust stability properties gain margin (GM), phase margin Φ_m, time delay margins (TDM) and corresponding gain-crossover frequencies $\omega_{gc,\Phi}$ and $\omega_{gc,TDM}$ for robust stability assessment of L1 adaptive controller with Eigenstructure Assignment without hedging at envelope points according to Table 2.2 generated for q loop cut (basic aircraft model)

Velocity $V\ \left[\frac{m}{s}\right]$	**GM** $[dB]$	$\Phi_m\ [^\circ]$	$\omega_{gc,\Phi}\ \left[\frac{rad}{s}\right]$	**TDM** $[s]$	$\omega_{gc,TDM}\ \left[\frac{rad}{s}\right]$
102.88	13.11	212.63	0.17	22.391	0.17
	$-\infty$	-62.24	0.13	-8.565	0.13
110.32	13.11	217.22	0.15	25.195	0.15
	$-\infty$	-70.12	0.12	-10.086	0.12
117.75	13.12	229.27	0.13	29.647	0.13
	$-\infty$	-83.90	0.12	-12.350	0.12
125.19	13.12	∞	0.00	∞	0.00
	$-\infty$	$-\infty$	0.00	$-\infty$	0.00
132.63	13.12	∞	0.00	∞	0.00
	$-\infty$	$-\infty$	0.00	$-\infty$	0.00
140.07	13.12	∞	0.00	∞	0.00
	$-\infty$	$-\infty$	0.00	$-\infty$	0.00
147.50	13.11	∞	0.00	∞	0.00
	$-\infty$	$-\infty$	0.00	$-\infty$	0.00
154.94	13.10	∞	0.00	∞	0.00
	$-\infty$	$-\infty$	0.00	$-\infty$	0.00
162.38	13.08	∞	0.00	∞	0.00
	$-\infty$	$-\infty$	0.00	$-\infty$	0.00
169.81	13.07	∞	0.00	∞	0.00
	$-\infty$	$-\infty$	0.00	$-\infty$	0.00
177.25	13.05	∞	0.00	∞	0.00
	$-\infty$	$-\infty$	0.00	$-\infty$	0.00
184.69	13.03	∞	0.00	∞	0.00
	$-\infty$	$-\infty$	0.00	$-\infty$	0.00
192.13	13.02	∞	0.00	∞	0.00
	$-\infty$	$-\infty$	0.00	$-\infty$	0.00
199.56	13.00	∞	0.00	∞	0.00
	$-\infty$	$-\infty$	0.00	$-\infty$	0.00
207.00	12.98	∞	0.00	∞	0.00
	$-\infty$	$-\infty$	0.00	$-\infty$	0.00

A.6. Robust stability of control laws (enhanced aircraft model)

A.6.1. Comparison between DPI and Plant Augmentation

Page intentionally left blank

Table A.57. – Robust stability properties gain margin (GM), phase margin Φ_m, time delay margins (TDM) and corresponding gain-crossover frequencies $\omega_{gc,\Phi}$ and $\omega_{gc,TDM}$ for robust stability comparison of DPI and Plant Augmentation with and without hedging at $V = 154.94\frac{m}{s}$ generated for α loop cut (enhanced aircraft model)

Controller	**GM** $[dB]$	$\Phi_m\,[^\circ]$	$\omega_{gc,\Phi}\left[\frac{rad}{s}\right]$	**TDM** $[s]$	$\omega_{gc,TDM}\left[\frac{rad}{s}\right]$
Baseline	7.72	63.12	0.40	2.777	0.40
	$-\infty$	-296.88	0.40	-13.063	0.40
DPI Augmentation	5.21	52.22	0.93	0.981	0.93
	-14.47	-307.78	0.93	-5.781	0.93
DPI Augmentation (no hedg.)	5.35	52.33	0.91	1.002	0.91
	-14.45	-307.67	0.91	-5.889	0.91
Plant Augmentation	5.34	51.43	0.96	0.935	0.96
	-13.54	-308.57	0.96	-5.609	0.96
Plant Augmentation (no hedg.)	5.49	51.55	0.94	0.955	0.94
	-13.52	-308.45	0.94	-5.714	0.94

Table A.58. – Robust stability properties gain margin (GM), phase margin Φ_m, time delay margins (TDM) and corresponding gain-crossover frequencies $\omega_{gc,\Phi}$ and $\omega_{gc,TDM}$ for robust stability comparison of DPI and Plant Augmentation with and without hedging at $V = 154.94\frac{m}{s}$ generated for q loop cut (enhanced aircraft model)

Controller	**GM** $[dB]$	$\Phi_m\,[^\circ]$	$\omega_{gc,\Phi}\left[\frac{rad}{s}\right]$	**TDM** $[s]$	$\omega_{gc,TDM}\left[\frac{rad}{s}\right]$
Baseline	21.76	∞	0.00	∞	0.00
	$-\infty$	$-\infty$	0.00	$-\infty$	0.00
DPI Augmentation	6.44	33.97	4.69	0.126	4.69
	-8.77	-79.55	0.88	-1.213	4.69
DPI Augmentation (no hedg.)	6.29	35.70	4.67	0.133	4.67
	-9.43	-80.56	0.86	-1.212	4.67
Plant Augmentation	6.53	34.77	4.70	0.129	4.70
	-9.09	-79.69	0.90	-1.208	4.70
Plant Augmentation (no hedg.)	6.38	36.58	4.67	0.137	4.67
	-9.79	-80.83	0.89	-1.207	4.67

A.6.2. Baseline Controller

Page intentionally left blank

Table A.59. – Robust stability properties gain margin (GM), phase margin Φ_m, time delay margins (TDM) and corresponding gain-crossover frequencies $\omega_{gc,\Phi}$ and $\omega_{gc,TDM}$ for robust stability assessment of baseline controller at envelope points according to Table 2.2 generated for α loop cut (enhanced aircraft model)

Velocity $V\ \left[\frac{m}{s}\right]$	**GM** $[dB]$	$\Phi_m\ [^\circ]$	$\omega_{gc,\Phi}\ \left[\frac{rad}{s}\right]$	**TDM** $[s]$	$\omega_{gc,TDM}\ \left[\frac{rad}{s}\right]$
102.88	10.65	66.37	0.41	2.842	0.41
	$-\infty$	-293.63	0.41	-12.575	0.41
110.32	9.75	65.63	0.40	2.857	0.40
	$-\infty$	-294.37	0.40	-12.814	0.40
117.75	9.12	64.87	0.40	2.858	0.40
	$-\infty$	-295.13	0.40	-13.003	0.40
125.19	8.69	64.40	0.39	2.850	0.39
	$-\infty$	-295.60	0.39	-13.083	0.39
132.63	8.34	63.98	0.39	2.838	0.39
	$-\infty$	-296.02	0.39	-13.128	0.39
140.07	8.08	63.63	0.39	2.821	0.39
	$-\infty$	-296.37	0.39	-13.138	0.39
147.50	7.86	63.33	0.39	2.800	0.39
	$-\infty$	-296.67	0.39	-13.115	0.39
154.94	7.72	63.12	0.40	2.778	0.40
	$-\infty$	-296.88	0.40	-13.063	0.40
162.38	7.59	62.97	0.40	2.753	0.40
	$-\infty$	-297.03	0.40	-12.985	0.40
169.81	7.52	62.85	0.40	2.725	0.40
	$-\infty$	-297.15	0.40	-12.883	0.40
177.25	7.48	62.89	0.41	2.702	0.41
	$-\infty$	-297.11	0.41	-12.764	0.41
184.69	7.47	62.59	0.41	2.656	0.41
	-21.29	-297.41	0.41	-12.620	0.41
192.13	7.49	62.48	0.41	2.633	0.41
	-11.87	-297.52	0.41	-12.539	0.41
199.56	7.53	63.23	0.42	2.621	0.42
	$-\infty$	-296.77	0.42	-12.303	0.42
207.00	7.58	63.45	0.43	2.589	0.43
	$-\infty$	-296.55	0.43	-12.102	0.43

Table A.60. – Robust stability properties gain margin (GM), phase margin Φ_m, time delay margins (TDM) and corresponding gain-crossover frequencies $\omega_{gc,\Phi}$ and $\omega_{gc,TDM}$ for robust stability assessment of baseline controller at envelope points according to Table 2.2 generated for q loop cut (enhanced aircraft model)

Velocity $V\ \left[\frac{m}{s}\right]$	**GM** $[dB]$	$\Phi_m\ [^\circ]$	$\omega_{gc,\Phi}\ \left[\frac{rad}{s}\right]$	**TDM** $[s]$	$\omega_{gc,TDM}\ \left[\frac{rad}{s}\right]$
102.88	13.43	142.39	1.93	1.289	1.93
	$-\infty$	-184.12	1.61	-1.970	1.93
110.32	15.26	∞	0.00	∞	0.00
	$-\infty$	$-\infty$	0.00	$-\infty$	0.00
117.75	17.31	∞	0.00	∞	0.00
	$-\infty$	$-\infty$	0.00	$-\infty$	0.00
125.19	18.12	∞	0.00	∞	0.00
	$-\infty$	$-\infty$	0.00	$-\infty$	0.00
132.63	18.87	∞	0.00	∞	0.00
	$-\infty$	$-\infty$	0.00	$-\infty$	0.00
140.07	19.72	∞	0.00	∞	0.00
	$-\infty$	$-\infty$	0.00	$-\infty$	0.00
147.50	20.68	∞	0.00	∞	0.00
	$-\infty$	$-\infty$	0.00	$-\infty$	0.00
154.94	21.76	∞	0.00	∞	0.00
	$-\infty$	$-\infty$	0.00	$-\infty$	0.00
162.38	23.01	∞	0.00	∞	0.00
	$-\infty$	$-\infty$	0.00	$-\infty$	0.00
169.81	24.44	∞	0.00	∞	0.00
	$-\infty$	$-\infty$	0.00	$-\infty$	0.00
177.25	26.14	∞	0.00	∞	0.00
	$-\infty$	$-\infty$	0.00	$-\infty$	0.00
184.69	28.20	∞	0.00	∞	0.00
	$-\infty$	$-\infty$	0.00	$-\infty$	0.00
192.13	31.01	∞	0.00	∞	0.00
	$-\infty$	$-\infty$	0.00	$-\infty$	0.00
199.56	34.52	∞	0.00	∞	0.00
	$-\infty$	$-\infty$	0.00	$-\infty$	0.00
207.00	40.20	∞	0.00	∞	0.00
	$-\infty$	$-\infty$	0.00	$-\infty$	0.00

A.6.3. DPI Augmentation

Page intentionally left blank

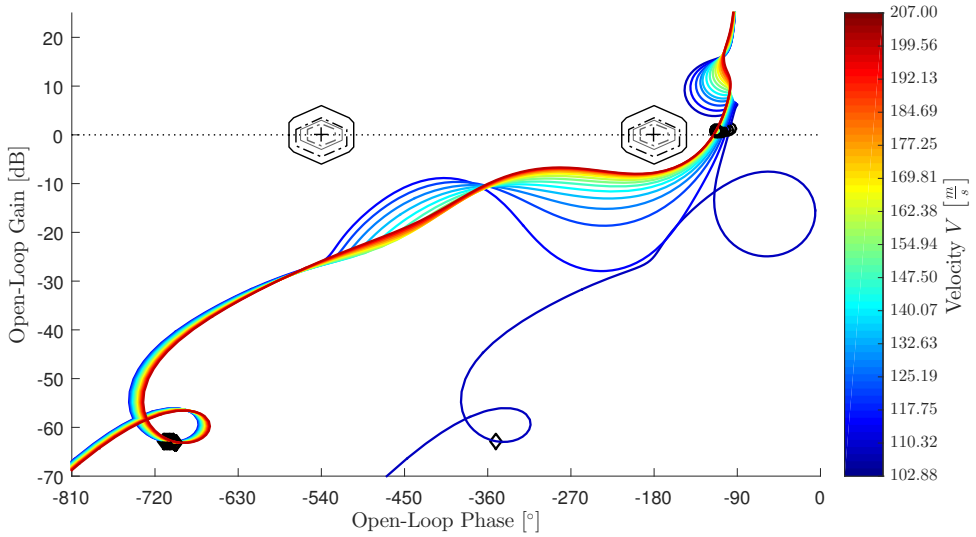

Figure A.43. – Nichols plot for robust stability assessment of DPI Augmentation at envelope points according to Table 2.2 generated for η_{cmd} (bottleneck) loop cut (enhanced aircraft model)

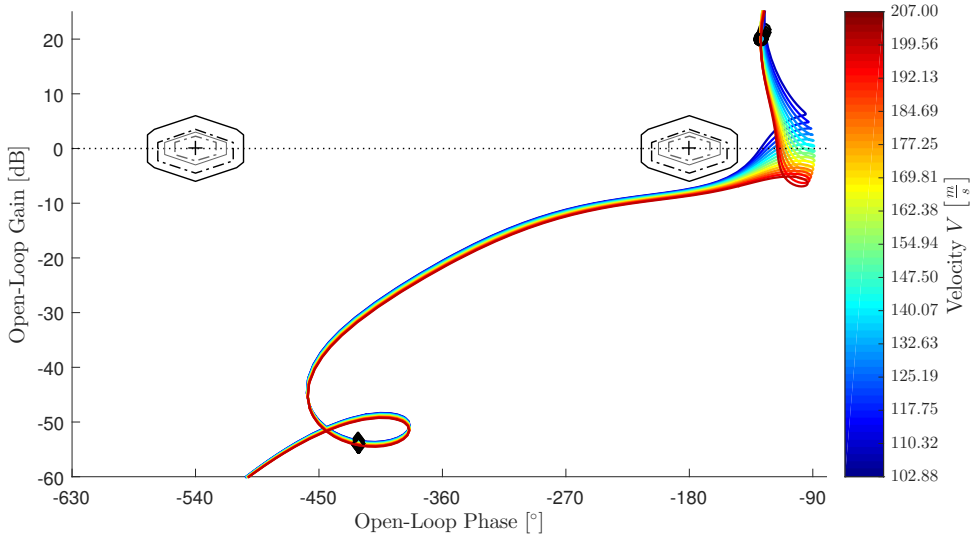

Figure A.44. – Nichols plot for robust stability assessment of DPI Augmentation without hedging at envelope points according to Table 2.2 generated for η_{cmd} (bottleneck) loop cut (enhanced aircraft model)

Table A.61. – Robust stability properties gain margin (GM), phase margin Φ_m, time delay margins (TDM) and corresponding gain-crossover frequencies $\omega_{gc,\Phi}$ and $\omega_{gc,TDM}$ for robust stability assessment of DPI Augmentation at envelope points according to Table 2.2 generated for η_{cmd} (bottleneck) loop cut (enhanced aircraft model)

Velocity $V\ \left[\frac{m}{s}\right]$	**GM** $[dB]$	$\Phi_m\ [^\circ]$	$\omega_{gc,\Phi}\ \left[\frac{rad}{s}\right]$	**TDM** $[s]$	$\omega_{gc,TDM}\ \left[\frac{rad}{s}\right]$
102.88	24.94	80.15	0.44	3.196	0.44
	$-\infty$	-279.85	0.44	-11.159	0.44
110.32	23.84	76.89	0.42	3.160	0.42
	$-\infty$	-283.11	0.42	-11.636	0.42
117.75	16.05	74.29	0.41	3.139	0.41
	$-\infty$	-285.71	0.41	-12.072	0.41
125.19	13.29	72.27	0.41	3.085	0.41
	$-\infty$	-287.73	0.41	-12.281	0.41
132.63	11.64	70.59	0.41	3.034	0.41
	$-\infty$	-289.41	0.41	-12.440	0.41
140.07	10.54	69.17	0.40	2.986	0.40
	$-\infty$	-290.83	0.40	-12.555	0.40
147.50	9.76	67.98	0.40	2.940	0.40
	$-\infty$	-292.02	0.40	-12.628	0.40
154.94	9.21	67.00	0.40	2.896	0.40
	$-\infty$	-293.00	0.40	-12.663	0.40
162.38	8.76	66.19	0.40	2.853	0.40
	$-\infty$	-293.81	0.40	-12.664	0.40
169.81	8.43	65.55	0.41	2.812	0.41
	$-\infty$	-294.45	0.41	-12.635	0.41
177.25	8.19	65.04	0.41	2.774	0.41
	$-\infty$	-294.96	0.41	-12.579	0.41
184.69	8.02	64.65	0.41	2.736	0.41
	$-\infty$	-295.35	0.41	-12.500	0.41
192.13	7.89	64.45	0.42	2.697	0.42
	$-\infty$	-295.55	0.42	-12.365	0.42
199.56	7.81	64.26	0.42	2.656	0.42
	$-\infty$	-295.74	0.42	-12.226	0.42
207.00	7.76	64.13	0.43	2.618	0.43
	$-\infty$	-295.87	0.43	-12.077	0.43

Table A.62. – Robust stability properties gain margin (GM), phase margin Φ_m, time delay margins (TDM) and corresponding gain-crossover frequencies $\omega_{gc,\Phi}$ and $\omega_{gc,TDM}$ for robust stability assessment of DPI Augmentation without hedging at envelope points according to Table 2.2 generated for η_{cmd} (bottleneck) loop cut (enhanced aircraft model)

Velocity $V\ \left[\frac{m}{s}\right]$	**GM** $[dB]$	$\Phi_m\ [^\circ]$	$\omega_{gc,\Phi}\ \left[\frac{rad}{s}\right]$	**TDM** $[s]$	$\omega_{gc,TDM}\ \left[\frac{rad}{s}\right]$
102.88	7.37	51.92	4.08	0.222	4.08
	$-\infty$	-308.08	4.08	-1.317	4.08
110.32	7.43	54.54	4.10	0.232	4.10
	$-\infty$	-305.46	4.10	-1.300	4.10
117.75	7.50	57.26	4.11	0.243	4.11
	$-\infty$	-302.74	4.11	-1.285	4.11
125.19	7.57	60.70	4.10	0.258	4.10
	$-\infty$	-299.30	4.10	-1.273	4.10
132.63	7.65	65.00	4.06	0.279	4.06
	$-\infty$	-295.00	4.06	-1.268	4.06
140.07	7.73	70.93	3.96	0.313	3.96
	$-\infty$	-289.07	3.96	-1.275	3.96
147.50	7.82	83.72	2.17	0.673	2.17
	$-\infty$	-276.28	2.17	-2.220	2.17
154.94	7.91	78.66	2.04	0.672	2.04
	$-\infty$	-281.34	2.04	-2.403	2.04
162.38	8.01	75.07	1.98	0.660	1.98
	$-\infty$	-284.93	1.98	-2.506	1.98
169.81	8.11	72.26	1.95	0.646	1.95
	$-\infty$	-287.74	1.95	-2.571	1.95
177.25	8.22	69.93	1.94	0.630	1.94
	$-\infty$	-290.07	1.94	-2.614	1.94
184.69	8.32	68.04	1.93	0.615	1.93
	$-\infty$	-291.96	1.93	-2.637	1.93
192.13	8.42	66.39	1.94	0.599	1.94
	$-\infty$	-293.61	1.94	-2.648	1.94
199.56	8.53	65.10	1.94	0.584	1.94
	$-\infty$	-294.90	1.94	-2.647	1.94
207.00	8.64	63.98	1.96	0.571	1.96
	$-\infty$	-296.02	1.96	-2.641	1.96

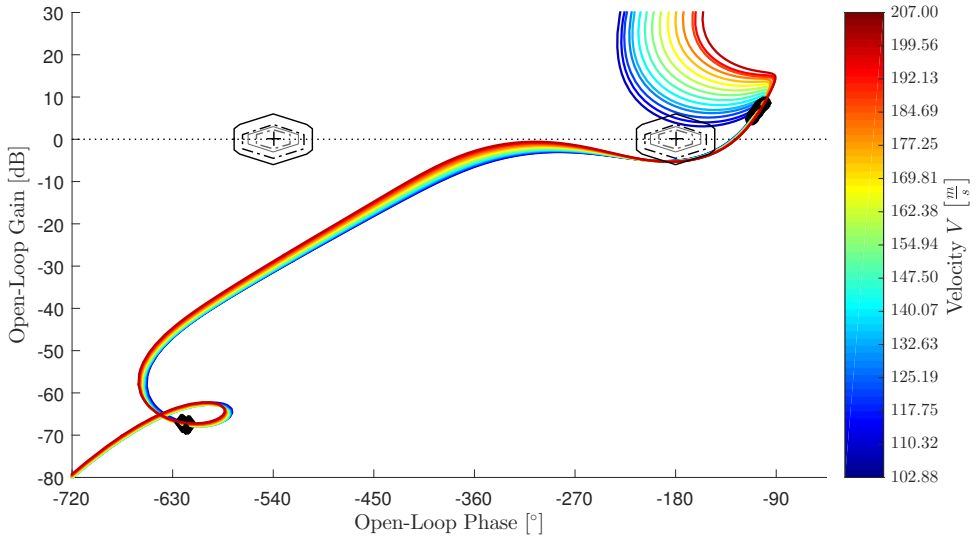

Figure A.45. – Nichols plot for robust stability assessment of DPI Augmentation at envelope points according to Table 2.2 generated for α loop cut (enhanced aircraft model)

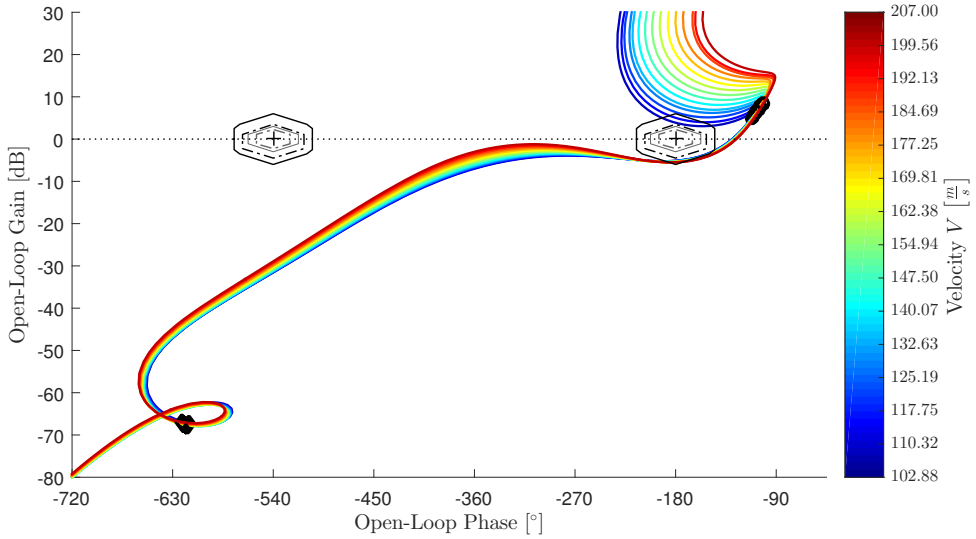

Figure A.46. – Nichols plot for robust stability assessment of DPI Augmentation without hedging at envelope points according to Table 2.2 generated for α loop cut (enhanced aircraft model)

Table A.63. – Robust stability properties gain margin (GM), phase margin Φ_m, time delay margins (TDM) and corresponding gain-crossover frequencies $\omega_{gc,\Phi}$ and $\omega_{gc,TDM}$ for robust stability assessment of DPI Augmentation at envelope points according to Table 2.2 generated for α loop cut (enhanced aircraft model)

Velocity $V\ \left[\frac{m}{s}\right]$	**GM** $[dB]$	$\Phi_m\ [^\circ]$	$\omega_{gc,\Phi}\ \left[\frac{rad}{s}\right]$	**TDM** $[s]$	$\omega_{gc,TDM}\ \left[\frac{rad}{s}\right]$
102.88	5.05	50.54	0.76	1.163	0.76
	-3.88	-309.46	0.76	-7.123	0.76
110.32	5.08	50.94	0.79	1.131	0.79
	-5.03	-309.06	0.79	-6.866	0.79
117.75	5.09	50.66	0.82	1.084	0.82
	-6.38	-309.34	0.82	-6.617	0.82
125.19	5.13	51.05	0.84	1.062	0.84
	-7.78	-308.95	0.84	-6.425	0.84
132.63	5.15	51.41	0.86	1.042	0.86
	-8.76	-308.59	0.86	-6.253	0.86
140.07	5.19	51.75	0.88	1.023	0.88
	-10.45	-308.25	0.88	-6.096	0.88
147.50	5.21	52.03	0.91	1.003	0.91
	-12.33	-307.97	0.91	-5.939	0.91
154.94	5.21	52.22	0.93	0.981	0.93
	-14.47	-307.78	0.93	-5.781	0.93
162.38	5.22	52.43	0.95	0.961	0.95
	-16.99	-307.57	0.95	-5.635	0.95
169.81	5.23	52.65	0.98	0.942	0.98
	-20.33	-307.35	0.98	-5.501	0.98
177.25	5.25	52.89	1.00	0.926	1.00
	-27.17	-307.11	1.00	-5.376	1.00
184.69	5.27	53.15	1.02	0.911	1.02
	$-\infty$	-306.85	1.02	-5.262	1.02
192.13	5.27	53.66	1.03	0.905	1.03
	$-\infty$	-306.34	1.03	-5.169	1.03
199.56	5.27	53.93	1.05	0.892	1.05
	$-\infty$	-306.07	1.05	-5.064	1.05
207.00	5.27	54.18	1.08	0.879	1.08
	$-\infty$	-305.82	1.08	-4.959	1.08

Table A.64. – Robust stability properties gain margin (GM), phase margin Φ_m, time delay margins (TDM) and corresponding gain-crossover frequencies $\omega_{gc,\Phi}$ and $\omega_{gc,TDM}$ for robust stability assessment of DPI Augmentation without hedging at envelope points according to Table 2.2 generated for α loop cut (enhanced aircraft model)

Velocity $V\ \left[\frac{m}{s}\right]$	**GM** $[dB]$	$\Phi_m\ [^\circ]$	$\omega_{gc,\Phi}\ \left[\frac{rad}{s}\right]$	**TDM** $[s]$	$\omega_{gc,TDM}\ \left[\frac{rad}{s}\right]$
102.88	5.11	50.49	0.75	1.173	0.75
	-3.87	-309.51	0.75	-7.189	0.75
110.32	5.17	50.94	0.78	1.145	0.78
	-5.03	-309.06	0.78	-6.948	0.78
117.75	5.18	50.68	0.81	1.098	0.81
	-6.38	-309.32	0.81	-6.702	0.81
125.19	5.22	51.07	0.83	1.076	0.83
	-7.77	-308.93	0.83	-6.511	0.83
132.63	5.26	51.43	0.85	1.057	0.85
	-8.75	-308.57	0.85	-6.341	0.85
140.07	5.31	51.77	0.87	1.039	0.87
	-10.44	-308.23	0.87	-6.185	0.87
147.50	5.33	52.10	0.89	1.022	0.89
	-12.32	-307.90	0.89	-6.042	0.89
154.94	5.35	52.33	0.91	1.002	0.91
	-14.45	-307.67	0.91	-5.889	0.91
162.38	5.38	52.54	0.93	0.981	0.93
	-16.97	-307.46	0.93	-5.743	0.93
169.81	5.41	52.77	0.96	0.963	0.96
	-20.31	-307.23	0.96	-5.608	0.96
177.25	5.42	53.01	0.98	0.947	0.98
	-27.12	-306.99	0.98	-5.483	0.98
184.69	5.45	53.26	1.00	0.932	1.00
	$-\infty$	-306.74	1.00	-5.367	1.00
192.13	5.46	53.78	1.01	0.926	1.01
	$-\infty$	-306.22	1.01	-5.273	1.01
199.56	5.46	54.10	1.03	0.915	1.03
	$-\infty$	-305.90	1.03	-5.177	1.03
207.00	5.47	54.41	1.05	0.905	1.05
	$-\infty$	-305.59	1.05	-5.082	1.05

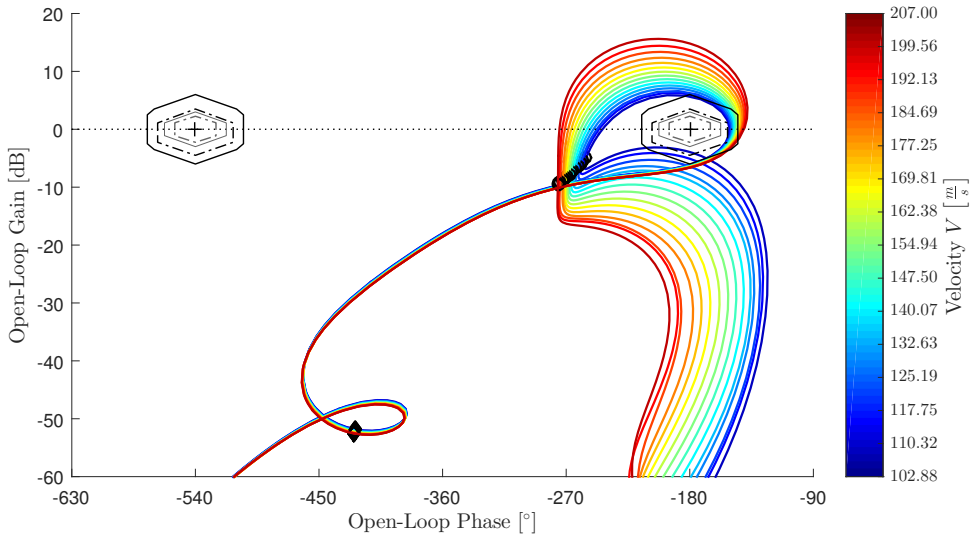

Figure A.47. – Nichols plot for robust stability assessment of DPI Augmentation at envelope points according to Table 2.2 generated for q loop cut (enhanced aircraft model)

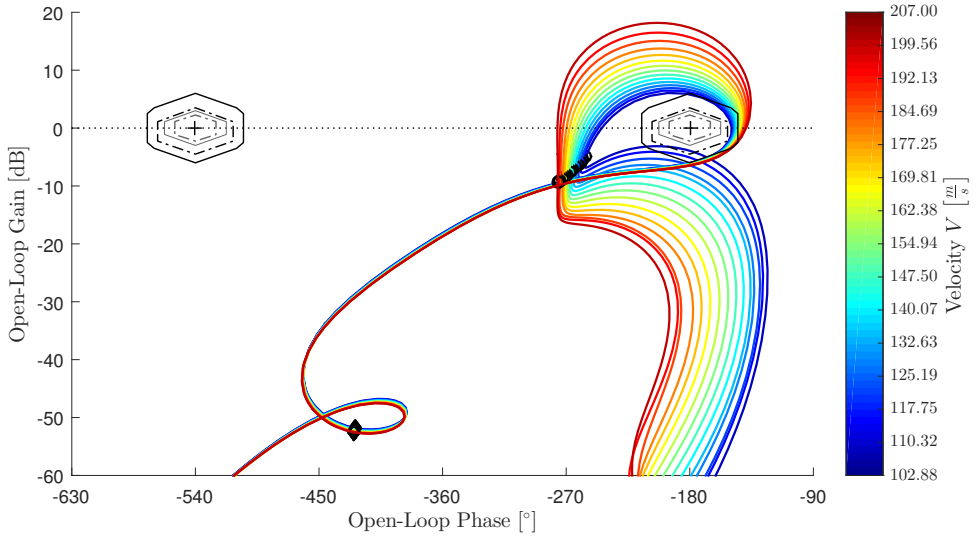

Figure A.48. – Nichols plot for robust stability assessment of DPI Augmentation without hedging at envelope points according to Table 2.2 generated for q loop cut (enhanced aircraft model)

Table A.65. – Robust stability properties gain margin (GM), phase margin Φ_m, time delay margins (TDM) and corresponding gain-crossover frequencies $\omega_{gc,\Phi}$ and $\omega_{gc,TDM}$ for robust stability assessment of DPI Augmentation at envelope points according to Table 2.2 generated for q loop cut (enhanced aircraft model)

Velocity $V\ \left[\frac{m}{s}\right]$	**GM** $[dB]$	$\Phi_m\ [^\circ]$	$\omega_{gc,\Phi}\ \left[\frac{rad}{s}\right]$	**TDM** $[s]$	$\omega_{gc,TDM}\ \left[\frac{rad}{s}\right]$
102.88	3.93	28.76	4.34	0.116	4.34
	-5.61	-63.53	0.72	-1.333	4.34
110.32	5.09	29.44	4.39	0.117	4.39
	-5.95	-66.09	0.74	-1.313	4.39
117.75	6.20	29.98	4.44	0.118	4.44
	-6.24	-67.74	0.77	-1.296	4.44
125.19	6.25	30.87	4.49	0.120	4.49
	-6.73	-70.17	0.79	-1.281	4.49
132.63	6.30	31.71	4.53	0.122	4.53
	-7.18	-72.52	0.81	-1.265	4.53
140.07	6.35	32.40	4.59	0.123	4.59
	-7.67	-74.91	0.83	-1.246	4.59
147.50	6.39	33.28	4.63	0.125	4.63
	-8.20	-77.22	0.86	-1.231	4.63
154.94	6.44	33.97	4.69	0.126	4.69
	-8.77	-79.55	0.88	-1.213	4.69
162.38	6.48	34.86	4.73	0.129	4.73
	-9.40	-81.81	0.90	-1.199	4.73
169.81	6.51	35.53	4.79	0.129	4.79
	-10.09	-84.06	0.92	-1.181	4.79
177.25	6.55	36.42	4.83	0.131	4.83
	-10.84	-86.27	0.94	-1.168	4.83
184.69	6.57	37.29	4.88	0.133	4.88
	-11.68	-88.46	0.96	-1.155	4.88
192.13	6.59	37.92	4.93	0.134	4.93
	-12.64	-90.90	0.98	-1.140	4.93
199.56	6.61	38.67	4.97	0.136	4.97
	-13.66	-92.93	1.00	-1.128	4.97
207.00	6.63	39.34	5.02	0.137	5.02
	-14.81	-94.91	1.02	-1.114	5.02

Table A.66. – Robust stability properties gain margin (GM), phase margin Φ_m, time delay margins (TDM) and corresponding gain-crossover frequencies $\omega_{gc,\Phi}$ and $\omega_{gc,TDM}$ for robust stability assessment of DPI Augmentation without hedging at envelope points according to Table 2.2 generated for q loop cut (enhanced aircraft model)

Velocity $V\ \left[\frac{m}{s}\right]$	**GM** $[dB]$	$\Phi_m\ [^\circ]$	$\omega_{gc,\Phi}\ \left[\frac{rad}{s}\right]$	**TDM** $[s]$	$\omega_{gc,TDM}\ \left[\frac{rad}{s}\right]$
102.88	3.93	30.39	4.28	0.124	4.28
	-5.78	-64.03	0.71	-1.344	4.28
110.32	5.09	31.07	4.34	0.125	4.34
	-6.16	-66.65	0.74	-1.322	4.34
117.75	6.08	31.77	4.39	0.126	4.39
	-6.57	-68.40	0.76	-1.305	4.39
125.19	6.12	32.51	4.45	0.128	4.45
	-7.04	-70.88	0.78	-1.285	4.45
132.63	6.17	33.29	4.50	0.129	4.50
	-7.56	-73.38	0.80	-1.266	4.50
140.07	6.21	34.09	4.56	0.130	4.56
	-8.13	-75.77	0.82	-1.248	4.56
147.50	6.25	34.86	4.62	0.132	4.62
	-8.75	-78.21	0.84	-1.229	4.62
154.94	6.29	35.70	4.67	0.133	4.67
	-9.43	-80.56	0.86	-1.212	4.67
162.38	6.33	36.42	4.74	0.134	4.74
	-10.18	-82.91	0.88	-1.193	4.74
169.81	6.36	37.32	4.78	0.136	4.78
	-11.03	-85.24	0.90	-1.178	4.78
177.25	6.39	38.15	4.83	0.138	4.83
	-11.97	-87.54	0.93	-1.163	4.83
184.69	6.42	38.93	4.88	0.139	4.88
	-13.04	-89.75	0.95	-1.147	4.88
192.13	6.44	39.65	4.94	0.140	4.94
	-14.31	-92.28	0.96	-1.133	4.94
199.56	6.46	40.32	4.99	0.141	4.99
	-15.70	-94.35	0.98	-1.118	4.99
207.00	6.48	40.98	5.05	0.142	5.05
	-17.35	-96.38	1.00	-1.103	5.05

A.6.4. Plant Augmentation

Page intentionally left blank

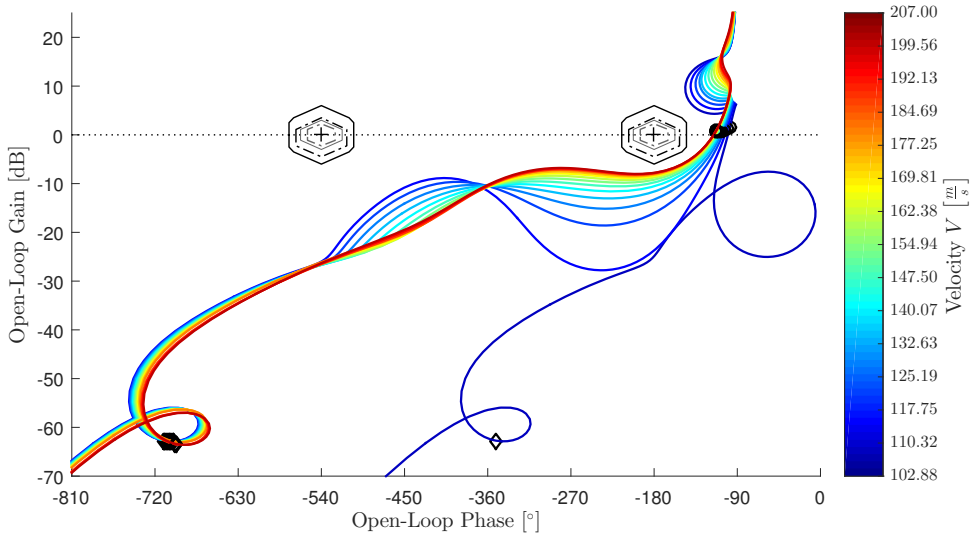

Figure A.49. – Nichols plot for robust stability assessment of Plant Augmentation at envelope points according to Table 2.2 generated for η_{cmd} (bottleneck) loop cut (enhanced aircraft model)

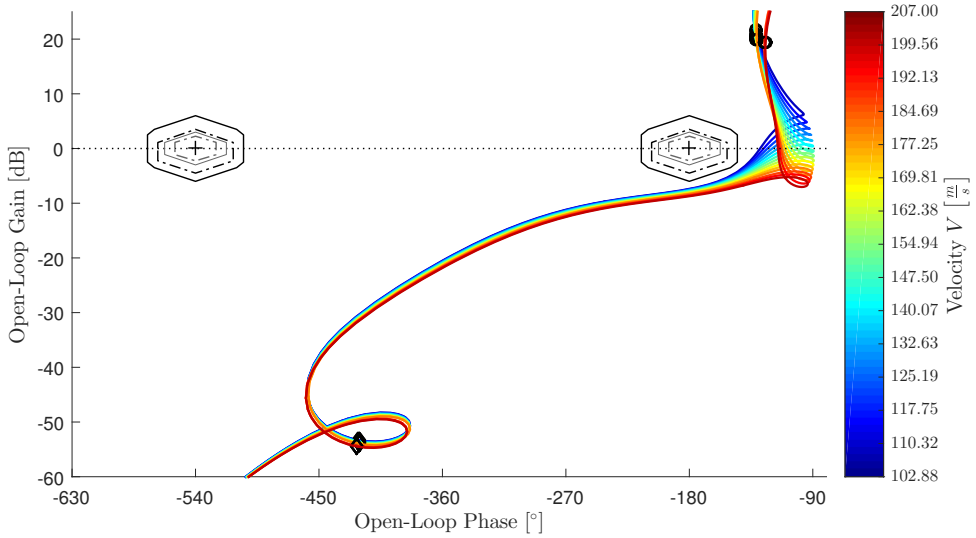

Figure A.50. – Nichols plot for robust stability assessment of Plant Augmentation without hedging at envelope points according to Table 2.2 generated for η_{cmd} (bottleneck) loop cut (enhanced aircraft model)

Table A.67. – Robust stability properties gain margin (GM), phase margin Φ_m, time delay margins (TDM) and corresponding gain-crossover frequencies $\omega_{gc,\Phi}$ and $\omega_{gc,TDM}$ for robust stability assessment of Plant Augmentation at envelope points according to Table 2.2 generated for η_{cmd} (bottleneck) loop cut (enhanced aircraft model)

Velocity $V\ \left[\frac{m}{s}\right]$	**GM** $[dB]$	$\Phi_m\ [^\circ]$	$\omega_{gc,\Phi}\ \left[\frac{rad}{s}\right]$	**TDM** $[s]$	$\omega_{gc,TDM}\ \left[\frac{rad}{s}\right]$
102.88	24.89	79.89	0.44	3.180	0.44
	$-\infty$	-280.11	0.44	-11.152	0.44
110.32	23.69	76.66	0.43	3.146	0.43
	$-\infty$	-283.34	0.43	-11.629	0.43
117.75	16.01	74.12	0.41	3.129	0.41
	$-\infty$	-285.88	0.41	-12.068	0.41
125.19	13.27	72.14	0.41	3.077	0.41
	$-\infty$	-287.86	0.41	-12.280	0.41
132.63	11.63	70.48	0.41	3.029	0.41
	$-\infty$	-289.52	0.41	-12.441	0.41
140.07	10.53	69.08	0.40	2.982	0.40
	$-\infty$	-290.92	0.40	-12.557	0.40
147.50	9.76	67.91	0.40	2.936	0.40
	$-\infty$	-292.09	0.40	-12.630	0.40
154.94	9.20	66.94	0.40	2.893	0.40
	$-\infty$	-293.06	0.40	-12.666	0.40
162.38	8.75	66.14	0.40	2.851	0.40
	$-\infty$	-293.86	0.40	-12.667	0.40
169.81	8.43	65.49	0.41	2.810	0.41
	$-\infty$	-294.51	0.41	-12.638	0.41
177.25	8.19	64.99	0.41	2.772	0.41
	$-\infty$	-295.01	0.41	-12.581	0.41
184.69	8.02	64.60	0.41	2.734	0.41
	$-\infty$	-295.40	0.41	-12.503	0.41
192.13	7.90	64.66	0.42	2.709	0.42
	$-\infty$	-295.34	0.42	-12.376	0.42
199.56	7.83	64.44	0.42	2.667	0.42
	$-\infty$	-295.56	0.42	-12.234	0.42
207.00	7.78	64.30	0.43	2.628	0.43
	$-\infty$	-295.70	0.43	-12.084	0.43

Table A.68. – Robust stability properties gain margin (GM), phase margin Φ_m, time delay margins (TDM) and corresponding gain-crossover frequencies $\omega_{gc,\Phi}$ and $\omega_{gc,TDM}$ for robust stability assessment of Plant Augmentation without hedging at envelope points according to Table 2.2 generated for η_{cmd} (bottleneck) loop cut (enhanced aircraft model)

Velocity $V\ \left[\frac{m}{s}\right]$	**GM** $[dB]$	$\Phi_m\ [^\circ]$	$\omega_{gc,\Phi}\ \left[\frac{rad}{s}\right]$	**TDM** $[s]$	$\omega_{gc,TDM}\ \left[\frac{rad}{s}\right]$
102.88	7.38	51.59	4.08	0.221	4.08
	-30.62	-308.41	4.08	-1.320	4.08
110.32	7.44	54.23	4.10	0.231	4.10
	$-\infty$	-305.77	4.10	-1.303	4.10
117.75	7.50	56.98	4.11	0.242	4.11
	$-\infty$	-303.02	4.11	-1.288	4.11
125.19	7.57	60.45	4.10	0.258	4.10
	$-\infty$	-299.55	4.10	-1.276	4.10
132.63	7.65	64.78	4.05	0.279	4.05
	$-\infty$	-295.22	4.05	-1.271	4.05
140.07	7.73	70.79	3.95	0.313	3.95
	$-\infty$	-289.21	3.95	-1.279	3.95
147.50	7.82	82.95	2.18	0.665	2.18
	$-\infty$	-277.05	2.18	-2.220	2.18
154.94	7.91	77.97	2.05	0.664	2.05
	$-\infty$	-282.03	2.05	-2.401	2.05
162.38	8.01	74.46	1.99	0.653	1.99
	$-\infty$	-285.54	1.99	-2.503	1.99
169.81	8.11	71.72	1.96	0.639	1.96
	$-\infty$	-288.28	1.96	-2.568	1.96
177.25	8.21	69.47	1.94	0.624	1.94
	$-\infty$	-290.53	1.94	-2.610	1.94
184.69	8.31	67.64	1.94	0.609	1.94
	$-\infty$	-292.36	1.94	-2.633	1.94
192.13	8.51	66.78	1.92	0.608	1.92
	$-\infty$	-293.22	1.92	-2.669	1.92
199.56	8.61	65.58	1.93	0.594	1.93
	$-\infty$	-294.42	1.93	-2.668	1.93
207.00	8.72	64.55	1.94	0.582	1.94
	$-\infty$	-295.45	1.94	-2.663	1.94

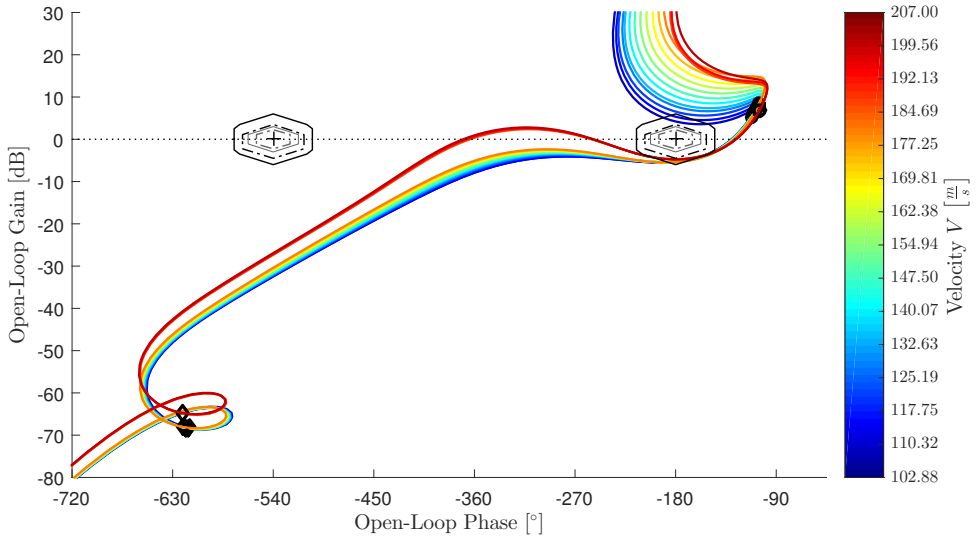

Figure A.51. – Nichols plot for robust stability assessment of Plant Augmentation at envelope points according to Table 2.2 generated for α loop cut (enhanced aircraft model)

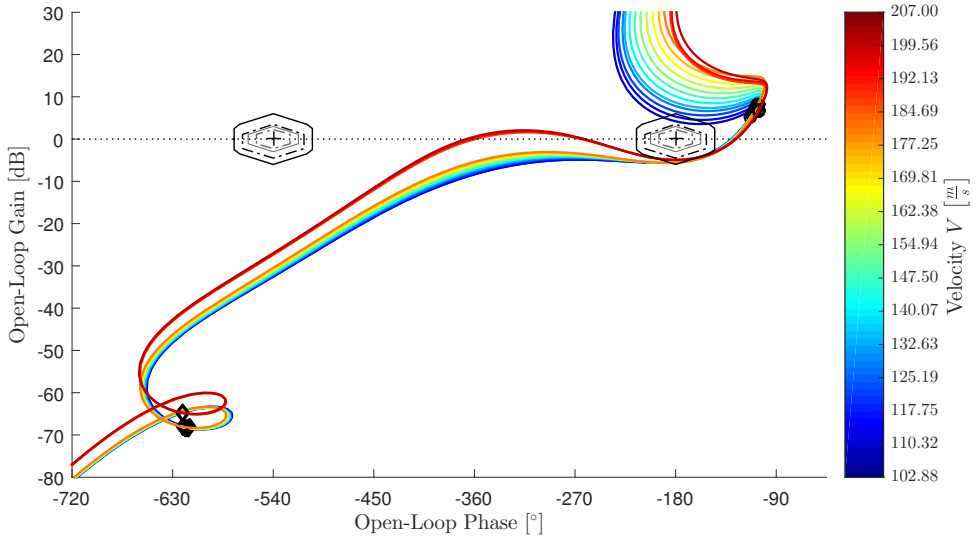

Figure A.52. – Nichols plot for robust stability assessment of Plant Augmentation without hedging at envelope points according to Table 2.2 generated for α loop cut (enhanced aircraft model)

Table A.69. – Robust stability properties gain margin (GM), phase margin Φ_m, time delay margins (TDM) and corresponding gain-crossover frequencies $\omega_{gc,\Phi}$ and $\omega_{gc,TDM}$ for robust stability assessment of Plant Augmentation at envelope points according to Table 2.2 generated for α loop cut (enhanced aircraft model)

Velocity $V\ \left[\frac{m}{s}\right]$	**GM** $[dB]$	$\Phi_m\ [^\circ]$	$\omega_{gc,\Phi}\ \left[\frac{rad}{s}\right]$	**TDM** $[s]$	$\omega_{gc,TDM}\ \left[\frac{rad}{s}\right]$
102.88	5.30	50.10	0.80	1.097	0.80
	-4.22	-309.90	0.80	-6.788	0.80
110.32	5.34	50.43	0.83	1.064	0.83
	-5.35	-309.57	0.83	-6.533	0.83
117.75	5.27	50.11	0.85	1.027	0.85
	-6.55	-309.89	0.85	-6.353	0.85
125.19	5.29	50.45	0.87	1.010	0.87
	-7.80	-309.55	0.87	-6.198	0.87
132.63	5.31	50.78	0.89	0.994	0.89
	-8.67	-309.22	0.89	-6.056	0.89
140.07	5.31	51.00	0.91	0.974	0.91
	-10.15	-309.00	0.91	-5.901	0.91
147.50	5.32	51.21	0.94	0.954	0.94
	-11.77	-308.79	0.94	-5.751	0.94
154.94	5.34	51.43	0.96	0.935	0.96
	-13.54	-308.57	0.96	-5.609	0.96
162.38	5.36	51.65	0.98	0.917	0.98
	-15.47	-308.35	0.98	-5.474	0.98
169.81	5.37	51.90	1.01	0.900	1.01
	-17.60	-308.10	1.01	-5.346	1.01
177.25	5.39	52.16	1.03	0.885	1.03
	-19.85	-307.84	1.03	-5.222	1.03
184.69	5.42	52.39	1.05	0.868	1.05
	-22.31	-307.61	1.05	-5.096	1.05
192.13	4.70	53.28	0.91	0.340	9.01
	-23.33	-75.23	6.53	-0.201	6.53
199.56	4.74	53.67	0.93	0.329	9.16
	-24.45	-74.17	6.60	-0.196	6.60
207.00	4.79	54.07	0.95	0.319	9.30
	$-\infty$	-73.39	6.67	-0.192	6.67

Table A.70. – Robust stability properties gain margin (GM), phase margin Φ_m, time delay margins (TDM) and corresponding gain-crossover frequencies $\omega_{gc,\Phi}$ and $\omega_{gc,TDM}$ for robust stability assessment of Plant Augmentation without hedging at envelope points according to Table 2.2 generated for α loop cut (enhanced aircraft model)

Velocity $V\ \left[\frac{m}{s}\right]$	**GM** $[dB]$	$\Phi_m\ [^\circ]$	$\omega_{gc,\Phi}\ \left[\frac{rad}{s}\right]$	**TDM** $[s]$	$\omega_{gc,TDM}\ \left[\frac{rad}{s}\right]$
102.88	5.37	50.10	0.79	1.110	0.79
	-4.21	-309.90	0.79	-6.863	0.79
110.32	5.43	50.44	0.82	1.077	0.82
	-5.34	-309.56	0.82	-6.611	0.82
117.75	5.37	50.14	0.84	1.041	0.84
	-6.54	-309.86	0.84	-6.434	0.84
125.19	5.38	50.48	0.86	1.024	0.86
	-7.79	-309.52	0.86	-6.282	0.86
132.63	5.40	50.81	0.88	1.009	0.88
	-8.66	-309.19	0.88	-6.141	0.88
140.07	5.43	51.12	0.90	0.994	0.90
	-10.14	-308.88	0.90	-6.006	0.90
147.50	5.46	51.33	0.92	0.974	0.92
	-11.76	-308.67	0.92	-5.856	0.92
154.94	5.49	51.55	0.94	0.955	0.94
	-13.52	-308.45	0.94	-5.714	0.94
162.38	5.50	51.78	0.96	0.937	0.96
	-15.46	-308.22	0.96	-5.579	0.96
169.81	5.53	52.03	0.99	0.921	0.99
	-17.58	-307.97	0.99	-5.450	0.99
177.25	5.57	52.29	1.01	0.905	1.01
	-19.83	-307.71	1.01	-5.325	1.01
184.69	5.58	52.57	1.03	0.890	1.03
	-22.29	-307.43	1.03	-5.207	1.03
192.13	4.87	53.32	0.89	0.347	9.10
	-23.31	-84.83	6.84	-0.216	6.84
199.56	4.92	53.70	0.91	0.332	9.28
	-24.43	-82.86	6.89	-0.210	6.89
207.00	4.98	54.09	0.93	0.319	9.44
	$-\infty$	-81.36	6.94	-0.205	6.94

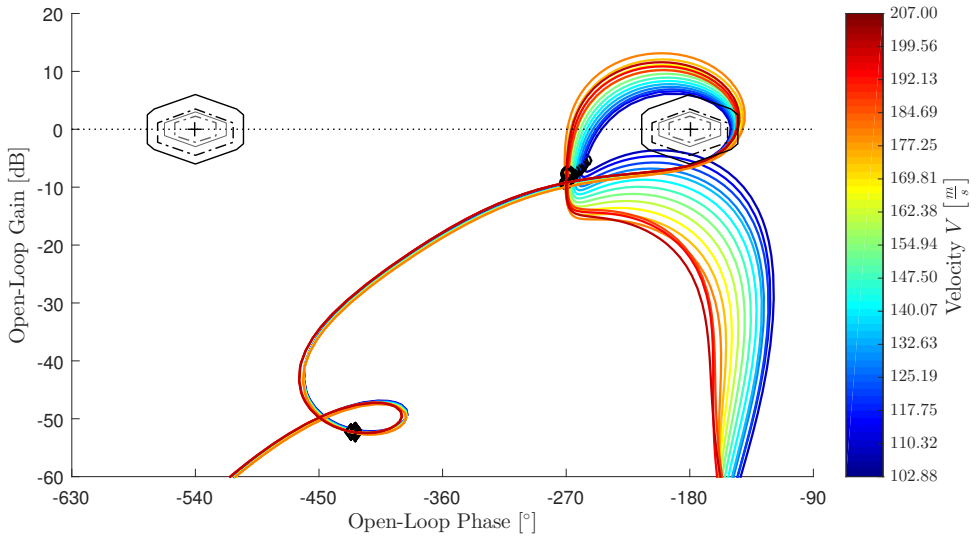

Figure A.53. – Nichols plot for robust stability assessment of Plant Augmentation at envelope points according to Table 2.2 generated for q loop cut (enhanced aircraft model)

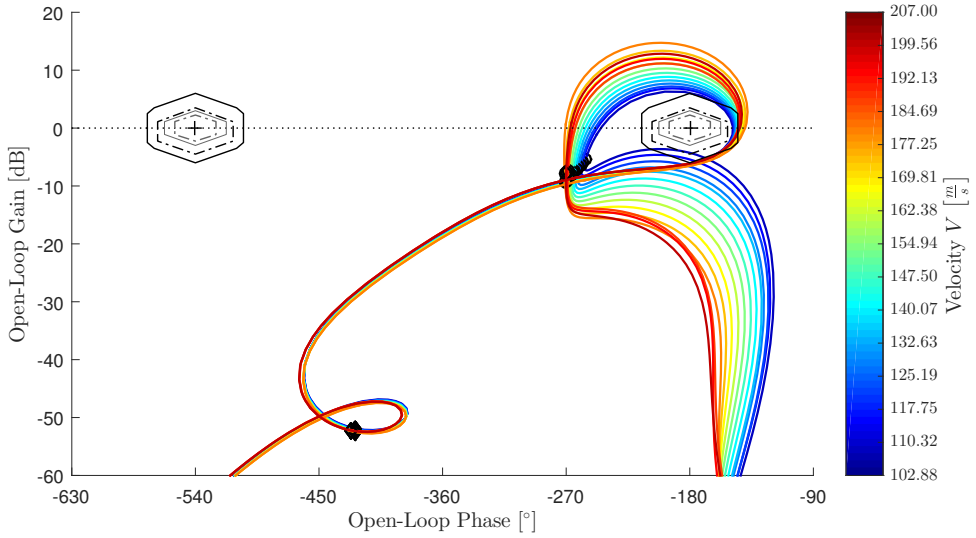

Figure A.54. – Nichols plot for robust stability assessment of Plant Augmentation without hedging at envelope points according to Table 2.2 generated for q loop cut (enhanced aircraft model)

Table A.71. – Robust stability properties gain margin (GM), phase margin Φ_m, time delay margins (TDM) and corresponding gain-crossover frequencies $\omega_{gc,\Phi}$ and $\omega_{gc,TDM}$ for robust stability assessment of Plant Augmentation at envelope points according to Table 2.2 generated for q loop cut (enhanced aircraft model)

Velocity $V\ \left[\frac{m}{s}\right]$	**GM** $[dB]$	$\Phi_m\ [^\circ]$	$\omega_{gc,\Phi}\ \left[\frac{rad}{s}\right]$	**TDM** $[s]$	$\omega_{gc,TDM}\ \left[\frac{rad}{s}\right]$
102.88	4.28	29.63	4.35	0.119	4.35
	-5.86	-64.14	0.75	-1.325	4.35
110.32	5.43	30.40	4.41	0.120	4.41
	-6.24	-66.77	0.78	-1.304	4.41
117.75	6.32	30.99	4.45	0.122	4.45
	-6.59	-68.20	0.80	-1.291	4.45
125.19	6.36	31.67	4.50	0.123	4.50
	-6.98	-70.50	0.82	-1.275	4.50
132.63	6.40	32.41	4.54	0.124	4.54
	-7.43	-72.80	0.84	-1.258	4.54
140.07	6.45	33.14	4.60	0.126	4.60
	-7.93	-75.08	0.86	-1.241	4.60
147.50	6.49	33.99	4.64	0.128	4.64
	-8.48	-77.41	0.88	-1.226	4.64
154.94	6.53	34.77	4.70	0.129	4.70
	-9.09	-79.69	0.90	-1.208	4.70
162.38	6.58	35.69	4.75	0.131	4.75
	-9.77	-82.07	0.93	-1.193	4.75
169.81	6.62	36.52	4.80	0.133	4.80
	-10.55	-84.36	0.95	-1.176	4.80
177.25	6.66	37.62	4.84	0.136	4.84
	-11.44	-86.79	0.98	-1.163	4.84
184.69	6.69	38.39	4.91	0.137	4.91
	-12.47	-89.15	1.01	-1.144	4.91
192.13	6.22	33.71	4.81	0.122	4.81
	-9.59	-82.62	0.84	-1.183	4.81
199.56	6.24	34.19	4.88	0.122	4.88
	-10.21	-84.26	0.85	-1.166	4.88
207.00	6.27	34.98	4.91	0.124	4.91
	-10.89	-86.01	0.87	-1.155	4.91

Table A.72. – Robust stability properties gain margin (GM), phase margin Φ_m, time delay margins (TDM) and corresponding gain-crossover frequencies $\omega_{gc,\Phi}$ and $\omega_{gc,TDM}$ for robust stability assessment of Plant Augmentation without hedging at envelope points according to Table 2.2 generated for q loop cut (enhanced aircraft model)

Velocity $V\ \left[\frac{m}{s}\right]$	**GM** $[dB]$	$\Phi_m\ [^\circ]$	$\omega_{gc,\Phi}\ \left[\frac{rad}{s}\right]$	**TDM** $[s]$	$\omega_{gc,TDM}\ \left[\frac{rad}{s}\right]$
102.88	4.28	31.34	4.30	0.127	4.30
	-6.03	-64.66	0.74	-1.335	4.30
110.32	5.42	32.26	4.35	0.129	4.35
	-6.56	-67.40	0.77	-1.314	4.35
117.75	6.19	32.65	4.41	0.129	4.41
	-6.86	-68.94	0.79	-1.297	4.41
125.19	6.23	33.43	4.45	0.131	4.45
	-7.32	-71.29	0.81	-1.280	4.45
132.63	6.26	34.06	4.52	0.132	4.52
	-7.83	-73.67	0.83	-1.260	4.52
140.07	6.30	34.95	4.56	0.134	4.56
	-8.41	-76.04	0.85	-1.244	4.56
147.50	6.34	35.63	4.63	0.134	4.63
	-9.06	-78.40	0.87	-1.223	4.63
154.94	6.38	36.58	4.67	0.137	4.67
	-9.79	-80.83	0.89	-1.207	4.67
162.38	6.42	37.33	4.74	0.137	4.74
	-10.62	-83.19	0.91	-1.187	4.74
169.81	6.46	38.40	4.78	0.140	4.78
	-11.58	-85.68	0.94	-1.173	4.78
177.25	6.50	39.19	4.85	0.141	4.85
	-12.69	-88.07	0.96	-1.153	4.85
184.69	6.53	40.31	4.90	0.144	4.90
	-14.03	-90.58	0.99	-1.140	4.90
192.13	6.09	34.97	4.85	0.126	4.85
	-10.55	-83.41	0.82	-1.171	4.85
199.56	6.11	35.85	4.88	0.128	4.88
	-11.31	-85.21	0.84	-1.160	4.88
207.00	6.13	36.48	4.93	0.129	4.93
	-12.16	-86.91	0.86	-1.145	4.93

A.6.5. $\Delta\dot{q}$ Compensation Law

Page intentionally left blank

Table A.73. – Robust stability properties gain margin (GM), phase margin Φ_m, time delay margins (TDM) and corresponding gain-crossover frequencies $\omega_{gc,\Phi}$ and $\omega_{gc,TDM}$ for robust stability comparison of $\Delta\dot{q}$ Compensation Law with and without $\dot{q}$ measurement at $V = 154.94\frac{m}{s}$ generated for α loop cut (enhanced aircraft model)

Controller	**GM** $[dB]$	$\Phi_m\,[^\circ]$	$\omega_{gc,\Phi}\left[\frac{rad}{s}\right]$	**TDM** $[s]$	$\omega_{gc,TDM}\left[\frac{rad}{s}\right]$
Baseline	7.72	63.12	0.40	2.777	0.40
	$-\infty$	-296.88	0.40	-13.063	0.40
$\Delta\dot{q}$ Compensator	8.81	50.68	1.41	0.626	1.41
	-20.15	-309.32	1.41	-3.820	1.41
$\Delta\dot{q}$ Compensator (no $\dot{q}$-meas.)	8.87	50.79	1.41	0.628	1.41
	-20.15	-309.21	1.41	-3.823	1.41

Table A.74. – Robust stability properties gain margin (GM), phase margin Φ_m, time delay margins (TDM) and corresponding gain-crossover frequencies $\omega_{gc,\Phi}$ and $\omega_{gc,TDM}$ for robust stability comparison of $\Delta\dot{q}$ Compensation Law with and without $\dot{q}$ measurement at $V = 154.94\frac{m}{s}$ generated for q loop cut (enhanced aircraft model)

Controller	**GM** $[dB]$	$\Phi_m\,[^\circ]$	$\omega_{gc,\Phi}\left[\frac{rad}{s}\right]$	**TDM** $[s]$	$\omega_{gc,TDM}\left[\frac{rad}{s}\right]$
Baseline	21.76	∞	0.00	∞	0.00
	$-\infty$	$-\infty$	0.00	$-\infty$	0.00
$\Delta\dot{q}$ Compensator	13.35	110.14	2.48	0.776	2.48
	$-\infty$	-164.83	1.53	-1.760	2.48
$\Delta\dot{q}$ Compensator (no $\dot{q}$-meas.)	7.26	44.99	5.36	0.146	5.36
	-19.28	-95.20	1.60	-1.025	5.36

Table A.75. – Robust stability properties gain margin (GM), phase margin Φ_m, time delay margins (TDM) and corresponding gain-crossover frequencies $\omega_{gc,\Phi}$ and $\omega_{gc,TDM}$ for robust stability assessment of $\Delta\dot{q}$ Compensation Law with $\dot{q}$ measurement at $V = 154.94\frac{m}{s}$ generated for $\dot{q}$ loop cut (enhanced aircraft model)

Controller	**GM** $[dB]$	$\Phi_m\,[^\circ]$	$\omega_{gc,\Phi}\left[\frac{rad}{s}\right]$	**TDM** $[s]$	$\omega_{gc,TDM}\left[\frac{rad}{s}\right]$
$\Delta\dot{q}$ Compensator	8.13	52.75	5.97	0.154	5.97
	-22.73	-79.61	2.52	-0.551	2.52

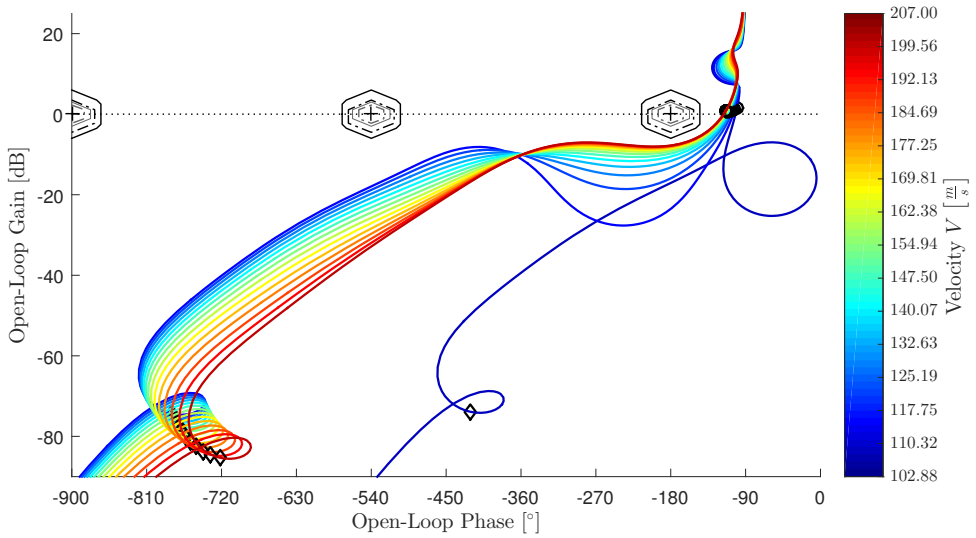

Figure A.55. – Nichols plot for robust stability assessment of $\Delta\dot{q}$ Compensation Law at envelope points according to Table 2.2 generated for η_{cmd} (bottleneck) loop cut (enhanced aircraft model)

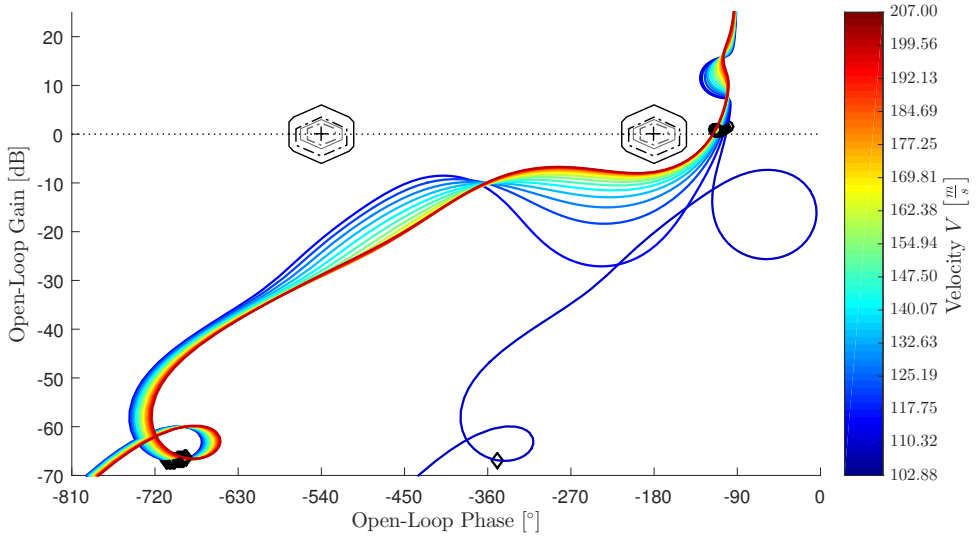

Figure A.56. – Nichols plot for robust stability assessment of $\Delta\dot{q}$ Compensation Law with $\dot{q}$ measurement at envelope points according to Table 2.2 generated for η_{cmd} (bottleneck) loop cut (enhanced aircraft model)

Table A.76. – Robust stability properties gain margin (GM), phase margin Φ_m, time delay margins (TDM) and corresponding gain-crossover frequencies $\omega_{gc,\Phi}$ and $\omega_{gc,TDM}$ for robust stability assessment of $\Delta\dot{q}$ Compensation Law at envelope points according to Table 2.2 generated for η_{cmd} (bottleneck) loop cut (enhanced aircraft model)

Velocity $V\ \left[\frac{m}{s}\right]$	**GM** $[dB]$	$\Phi_m\ [^\circ]$	$\omega_{gc,\Phi}\ \left[\frac{rad}{s}\right]$	**TDM** $[s]$	$\omega_{gc,TDM}\ \left[\frac{rad}{s}\right]$
102.88	17.08	77.83	0.45	3.025	0.45
	$-\infty$	-282.17	0.45	-10.966	0.45
110.32	17.94	75.02	0.43	3.020	0.43
	$-\infty$	-284.98	0.43	-11.472	0.43
117.75	15.93	72.65	0.42	3.009	0.42
	$-\infty$	-287.35	0.42	-11.902	0.42
125.19	13.22	70.87	0.42	2.978	0.42
	$-\infty$	-289.13	0.42	-12.147	0.42
132.63	11.62	69.36	0.41	2.943	0.41
	$-\infty$	-290.64	0.41	-12.329	0.41
140.07	10.52	68.08	0.41	2.906	0.41
	$-\infty$	-291.92	0.41	-12.458	0.41
147.50	9.75	67.02	0.41	2.869	0.41
	$-\infty$	-292.98	0.41	-12.543	0.41
154.94	9.20	66.14	0.41	2.833	0.41
	$-\infty$	-293.86	0.41	-12.589	0.41
162.38	8.76	65.42	0.41	2.798	0.41
	$-\infty$	-294.58	0.41	-12.599	0.41
169.81	8.43	64.85	0.41	2.764	0.41
	$-\infty$	-295.15	0.41	-12.578	0.41
177.25	8.20	64.40	0.41	2.730	0.41
	$-\infty$	-295.60	0.41	-12.530	0.41
184.69	8.03	64.08	0.41	2.697	0.41
	$-\infty$	-295.92	0.41	-12.455	0.41
192.13	7.89	63.55	0.42	2.647	0.42
	$-\infty$	-296.45	0.42	-12.350	0.42
199.56	7.83	63.77	0.42	2.633	0.42
	$-\infty$	-296.23	0.42	-12.229	0.42
207.00	7.78	63.68	0.43	2.597	0.43
	$-\infty$	-296.32	0.43	-12.084	0.43

Table A.77. – Robust stability properties gain margin (GM), phase margin Φ_m, time delay margins (TDM) and corresponding gain-crossover frequencies $\omega_{gc,\Phi}$ and $\omega_{gc,TDM}$ for robust stability assessment of $\Delta\dot{q}$ Compensation Law with $\dot{q}$ measurement at envelope points according to Table 2.2 generated for η_{cmd} (bottleneck) loop cut (enhanced aircraft model)

Velocity $V\ \left[\frac{m}{s}\right]$	**GM** $[dB]$	$\Phi_m\ [^\circ]$	$\omega_{gc,\Phi}\ \left[\frac{rad}{s}\right]$	**TDM** $[s]$	$\omega_{gc,TDM}\ \left[\frac{rad}{s}\right]$
102.88	20.19	77.82	0.45	3.024	0.45
	$-\infty$	-282.18	0.45	-10.966	0.45
110.32	21.49	75.02	0.43	3.020	0.43
	$-\infty$	-284.98	0.43	-11.472	0.43
117.75	15.79	72.64	0.42	3.009	0.42
	$-\infty$	-287.36	0.42	-11.901	0.42
125.19	13.14	70.87	0.42	2.977	0.42
	$-\infty$	-289.13	0.42	-12.147	0.42
132.63	11.54	69.36	0.41	2.942	0.41
	$-\infty$	-290.64	0.41	-12.329	0.41
140.07	10.47	68.08	0.41	2.905	0.41
	$-\infty$	-291.92	0.41	-12.457	0.41
147.50	9.71	67.01	0.41	2.869	0.41
	$-\infty$	-292.99	0.41	-12.543	0.41
154.94	9.16	66.13	0.41	2.833	0.41
	$-\infty$	-293.87	0.41	-12.588	0.41
162.38	8.72	65.41	0.41	2.798	0.41
	$-\infty$	-294.59	0.41	-12.599	0.41
169.81	8.40	64.84	0.41	2.763	0.41
	$-\infty$	-295.16	0.41	-12.578	0.41
177.25	8.16	64.40	0.41	2.730	0.41
	$-\infty$	-295.60	0.41	-12.530	0.41
184.69	8.00	64.08	0.41	2.697	0.41
	$-\infty$	-295.92	0.41	-12.455	0.41
192.13	7.86	63.54	0.42	2.647	0.42
	$-\infty$	-296.46	0.42	-12.350	0.42
199.56	7.80	63.76	0.42	2.632	0.42
	$-\infty$	-296.24	0.42	-12.229	0.42
207.00	7.75	63.68	0.43	2.597	0.43
	$-\infty$	-296.32	0.43	-12.084	0.43

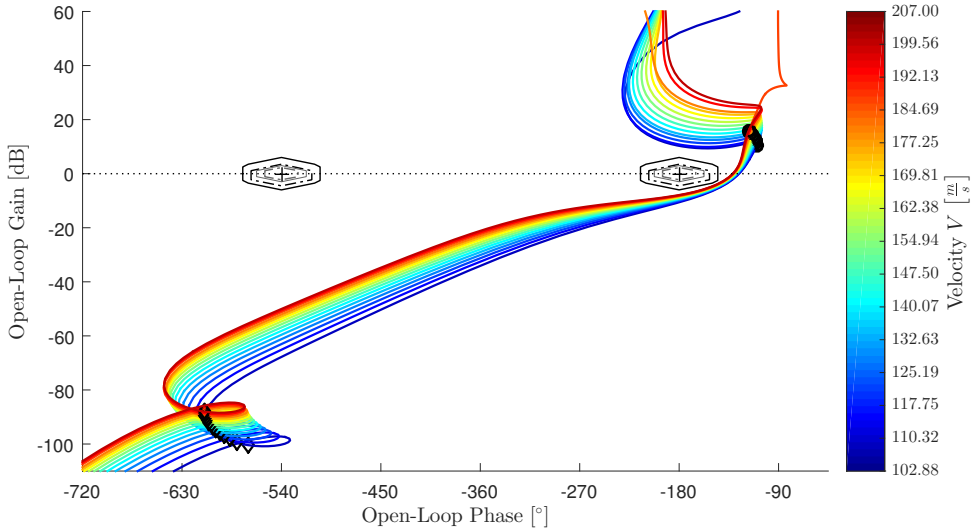

Figure A.57. – Nichols plot for robust stability assessment of $\Delta\dot{q}$ Compensation Law at envelope points according to Table 2.2 generated for α loop cut (enhanced aircraft model)

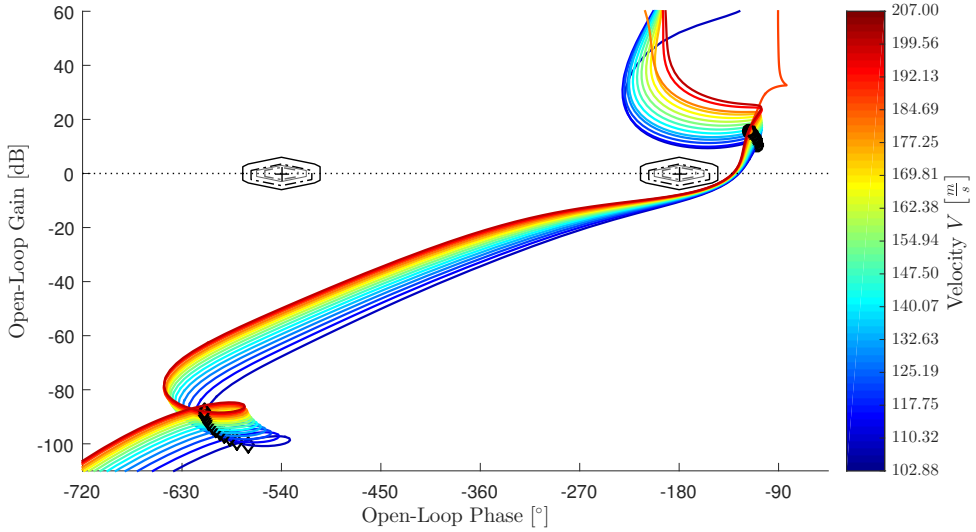

Figure A.58. – Nichols plot for robust stability assessment of $\Delta\dot{q}$ Compensation Law with $\dot{q}$ measurement at envelope points according to Table 2.2 generated for α loop cut (enhanced aircraft model)

Table A.78. – Robust stability properties gain margin (GM), phase margin Φ_m, time delay margins (TDM) and corresponding gain-crossover frequencies $\omega_{gc,\Phi}$ and $\omega_{gc,TDM}$ for robust stability assessment of $\Delta\dot{q}$ Compensation Law at envelope points according to Table 2.2 generated for α loop cut (enhanced aircraft model)

Velocity $V\ \left[\frac{m}{s}\right]$	**GM** $[dB]$	$\Phi_m\ [^\circ]$	$\omega_{gc,\Phi}\ \left[\frac{rad}{s}\right]$	**TDM** $[s]$	$\omega_{gc,TDM}\ \left[\frac{rad}{s}\right]$
102.88	10.57	54.21	1.14	0.833	1.14
	-10.30	-305.79	1.14	-4.700	1.14
110.32	10.24	53.74	1.18	0.797	1.18
	-10.81	-306.26	1.18	-4.541	1.18
117.75	9.95	52.98	1.21	0.762	1.21
	-12.28	-307.02	1.21	-4.413	1.21
125.19	9.70	52.50	1.26	0.730	1.26
	-13.70	-307.50	1.26	-4.273	1.26
132.63	9.46	52.03	1.30	0.700	1.30
	-14.76	-307.97	1.30	-4.145	1.30
140.07	9.25	51.58	1.34	0.674	1.34
	-16.43	-308.42	1.34	-4.029	1.34
147.50	9.05	51.17	1.37	0.650	1.37
	-18.23	-308.83	1.37	-3.922	1.37
154.94	8.87	50.79	1.41	0.628	1.41
	-20.15	-309.21	1.41	-3.823	1.41
162.38	8.70	50.35	1.45	0.605	1.45
	-22.18	-309.65	1.45	-3.718	1.45
169.81	8.54	49.91	1.50	0.582	1.50
	-24.37	-310.09	1.50	-3.617	1.50
177.25	8.39	49.53	1.54	0.562	1.54
	-26.53	-310.47	1.54	-3.523	1.54
184.69	8.26	49.21	1.58	0.544	1.58
	-27.94	-310.79	1.58	-3.436	1.58
192.13	8.14	49.01	1.62	0.530	1.62
	$-\infty$	-310.99	1.62	-3.361	1.62
199.56	8.02	48.84	1.65	0.516	1.65
	-32.06	-311.16	1.65	-3.286	1.65
207.00	7.90	48.56	1.70	0.500	1.70
	-35.06	-311.44	1.70	-3.206	1.70

Table A.79. – Robust stability properties gain margin (GM), phase margin Φ_m, time delay margins (TDM) and corresponding gain-crossover frequencies $\omega_{gc,\Phi}$ and $\omega_{gc,TDM}$ for robust stability assessment of $\Delta\dot{q}$ Compensation Law with $\dot{q}$ measurement at envelope points according to Table 2.2 generated for α loop cut (enhanced aircraft model)

Velocity $V\ \left[\frac{m}{s}\right]$	**GM** $[dB]$	$\Phi_m\ [^\circ]$	$\omega_{gc,\Phi}\ \left[\frac{rad}{s}\right]$	**TDM** $[s]$	$\omega_{gc,TDM}\ \left[\frac{rad}{s}\right]$
102.88	10.48	54.11	1.14	0.830	1.14
	-10.30	-305.89	1.14	-4.695	1.14
110.32	10.16	53.63	1.18	0.794	1.18
	-10.81	-306.37	1.18	-4.537	1.18
117.75	9.87	52.88	1.22	0.759	1.22
	-12.28	-307.12	1.22	-4.410	1.22
125.19	9.63	52.39	1.26	0.727	1.26
	-13.70	-307.61	1.26	-4.269	1.26
132.63	9.40	51.91	1.30	0.698	1.30
	-14.76	-308.09	1.30	-4.142	1.30
140.07	9.19	51.47	1.34	0.671	1.34
	-16.43	-308.53	1.34	-4.026	1.34
147.50	8.99	51.05	1.38	0.648	1.38
	-18.23	-308.95	1.38	-3.919	1.38
154.94	8.81	50.68	1.41	0.626	1.41
	-20.15	-309.32	1.41	-3.820	1.41
162.38	8.65	50.23	1.46	0.602	1.46
	-22.18	-309.77	1.46	-3.715	1.46
169.81	8.50	49.79	1.50	0.580	1.50
	-24.37	-310.21	1.50	-3.615	1.50
177.25	8.36	49.41	1.54	0.560	1.54
	-26.53	-310.59	1.54	-3.521	1.54
184.69	8.21	49.09	1.58	0.542	1.58
	-27.94	-310.91	1.58	-3.434	1.58
192.13	8.08	48.89	1.62	0.528	1.62
	$-\infty$	-311.11	1.62	-3.359	1.62
199.56	7.96	48.73	1.65	0.514	1.65
	-32.06	-311.27	1.65	-3.285	1.65
207.00	7.86	48.44	1.70	0.498	1.70
	-35.06	-311.56	1.70	-3.205	1.70

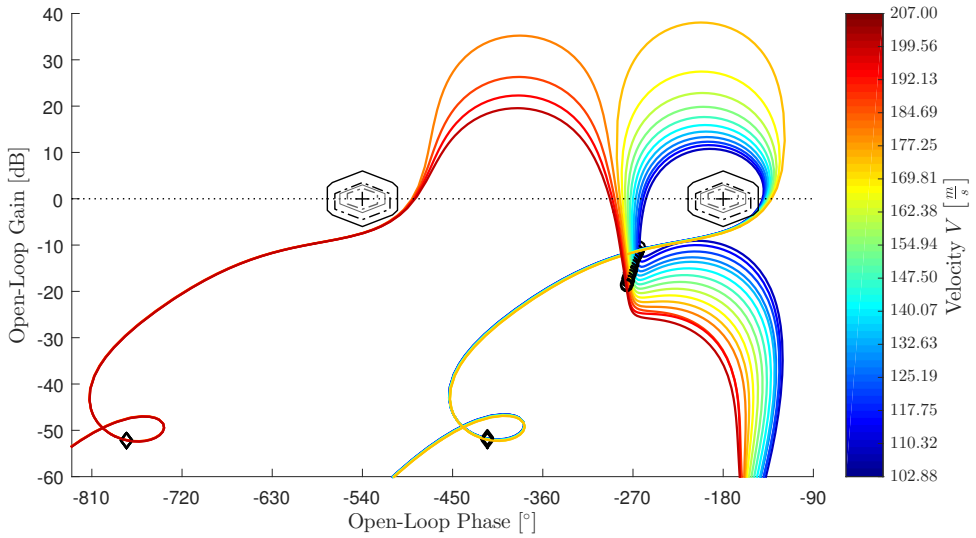

Figure A.59. – Nichols plot for robust stability assessment of $\Delta\dot{q}$ Compensation Law at envelope points according to Table 2.2 generated for q loop cut (enhanced aircraft model)

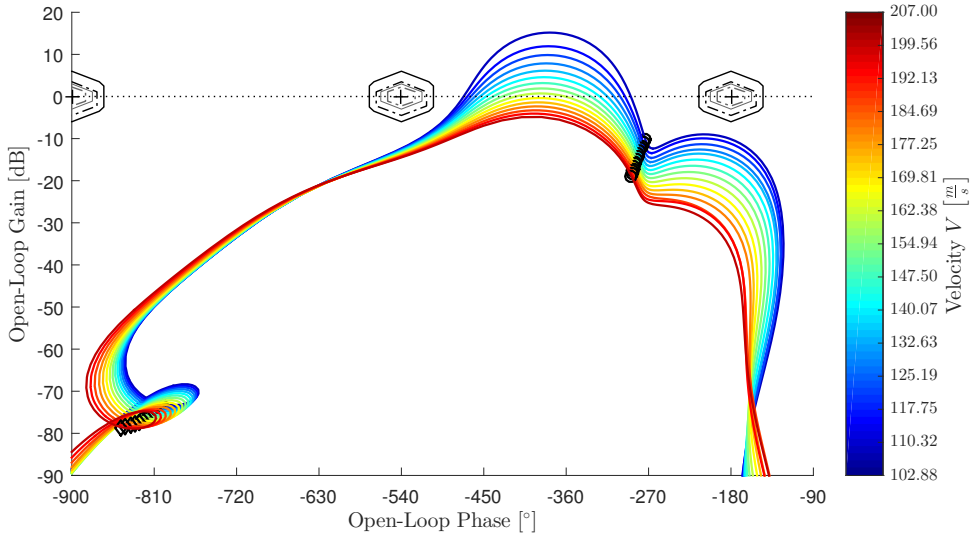

Figure A.60. – Nichols plot for robust stability assessment of $\Delta\dot{q}$ Compensation Law with $\dot{q}$ measurement at envelope points according to Table 2.2 generated for q loop cut (enhanced aircraft model)

Table A.80. – Robust stability properties gain margin (GM), phase margin Φ_m, time delay margins (TDM) and corresponding gain-crossover frequencies $\omega_{gc,\Phi}$ and $\omega_{gc,TDM}$ for robust stability assessment of $\Delta\dot{q}$ Compensation Law at envelope points according to Table 2.2 generated for q loop cut (enhanced aircraft model)

Velocity $V\ \left[\frac{m}{s}\right]$	**GM** $[dB]$	$\Phi_m\ [^\circ]$	$\omega_{gc,\Phi}\ \left[\frac{rad}{s}\right]$	**TDM** $[s]$	$\omega_{gc,TDM}\ \left[\frac{rad}{s}\right]$
102.88	7.03	39.13	4.83	0.142	4.83
	-10.48	-77.05	1.12	-1.161	4.83
110.32	7.06	40.03	4.89	0.143	4.89
	-11.25	-79.88	1.18	-1.143	4.89
117.75	7.08	40.46	4.98	0.142	4.98
	-11.96	-81.85	1.25	-1.120	4.98
125.19	7.11	41.52	5.03	0.144	5.03
	-12.93	-84.51	1.31	-1.104	5.03
132.63	7.15	42.15	5.13	0.143	5.13
	-14.08	-87.26	1.38	-1.082	5.13
140.07	7.18	43.28	5.18	0.146	5.18
	-15.44	-89.93	1.45	-1.066	5.18
147.50	7.22	43.98	5.29	0.145	5.29
	-17.13	-92.59	1.52	-1.043	5.29
154.94	7.26	44.99	5.36	0.146	5.36
	-19.28	-95.20	1.60	-1.025	5.36
162.38	7.29	46.05	5.44	0.148	5.44
	-22.23	-97.80	1.69	-1.008	5.44
169.81	7.33	47.15	5.51	0.149	5.51
	-26.82	-100.36	1.78	-0.986	1.78
177.25	7.37	48.30	5.57	0.151	5.57
	-37.37	-102.93	1.87	-0.960	1.87
184.69	7.41	49.48	5.64	0.153	5.64
	$-\infty$	-105.45	1.97	-0.935	1.97
192.13	7.43	50.67	5.70	0.155	5.70
	$-\infty$	-108.27	2.06	-0.917	2.06
199.56	7.46	51.59	5.79	0.156	5.79
	$-\infty$	-110.65	2.16	-0.895	2.16
207.00	7.48	52.57	5.87	0.156	5.87
	$-\infty$	-112.99	2.26	-0.872	2.26

Table A.81. – Robust stability properties gain margin (GM), phase margin Φ_m, time delay margins (TDM) and corresponding gain-crossover frequencies $\omega_{gc,\Phi}$ and $\omega_{gc,TDM}$ for robust stability assessment of $\Delta\dot{q}$ Compensation Law with $\dot{q}$ measurement at envelope points according to Table 2.2 generated for q loop cut (enhanced aircraft model)

Velocity $V\ \left[\frac{m}{s}\right]$	**GM** $[dB]$	$\Phi_m\ [^\circ]$	$\omega_{gc,\Phi}\ \left[\frac{rad}{s}\right]$	**TDM** $[s]$	$\omega_{gc,TDM}\ \left[\frac{rad}{s}\right]$
102.88	10.15	67.96	2.65	0.448	2.65
	$-\infty$	-109.45	0.94	-1.924	2.65
110.32	11.21	72.01	2.65	0.474	2.65
	$-\infty$	-115.76	1.00	-1.898	2.65
117.75	12.58	75.80	2.66	0.498	2.66
	$-\infty$	-121.03	1.06	-1.867	2.66
125.19	12.71	80.45	2.65	0.530	2.65
	$-\infty$	-127.65	1.13	-1.842	2.65
132.63	12.86	85.90	2.63	0.569	2.63
	$-\infty$	-135.02	1.20	-1.816	2.63
140.07	13.02	92.37	2.60	0.619	2.60
	$-\infty$	-143.29	1.29	-1.794	2.60
147.50	13.18	100.28	2.56	0.685	2.56
	$-\infty$	-153.00	1.40	-1.774	2.56
154.94	13.35	110.14	2.48	0.776	2.48
	$-\infty$	-164.83	1.53	-1.760	2.48
162.38	13.53	124.99	2.34	0.932	2.34
	$-\infty$	-181.19	1.73	-1.752	2.34
169.81	13.70	∞	0.00	∞	0.00
	$-\infty$	$-\infty$	0.00	$-\infty$	0.00
177.25	13.87	∞	0.00	∞	0.00
	$-\infty$	$-\infty$	0.00	$-\infty$	0.00
184.69	14.04	∞	0.00	∞	0.00
	$-\infty$	$-\infty$	0.00	$-\infty$	0.00
192.13	14.21	∞	0.00	∞	0.00
	$-\infty$	$-\infty$	0.00	$-\infty$	0.00
199.56	14.34	∞	0.00	∞	0.00
	$-\infty$	$-\infty$	0.00	$-\infty$	0.00
207.00	14.47	∞	0.00	∞	0.00
	$-\infty$	$-\infty$	0.00	$-\infty$	0.00

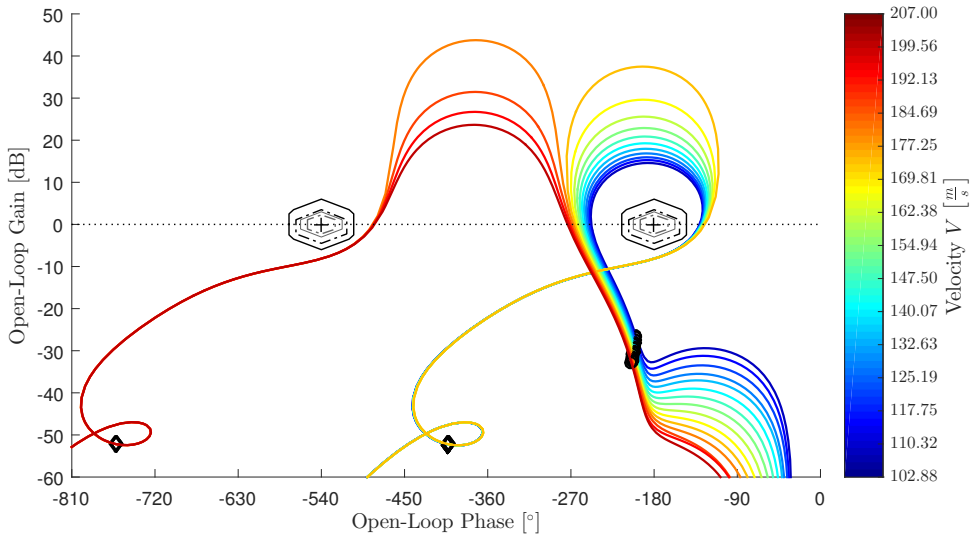

Figure A.61. – Nichols plot for robust stability assessment of $\Delta\dot{q}$ Compensation Law with $\dot{q}$ measurement at envelope points according to Table 2.2 generated for $\dot{q}$ loop cut (enhanced aircraft model)

Table A.82. – Robust stability properties gain margin (GM), phase margin Φ_m, time delay margins (TDM) and corresponding gain-crossover frequencies $\omega_{gc,\Phi}$ and $\omega_{gc,TDM}$ for robust stability assessment of $\Delta\dot{q}$ Compensation Law with $\dot{q}$ measurement at envelope points according to Table 2.2 generated for $\dot{q}$ loop cut (enhanced aircraft model)

Velocity $V\ \left[\frac{m}{s}\right]$	**GM** $[dB]$	$\Phi_m\ [^\circ]$	$\omega_{gc,\Phi}\ \left[\frac{rad}{s}\right]$	**TDM** $[s]$	$\omega_{gc,TDM}\ \left[\frac{rad}{s}\right]$
102.88	8.12	48.99	5.50	0.155	5.50
	-14.51	-67.82	2.08	-0.569	2.08
110.32	8.12	49.62	5.55	0.156	5.55
	-15.19	-69.41	2.14	-0.565	2.14
117.75	8.12	50.23	5.60	0.157	5.60
	-15.84	-70.53	2.20	-0.559	2.20
125.19	8.12	50.75	5.66	0.156	5.66
	-16.75	-72.27	2.26	-0.557	2.26
132.63	8.12	51.27	5.73	0.156	5.73
	-17.84	-74.24	2.33	-0.556	2.33
140.07	8.13	51.84	5.80	0.156	5.80
	-19.13	-75.85	2.39	-0.554	2.39
147.50	8.13	52.22	5.89	0.155	5.89
	-20.72	-77.63	2.45	-0.552	2.45
154.94	8.13	52.75	5.97	0.154	5.97
	-22.73	-79.61	2.52	-0.551	2.52
162.38	8.13	53.33	6.04	0.154	6.04
	-25.42	-81.67	2.59	-0.550	2.59
169.81	8.13	53.93	6.12	0.154	6.12
	-29.43	-83.60	2.66	-0.548	2.66
177.25	8.13	54.57	6.19	0.154	6.19
	-37.27	-85.45	2.73	-0.546	2.73
184.69	8.13	55.23	6.26	0.154	6.26
	$-\infty$	-87.42	2.80	-0.544	2.80
192.13	8.12	55.90	6.33	0.154	6.33
	$-\infty$	-89.58	2.88	-0.544	2.88
199.56	8.12	56.60	6.39	0.154	6.39
	$-\infty$	-91.57	2.95	-0.541	2.95
207.00	8.12	57.33	6.46	0.155	6.46
	$-\infty$	-93.61	3.04	-0.538	3.04

A.6.6. L1 adaptive controller with Eigenstructure Assignment

Page intentionally left blank

Table A.83. – Robust stability properties gain margin (GM), phase margin Φ_m, time delay margins (TDM) and corresponding gain-crossover frequencies $\omega_{gc,\Phi}$ and $\omega_{gc,TDM}$ for robust stability comparison of L1 adaptive controller with Eigenstructure Assignment with and without hedging at V = 154.94$\frac{m}{s}$ generated for α loop cut (enhanced aircraft model)

Controller	**GM** $[dB]$	Φ_m $[^\circ]$	$\omega_{gc,\Phi}$ $\left[\frac{rad}{s}\right]$	**TDM** $[s]$	$\omega_{gc,TDM}$ $\left[\frac{rad}{s}\right]$
Baseline	7.72	63.12	0.40	2.777	0.40
	$-\infty$	-296.88	0.40	-13.063	0.40
L1 Standalone	9.85	85.76	1.99	0.754	1.99
	-25.51	-274.24	1.99	-2.411	1.99
L1 Standalone (no hedg.)	9.87	87.08	1.88	0.807	1.88
	-25.76	-272.92	1.88	-2.531	1.88

Table A.84. – Robust stability properties gain margin (GM), phase margin Φ_m, time delay margins (TDM) and corresponding gain-crossover frequencies $\omega_{gc,\Phi}$ and $\omega_{gc,TDM}$ for robust stability comparison of L1 adaptive controller with Eigenstructure Assignment with and without hedging at V = 154.94$\frac{m}{s}$ generated for q loop cut (enhanced aircraft model)

Controller	**GM** $[dB]$	Φ_m $[^\circ]$	$\omega_{gc,\Phi}$ $\left[\frac{rad}{s}\right]$	**TDM** $[s]$	$\omega_{gc,TDM}$ $\left[\frac{rad}{s}\right]$
Baseline	21.76	∞	0.00	∞	0.00
	$-\infty$	$-\infty$	0.00	$-\infty$	0.00
L1 Standalone	12.77	∞	0.00	∞	0.00
	$-\infty$	$-\infty$	0.00	$-\infty$	0.00
L1 Standalone (no hedg.)	12.33	∞	0.00	∞	0.00
	$-\infty$	$-\infty$	0.00	$-\infty$	0.00

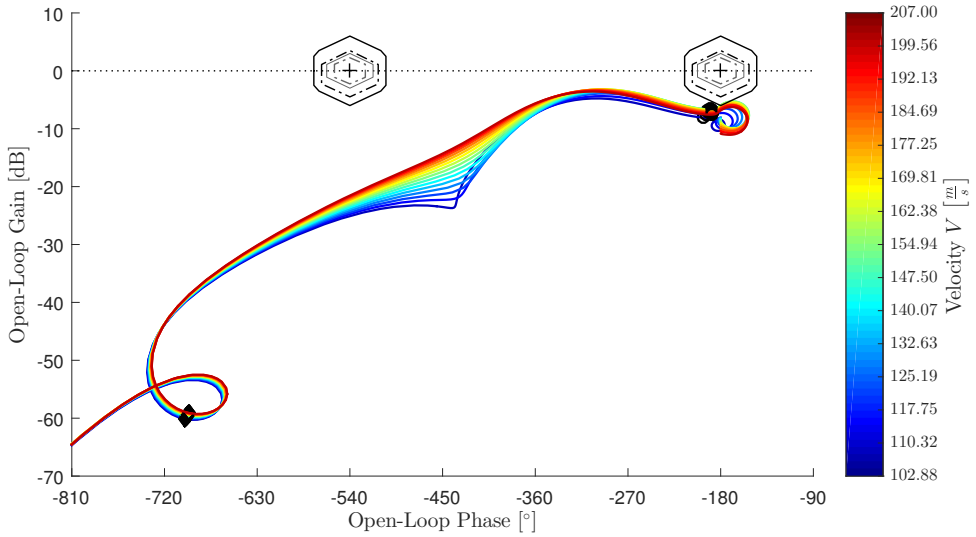

Figure A.62. – Nichols plot for robust stability assessment of L1 adaptive controller with Eigenstructure Assignment at envelope points according to Table 2.2 generated for η_{cmd} (bottleneck) loop cut (enhanced aircraft model)

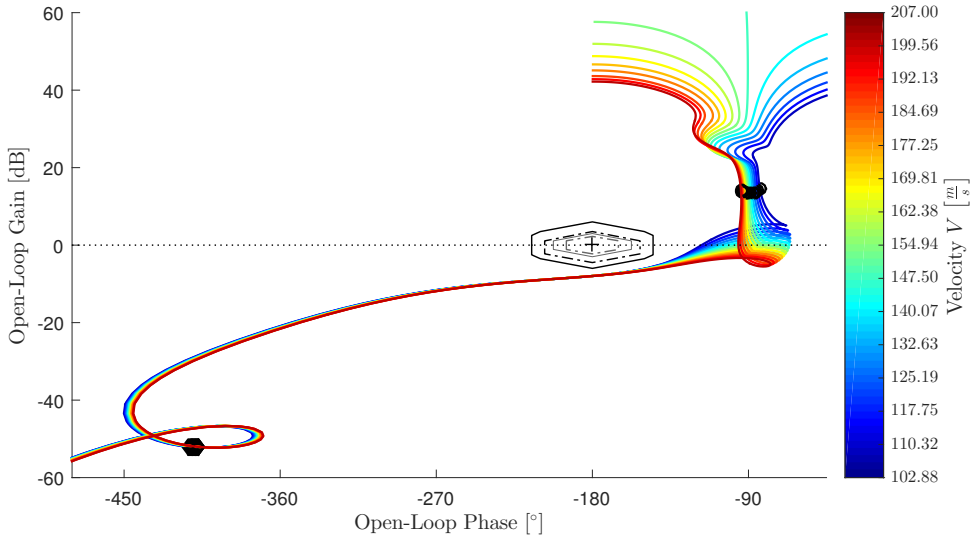

Figure A.63. – Nichols plot for robust stability assessment of L1 adaptive controller with Eigenstructure Assignment without hedging at envelope points according to Table 2.2 generated for η_{cmd} (bottleneck) loop cut (enhanced aircraft model)

Table A.85. – Robust stability properties gain margin (GM), phase margin Φ_m, time delay margins (TDM) and corresponding gain-crossover frequencies $\omega_{gc,\Phi}$ and $\omega_{gc,TDM}$ for robust stability assessment of L1 adaptive controller with Eigenstructure Assignment at envelope points according to Table 2.2 generated for η_{cmd} (bottleneck) loop cut (enhanced aircraft model)

Velocity $V\ \left[\frac{m}{s}\right]$	**GM** $[dB]$	$\Phi_m\ [^\circ]$	$\omega_{gc,\Phi}\ \left[\frac{rad}{s}\right]$	**TDM** $[s]$	$\omega_{gc,TDM}\ \left[\frac{rad}{s}\right]$
102.88	8.41	∞	0.00	∞	0.00
	$-\infty$	$-\infty$	0.00	$-\infty$	0.00
110.32	7.30	∞	0.00	∞	0.00
	$-\infty$	$-\infty$	0.00	$-\infty$	0.00
117.75	6.67	∞	0.00	∞	0.00
	$-\infty$	$-\infty$	0.00	$-\infty$	0.00
125.19	6.34	∞	0.00	∞	0.00
	$-\infty$	$-\infty$	0.00	$-\infty$	0.00
132.63	6.11	∞	0.00	∞	0.00
	$-\infty$	$-\infty$	0.00	$-\infty$	0.00
140.07	6.00	∞	0.00	∞	0.00
	$-\infty$	$-\infty$	0.00	$-\infty$	0.00
147.50	5.97	∞	0.00	∞	0.00
	$-\infty$	$-\infty$	0.00	$-\infty$	0.00
154.94	5.98	∞	0.00	∞	0.00
	$-\infty$	$-\infty$	0.00	$-\infty$	0.00
162.38	6.05	∞	0.00	∞	0.00
	$-\infty$	$-\infty$	0.00	$-\infty$	0.00
169.81	6.15	∞	0.00	∞	0.00
	$-\infty$	$-\infty$	0.00	$-\infty$	0.00
177.25	6.28	∞	0.00	∞	0.00
	$-\infty$	$-\infty$	0.00	$-\infty$	0.00
184.69	6.43	∞	0.00	∞	0.00
	$-\infty$	$-\infty$	0.00	$-\infty$	0.00
192.13	6.48	∞	0.00	∞	0.00
	$-\infty$	$-\infty$	0.00	$-\infty$	0.00
199.56	6.63	∞	0.00	∞	0.00
	$-\infty$	$-\infty$	0.00	$-\infty$	0.00
207.00	6.86	∞	0.00	∞	0.00
	$-\infty$	$-\infty$	0.00	$-\infty$	0.00

Table A.86. – Robust stability properties gain margin (GM), phase margin Φ_m, time delay margins (TDM) and corresponding gain-crossover frequencies $\omega_{gc,\Phi}$ and $\omega_{gc,TDM}$ for robust stability assessment of L1 adaptive controller with Eigenstructure Assignment without hedging at envelope points according to Table 2.2 generated for η_{cmd} (bottleneck) loop cut (enhanced aircraft model)

Velocity $V\ \left[\frac{m}{s}\right]$	**GM** $[dB]$	$\Phi_m\ [^\circ]$	$\omega_{gc,\Phi}\ \left[\frac{rad}{s}\right]$	**TDM** $[s]$	$\omega_{gc,TDM}\ \left[\frac{rad}{s}\right]$
102.88	7.97	62.97	4.03	0.273	4.03
	$-\infty$	-297.03	4.03	-1.287	4.03
110.32	7.97	65.38	4.09	0.279	4.09
	$-\infty$	-294.62	4.09	-1.257	4.09
117.75	7.97	67.74	4.15	0.285	4.15
	$-\infty$	-292.26	4.15	-1.230	4.15
125.19	7.97	70.61	4.18	0.295	4.18
	$-\infty$	-289.39	4.18	-1.207	4.18
132.63	7.97	73.94	4.20	0.307	4.20
	$-\infty$	-286.06	4.20	-1.188	4.20
140.07	7.97	78.03	4.20	0.324	4.20
	$-\infty$	-246.27	2.43	-1.172	4.20
147.50	7.97	83.61	4.14	0.352	4.14
	$-\infty$	-248.93	2.97	-1.165	4.14
154.94	7.97	96.64	3.80	0.444	3.80
	$-\infty$	-261.65	3.73	-1.211	3.80
162.38	7.96	94.92	1.69	0.981	1.69
	$-\infty$	-265.08	1.69	-2.740	1.69
169.81	7.96	92.39	1.69	0.957	1.69
	$-\infty$	-267.61	1.69	-2.771	1.69
177.25	7.96	90.25	1.69	0.929	1.69
	$-\infty$	-269.75	1.69	-2.778	1.69
184.69	7.96	88.42	1.71	0.901	1.71
	$-\infty$	-271.58	1.71	-2.766	1.71
192.13	7.97	86.79	1.74	0.873	1.74
	$-\infty$	-273.21	1.74	-2.748	1.74
199.56	7.98	85.42	1.76	0.845	1.76
	$-\infty$	-274.58	1.76	-2.716	1.76
207.00	7.98	84.15	1.80	0.818	1.80
	$-\infty$	-275.85	1.80	-2.682	1.80

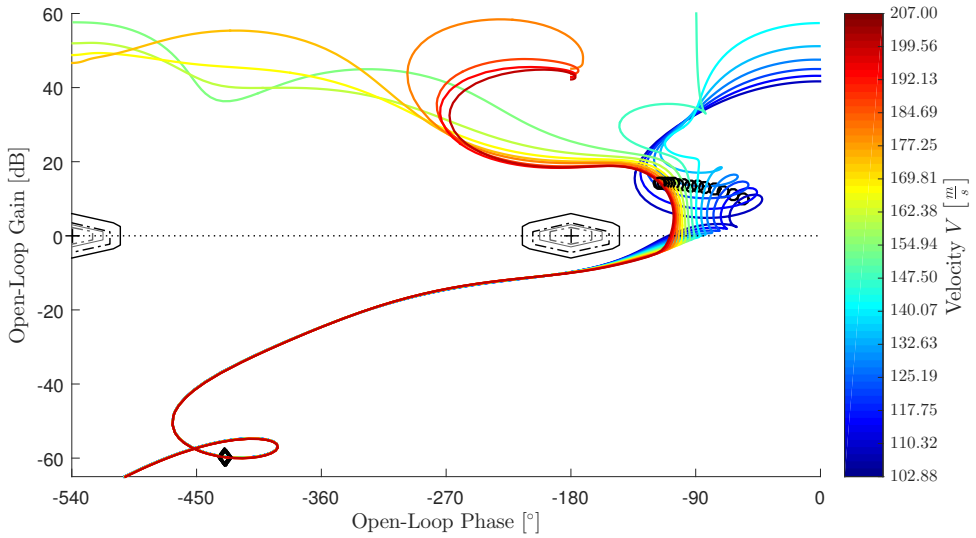

Figure A.64. – Nichols plot for robust stability assessment of L1 adaptive controller with Eigenstructure Assignment at envelope points according to Table 2.2 generated for α loop cut (enhanced aircraft model)

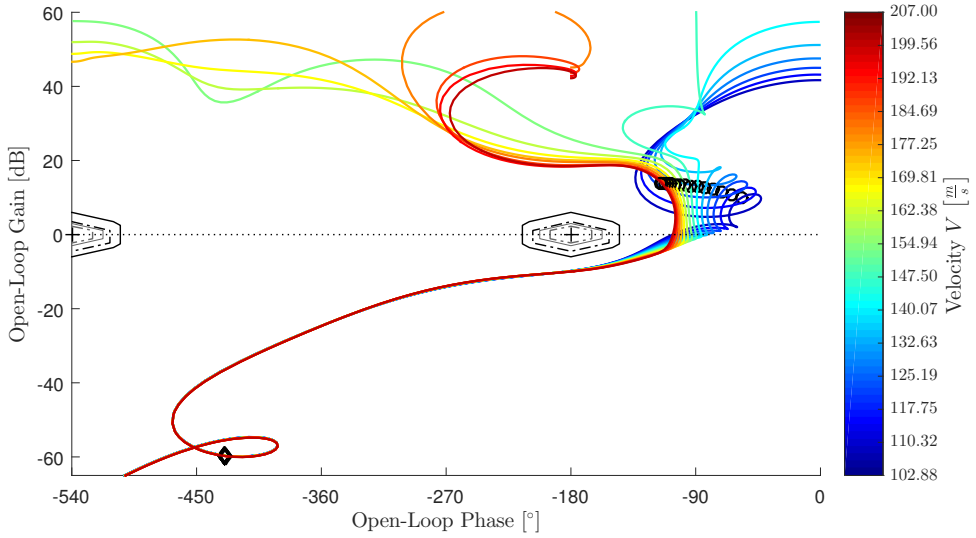

Figure A.65. – Nichols plot for robust stability assessment of L1 adaptive controller with Eigenstructure Assignment without hedging at envelope points according to Table 2.2 generated for α loop cut (enhanced aircraft model)

Table A.87. – Robust stability properties gain margin (GM), phase margin Φ_m, time delay margins (TDM) and corresponding gain-crossover frequencies $\omega_{gc,\Phi}$ and $\omega_{gc,TDM}$ for robust stability assessment of L1 adaptive controller with Eigenstructure Assignment at envelope points according to Table 2.2 generated for α loop cut (enhanced aircraft model)

Velocity $V\ \left[\frac{m}{s}\right]$	**GM** $[dB]$	$\Phi_m\ [^\circ]$	$\omega_{gc,\Phi}\ \left[\frac{rad}{s}\right]$	**TDM** $[s]$	$\omega_{gc,TDM}\ \left[\frac{rad}{s}\right]$
102.88	9.78	70.23	3.36	0.364	3.36
	$-\infty$	-289.77	3.36	-1.503	3.36
110.32	9.79	73.69	3.29	0.390	3.29
	$-\infty$	-286.31	3.29	-1.517	3.29
117.75	9.80	77.66	3.20	0.424	3.20
	$-\infty$	-282.34	3.20	-1.542	3.20
125.19	9.80	83.40	3.00	0.485	3.00
	$-\infty$	-276.60	3.00	-1.609	3.00
132.63	9.82	93.48	2.47	0.661	2.47
	$-\infty$	-266.52	2.47	-1.884	2.47
140.07	9.83	92.95	2.07	0.784	2.07
	$-\infty$	-267.05	2.07	-2.252	2.07
147.50	9.84	89.12	2.01	0.775	2.01
	$-\infty$	-270.88	2.01	-2.355	2.01
154.94	9.85	85.76	1.99	0.754	1.99
	-25.51	-274.24	1.99	-2.411	1.99
162.38	9.87	82.79	1.99	0.726	1.99
	-22.32	-277.21	1.99	-2.432	1.99
169.81	9.89	80.22	2.01	0.698	2.01
	-20.91	-279.78	2.01	-2.435	2.01
177.25	9.90	77.98	2.03	0.671	2.03
	-20.09	-282.02	2.03	-2.426	2.03
184.69	9.92	76.03	2.06	0.645	2.06
	-19.60	-283.97	2.06	-2.411	2.06
192.13	9.95	74.22	2.09	0.621	2.09
	-18.75	-285.78	2.09	-2.390	2.09
199.56	9.97	72.80	2.12	0.600	2.12
	-18.40	-287.20	2.12	-2.365	2.12
207.00	9.99	71.56	2.15	0.580	2.15
	-18.51	-288.44	2.15	-2.339	2.15

Table A.88. – Robust stability properties gain margin (GM), phase margin Φ_m, time delay margins (TDM) and corresponding gain-crossover frequencies $\omega_{gc,\Phi}$ and $\omega_{gc,TDM}$ for robust stability assessment of L1 adaptive controller with Eigenstructure Assignment without hedging at envelope points according to Table 2.2 generated for α loop cut (enhanced aircraft model)

Velocity $V\ \left[\frac{m}{s}\right]$	**GM** $[dB]$	$\Phi_m\ [^\circ]$	$\omega_{gc,\Phi}\ \left[\frac{rad}{s}\right]$	**TDM** $[s]$	$\omega_{gc,TDM}\ \left[\frac{rad}{s}\right]$
102.88	9.82	73.26	3.27	0.392	3.27
	$-\infty$	-286.74	3.27	-1.532	3.27
110.32	9.82	77.08	3.19	0.421	3.19
	$-\infty$	-282.92	3.19	-1.547	3.19
117.75	9.83	81.37	3.08	0.461	3.08
	$-\infty$	-278.63	3.08	-1.577	3.08
125.19	9.83	88.45	2.84	0.544	2.84
	$-\infty$	-271.55	2.84	-1.671	2.84
132.63	9.84	98.36	2.04	0.843	2.04
	$-\infty$	-261.64	2.04	-2.242	2.04
140.07	9.85	94.21	1.91	0.860	1.91
	$-\infty$	-265.79	1.91	-2.427	1.91
147.50	9.86	90.39	1.88	0.840	1.88
	$-\infty$	-269.61	1.88	-2.507	1.88
154.94	9.87	87.08	1.88	0.807	1.88
	-25.76	-272.92	1.88	-2.531	1.88
162.38	9.88	84.23	1.89	0.777	1.89
	-22.35	-275.77	1.89	-2.543	1.89
169.81	9.89	81.76	1.91	0.747	1.91
	-20.90	-278.24	1.91	-2.541	1.91
177.25	9.91	79.62	1.93	0.719	1.93
	-20.08	-280.38	1.93	-2.530	1.93
184.69	9.92	77.75	1.97	0.690	1.97
	-19.59	-282.25	1.97	-2.506	1.97
192.13	9.95	76.02	2.00	0.663	2.00
	-18.74	-283.98	2.00	-2.478	2.00
199.56	9.96	74.66	2.03	0.641	2.03
	-18.37	-285.34	2.03	-2.449	2.03
207.00	9.98	73.47	2.07	0.620	2.07
	-18.49	-286.53	2.07	-2.418	2.07

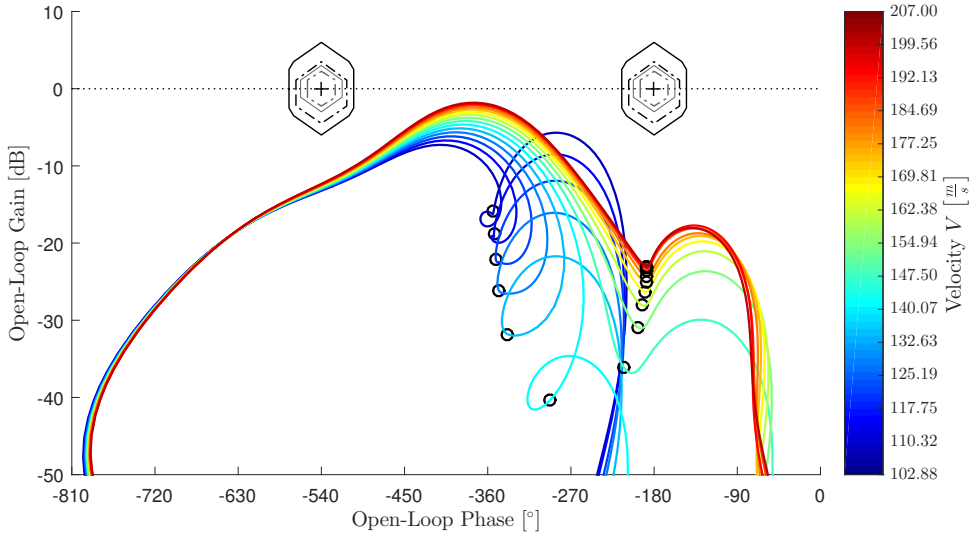

Figure A.66. – Nichols plot for robust stability assessment of L1 adaptive controller with Eigenstructure Assignment at envelope points according to Table 2.2 generated for q loop cut (enhanced aircraft model)

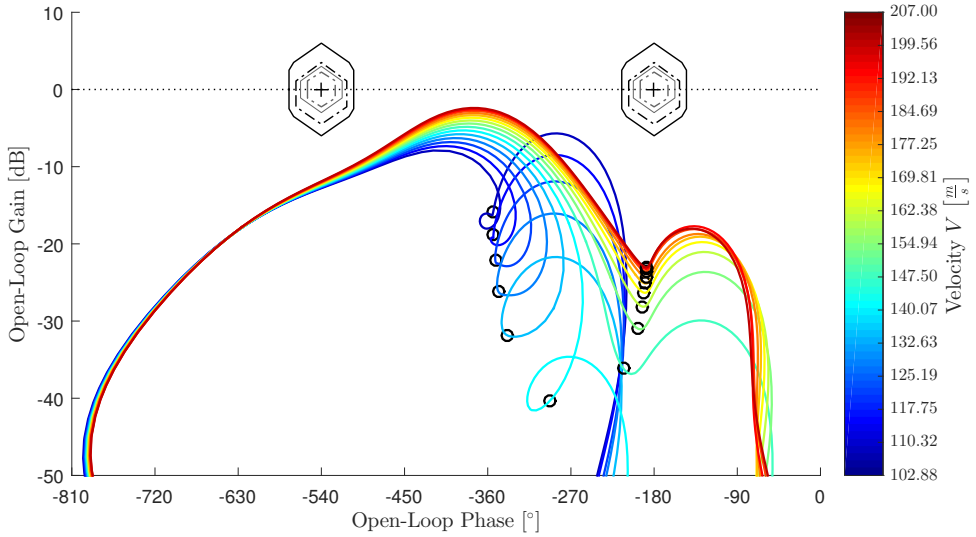

Figure A.67. – Nichols plot for robust stability assessment of L1 adaptive controller with Eigenstructure Assignment without hedging at envelope points according to Table 2.2 generated for q loop cut (enhanced aircraft model)

Table A.89. – Robust stability properties gain margin (GM), phase margin Φ_m, time delay margins (TDM) and corresponding gain-crossover frequencies $\omega_{gc,\Phi}$ and $\omega_{gc,TDM}$ for robust stability assessment of L1 adaptive controller with Eigenstructure Assignment at envelope points according to Table 2.2 generated for q loop cut (enhanced aircraft model)

Velocity $V\ \left[\frac{m}{s}\right]$	**GM** $[dB]$	$\Phi_m\ [^\circ]$	$\omega_{gc,\Phi}\ \left[\frac{rad}{s}\right]$	**TDM** $[s]$	$\omega_{gc,TDM}\ \left[\frac{rad}{s}\right]$
102.88	13.22	∞	0.00	∞	0.00
	$-\infty$	$-\infty$	0.00	$-\infty$	0.00
110.32	13.15	∞	0.00	∞	0.00
	$-\infty$	$-\infty$	0.00	$-\infty$	0.00
117.75	13.10	∞	0.00	∞	0.00
	$-\infty$	$-\infty$	0.00	$-\infty$	0.00
125.19	13.03	∞	0.00	∞	0.00
	$-\infty$	$-\infty$	0.00	$-\infty$	0.00
132.63	12.97	∞	0.00	∞	0.00
	$-\infty$	$-\infty$	0.00	$-\infty$	0.00
140.07	12.90	∞	0.00	∞	0.00
	$-\infty$	$-\infty$	0.00	$-\infty$	0.00
147.50	12.84	∞	0.00	∞	0.00
	$-\infty$	$-\infty$	0.00	$-\infty$	0.00
154.94	12.77	∞	0.00	∞	0.00
	$-\infty$	$-\infty$	0.00	$-\infty$	0.00
162.38	12.70	∞	0.00	∞	0.00
	$-\infty$	$-\infty$	0.00	$-\infty$	0.00
169.81	12.64	∞	0.00	∞	0.00
	$-\infty$	$-\infty$	0.00	$-\infty$	0.00
177.25	12.57	∞	0.00	∞	0.00
	$-\infty$	$-\infty$	0.00	$-\infty$	0.00
184.69	12.51	∞	0.00	∞	0.00
	$-\infty$	$-\infty$	0.00	$-\infty$	0.00
192.13	12.45	∞	0.00	∞	0.00
	$-\infty$	$-\infty$	0.00	$-\infty$	0.00
199.56	12.39	∞	0.00	∞	0.00
	$-\infty$	$-\infty$	0.00	$-\infty$	0.00
207.00	12.33	∞	0.00	∞	0.00
	$-\infty$	$-\infty$	0.00	$-\infty$	0.00

Table A.90. – Robust stability properties gain margin (GM), phase margin Φ_m, time delay margins (TDM) and corresponding gain-crossover frequencies $\omega_{gc,\Phi}$ and $\omega_{gc,TDM}$ for robust stability assessment of L1 adaptive controller with Eigenstructure Assignment without hedging at envelope points according to Table 2.2 generated for q loop cut (enhanced aircraft model)

Velocity $V\ \left[\frac{m}{s}\right]$	**GM** $[dB]$	$\Phi_m\ [^\circ]$	$\omega_{gc,\Phi}\ \left[\frac{rad}{s}\right]$	**TDM** $[s]$	$\omega_{gc,TDM}\ \left[\frac{rad}{s}\right]$
102.88	12.79	∞	0.00	∞	0.00
	$-\infty$	$-\infty$	0.00	$-\infty$	0.00
110.32	12.72	∞	0.00	∞	0.00
	$-\infty$	$-\infty$	0.00	$-\infty$	0.00
117.75	12.66	∞	0.00	∞	0.00
	$-\infty$	$-\infty$	0.00	$-\infty$	0.00
125.19	12.60	∞	0.00	∞	0.00
	$-\infty$	$-\infty$	0.00	$-\infty$	0.00
132.63	12.53	∞	0.00	∞	0.00
	$-\infty$	$-\infty$	0.00	$-\infty$	0.00
140.07	12.47	∞	0.00	∞	0.00
	$-\infty$	$-\infty$	0.00	$-\infty$	0.00
147.50	12.40	∞	0.00	∞	0.00
	$-\infty$	$-\infty$	0.00	$-\infty$	0.00
154.94	12.33	∞	0.00	∞	0.00
	$-\infty$	$-\infty$	0.00	$-\infty$	0.00
162.38	12.27	∞	0.00	∞	0.00
	$-\infty$	$-\infty$	0.00	$-\infty$	0.00
169.81	12.20	∞	0.00	∞	0.00
	$-\infty$	$-\infty$	0.00	$-\infty$	0.00
177.25	12.13	∞	0.00	∞	0.00
	$-\infty$	$-\infty$	0.00	$-\infty$	0.00
184.69	12.07	∞	0.00	∞	0.00
	$-\infty$	$-\infty$	0.00	$-\infty$	0.00
192.13	12.01	∞	0.00	∞	0.00
	$-\infty$	$-\infty$	0.00	$-\infty$	0.00
199.56	11.95	∞	0.00	∞	0.00
	$-\infty$	$-\infty$	0.00	$-\infty$	0.00
207.00	11.90	∞	0.00	∞	0.00
	$-\infty$	$-\infty$	0.00	$-\infty$	0.00

A.7. Performance of control laws

A.7.1. Comparison of control laws

Page intentionally left blank

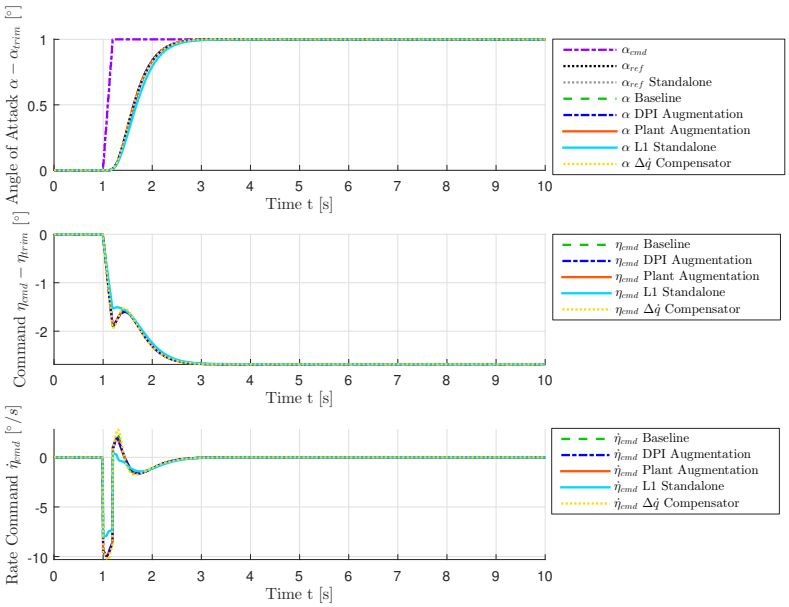

Figure A.68. – Comparison of α_{cmd} step responses of basic, linear aircraft model containing only the short-period approximation in combination with baseline controller, L1 Adaptive Augmentations, $\Delta\dot{q}$ Compensation Law and L1 adaptive controller with Eigenstructure Assignment at $V_0 = 154.94\frac{m}{s}$

Table A.91. – Comparison of performance metrics $M_{\mathcal{L}_2}$, $M_{\mathcal{L}_\infty}$ and $M_{\mathcal{L}_{2,act}}$ generated from step responses of basic, linear aircraft model containing only the short-period approximation in combination with baseline controller, L1 Adaptive Augmentations, $\Delta\dot{q}$ Compensation Law and L1 adaptive controller with Eigenstructure Assignment at $V_0 = 154.94\frac{m}{s}$

Controller	$M_{\mathcal{L}_2}$ $[-]$	$M_{\mathcal{L}_\infty}$ $[-]$	$M_{\mathcal{L}_{2,act}}$ $[-]$
Baseline	0.004	0.0003	0.784
DPI Augmentation	0.004	0.0003	0.773
Plant Augmentation	0.003	0.0002	0.770
L1 Standalone	0.029	0.0014	0.629
$\Delta\dot{q}$ Compensator	0.005	0.0003	0.804

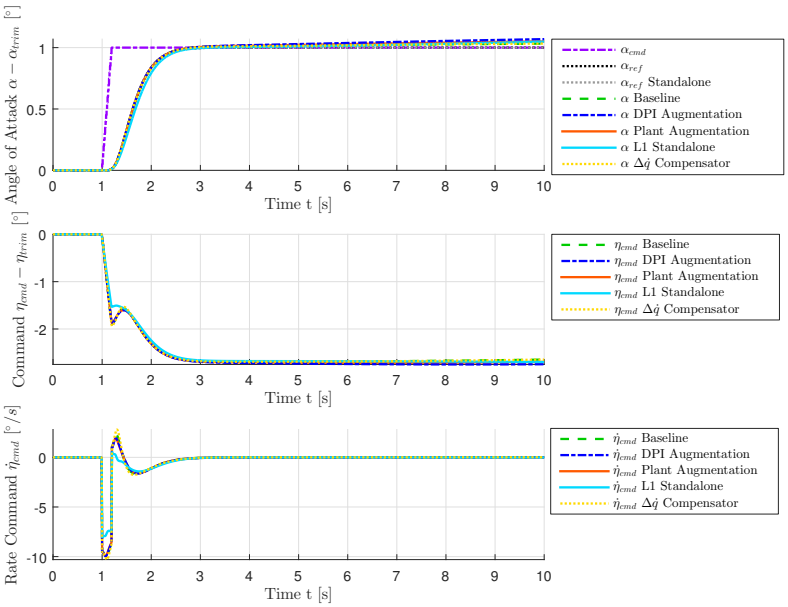

Figure A.69. – Comparison of α_{cmd} step responses of basic, linear aircraft model in combination with baseline controller, L1 Adaptive Augmentations, $\Delta\dot{q}$ Compensation Law and L1 adaptive controller with Eigenstructure Assignment at $V_0 = 154.94\frac{m}{s}$

Table A.92. – Comparison of performance metrics $M_{\mathcal{L}_2}$, $M_{\mathcal{L}_\infty}$ and $M_{\mathcal{L}_{2,act}}$ generated from step responses of basic, linear aircraft model in combination with baseline controller, L1 Adaptive Augmentations, $\Delta\dot{q}$ Compensation Law and L1 adaptive controller with Eigenstructure Assignment at $V_0 = 154.94\frac{m}{s}$

Controller	$M_{\mathcal{L}_2}$ $[-]$	$M_{\mathcal{L}_\infty}$ $[-]$	$M_{\mathcal{L}_{2,act}}$ $[-]$
Baseline	0.032	0.0006	0.784
DPI Augmentation	0.066	0.0012	0.774
Plant Augmentation	0.049	0.0009	0.770
L1 Standalone	0.047	0.0014	0.629
$\Delta\dot{q}$ Compensator	0.033	0.0006	0.804

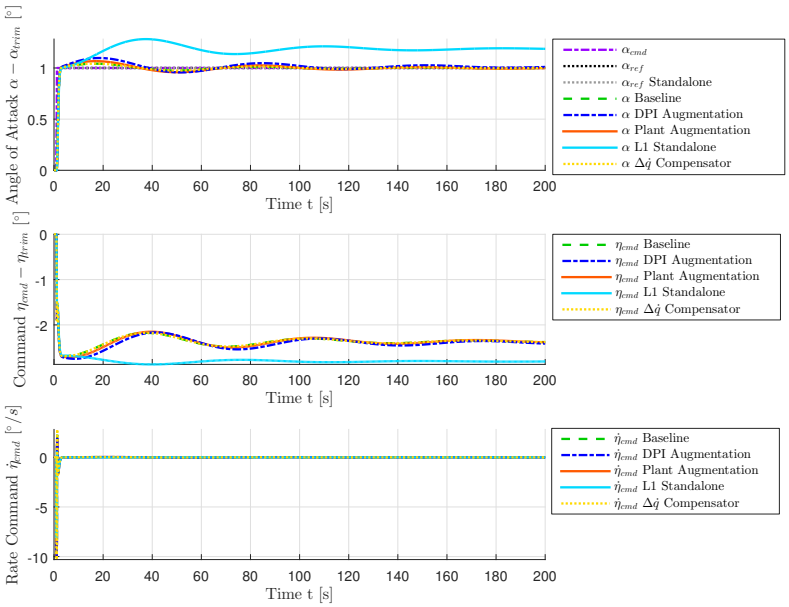

Figure A.70. – Comparison of α_{cmd} step responses of basic, linear aircraft model in combination with baseline controller, L1 Adaptive Augmentations, $\Delta\dot{q}$ Compensation Law and L1 adaptive controller with Eigenstructure Assignment at $V_0 = 154.94\frac{m}{s}$ for large timescale

Table A.93. – Comparison of performance metrics $M_{\mathcal{L}_2}$, $M_{\mathcal{L}_\infty}$ and $M_{\mathcal{L}_{2,act}}$ generated from step responses of basic, linear aircraft model in combination with baseline controller, L1 Adaptive Augmentations, $\Delta\dot{q}$ Compensation Law and L1 adaptive controller with Eigenstructure Assignment at $V_0 = 154.94\frac{m}{s}$ for large timescale

Controller	$M_{\mathcal{L}_2}$ $[-]$	$M_{\mathcal{L}_\infty}$ $[-]$	$M_{\mathcal{L}_{2,act}}$ $[-]$
Baseline	0.117	0.0007	0.784
DPI Augmentation	0.280	0.0017	0.774
Plant Augmentation	0.190	0.0012	0.771
L1 Standalone	1.473	0.0049	0.629
$\Delta\dot{q}$ Compensator	0.117	0.0007	0.804

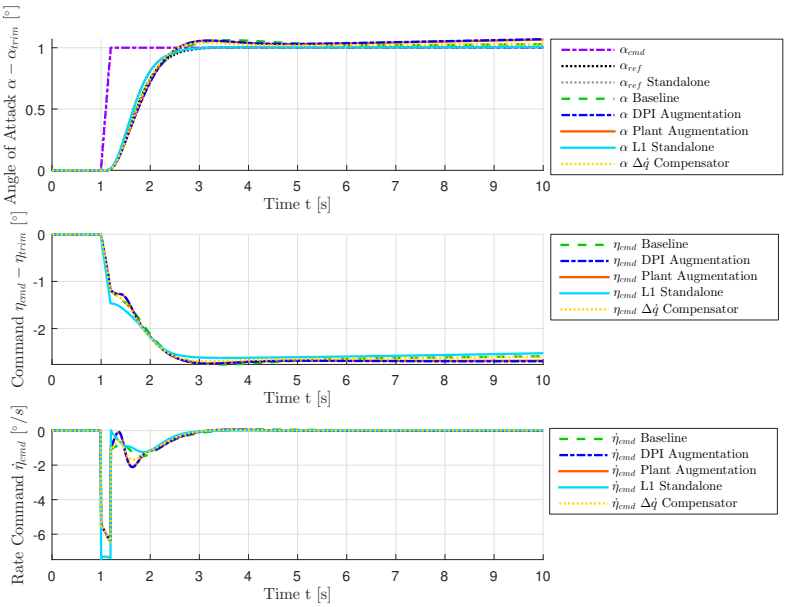

Figure A.71. – Comparison of α_{cmd} step responses of enhanced, nonlinear aircraft model in combination with baseline controller, L1 Adaptive Augmentations, $\Delta\dot{q}$ Compensation Law and L1 adaptive controller with Eigenstructure Assignment at $V_0 = 154.94\frac{m}{s}$

Table A.94. – Comparison of performance metrics $M_{\mathcal{L}_2}$, $M_{\mathcal{L}_\infty}$ and $M_{\mathcal{L}_{2,act}}$ generated from step responses of enhanced, nonlinear aircraft model in combination with baseline controller, L1 Adaptive Augmentations, $\Delta\dot{q}$ Compensation Law and L1 adaptive controller with Eigenstructure Assignment at $V_0 = 154.94\frac{m}{s}$

Controller	$M_{\mathcal{L}_2}$ $[-]$	$M_{\mathcal{L}_\infty}$ $[-]$	$M_{\mathcal{L}_{2,act}}$ $[-]$
Baseline	0.048	0.0010	0.516
DPI Augmentation	0.069	0.0011	0.526
Plant Augmentation	0.066	0.0011	0.526
L1 Standalone	0.005	0.0002	0.599
$\Delta\dot{q}$ Compensator	0.038	0.0008	0.520

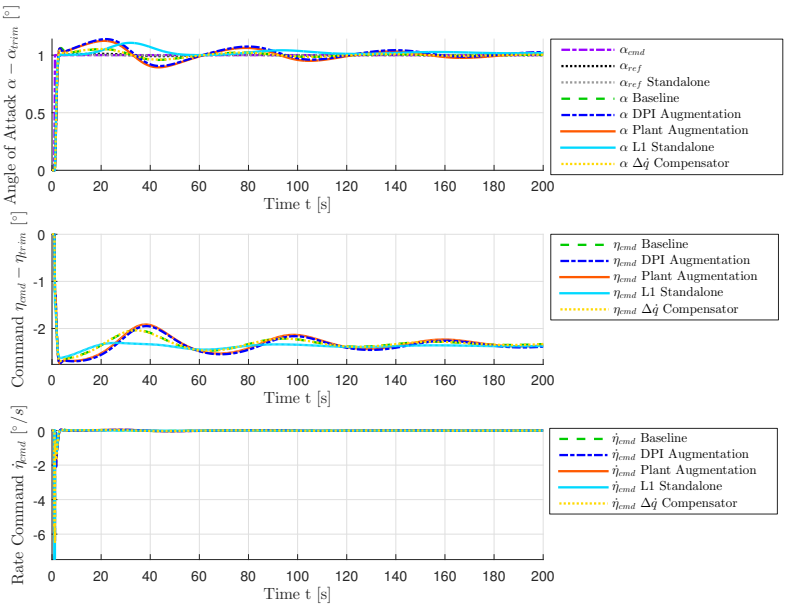

Figure A.72. – Comparison of α_{cmd} step responses of enhanced, nonlinear aircraft model in combination with baseline controller, L1 Adaptive Augmentations, $\Delta\dot{q}$ Compensation Law and L1 adaptive controller with Eigenstructure Assignment at $V_0 = 154.94\frac{m}{s}$ for large timescale

Table A.95. – Comparison of performance metrics $M_{\mathcal{L}_2}$, $M_{\mathcal{L}_\infty}$ and $M_{\mathcal{L}_{2,act}}$ generated from step responses of enhanced, nonlinear aircraft model in combination with baseline controller, L1 Adaptive Augmentations, $\Delta\dot{q}$ Compensation Law and L1 adaptive controller with Eigenstructure Assignment at $V_0 = 154.94\frac{m}{s}$ for large timescale

Controller	$M_{\mathcal{L}_2}$ $[-]$	$M_{\mathcal{L}_\infty}$ $[-]$	$M_{\mathcal{L}_{2,act}}$ $[-]$
Baseline	0.126	0.0010	0.517
DPI Augmentation	0.375	0.0022	0.528
Plant Augmentation	0.353	0.0020	0.527
L1 Standalone	0.277	0.0019	0.599
$\Delta\dot{q}$ Compensator	0.122	0.0008	0.521

A.7.2. Baseline Controller

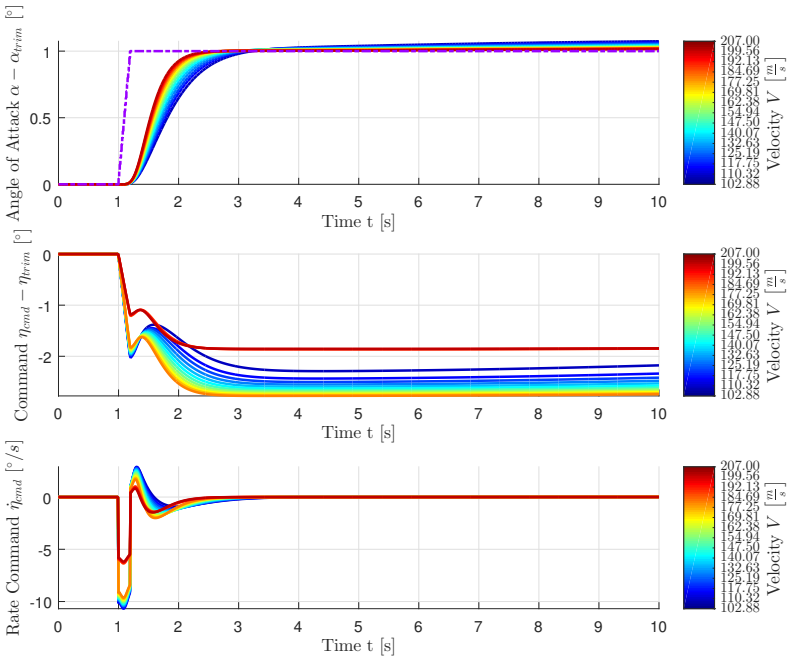

Figure A.73. – α_{cmd} step responses of basic, linear aircraft model and baseline controller at envelope points according to Table 2.2

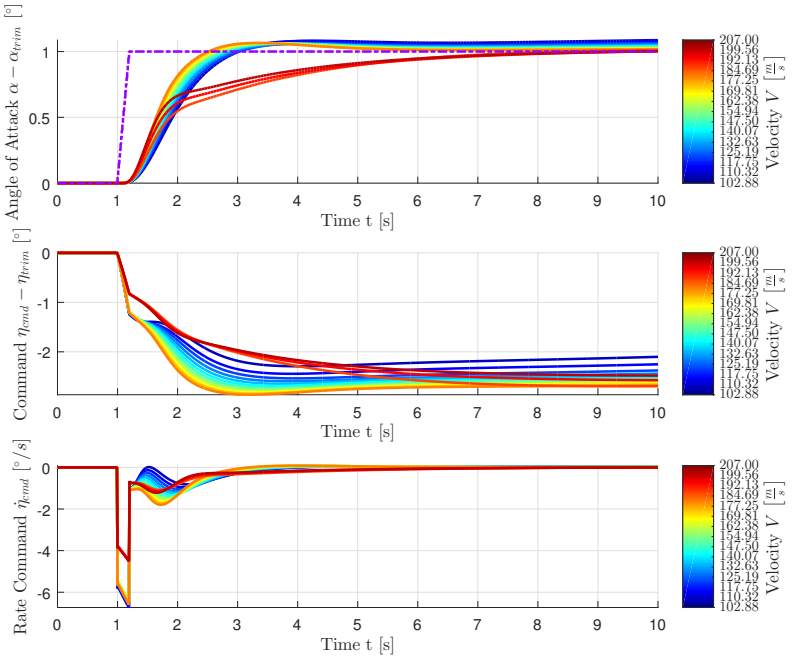

Figure A.74. – α_{cmd} step responses of enhanced, nonlinear aircraft model and baseline controller at envelope points according to Table 2.2

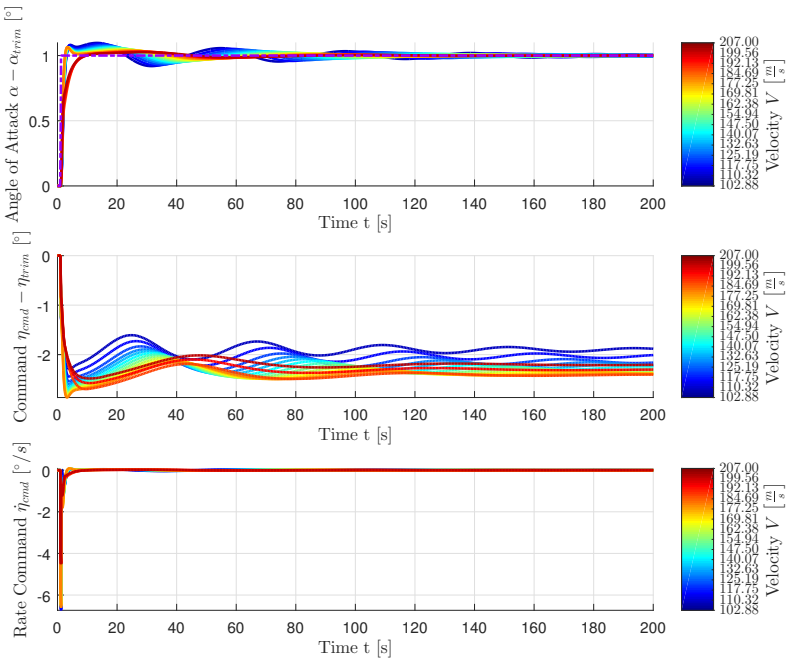

Figure A.75. – α_{cmd} step responses of enhanced, nonlinear aircraft model and baseline controller at envelope points according to Table 2.2 for large timescale

A.7.3. DPI Augmentation

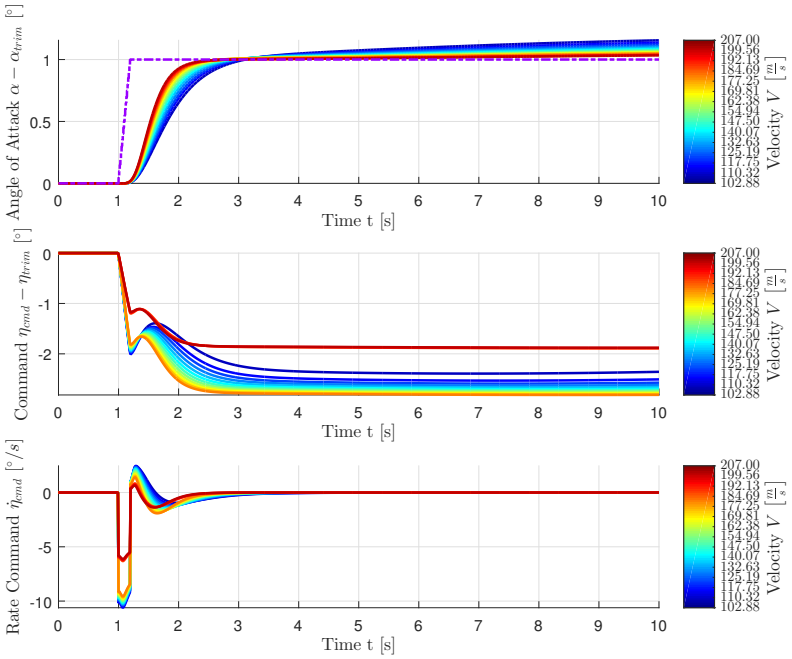

Figure A.76. – α_{cmd} step responses of basic, linear aircraft model and DPI Augmentation at envelope points according to Table 2.2

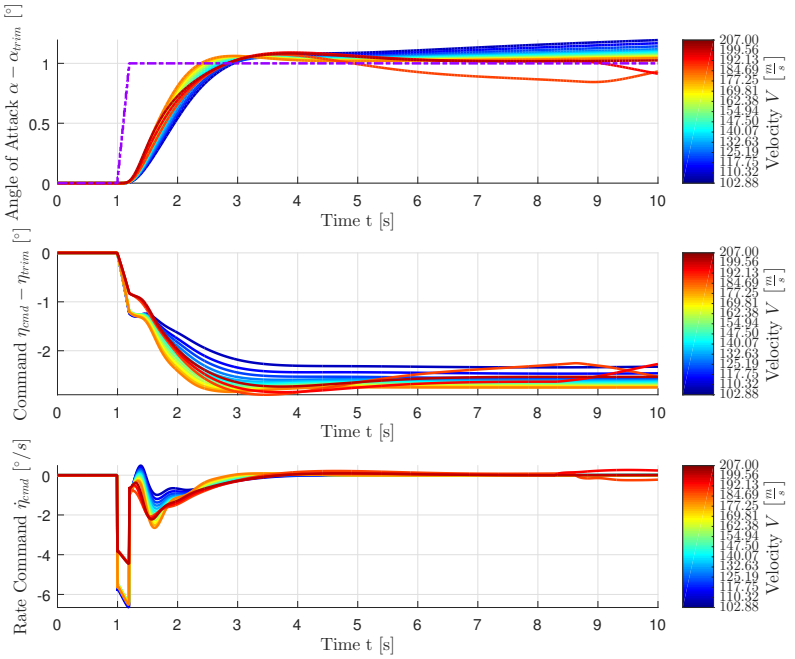

Figure A.77. – α_{cmd} step responses of enhanced, nonlinear aircraft model and DPI Augmentation at envelope points according to Table 2.2

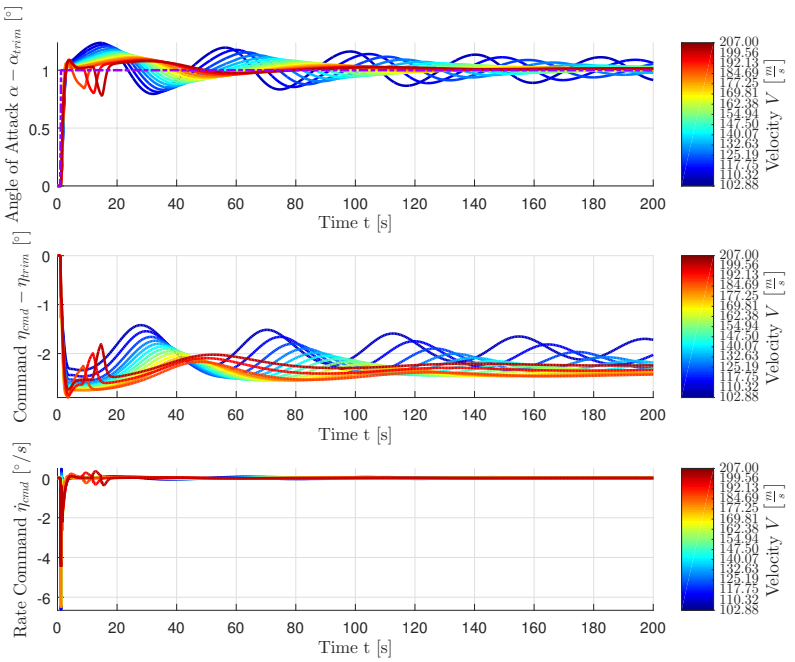

Figure A.78. – α_{cmd} step responses of enhanced, nonlinear aircraft model and DPI Augmentation at envelope points according to Table 2.2 for large timescale

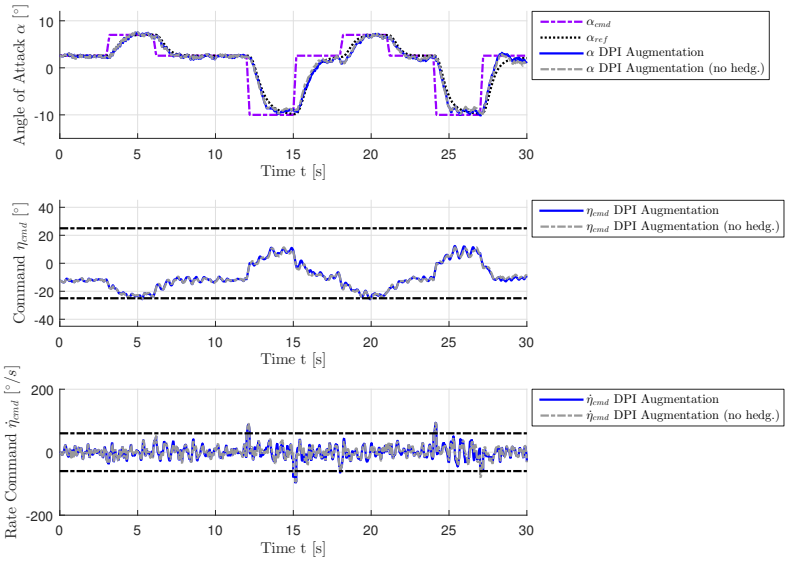

Figure A.79. – Angle of attack α, elevator command η_{cmd} and elevator command rate $\dot{\eta}_{cmd}$ for example maneuver performed by enhanced, nonlinear aircraft model with DPI Augmentation with and without hedging applied at $V_0 = 154.94\frac{m}{s}$ and $h_0 = 5000m$

A.7.4. Plant Augmentation

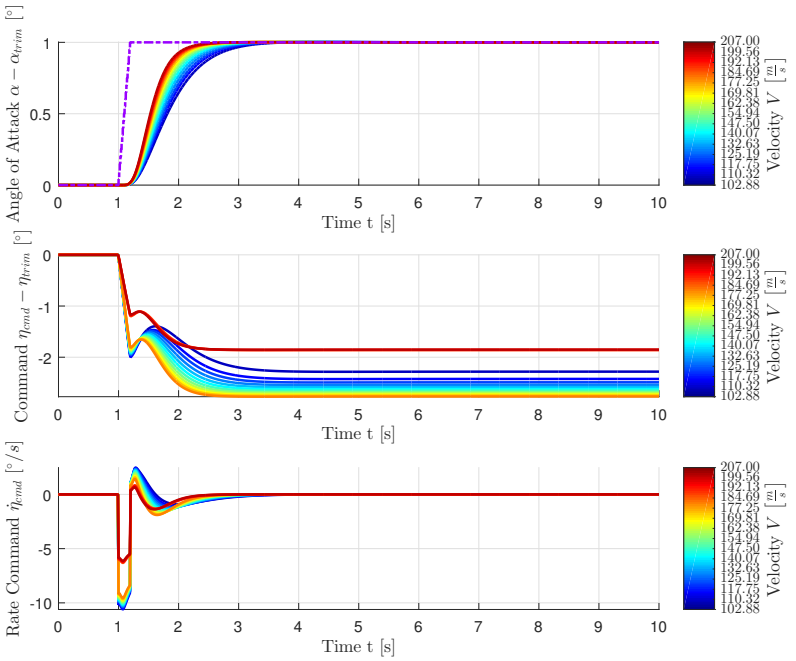

Figure A.80. – α_{cmd} step responses of basic, linear aircraft model containing only the short-period approximation and Plant Augmentation at envelope points according to Table 2.2

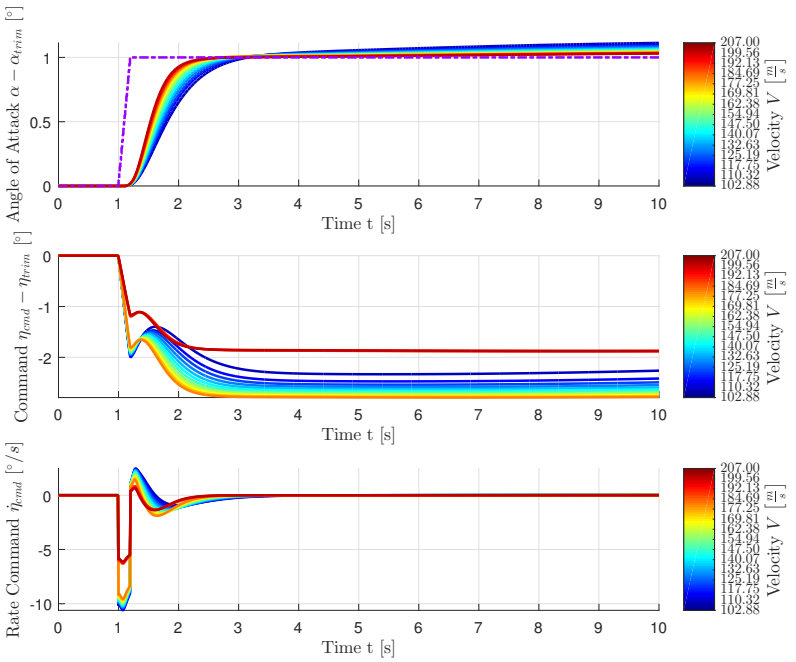

Figure A.81. – α_{cmd} step responses of basic, linear aircraft model and Plant Augmentation at envelope points according to Table 2.2

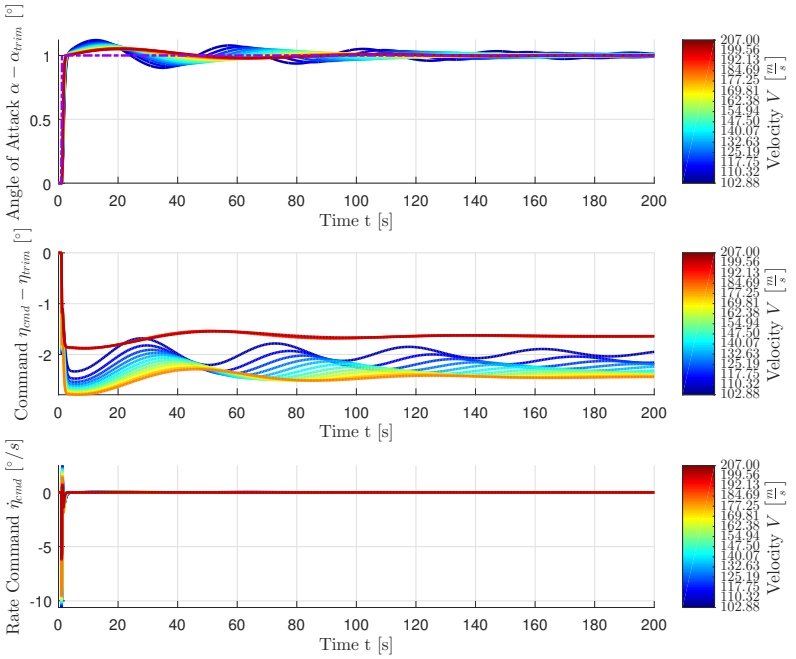

Figure A.82. – α_{cmd} step responses of basic, linear aircraft model and Plant Augmentation at envelope points according to Table 2.2 for large timescale

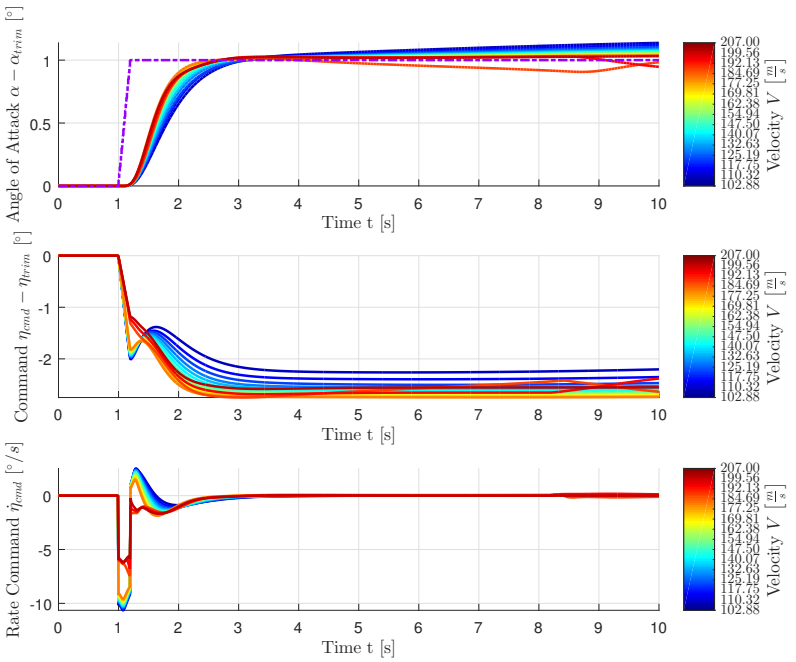

Figure A.83. – α_{cmd} step responses of basic, nonlinear aircraft model and Plant Augmentation at envelope points according to Table 2.2

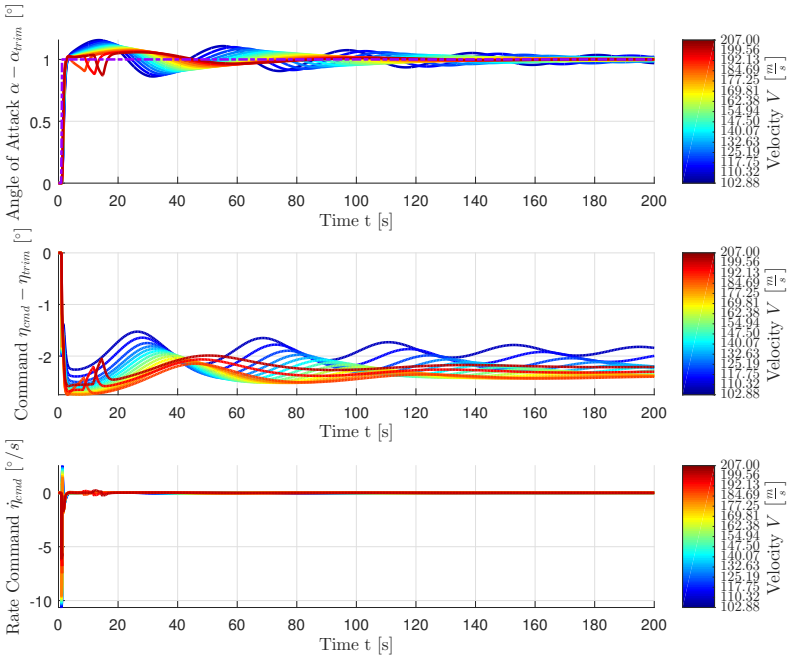

Figure A.84. – α_{cmd} step responses of basic, nonlinear aircraft model and Plant Augmentation at envelope points according to Table 2.2 for large timescale

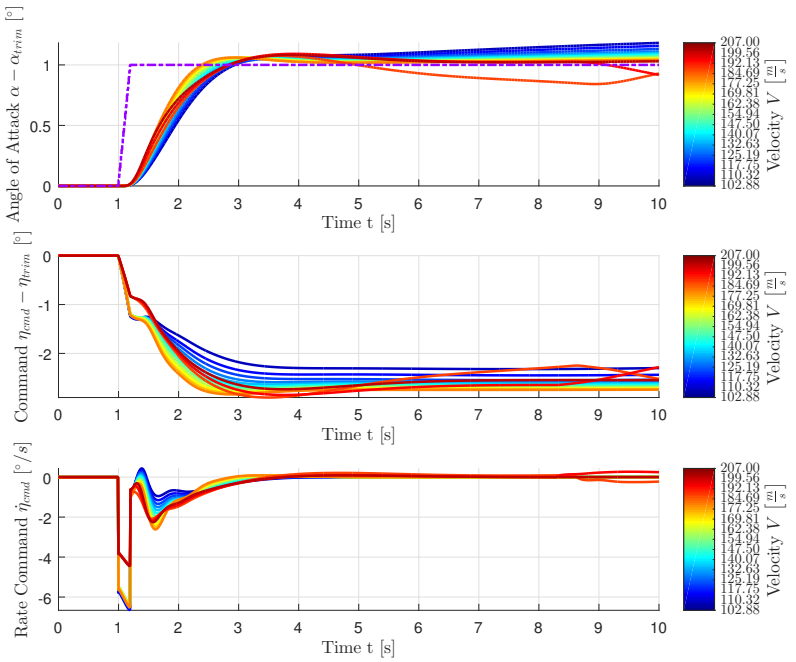

Figure A.85. – α_{cmd} step responses of enhanced, nonlinear aircraft model and Plant Augmentation at envelope points according to Table 2.2

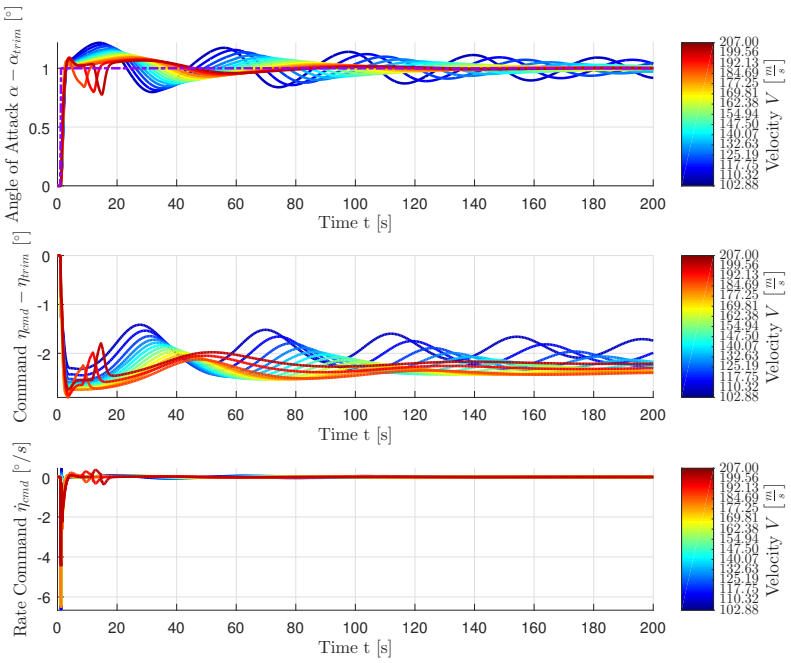

Figure A.86. – α_{cmd} step responses of enhanced, nonlinear aircraft model and Plant Augmentation at envelope points according to Table 2.2 for large timescale

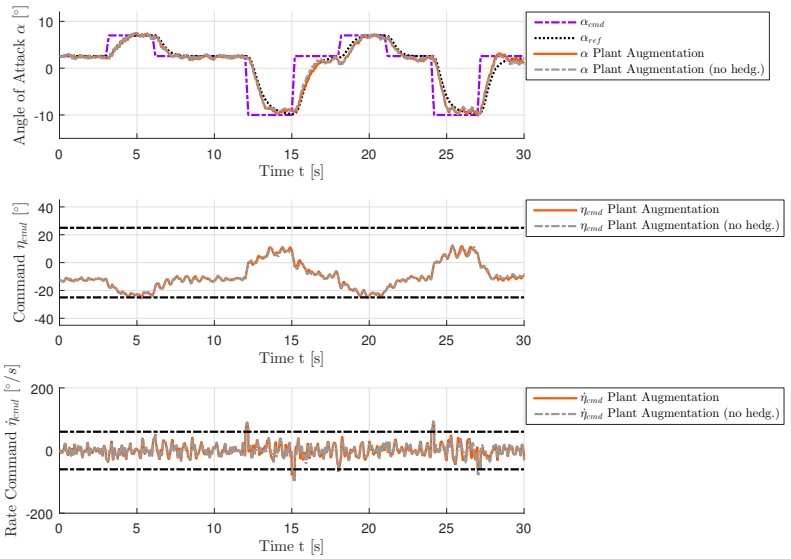

Figure A.87. – Angle of attack α, elevator command η_{cmd} and elevator command rate $\dot{\eta}_{cmd}$ for example maneuver performed by enhanced, nonlinear aircraft model with Plant Augmentation with and without hedging applied at $V_0 = 154.94\frac{m}{s}$ and $h_0 = 5000m$

A.7.5. $\Delta\dot{q}$ Compensation Law

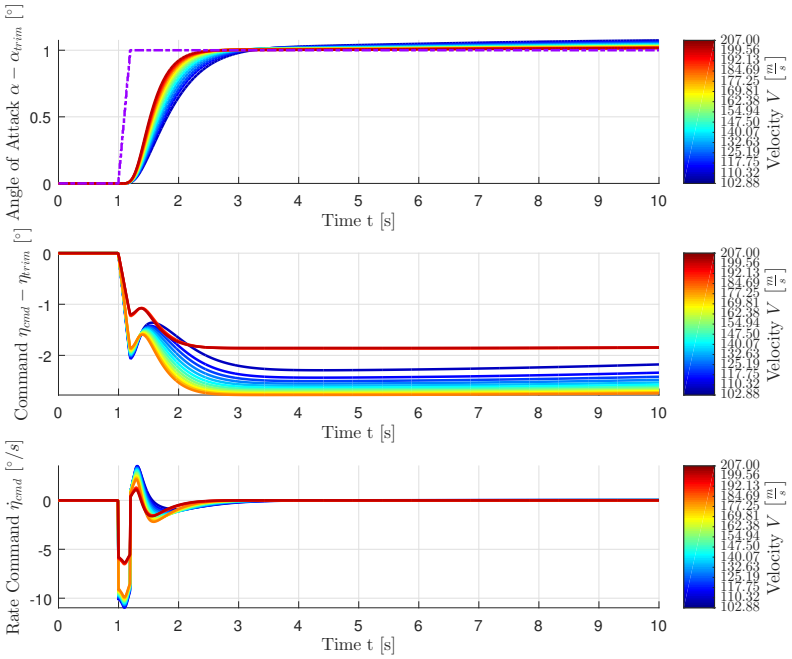

Figure A.88. – α_{cmd} step responses of basic, linear aircraft model and $\Delta\dot{q}$ Compensation Law at envelope points according to Table 2.2

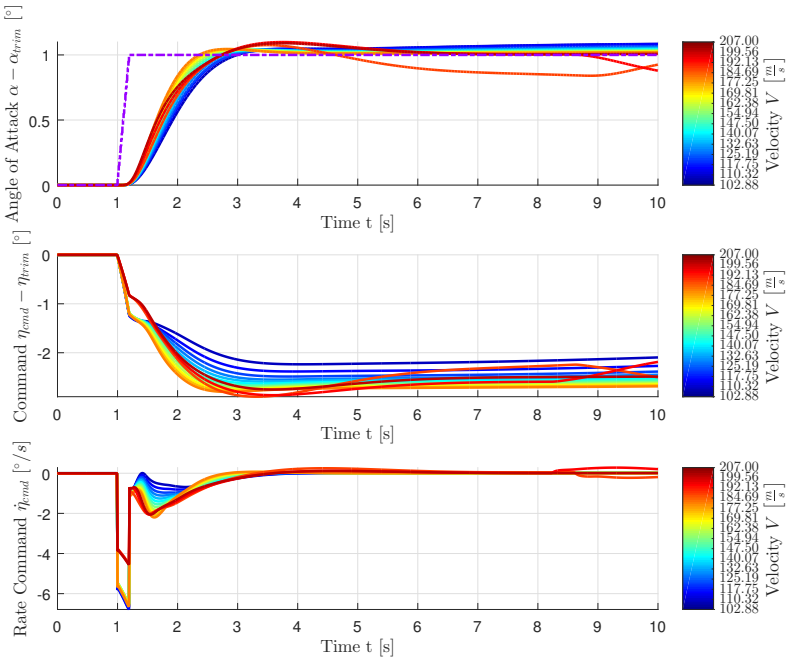

Figure A.89. – α_{cmd} step responses of enhanced, nonlinear aircraft model and $\Delta\dot{q}$ Compensation Law at envelope points according to Table 2.2

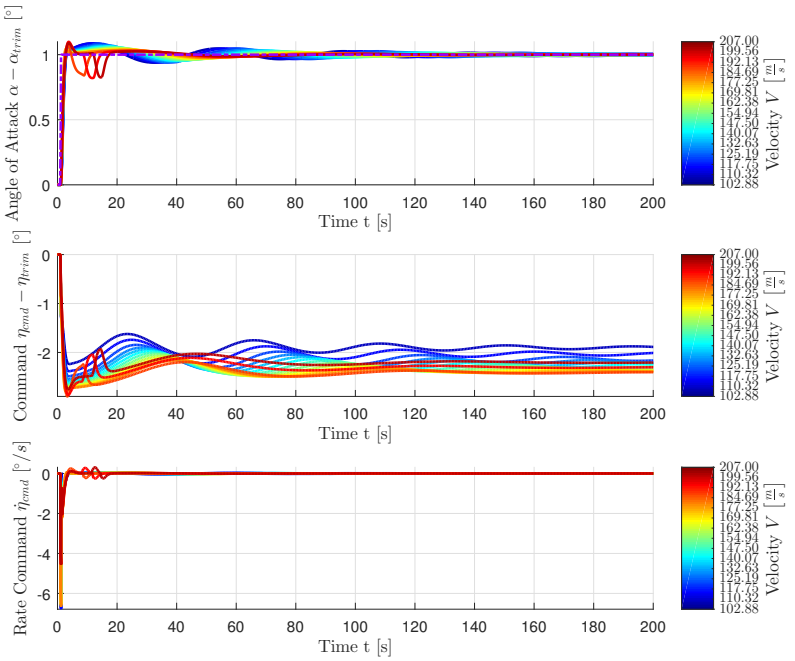

Figure A.90. – α_{cmd} step responses of enhanced, nonlinear aircraft model and $\Delta\dot{q}$ Compensation Law at envelope points according to Table 2.2 for large timescale

A.7.6. L1 adaptive controller with Eigenstructure Assignment

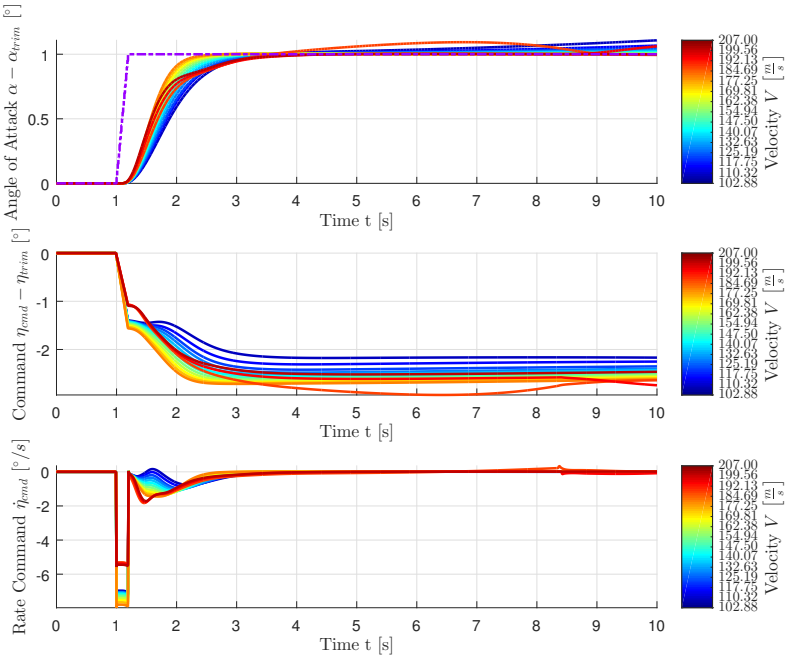

Figure A.91. – α_{cmd} step responses of enhanced, nonlinear aircraft model and L1 adaptive controller with Eigenstructure Assignment at envelope points according to Table 2.2

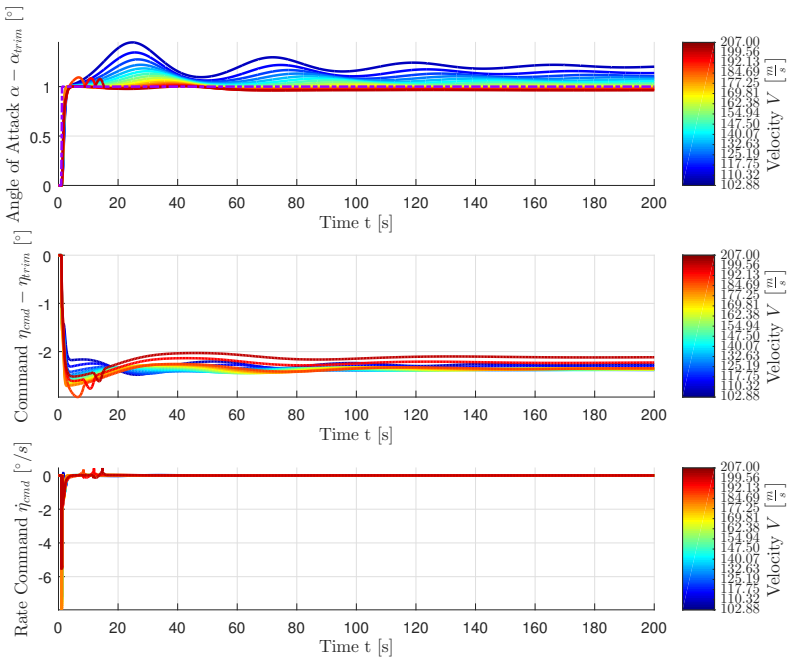

Figure A.92. – α_{cmd} step responses of enhanced, nonlinear aircraft model and L1 adaptive controller with Eigenstructure Assignment at envelope points according to Table 2.2 for large timescale